

LDEF- 69 Months in Space

Third Post - Retrieval Symposium

November 8-12, 1993
Williamsburg, Virginia

Sponsors:

LDEF Science Office
NASA Langley Research Center

American Institute of
Aeronautics and Astronautics

NASA Conference Publication 3275
Part 3

N95-27629
--THRU--
N95-27671
Unclass

H1/99 0047190

(NASA-CP-3275-pt-3) LDEF: 69
MONTHS IN SPACE. THIRD
POST-RETRIEVAL SYMPOSIUM, PART 3
(NASA. Langley Research Center)
515 p



National Aeronautics and
Space Administration



American Institute of
Aeronautics and Astronautics

LDEF— 69 Months in Space

NASA Conference Publication 3275

Part 3

Third Post - Retrieval Symposium

Edited by
Arlene S. Levine
NASA Langley Research Center
Hampton, Virginia

Proceedings of a symposium sponsored by
the National Aeronautics and Space
Administration, Washington, D.C., and the
American Institute of Aeronautics and
Astronautics, Washington, D.C., and held in
Williamsburg, Virginia
November 8-12, 1993



National Aeronautics and
Space Administration
Office of Management
Scientific and Technical
Information Program

1993

The use of trade names of manufacturers in this report does not constitute an official endorsement of such products or manufacturers, either expressed or implied, by the National Aeronautics and Space Administration.

This publication is available from the following sources:

NASA Center for AeroSpace Information
800 Elkridge Landing Road
Linthicum Heights, MD 21090-2934
(301) 621-0390

National Technical Information Service (NTIS)
5285 Port Royal Road
Springfield, VA 22161-2171
(703) 487-4650

FOREWORD

The third LDEF Post-Retrieval Symposium was held at the Williamsburg Lodge in Williamsburg, Virginia, November 8–12, 1993. Approximately 140 papers, posters, and demonstrations were presented. The Symposium represents the transition from focusing solely on a single spacecraft (LDEF) and its exposure to the low Earth orbit, to focusing on a broad approach to study the space environment and its effects. The LDEF program has provided a benchmark and means of comparison for other programs defining the low Earth orbit environment and its effects on spacecraft materials, systems, and structures. This Symposium included the preliminary results of European Retrievable Carrier (EURECA), the Evaluation of Oxygen Interactions with Materials III (EOIM-III) flight experiment, Salyut-7, and future flight experiments.

We have been challenged to design cheaper, better, and longer lasting spacecraft. NASA, other domestic and foreign agencies, and industry have contributed to the experiments and technologies now used to provide more accurate environmental definition and life prediction, lighter, long-lasting materials and structures, and more efficient systems. NASA's mission has always been to disseminate knowledge, and now we have been challenged to see that this knowledge is transformed into relevant technology.

The editor would like to thank all participants at the third Post-Retrieval Symposium for their contributions leading to the transfer of this technology. I would also like to thank all the contributing authors, as well as all those researchers who performed peer reviews of the enclosed papers. A special word of thanks goes to Bland Stein, Don Humes, and Steve Koontz, who reviewed more than their fair share of papers. I would like to thank the Symposium session chairs:

Darrel Tenney, *Opening Session*
Gale Harvey, *Induced Environment*
Alan Dover, *EURECA*
Thomas Parnell and James Adams, *Ionizing Radiation*
Friedrich Hörz, Dale Atkinson, J.A.M. McDonnell, Michael Zolensky, Donald Kessler,
Donald Humes, and Jean-Claude Mandeville, *Meteoroid and Debris*
Philip Young, Ann Whitaker, Gary Pippin, James Zwiener, Joan Funk, and Bruce
Banks, *Materials*
Steve Koontz and Wayne Stuckey, *EOIM-III*
James Mason, *Systems*
Ranty Liang and William Kinard, *Future Activities*

Many thanks to Susan Hurd (Mason and Hanger) for her patient, gracious, and invaluable editing and to Maureen Sgambelluri (Troy Systems) for her patience and skill in reformatting papers to meet our requirements.

NASA CP-3275 is the third LDEF Post-Retrieval Symposium. The first Symposium, NASA CP-3134, was held in 1991 in Kissimmee, Florida, and the second Symposium, NASA CP-3194, was held in San Diego, California, in 1992. You may request copies of either or both proceedings. For information please contact

Arlene S. Levine
Mail Stop 404
NASA Langley Research Center
Hampton, Virginia 23681-0001
phone: 804 864-3318/fax: 804 864-8094
e-mail: a.s.levine@larc.nasa.gov

CONTENTS

FOREWORD	iii
Author Index	xv

PART 1*

NATURAL AND INDUCED ENVIRONMENTS

LDEF Environment Modeling Updates	3
Tim Gordon, Ray Rantanen, Ann Whitaker	
Outgassing Products from Orbiter TPS Materials	13
Gale A. Harvey, Tom J. Lash, J. Richard Rawls	

EUROPEAN RETRIEVABLE CARRIER (EURECA)

EURECA 11 Months in Orbit: Initial Post Flight Investigation Results	23
Alan Dover, Roberto Aceti, Gerhard Drolshagen	
Dosimetric Results on EURECA	37
G. Reitz	
Preliminary Results of Radiation Measurements on EURECA	43
E.V. Benton, A.L. Frank	
Performance Characterizations of EURECA Retroreflectors with Fluoropolymer-Filled SiO_x Protective Coatings	51
Bruce A. Banks, Sharon K. Rutledge, Michael Cales	
Effect of the Space Environment on Materials Flown on the EURECA/TICCE-HVI Experiment	65
Carl R. Maag, William G. Tanner, Tim J. Stevenson, Mare Crisium, Janet Borg	
Material Inspection of EURECA: First Findings and Recommendations	71
Marc Van Eesbeek, Michael Froggatt, Georges Gourmelon	

IONIZING RADIATION

LDEF Contributions to Cosmic Ray and Radiation Environments Research . .	89
Thomas A. Parnell	
Trapped Iron Measured on LDEF	91
R. Beaujean, D. Jonathal, S. Barz, W. Enge	
Characteristics of Low Energy Ions in the Heavy Ions in Space (HIIS) Experiment	101
Thomas Kleis, Allan J. Tylka, Paul R. Boberg, James H. Adams, Jr., Lorraine P. Beahm	

*Part 1 is presented under separate cover.

Results from the Heavy Ions in Space (HIIS) Experiment on the Ionic Charge State of Solar Energetic Particles	113
Allan J. Tylka, Paul R. Boberg, James H. Adams, Jr., Lorraine P. Beahm, Thomas Kleis	
Early Results from the Ultra Heavy Cosmic Ray Experiment	129
D. O'Sullivan, A. Thompson, J. Bosch, R. Keegan, K.-P. Wenzel, F. Jansen, C. Domingo	
Absorbed Dose and LET Spectra Measurements on LDEF	135
E.V. Benton, I. Csige, A.L. Frank, E.R. Benton, L.A. Frigo, T.A. Parnell, J. Watts, A. Harmon	
Fission Foil Measurements of Neutron and Proton Fluences in the A0015 Experiment	149
A.L. Frank, E.V. Benton, T.W. Armstrong, B.L. Colborn	
Measurement of Trapped Proton Fluences in Main Stack of P0006 Experiment	159
N. Nefedov, I. Csige, E.V. Benton, R.P. Henke, E.R. Benton, L.A. Frigo	
Contribution of Proton-Induced Short Range Secondaries to the LET Spectra on LDEF	167
E.R. Benton, I. Csige, E.V. Benton, L.A. Frigo	
Charge, Energy and LET Spectra of High LET Primary and Secondary Particles in CR-39 Plastic Nuclear Tract Detectors of the P0006 Experiment	179
I. Csige, L.A. Frigo, E.V. Benton, K. Oda	
Predictions of LET Spectra Measured on LDEF	181
T.W. Armstrong, B.L. Colborn, E.V. Benton	
Doing Photons with Merlin II at Oroville	189
Alan R. Smith, Donna L. Hurley	
Status of LDEF Activation Measurements and Archive	199
B. Alan Harmon, Thomas A. Parnell, Christopher E. Laird	
Predictions of LDEF Radioactivity and Comparison with Measurements	203
T.W. Armstrong, B.L. Colborn, B.A. Harmon, C. E. Laird	
Status of LDEF Radiation Modeling	217
John W. Watts, T.W. Armstrong, B.L. Colborn	
¹⁰Be in Terrestrial Bauxite and Industrial Aluminum: An LDEF Fallout	227
J.C. Gregory, A. Albrecht, G. Herzog, J. Klein, R. Middleton, B.A. Harmon, T.A. Parnell	
Germination, Growth Rates, and Electron Microscope Analysis of Tomato Seeds Flown on the LDEF	231
Ernest C. Hammond, Jr., Kevin Bridgers, Cecelia Wright Brown	

SPACE ENVIRONMENTS
Meteoroid and Debris

Status of LDEF Contributions to Current Knowledge of Meteoroid and Manmade Debris Environments and Their Effects on Spacecraft in LEO . . .	255
William H. Kinard	
LDEF Meteoroid and Debris Special Investigation Group Investigations and Activities at the Johnson Space Center	257
Thomas H. See, Michael E. Zolensky, Ronald P. Bernhard, Jack L. Warren, Clyde A. Sapp, Claire B. Dardano	
Micrometeoroids and Debris on LDEF: Comparison With MIR Data	275
Jean-Claude Mandeville, Lucinda Berthoud	
Small Craters on the Meteoroid and Space Debris Impact Experiment	287
Donald H. Humes	
Long-Term Microparticle Impact Fluxes on LDEF Determined from Optical Survey of Interplanetary Dust Experiment (IDE) Sensors	323
C.G. Simon, J.P. Oliver, W.J. Cooke, K.I. Downey, P.C. Kassel	
Penetration Rates Over 30 Years in the Space Age	337
J.A.M. McDonnell, J.M. Baron	
LDEF Interplanetary Dust Experiment (IDE) Results	353
John P. Oliver, S.F. Singer, J.L. Weinberg, C.G. Simon, W.J. Cooke, P.C. Kassel, W.H. Kinard, J.D. Mulholland, J.J. Wortman	
The Orbital Characteristics of Debris Particle Rings as Derived from IDE Observations of Multiple Orbit Intersections with LDEF	361
William J. Cooke, John P. Oliver, Charles G. Simon	
Orbital Debris and Meteoroid Population as Estimated from LDEF Impact Data	373
Jingchang Zhang, Donald J. Kessler	
Hypervelocity Impact Survivability Experiments for Carbonaceous Impactors: Part II	385
T.E. Bunch, Julie M. Paque, Luann Becker, James F. Vedder, Jozef Erlichman	
Analytical Electron Microscopy of LDEF Impactor Residues	401
Ronald P. Bernhard, Ruth A. Barrett, Michael E. Zolensky	
Natural and Orbital Debris Particles on LDEF's Trailing and Forward-Facing Surfaces	415
Friedrich Hörz, Ronald P. Bernhard, Thomas H. See, Donald E. Brownlee	
Debris and Meteoroid Proportions Deduced from Impact Crater Residue Analysis	431
Lucinda Berthoud, Jean-Claude Mandeville, Christian Durin, Janet Borg	
Micro-Abrasion Package Capture Cell Experiment on the Trailing Edge of LDEF: Impactor Chemistry and Whipple Bumper Shield Efficiencies	445
Howard J. Fitzgerald, Hajime Yano	

Secondary Ion Mass Spectrometry (SIMS) Analysis of Hypervelocity Microparticle Impact Sites on LDEF Surfaces	459
C.G. Simon, A.J. Buonaquisti, D.A. Batchelor, J.L. Hunter, D.P. Griffis, V. Misra, D.R. Ricks, J.J. Wortman, D.E. Brownlee, S.R. Best, M.S. Crumpler, B. Arad, S. Eliezer, S.E. Moshe, S. Maman, I. Gilath	
SIMS Chemical and Isotopic Analysis of Impact Features from LDEF Experiments AO187-1 and AO187-2	461
Frank J. Stadermann, Sachiko Amari, John Foote, Pat Swan, Robert M. Walker, Ernst Zinner	
Image and Compositional Characteristics of the "Big Guy" LDEF Impact Crater	475
T.E. Bunch, Julie M. Paque, Michael Zolensky	
The Effect of Impact Angle on Craters Formed by Hypervelocity Particles	483
David C. Hill, M. Frank Rose, Steve R. Best, Michael S. Crumpler, Gary D. Crawford, Ralph H-C. Zee, Michael J. Bozack	
Experimental Investigation of the Relationship Between Impact Crater Morphology and Impacting Particle Velocity and Direction	499
N.G. Mackay, S.F. Green, D.J. Gardner, J.A.M. McDonnell	
Determining Orbital Particle Parameters of Impacts into Germanium Using Morphology Analysis and Calibration Data from Hypervelocity Impact Experiments in the Laboratory	509
Klaus G.Paul	
Cratering and Penetration Experiments in Teflon Targets at Velocities from 1 To 7 KM/S	521
Friedrich Hörz, Mark J. Cintala, Ronald P. Bernhard, Thomas H. See	
Dimensional Scaling for Impact Cratering and Perforation	523
Alan J. Watts, Dale Atkinson	

PART 2*

MATERIALS

Summary and Review of Materials Special Investigation Group Evaluations of Hardware from the Long Duration Exposure Facility	539
Ann F. Whitaker, Joan Funk, Gary Pippin and Harry Dursch	
Recent Results from Long Duration Exposure Facility Materials Testing	555
H.G. Pippin, H.W. Dursch	
LDEF Polymeric Materials: A Summary of Langley Characterization	567
Philip R. Young, Wayne S. Slemph, Karen S. Whitley, Carol R. Kalil, Emilie J. Siochi, James Y. Shen, A. C. Chang	

*Part 2 is presented under separate cover.

Surface Characterization of LDEF Carbon Fiber/Polymer Matrix Composites	601
Holly L. Grammer, James P. Wightman, Philip R. Young, Wayne S. Slemp	
Space Environmental Effects on Polymer Matrix Composites as a Function of Sample Location on LDEF	613
R.C. Tennyson, G.R. Cool, D.G. Zimcik	
Nonlinear Viscoelastic Characterization of Polymer Materials Using a Dynamic-Mechanical Methodology	631
Thomas W. Strganac, Debbie Flowers Payne, Bruce A. Biskup, Alan Letton	
The Effect of Simulated Low Earth Orbit Radiation on Polyimides (UV Degradation Study)	645
John S. Forsythe, Graeme A. George, David J.T. Hill, James H. O'Donnell, Peter J. Pomery, Firas A. Rasoul	
The Surface Properties of Fluorinated Polyimides Exposed to VUV and Atomic Oxygen	657
John S. Forsythe, Graeme A. George, David J.T. Hill, James H. O'Donnell, Peter J. Pomery, Firas A. Rasoul	
Collection and Review of Metals Data Obtained from LDEF Experiment Specimens and Support Hardware	667
Roger Bourassa, Gary Pippin	
Measurements of the Optical Properties of Thin Films of Silver and Silver Oxide	689
Palmer N. Peters, Robert C. Sisk, Yolanda Brown, John C. Gregory, Pallob K. Nag, Ligia Christl	
Changes in Chemical and Optical Properties of Thin Film Metal Mirrors on LDEF	703
Palmer N. Peters James M. Zwiener, John C. Gregory, Ganesh N. Raikar, Ligia C. Christl, Donald R. Wilkes	
Further Investigations of Experiment AO034 Atomic Oxygen Stimulated Outgassing	727
Roger C. Linton, Miria M. Finckenor, Rachel R. Kamenetzky	
Atomic Oxygen Interactions with Protected Organic Materials on the Long Duration Exposure Facility (LDEF)	737
Bruce A. Banks, Kim K. de Groh, Justine L. Bucholz, Michael R. Cales	
Trend Analysis of In-Situ Spectral Reflectance Data from the Thermal Control Surfaces Experiment (TCSE)	755
D.R. Wilkes, P.S. LeMaster, R.J. Mell, E.R. Miller, J.M. Zwiener	
Whisker/Cone Growth on the Thermal Control Surfaces Experiment #S0069	771
James M. Zwiener, James E. Coston, Jr., Donald R. Wilkes, Edgar R. Miller, Richard J. Mell	

Durability of Reflector Materials in the Space Environment	791
Ann F. Whitaker, Miria M. Finckenor, David Edwards, Rachel R. Kamenetzky, Roger C. Linton	
Four Space Application Materials Coatings on the Long-Duration Exposure Facility (LDEF)	803
John J. Scialdone and Carroll Clatterbuck	
Organic Matrix Composite Protective Coatings for Space Applications	825
Harry Dursch and Pete George	
Structure and Properties of Polymeric Composite Materials During 1501 Days Outer Space Exposure on the "Salyut-7" Orbital Station	843
Oleg V. Startsev, Eugene F. Nikishin	
Overview of the LDEF MSIG Databasing Activities	859
Joan G. Funk	

PART 3

EVALUATION OF OXYGEN INTERACTIONS WITH MATERIALS III (EOIM-III)

An Overview of the Evaluation of Oxygen Interactions with Materials III Experiment: Space Shuttle Mission 46, July - August 1992 . . .	869
Steven L. Koontz, Lubert J. Leger, James T. Visentine, Don E. Hunton, Jon B. Cross, Charles L. Hakes	
Evaluation of Oxygen Interactions with Materials III — Mission and Induced Environments	903
Steven L. Koontz, Lubert J. Leger, Steven L. Rickman, Charles L. Hakes, David T. Bui, Donald Hunton, Jon B. Cross,	
Spacecraft Materials Studies on the Aerospace Corporation Tray on EOIM-III	917
Wayne K. Stuckey, Carol S. Hemminger, Gary L. Steckel, Malina M. Hills, Michael R. Hilton	
Exposure of LDEF Materials to Atomic Oxygen: Results of EOIM-III	931
C.H. Jagers, M.J. Meshishnek	
Atomic Oxygen Dosimetry Measurements Made on STS-46 by CONCAP-II . .	957
J.C. Gregory, G.P. Miller, P.J. Pettigrew, G.N. Raikar, J.B. Cross, E. Lan, C.L. Renschler, W.T. Sutherland	
Inflight Resistance Measurements on High-T_c Superconducting Thin Films Exposed to Orbital Atomic Oxygen on CONCAP-II (STS-46)	971
J.C. Gregory, G.N. Raikar, J.A. Bijvoet, P.D. Nerren, W.T. Sutherland, A. Mogro-Campero, L.G. Turner, Hoi Kwok, I.D. Raistrick, J.B. Cross, D.W. Cooke, C. Mombourquette, R.J. Houlton, F.H. Garzon, R. Herschitz	
LEO Degradation of Graphite and Carbon-Based Composites Aboard Space Shuttle Flight STS-46	989
Blaine R. Spady, R.A. Synowicki, Jeffrey S. Hale, M.J. De Vries, John A. Woollam, Arthur W. Moore, Max Lake	

Orbital Atomic Oxygen Effects on Materials: An Overview of MSFC Experiments on the STS-46 EOIM-3	999
Roger C. Linton, Jason A. Vaughn, Miria M. Finckenor, Rachel R. Kamenetzky, Robert F. DeHaye, Ann F. Whitaker	
Effects of Atomic Oxygen on Polymeric Materials Flown on EOIM-3	1011
Rachel R. Kamenetzky, Roger C. Linton, Miria M. Finckenor, Jason A. Vaughn	
Thermal Control Materials on EOIM-3	1025
Miria M. Finckenor, Roger C. Linton, Rachel R. Kamenetzky, Jason A. Vaughn	
Solid Film Lubricants and Thermal Control Coatings Flown Aboard the EOIM-3 MDA Sub-Experiment	1037
Taylor J. Murphy, Kaia E. David, Hank W. Babel	
Evaluation of Space Environmental Effects on Metals and Optical Thin Films on EOIM-3	1053
Jason A. Vaughn, Roger C. Linton, Miria M. Finckenor, Rachel R. Kamenetzky	
Analysis of Selected Specimens from the STS-46 Energetic Oxygen Interaction with Materials-III Experiment	1067
Johnny L. Golden, Roger J. Bourassa, Harry W. Dursch, H. Gary Pippin	
Molecular Beam Scattering from ¹³C-Enriched Kapton and Correlation with the EOIM-3 Carousel Experiment	1095
Timothy K. Minton, Teresa A. Moore	
BMDO Materials Testing in the EOIM-3 Experiment	1115
Shirley Y. Chung, David E. Brinza, Timothy K. Minton, Ranty H. Liang	
STS-46 Plasma Composition Measurements Using the EOIM-3 Mass Spectrometer	1129
Donald E. Hunton, Edmund Trzcinski, Roger Gosselin, Steve Koontz, Lubert Leger, Jim Visentine	
Point Defect Formation in Optical Materials Exposed to the Space Environment	1131
J. L. Allen, N. Seifert, Y. Yao, R.G. Albridge, A.V. Barnes, N.H. Tolk, A.M. Strauss, R.C. Linton, R.R. Kamenetzky, J.A. Vaughn, M.M. Finckenor	
SYSTEMS	
LDEF Systems Special Investigation Group Overview	1149
Jim Mason, Harry Dursch	
System Results from FRECOPA	1153
Christian Durin, Lucinda Berthoud, Jean-Claude Mandeville	
Space Environmental Effects on Solar Cells: LDEF and Other Flight Tests . .	1167
Peter Gruenbaum, Harry Dursch	
A Final Look at LDEF Electro-Optic Systems Components	1179
M.D. Blue	

Effects of the LDEF Orbital Environment on the Reflectance of Optical Mirror Materials	1189
Howard Herzig, Charles M. Fleetwood, Jr.	
Effects of Low Earth Orbit on the Optical Performance of Multilayer Enhanced High Reflectance Mirrors	1205
Terence Donovan, Linda Johnson, Karl Klemm, Rick Scheri, Jean Bennett, Jon Erickson, Filippo di Brozolo	
Effects of Long Term Space Environment Exposure on Optical Substrates and Coatings (S0050-2)	1227
John Vallimont, E. Steven Brandt, Keith Havey, Arthur Mustico	
Long Duration Exposure Facility (LDEF) Space Optics Handbook	1229
William T. Kemp, Edward Taylor, Robert Champetier, Alan Watts, Dale Atkinson	
Space Environmental Effects Observed on the Hubble Space Telescope	1231
Joel E. Edelman, James B. Mason	
Hardware Cleanliness Methodology and Certification	1237
Gale A. Harvey, Thomas J. Lash, J. Richard Rawls	

FUTURE ACTIVITIES

From LDEF to a National Space Environment and Effects (SEE) Program: A Natural Progression	1247
David E. Bowles, Robert L. Calloway, Joan G. Funk, William H. Kinard, Arlene S. Levine	
Long Duration Exposure Facility (LDEF) Archive System	1249
Brenda K. Wilson	
The Long Duration Exposure Facility (LDEF) Annotated Bibliography	1263
Arlene S. Levine	
The Long Duration Exposure Facility (LDEF) Photographic Survey Special Publication	1267
Robert L. O'Neal, Arlene S. Levine, Carol C. Kiser	

SPACE STATION

LDEF's Contribution to the Selection of Thermal Control Coatings for the Space Station	1273
Henry W. Babel	
Space Station Program Status and Research Capabilities	1285
Alan C. Holt	
Space Station as a Long Duration Exposure Facility	1289
Adrienne Folley, Jim Scheib	
A Materials Exposure Facility	1301
Wayne S. Slempp, Don E. Avery	

OTHER SPACECRAFT

An LDEF Follow-on Spacecraft Concept 1307
Vernon Keller, Larry Breazeale, Don Perkinson, William H. Kinard

**Long Duration Exposure Facility Post-Flight Data as It Influences
the Tropical Rainfall Measuring Mission** 1309
Sharon A. Straka

EXPERIMENTS

Element Material Exposure Experiment by EFFU 1321
Yoshihiro Hashimoto, Masaaki Ichikawa, Mitsuru Takei, Yoshihiro Torii, Kazuo Ota

Orbiting Meteoroid and Debris Counting Experiment 1331
William H. Kinard, Dwayne Armstrong, Sharon K. Crockett, James L. Jones, Jr.,
Philip C. Kassel, Jr., J.J. Wortman

**The Strategic Technologies for Automation and Robotics (STEAR)
Program Protection of Materials in the Space Environment Subprogram** 1341
L R. Schmidt, J. Francoeur, A. Agüero, M.R. Wertheimer, J.E. Klemberg-Sapieha,
L. Martinu, J. W. Blezius, M. Olivier, A. Singh

**The Orbital Debris Detector Consortium: Suppliers of Instruments for
In Situ Measurements of Small Particles in the Space Environment** 1361
C.G. Simon, R. Münzenmeyer, W.G. Tanner, Jr., O.M. Uy, R.A. Skrivanek, Jr.,
A.J. Tuzzolino, C. Maag, J.J. Wortman

A New Technique for Ground Simulation of Hypervelocity Debris 1379
R. Roybal, J. Shively, C. Stein, C. Miglionico, R. Robertson

AUTHOR INDEX



84-5648

xv

PRECEDING PAGE BLANK NOT FILMED

AUTHOR INDEX

Part 1 — pages 1—536
Part 2 — pages 537—866
Part 3 — pages 867—1388

A

Aceti, Roberto 23
Adams, James H., Jr. 101, 113
Agüero, A. 1341
Albrecht, A. 227
Albridge, R.G. 1131
Allen, J.L. 1131
Amari, Sachiko 461
Arad, B 459
Armstrong, Dwayne 1331
Armstrong, T.W. 149, 181, 203, 217
Atkinson, Dale 523, 1229
Avery, Don E. 1301

B

Babel, Henry W. 1037, 1273
Banks, Bruce A. 51, 737
Barnes, A.V. 1131
Baron, J.M. 337
Barrett, Ruth A. 401
Barz, S. 91
Batchelor, D.A. 459
Beahm, Lorraine P. 101, 113
Beaujean, R. 91
Becker, Luann 385
Bennett, Jean 1205
Benton, E.R. 135, 159, 167
Benton, E.V. 43, 135, 149, 159, 167, 179, 181
Bernhard, Ronald P. 257, 401, 415, 521
Berthoud, Lucinda 275, 431, 1153
Best, Steve R. 459, 483
Bijvoet, J.A. 971
Biskup, Bruce 631
Blezius, J.W. 1341
Blue, M.D. 1179
Boberg, Paul R. 101, 113
Borg, Janet 65, 431
Bosch, J. 129
Bourassa, Roger 667, 1067
Bowles, David E. 1247
Bozack, Michael J. 483
Brandt, E. Steven 1227
Breazeale, Larry 1307

Bridgers, Kevin 231
Brinza, David E. 1115
Brown, Cecelia Wright 231
Brown, Yolanda 689
Brownlee, Donald E. 415, 459
Bucholz, Justine L. 737
Bui, David T. 903
Bunch, T.E. 385, 475
Buonaquisti, A.J. 459

C

Cales, Michael 51, 737
Calloway, Robert L. 1247
Champetier, Robert 1229
Chang, A.C. 567
Christl, Ligia 689, 703
Chung, Shirley Y. 1115
Cintala, Mark J. 521
Clatterbuck, Carroll 803
Colborn, B.L. 149, 181, 203, 217
Cooke, D.W. 971
Cooke, William J. 323, 353, 361
Cool, G.R. 613
Coston, James, E., Jr. 771
Crawford, Gary D. 483
Crisium, Mare 65
Crockett, Sharon K. 1331
Cross, Jon B. 869, 903, 957, 971
Crumpler, Michael S. 459, 483
Csige, I. 135, 159, 167, 179

D

Dardano, Claire B. 257
David, Kaia E. 1037
de Groh, Kim K. 737
DeHaye, Robert F. 999
DeVries, M.J. 989
di Brozolo, Filippo 1205
Domingo, C. 129
Donovan, Terence 1205
Dover, Alan 23
Downey, K.I. 323
Drolshagen, Gerhard 23
Durin, Christian 431, 1153
Dursch, H.W. 539, 555, 825, 1067, 1149, 1167

E

Edelman, Joel E. 1231
Edwards David 791
Eliezer, S. 459
Enge, W. 91

Erickson, Jon 1205
Erlichman, Jozef 385

F

Finckenor, Miria M. 727, 791, 999, 1011, 1025, 1053, 1131
Fitzgerald, Howard J. 445
Fleetwood, Charles M., Jr. 1189
Folley, Adrienne 1289
Foote, John 461
Forsythe, John S. 645, 657
Francoeur, J. 1341
Frank, A.L. 43, 135, 149
Frigo, L.A. 135, 159, 167, 179
Froggatt, Michael 71
Funk, Joan G. 539, 859, 1247

G

Gardner, D.J. 499
Garzon, F.H. 971
George, Graeme A. 645, 657
George, Pete 825
Gilath, I. 459
Golden, Johnny L. 1067
Gordon, Tim 3
Gosselin, Roger 1129
Gourmelon, Georges 71
Grammer, Holly L. 601
Green, S.F. 499
Gregory, J.C. 227, 689, 703, 957, 971
Griffis, D.P. 459
Gruenbaum, Peter 1167

H

Hakes, Charles L. 869, 903
Hale, Jeffrey S. 989
Hammond, Ernest C., Jr. 231
Harmon, B. Alan 135, 199, 203, 227
Harvey, Gale A. 13, 1237
Hashimoto, Yoshihiro 1321
Havey, Keith 1227
Hemminger, Carol S. 917
Henke, R.P. 159
Herschitz, R. 971
Herzig, Howard 227, 1189
Herzog, G. 227
Hill, David C. 483
Hill, David J.T. 645, 657
Hills, Malina M. 917
Hilton, Michael R. 917
Holt, Alan C. 1285

Hörz, Friedrich 415, 521
Houlton, R.J. 971
Humes, Donald H. 287
Hunter, J.L. 459
Hunton, Don E. 869, 903, 1129
Hurley, Donna L. 189

I

Ichikawa, Masaaki 1321

J

Jaggers, C.H. 931
Jansen, F. 129
Johnson, Linda 1205
Jonathal, D. 91
Jones, James L. Jr. 1331

K

Kalil, Carol R. 567
Kamenetzky, Rachel R. 727, 791, 999, 1011, 1025, 1053, 1131
Kassel, P.C. 323, 353, 1331
Keegan, R. 129
Keller, Vernon 1307
Kemp, William T. 1229
Kessler, Donald J. 373
Kinard, W.H. 255, 353, 1247, 1307, 1331
Kiser, Carol 1267
Klein, J. 227
Kleis, Thomas 101, 113
Klemberg-Sapieha, J.E. 1341
Klemm, Karl 1205
Koontz, Steven L. 869, 903, 1129
Kwok, Hoi 971

L

Laird, Christopher E. 199, 203
Lake, Max 989
Lan, E. 957
Lash, Tom J. 13, 1237
Leger, Lubert J. 869, 903, 1129
LeMaster, P.S. 755
Letton, Alan 631
Levine, Arlene S. 1247, 1263, 1267
Liang, Ranty H. 1115
Linton, Roger.C. 727, 791, 999, 1011, 1025, 1053, 1131

M

Maag, Carl R. 65, 1361
Mackay, N.G. 499

Maman, S. 459
Mandeville, Jean-Claude 275, 431, 1153
Martinu, L. 1341
Mason, James B. 1149, 1231
McDonnell, J.A.M. 337, 499
Mell, Richard J. 755, 771
Meshishnek, M.J. 931
Middleton, R. 227
Miglionico, C. 1379
Miller, Edgar R. 755, 771
Miller, G.P. 957
Minton, Timothy K. 1095, 1115
Misra, V. 459
Mombourquette, C. 971
Mogro-Campero, A. 971
Moore, Arthur W. 989
Moore, Teresa A. 1095
Moshe, S.E. 459
Mulholland, J.D. 353
Murphy, Taylor J. 1037
Münzenmeyer, R. 1361
Mustico, Arthur 1227

N

Nag, Pallob, K. 689
Nefedov, N. 159
Nerren, P.D. 971
Nikishin, Eugene F. 843

O

Oda, K. 179
O'Donnell, James H. 645, 657
O'Neal, Robert L. 1267
O'Sullivan, D. 129
Oliver, John P. 323, 353, 361
Olivier, M. 1341
Ota, Kazuo 1321

P

Paque, Julie M. 385, 475
Parnell, Thomas A. 89, 135, 199, 227
Paul, Klaus G. 509
Payne, Debbie F. 631
Perkinson, Don 1307
Peters, Palmer N. 689, 703
Pettigrew, P. J. 957
Pippin, H. Gary 539, 555, 667, 1067
Pomery, Peter J. 645, 657

R

Raikar, G.N. 703, 957, 971
Raistrick, I.D. 971
Rantanen, Ray 3
Rasoul, Firas A. 645, 657
Rawls, J. Richard 13, 1237
Reitz, G. 37
Renschler, C.L. 957
Rickman, Steven L. 903
Ricks, D.R. 459
Robertson, R. 1379
Rose, M. Frank 483
Roybal, R. 1379
Rutledge, Sharon K. 51

S

Sapp, Clyde A. 257
Scheib, Jim 1289
Scheri, Rick 1205
Schmidt, L.R. 1341
Scialdone, John J. 803
See, Thomas H. 257, 415, 521
Seifert, N. 1131
Shen, James Y. 567
Shively, J. 1379
Simon, Charles G. 323, 353, 361, 459, 1361
Singer, S.F. 353
Singh, A. 1341
Siochi, Emilie J. 567
Sisk, Robert C. 689
Skrivanek, R.A. 1361
Slemp, Wayne S. 567, 601, 1301
Smith, Alan R. 189
Spady, Blaine R. 989
Stadermann, Frank J. 461
Startsev, Oleg V. 843
Steckel, Gary L. 917
Stein, C. 1379
Stevenson, Tim J. 65
Straka, Sharon A. 1309
Strauss, A.M. 1131
Strganac, Thomas W. 631
Stuckey, Wayne K. 917
Sutherland, W.T. 957, 971
Swan, Pat 461
Synowicki, R.A. 989

T

Takei, Mitsuru 1321
Tanner, W.G. 65, 1361

Taylor, Edward 1229
Tennyson, R.C. 613
Thompson, A. 129
Tolk, N.H. 1131
Torii, Yoshihiro 1321
Trzcinski, Edmund 1129
Turner, L.G. 971
Tylka, Allan J. 101, 113
Tuzzolino, A.J. 1361

U

Uy, O.M. 1361

V

Vallimont, John 1227
Van Eesbeek, Marc 71
Vaughn, Jason A. 999, 1011, 1025, 1053, 1131
Vedder, James F. 385
Visentine, James T. 869, 1129

W

Walker, Robert M. 461
Warren, Jack L. 257
Watts, Alan J. 523, 1229
Watts, John W. 135, 217
Weinberg, J.L. 353
Wenzel, K.-P. 129
Wertheimer, M.R. 1341
Whitaker, Ann F. 3, 539, 791, 999
Whitley, Karen S. 567
Wightman, James P. 601
Wilkes, Donald R. 703, 755, 771
Wilson, Brenda K. 1249
Woollam, John A. 989
Wortman, J.J. 353, 459, 1331, 1361

Y

Yao, Y. 1131
Yano, Hajime 445
Young, Philip R. 567, 601

Z

Zee, Ralph H-C. 483
Zhang, Jingchang 373
Zimcik, D.G. 613
Zinner, Ernst 461
Zolensky, Michael E. 257, 401, 475
Zwiener, James M. 703, 755, 771

PART 3

**EVALUATION OF OXYGEN INTERACTIONS
WITH MATERIALS III (EOIM-III)**



KSC-392C-4225.17

PART 3

**An Overview of the Evaluation of Oxygen Interactions with Materials III
Experiment: Space Shuttle Mission 46, July-August 1992.**

**Steven L. Koontz, Lubert J. Leger, James T. Visentine; NASA Johnson Space Center,
Houston, TX, 77058, (713)-483-8916**

**Don E. Hunton, USAF Phillips Laboratory,
Hanscomb Air Force Base, MA, 01731, (617)-377-4057**

**Jon B. Cross, Los Alamos National Laboratory,
CS2, J-565, Los Alamos, NM., 87545, (505)-667-0511**

**Charles L. Hakes, Lockheed Engineering & Sciences Company,
Houston, TX, 77058, (713)-333-7804**

ABSTRACT

The Evaluation of Oxygen Interactions with Materials III (EOIM-III) flight experiment was developed to obtain benchmark atomic oxygen reactivity data and was conducted during Space Transportation System Mission 46 (STS-46), July 31 to August 7, 1992. In this paper, we present an overview of EOIM-III and the results of the Lyndon B. Johnson Space Center (JSC) materials reactivity and mass spectrometer/carousel experiments. Mass spectrometer calibration methods are discussed briefly, as a prelude to a detailed discussion of the mass spectrometric results produced during STS-46. Mass spectrometric measurements of ambient O-atom flux and fluence are in good agreement with the values calculated using the MSIS-86 model of the thermosphere as well as estimates based on the extent of O-atom reaction with Kapton polyimide. Mass spectrometric measurements of gaseous products formed by O-atom reaction with C¹³ labeled Kapton revealed CO, CO₂, H₂O, NO and NO₂. Finally, by operating the mass spectrometer so as to detect naturally occurring ionospheric species, we characterized the ambient ionosphere at various times during EOIM-III and detected the gaseous reaction products formed when ambient ions interacted with the C¹³ Kapton carousel sector. By direct comparison of the results of on-orbit O-atom exposures with those conducted in ground-based laboratory systems, which provide known O-atom fluences and translational energies, we have demonstrated the strong translational energy dependence of O-atom reactions with a variety of polymers. A "line-of-centers" reactive scattering model was shown to provide a reasonably accurate description of the translational energy dependence of polymer reactions with O atoms at high atom kinetic energies while a Beckerle-Ceyer model provided an accurate description of O-atom reactivity over a three order-of-magnitude range in translational energy and a four order-of-magnitude range in reaction efficiency. Postflight studies of the polymer samples by x-ray photoelectron spectroscopy and infrared spectroscopy demonstrate that O-atom attack is confined to the near-surface region of the sample, i.e. within 50 to 100 Angstroms of the surface.

INTRODUCTION

Oxygen atoms are the most abundant neutral constituents of the Earth's ionosphere at altitudes ranging from 200 to 700 km^{refs 1-3} and have been shown to be one of the more important environmental factors involved in the degradation of several important classes of spacecraft materials^{ref 4,5}. The primary objective of the EOIM-III experiment was to produce benchmark atomic oxygen reactivity data for a wide range of materials^{ref 6}. Secondary objectives included: 1) mass spectrometric characterization of the gaseous reaction and scattering products formed when the ambient atmosphere interacts with various materials, 2) characterizing the induced environment produced by interaction of the ambient atmosphere with the EOIM-III experiment and the Space Shuttle cargo bay, and 3) characterizing the chemical reaction dynamics of the reaction between O-atoms and polymers. In this paper, we present an overview of the EOIM-III experiment as performed during STS-46 during early August 1993. EOIM-III was a team effort with coinvestigators from all major NASA field centers, the United States Air Force, the European, Japanese and Canadian space agencies and the Ballistic Missile Defense Office.

Our approach to achieving EOIM-III objectives was based on comparing measurements of materials samples after exposure to known O-atom fluences in three well-characterized environments: 1) The low-Earth-Orbit (LEO) environment, 2) the high-velocity neutral-atom beam (HVAB) system at the Los Alamos National Laboratory (LANL), and 3) a flowing discharge or downstream plasma system at JSC. Detailed characterization of the exposure environments was accomplished by determining such factors as O-atom flux and fluence as well as O-atom kinetic energy distribution function, sample temperature, ultraviolet/vacuum ultraviolet (UV/VUV) radiation dose and surface contamination.

The methods and results of the EOIM-III environment characterization effort are described in detail in the accompanying paper^{ref 1}. Briefly, the atomic oxygen fluence was determined by calculation using the MSIS-86 model of the thermosphere combined with as flown trajectory and vehicle attitude data^{ref 7} as well as daily average values (24-hours average) of the solar activity indices. A second estimate of the O-atom fluence was obtained from direct measurements of the O-atom flux using a mass spectrometer^{ref 8} provided by the USAF Phillips Laboratory^{ref 9}. Kapton polymer film standards were also used to obtain an additional estimate of O-atom fluence by simply measuring mass loss and surface recession after the mission and using the widely-accepted value of $3.0 \times 10^{-24} \text{cm}^3/\text{atom}$ ^{ref 10} as the Kapton reaction efficiency.

The thermal history of the payload was recorded with an array of thermocouple sensors^{ref 1}, and the solar UV/VUV dose was estimated using daily average solar flux data from the Upper Atmosphere Research Satellite^{ref 1} combined with a detailed analysis of the Space Shuttle attitude history. Payload contamination was evaluated by post flight X-ray photoelectron spectroscopy of selected samples and monitored during

the mission with an array of Temperature Controlled Quartz Crystal Microbalances (TQCMs)^{ref 1}.

EOIM-III Flight Experiment: Description and Performance

The EOIM-III flight hardware is briefly described below. Photographs of the EOIM-III payload, after installation in the Space Shuttle Atlantis and removal of protective covers, are shown in figure 1. A line drawing of EOIM-III identifying the various sub-assemblies and experiments is shown in figure 2 and can be used to identify the various features shown in figure 1. The overall cargo bay layout of STS-46 is shown in figure 3. EOIM-III was mounted on a Multipurpose Payload and Experiment Support Structure ("MPRESS" structure), on the starboard side of the Space Shuttle Atlantis, near the aft bulkhead, and at the level of the orbiter sill longeron, i.e., at the level of the cargo bay door hinge line. The carousel and mass spectrometer are visible in the middle of the EOIM-III pallet, with the passive sample carriers on the outboard side and the heated trays and environmental monitor package inboard, toward the center of the Space Shuttle cargo bay. In figure 1 the mass spectrometer is pointed along the cargo bay normal (-Z in orbiter coordinates) and the motorized lid is closed. The mass spectrometer ion source was of the semi-open variety as defined by Hayden, Neir, et al.,^{ref 11} and was capable of receiving neutral gas from a 180-degree field of view. Only the vertical stabilizer, several cargo bay components including the aft bulkhead, and the orbital maneuvering system pods are line-of-sight to the mass spectrometer ion source (although only occupying a small, peripheral fraction of the field of view) and, by implication, the rest of the payload^{ref 1}. A cross sectional drawing of the mass spectrometer is shown in figure 4.

The as-flown altitude and attitude timelines for STS-46 are shown in figures 5 and 6. The attitude timeline shows the angle between the cargo bay normal (-Z in orbiter coordinates) and the orbiter velocity vector. The angle shown in figure 6 runs from 0 degrees, corresponding to the -ZVV or ram orientation, to 180 degrees, corresponding to ZVV or antiram (heat shield into the velocity vector). The oscillations between 0 and 180 degrees visible during earlier parts of the mission correspond to inertial hold attitudes or roll maneuvers. The orbital inclination was 28.5 degrees and the beta angle (the angle between the Sun pointing vector and the plane of the Space Shuttle orbit) varied between 17.5 and 24.3 degrees. EOIM-III was initiated at Mission Elapsed Time (MET) 5 days, 22 hours, 30 minutes (5:22:30 = 142.5 hrs.), shortly after reducing orbital altitude to 123-124 nmi. A waste-water dump was conducted between MET 5:20:37 and MET 5:22:30 with the orbiter attitude adjusted to minimize the chance of particles from the waste stream recontacting the orbiter. The orbiter was placed in the -ZVV attitude for EOIM-III at MET = 142.5 hrs.

In general, the EOIM-III flight hardware performed well during the mission. Primary electric power was applied to the payload at MET 0:3:22 and telemetry was then enabled. Before EOIM-III was initiated, the mass spectrometer was operated only as

needed in order to obtain natural and induced environment data for selected vehicle attitudes and operations. The mass spectrometer was pointed in the -Z direction, as shown in figures 1 and 2, throughout the pre EOIM-III portion of the mission and operated so as to alternately collect mass spectra of neutral gases (the electron impact ionization filaments and a repeller grid to exclude ambient ions were both powered on) in neutral mode, or ambient ions (filaments and repeller grid off) in ion mode during alternating 1 minute intervals. In addition, payload temperature data were recorded throughout the mission using thermocouples placed as described in the accompanying mission and induced environments paper^{ref 1}.

After initiation of the EOIM-III experiment, the EOIM-III payload executed a series of timed operating cycles in which mass spectrometric measurements of the ambient atmosphere and ionospheric constituents alternated with mass spectrometric measurements of reaction and scattering products formed when ambient species interacted with various carousel sectors each of which was coated with one of the following materials: 1) C¹³ labeled Kapton polyimide prepared by the Jet Propulsion Laboratory; 2) anodized aluminum; 3) Chemglaze Z-306 black polyurethane based space paint; 4) FEP Teflon, 5) Parylene-C coated stainless steel. The carousel sectors were designed so that the geometric field of view of the mass spectrometer ion source contained only carousel sector surfaces. A movable carousel sector cover blocked direct incidence of atmospheric species during a portion of each carousel sector observation period so that the induced environment from both direct ram and scattered ram could be measured.

In addition to carousel/mass spectrometer operations, heated tray temperatures were established at 60, 120 and 200 degrees Centigrade (prior to placing the orbiter in the ram -ZVV attitude for EOIM-III) and timed sample tray cover movements for the variable exposure trays (VET) and solar ultraviolet (SUV) trays were initiated. The VET cover failed to operate correctly, and all sample specimens received the same nominal O-atom fluence. The SUV and heated tray experiments operated properly. Two payload-switching problems were encountered which have not been explained to date. First, the mass spectrometer did not respond to a power-off command leading to 13.6 hours of unplanned operation early in the mission. Second, the preprogrammed mass spectrometer/carousel cycle did not initiate properly on the first try so that the carousel observations were delayed by about 6 hours. Despite the switching problem, neutral mode mass spectra were obtained for all carousel segments and ion mode spectra were obtained for the Z-306 and the C¹³ labeled sectors.

The reactivities of EOIM-III polymer samples were determined by two complementary methods: 1) weight loss and 2) profilometry. In most cases, two disk samples of each polymer were placed in each sample holder opening. The top sample was directly exposed to the space environment and interacted with atomic oxygen, UV/VUV radiation and other space environment factors while the underlying sample was exposed only to thermal vacuum. Both samples were subjected to high-vacuum baking and were weighed before and after the mission. Both samples were cleaned by rinsing

briefly with Q Cleantm Solvent, (Thermo Analytical Inc., Monrovia Calif.) an ultra-high-purity cleaning solvent, and were then air dried in a laminar flow hood prior to installation in the EOIM-III sample holders. Polymer film samples were tested for short-term compatibility with Q Cleantm before cleaning. The top sample was also covered with a high-transparency metal grid which acted as an etch mask. In this way, the well-known highly-directional nature of high-velocity O atom reactions with polymeric materials was exploited to advantage by producing a regular pattern of ridges on O-atom reactive polymers. The regular pattern of ridges produced with the etch mask makes profilometry more accurate in the presence of the natural surface irregularities always present on polymer film samples. All polymer film specimens were used as-received from the vendors except for the vacuum baking and cleaning process described above. However, the two liquid crystal polymers, Xydar and LCP-4100, were also polished because the surface roughness of the as-received material was too great to permit accurate profilometry even with use of the metal screen etch masks.

EOIM-III Laboratory Support Instrumentation: Apparatus and Methods

Laboratory measurements and calibrations were a key component of the EOIM-III experiment. Effects resulting from sample exposure to laboratory O-atom systems were compared to those resulting from on-orbit O-atom exposure to gain insight into reaction mechanism and to verify various approaches to ground-based testing. In addition, the EOIM-III mass spectrometer was calibrated in a ground-based, high-velocity O-atom beam system. Finally, most materials reactivity determinations were made by post exposure laboratory measurements of exposed specimens for comparison with controls. Weight loss, surface recession by profilometry, scanning electron microscope images, x-ray photoelectron spectroscopy, thermomechanical analysis, and transmission infrared spectroscopy were the most important sample characterization techniques used for the JSC samples. Two laboratory O-atom systems were used to provide comparison data: 1) the flowing discharge and 2) the HVAB. In general, polymer specimens were prepared as for flight on EOIM-III (see proceeding section). Polymers exposed to the HVAB beam were, however, bonded to aluminum heat sinks using a silicone-free epoxy cement so as to assure known sample surface temperatures despite heating by beam-source thermal radiation.

The methods and apparatus used to determine the O-atom reactivities of polymers in the flowing discharge (remote plasma) apparatus have been described^{ref 12,13}. Briefly, a working gas (10% O₂/90% Ar), at total pressures on the order of 2 Torr, was passed through a 2.45 GHz Evenson discharge cell and flowed downstream from the discharge before coming into contact with the polymer samples so that the gas had cooled to room temperature but still contained oxygen atoms in the O³P electronic ground state. The O-atom concentration was determined by chemiluminescent titration using NO₂^{ref 14,15} and the atom flux on sample surfaces is determined using well-known methods for modeling flowing reaction-diffusion systems^{ref 16}. Both the samples and the reactive gas could be heated to determine Arrhenius activation energies. Unlike the

atom beam and space flight experiment experiment, both of which deliver O-atoms to the polymer surface in the form of a directed beam, the flowing discharge delivers O-atoms to the polymer surface by diffusion from an isotropic gas in thermal equilibrium with the polymer sample. This does not necessarily imply that the comparison of flowing discharge and directed beam O-atom processes is invalid in an "apples and oranges" sense simply because the O-atom reaction with the sample surface still depends on an O-atom surface collision. In addition, the flux of molecular oxygen was much higher in the flowing discharge than in the LEO or HVAB environments described above, though large variations in O₂ partial pressure revealed no effects on the reactivity of Kapton, Mylar or polyethylene in the flowing discharge system^{ref 13,16}. Polymer reactivity in this system was determined by periodically venting the system and weighing the polymer specimens on a six-place laboratory balance. The observed mass loss was always significantly greater than any water adsorption or desorption effects.

The HVAB has been described^{ref 17,18}. Briefly, a laser-sustained gaseous discharge (50% O₂/Ar or O₂/Ne at pressures on the order of 2000 Torr) undergoes supersonic nozzle expansion to form a seeded beam of oxygen atoms (O³P electronic ground state) and inert gas atoms. The average kinetic energy can be varied between 0.4 and 3 eV. Beam velocity distribution functions were determined directly using well-known time of flight (TOF), methods^{ref 17,18} with phase-sensitive (modulated atom beam) mass spectrometric detection to reject vacuum system background. The mass spectrometer used for beam characterization was not the EOIM-III mass spectrometer but, rather, a component of the HVAB system.

The O-atom flux in the beam was determined using both relative abundance from the mass spectrometric measurements of beam composition using TOF methods and the pressure rise in an accommodation chamber (measured with a spinning rotor type pressure gauge and residual gas analyzer) as was previously reported^{ref 9}. Given the inert gas flux in the beam and the relative abundances of the various high-velocity beam species from phase-sensitive mass spectrometry, the fluxes of all other beam species, including atomic oxygen, were calculated using known values of electron impact cross sections, the mass spectrometric transmission function, and the change in mass spectrometer sensitivity with atom or molecule velocity^{ref 18}. The well characterized O-atom beam used for calibration and characterization of the EOIM-III flight mass spectrometer was also used to support polymer reaction efficiency measurements in this system.

The typical polymer film temperature during exposure to the O-atom beam was 45 degrees centigrade, and the samples could be heated to determine Arrhenius activation energies. Gaseous reaction products were detected using phase-sensitive (modulated beam) mass spectrometric detection techniques^{ref 18} to reject vacuum system background.

Results and Discussion of Results: Mass Spectrometer/Carousel

The mass spectrometer carousel system produced about 48,000 neutral and ion mass spectra during STS-46. Typical ram mass spectra taken: 1) during the post Eureka deployment ram orientation period (altitude = 430 km) and 2) at the beginning of the EOIM-III (altitude = 230 km) are shown in figures 7a and 7b, respectively. For comparison purposes, a typical mass spectrum produced during the calibration process at LANL is shown in figure 8. Atomic oxygen is visible at mass 16 in figures 7 and 8, with water at mass 18 and the OH^+ ion at mass 17. Molecular oxygen is visible at mass 32 in both figures and is formed by recombination of atomic oxygen in the mass spectrometer ion source (neither the HVAB beam nor the LEO environment contains significant amounts of O_2). The mass 40 and 20 peaks in figure 8 are from Ar^+ and Ar^{++} respectively. Figures 7 and 8 show a number of features not apparent in figure 18. The intense peak at mass 28 amu is produced by molecular nitrogen, a natural component of the atmosphere at Shuttle operating altitudes, and the associated atomic nitrogen fragment is visible at mass 14. The mass peak at 44, with an associated doubly charged peak at 22, as well as an atomic carbon fragment peak at mass 12, is attributed to CO_2 . The CO peak (mass 28) is obscured by the N_2 peak at mass 28. H_2O and CO_2 are not components of the natural environment at shuttle operating altitudes but can be produced by both active (O-atom reactions with cargo bay materials) and passive outgassing of space shuttle cargo bay components and the mass spectrometer itself. The low intensity mass peaks at 23 and 39 amu correspond to sodium and potassium, also not components of the natural environment, and have been reported in mass spectra produced by satellite borne instruments^{ref 31}.

The high-background current visible in the calibration spectrum (figure 8) is the result of scattered UV/VUV radiation from the HVAB source which was coaxial with the ion flight path of the mass spectrometer. The same high background current would be visible in the EOIM-III mass spectra if the instrument had been directly facing the Sun, but the combination of orbital inclination, beta angle (the angle between the Sun vector and the orbital plane), and vehicle attitude precluded that event during STS-46 (the 180° field of view applies to the ion source only, not the complete path from ion source to secondary electron multiplier). During EOIM-III and the various HVAB calibration experiments, the mass spectrometric sensitivity decreased as a function of O-atom fluence. However, the O-atom fluence dependence of the mass spectrometer was different in the on-orbit and high velocity atom beam environments^{ref 1}.

Only a 30 percent loss of signal was noted in the photocurrent background at LANL while a factor of 6 decrease in ion current was noted under constant O-atom flux conditions. The effect of O-atom fluence on mass spectrometer sensitivity is believed to be due to the formation of gold oxide on the surfaces of the gold-plated ion source optics in the EOIM-III mass spectrometer. This effect was previously reported to occur during mass spectrometric sampling of ions from flowing discharges with gold sampling orifices^{ref 19}. Formation of a dielectric layer on the ion optical elements

degrades the sampling efficiency of the ion source. Some degradation of secondary electron multiplier performance was observed via changes in the amplitude of the photocurrent background during high fluence calibration experiments at LANL; the effect is small compared to the observed mass spectral sensitivity loss. The formation of gold oxide (Au_2O_3) from gold and molecular oxygen is not observed because the process is endothermic at 19.3 kcal/mole. In contrast, the formation of gold oxide from gold and atomic oxygen is exothermic at -159 kcal/mole.

Finally, it is interesting to note that different O_2/O ratios were obtained on orbit and in the laboratory ($\text{O}_2/\text{O} = 2.8$ on orbit; $\text{O}_2/\text{O} = 1.5$ at LANL). Since O_2 constituted less than 3 percent of the high-velocity gas entering the mass spectrometer in both environments, the very different O_2/O ratios observed suggest that O-atom recombination and transport processes were following different kinetic laws in the two environments.

The immediate conclusion obtained from the comparison of mass spectrometric performance on orbit and in the laboratory is that simple direct application of the LANL calibration results to the on-orbit data will not give the best accuracy. O-atom fluence estimates based on mass spectrometric data range from 2.2×10^{20} to 4.7×10^{20} atoms per square centimeter depending on the approach we used in applying the calibration results to the on-orbit data. As of this writing, the mass spectrometric fluence estimate is $2.3 \pm 0.7 \times 10^{20}$ O atoms/cm². This fluence estimate was calculated as follows. First, the calibration factor at zero O-atom fluence is taken as 2.3×10^{23} (atoms/cm²)/amp, as determined in the HVAB facility at LANL. The corrected mass 16-peak areas (corrected by subtraction of 26 percent of the mass 32-peak area, 0.15 percent of the mass 18-peak area) are multiplied by the sensitivity decay function to correct for O-atom fluence dependent instrument sensitivity loss. The sensitivity decay function was obtained by fitting an exponential decay function to the on-orbit mass 16-peak area data (i.e. except for diurnal variations, the O-atom flux was assumed to be approximately constant). Finally, the corrected mass 16 peak areas were multiplied by the zero fluence calibration factor to obtain the O-atom flux. The flux is calculated at regular time intervals and summed to obtain the mass spectrometer O-atom fluence measurement for those time periods when the mass spectrometer was on and producing O-atom flux measurements. Division of the mass spectrometric fluence calculated above by the duty cycle, i.e. the fractional time on and measuring O-atom flux, gives the final value for the mass spectrometric O-atom fluence.

Typical mass spectra of the induced neutral environment in the C^{13} labeled Kapton carousel sector are shown in figures 9 (sector open to direct ram flux) and 10 (sector cover on blocking direct ram flux). Comparison with the typical ram mass spectra (figure 7) shows that scattered ambient species dominate the induced environment. Gaseous reaction products are a significant part of the spectra, however, and C^{13}O_2 and C^{13}O are visible in figures 9 and 10. Gaseous reaction products formed during exposure of an identical C^{13} Kapton sample to the HVAB at LANL is compared with

EOIM-III measurements in figure 11 demonstrating that the same gaseous reaction products are produced in both environments. The higher levels of NO at mass 30 in flight is probably formed by environmental interaction processes not directly related to O-atom reactions with polymers. Mechanisms previously proposed to explain the visible spacecraft glow phenomena may explain the high NO signal observed^{ref 30}.

Moving the cover over the carousel sector produced little effect except for a net reduction in spectral intensity (figures 9&10). The fact that the sector cover had little effect is attributed to the scattering of ambient ram species from the EOIM-III pallet, near the opening to the carousel sector, as well as scattering of cargo bay induced environment gases from aft bulkhead surfaces. With the cover in position over the carousel sector, incomplete momentum accommodation (on surface collision) can result in relatively high kinetic energy (i.e., high reactivity) O atoms colliding with the carousel sample surfaces after only two reflections, one from the EOIM-III pallet and one from the sector cover surface which faces the sample compartment.

The EOIM-III mass spectrometer measured ions in the natural and induced environment when the electron impact ionizer and the repeller grid were turned off as described above. A typical ambient ion mass spectrum taken with the mass spectrometer ion source in a ram orientation during EOIM-III operations at a 230 km altitude is shown in figure 12. Mass spectra of the induced ionic environment, formed by interaction of naturally occurring ionospheric ions with the C¹³ Kapton carousel sector, are shown in figures 13 (sector cover off) and 14 (sector cover on). The difference between the ambient ram mass spectra and the induced environments spectra is more notable in this case than in the neutral case of figures 9 and 10. Isotope-labeled reaction products are visible in the mass spectra of the Kapton carousel sector and may result either from direct reaction of O⁺ ions with the carousel sector surfaces or gas phase charge exchange of O⁺ ions with the gaseous reaction produced by neutral O-atom attack on the polymer. It is also interesting to note that in contrast with the induced neutral environment mass spectra of the same carousel sector, mass spectra of the induced ionic or plasma environments showed a dramatic decrease in intensity when the carousel sector cover moved into position showing that ionospheric plasma ions are efficiently neutralized during collisions with payload surfaces.

Results and Discussion: O-Atom Reactions with Polymeric Materials.

Polymer reaction efficiencies (cm³ of material removed per incident O atom) determined following exposure on orbit in the EOIM-III passive trays, are shown in table 1, where EOIM-III measurements are compared with those made following previous flight experiments. The reaction efficiencies reported in table 1 were determined by weight loss only; the repeatability of the measurement is indicated as the difference between the largest and smallest measurement, if more than one sample was exposed on orbit. Comparison of the EOIM-III reaction efficiency column in table 1

with those of previous missions demonstrates that the polymer reaction efficiency data base has been both enlarged and verified.

Table 1. Polymer Reaction Efficiencies

POLYMER	Re (EOIM-III) x 10 ²⁴	Re (STS-8) x 10 ²⁴	Re (STS-41) x 10 ²⁴	Re LDEF x 10 ²⁴
KAPTON (LeRC R.R.)	3.1	3.0	3.3	3.0
EYMYD-F (ETHYL CORP.)	2.7			
CR-39 POLYCARBONATE	6.1	6.0		
PEEK (ICI)	3.4		4.3	
XYDAR (AMOCO)	2.9			
LCP-4100 (DuPont)	3.2			
MYLAR A (DuPont)	3.8	3.9		
POLYETHYLENE (PE)	4.4	3.7		
HDPE (PHILLIPS, EMH6606)	3.7	3.7	3.5	
POLYMETHYLPENTENE (PMP, MITSUI)	5.3			
POLYPROPYLENE	5.5		4.4	
TEDLAR (DuPont)	3.5	3.2		
TEFZEL (CLEAR, DuPont)	0.9		0.2	
TEFZEL (BLUE, RAYCHEM)	1.1			
TEFZEL (WHITE, RAYCHEM)	0.9			
KYNAR (PENWALT)	1.2			
KEL-F (PCTFE, 3M)	0.9			
HALAR (ALLIED)	1.9			
ACLAR 33C (ALLIED)	1.0			
FEP TEFLON (LeRC R.R.)	0.05	<0.03	<0.03	0.3
TFE TEFLON (DuPont)	0.06	<0.03		0.5
EYPEL-F, (ETHYL CORP.) POLY(BISTRIFLUOROPRO- PYLPHOSPHAZENE)	<0.03			

The results of replicate measurements of the reaction efficiency of Kapton polyimide demonstrate excellent agreement between the profilometry and weight loss measurements. Weight loss on four Kapton samples produced a reaction efficiency of $3.05 \pm 0.1 \times 10^{-24}$ cm³/atom while profilometry of four different Kapton samples produced a reaction efficiency of $3.16 \pm 0.1 \times 10^{-24}$ cm³/atom, using 2.3×10^{20} atoms/cm² as the fluence estimate. Both numbers are in excellent agreement with the Kapton reaction efficiencies produced by other on-orbit materials experiments such as STS-8^{ref 21} (3×10^{-24}), the Long-Duration Exposure Facility^{ref 22} (LDEF) (3.0×10^{-24}) and the Intelsat Solar Array Coupon (ISAC) experiment flown on STS-41^{ref 5} (3.1×10^{-24}). The HVAB at LANL was used to produce an independent (independent of MSIS-86 calculations) estimate of the Kapton reaction efficiency as

described below. The value of the Kapton reaction efficiency determined in the HVAB is 3.3×10^{-24} , within 10 percent of the values produced by the flight experiments.

Several general trends in the relationship between O-atom reactivity and molecular structure are visible in table 1. For example, polyethylene, Tedlar, Tefzel, Kynar and Teflon are all linear carbon chain polymers with increasing fluorine content and decreasing hydrogen content as we move along the series from polyethylene, $(\text{CH}_2-\text{CH}_2)_n$, or polypropylene, to Teflon, $(\text{CF}_2-\text{CF}_2)_n$, or FEP Teflon. As can be seen in table 1, increasing fluorine content results in decreasing O-atom reaction efficiency, as we would expect if hydrogen atom abstraction is a rate-limiting process and fluorine atom abstraction occurs to a very limited extent, if at all. The EOIM-III reaction efficiency for Teflon is intermediate between that reported from STS-8^{ref 20} and LDEF^{ref 21}. We attribute the observed range of reaction efficiency values to different net doses of solar UV/VUV radiation in the different mission environments. Vacuum ultraviolet photochemistry has been shown to be the controlling factor in the O-atom chemistry of Teflon and Kel-F^{ref 22,23}. The EOIM-III payload received a larger VUV radiation dose than STS-8 as a result of the solar inertial hold period following deployment of the Eureka satellite during an earlier portion of the STS-46 mission.

In contrast, incorporating two CF_3 groups into a polyimide structure results in little or no change in reaction efficiency, as can be seen by comparing the reaction efficiencies of Kapton polyimide and Eymyd-F. In general, the aromatic polymers displayed significantly lower reaction efficiencies than the linear straight-chain hydrocarbons, with the notable exception of the polycarbonate. The very low reaction efficiency of the poly(bistrifluoropropylphosphazene) based polymers X-221, X-222, and Eypel-F, all showing little or no evidence of reaction, confirms earlier work in ground-based test facilities^{ref 24}. Eypel-F is a durable, high-temperature elastomer which may find use in spacecraft atomic oxygen environments.

Table 2 shows the temperature dependence of the polymer reaction efficiencies determined following exposure to known O-atom fluences on the EOIM-III heated trays in the flowing discharge apparatus and in the HVAB. The temperature dependence of the O-atom reaction efficiency is shown as an empirical Arrhenius activation energy, i.e., the natural logarithm of the reaction efficiency is plotted against the reciprocal of the polymer sample temperature in degrees Kelvin, and the activation energy is reported as the slope. It should be noted that atom kinetic energy appears nowhere in this expression. For all the cases examined to date, straight-line Arrhenius plots have been obtained with correlation coefficients between 0.95 and 0.99. Inspection of table 2 shows that a large decrease in the Arrhenius activation energy is obtained on going from the flowing discharge to the HVAB or orbital environments. The large decrease in activation energy is accompanied by the large increase in reaction efficiency.

TABLE 2. The effects of atom-surface collision energy on the reaction efficiency, Re , and the parameters of the empirical Arrhenius equation, $Re = A \times \text{EXP}(-E_a/kT_s)$, where T_s is polymer surface temperature and E_a is the activation energy in eV. Re is in cm^3/atom .

POLYMER	Re , LEO	E_a , LEO	Re ,HVAB	E_a ,HVAB	Re , FDS	E_a , FDS
KAPTAN	3.1E-24	0.02 eV	3.3E-24	0.01 eV	2 E-28	0.3 eV
MYLAR	3.8E-24	0.05 eV	-----	-----	3 E-28	0.4 eV
D4 POLYETHYLENE	3.8E-24	0.0 eV	-----	-----	2 E-27	0.2 eV
POLYETHYLENE (PE)	3.7E-24	0.0 eV	-----	-----	4 E-27	0.2 eV
KYNAR	1.2E-24	0.0 eV	-----	-----	3 E-29	0.4 eV
TEFZEL	0.9E-24	0.04 eV	-----	-----	3 E-29	0.5 eV
LCP-4100	3.2E-24	0.04 eV	-----	-----	-----	-----
XYDAR	2.9E-24	0.05 eV	-----	-----	-----	-----
CR-39	6.1E-24	0.04 eV	-----	-----	-----	-----
EYMYD-F	2.7E-24	0.03 eV	-----	-----	-----	-----
PEEK	3.4E-24	0.03 eV	-----	-----	-----	-----

O-atom kinetic energy, on impact with the polymer surface, does not appear in the Arrhenius equation. As a result, the activation energy calculated by this method can vary with O-atom kinetic energy, if atom kinetic energy is available to overcome energetic barriers to reaction as has been previously proposed^{ref 13,25}. Alternately, the mechanism of reaction could change as atom-kinetic energy approaches a threshold value. Simple, semiempirical power laws or exponential functions have been shown to produce reasonable agreement with the limited data then available in the 0.065 to 5.0 eV translational energy range which suggests that a single reaction mechanism, as well as a single energetic barrier to reaction, may determine the reaction efficiency in the O-atom kinetic energy domain of interest. The question cannot be resolved without reaction efficiency data taken at several translational energies between 0.1 and 1.0 eV.

The LANL HVAB was used to obtain reaction efficiency data on Kapton polyimide at average atom kinetic energies of 0.44, 0.72, 0.79, and 2.1 eV. Velocity distribution functions and HVAB composition were measured as described in the apparatus and methods section above. The four O-atom kinetic energy distribution functions are shown in figure 15. For comparison purposes the kinetic energy distribution functions for ram-incident O atoms in LEO (average kinetic energy = 5.6 eV) and for O atoms striking a surface immersed in flowing discharge gas (average kinetic energy = 0.065 eV) are shown in figure 16.

It should be noted that the component of the kinetic energy normal to the surface plane during collision with the surface and the total O-atom kinetic energy are the same for the O-atom directed beam on-orbit and in the HVAB. In the case of the thermalized gas in the flowing discharge, the component of the kinetic energy which is normal to the surface plane during collision with the surface and the total O-atom kinetic energy are not the same. The total kinetic energy distribution on surface collision in the flowing discharge shown in figure 16 was calculated using well known molecular

effusion beam methods. The component of the total kinetic energy normal to the surface plane is often used in surface reactive scattering experiments on surfaces having well defined surface structures^{ref 27}. The total kinetic energy on surface collision is probably more appropriate in the case of polymer films which are expected to be rough on a molecular scale and show no preferred orientation of chemical bonds.

The measured reaction efficiency of Kapton polyimide is plotted against the first moment (average value) of the kinetic energy distributions described in the previous paragraph (figures 15 and 16) in figure 17. A rapid increase in reaction efficiency is seen between 0.065 and 1.0 eV followed by relatively little change between 1.0 and 5.6 eV. The data shown in figure 17 suggest that the dynamics of the reaction of O-atoms with polymers may be described with a line-of-centers^{ref 26}, a Berckele et al^{ref 27}, or a microcanonical transition state^{ref 28} model of the kinetic energy dependence of the reaction probability. Such models have proven highly successful in describing the translational energy dependence of a number of gas phase and surface reactive scattering processes^{ref 26-29}. A simple direct fit of the data plotted in figure 17 to such a model is a gross oversimplification given the width of the velocity distribution functions. A more accurate test of the translational energy dependence hypothesis is needed.

To test the hypothesis that the simple reactive scattering models provide a reasonable description of the reaction dynamics of O atoms with polymers, we form the convolution integral of the function which describes the kinetic energy dependence of the reaction probability with the normalized kinetic energy distribution function, $f(Et)$, as shown in the equations below and then determine if the Re vs. Et data can be fit to the resulting function. Finally, we ask if the Re equation, with parameters determined by least squares curve fitting to the HVAB data, can predict values of Re for the flowing discharge and on-orbit environments.

Line of Centers Model

$$Re = \int_0^{\infty} A \left(1 - \frac{Ea}{Et}\right) f(Et) d(Et),$$

$$A = 5.10 \times 10^{-24} \text{ cm}^3 / \text{atom} \quad Ea = 0.62 \text{ eV} \quad \Delta = 0.036 \quad (1)$$

Beckerle-Ceyer Model

$$Re = \int_0^{\infty} \frac{A}{1 + \exp - n(Et - Ea)} \times f(Et) d(Et)$$

$$A = 3.7 \times 10^{-24} \quad n = 10 \quad Ea = 0.98 \quad \Delta = 0.008 \quad (2)$$

R_e , as defined by the R_e equations above, is the average of a large number of reaction efficiencies, one for each kinetic energy interval in the kinetic energy distribution function of interest. The R_e equations allow us to calculate the reaction efficiency given the normalized kinetic energy distribution function, $f(E_t)$, and values for the parameters E_a , the magnitude of the energetic barrier to reaction, and A , the limiting reaction efficiency at high kinetic energies. The Δ term is the residual sum of squares error at the conclusion of the curve-fitting process.

We test the hypothesis represented by an R_e equation as follows. First, because a priori values for A and E_a are not available, a gaussian least squares curve-fitting process is used with A and E_a as adjustable parameters. A , E_a , and any other adjustable parameters are varied until the R_e equation gives the best fit (minimum Δ) to the R_e data produced by exposing Kapton samples in the four different atom beam kinetic energy distribution functions shown in figure 16. The success of the curve-fitting operation both in terms of the reasonableness of the A and E_a values obtained and the magnitude of the sum of squares error at the end of the curve-fitting process is one test of the validity of the hypothesis. A second test involves asking how accurately an R_e equation, with A and E_a values determined as described above, can predict R_e values for kinetic energy distributions well outside the range of values used in the least squares process. Specifically, can an R_e equation, with A and E_a determined with HVAB data, predict R_e values obtained from the flowing discharge and EOIM-III experiments?

The predictions of the R_e equations are plotted with the measured R_e values in figure 17. Clearly, both R_e equations provide a reasonably accurate description of the kinetic energy dependence of the Kapton R_e for the HVAB and on-orbit data. The two models differ significantly in their ability to accurately predict the R_e in the flowing discharge apparatus. The Beckerle-Ceyer model produces reasonably accurate predictions of the Kapton R_e over a three order of magnitude range of O-atom kinetic energy and a four order of magnitude range in R_e . Failure of the line-of-centers model to predict R_e at thermal energies suggests that the potential energy surface describing the reactive collision may change in such a way that E_a varies with collision energy. Finally, it is useful to note that the Beckerle-Ceyer model, with parameters estimated for Kapton, is a useful tool for making reasonable estimates of R_e for a variety of polymers in both thermal and hyperthermal O-atom environments as can be seen by comparison of the data in tables 1 and 2 with figure 17.

The results of x-ray photoelectron spectroscopic (XPS) studies of several polymers are shown in table 3 where samples exposed to the O-atom flux during EOIM-III are compared with flight controls (i.e., samples exposed to the space vacuum during EOIM-III, but not to O-atom flux). All the polymer samples show significant increases in surface oxygen content accompanied by surface depletion of carbon. However the net disturbance of the surface atomic composition is relatively small at 10 to 15 atom percent. In contrast, infrared adsorption spectra of polymer sample films show no significant difference between the oxygen exposed samples and the controls, except a

slightly smaller absorbance value for the O-atom exposed samples which were thinner than the controls as a result of O-atom reaction. Because the XPS method has a sampling depth on the order of 0 to 50 Angstroms we can conclude that O-atom reaction processes are confined to the near surface region of the polymer with no significant reaction processes occurring at the greater depths samples by infrared spectroscopy. Typical infrared adsorbance spectra of Kapton and polyethylene which were exposed to the ram O-atom flux during EOIM-III are compared to those of the corresponding flight controls in figure 18. The small differences in absorbance peak heights are the result variability in final film thickness after pressing, not O-atom reaction effects.

Table 3. Surface composition of EOIM-III polymer films, expressed as atom percent, as determined by X-ray photoelectron spectroscopy. The surface exposed to ram atomic oxygen during EOIM-III is compared with the control sample.

Polymer	O-atom Reaction Surface					Control Surface				
	C	O	N	F	Si	C	O	N	F	Si
Kapton	64.3	23.2	5.7	0.0	6.8	79.7	13.3	5.7	0.0	1.1
Mylar	71.2	24.2	0.6	0.8	2.2	75.1	22.7	0.1	0.3	1.8
PEEK	49.3	36.1	2.4	5.2	6.9	81.0	15.9	0.6	0.4	2.2
PE	80.4	14.2	1.5	0.0	3.8	94.8	3.4	0.0	0.0	1.8
PMP	86.9	9.1	0.3	0.5	3.2	97.3	1.8	0.0	0.0	0.9

Finally, profilometry and weight-loss measurements on JSC polymer samples revealed some interesting configuration interaction effects produced by the sample holders themselves. Thin metal screens were placed in front of most polymer samples on EOIM-I to act as etch masks, helping to provide for more accurate profilometry. However, the profilometry measurements showed more surface recession near the edge of the 2.65 centimeter diameter sample holder opening and less recession near the center as shown in figure 20. The effect is probably a result of the 45 degree bevel machined into the circular sample openings in the sample holders. High-velocity oxygen atoms can scatter off the beveled surface and onto the sample, effectively increasing the O-atom flux and fluence nearest the edge of the sample holder opening.

Summary and Conclusions

Despite some minor payload timing and switching problems, the EOIM-III flight experiment achieved all of its objectives. A well-characterized, short-term, high-fluence O-atom exposure was provided for a large number of materials, many of which had never been exposed to the atomic oxygen environment in LEO before. Detailed definition of the sample exposure history is provided in reference 1. The mass spectrometer/carousel experiment produced over 46,000 mass spectra providing detailed characterization of both the natural and induced environments. The mass

spectrometric data base will prove a valuable resource in future years for the verification of various models of rarefied gas and plasma flow around spacecraft. The gaseous reaction products of various polymer species have been determined in the LEO environment and direct reactions of ambient O^+ ions with surfaces have been observed. Finally, by combining measurements of polymer reaction efficiency, we have determined the dependence of polymer reaction efficiency on O-atom kinetic energy in an unequivocal way. Reaction efficiency data produced in the HVAB system at several different O-atom kinetic energies were shown to be described by the Beckerle^{ref 29} reactive scattering model with an energy barrier of 0.98 eV. The same equation made reasonably accurate predictions of reaction efficiencies in the LEO environment and in the laboratory flowing discharge at JSC. The activation energy for the mass removal or surface recession process, defined in terms of polymer temperature only, showed a marked decrease in magnitude as O-atom translational energy is increased, a result which is expected if O-atom kinetic energy is directly available to overcome energetic barriers to reaction.

References

- 1) Koontz S. L., Leger, L. J., Rickman, S. L., Cross, J. B., Hakes, C. L., Bui, D. T.; "The Evaluation of Oxygen Interactions with Materials III (EOIM-III) Mission and Induced Environments," Proceedings of the Third LDEF Post-Retrieval Symposium, Williamsburg, VA, November 8-12, 1993, NASA CP-3275.
- 2) Jursa, A. S., editor; Handbook of Geophysics and the Space Environment, Air Force Geophysics Laboratory, United States Air Force, 1985 (National Technical Information Service).
- 3) Hedin, A. E., "A Revised Thermospheric Model Based on Mass Spectrometer and Incoherent Scatter Data: MSIS-83," J. Geophys. Res., Vol. 88, No. 10, pp 170-188, 1983.
- 4) Leger, L. J., Visentine, J. T., Santos-Mason, B.; "Selected Materials Issues Associated with Space Station Freedom," in the SAMPE Quarterly, Vol. 18, No. 2, pp 48-54, Jan. 1987.
- 5) Koontz, S., King, G., Dunnet, A., Kirkendahl, T., Linton, R., Vaughn, J.; "The ISAC Atomic Oxygen Flight Experiment," J. Spacecraft., in press, 1994.
- 6) Visentine, J. T., Leger, L. J.; "Materials Interactions with the Low-Earth Orbit Environment: Accurate Reaction Rate Measurements," AIAA paper AIAA 85-7019, AIAA Shuttle Environments and Operations II Conference, Nov. 1985, p 168.

- 7) Leger, L. J., Visentine, J. T., Schleising, J. A.; "A Consideration of Atomic Oxygen Interactions with Space Station," AIAA-85-0476, AIAA 23rd Aerospace Sciences Meeting, Jan. 14-17, 1985, Reno, Nevada.
- 8) Hunton, D. E., Trzcinski, E., Wlodyka, L., Federico, G., Dorian, J. 1Lt, USAF; "Quadrupole Ion-Neutral Mass Spectrometer for Space Shuttle Applications," AFCEC-TR-86-0084, Environmental Engineering Paper No. 953.
- 9) Kooztz, S. L., Cross, J. B., Lan, E.; "Characterization and Calibration of the EO I-III Flight Mass Spectrometer in a High Velocity Atom Beam," in Materials Degradation in Low-Earth Orbit (LEO), Srinivasan, V., Banks, B. A., eds., The Materials, Metals and Minerals Society, 1990.
- 10) Visentine, J. T., comp.; NASA Technical Memorandum 100459, "Atomic Oxygen Effects Measurements for Shuttle Missions STS-8 and STS-41G: Vol. I-III," Sept. 1988.
- 11) Hayden, L. J., Nier, A. O., French, J. B., Reid, N. M., and Duckett R. J.; "The Characteristics of an Open Source Mass Spectrometer Under Conditions Simulation Upper Atmosphere Flight," *Int. J. Mass Spectrom. Ion Phys.* 15, pp 37-47, 1974.
- 12) Kooztz, S. L., Albyn, K., Leger, L. J.; "Atomic Oxygen Testing with Thermal Atom Systems: A Critical Evaluation," *J. Spacecraft*, Vol. 28, No. 3, pp 315-323, May/June, 1991.
- 13) Kooztz, S. L., Albyn, K., Leger, L.; "Materials Selection for Long Life in Low Earth Orbit," *Journal of the IES*, March/April 1990, pp 50-59.
- 14) Clyne M. A. A., Nip, W. S.; "Generation and Measurement of Atom and Radical Concentrations in Flow Systems," in Reactive Intermediates in the Gas Phase, Setzer, D. W., Editor, Academic Press, New York, pp 1-57, 1979.
- 15) Huie R. E., Herron, J. T.; "Reactions of Atomic Oxygen (O^3P) with Organic Compounds," *Progress in Reaction Kinetics*, Vol.8, No. 1, pp1-80, 1975.
- 16) Kooztz, S. L., Nordine, P.; "The Reaction Efficiency of Thermal Energy Oxygen Atoms with Polymeric Materials," in Materials Degradation in Low Earth Orbit (LEO), Banks, B. A., Srinivasan, V., Eds. pp 189-205, The Minerals, Metals and Materials Society, Warrendale Penn., 1990.
- 17) Cross, J. B., Blais, N. C.; "High Energy/Intensity CW Atomic Oxygen Beam Source," *Progress in Aeronautics and Astronautics*, Vol. 116, pp 143-155, American Institute of Aeronautics and Astronautics, Washington, DC, 1989,

- 18) Cross J., B., Koontz, S. L., Gregory, J. C., Edgell, M. J.; "Hyperthermal Atomic Oxygen Reactions with Kapton and Polyethylene," in Materials Degradation in Low Earth Orbit (LEO), Banks, B. A., Srinivasan, V., Eds. pp 1-13, The Minerals, Metals and Materials Society, Warrendale Penn., 1990.
- 19) Fergeson, E. E., Feshenfeld, F. C., Schmeltenkoph, A. L.; "Flowing Afterglow Measurements," in Advances in Atomic and Molecular Physics, Vol.5, pp 12-13, Academic Press, New York, 1969.
- 20) Visentine, J. T., Leger, L. J., Kuminecz, J. F., Spiker, I. K.; "STS-8 Atomic Oxygen Effects Experiment, " AIAA paper AIAA-85-0415, 23rd Aerospace Sciences Meeting, Jan. 14-17, 1985, Reno, Nevada.
- 21) Personal communication, Professor John Gregory, Chemistry Department, University of Alabama, Huntsville, Alabama.
- 22) Koontz, S. L., Leger, L. J., Albyn, K. A., and Cross, J.; "Ultraviolet Radiation/ Atomic Oxygen Synergism in Materials Reactivity," J. Spacecraft, Vol. 27, No. 5, pp 346-348, May-June 1990.
- 23) Steigman, A. E., Brinza, D. E., Anderson, M. S., Minton, T. K., Laue, E. G., Liang, R. H.; "An Investigation of the Degradation of Fluorinated Ethylene Propylene (FEP) Copolymer Thermal Blanketing Materials Aboard LDEF and in the Laboratory," JPL publication 91-10, May 15, 1991, Jet Propulsion Laboratory, Pasadena, California.
- 24) Fewell, L., Fenney, L.; Polymer Comm., Vol. 32, No. 13, pp 393-396, 1991.
- 25) Arnold, G. S.; Peplinski, D. R.; Cascarano, F. M.; "Translational Energy Dependence of the Reaction of atomic Oxygen with Polyimide Films," J. Spacecraft, 24(5), pp 454-458, 1987.
- 26) Berkerle, J.D.; Johnson, A.D.; Yang Q. Y.; Ceyer, S. T. "Collision Induced Dissociative Chemisorption of CH₄ on Ni: The Mechanism for Chemistry With a Hammer," J. Chem. Phys., 91(9), pp 5756-5777, 1989.
- 27) Stienfeld, J. I.; Francisco, J. S.; Hase, W. L. Chemical Kinetics and Dynamics, Chapter 8, "Dynamics of Bimolecular Collisions," Printice Hall, New Jersey, 1989.
- 28) Zeiri, Y.; Lucchese, R. R. "Collision of hyperthermal atoms with an absorbate covered solid surface II: Collision induced desorption," Surface Science, 264, pp 197-206, 1992.

- 29) Gonzalez Urena, A, "Influence of Translational Energy upon Reactive Scattering Cross Section: Neutral-Neutral Collisions," in *Advances in Chemical Physics*, Prigogine, I and Rice S. A. Eds. Vol. LXVI, John Wiley and Sons, New York, 1987, pp 231-335.
- 30) Swenson, G. R., Meyerott, R. E.; "Spacecraft Ram Cloud Exchange and N₂ LBH Glow," *Geophys. Res. Lett.*, 15, 2, pp245-248, March 1988.
- 31) Hanson, W. B., Sanatani, S., Hoffman, J. H.; "Ion Sputtering from Satellite Surfaces," *J. Geophys. Res.*, 86, A13, pp 11,350-11,356, Dec. 1981.

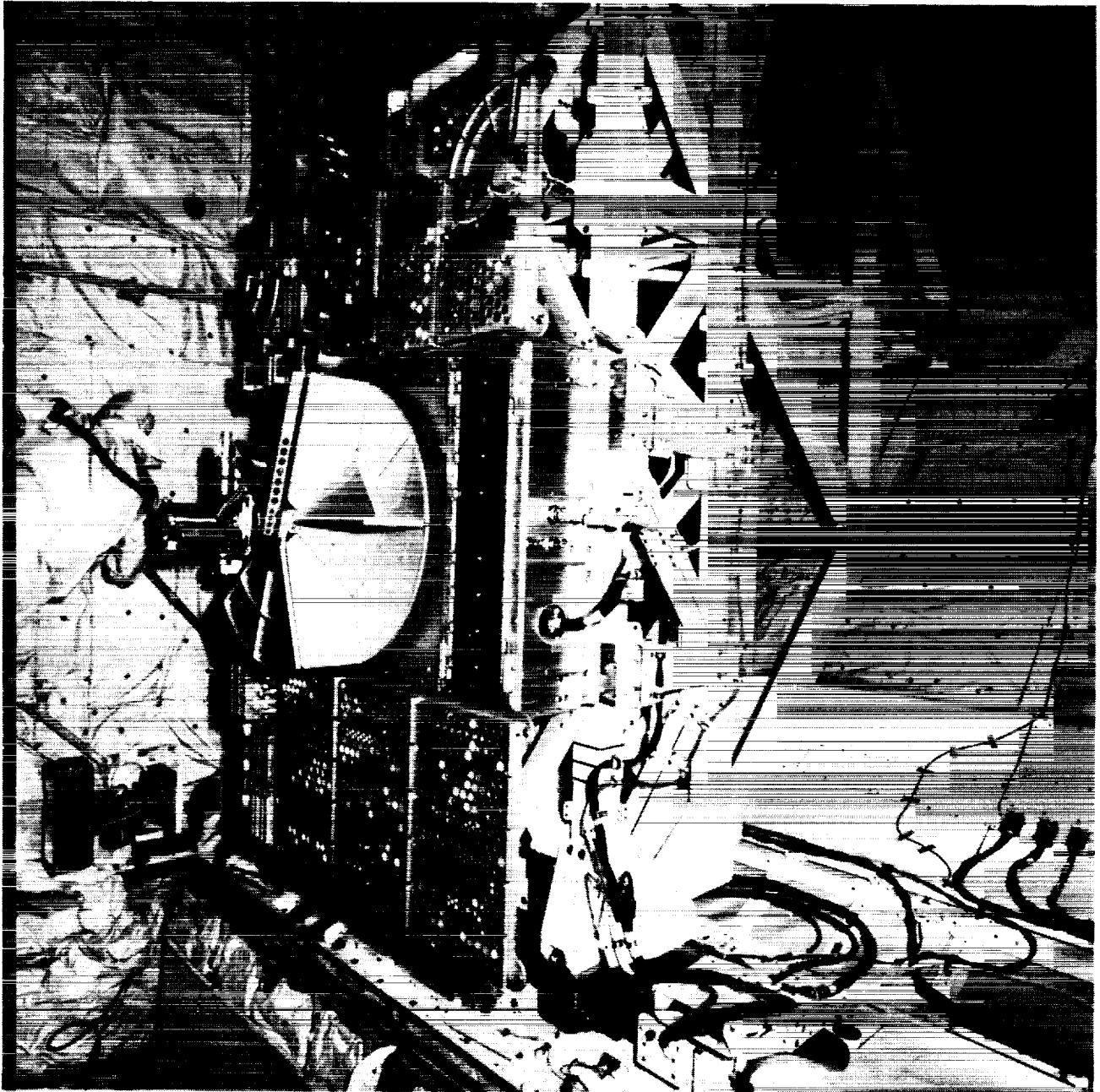
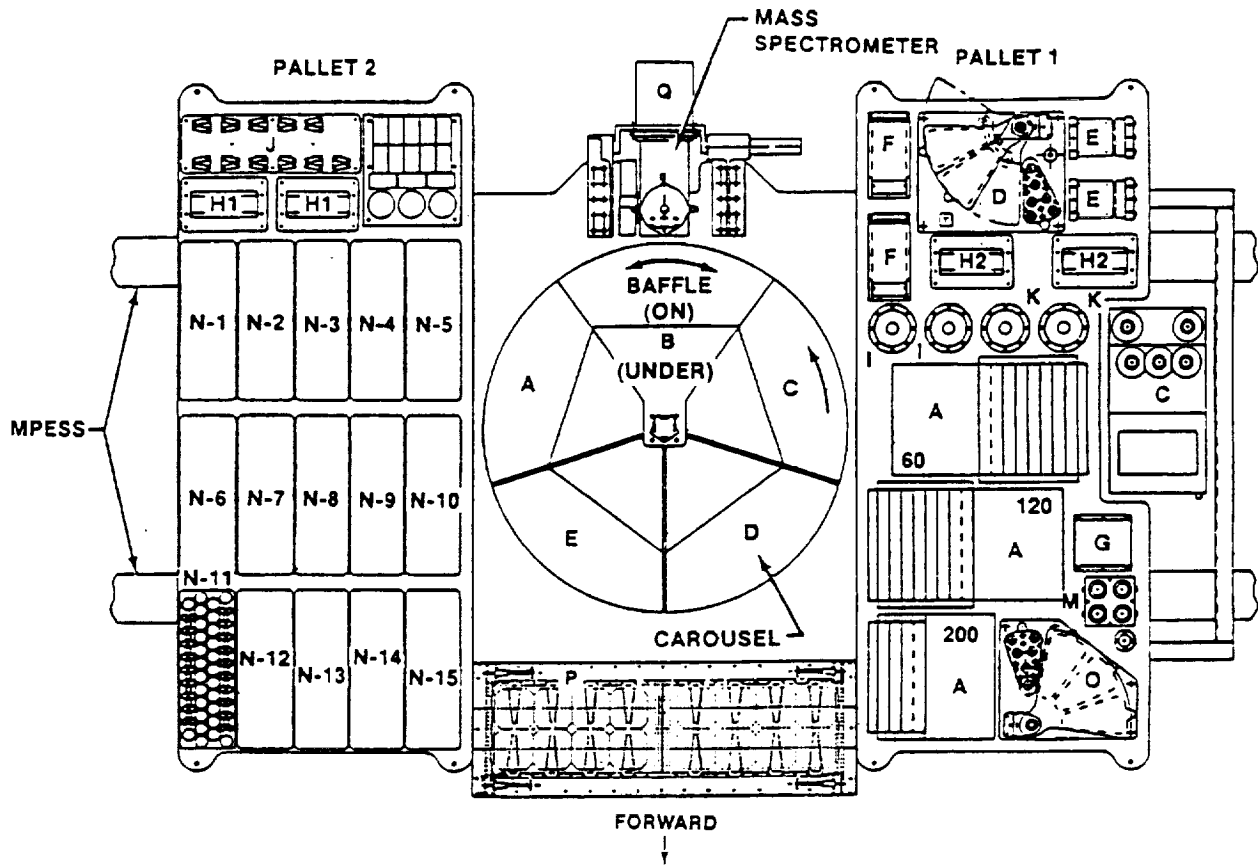


Figure 1: A launch pad close-out photo of the EOIM-III payload in the cargo bay of the Space Shuttle Atlantis. The aft bulkhead of the cargo bay is visible at the bottom of the photograph.



ATOMIC INTERACTION EXPERIMENTS:

- A - HEATED PLATE (JSC), 3EA
- B - ATOM SCATTERING EXPERIMENT (UAH), 1EA
- C - ENVIRONMENT MONITOR PACKAGE (GSFC), 1EA
- D - SOLAR UV EXPERIMENT (JSC), 1EA
- E - STATIC STRESS FIXTURE (MSFC), 2 EA
- F - UNIFORM STRESS FIXTURE (MSFC), 2 EA
- G - ATOMIC OXYGEN MONITOR (MSFC), 1 EA
- H1 - COMPOSITE STRESS FIXTURE(LaRC), 2EA
- H2 - COMPOSITE STRESS FIXTURE (JSC), 2 EA

- I - SCATTEROMETER (JPL), 2 EA
- J - MECHANICAL STRESS FIXTURE (LeRC), 11 EA
- K - REFLECTOMETER (LeRC), 2 EA
- L - PINHOLE CAMERA (LeRC), 1 EA
- M - SCATTEROMETER (AEROSPACE CORP.), 1EA
- N - PASSIVE SAMPLE CARRIERS, 15 EA
- O - VARIABLE EXPOSURE TRAY, 1EA
- P - FREEDOM ARRAY MATERIALS EXPOSURE EXPERIMENT(LeRC), 1 EA
- Q - QUADRUPLE MASS SPECTROMETER, 1 EA

Figure 2: A line drawing of EOIM-III, as viewed from directly above, showing the identification of various sub-experiments and assemblies.

STS-46 CONFIGURATION

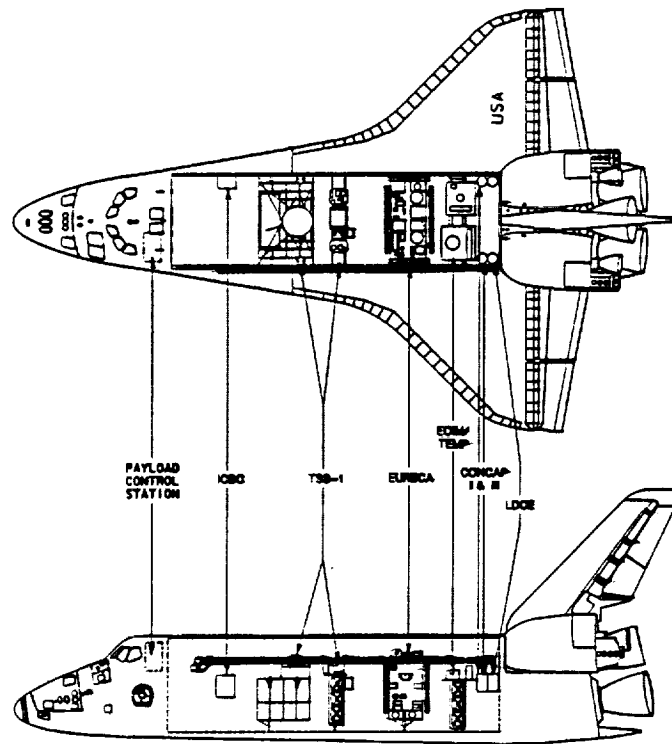


Figure 3: Cargo bay configuration for STS-46.

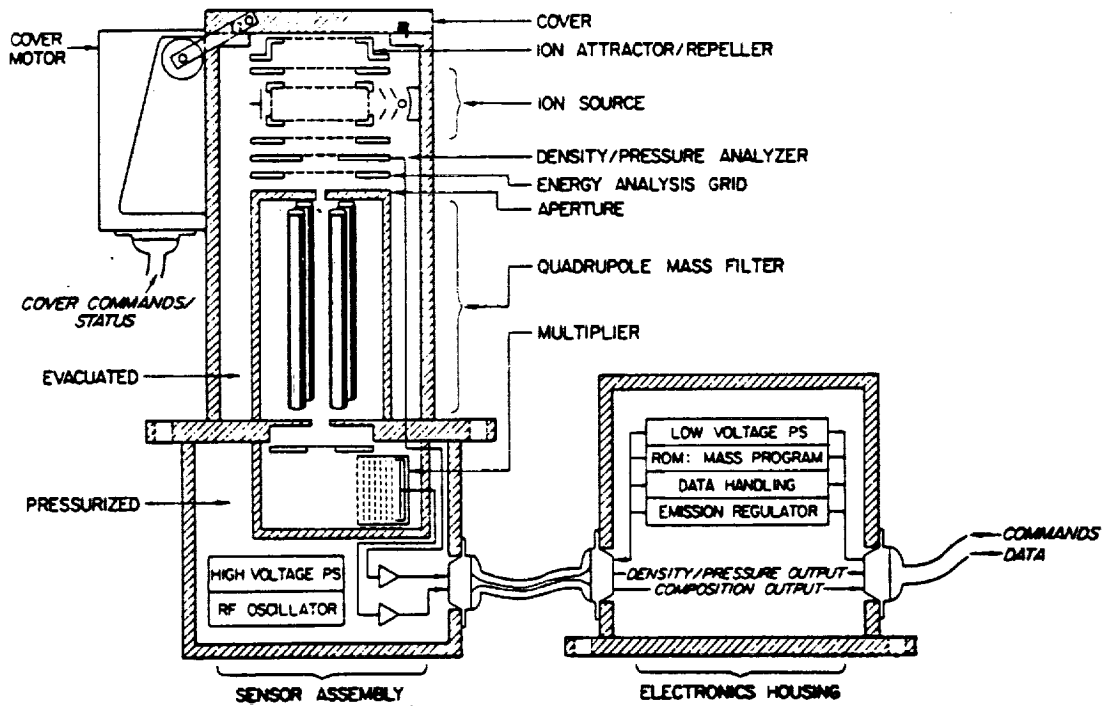


Figure 4: A cross sectional drawing of the EOIM-III mass spectrometer.

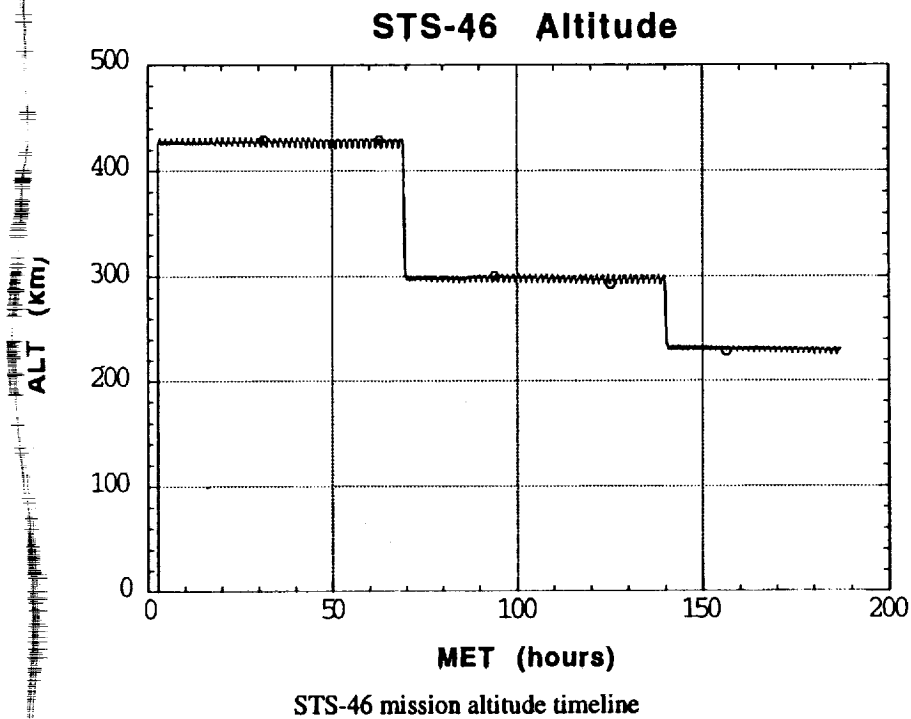


Figure : The altitude history of STS-46 as determined by post-flight analysis of tracking and pointing data.

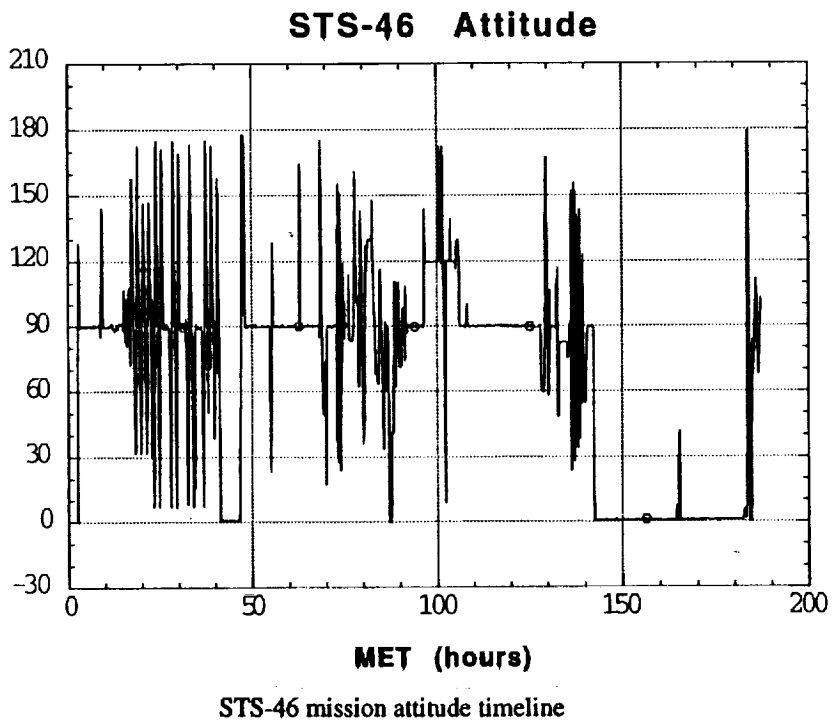
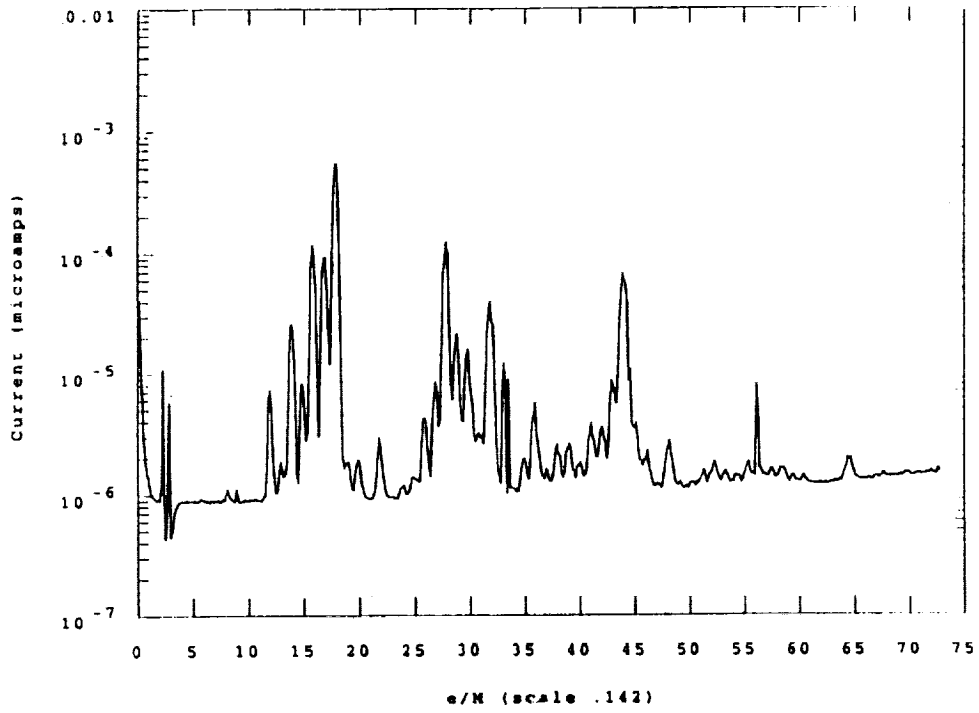


Figure () The vehicle attitude history of STS-46 as determined by post-flight analysis of tracking and pointing data. The attitude variable of interest for atomic oxygen fluence calculations, the angle between the cargo bay verticle (-Z) and the velocity vector (), is shown here.

Neutral Ram at 231 nmi



MET 576000-576300

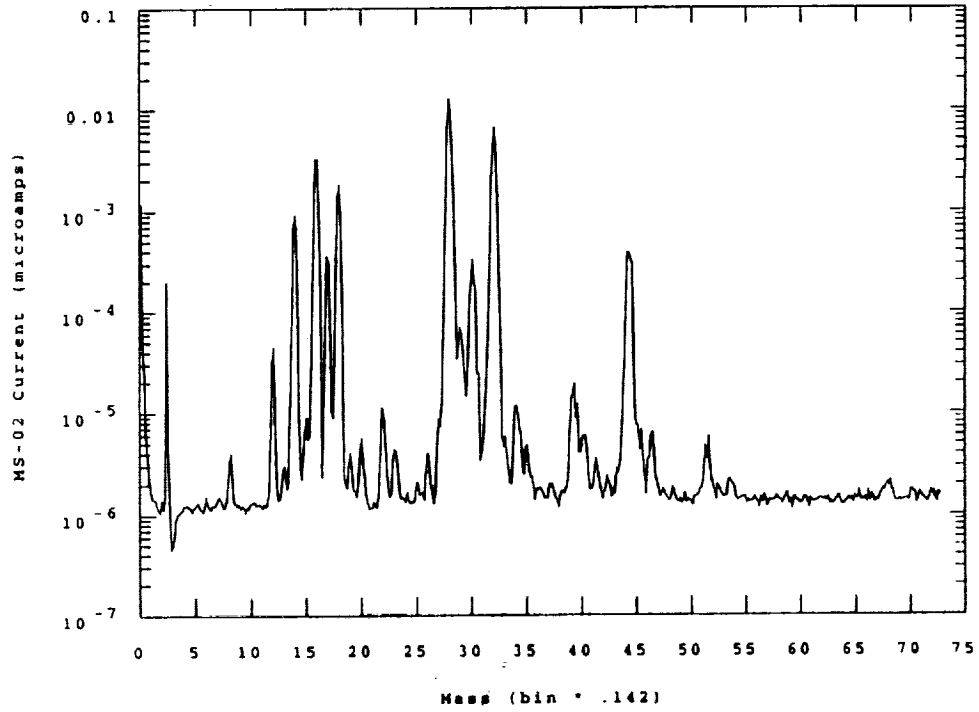


Figure 7: Typical mass spectra produced with both the mass spectrometer axis and the space shuttle -Z axis aligned with the velocity vector (i.e., ram oriented). a) altitude= 231 nmi, b) altitude=123 nmi.

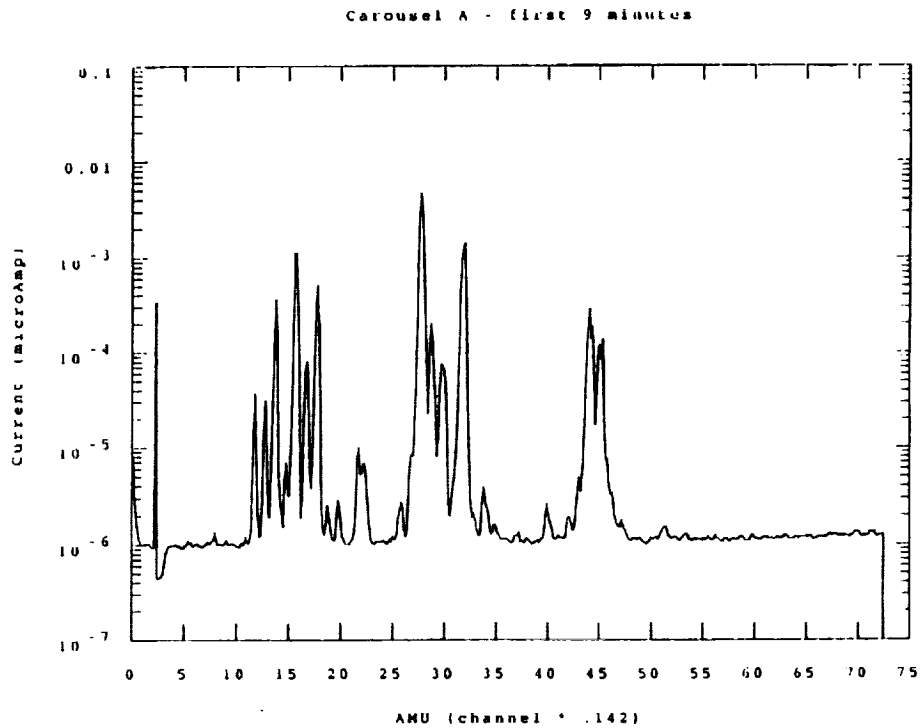


Figure 9: A typical mass spectrum of the induced neutral gaseous environment in the C^{13} labeled Kapton carousel sector. The sector was open to direct ram ambient atmosphere.

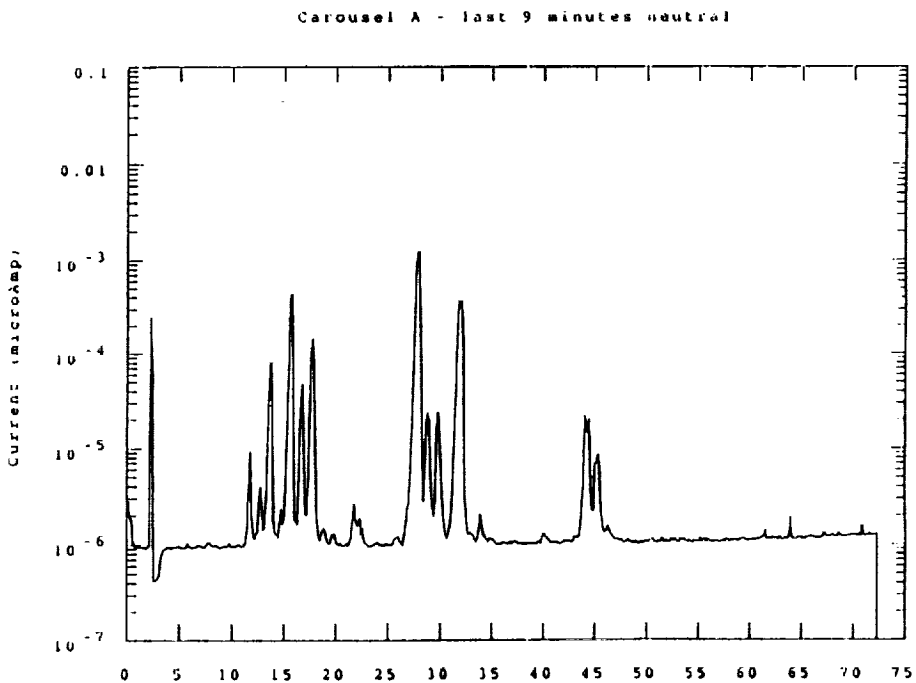


Figure 10: A typical mass spectrum of the induced gaseous environment in the C^{13} labeled Kapton carousel sector. The sector cover blocked direct ram ambient atmosphere in this case.

Isotopically Labeled (^{13}C) Kapton Reaction Products
 Agree Between LEO Simulation and LEO Flight

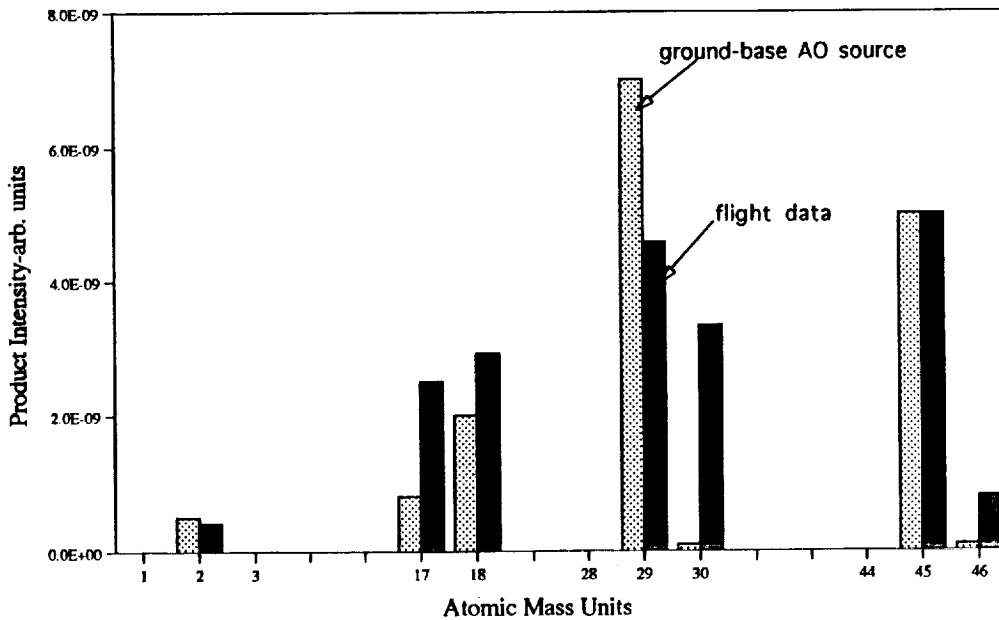


Figure 11: A comparison of the gaseous reaction products formed by O-atom reaction with C^{13} labeled Kapton on-orbit and in the HVAB at LANL.

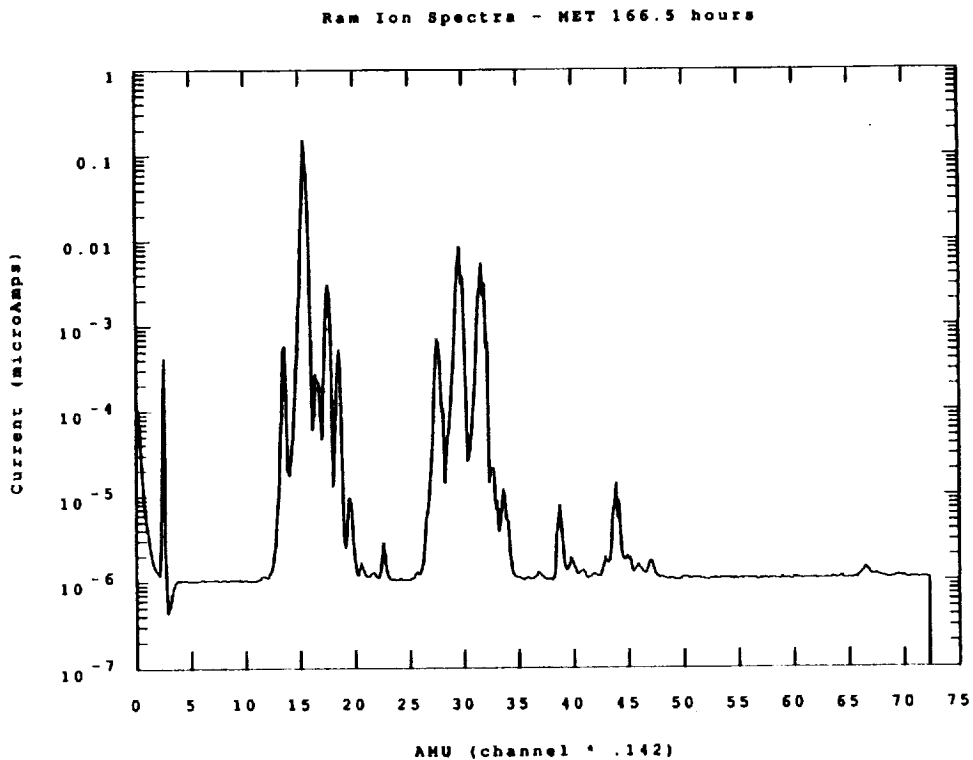


Figure 12: A typical mass spectrum of the natural ionospheric plasma environment at 123 nmi taken with the mass spectrometer configured to sample naturally occurring ionic species.

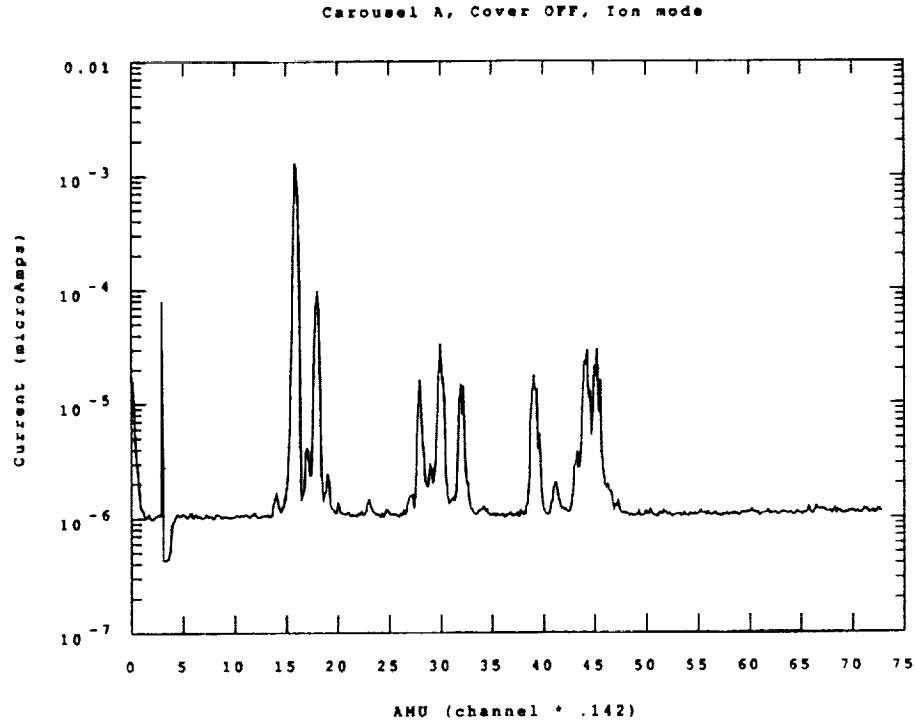


Figure 13: A typical mass spectrum of the induced plasma environment in the C¹³ labeled Kapton carousel sector. The sector cover was open to direct ram ambient atmosphere.

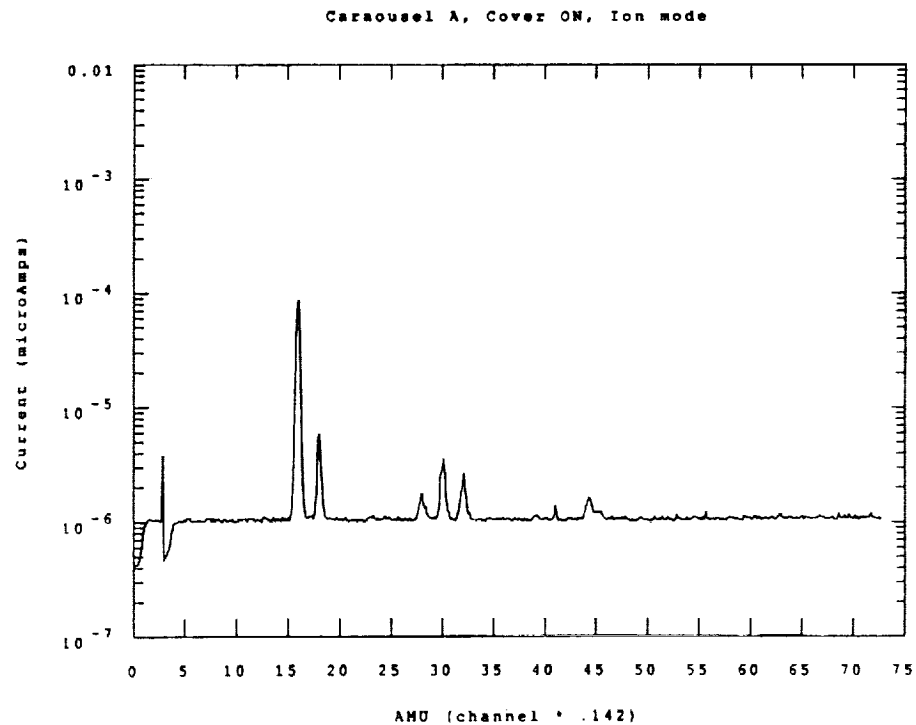


Figure 14: A typical mass spectrum of the induced plasma environment in the C¹³ labeled Kapton carousel sector. The sector cover blocked direct ram ambient atmosphere in this case.

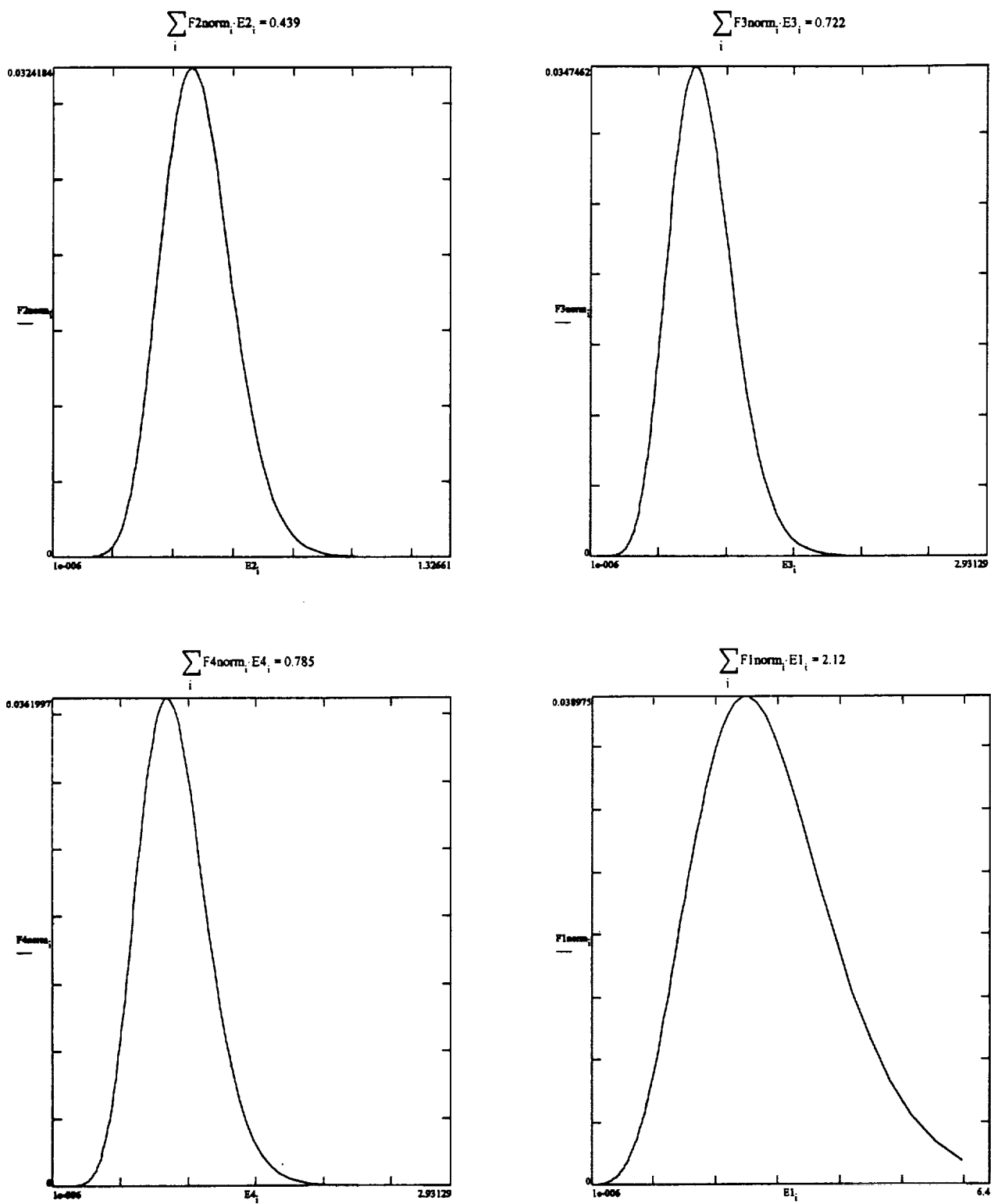
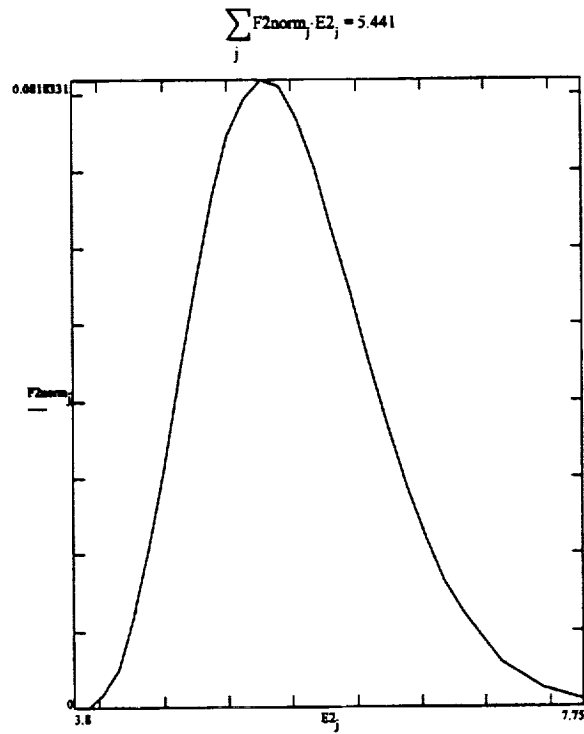
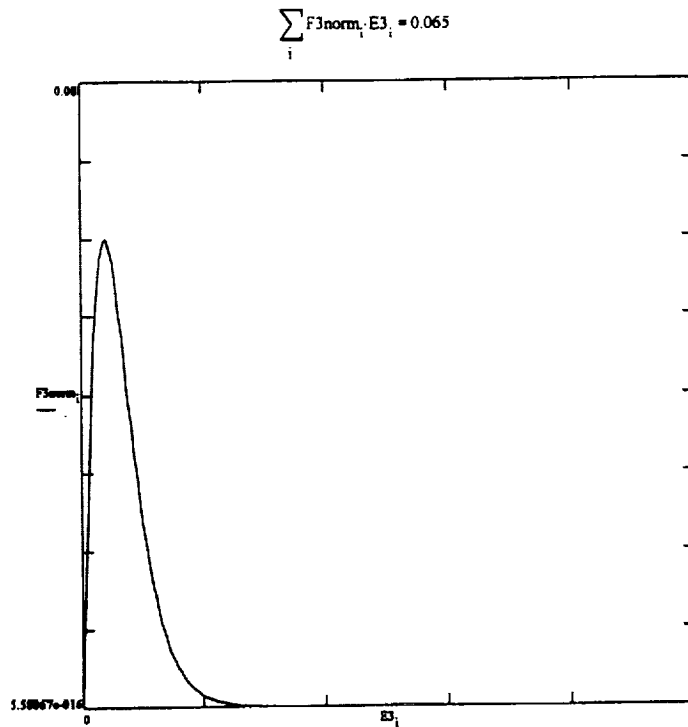


Figure 15: O-atom kinetic energy distribution functions (kinetic energy on collision with the polymer surface) and the corresponding average kinetic energies (first moments) for the HVAB O-atom beams used in developing the formula relating reaction efficiency to atom kinetic energy in eV.



a)



b)

Figure 16: O-atom kinetic energy (kinetic energy on collision with the polymer surface) distribution functions for, a) the LEO environment and b) the flowing discharge Energy in eV.

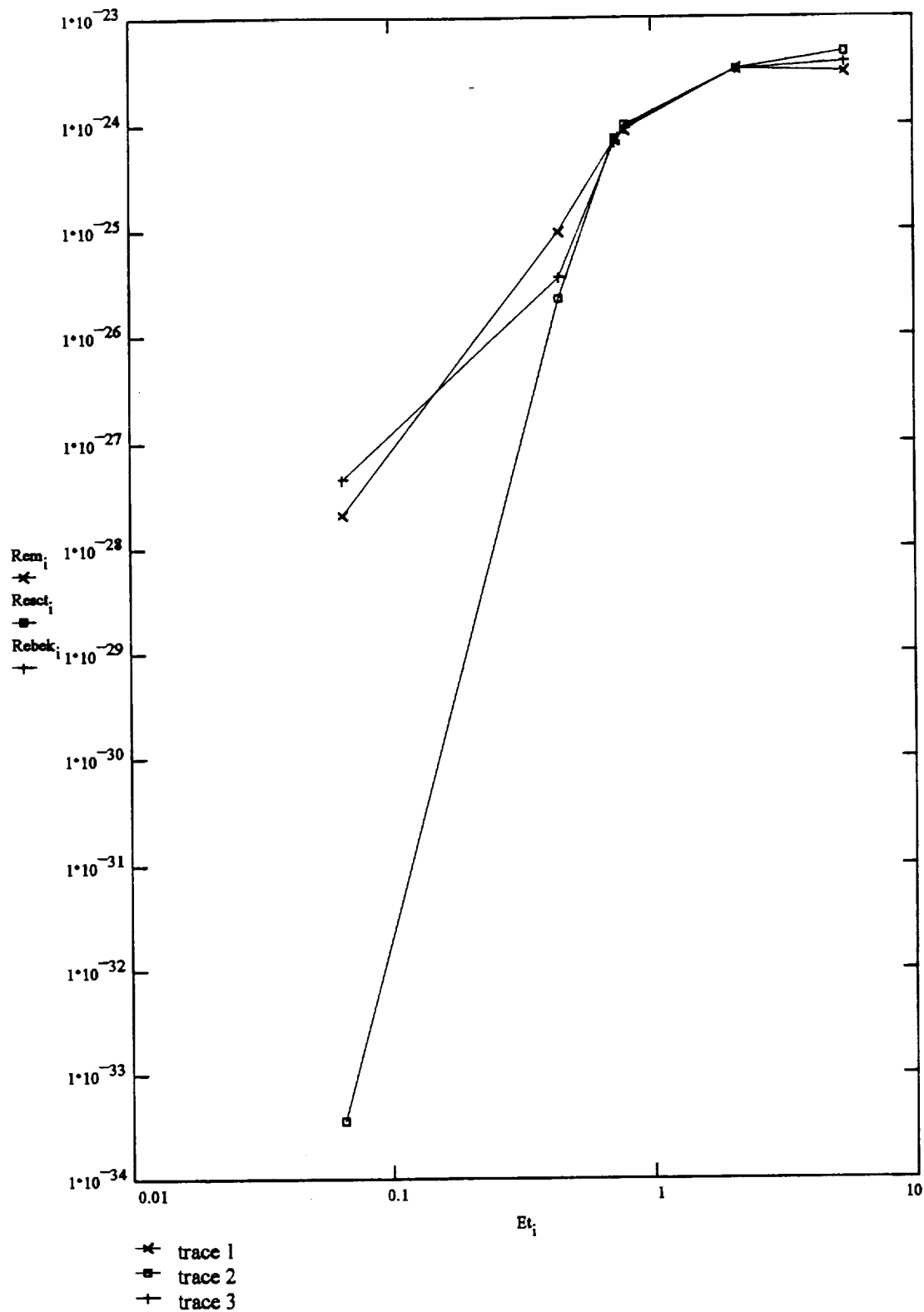


Figure 17: The measured and predicted (equations 1-3) Re values for Kapton polyimide plotted against the average value of the O-atom kinetic energy on collision with the polymer surface for the environments of figures 18 and 19: Rem = measured values, React = line-of-centers model, Rebeek = Beckerle-Ceyer model.

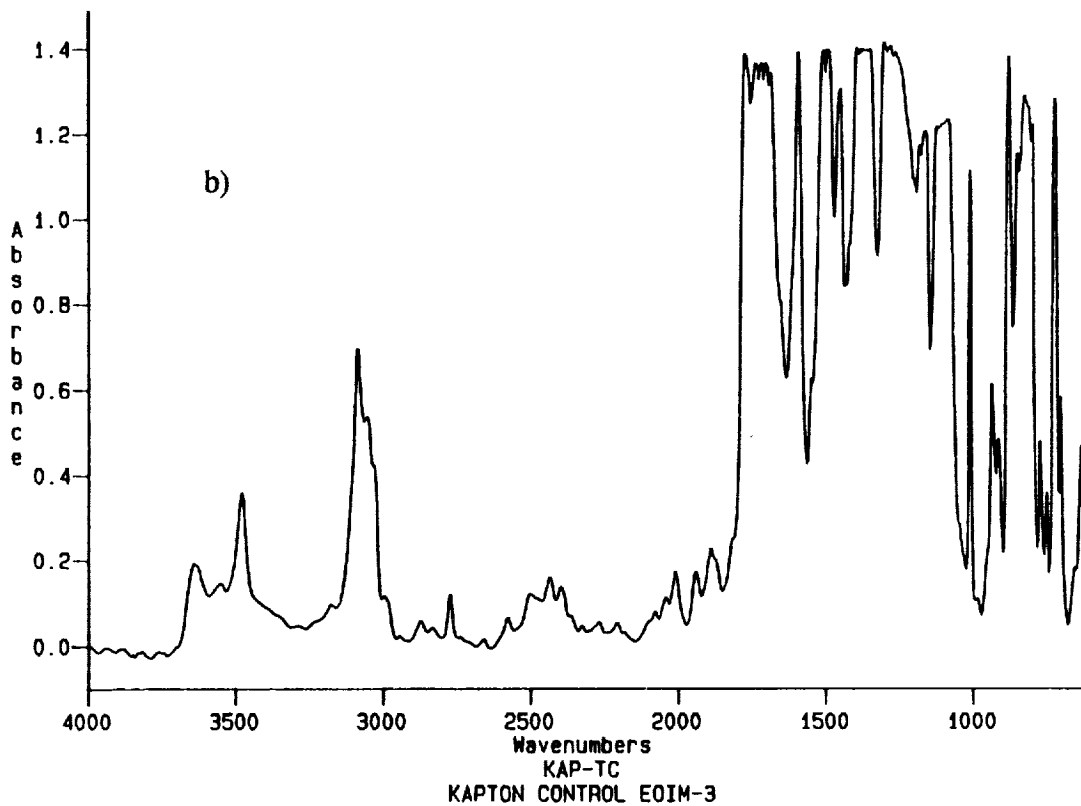
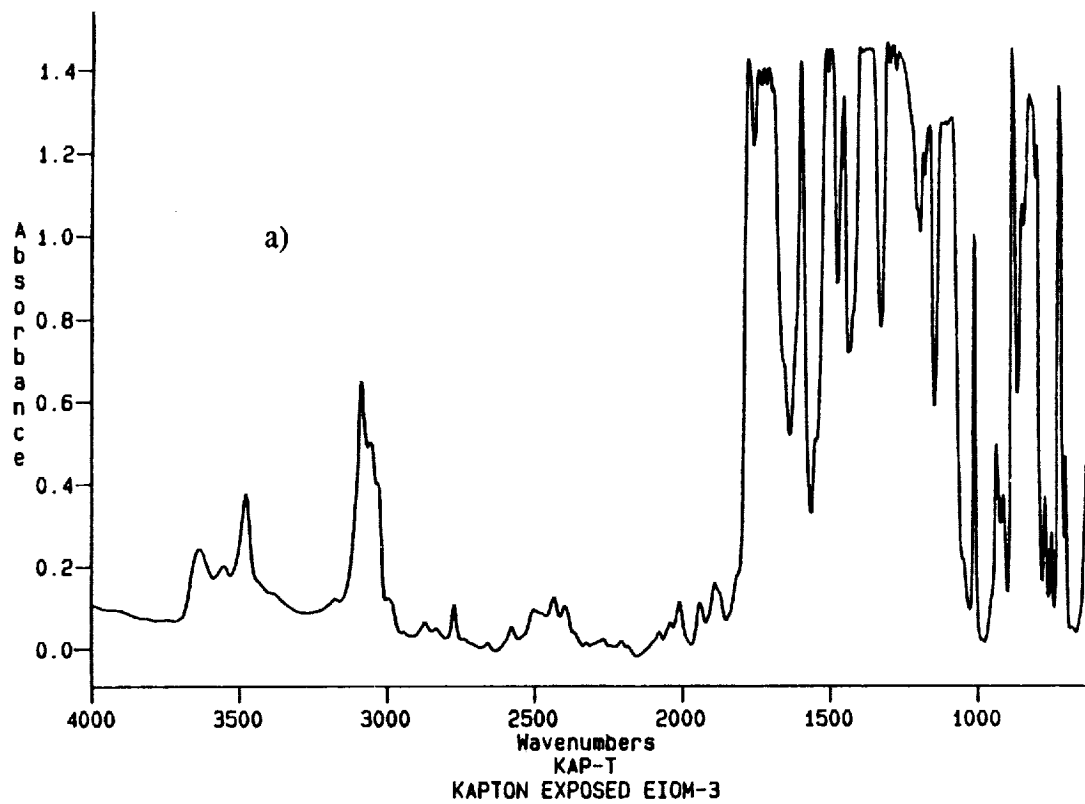


Figure 18: Typical infrared absorbance spectra of Kapton and polyethylene from EOIM-III: a) Kapton exposed to O atoms during EOIM-III, b) Kapton control, c) Polyethylene exposed to O atoms during EOIM-III, d) polyethylene control.

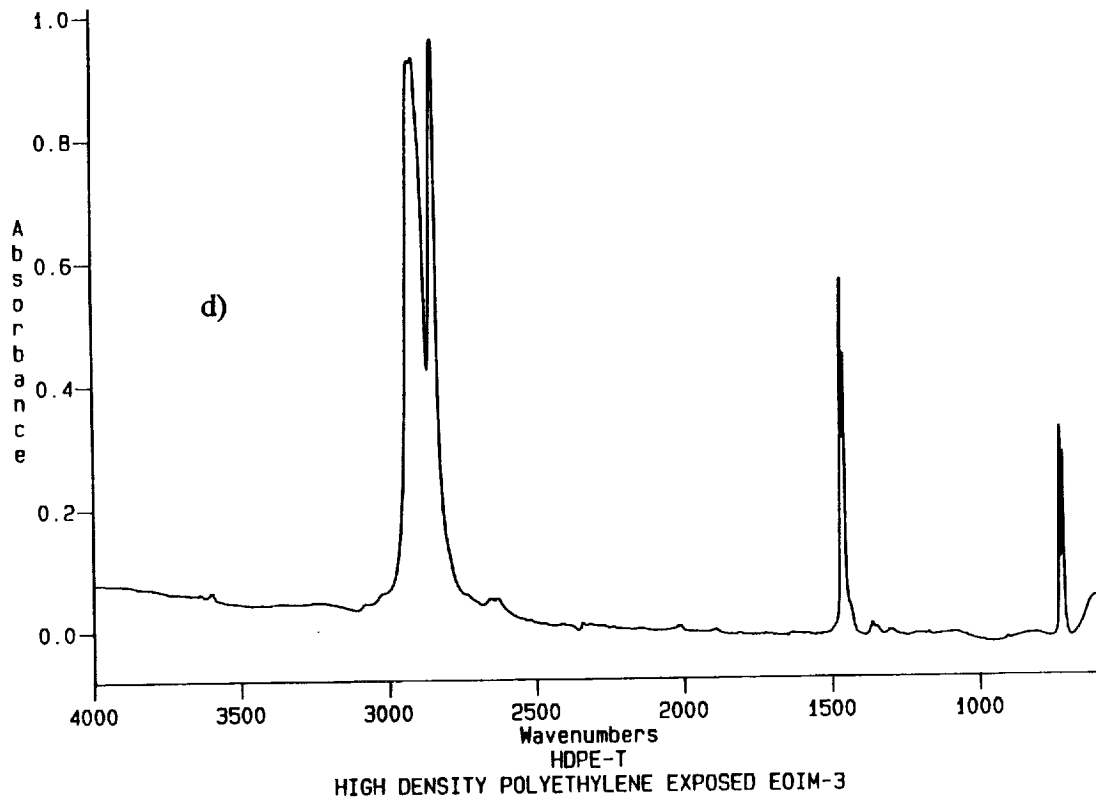
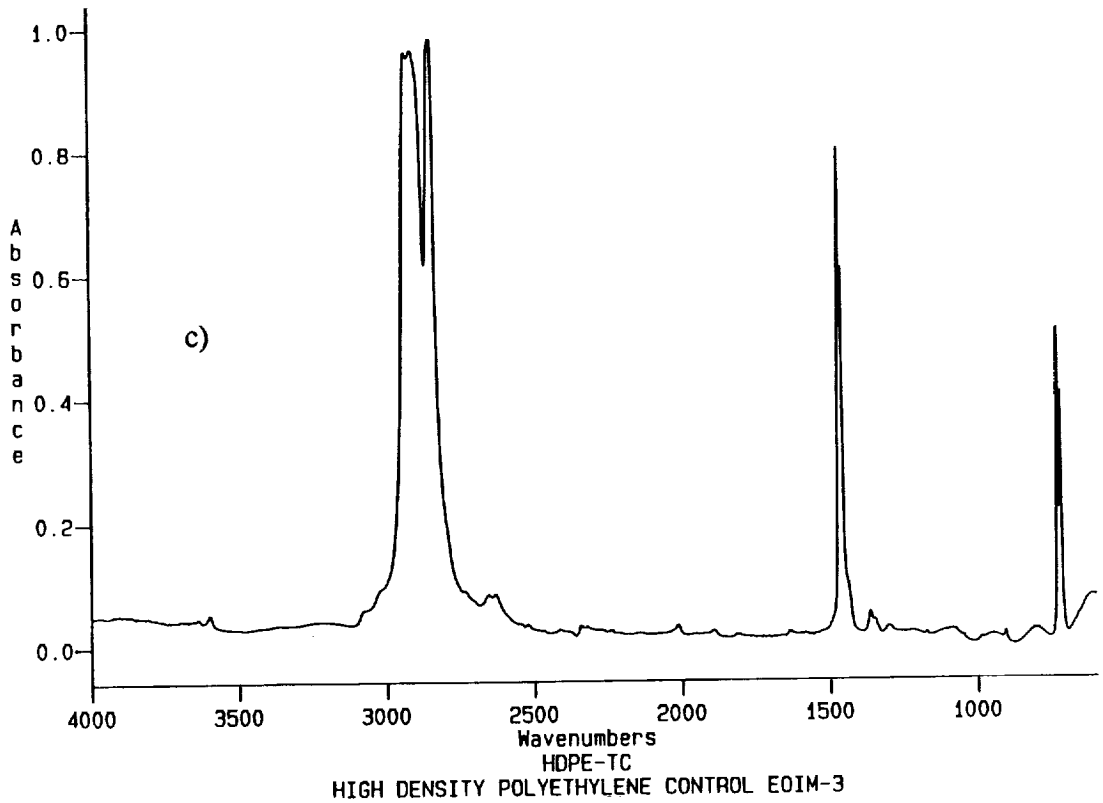


Figure 18: Typical infrared absorbance spectra of Kapton and polyethylene from EOIM-III: a) Kapton exposed to O atoms during EOIM-III, b) Kapton control, c) Polyethylene exposed to O atoms during EOIM-III, d) polyethylene control.

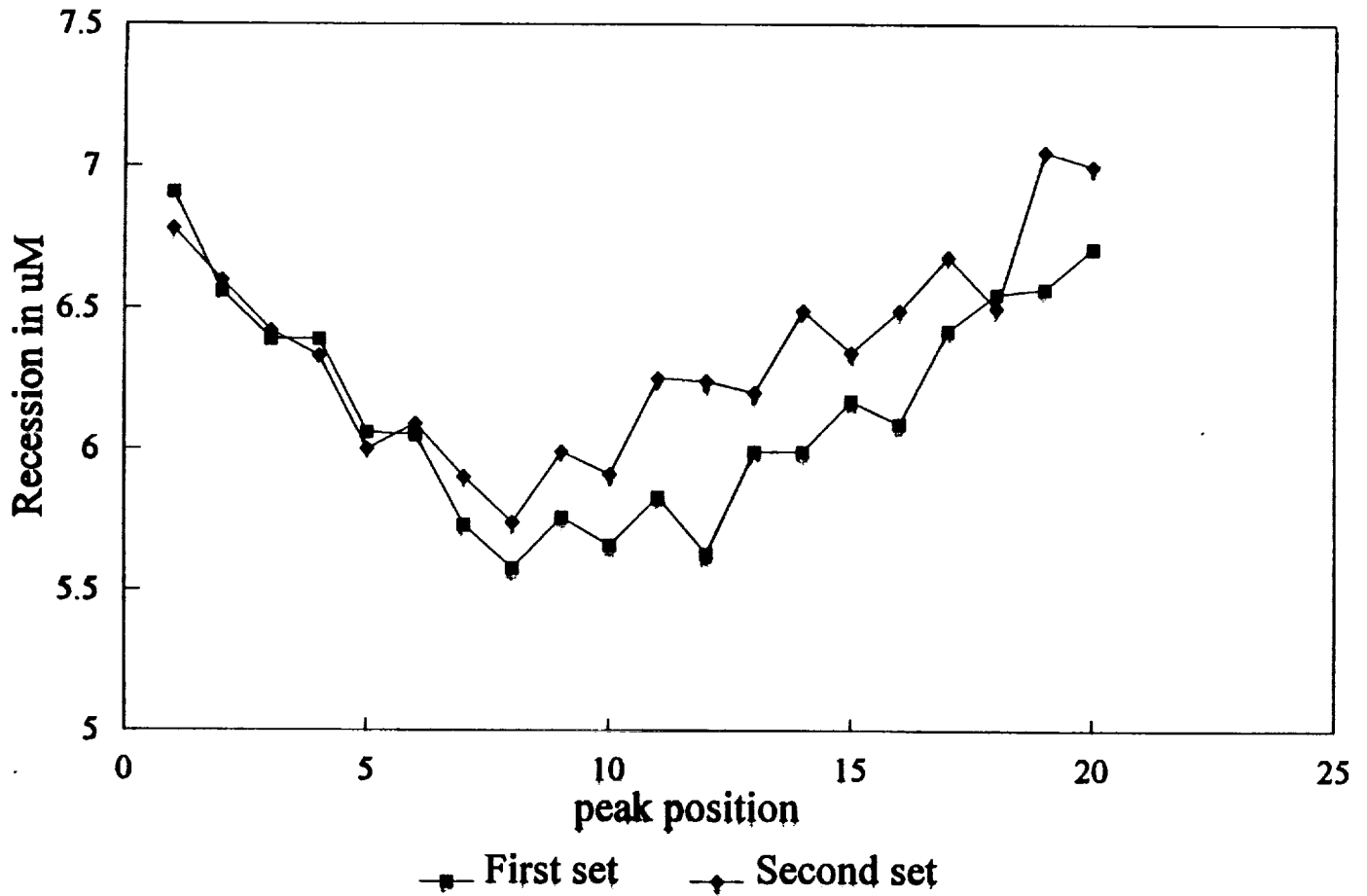


Figure 19: Configuration interaction between sample holders and ram O atoms revealed by profilometry of Kapton film specimens covered with a high transparency metal grid etch mask. Measured recession increases on moving toward the edge from the center of the sample as a result of atom scattering from the 45 degree bevel on the sample holder opening shown in the insert.

EVALUATION OF OXYGEN INTERACTIONS WITH MATERIALS III — MISSION AND INDUCED ENVIRONMENTS

Steven L. Koontz, Lubert J. Leger, Steven L. Rickman
NASA Lyndon B. Johnson Space Center, Houston, TX 77058
Phone: 713/483-5906, Fax: 713/483-2162

Charles L. Hakes, David T. Bui
Lockheed Engineering & Sciences Company, Houston, Texas 77058
Phone: 713/333-7804, Fax: 713/333-7727

Donald Hunton
USAF Phillips Laboratory, Hanscom Air Force Base, MA 01731
Phone: 617/377-4057, Fax: 617/377-7091

Jon B. Cross
Los Alamos National Laboratory, Los Alamos, NM 87545
Phone: 505/667-0511, Fax: 505/665-4631

ABSTRACT

The Evaluation of Oxygen Interactions with Materials III (EOIM-III) flight experiment was developed to obtain benchmark atomic oxygen/material reactivity data. The experiment was conducted during Space Shuttle mission 46 (STS-46), which flew July 31 to August 7, 1992. Quantitative interpretation of the materials reactivity measurements requires a complete and accurate definition of the space environment exposure, including the thermal history of the payload, the solar ultraviolet exposure, the atomic oxygen fluence, and any spacecraft outgassing contamination effects. The thermal history of the payload was measured using twelve thermocouple sensors placed behind selected samples and on the EOIM-III payload structure. The solar ultraviolet exposure history of the EOIM-III payload was determined by analysis of the as-flown orbit and vehicle attitude combined with daily average solar ultraviolet and vacuum ultraviolet (UV/VUV) fluxes. The atomic oxygen fluence was assessed in three different ways. First, the O-atom fluence was calculated using a program that incorporates the MSIS-86 atmospheric model, the as-flown Space Shuttle trajectory, and solar activity parameters. Second, the oxygen atom fluence was estimated directly from Kapton film erosion. Third, ambient oxygen atom measurements were made using the quadrupole mass spectrometer on the EOIM-III payload. Our best estimate of the oxygen atom fluence as of this writing is $2.3 \pm 0.3 \times 10^{20}$ atoms per square centimeter. Finally, results of post-flight X-ray photoelectron spectroscopy (XPS) surface analyses of selected samples indicate low levels of contamination on the payload surface.

INTRODUCTION

Previous studies^(ref. 1) of atomic oxygen reactivity with materials used on low-Earth-orbiting spacecraft have been based on material changes measured in the laboratory and normalized to atomic oxygen fluence as derived from spacecraft flight conditions and ambient density predictions (MSIS-86).^(refs. 2,3) Some questions regarding the validity of using long-term-based ambient density models for short-term flight experiments have arisen.^(refs. 4,5) In an attempt to resolve this uncertainty, the Evaluation of Oxygen Interactions with Materials III (EOIM-III) flight experiment was conducted on Space Shuttle mission 46 (STS-46), which flew July 31 to August 7, 1992. This paper presents a detailed description of the space environment exposure for STS-46 and the EOIM-III flight experiment. An overview of the EOIM-III flight measurements and supporting ground measurements is included in reference 6.

FLIGHT SUMMARY

The STS-46 mission altitudes and attitudes were scheduled to accommodate three primary payloads, of which the EOIM-III was sequentially the third and final. The orbital inclination was 28.5 degrees and the solar beta angle (the angle between the orbit plane and the Earth-Sun vector) varied between 17.5 and 24.3 degrees. The STS-46 altitudes as a function of Mission Elapsed Time (MET) are shown in figure 1. The highest (430 km) orbit, occurring from MET 0-70 hours, was flown to support the release of the European Retrievable Carrier (EURECA) satellite. The second (300 km) orbit, occurring from MET 70-140 hours, was for Tethered Satellite System (TSS) operations. The lowest (230 km) orbit supported the EOIM-III experiment, exposing the orbiter and all payloads to a far denser atmosphere than the earlier, higher orbits. The molecular density of the atmosphere at the EOIM-III altitude was approximately 10 times higher than the density at the TSS-deploy altitude, and approximately 100 times higher than the EURECA-release altitude. Because of the density increase at low altitudes and the non-ram orientations flown during most of the rest of the flight, approximately 95 percent of the total atomic oxygen fluence occurred during the EOIM-III portion of the mission.

The environmental exposure of the EOIM-III payload also depended on the attitude of the orbiter with respect to the direction of flight (ram direction), and with respect to the Sun. The attitude timeline in figure 2 shows the angle between the cargo bay normal (-Z in orbiter body coordinates) and the orbiter velocity vector. The angle shown in figure 2 runs from 0 degrees, corresponding to the -ZVV or ram orientation, to 180 degrees, corresponding to ZVV or anti-ram (heat shield into the velocity vector). The oscillations between 0 and 180 degrees visible during earlier parts of the mission correspond to inertial hold attitudes or roll maneuvers. The EURECA-release portion of the flight included periods of ram attitude and periods of a solar inertial hold, during which time the cargo bay was facing the Sun. The EOIM-III mass spectrometer was on for approximately 17 hours during this part of the flight. The TSS-deploy portion of the flight comprised mostly an "airplane mode" orientation, where the cargo bay was facing away from Earth. The mass spectrometer was on for about 4 hours during TSS operations.

THERMAL HISTORY

The thermal history of the EOIM-III payload was measured by 11 thermocouple sensors placed behind selected samples and on the EOIM-III payload structure, as shown in figure 3. Because of noise in the temperature data, and the large number of measurements from each sensor (one sample per second), the data were appropriately filtered and time-averaged before plotting. Figures 4.1 through 4.11 show the filtered output of the sensors. Temperature variations are consistent with vehicle flight conditions, with the hottest period for the passive plates occurring during the EURECA-release portion of the flight. Diurnal variations in temperature are visible in the data (note MET 100-130 hours on the

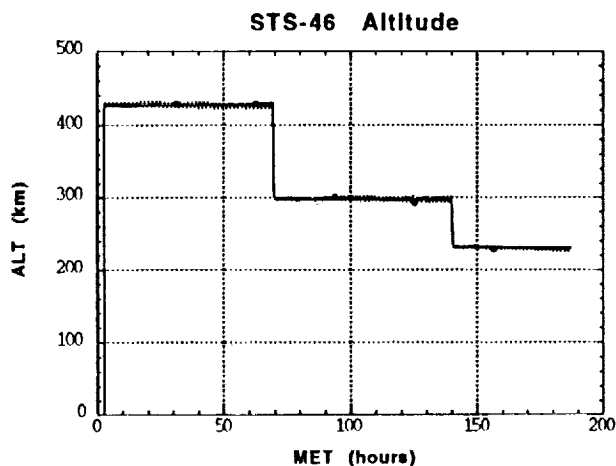


Figure 1 - STS-46 mission altitude timeline.

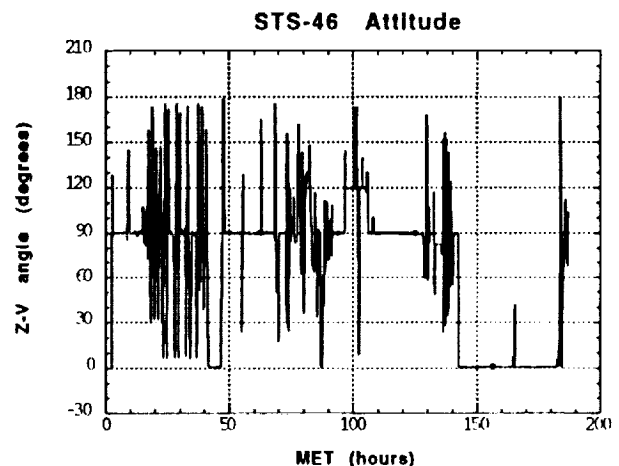


Figure 2 - STS-46 mission attitude timeline.

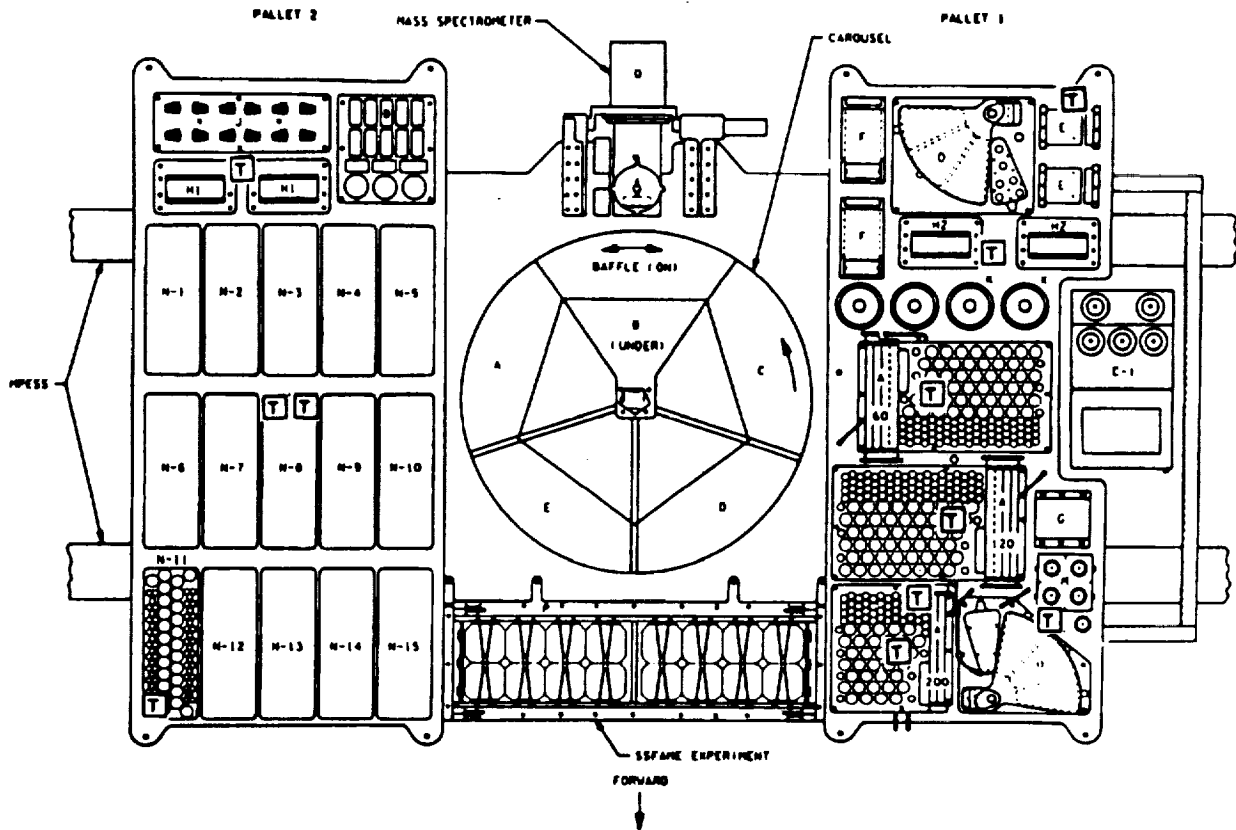


Figure 3 – EOIM-III Temperature sensor locations (marked with boxed T).

figures). Other temperature variations are due to vehicle attitude or operations of heaters on the temperature-controlled plates.

The thermal mass, thermal conductivity and thermo-optical properties of the thermocouple mounting assembly determine the temperature reported by the thermocouple sensor. This temperature is only an approximation of the temperature of any nearby materials samples. The effects of sample thermo-optical property variations can be gauged by a comparison of the two thermocouple readings from the

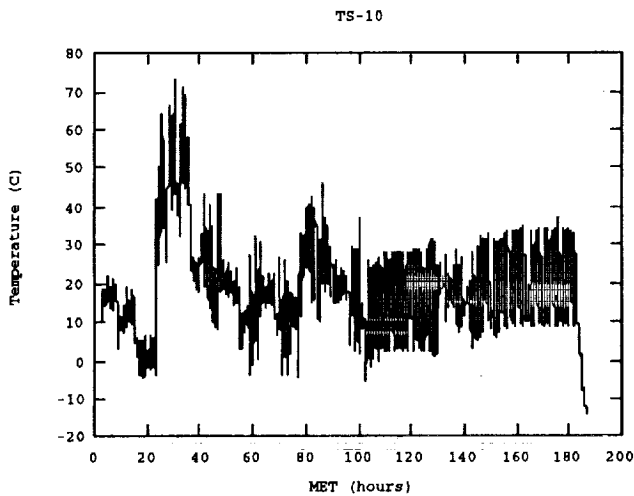


Figure 4.1 – Temperature recorded by the sensor on the Pallet 2 Sample Disk/Carrier N-8. The temperature sensor was mounted under aluminized Kapton film with the Kapton side up.

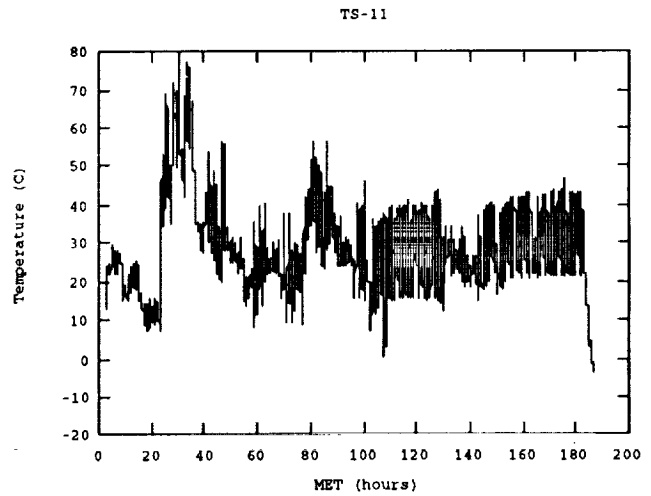


Figure 4.2 – Temperature recorded by the sensor on the Pallet 2 Sample Disk/Carrier N-8. The temperature sensor was mounted under aluminized Kapton film with the Aluminum side up.

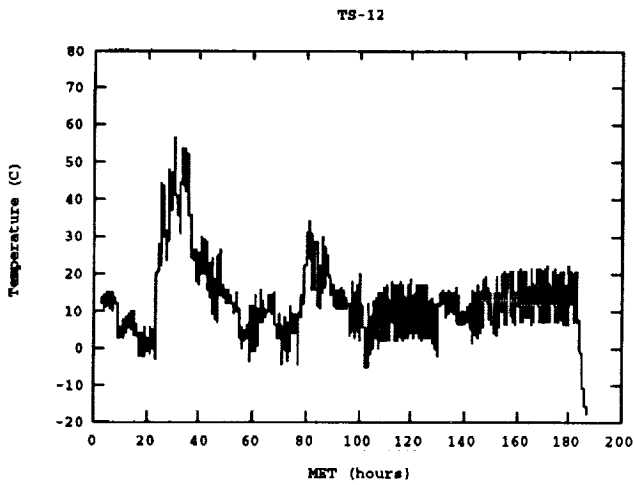


Figure 4.3 – Temperature recorded by the sensor on the Pallet 2 Sample Carrier N-11.

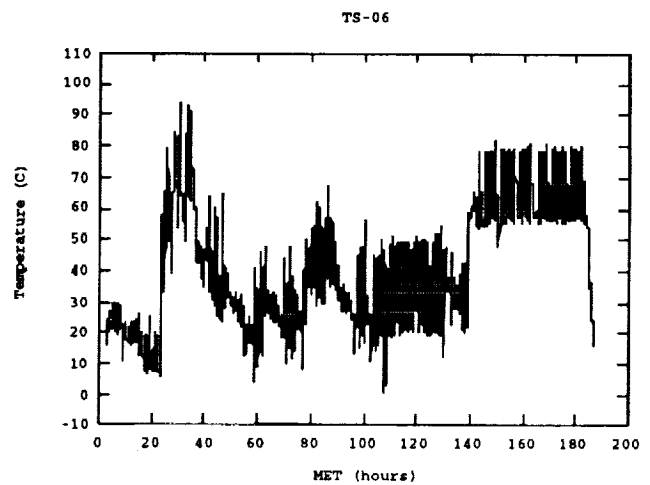


Figure 4.4 – Temperature recorded by the sensor on the Pallet 1 (60°C) heated plate at the sample disk.

Pallet 2 Sample Disk Carrier Number 8 sample cells, shown in figures 4.1 and 4.2. The physical configuration of the two thermocouple sensors was identical, except for sample thermo-optical properties, and the sensor assemblies were adjacent to each other on the sample carrier (adjacent sample cells). Thermo-optical properties were determined by the choice of sample material mounted on top of each sensor; aluminized Kapton film with the aluminum side up in one case ($\alpha = 0.12$, $\epsilon = 0.04$, $\alpha/\epsilon = 3$) and the Kapton side up in the other ($\alpha = 0.33$, $\epsilon = 0.82$, $\alpha/\epsilon = 0.4$). The effect of the rather large change in α/ϵ can be seen in figures 4.1 and 4.2, where the aluminum-side-up shows significantly higher temperatures throughout the mission. During the 42 hour EOIM-III period, the average temperatures were 30.6 degrees Centigrade and 20.0 degrees Centigrade for the aluminum-side-up sensor and the Kapton-side-up sensor respectively. The extremes of temperature resulting from diurnal variations in solar heating were from 16.5 to 47.0 degrees Centigrade for the aluminum-side-up sensor and from 5.3 to 36.9 degrees Centigrade for the Kapton-side-up sensor.

Thermocouple sensors on the 200 degree heated tray were placed both on the tray thermostat and in a sample holder cell. The thermo-optical properties for the sample cell sensor were determined by an anodized aluminum disk that was identical to the rest of the payload aluminum, so that any differences between the sensor readings were due to configuration interactions alone. As shown in figures 4.6 and 4.7, the thermostat sensor on the 200 degree tray shows a much smaller diurnal temperature variation and a significantly higher mean temperature than the sample cell sensor. The mean, maximum, and minimum temperatures during the EOIM-III exposure (excluding the large temperature drop that

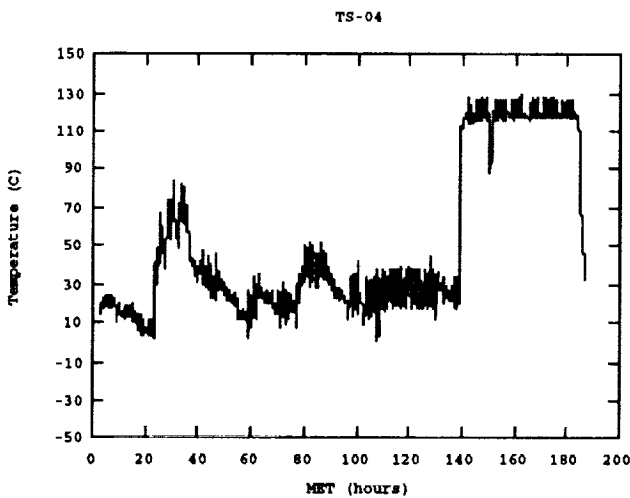


Figure 4.5 – Temperature recorded by the sensor on the Pallet 1 (120°C) heated plate at the sample disk.

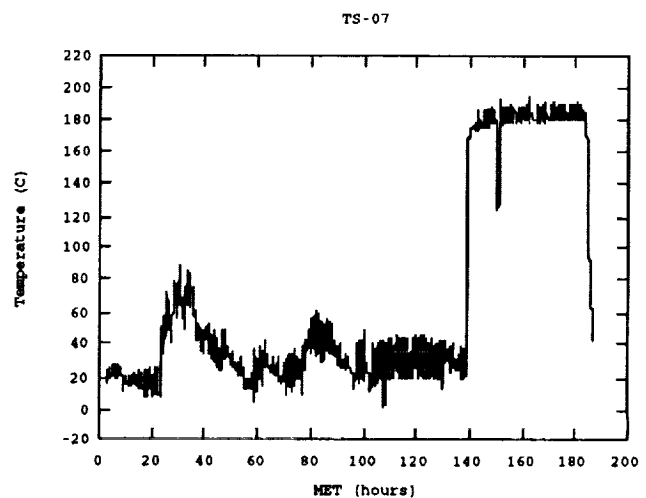


Figure 4.6 – Temperature recorded by the sensor on the Pallet 1 (200°C) heated plate at the sample disk.

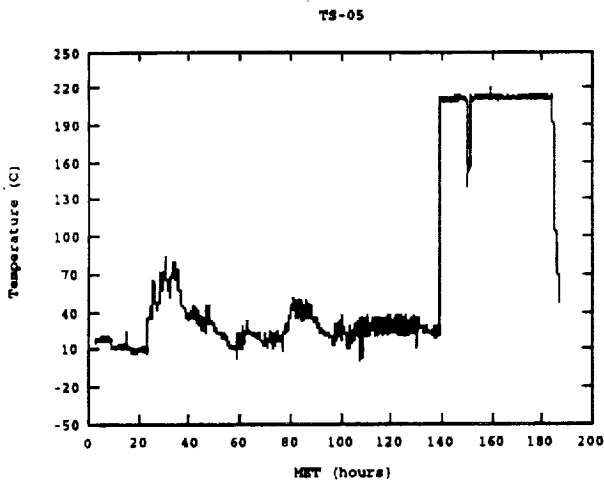


Figure 4.7 – Temperature recorded by the sensor on the Pallet 1 (200°C) heated plate at the thermostat.

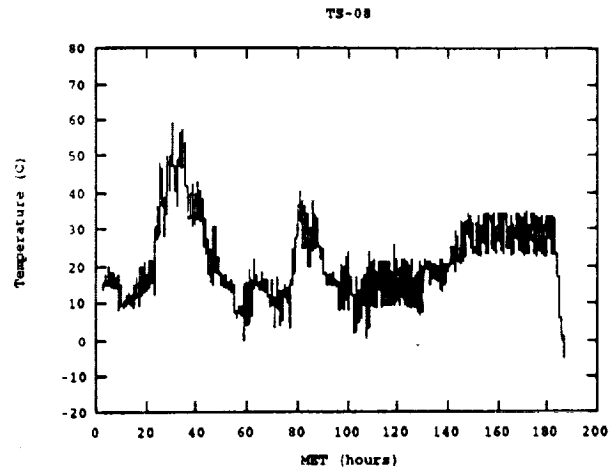


Figure 4.10 – Temperature recorded by the sensor on the Pallet 1 Scatterometer (Aerospace).

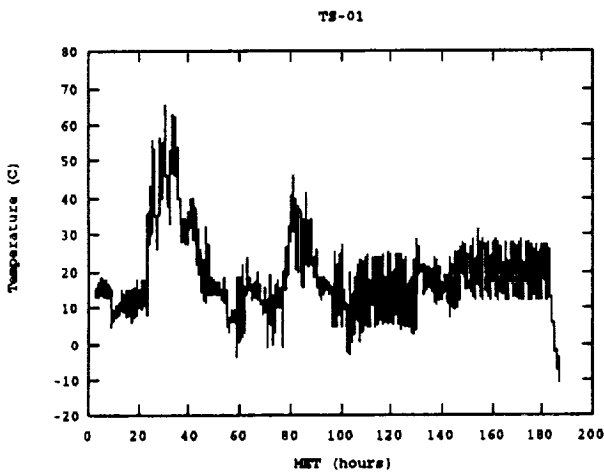


Figure 4.8 – Temperature recorded by the sensor on the Pallet 1 Static Stress Fixture (MSFC).

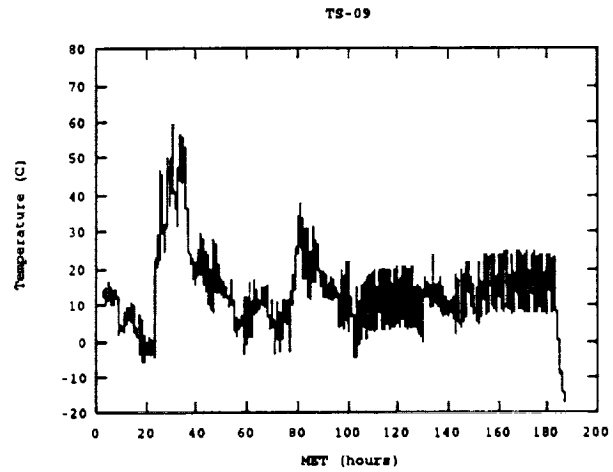


Figure 4.11 – Temperature recorded by the sensor on the Pallet 2 Composite Stress Fixture (LaRC).

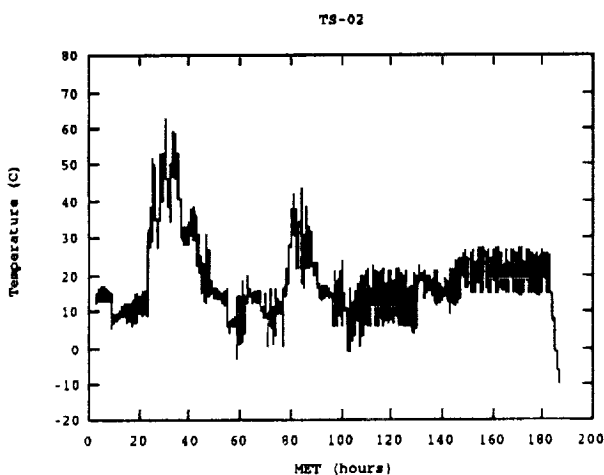


Figure 4.9 – Temperature recorded by the sensor on the Pallet 1 Composite Stress Fixture (JSC).

occurred when the heater was off near MET 150 hours) were 212.0, 210.2, 215.1 degrees Centigrade for the thermostat sensor and 183.7, 179.3, 191.7 degrees Centigrade for the sample cell sensor.

SOLAR UV/VUV EXPOSURE

An analytical determination of the equivalent Sun hours (the energy received by a surface with the Sun normally incident to it for 1 hour) experienced by the EOIM-III payload was performed in order to determine the solar ultraviolet and vacuum ultraviolet (UV/VUV) doses to exposed materials. EOIM-III operations consisted of only a few attitudes. Prior to EOIM-III operations, however, numerous

attitudes were flown. Hence, two different methods were used to calculate the solar exposure.

The Thermal Interactive Mission Evaluation System (TIMES89)^(ref. 7) computer program was used to characterize the solar exposure in the period prior to EOIM-III experiment operations. This program allows analysis of unshadowed sensing surfaces as they move and re-orient throughout their orbit. The solar irradiance on the experiment was calculated using the as-flown mission attitude timeline and the known orbit parameters. While all major attitudes were analyzed (both local vertical-local horizontal and inertially referenced), simplifying assumptions in the TIMES89 code prohibit modeling of attitude-to-attitude transitions. Thus, exposure during these periods was approximated by holding the previous attitude until halfway through the transition period and then instantaneously switching to the new attitude. The unshadowed sample surface assumption should hold reasonably well for this configuration as the Sun sensor was located high in the cargo bay and had few potential solar illumination blockers.

For the period of time encompassing EOIM-III operations, the cargo bay was facing into the velocity vector direction and the majority of the time was spent in either a biased tail-to-Earth or nose-to-Earth attitude. Since this period of time was of specific interest, a more detailed assessment of the potential blockage by orbiter components was performed. A detailed geometric model of the configuration was used and the location of the onset of solar blockage was assessed based on line-of-sight considerations using the Thermal Synthesizer System (TSS) software.^(ref. 8) These data were used in conjunction with the following equation to determine the accumulated solar flux:

$$F_{ACC} = S \cos \beta \int_{\alpha_1}^{\alpha_2} (-\sin \alpha \, d\alpha) = S \cos \beta [\cos \alpha]_{\alpha_1}^{\alpha_2}$$

where... F_{ACC} is the accumulated direct solar flux;
 S is the solar flux (assumed unity here, so that F_{ACC} is essentially a scaling factor);
 α_1 is the terminator exit angle;
 α_2 is the orbit angle where blockage begins;
 β is the angle between the solar vector and the orbit plane (assumed constant over a single orbit).

Note that this equation applies only to the case where the orbiter cargo bay faces into the velocity vector direction. Also, for all locations other than between the orbit angles α_1 and α_2 , $F_{ACC} = 0$ due to blockage or angles greater than 90 degrees with respect to the solar vector.

If the accumulated direct solar flux is divided by the product of the solar constant and the orbit

Table 1 – Solar Ultraviolet Exposure History

Mission Days*	Sun Hours	250-200 nm mW/cm ²	200-150 nm mW/cm ²	150-119 nm mW/cm ²	121.5 nm mW/cm ²	119-10 nm mW/cm ²
0 - 2.0	5.8	2.00x10 ⁻¹	9.82x10 ⁻³	1.10x10 ⁻³	8.81x10 ⁻⁴	3.4x10 ⁻⁴
2.0 - 4.0	6.8	2.01x10 ⁻¹	9.85x10 ⁻³	1.13x10 ⁻³	9.10x10 ⁻⁴	3.6x10 ⁻⁴
4.0 - 5.8	10.4	2.01x10 ⁻¹	9.89x10 ⁻³	1.16x10 ⁻³	9.31x10 ⁻⁴	3.7x10 ⁻⁴
5.8 - 6.0†	0.5	2.02x10 ⁻¹	9.93x10 ⁻³	1.17x10 ⁻³	9.45x10 ⁻⁴	3.7x10 ⁻⁴
6.0 - 7.0†	4.4	2.02x10 ⁻¹	9.95x10 ⁻³	1.18x10 ⁻³	9.51x10 ⁻⁴	3.8x10 ⁻⁴
7.0 - 8.0†	3.0	2.02x10 ⁻¹	9.99x10 ⁻³	1.19x10 ⁻³	9.63x10 ⁻⁴	3.8x10 ⁻⁴
	Hours	J/cm ²	J/cm ²	J/cm ²	J/cm ²	J/cm ²
Cumulative	30.9	22.4	1.10	.128	.103	.04

* Mission-elapsed time in days. The numbers shown represent the beginning time and end time of the measurement interval in days.

† EOIM-III exposure period.

period, the result is equivalent Sun hours. The solar exposure is calculated by multiplying the equivalent sun hours by the UV/VUV fluxes measured by the Solar-Stellar Comparison Experiment 1 (SOLSTICE)(refs. 9,10,11) on the Upper Atmosphere Research Satellite (UARS). The resulting solar exposure values are presented in table 1. It should be noted that the short wavelength limit for SOLSTICE is 119nm, so the interval 119 to 10 nm are not measurements, but are from a model that uses the solar 10.7 cm radio flux.(ref. 12) Due to the shape of the solar spectrum, the 150-200 nm irradiance consists of about 80 percent from the 180-200 nm flux, and the 119-150 nm irradiance consists of about 80 percent from the Lyman- α flux at 121.5 nm. The 1- σ uncertainty for UARS measurements is 5 percent, and the 1- σ uncertainty for the extreme ultraviolet model results is 30 percent.

ATOMIC OXYGEN FLUENCE

The atomic oxygen fluence is determined in three different ways. First, the AOFLUX computer program(ref. 13), which incorporates the MSIS-86 atmospheric model and the as-flown Space Shuttle trajectory, was used to calculate oxygen atom fluence. Second, the oxygen atom fluence was measured directly from Kapton film erosion, as corrected for configuration interactions produced by the sample holder. The Kapton film erosion measurements are discussed in detail in reference 6. Finally, ambient oxygen atom measurements were made using a mass spectrometer that was calibrated before and after the mission in the High Velocity O-atom Beam (HVAB) system at the Los Alamos National Laboratory (LANL).(ref. 14) All fluence estimates are summarized in table 3.

AOFLUX Calculations

The AOFLUX program(ref. 13), written to calculate the expected O-atom fluence, was based on the MSIS-86 atmospheric model(refs. 2,3) and the as-flown timeline, which included the altitude, latitude and longitude. Solar activity parameters recorded during STS-46 at the Space Environment Services Center (National Oceanic and Atmospheric Administration) were used to account for the magnetic substorm activity observed during EOIM-III. Mission-specific values for the daily-average A_p geomagnetic activity and the daily solar F10.7 values are given in table 2.(ref. 15)

The O-atom densities calculated from MSIS-86 were used with the velocity of the spacecraft to calculate the total flux to the spacecraft. Integrating the total flux throughout the mission gives a total fluence to the spacecraft (before orientation effects are included) of 3.4×10^{20} O-atoms/cm². The total flux at each time increment was multiplied by the cosine of the ram angle (shown in figure 2) to obtain the net flux to the EOIM-III payload (shown in figure 5). Note that the fluxes for angles greater than 90 degrees were simply set to zero. By integrating the net flux throughout the mission, the fluence to the EOIM-III payload is calculated to be 2.3×10^{20} O-atoms/cm² (see table 3). Ninety-five percent of this net fluence occurs during the low-altitude ram orientation, as can be seen in figure 5.

Kapton Recession Measurements

Measurements of Kapton polyimide surface recession or weight loss made following several previous Low Earth Orbit (LEO) flight experiments(refs. 4,16,17) have produced the widely accepted value of the Kapton reaction efficiency of $3.0 \pm 0.3 \times 10^{-24}$ cm³/atom. MSIS-86 was used to calculate the O-atom fluence needed to calculate polymer reaction efficiencies in all previous LEO flight experiments. In order to determine the EOIM-III O-atom fluence using Kapton surface recession or weight loss measurements, without referring indirectly to MSIS-86 calculations, an

Table 2 – Daily-Average A_p Geomagnetic Activity Values and the Daily Solar F10.7 Microwave Flux Values Used in the AOFLUX/MSIS-86 Calculations(ref. 15)

Date	Daily A_p	Daily F10.7	90 day average F10.7
07/31/1992	11	103.0	125.0
08/01/1992	09	110.0	125.0
08/02/1992	06	125.0	124.0
08/03/1992	05	131.0	124.0
08/04/1992	13	131.0	124.0
08/05/1992	43	131.0	124.0
08/06/1992	19	138.0	124.0
08/07/1992	42	141.0	125.0
08/08/1992	22	144.0	125.0

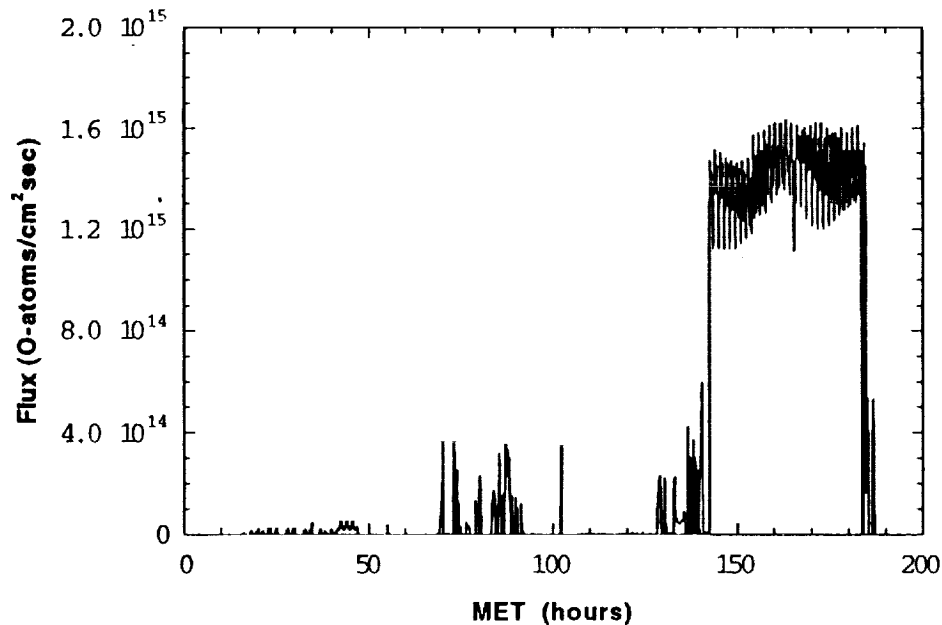


Figure 5 – Atomic oxygen flux on the EOIM-III payload during STS-46, as calculated using the MSIS-86 atmospheric model with daily average Λ_p and F10.7 values. Note the magnitude of the diurnal variations during the ram period between hours 142 and 185.

independent measurement of Kapton reaction efficiency was conducted in the HVAB at LANL as described in reference 6. The EOIM-III O-atom fluence based on the LANL measurement of the Kapton polyimide reaction efficiency is $2.3 \pm 0.07 \times 10^{20}$ atoms/cm² based on weight loss and $2.4 \pm 0.09 \times 10^{20}$ O-atoms/cm² based on surface recession measured by profilometry. The various O-atom fluence determinations for EOIM-III are summarized in table 3 where it can be seen that MSIS-86 calculations, mass spectrometer measurements and Kapton weight loss or profilometry measurements produce nearly identical fluence determinations.

Mass Spectrometer Measurements

The EOIM-III quadrupole ion/neutral mass spectrometer^(ref. 18) scanned a mass to charge ratio range of 0 to 72 amu/unit charge every 5.12 seconds with a digital resolution of 0.142 M/e/channel (512 digital data channels corresponding to 0-72 amu/unit charge). The mass spectrometer resolution ($\Delta M/M$) calculated as mass peak width (full width at half maximum) at mass 28 was .011 throughout the mission and during the pre and post flight calibrations. The mass spectrometer output signal was logarithmically amplified, which permitted the display of seven orders of magnitude in mass spectrometer detector current in a 0 to 5 volt analog signal that was then digitized with an 8-bit analog-to-digital converter. Mass spectra were produced in either ion or neutral operating mode. In neutral mode, a repeller grid excluded naturally occurring ionospheric ions and neutral gaseous species entering the ion source were ionized by electron impact. In ion mode, the repeller grid and the filaments producing electrons for electron impact ionization were shut off and naturally occurring ionospheric ions entering the ion source volume were mass analyzed and detected.

Approximately 46,000 mass spectra were recorded during STS-46. Prior to the beginning of EOIM-III operations, the mass spectrometer operated in the ion and neutral mode in alternating one minute time periods. During EOIM-III operations, ion and neutral mass spectra were recorded according to a predetermined sequence which also involved periodic observation of the gaseous and plasma environments in the various carousel sectors. For a comparison of mass spectrometer to MSIS-86 data, it is useful to calculate the MSIS-86 fluence during the time that the mass spectrometer was on, tilted up, and measuring neutral species. The on-time MSIS-86 fluence is 1.1×10^{20} O-atoms/cm², or 48 percent of the net MSIS-calculated fluence.

The primary objective of the EOIM-III mass spectrometer experiment was to measure the O-atom fluence for comparison with the fluence calculated using the MSIS-86 model of the thermosphere. The mass spectrometer was subjected to an extensive calibration process both before and after the flight (ref. 14) to permit accurate quantitative estimates of O-atom flux and fluence from the mass spectrometer data. The O-atom fluence was determined from the mass spectrometer data as follows. First, the mass spectrometer data were divided into 5-minute intervals corresponding to the 5-minute intervals used in the MSIS-86 calculations. Within each 5-minute interval, all complete, valid spectra appropriate for use in neutral flux and fluence calculations were averaged. Figure 6 shows a typical 5-minute-average spectrum taken early in the EOIM-III ram exposure period. Figure 7 shows an overview of the 5-minute-average spectra taken throughout STS-46. In figure 7, an additional averaging of 12 adjacent 5-minute-average spectra was included to reduce the line density of the plot.

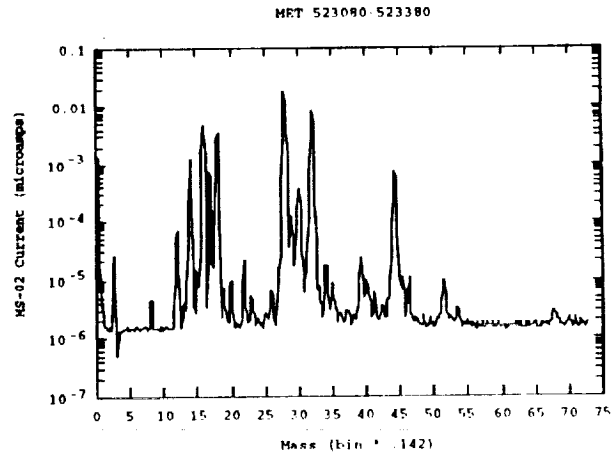


Figure 6 – A typical five-minute-average spectrum from the early part of the low altitude ram period.

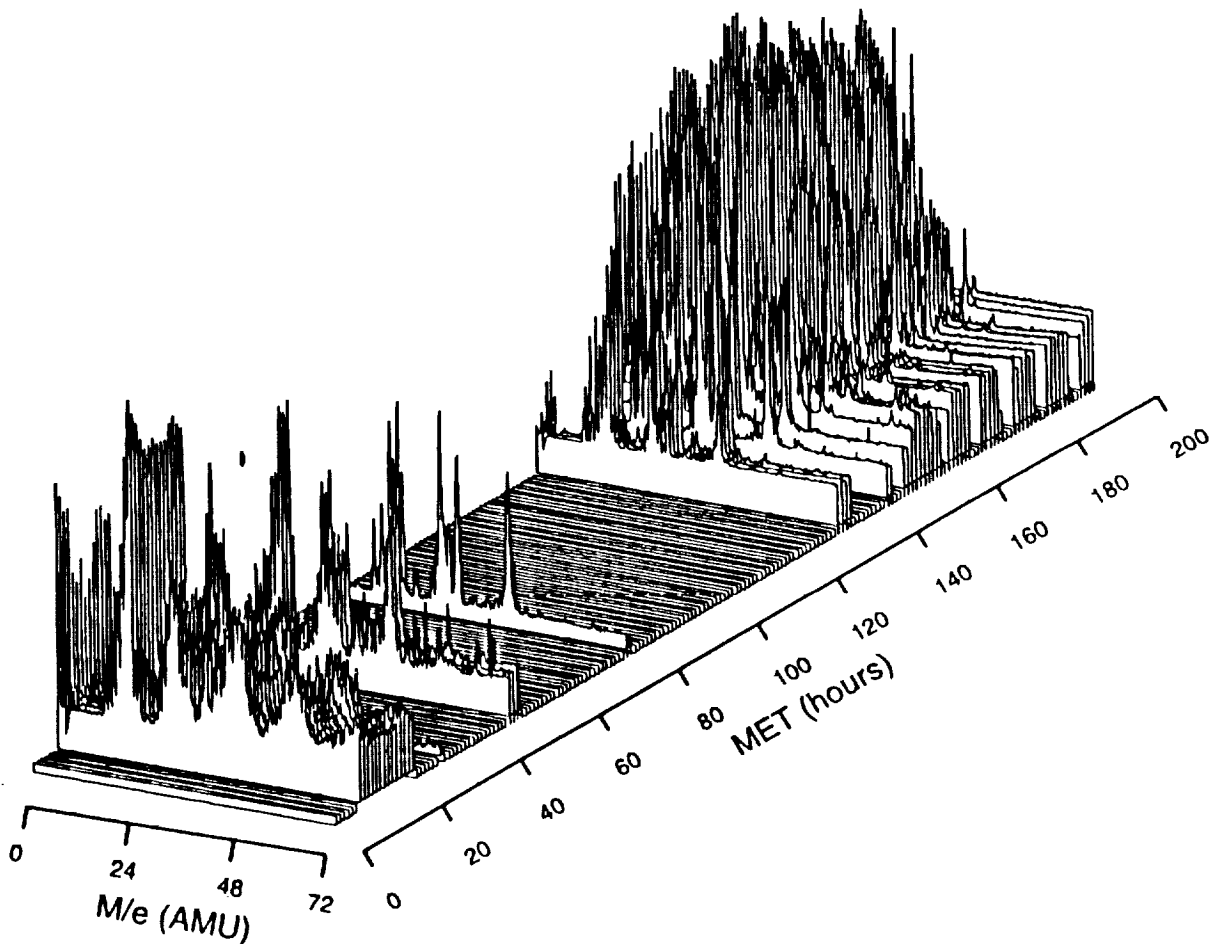


Figure 7 – Neutral spectra from the EOIM-III mass spectrometer. The data have been averaged into 1-hour time blocks for a qualitative view of the entire STS-46 mission. The start of the mission is towards the front of the picture, and flat lines indicate the times when the mass spectrometer was either turned off, facing the carousel, or in ion mode.

The 5-minute-average spectra were used to calculate O-atom fluence. Mass peak areas (peak sums), not peak heights, were used throughout in order to obtain the best possible signal to noise ratio. Peak sums, which retained the units of Amperes, were calculated by summing the mass spectrometer signal amplitude in the seven adjacent digital data channels containing a mass peak. The unmodified peak sums for the $M/e = 16$, 28, and 32 peaks (O, N_2 , and O_2) are shown in figures 8 through 10. To calculate the O-atom flux, the peak sum at $M/e = 16$ was corrected for contributions from $M/e = 16$ fragment ions from molecular oxygen and water by subtracting 26 percent of the $M/e = 32$ (O_2) peak sum and 1.7 percent of the $M/e = 18$ (H_2O) peak sum, as shown in figure 12. The O-atom flux that produced each 5-minute-average spectrum was then calculated by multiplying the corrected $M/e = 16$ peak sum by a calibration function described below. The O-atom fluence was then determined by adding up the fluences for the various 5-minute periods.

The calibration function was derived from both ground based calibration of the mass spectrometer in the HVAB at LANL and mass spectrometer performance data from STS-46 itself. The EOIM-III mass spectrometer showed an O-atom fluence dependent sensitivity decay both in the HVAB at LANL and during STS-46. However, different sensitivity decay functions were observed in the lab and on orbit as shown in figure 11. For this reason, the zero-fluence O-atom flux calibration factor determined in the HVAB at LANL was used with an empirical sensitivity decay function derived from a fit to the corrected $M/e = 16$ peak sum data from STS-46 to produce the calibration function:

$$y = \frac{0.006}{0.0047968 - 0.0022472 \cdot \log(\text{MET} - 142.5)}$$

Using this calibration function, the corrected O-atom peak sums, and the percentage of mass spectrometer on-time, the measured EOIM-III mission fluence is $2.3 \pm 0.7 \times 10^{20}$ O-atoms/cm².

The EOIM-III mass spectrometer was calibrated for direct measurement of high velocity O-atom flux both before and after flight on STS-46 in the HVAB at LANL. Details of the calibration methodology, and a summary of calibration methods and results have been reported previously (ref. 14). Calibration studies were conducted over a period of several years

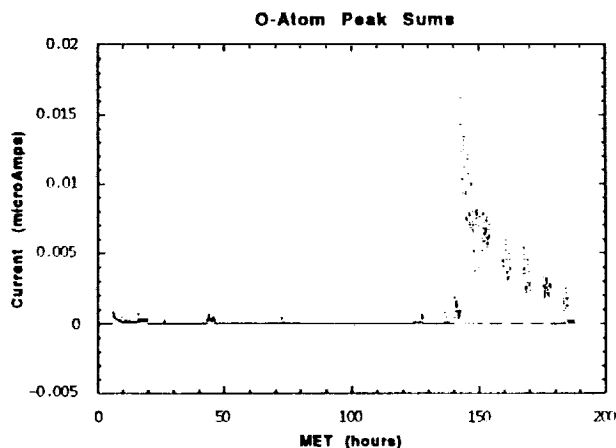


Figure 8 – O-atom ($e/M=16$) current measured by the mass spectrometer.

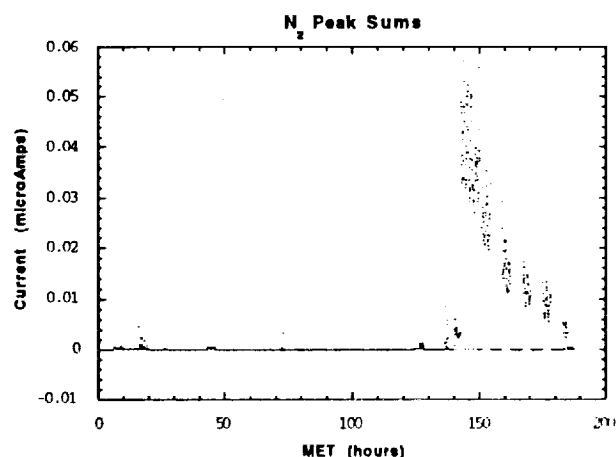


Figure 9 – N_2 ($e/M=28$) current measured by the mass spectrometer.

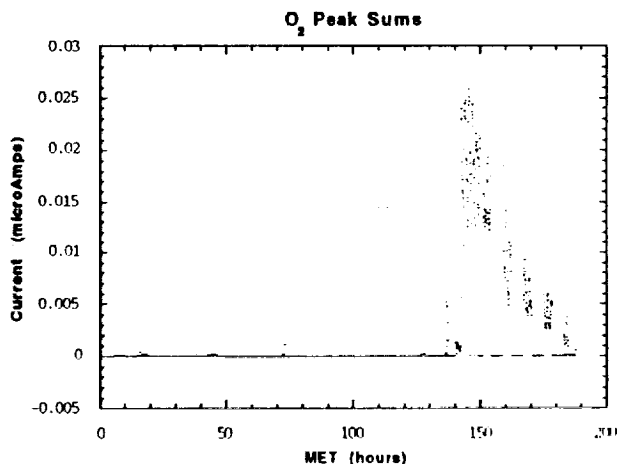


Figure 10 – O_2 ($e/M=32$) current measured by the mass spectrometer.

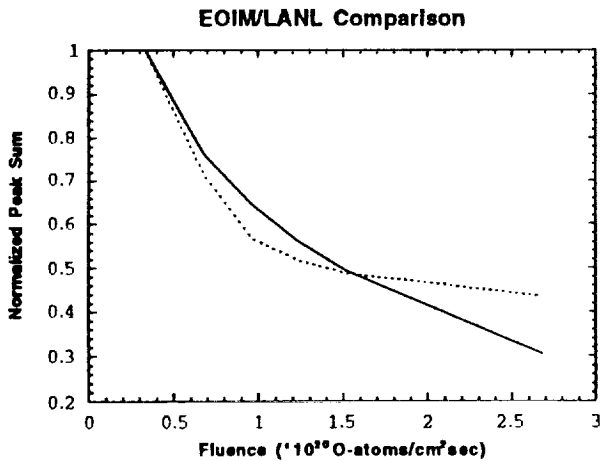


Figure 11- Comparison of O-atom peak decay during flight and laboratory exposure.

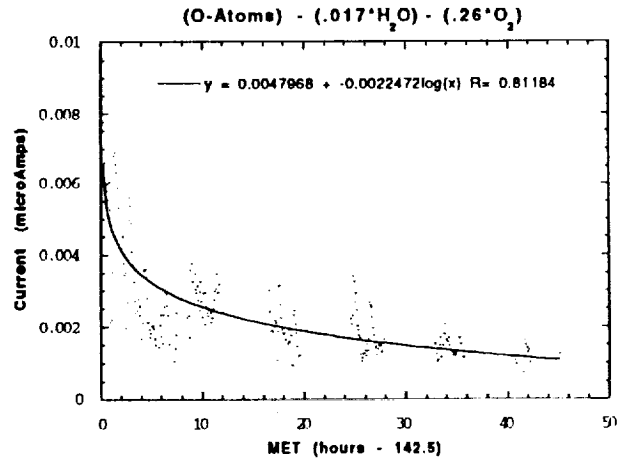


Figure 12 - Logarithmic fit to the corrected O-atom peak as a function of MET after 142.5 hours.

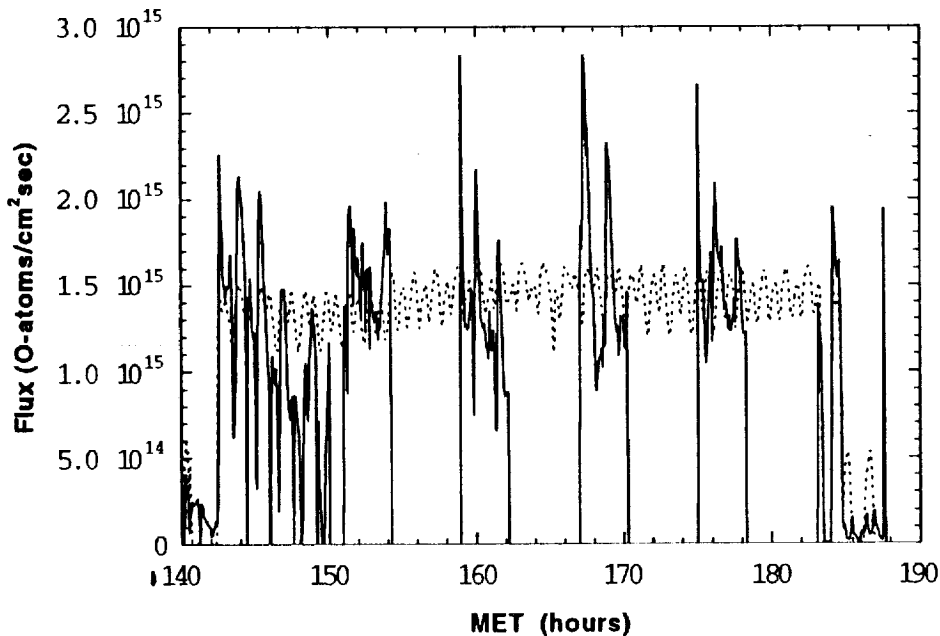


Figure 13 - Atomic oxygen flux calculated using the empirical fit to the O-atom peak (solid line). For comparison, the MSIS-86 flux is shown (dashed line).

prior to STS-46 as well as after the mission. In general the EOIM-III mass spectrometer showed excellent stability with the O-atom flux at low O-atom fluence, showing a maximum variation of 5 percent and the partial pressure sensitivity for nitrogen gas varying by less than 10 percent. Some changes in the fragmentation yield of O_2^+ were, however, observed so that the 10 percent correction factor reported in reference 14 was increased to 26 percent for O-atom fluence calculations as a result of thermal gas calibration measurements conducted prior to and just after STS-46. It should be noted that the calibration results reported in reference 14 were obtained before the O-atom fluence sensitivity decay was observed. A more complete description of mass spectrometer calibration is forthcoming.

EOIM-III CONTAMINATION

Since atomic oxygen effects are affected by contamination, deposits on sample surfaces were measured both in flight and post flight. In flight measurements were made using quartz crystal

Table 3 – Summary of EOIM-III Atomic Oxygen Fluence Estimates

Measurement Method	Fluence	Measurement Uncertainty
AOFLUX (MSIS-86) calculation	2.3×10^{20}	$\pm 0.35 \times 10^{20}$ (15% estimated from MSIS)
Kapton Erosion Weight Loss (3 Samples)	2.34×10^{20}	$\pm 0.07 \times 10^{20}$ (weight loss uncertainty)
Kapton Erosion Profilometry (4 Samples)	2.41×10^{20}	$\pm 0.09 \times 10^{20}$ (profilometry uncertainty)
Mass Spectrometer - Empirical Calibration from In-Flight Data	2.3×10^{20}	(TBD)

microbalances (QCMs) in the Environment Monitor Package (EMP) provided by Goddard Spaceflight Center. (ref. 19) The EMP contained five QCMs — four coated with reactive materials and one not overcoated — and was located to the side of pallet one as shown on the right in figure 3. Response from the uncoated crystal for the entire mission is shown in figure 14 and is representative of the response of all five microbalances. A large amount of contamination (~ several thousand Angstroms) is indicated and most of the deposition occurs during the EOIM-III portion of flight. Because of the inconsistency of these results with the numerous post flight XPS surface analyses which show only small amounts of contamination on the top plates of the experiment, it is expected that the EMP was contaminated from a source below the pallet top, but within the EOIM-III hardware.

**EMP QCM #1 DEPOSITION
UNCOATED CRYSTAL**

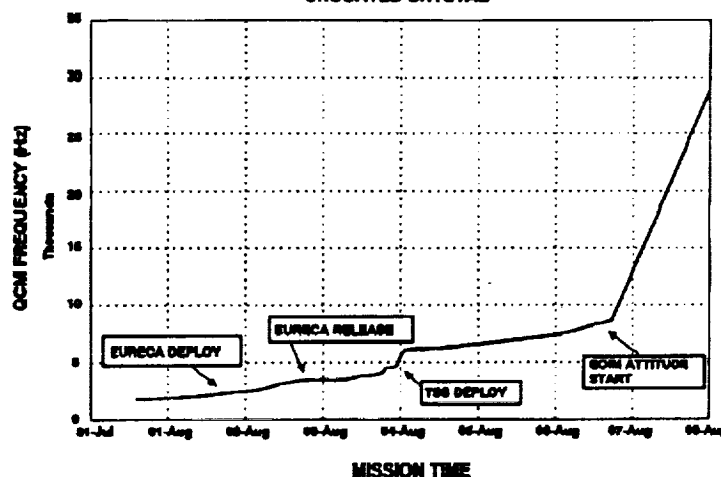


Figure 14 – EMP QCM #1 (uncoated crystal) frequency change during the flight.

The results of the post flight contamination survey of the EOIM-III payload are shown in table 4. X-ray photoelectron spectroscopy (XPS) was used to provide measurements of the elemental composition and state of chemical combination of the near-surface region (10-50 Angstroms from the surface) of the sample. Samples were surveyed for a variety of elements but only silicon was identified as different from the substrate composition and is reported in table 4. For all the surfaces measured, the substrate elements were evident in the XPS spectra indicating that the contaminant layer was less than 20 Angstroms. It can be concluded from the XPS results that a small amount of contamination did deposit on the experiment top pallets but is insignificant and should not affect the atomic oxygen measurements.

Additional evidence confirming the relatively low levels of contamination occurring on EOIM-III samples are the measured reaction efficiencies of Kapton and other polymer films which were in good agreement with measurements made on STS-8 and STS-41 and LDEF, as well as the performance of the atomic oxygen monitors (AOMs) provided by Marshall Space Flight Center. (ref. 20) The AOM consisted of an array of thin film carbon resistors which showed increasing resistance as the carbon is removed by O-atom reaction. The AOMs showed a constant or slightly increasing rate of resistance change throughout the EOIM-III ram period which would not be observed if a coating of SiO₂ were accumulating on the carbon resistor surfaces at the rates indicated by the EMP.

Table 4 – EOIM-III X-ray Photoelectron Spectroscopy contamination survey

PAYLOAD LOCATION	SAMPLE TYPE	ATOM % Si
mass spec. ram	Silver/Teflon	4.4
mass spec. payload bay view	Silver/Teflon	12.2
mass spec. starboard	Silver/Teflon	0.0
mass spec. ram	Kapton tape (exposed)	3.2
mass spec. ram	Kapton tape (unexposed)	0.0
VET mount	steel washer (exposed)	2.7
SUV mount	steel washer (exposed)	0.0
60° C tray	steel ground strap	3.8
	polysulfone (exposed)	0.8
	polysulfone (unexposed)	0.0
	Mylar-A (exposed)	2.4
	Mylar-A (unexposed)	0.0
	aluminum	7.1
120° C tray	steel washer	7.7
	Kapton (exposed)	2.0
	Kapton (unexposed)	0.0
	aluminum	9.4
	aluminum	6.6
passive tray 7&8	7 polymer films	3.8 ± 2.6

SUMMARY AND CONCLUSIONS

A detailed characterization of the EOIM-III materials exposure environment has been completed. The atomic oxygen fluence calculated using the MSIS-86 model of the thermosphere and as-flown Space Shuttle trajectory data (combined with the daily measurements of the solar activity and geomagnetic indices) is in good agreement with mass spectrometer and O-atom dosimeter measurements made during STS-46. Temperature measurements made during EOIM-III provide a complete thermal history of the payload and provide the investigators with useful sample temperature histories. UARS investigators provided solar UV and VUV measurements which, combined with the STS-46 trajectory and vehicle attitude data, allow calculation of net solar UV and VUV radiation doses to the EOIM-III materials samples. Post flight XPS analysis of materials samples as well as in-flight performance of the AOM both demonstrate that contamination of EOIM-III was, in fact, nominal and in no way interfered with the scientific and programmatic objectives of the payload. The severe contamination indicated by the TQCM sensors in the EMP component of EOIM-III was localized in the immediate vicinity of the EMP.

The detailed characterization of LEO exposure conditions during STS-46 reported above provides the investigator community with the necessary foundation for a complete interpretation of the effects of the LEO space environment on the materials and instruments flown on EOIM-III.

REFERENCES

1. J. T. Visentine, and L. J. Leger, "Material Interaction with the Low Earth Orbital Environment: Accurate Reaction Rate Measurements," in Proceedings of the NASA Workshop on Atomic Oxygen Effects, Nov. 10-11, 1986, D. E. Brinza, Ed., JPL Publication 84-14, pp. 11-20, June 1, 1987.
2. A. E. Heddin, MSIS-86 Thermospheric Model, Journal of Geophys. Res., vol.92, No. A5, pp. 4649-4662, May 1, 1987.

3. A. E. Heddin, High Altitude Atmospheric Modeling, NASA Technical Memorandum 100707, October 1988.
4. J. T. Visentine, L. J. Leger, J. F. Kuminecz, I. K. Spiker, "STS-8 Atomic Oxygen Effects Experiment", AIAA paper AIAA-85-0415, 23rd Aerospace Sciences Meeting, Reno, Nevada, Jan. 14-17, 1985.
5. J. T. Visentine, L. J. Leger, "Materials Interactions with the Low-Earth Orbital Environment: Accurate Reaction Rate Measurements", AIAA paper AIAA-85-7019, AIAA Shuttle Environments and Operations II Conference, p 168, Nov. 1985.
6. Lubert Leger, Steve Koontz, Jim Visentine, Don Hunton, Jon Cross, Charles Hakes, "An Overview of the Evaluation of Oxygen Interactions with Materials III Experiment: Space Shuttle Mission 46; July-August, 1992." Third LDEF Post-Retrieval Symposium, Williamsburg, Virginia, Nov. 1993.
7. S. L. Rickman, C. R. Ortiz, Thermal Interactive Mission Evaluation System (TIMES89), NASA publication JSC-23852, Sept. 1989.
8. Thermal Synthesizer System (TSS) Users Manual, LMSC/F191409, developed under contract NAS 9-17923, Dec. 1992.
9. Gary Rottman and Tom Woods, High Altitude Observatory, National Center for Atmospheric Research, private communication to Steve Koontz.
10. Gary J. Rottman, Thomas N. Woods, Thomas P. Sparn, Solar-Stellar Irradiance Comparison Experiment 1: 1. Instrument Design and Operation, J. Geophys. Res., vol. 98, no. D6, p. 10667, June 20, 1993.
11. Thomas N. Woods, Gary J. Rottman, Gregory J. Ucker, Solar-Stellar Irradiance Comparison Experiment 1: 2. Instrument Calibrations, J. Geophys. Res., vol. 98, no. D6, p. 10679, June 20, 1993.
12. Hans E. Hinteregger, Katsura Fukui, Observational, Reference and Model Data on Solar EUV, from Measurements on AE-E, Geophys. Res. Let., vol. 8, no. 11, p.1147, Nov. 1981.
13. Charles L. Hakes, David T. Bui, AOFLUX program, Lockheed Engineering & Sciences Company, developed under contract NAS 9-17900, 1993.
14. S. L. Koontz, J. B. Cross, D. Hunton, E. Lan, "Characterization and Calibration of the EOIM-III Flight Mass Spectrometer in a High Velocity Oxygen Atom Beam", Materials Degradation in Low Earth Orbit (LEO), V. Srinivasan and B. A. Banks, Ed., The Minerals, Metals & Materials Society, 1990.
15. Space Environment Services Center (Mission-specific values for the daily-average A_p geomagnetic activity and the daily solar F10.7 values), private communication to Steve Koontz.
16. D. G. Zimcik, C. R. Magg, "Results of Apparent Oxygen Reactions with Spacecraft Materials During Shuttle Flight STS-41-G," J. Spacecraft, vol. 25, no. 2, March-April 1988.
17. S. Koontz, G. King, A. Dunnet, T. Kirkendahl, R. Linton, J. Vaughn, "The ISAC Atomic Oxygen Flight Experiment," J. Spacecraft, in press, 1994.
18. D. E. Hunton, E. Trzcinski, L. Wlodyka, G. Federico, and J. Dorian, "Quadrupole Ion/Neutral Mass Spectrometer (for Space Shuttle Applications)", AFGL-TR-86-0084, Air Force Geophysics Laboratory, Hanscomb Air Force Base, MA, April 7, 1987.
19. P. Chen and S. A. Straka, Goddard Space Flight Center, private communication to Steve Koontz.
20. R. C. Linton, J. A. Vaughn, M. M. Fincknor, R. R. Kamenetzky, R. F. DeHaye, A. F. Whitaker, "Orbital Atomic Oxygen Effects on Materials: An Overview of MSFC Experiments on the STS-46 EOIM-3," AIAA paper AIAA-93-4102, AIAA Space Programs and Technologies Conference and Exhibit, Huntsville, AL, Sept. 21-23, 1993.

SPACECRAFT MATERIALS STUDIES ON THE AEROSPACE CORPORATION TRAY ON EOIM-III

Wayne K. Stuckey, Carol S. Hemminger, Gary L. Steckel, Malina M. Hills, and Michael R. Hilton
Mechanics and Materials Technology Center
The Aerospace Corporation
2350 East El Segundo Blvd.
El Segundo, CA 90245
Phone: 310/336-7389, Fax: 310/336-5846

SUMMARY

A passive tray was flown on the Effects of Oxygen Interaction with Materials experiment on STS-46 (EOIM-III) with 82 samples from The Aerospace Corporation. A variety of advanced materials related to potential uses on future spacecraft were included for evaluation representing optical coatings, lubricants, polymers, composites, carbon-carbon composite protective coatings, graphite protective coatings, thermal-control materials, and some samples of current materials. An overview of the available results from the investigations of these materials is presented.

INTRODUCTION

The third experiment on the Effects of Oxygen Interaction with Materials (EOIM-III) was flown on STS-46. This mission was launched on July 31, 1992. On day 5, after deployment of Eureka and the tests of the Tethered Satellite System, the shuttle altitude was dropped to 124 nmi. The shuttle was oriented in a -Z orientation for 42 h, with the nose of the shuttle towards earth and the cargo bay into the velocity vector for the EOIM exposure to atomic oxygen. The fluence for the exposure was determined to be $2.3 \pm 0.1 \times 10^{20}$ oxygen atoms/cm² based on Kapton film erosion measurements, flux calculations using MSIS-86 with the as-flown orbit, and mass spectrometer measurements on EOIM-III.

The EOIM-III experiment submitted by The Aerospace Corporation consisted of one ambient-temperature tray with 82 samples (see Appendix I) and 19 samples placed on trays designed to have controlled temperature at 60°C, 120°C, and 200°C (see Appendix II). The actual temperatures from flight data showed that the ambient-temperature trays varied from 0°C to 43°C during the 42-h exposure, and the controlled-temperature trays were 58–80°C, 114–129°C, and 178–186°C.

The ambient-temperature tray was supplied by NASA-Johnson Space Center (ID No. 12). The samples were loaded into the tray at Aerospace and included a sample facing down in the tray as a flight control whenever possible. In addition, many samples had ground controls that were not flown. Many of the samples are vacuum-deposited coatings that did not initially experience additional vacuum conditioning upon receipt at Aerospace. The other samples had all experienced at least 24 h of 10^{-6} torr or less at room temperature. Many of the samples had also been in high-vacuum systems for pre-flight analyses by X-ray photoelectron spectroscopy (XPS) or scanning electron microscopy (SEM). Samples 22 and 23, with RTV 566 adhesive bonding silver interconnects, were held at 65°C for 24 h at pressures reaching into the 10^{-9} torr range. In response to a NASA request, the assembled tray with all samples except numbers 28, 29, 30 and 31 was placed in a vacuum chamber on a table maintained at 65–73°C for an additional 72 h. Pressures of $\sim 2.1 \times 10^{-6}$ torr were obtained initially and reached 5×10^{-8} at the conclusion of the bakeout. A residual gas analysis during the outgassing detected only water vapor. At room temperature, the final pressure was 5×10^{-9} torr. A Germanium ATR witness plate was placed in the chamber during the outgassing and showed

no detectable IR bands. Samples 28 and 29 were vacuum deposited and maintained at 65°C for 24 h with pressures of 2×10^{-8} to 5×10^{-9} torr. Samples 30 and 31 are typical optical components vacuum deposited by OCLI with preflight characterization that could not be repeated if included in the 65°C outgassing. All other samples, including all tray hardware, were included during the 65°C outgassing.

After the mission, the ambient tray was retrieved at NASA Kennedy Space Center and returned to Aerospace. Each sample was photographed immediately after removal from the tray. The controlled-temperature samples were removed from their fixture at NASA JSC and returned to Aerospace. The samples were then returned to the individual investigators for further study. Results on thermal-control materials are included elsewhere in these proceedings (ref. 1). Selected results will be presented here to give an overview of the results from the Aerospace tray.

RESULTS

Surface Contamination Analysis

Surface analysis by XPS of eight of the EOIM-III samples, which did not intrinsically contain silicon, listed in Table I, was used to evaluate surface contamination effects. Post-flight analysis of each sample was compared either to the pre-flight analysis results for the same sample, or to analysis of a ground-control sample made at the time of the post-flight analyses. A variety of surface changes was measured in the post-flight analyses, including contaminant deposition, surface oxidation, and surface stoichiometry changes. The major class of surface contaminant appears to have consisted of silicones. Surface silicon concentration increased from 4 to 11 atom % post-flight, with an average of 7 atom %. This implies the deposition of more than one monolayer of silicone on the flight-exposed samples.

The measured silicon concentrations were higher by a factor of 2 on the vanadium carbide samples located on the heated trays, compared to the silicon concentrations on the other samples in Table II located on the ambient-temperature tray. A quartz crystal microbalance experiment from NASA-Goddard located near the EOIM-III heated trays experienced significant weight gain on flight, which has not yet been

Table I. Silicon Concentration from XPS Analysis

Material	Atom %			
	Ground Control	Pre-flight Analysis	Post-flight Analysis	Increase in SI
SXA Mirror, E3-40	--	not detected	7.5	7.5
Cr on Graphite, E3-53	0.5	--	6.1	5.6
VC on Graphite, 60°C, E3-60-4	0.4	--	10	10
VC on Graphite, 120°C, E3-120-4	0.4	--	11	11
VC on Graphite, 200°C, E3-200-3	0.4	--	11	11
Anodized Al, E3-9†	--	5.7	11	5
ChemglazeA276, E3-25†	--	5.5	12	6
Z306, E3-10†	--	15	19	4

†Sample cut from exposed LDEF hardware, trailing edge.

completely explained. These data indicate the possibility for non-uniform contaminant deposition from localized sources on the EOIM-III experiment or from the Shuttle.

The contamination levels on the EOIM-III samples can be compared to those measured by XPS on a variety of LDEF samples (ref. 2). The average post-flight increase in silicon concentration for non-polymeric, leading-edge LDEF samples exposed for the duration of the mission was 17 atom %. By contrast, a nickel mirror sample exposed on-orbit only for 300 days had only a 2.5 atom % increase in Si surface concentration. This implies that both EOIM-III and LDEF samples may have received some silicone contamination from Shuttle sources.

Polymers

Polymers flown on the Aerospace EOIM-III experiment are shown in Table II. The atomic-oxygen erosion was determined by both weight loss measurements and profilometry. All of the samples were weighed pre-flight after conditioning to constant weight in a desiccator. Post-flight weights were measured in the same manner to determine the mass loss due to atomic-oxygen erosion of the polymer. In addition, an erosion step was formed by the beveled retainer ring on the front edge of the samples. This retainer created a protected and an exposed region that formed a circular crater on the sample. Surface profiles were determined with a Sloan Dektac 3030 at a minimum of three locations around the circumference of the crater to measure the step created from erosion of the polymer. There was good agreement between the two reactivity measurements. For reference, Kapton reactivity has been measured many times and is accepted to be $3.0 \times 10^{-24} \text{ cm}^3/\text{O atom}$. The black Kapton included in this test was carbon-filled and consistently indicated a difference in reactivity between the old and new black Kapton obtained at different times. The measurements of the fluorinated polymers are slightly more variable.

Table II. Atomic Oxygen Erosion of Polymers

Material	Reactivity ($\text{cm}^3 \times 10^{-24}/\text{O Atom}$)	
	Profilometry	Weight
Black Kapton (Old)	2.1 ± 0.3	2.6
Black Kapton (New)	1.2 ± 0.1	1.0
6FDA + APB (spin)	2.6 ± 0.3	2.1
6FDA + APB (spray)	2.4 ± 0.6	1.6
6FDA + APB (both)	2.5 ± 0.5	1.85
6FDA + DDSO2	1.3 ± 0.3	0.3
BFDA + 4BDAF	2.3 ± 0.1	1.9
BTDA + 4,4ODA	3.4 ± 0.5	2.7

For the black Kapton samples, thermal property measurements were also performed (Table III). Some increase in solar absorptance was observed from erosion of the Kapton. The emissivity changes were slightly higher for the old black Kapton for the atomic-oxygen fluence experienced on EOIM-III, but no significant change was seen for the α/ϵ ratio.

Table III. Thermal Property Changes of Black Kapton on EOIM-III

Sample	Orientation In Tray	Solar Absorptance (α)	Emissivity (ϵ)	α/ϵ
"Old" Black Kapton	Up	0.988	0.928	1.06
"Old" Black Kapton	Down	0.930	0.887	1.05
"New" Black Kapton	Up	0.989	0.867	1.14
"New" Black Kapton	Down	0.929	0.871	1.07

Zinc Sulfide

Another EOIM-III experiment examined the oxidation of zinc-sulfide-coated lenses of an Earth-viewing sensor. Degradation of these lenses (loss of transmission at 14–16 μm) has been observed during solar maxima, when the density of atomic oxygen (AO) is highest. The degradation was, therefore, postulated to result from the interaction of AO with the lens material. In order to measure the kinetics of oxygen diffusion and reaction with the zinc sulfide coating, and thereby predict the extent of oxidation on the orbiting satellite, samples were flown on EOIM-III at three different temperatures: ambient, 60°C, and 120°C.

The EOIM-III lens samples exhibited no change in their infrared optical properties. However, all lens samples exhibited extensive visible degradation in the area of AO exposure. X-ray photoelectron spectroscopic (XPS) measurements of the surfaces of the lens samples indicated that they were severely oxidized (see Table IV), and that the extent of oxidation increased with temperature. This temperature dependence suggests that the oxidation is diffusion-limited. Secondary Ion Mass Spectrometry (SIMS) of the lenses was also performed to measure the oxygen concentration profile as a function of depth. The SIMS data showed that the higher the temperature of the lens during the Shuttle exposure, the greater the depth of oxidation.

Table IV. Increase in oxygen content of zinc sulfide lens surfaces as determined by XPS.

Lens sample	Increase in Oxygen (atomic %)
Ambient #3	18
Ambient #4	16
60 °C	22
120 °C	31

Currently, the oxygen concentration data are being fit to a diffusion model. Preliminary modeling results suggest that the energy of diffusion is quite low ($E_{\text{dif}} < 10$ kcal/mole). The sensor lenses are exposed to a lower AO flux environment on the satellite than in the Shuttle bay, but are exposed to AO for a much longer period. The low energy of diffusion suggests that the extent of oxidation of the lenses on the satellite would be less than that observed on the EOIM-III samples. The lens degradation on the satellite would, therefore, have to be attributed to another degradation mechanism, such as contamination, or to synergistic effects such as simultaneous exposure to AO and UV light. (The lenses on the satellite were exposed to a higher intensity of UV light.) Completion of this modeling effort will clarify these results.

Optical Coatings

The optical coating configurations flown on the Aerospace tray are shown in Table V. Five of the samples were in virgin condition, and three received combined electron/proton/UV exposure in an experiment designed to ascertain the effect of on-orbit radiation on the optical and nuclear survivability of the coatings. These three samples were otherwise duplicates of three of the five virgin samples. The preconditioned samples received a dose of 2×10^{16} electrons/cm² at 40 keV, 3×10^{16} protons/cm² at 40 keV, and 1000 equivalent sun-hours UV exposure at a rate of 2 suns.

Companion samples to those flown on the Aerospace tray were tested at the atomic-oxygen exposure facility at Los Alamos National Laboratory. The fluence was 2×10^{20} atoms/cm² except for 240A-2, which received 1.8×10^{20} atoms/cm². The optical scatter from each sample was characterized before and after each atomic-oxygen exposure.

Comparison of the results of sample exposure on EOIM-III and at Los Alamos National Laboratory do not prove to be consistent. Two of the coating configurations show more scatter increase when fielded at

LANL, and four configurations showed greater increase on the EOIM-III experiment. However, many of these coatings also showed extensive deterioration of laboratory control samples (ref. 3).

Table V. Optical Coatings

Composition	EOIM-III Results	LANL Results
100 Å Al ₂ O ₃ / 2400 Å BN // Fused Silica	Increase in scatter (129%) Blister diameter increase by 258% Slight erosion	Increase in scatter (111%) Blister diameter increase by 118% Slight erosion
100 Å Al ₂ O ₃ / 2400 Å BN // FS (pre-exposed to e ⁻ /UV/H ⁺)	Decrease in scatter (74%) Blister diameter increase by 223% Heavy erosion	No change in scatter (103%) No change in blister diameter Moderate erosion
2150 Å BN // Fused Silica	HUGE increase in scatter (261%) slight erosion	Increase in scatter (121%) Many small blisters
2150 Å BN // Fused Silica (pre-exposed to e ⁻ /UV/H ⁺)	No change in scatter (103%) Moderate erosion	Increase in scatter (121%) Moderate erosion
1500 Å BN / 300Å Al // FS	Increase in scatter (141%) No erosion evident	No change in scatter (103%) Exposed area appears brighter No erosion evident
1500 Å BN / 300Å Al // FS (pre-exposed to e ⁻ /UV/H ⁺)	Increase in scatter (116%) No erosion evident	Not tested
Magnesia-doped Al ₂ O ₃ / SiO ₂ Multilayer // FS	No change in scatter (99%) No other response	Not tested
200 Å SiO ₂ / 1000 Å TiN // FS	Increase in scatter (132%) No erosion evident	Increase in scatter (112%) No erosion evident

TiN and BN samples provided by Jaycor

Lubricants

Sputter-deposited MoS₂ lubricant films are used on a variety of spacecraft mechanisms, including release/deployment devices and some precision bearings. However, MoS₂ can oxidize into MoO₃, which is an inferior lubricant having low endurance and a relatively higher friction coefficient. Humid ground storage promotes oxidation (ref. 4). Atomic-oxygen exposure in ground tests has been found to cause surface oxidation to a depth of 9 nm (ref. 5). Most MoS₂ films have generally had as-deposited porous microstructures with (100) or (110) orientation. During sliding or rolling contact, lubricant particles would detach and reorient such that the (001) orientation (the active plane of slip) would become parallel to the surface. This bur-nished orientation is believed to have more oxidation stability. Films having dense, (001) oriented microstructures as-deposited have recently become available (ref. 6). These newer films were developed under BMDO auspices (PMA F1504 Materials and Structures Program) for precision gimbal bearings that would be used in sensor acquisition, tracking, and pointing mechanisms.

A series of MoS₂ films (deposited onto 440C steel) having different microstructures were flown on EOIM-III on several trays. The films were characterized structurally (SEM), chemically (AES/XPS), and tribologically (sliding friction coefficients in air and in UHV) by Sandia (PI: Michael T. Dugger) (ref. 7). Films having traditional (100)-oriented microstructures, prepared by Aerospace, were loaded onto a tray of the University of Alabama. Films with denser microstructures were flown on a JPL tray (Ovonic/OSMIC

0.7nm Ni/10nm multilayer MoS₂ film with 50 nm overlayer of pure MoS₂; Hohman cosputtered 20% SbO_x-MoS₂) or an Aerospace tray (Ovonics/OSMIC 0.9nm Au-20% Pd/10nm multilayer film with 50 nm overlayer of pure MoS₂; Naval Research Lab MoS₂ prepared using ion-beam-assisted deposition [IBAD]). All films were 1-μm thick. Duplicate samples were flown so that for each film type, one sample was exposed to AO, and one was shielded (flight control). Additional ground-control samples were prepared and characterized.

Post-flight analyses of these films are still in progress, though there is some preliminary data available (ref. 7). Of the newer films, microscopy has shown that the Ni-multilayer films exposed to flight AO have developed cracks and delaminated regions. The Au-multilayer (SbO_x-cosputtered) and the IBAD films did not have cracks or delaminated regions. Post-flight sliding tests in air have been conducted on these dense films. In the AO exposed regions, initial friction coefficients 3–4× above baseline were observed for the first 10 to 100 cycles before friction values dropped to baseline levels. The data suggests that a thin layer of MoO₃ had formed, which was quickly removed in sliding; this is consistent with the ground test AO experiments (ref. 5). From a design viewpoint, the preliminary data indicates that the Ni-multilayer films should be avoided for use as a lubricant on AO-exposed mechanisms because of coating fracture/delamination. The other dense lubricants may be more suitable for such mechanisms if the devices are not used continuously, although designers should anticipate higher initial friction coefficients after periods of inaction on exposed mechanisms if these lubricants are used. If the mechanisms are used continuously, these lubricants would appear to require shielding from AO to avoid continual oxide formation that would accelerate wear.

Composite Materials

Three composite samples were flown—two graphite-fiber-reinforced, polymer-matrix composites and one silicon-carbide, whisker-reinforced, metal-matrix composite. The metal-matrix composite was a flat mirror fabricated by Advanced Composite Materials Corporation (ACMC) and provided to NSWC. The mirror consisted of a low-density (0.42 g/cc) silicon carbide/aluminum (SiC/Al) foam core approximately 0.2-in. thick with SiC/Al surface foils. The 0.020-in. thick surface foils were applied with Sn96 Sn-Ag solder after an electroless nickel coating was applied to both bond surfaces. The planar mirror surface was then prepared by OCA Applied Optics. One of the SiC/Al face sheets was plated with an electroless nickel coating, which was polished to form the planar mirror finish. The final subsize mirror was 0.25-in. thick and 0.5-in. in diameter and had a density of approximately 2.0 g/cc.

The mirror surface was characterized preflight and postflight by total integrated scattering (TIS) to quantify its reflective properties and by XPS to determine the surface chemistry. The XPS data (see Table VI) provided evidence of several surface effects from the low earth orbit exposure, including contamination deposition, oxidation, and stoichiometry changes. Electroless nickel typically contains several percent phosphorous, which is in solution in the Ni or present as nickel phosphide, depending upon the concentration and heat treatment (ref. 8). The target phosphorous concentration for the mirror surface was relatively high (12 wt.%) so that a high fraction of Ni₃P would be expected. XPS indicated that the Ni:P atom ratio

Table VI. XPS Data for SXA Mirror, EOIM-III

	Surface Atom % (Normalized)									
	C	O	SI	NI	P	N	S	Cl	Na	Ca
Pre-Flight	25	31	nd	29	13	nd	nd	nd	1.3	1.0
Post-Flight	16	53	7.5	21	0.5	nd	0.2	0.2	0.5	0.3

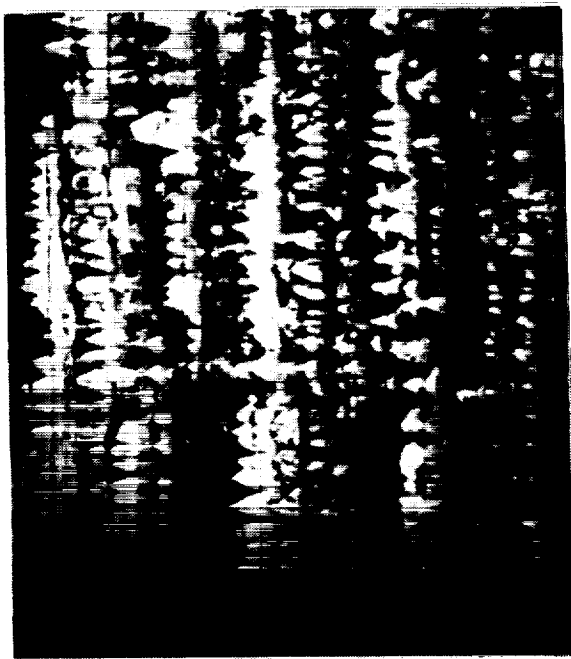
Note: nd = not detected and tr = trace.

on the surface changed from 2.2 preflight to 42 post-flight, while the phosphide-to-phosphate ratio changed from 2:1 to 1:1. These results indicate surface oxidation accompanied by a depletion of phosphorous from exposure to atomic oxygen. The extreme phosphorous depletion is assumed to result from the formation of volatile oxides and could lead to serious long-term surface degradation, such as pitting. SEM did not reveal any damage to the polished surface from the short-term EOIM-III exposure. However, atomic force microscopy performed by Advanced Materials Laboratory, Incorporated (ref. 9) gave indications of isolated pitting. Surface roughness measured over a 1- μm square was around 4 nm in the pitted areas versus less than 1 nm in typical areas. However, for most areas evaluated, the surface roughness was essentially the same in the exposed areas as in masked areas that were protected from atomic oxygen. The scattering measurements indicated that mirror performance was degraded. TIS increased by 100% from 0.0073 preflight to 0.0146 postflight, and the total hemispherical reflectance decreased by 7% from 0.537 to 0.498. Thus, some degradation of the mirror surface occurred and is probably related to the chemical changes. Similar results were reported (ref. 10) for polished electroless nickel surfaces flown on STS-5.

The polymer matrix composites included a P75S/934 graphite/epoxy composite with an eight-ply $(90/\pm 30/90)_s$ lay-up and an AS4/PEEK graphite/thermoplastic composite with an eight-ply $(0/45/90/-45)_s$ lay-up. Mounted and polished cross sections were flown to obtain atomic-oxygen erosion surfaces in which the fibers and matrix were clearly distinguishable to serve as standards for the interpretation of LDEF erosion morphologies. Most polymer matrix composites flown on LDEF had either the coarse "Christmas tree" or cone-like structure exemplified by P75S/934 in Fig. 1a, or a fine, acicular structure as shown by Celion 6000/PMR-15 graphite/polyimide in Fig. 1b. The initial surfaces on LDEF samples were all as-fabricated surfaces so that it was not possible to distinguish between fiber and matrix areas on the eroded surfaces. Although it was not possible to identify parameters that controlled the erosion morphology, there did appear to be some correlation between the graphite-fiber type and the erosion features. Composites with higher-

**P75S/934
GR/EPOXY**

**CELION 6000/PMR-15
GR/POLYIMIDE**



(a)

60 μm

(b)

Figure 1. Scanning electron micrographs of atomic-oxygen erosion features of graphite-fiber-reinforced polymer matrix composites flown on LDEF.

modulus fibers (P75S and GY70) usually had the coarse Christmas tree features, while composites with lower-modulus fibers (Celion 6000 and T300) had the finer, acicular structure (ref. 11). Therefore, this experiment was performed to obtain controlled-erosion surfaces in which the fibers and matrix could be distinguished from each other. The composite systems were selected based on the differences between the relatively low modulus (34×10^6 psi), polyacrylonitrile-precursor AS4 fiber and the higher modulus (75×10^6 psi), mesophase pitch-precursor P75S fiber.

Several observations were made from SEMs of the erosion surfaces as shown in Fig. 2. The 934 epoxy and PEEK thermoplastic matrix erosion rates were significantly higher than those for the P75S and AS4 graphite fiber, respectively. The erosion morphologies were similar for the two polymer matrices. Similar erosion features were observed on the ends of the AS4 fibers, perpendicular to the fiber axis, and on the sides of the fibers, parallel to the fiber axis. Although not shown in Fig. 2, the P75S fiber also showed no orientation dependence for the erosion morphology. Finally, the P75S fiber eroded with a more uniform, finer structure than the AS4 fiber. This is contrary to the result anticipated from LDEF observations. Unfortunately, this experiment did not enable interpretation of LDEF atomic-oxygen erosion morphologies.

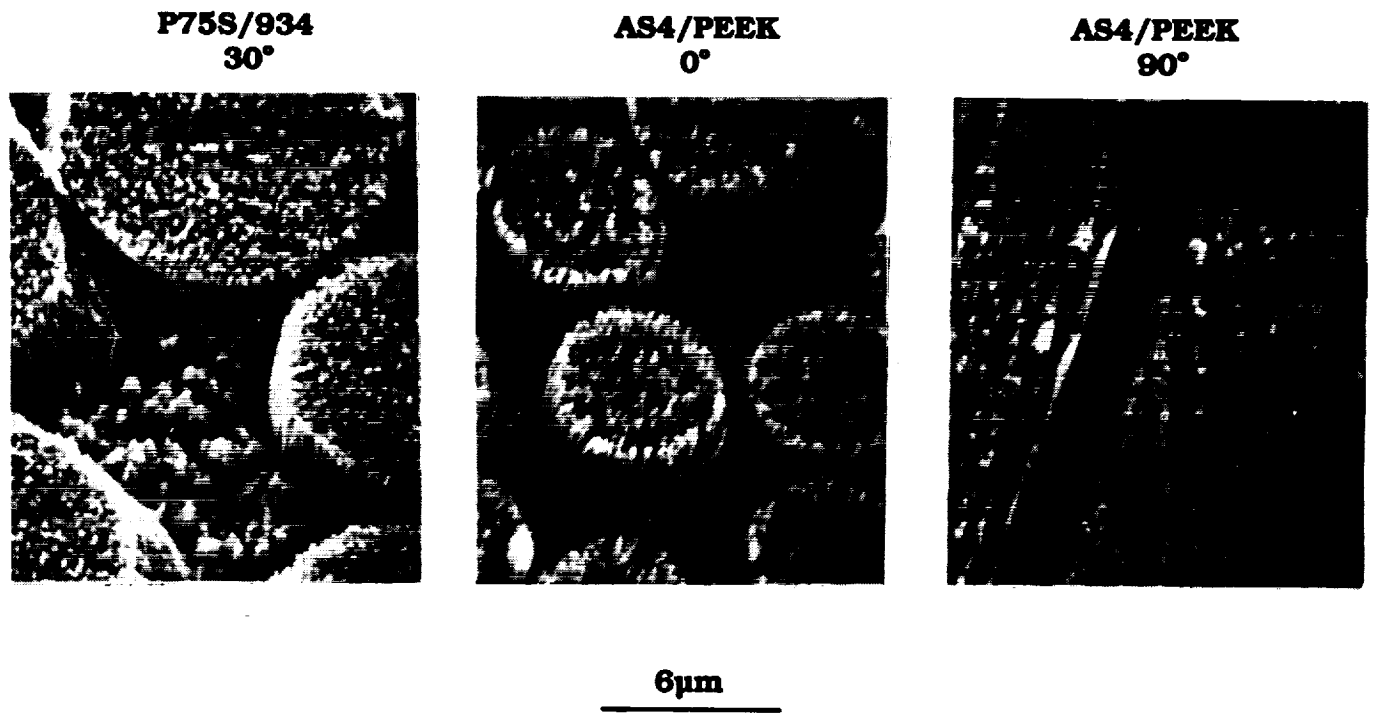


Figure 2. Scanning electron micrographs of atomic-oxygen erosion features for graphite-fiber-reinforced polymer matrix composites flown on EOIM-III. The fiber axis orientation relative to the atomic-oxygen velocity vector is shown for each micrograph.

Coated Graphite and Carbon-Carbon Samples

A variety of coatings over AXF-5Q polycrystalline graphite or carbon-carbon substrates was flown on the Aerospace ambient tray and the heated trays. The samples are described under sample numbers 45 through 64 in Appendix I for the ambient tray and the vanadium- and titanium-coated carbide samples on the heated tray summary in Appendix II. The carbide and boride coatings were deposited by CVD with ~100 μm thickness. Other coatings were either sputtered or deposited from a phosphoric-acid slurry. The reactivity of the uncoated carbon-carbon sample was indicated to be $1.4 \times 10^{-24} \text{ cm}^3/\text{O Atom}$ by weight-loss measurements. All of the coated specimens had reactivities at least a factor of 10 lower.

Three samples of ~1 μm chromium deposited on graphite were surface-analyzed by XPS: a ground control, a flight control (flown facing downward), and a flight exposed. The major surface changes observed were contaminant deposition and surface oxidation. The XPS composition data for the chromium-on-graphite samples is shown in Table VII. The major surface contaminants detected on the exposed sample were silicone and fluorocarbon residues. The silicon concentration was increased about 6 atom % relative to the ground and flight controls. The fluorine concentration was increased by a factor of 5 on both the flight control and flight exposed surfaces relative to the ground control. There was no evidence for fluorocarbon contamination greater than 1 atom % on the other EOIM-III flight samples analyzed by XPS in our laboratory. It is probable that the flight samples of chromium on graphite were contaminated pre-flight. The ground control had 4 atom % fluorine detected on its surface, indicating that variable levels of fluorocarbon contamination were deposited during fabrication or handling. A decrease in total surface carbon contamination was observed for the flight-exposed sample relative to the ground control, even with the deposition of silicone and fluorocarbon residues. This was typical of LDEF exposed surfaces as well (ref. 2) and is attributed primarily to volatilization of atomic oxygen reaction products such as CO and CO₂.

The increase in surface oxygen concentration by a factor of 2 on the flight sample relative to the ground control is due both to silicone contaminant residues and an increase in the surface oxidation of the chromium. XPS curve fit data for the Cr2p_{3/2} peak of the three samples analyzed is shown in Table VIII. The flight-exposed surface has a significant decrease in the zerovalent chromium detected relative to the control surfaces. The peak attributed to CrO₂ and Cr₂O₃ increased on the exposed surface, and a new peak attributed to CrO₃ was also detected.

Table VII. XPS Composition Data for Chromium on Graphite Samples

Sample		Surface Atom %, Normalized								
		Cr	O	C	Si	F	N	Cl	Ca	Zn
	Ground Control	12	22	59	0.5	3.8	0.5	0.3	1.2	0.3
E3-53	Flown Down	10	27	35	0.6	25	0.6	0.7	0.8	0.2
E3-53	Exposed	6.7	41	26	6.1	19	1.0	0.2	0.6	0.2

Table VIII. Cr2p_{3/2} Curve Fit Data for Chromium on Graphite EOIM-III Samples

Sample		Cr2p _{3/2} Curve Fit Results, Normalized Percent		
		Zerovalent Cr	CrO ₂ , Cr ₂ O ₃	CrO ₃
	Ground Control	43	57	—
E3-53	Flown Down	36	64	—
E3-53	Exposed	9	70	21

Four samples of vanadium carbide on graphite were surface-analyzed by XPS: a ground control, and three flight-exposed samples from the 60°C, 120°C, and 200°C heated trays. The major surface changes observed were contaminant deposition and surface oxidation. The XPS composition data for the vanadium carbide on graphite samples is shown in Table IX. The major surface contaminants detected on the exposed sample were silicone residues. The silicon concentration was increased on the heated samples about 10 atom % relative to the ground control. This was a larger concentration increase than observed for flight-exposed samples of other material on the ambient-temperature tray of the experiment. The vanadium carbide films in this study were apparently not of high purity. Significant, but variable, concentrations of tantalum, tin, niobium, zirconium, and potassium were detected. It was not possible to deduce from the XPS data whether or not there were changes in the stoichiometry of the carbide film induced by the flight exposure since the extent of pre-flight composition variability was not known.

A decrease in total surface carbon concentration was observed for the flight-exposed samples relative to the ground control, even with the deposition of silicone residues. This indicates a loss of surface carbide and carbonaceous contamination by volatilization of atomic-oxygen reaction products such as CO and CO₂. The concentration of carbide carbon on the ground-control surface was about 6 atom % (determined by a curve fit of the C1s peak). Both vanadium and tantalum had surface carbide and oxide states present. The concentration of carbide carbon on the 60°C sample was about 0.5 atom %, and no carbide could be detected on the 120°C or 200°C sample surfaces. The metals were all detected predominantly as oxides on all three of the flight-exposed samples. The increase in surface oxygen concentration by a factor of 2 on the flight samples relative to the ground control is due both to silicone contaminant residues and an increase in the surface oxidation of the vanadium and other metals.

Table IX. XPS Composition Data for Vanadium Carbide on Graphite EOIM-III Samples

Sample	Surface Atom %, Normalized									
	V	C	O	Si	F	Ta	Sn	Nb	Zr	K
Ground Control	8.3	61	25	0.4	0.4	4.4	0.4	0.8	0.1	nd
E3-60-4 Exposed, 60°C	10	13	65	10	0.3	0.4	0.1	0.1	0.3	0.2
E3-120-4 Exposed, 120°C	14	15	60	11	0.2	0.6	nd	tr	tr	0.1
E3-200-3 Exposed, 200°C	9.2	11	66	11	tr	2.2	0.1	0.4	tr	0.2

nd = not detected

tr = trace

Miscellaneous Samples

A variety of materials contributed by Hughes Space and Communications was flown on the Aerospace tray (ref. 12). Preliminary results are shown in Table X. Values shown for the solar absorptance and normal emittance are differences between the flight and control measurements. The value for the rhodium-plated molybdenum in the ambient tray was apparently the largest change, but an opposite trend was observed for the companion sample at 200°C. The erosion for the two polymeric resins was measured by microscopic examination.

Table X. Results on Hughes Space and Communications Samples

Sample Description	Sample Tray	Sample No.	Solar Absorptance Difference*	Normal Emittance Difference*	Measured Erosion (Microns)	Reaction Efficiency (cm ³ /O Atom)
SPEREX Conductive Black Paint	Ambient	E3-75	-0.011	-0.039		
SPEREX Conductive Black Paint	200 °C	E3-200-5	-0.005	-0.053		
SPEREX White Paint, SP101	Ambient	E3-76	-0.009	-0.046		
SPEREX White Paint, SP101	200 °C	E3-200-6	0.021	-0.102		
Germanium/ Kapton	Ambient	E3-77	-0.005	-0.004		
Germanium/ Kapton	120 °C	E3-200-1	-0.003	-0.003		
Rhodium-Plated Molybdenum	Ambient	E3-77	0.090	0.002		
Rhodium-Plated Molybdenum	200 °C	E3-200-4	-0.064	-0.005		
954-3 Cyanate Ester Resin	Ambient	E3-78			6.0	2.6 X 10 ⁻²⁴
934 Epoxy Resin	Ambient	E3-79			6.5	2.8 X 10 ⁻²⁴

*Flown Value minus Control Value

SUMMARY

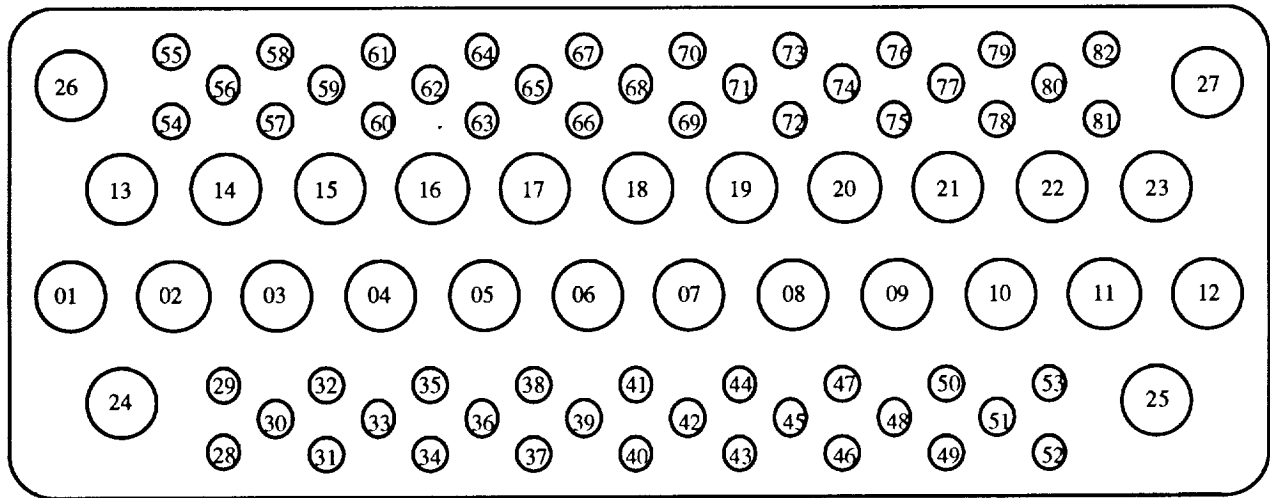
A variety of candidate spacecraft materials were flown on EOIM-III on the STS-46 shuttle mission. One full tray of 82 samples was flown at the ambient temperature during the mission, and samples were also on three trays held at fixed temperatures during the exposure. Results have been summarized on the observation of silicon contamination on the returned samples, the degradation of polymer samples, scatter properties of optical coatings, and the changes observed with zinc sulfide optical films, lubricants, composite materials, and coated carbonaceous materials.

Acknowledgments. The work on the silicon carbide/aluminum mirror and the coated graphite and carbon-carbon samples was supported by the Naval Surface Warfare Center. All other work reported was funded by the Air Force Materiel Command, Space and Missile Systems Center, under contract F04701-93-C-0094.

REFERENCES

1. M. J. Meshishnek and C. H. Jagers, "Exposure of LDEF Materials to Atomic Oxygen: Results of EOIM-III," Third LDEF Post-Retrieval Symposium, November 8-12, 1993.
2. C. S. Hemminger, "Surface Contamination on LDEF Exposed Materials," LDEF Materials Workshop '91, NASA CP-3162, September, 1992, pp. 159-174.
3. M. L. Boeck and D. J. Speece, "Effect of Combined Electron/Proton/UV Exposure on Optical Coating Materials," TOR-93(3089)-2, The Aerospace Corporation, El Segundo, CA (15 May 1993).
4. P. D. Fleischauer, ASLE Trans, 27(1) (1983) 82.
5. J. R. Martin, J. B. Cross, and L. E. Pope, Mat. Res. Soc. Symp. Proc., 140 (1989) 271.
6. M. R. Hilton and P. D. Fleischauer, Surf. Coat. Technol., 54/55 (1992) 435.
7. Michael T. Dugger, Sandia National Laboratories, P. O. Box 5800, M/S 0340, Albuquerque, NM 87185-0340, Tel: 505-844-1091. Personal communication to M. R. Hilton, Aerospace Corp., 4/20/94.
8. The Engineering Properties of Electroless Nickel Deposits, International Nickel, The International Nickel Co., Inc., New York, NY, 1971.
9. T. L. Altshuler, "Atomic Force Microscopy of a Polished Nickel Plated Mirror EOIM3 E3-40 Exposed to Space on the August 1992 Shuttle Flight," Advanced Materials Laboratory, Inc. Report No. AML TR 93-13, May 6, 1993.
10. M. J. Meshishnek, W. K. Stuckey, G. S. Arnold, and D. R. Peplinski, "Effects on Advanced Materials: Results of the STS-8 EOIM Experiment," Atomic Oxygen Effects Measurements for Shuttle Missions STS-8 and 41-G, NASA Technical Memorandum 100459, Vol. II, pp. 5-6, Sept. 1988.
11. G. L. Steckel, T. Cookson, and C. Blair, "Polymer Matrix Composites on LDEF Experiments M0003-9 & 10," LDEF Materials Workshop '91, NASA CP-3162, pp. 515-542, 1992.
12. Bruce Drolin, private communication, Hughes Space and Communications, El Segundo, CA.

APPENDIX I. AMBIENT EOIM-III TRAY - THE AEROSPACE CORPORATION



1	100 Å Al ₂ O ₃ / 2400 Å BN // Fused Silica (exposed to e ⁻ /UV/H ⁺) #SE1-01
2	100 Å Al ₂ O ₃ / 2400 Å BN // Fused Silica #SE1-05
3	2150 Å BN // Fused Silica (exposed to e ⁻ /UV/H ⁺) #SE2-01
4	2150 Å BN // Fused Silica #SE2-05
5	1500 Å BN / 300Å Al // Fused Silica (exposed to e ⁻ /UV/H ⁺) #6A7-5
6	1500 Å BN / 300Å Al // Fused Silica #6A7-3
7	Magnesia-doped Al ₂ O ₃ / SiO ₂ Multilayer // Fused Silica #B-1
8	200 Å SiO ₂ / 1000 Å TiN // Fused Silica #SE5-02
9	LDEF Anodized Aluminum # 1-1
10	LDEF Z306 #4-1
11	LDEF S13GLO Leading Edge #3-1
12	LDEF S13GLO Trailing Edge #2-1
13	Ovonics Au-MoS ₂ multilayer film on 440C steel #071091-013
14	Ovonics Au-MoS ₂ multilayer film on 440C steel #071091-015
15	NRL MoS ₂ films #102591-002
16	NRL MoS ₂ films #102591-004
17	Diamond-like Film (C) #071091-003/Ag Mask
18	Diamond-like Film (C) #071091-009/Ag Mask
19	Black Kapton- Old #1
20	Black Kapton-New #1
21	Germanium/Kapton
22	Silver Interconnect
23	Silver Interconnect

24	Anodized&Nickel Plated/ SiC-Aluminum
25	LDEF A276 Trailing Edge #1-1
26	6FDA + APB Spin Coated #1
27	6FDA + APB Spray Coated #1
28	Fluorinated Corning 7940
29	Fluorinated Corning 7940
30	Ambient Lens 3
31	Ambient Lens 4
32	ZnS/Silicon #ZnS-5
33	ZnS/Silicon #ZnS-7
34	TiO ₂ /Silicon #MOCVD 92-111
35	TiO ₂ /Fused Silica #MOCVD 92-112
36	TiO ₂ /Involute Carbon-Carbon #MOCVD 92-114
37	TiO ₂ /Braided Carbon-Carbon #MOCVD 92-115
38	TiO ₂ /POCO Graphite #MOCVD 92-116
39	TiO ₂ -SiO ₂ /Silicon #MOCVD 92-117
40	Nickel Plated/ SiC-Aluminum Mirror
41	Silicon Carbide Mirror
42	P75/934 Graphite Epoxy
43	AS4/PEEK
44	6FDA + DDSO ₂ #1
45	TiC / POCO AXF-5Q Graphite #1
46	VC / POCO AXF-5Q Graphite #1
47	TiB ₂ /POCO AXF-5Q Graphite #1
48	TiC / POCO AXF-5Q Graphite #1
49	NiAl #1
50	NiBe/POCO AXF-5Q Graphite #1
51	Ti ₂ Be ₁₇ / POCO AXF-5Q Graphite #1
52	V / POCO AXF-5Q Graphite #1

53	Cr/ POCO AXF-5Q Graphite #1
54	Si&SiC / Carbon-Carbon #1
55	SiO ₂ /Si&SiC/Carbon-Carbon #1
56	Al ₂ O ₃ /Si&SiC/Carbon-Carbon #1
57	Rh/Si&SiC/Carbon-Carbon #1
58	ZrP ₂ O ₇ / Carbon-Carbon #1
59	SiO ₂ /ZrP ₂ O ₇ /Carbon-Carbon #1
60	SiP ₂ O ₇ /Carbon-Carbon #1
61	SiO ₂ /SiP ₂ O ₇ /Carbon-Carbon #1
62	Carbon-Carbon Composite #1
63	AlPO ₄ / Carbon-Carbon #1
64	SiO ₂ /AlPO ₄ / Carbon-Carbon #1
65	NRL Diamond-like Film (Si) #D"
66	NRL Diamond-like Film (Si) #1
67	BFDA + 4BDAF #1
68	6FDA + APB Spin Coated #1
69	6FDA + APB Spray Coated #1
70	BTDA + 4,4ODA #1
71	Liquid Crystalline Epoxy/PDA
72	EPON 825/PDA
73	Vectra 4950 Liquid Crystalline Polymer
74	XYDAR SRT 300 Liquid Crystalline Polymer
75	Sperex Conductive Black Paint
76	Sperex White Paint SP101
77	Rhodium-plated Molybdenum
78	954-3 Cyanate Ester
79	934 Epoxy
80	High Temperature Adhesive
81	CV1144 Protective Silicone on Gr/Ep
82	AO Resistant Polyimide

APPENDIX II. HEATED SAMPLE CARRIER SUMMARY - THE AEROSPACE CORPORATION

Number	Size	Material	Investigator
60 °C Tray			
E3-60-1	1"	Germanium/ Kapton	Drolin
E3-60-2	1"	Solar Cell Interconnect Silver #11	Drolin
E3-60-3	0.5"	Lens 1	Hills
E3-60-4	0.5"	VC/Graphite	Foltz/Opeka
E3-60-5	0.5"	TiC/Graphite	Foltz/Opeka
E3-60-6	0.5"	CV1144 Silicone on Gr/Ep	Drolin
E3-60-7	0.5"	Silicone/Polyimide (Unannealed)	Gilman
E3-60-8	0.5"	Silicone/Polyimide (Annealed)	Gilman
120 °C Tray			
E3-120-1	1"	Germanium/ Kapton	Drolin
E3-120-2	1"	Solar Cell Interconnect Silver #6	Drolin
Lens 1	0.5"	Lens 2	Hills
E3-120-4	0.5"	VC/Graphite	Foltz/Opeka
E3-120-5	0.5"	Silicone/Polyimide (Unannealed)	Gilman
E3-120-6	0.5"	Silicone/Polyimide (Annealed)	Gilman
200 °C Tray			
E3-200-1	1"		
E3-200-2	1"	Solar Cell Interconnect Silver #8	Drolin
E3-200-3	0.5"	VC/Graphite	Foltz/Opeka
E3-200-4	0.5"	Rhodium-plated Molybdenum	Drolin
E3-200-5	0.5"	SPEREX Black	Drolin
E3-200-6	0.5"	SPEREX White	Drolin

EXPOSURE OF LDEF MATERIALS TO
ATOMIC OXYGEN: RESULTS OF EOIM III

C.H. Jagers
M.J. Meshishnek

The Aerospace Corporation
Mechanics and Materials Technology Center
El Segundo, CA 90245
Phone: 310/336-68760, Fax: 310/336-5846

ABSTRACT

The third Effects of Oxygen Atom Interaction with Materials (EOIM III) experiment flew on STS-46 from July 31 to August 8, 1992. The EOIM-III sample tray was exposed to the low-earth orbit space environment for 58.55 hours at an altitude of 124 nautical miles resulting in a calculated total atomic oxygen (AO) fluence of 1.99×10^{20} atoms/cm². Five samples previously flown on the Long Duration Exposure Facility (LDEF) Experiment M0003 were included on the Aerospace EOIM III experimental tray: (1) Chemglaze A276 white thermal control paint from the LDEF trailing edge (TE); (2) S13GLO white thermal control paint from the LDEF TE; (3) S13GLO from the LDEF leading edge (LE) with a visible contamination layer from the LDEF mission; (4) Z306 black thermal control paint from the LDEF TE with a contamination layer from the LDEF mission; and (5) anodized aluminum from the LDEF TE with a contamination layer from the LDEF mission. The purpose of this experiment was twofold: (1) investigate the response of trailing edge LDEF materials to atomic oxygen exposure, thereby simulating LDEF leading edge phenomena; (2) investigate the response of contaminated LDEF samples to atomic oxygen in attempts to understand LDEF contamination-atomic oxygen interactions.

This paper describes the response of these materials to atomic oxygen exposure, and compares the results of the EOIM III experiment to the LDEF mission and to ground-based atomic oxygen exposure studies.

INTRODUCTION

Specimens retrieved from the Long Duration Exposure Facility (LDEF) showed dramatic differences between the response of materials located on the leading edge (LE) and those on the trailing edge (TE). These differences are largely attributed to the high fluence of atomic oxygen to which the leading edge specimens were exposed.⁽¹⁾ The synergistic effects between UV radiation and atomic oxygen have also received much attention since the return of LDEF. Typical responses of white thermal control paints on the trailing edge included darkening due to the UV exposure. However, paint specimens on the leading edge of LDEF in many cases retained their white properties, presumably due to the scrubbing effects of atomic oxygen which removed the UV damaged layer.⁽¹⁻³⁾ Contamination on LDEF has, and continues to be, actively investigated, especially with respect to reaction with UV and atomic oxygen.⁽⁴⁻⁸⁾

The purpose of this experiment was twofold. First, we wished to simulate LDEF LE phenomena by exposing TE samples of white paints to low Earth orbit atomic oxygen. Second, we wanted to

see if contamination layers on TE specimens could be removed and/or chemically altered by the atomic oxygen exposure. The exposure of these materials on EOIM III can be compared to recent results obtained from ground-based atomic oxygen exposures using O-atom facilities at Los Alamos National Laboratory (LANL).

FLIGHT DESCRIPTION

The third Effects of Oxygen Atom Interaction with Materials (EOIM III) experiment flew on STS-46 from July 31 to August 8, 1992. The EOIM-III sample tray was exposed to the low-Earth orbit space environment for 58.55 hours at an altitude of 124 nautical miles. The sample tray was exposed to a calculated total atomic oxygen (AO) fluence of 1.99×10^{20} atoms/cm². Five samples previously flown on the M0003 LDEF experiment were included on the Aerospace experimental tray: (1) Chemglaze A276 white thermal control paint from the LDEF trailing edge (TE); (2) S13GLO white thermal control paint from the LDEF TE; (3) S13GLO from the LDEF leading edge (LE) with a visible contamination layer from the LDEF mission; (4) Z306 black thermal control paint from the LDEF TE with a contamination layer; and (5) anodized aluminum from the LDEF TE with a contamination layer.

SAMPLE DESCRIPTION AND PREPARATION

Chemglaze A276 is a white thermal control paint manufactured by Lord Corporation that consists of primarily a titanium dioxide pigment in a polyurethane binder. This paint was used on LDEF as a thermal control coating on the Experiment Power and Data System (EPDS) sunshields. The samples used for EOIM III were sectioned from the Aerospace Corporation LDEF experiment EPDS sunshield located on the LDEF trailing edge at D4.⁽¹⁾ The sunshield exposure was 10,400 equivalent sun hours of UV radiation and an atomic oxygen fluence of 2.31×10^5 atoms/cm² during the LDEF mission.^(9,10) Unlike leading edge samples of Chemglaze A276, these samples did not show evidence of atomic oxygen erosion from the LDEF mission due to their exposure to a much lower atomic oxygen fluence (by about seventeen orders of magnitude).^(1,3) The samples rather had been considerably darkened from UV radiation but remained quite glossy and specular.

S13GLO is a white thermal control paint manufactured by IITRI that incorporates a zinc oxide pigment in a methyl silicone binder. The ZnO pigment is encapsulated with potassium silicate for increased radiation stability. The samples were sectioned from the leading and trailing edge signal conditioning unit covers (SCU) on trays D8 and D4, respectively.⁽¹⁾ The LE samples had previously been exposed to 9400 equivalent sun hours of UV radiation and an atomic oxygen fluence of 8.99×10^{21} atoms/cm².^(9,10) The LE samples used for the EOIM III experiment were contaminated with a dark brown/tan contamination layer which significantly increased the paint's solar absorptance. However, the samples were taken from the side of the SCU cover so they saw no direct exposure to atomic oxygen but may have seen some reflected or scattered AO during the LDEF mission. The contamination was the result of venting of contamination from the interior of LDEF.

The TE S13GLO samples, used for the EOIM III experiment, like the Chemglaze A276 TE samples, were exposed to 10,400 equivalent sun hours of UV radiation and an atomic oxygen fluence of 2.31×10^5 atoms/cm².^(9,10) These samples had also been significantly darkened by the UV exposure.⁽¹⁾ There was no significant contamination layer on these samples as was the case for the LE specimens.

Chemglaze Z306 is a black thermal control paint manufactured by Lord Corporation that incorporates a carbon black pigment in a polyurethane binder. Samples were sectioned from a module backing plate on the LDEF trailing edge tray at location D3. This painted surface was facing inside of LDEF, and therefore was not subjected to UV radiation or atomic oxygen impingement. The backing plate did, however, have a visible contamination layer from the outgassing of various components and/or experiments on LDEF.

Anodized aluminum samples were sectioned from the environmental exposure control canister (EECC) located on the LDEF trailing edge at D4. Consequently, it had been exposed to 10,400 equivalent sun hours of UV radiation and an atomic oxygen fluence of 2.31×10^5 atoms/cm².^(9,10) A light brown contamination layer was present on the surface due to the outgassing of various components and/or experiments on LDEF, and their subsequent photo-fixing from the UV exposure.⁽¹⁾

The samples were sectioned into several 1"-diameter discs. The following sample notation and descriptions were used for identification purposes:

EOIM3-X-Y

- where
- | | |
|------------|---------------------------------------------------------------------------------------------------------------------------------------------------------------------------------------------------------------------------------------------------------------------------------------------------------------------------------------------------------------------------------------------------------------------------------------------------------------------------------------------------------------------------------------------------------------------------------------------------------------------------------------------------------------------------------------------------------|
| X = | Material Designation as follows:
1 = Chemglaze A276 white thermal control paint on aluminum substrate from trailing edge of LDEF (D4 sunshield)
2 = S13GLO white thermal control paint on aluminum substrate from trailing edge of LDEF (D4 signal conditioning unit cover)
3 = S13GLO white thermal control paint on aluminum substrate from leading edge of LDEF with contamination stain (D8 signal conditioning unit cover)
4 = Z306 black thermal control paint on aluminum substrate from trailing edge of LDEF with contamination stain (Interior module backing plate from tray D3)
5 = Aluminum section from trailing edge of LDEF with contamination stain (D4 EECC sunshield) |
| Y = | Sample use designation as follows:
1 = Flight sample
2 = Control Sample
3-5 = LANL, Analysis samples |

All samples were baked for at least 24 hours at a minimum temperature of 65°C and a maximum pressure of 2×10^{-6} torr to meet EOIM III flight contamination requirements.

EXPERIMENTAL

The flight samples were characterized before and after the EOIM III mission and compared to the control samples. Sample weight, solar absorptance, surface analysis, and surface morphology were all determined for each sample by the methods described below.

Change in the optical properties of thermal control materials, especially solar absorptance, is the primary indication of degradation after exposure to the space environment. Diffuse reflectance spectra of the samples from 250-2500 nm were obtained using a Perkin-Elmer Lambda 9

UV/VIS/NIR spectrophotometer equipped with a barium sulfate integrating sphere. Solar absorbance values for each sample were calculated from the spectra after normalization to an NIST diffuse reflectance standard. The precision of the measurement is ± 0.003 , however absorption of the material outside the range of measurement can produce errors in accuracy of 4%.

X-ray Photoelectron Spectroscopy (XPS) was used to investigate the surface chemistry of the samples and to detect any surface compositional changes. A VG Scientific MICROLAB MK II multiprobe instrument was used for the XPS analyses. The samples were mounted on sample stubs with double-sided tape. Survey scans from 0 to 1100 eV binding energy were acquired with a Mg K α source to qualitatively determine the sample surface composition. Analysis areas were about 4 x 5 mm in size and to a depth of 50-100Å. High resolution elemental scans were subsequently run to obtain semi-quantitative elemental analyses from peak area measurements and chemical state information from the details of binding energy and shape. Measured peak areas for all detected elements were corrected by elemental sensitivity factors before normalization to give surface mole %. The quantitation error on a relative basis is $\leq 10\%$ of the measurement for components with a surface concentration >1 mole %. Large uncertainties in the relative elemental sensitivity factors can introduce absolute errors of a factor of 2 or even greater. The detection limit is about 0.1 surface mole %, but spectral overlaps between large peaks and small peaks can make it impossible to detect minor components, particularly when more than one chemical state is present for a given element.⁽¹¹⁾

Changes in surface composition and structure were also investigated using Fourier-Transform Infrared Spectroscopy (FTIR). FTIR spectra were obtained by the diffuse reflectance method using a Nicolet MX-1 infrared spectrometer scanning from 4000 to 400 cm⁻¹.

The surface morphologies of the control and flight samples were compared using a JEOL JSM-840 Scanning Electron Microscope (SEM). An accelerating voltage of 15 KeV was used for all sample observations. Photographs of the samples were taken at magnifications from 100-5000X. It was necessary to carbon-coat the paint samples prior to analyses to eliminate the surface charging effects that distorted the SEM images.

RESULTS

Optical and surface analysis measurements were performed on all of the flight and control samples, both before and after the EOIM III mission. However, due to the destructive nature of the SEM investigations (i.e., carbon-coating the samples), no preflight SEM analyses were performed on the flight samples. Thus, comparisons were made between post-flight and control samples.

Pre- and post-flight weight measurements of the samples are listed in Table 1. Quantitative conclusions from these measurements are difficult, since there was some contamination of many samples during the EOIM III mission. However, the measurements are qualitatively consistent with the other results, as discussed below. The net weight gain for the S13GLO samples is unusual and may be due to re-absorption of water vapor postflight.

Chemglaze A276 (TE). The trailing edge LDEF sample (EOIM3-1-1) of Chemglaze A276 showed marked changes due to the EOIM III exposure, as expected. Visual inspection revealed that the sample changed from brown to white during the experiment and the surface became more diffuse. A photograph of the post-flight sample is shown in figure 1. The UV-VIS-NIR spectra (Figure 2) show increased reflectance after the exposure and that the change in the

material primarily occurred in the visible wavelength range. The solar absorptance decreased from 0.528 to 0.295 (Table 2)

Investigation of the surface morphology by SEM (Figure 3) indicates the expected changes due to the atomic oxygen exposure. The flight sample, in comparison to the ground control, indicates a significant roughening of the surface from erosion. The control sample, which has not been exposed to significant amounts of atomic oxygen, appears to be relatively intact with the titanium dioxide pigment particles dispersed throughout the polyurethane binder. However, the polyurethane binder on the surface of the flight sample was eroded away leaving a surface that is primarily titanium dioxide pigment. These differences were also seen between LDEF leading and trailing edge samples.^(1,3)

The preflight and postflight FTIR spectra of the Chemglaze A276 sample are shown in figure 4. There is an apparent reduction in infrared absorption throughout the wavelength range suggesting a thinning of the polyurethane binder layer from atomic oxygen erosion. This is consistent with the SEM observations. However no significant spectral shifts or intensity ratio changes were observed, suggesting uniform erosion of the polyurethane. There appears to be a small change in the absorption ratio at 750 cm^{-1} , which may be due to removal of aromatic hydrogens in the polyurethane.

The XPS results for the Chemglaze A276 sample (Table 3) indicate changes to the surface chemical composition.⁽¹²⁾ The preflight surface silicon is presumably due to contamination. An increase of 6.5 atom % of surface silicon was detected on the post-flight sample which is attributed to flight contamination and to an aluminum silicate filler/extender that is used in the Chemglaze paints being uncovered as the binder erodes away (2). The corresponding increase in aluminum is consistent with this hypothesis. The 40% decrease in carbon concentration is explained by loss of the polyurethane binder by reaction with the atomic oxygen. The increase in surface oxygen could be due to deposition of silicone contaminants during the EOIM III mission, exposure of the aluminum silicate, or some oxidation of surface silicones to silicates. However, the shift in the Si2p binding energy was not significant. Other samples on the Aerospace EOIM III tray had postflight increases in surface silicon which had to have been caused by flight contamination.⁽¹²⁾ The small increase in titanium signal and decrease in nitrogen concentration are also consistent with loss of surface binder. Pre-flight contamination is presumed responsible for the surface tin signal.

The sample weight (Table 1) shows a net decrease, which is consistent with the observation that atomic oxygen erosion caused removal of the polyurethane binder.

S13GLO (TE). The S13GLO sample from the trailing edge of LDEF visually appeared whiter in comparison to the control sample and to the masked region of the flight sample (figure 5). The sample exhibited increased postflight reflectance in the visible wavelength range (Figure 6), resulting in a decreased solar absorptance from 0.417 to 0.355 (Table 1).

Investigation of the surface morphology with SEM (Figure 7) indicates that exposure to atomic oxygen resulted in minor changes. The surface of the flight sample appears to have been slightly eroded by atomic oxygen, although not as extensively as the Chemglaze A276 sample. As with Chemglaze A276, the erosion was probably due to atomic oxygen erosion of the binder. However in this case erosion of the silicone is much less than the polyurethane used in the Chemglaze paints. Erosion of the S13GLO binder was not observed on M0003 LDEF samples.^(1,3)

Figure 8 gives the preflight and postflight FTIR spectra for the TE S13GLO sample. Some decreased absorbance is noted for the sample after the exposure. There is a significant but small decrease in the absorption at 3000 cm^{-1} due to the C-H stretch indicating oxidative removal of the methyl groups attached to the silicone polymer. This effect has been observed on earlier EOIM flights.⁽¹³⁾

XPS post-flight analysis showed a significant decrease in the surface carbon concentration, an increase in the surface silicon concentration, and a small increase in the surface oxidation relative to the pre-flight analysis (Table 3).⁽⁵⁾ The increase in silicon concentration is probably due to contaminant deposition, although it is impossible to distinguish between the possible sources of silicon (contaminant silicones, methyl silicone binder, potassium silicate encapsulate). There is indication that oxidation of silicone to silica on the surface occurred, as supported by a shift of the Si2p binding energy peak. Silica was the predominant state on the pre-flight sample, but some additional oxidation of surface silicones or silicates has probably occurred due to the atomic oxygen exposure. The increase in potassium and larger increase in zinc signal indicates that some loss of surface binder occurred.

The sample weight (Table 1) increased slightly during the EOIM III experiment. However, it did not increase as much as for the S13GLO (LE, contaminated) sample, which was relatively inert to atomic oxygen exposure (see next section). These facts are consistent with the hypothesis that atomic oxygen erosion of the methyl silicone binder did occur but the total weight loss was slightly less than the weight gain due to flight contamination or re-absorbed water vapor.

S13GLO (LE, contaminated). The S13GLO sample from the side of the SCU cover on the leading edge of LDEF was recovered still visibly contaminated with a brown "nicotine" stain. The post-flight photo of this sample is shown in figure 9. The reflectance spectra in Figure 10 indicate very little change resulting from atomic oxygen exposure; the solar absorptance increased insignificantly from 0.507 to 0.515 (Table 2).

The SEM photographs in Figure 11 show a significantly different surface morphology than the S13GLO LDEF TE sample, presumably due to the contamination layer. From the SEM photographs, it appears the contamination layer grows from nucleation sites on the surface in an upward direction, away from the surface. Both the flight sample (after atomic oxygen exposure) and the control sample (no atomic oxygen exposure) have similar surface morphologies, indicating that atomic oxygen had little effect on this contamination layer.

The FTIR spectra for the LE S13GLO sample are given in figure 12. Essentially no changes occurred due to the atomic oxygen exposure. Overall absorption changes are evident due to thickness differences in different areas of the paint sample.

Post-flight XPS analysis of the sample showed very little significant change in the surface composition (Table 3).⁽⁵⁾ A small decrease in the surface carbon concentration was noted. The contamination layer from the LDEF exposure appears to be quite stable to further atomic oxygen exposure. The binding energy of the Si2p peak indicates that the predominant surface state is silica, which is consistent with its stability to the space environment.

The sample weight increased after the EOIM III exposure (Table 1). The sample analyses show that this sample was relatively inert to atomic oxygen, thus causes for the apparent weight gain are unknown. However it may be unique to the material S13GLO since both EOIM III samples gained weight. Reabsorbed water is a possible source.

Z306 (TE, contaminated). The sample of Z306 from the trailing edge of LDEF flown on EOIM III exhibited only a slight change in its reflectance post-flight, resulting in a negligible increase in its solar absorptance from 0.955 to 0.960 (Table 2). Visually the sample appeared the same as before the flight (figure 13). The reflectance spectra are shown in figure 14. However, XPS and SEM results indicate significant changes did occur due to atomic oxygen erosion.

The XPS data in Table 3 shows a significant loss of surface carbon, which may be due to a loss of either carbon black pigment and/or polyurethane binder. A decrease of surface nitrogen concentration indicates a minor loss of surface binder. The large preflight surface silicon is due to the contamination layer on the sample. The increase in silicon may be due to flight contamination or the exposure of a silicate filler due to erosion of the binder.

The surface morphology of the Z306 sample was clearly altered as indicated by the SEM photographs in Figure 15. The flight sample has what appears to be a pitted or cratered surface, where portions of the surface were eroded away. This effect is not uniform across the surface, resulting in fairly large craters or pits. In contrast, the control sample has a fairly uniform texture, evenly distributed over the entire surface. The reasons for this erosion behavior are not understood.

The FTIR spectra for this sample as shown in figure 16 do not indicate any significant chemical changes in the sample due to the atomic oxygen exposure.

The Z306 sample experienced weight loss due to the EOIM III exposure (Table 1). This weight loss is consistent with the erosion of the surface; however, the magnitude of this erosion appears more significant than indicated by the sample weight change. Some of this erosion could have been offset by a weight gain due to contamination during the flight exposure.

Anodized Aluminum (TE, contaminated). The anodized aluminum sample from the trailing edge of LDEF with a visible contamination layer is shown in figure 17, post-flight. The sample exhibited an increase in its reflectance post-flight (Figure 18), resulting in a decrease in its solar absorptance from 0.394 to 0.330 (Table 2). The preflight XPS analysis indicated that the sample was contaminated with a layer of silica and silicones/silicates based on the Si2p peak.

Post-flight surface analysis showed additional surface deposition of silicon, increased surface oxidation and decreased surface carbon concentration. The silicon concentration increased by 5 atom % with new contaminant deposition. The decreased carbon signal, combined with the increased aluminum substrate signal, indicates that a significant portion of the carbon in the contaminant layer was removed by atomic oxygen during the flight. The increased silicon signal gives the most reliable data of the five samples, indicating that contamination occurred during the EOIM III mission. The FTIR spectra shown in figure 19 indicate that the contaminant layer has probably been thinned due to the exposure. Even with the silicon contamination, the sample still lost weight as indicated in table 1.

COMPARISON TO GROUND-BASED EXPERIMENTS

For comparison to the EOIM III results, two LDEF samples of Chemglaze A276 (TE) and S13GLO (TE) similar to the samples flown on EOIM III were exposed in the Hyperthermal Atomic Oxygen Facility at Los Alamos National Laboratory (LANL). These samples were cut from the same areas as the EOIM III specimens.

The atomic oxygen facility at LANL consists of a continuous-wave laser sustained discharge source producing O-atoms having a variable energy of 1 to 5 eV at a flux of 10^{16} to 10^{17} atoms/cm² sec. A detailed description of the facility including flux calculations has been published previously.^(14,15) In this experiment, exposures were made using a 50% Ar/50% O₂ gas mixture, with an estimated dissociation of O₂ of 95%. The kinetic energy of the atoms was 2 eV with a full-width-half maximum on the energy distribution curve of 1.5 eV. The total atomic oxygen exposure for the samples was 2.0×10^{20} atoms/cm² for Chemglaze A276 and 1.6×10^{20} atoms/cm² for S13GLO, which were similar to the total sample exposures on EOIM III.

Chemglaze A276 (TE). The LANL Chemglaze A276 sample showed similar effects to the EOIM III flight sample. Visually, the sample changed from brown to white, as evident by the increased reflectance below 1500 nm (Figure 20) and the decreased solar absorptance from 0.536 to 0.258 (Table 2). Comparison with the reflectance data obtained from EOIM III on the same material, the LANL paint sample exhibited greater increased reflectance post-test than the flight sample. Since both samples received the same atomic oxygen dose, the reasons for this are not clear.

Atomic oxygen erosion of the polyurethane binder accounts for the changes in the surface morphology, as evident in the SEM photographs in Figure 21. Like the EOIM III flight sample, exposure of the sample to atomic oxygen at LANL resulted in preferential erosion of the polyurethane binder, leaving a predominantly titanium dioxide pigment surface.

The XPS data for the Chemglaze A276 sample is shown in Table 3. Comparable decreases in surface carbon concentration, about 40% relative, were noted after AO exposure at LANL and on EOIM III. As discussed earlier, this loss of carbon is most likely due to the reaction of atomic oxygen with the polyurethane binder, creating volatile molecules which leave the surface. The surface silicon is probably due to surface contamination. However the relative increase in the surface silicon concentration could be due to the loss of surface carbon or to the aluminum silicate filler that is present in the chemglaze paints. Both the EOIM III sample and the LANL sample experienced similar increases in the silicon concentrations. Based on the Si2p binding energy, the predominant state of silicon appears to be silica.⁽¹¹⁾ Similar to the EOIM III sample, an increase in aluminum concentration is observed which is attributed to the aluminum silicate filler. Importantly, no cracking or delaminations was seen in either the LANL or EOIM III sample. Thus, the aluminum signal is not due to the paint substrate.

S13GLO (TE). The S13GLO TE sample lightened during the ground-based atomic oxygen exposure at LANL, but visually it did not lighten as much as the EOIM III flight sample. However, the change in the reflectance curve (Figure 22) is similar to the change observed for the flight sample (Figure 6). The change in solar absorptance from 0.422 to 0.386 is a little over half that observed for the flight sample (Table 2).

Investigation of the surface morphology with SEM (Figure 23) shows slight changes due to atomic oxygen exposure. These changes are minor, and again, qualitatively are less than observed for the EOIM III sample.

The pre-exposure XPS analysis of the LANL sample indicated similar surface composition to the EOIM III flight sample (Table 3). Post-experiment analyses of the LANL AO experiment sample and the EOIM III flight sample showed similar decreases in surface carbon concentration, increases in surface silicon concentration, and increases in surface oxygen. The decrease in surface carbon concentration of 30% relative is due to the loss of volatile molecules formed by atomic oxygen reactions, and also accounts for much of the relative increase in surface silicon and oxygen

concentrations. The Si2p binding energy indicates that the predominant state on both surfaces is SiO₂. Additionally, a shift in the charge-corrected binding energy of this peak of about half a volt indicates that some additional oxidation of residual surface silicones or silicates probably occurred during LANL AO exposure.⁽¹¹⁾

Increases in surface potassium and zinc only occurred on the EOIM III sample, indicating that the LANL AO experiment sample did not experience a significant loss of surface binder. In contrast, the EOIM III sample showed an increase in potassium and a large increase in zinc, indicating that some loss of binder did occur. This difference may be caused by differences in thermal cycling and VUV exposure between the two AO exposure environments. Additionally, the EOIM III sample was exposed to a 25% greater fluence than the ground-based LANL AO exposure sample, which could directly affect the amount of binder removed from the surface, thereby affecting the degree of exposure of the pigment to the XPS instrument. AO exposure at LANL also resulted in a 60% relative decrease in surface nitrogen, while no decrease was noted for the EOIM III sample. This discrepancy may indicate that nitrogen-containing contaminant deposition occurred on EOIM III, balancing nitrogen loss due to AO reactions.⁽¹¹⁾

SUMMARY

The results from EOIM III are consistent with the results and conclusions from LDEF. Several generalizations can be made, which include the following:

- Exposure of retrieved TE LDEF paints to atomic oxygen either in ground-based facilities or on Shuttle sorties approximates LE phenomena observed on LDEF.
- While quite similar results were obtained between EOIM III and LANL exposure studies, there are some small differences in the response of the paints to these two environments.
- Organic paint binders such as methyl silicone or polyurethane react with atomic oxygen to form volatile carbon-based molecules which are removed from the paint surface.
 - The methyl silicone binder in S13GLO, although still susceptible to reaction with atomic oxygen, is not as reactive as the Chemglaze A276 polyurethane binder.
- Depending on the chemical composition of the paint binder, erosion can occur which results in the exposure of pigment particles, which can affect the solar absorptance of the paint surface.
 - The polyurethane binder in Chemglaze A276 degrades upon exposure to UV radiation, resulting in a significant increase in solar absorptance. Exposure of this surface to atomic oxygen results in erosion of the binder surface layers, resulting in a predominantly titanium-dioxide pigment surface and a significant decrease in solar absorptance.
- Silicones and/or silicates tend to be oxidized by atomic oxygen to form silica, SiO₂. Erosion of the silicone occurs at the methyl groups, leading to a silicate and eventually, silica.
- Not all surfaces are susceptible to atomic oxygen erosion, as displayed by the contamination layer on the S13GLO LE sample.
 - Contaminated surfaces containing silicones which have been oxidized to silicates or silica are resistant to further erosion.

REFERENCES

1. Meshishnek, M. J., Gyetvay, S. R. and Jagers, C. H., "Long Duration Exposure Facility Experiment M0003 Deintegration/Findings and Impacts", LDEF--69 Months in Space, First Post-Retrieval Symposium, NASA Conference Publication 3134, p 1073 - 1108 (1991).
2. Golden, J. L., "Results of the Examination of the A276 White and Z306 Black Thermal Control Paint Disks Flown on LDEF", LDEF--69 Months in Space, First Post-Retrieval Symposium, NASA Conference Publication 3134, p 975 - 987 (1991).
3. Jagers, C. H., Coggi, J. M. and Meshishnek, M. J., "Thermal Control Paints on LDEF: Results of M0003 Sub-Experiment 18", LDEF--69 Months in Space, Second LDEF Post-Retrieval Symposium, NASA Conference Publication 3194, p 1075-1092 (1993).
4. Crutcher, E. R. and Warner, E. J., "Molecular Films Associated with LDEF", LDEF--69 Months in Space, First Post-Retrieval Symposium, NASA Conference Publication 3134, p 155-177 (1991).
5. Harvey, G. A., "Organic Contamination on LDEF", LDEF--69 Months in Space, First Post-Retrieval Symposium, NASA Conference Publication 3134, p 179-196 (1991).
6. Banks, B. A., Dever, J. A., Gebauer, L. and Hill, C. M., "Atomic Oxygen Interactions with FEP Teflon and Silicones on LDEF", LDEF--69 Months in Space, First Post-Retrieval Symposium, NASA Conference Publication 3134, p 801-815 (1991).
7. Pippin, G. and Crutcher, R., "Contamination of LDEF: Sources, Distribution and History", LDEF--69 Months in Space, Second LDEF Post-Retrieval Symposium, NASA Conference Publication 3194, p 1023-1033 (1993).
8. Blakkolb, B. K., Ryan, L.E., Bowen, H. S. and Kotic, T. J., "Optical Characterization of LDEF Contaminant Film", LDEF--69 Months in Space, Second LDEF Post-Retrieval Symposium, NASA Conference Publication 3194, 1035-1040 (1993).
9. Stein, B. A., "LDEF Materials: An overview of the Interim Findings", LDEF Materials Workshop '91, NASA Conference Publication 3162, p 1-56, (1991).
10. Stein, B. A., "LDEF Materials Overview", LDEF--69 Months in Space, Second LDEF Post-Retrieval Symposium, NASA Conference Publication 3194, p 741-789, (1993).
11. Hemminger, C.S., "XPS Analysis of Paint Samples Exposed to Atomic Oxygen at Los Alamos National Laboratory", Aerospace Technical Memorandum 93(3068-02)-1, 10 March 1993.
12. Hemminger, C.S., "Surface Changes Measured by XPS on Select Samples Exposed to the Space Environment on EOIM-3", Aerospace Technical Memorandum 92(2935-15)-8, 24 September 1992.
13. Meshishnek, M. J., Stuckey, W. K., Evangelides, J. S., Feldman, L. A. and Peterson, R. V., "Effects on Advanced Materials: Results of the STS-8 EOIM Experiment", NASA Technical Memorandum 100459, Atomic Oxygen Effects For Shuttle Missions STS-8 and 41-G., Volume II, September 1988.

14. Cross, J. B., Spangler, L. H., Hoffbauer, M. A. and Archuleta, F. A., "High Intensity 5 eV cw Laser Sustained O-atom Exposure Facility for Material Degradation Studies", SAMPE Quarterly **18**, 41 (1987).
15. Cross, J. B. and Blais, N. C., "High Energy/Intensity Atomic Oxygen Beam Source for Low Earth Orbit Materials Degradation Studies", Proceedings of the Sixteenth International Symposium on Rarefied Gas Dynamics, Pasadena, CA (1988).

Acknowledgements: The authors wish to thank Lt. Col. Michael Obal of the Ballistic Missile Defense Organization (BMDO) for funding a portion of this work as part of the BMDO Space Environment Effects (SEE) program. We also wish to express our sincere appreciation to John Cross at Los Alamos National Laboratory for the use of his facility for the ground based exposures and to Carol Hemminger for the XPS analyses of the specimens. The following individuals also contributed to this work: Wayne Stuckey, Sandra Gyetvay, John Coggi, Tom Park, Dana Speece, Gloria To and John Golden.

Table 1. Weights of EOIM III Samples

Sample	Sample ID	Weight (g)		Change
		Pre-flight	Post-flight	
Chemglaze A276	EOIM3-1-1	1.394380	1.394300	-0.000080
S13GLO TE	EOIM3-2-1	1.323910	1.324040	+0.000130
S13GLO LE	EOIM3-3-1	1.300280	1.300810	+0.000530
Chemglaze Z306	EOIM3-4-1	2.191500	2.191410	-0.000090
Aluminum	EOIM3-5-1	2.241205	2.241180	-0.000025

Table 2. Solar Absorptance Calculations of EOIM III Samples

Sample	Sample ID		Solar Absorptance		Change
			Pre-flight	Post-flight	
Chemglaze A276	EOIM3-1-1	Flight	0.528	0.295	-0.233
	EOIM3-1-2	Control	0.537	0.534	-0.003
	EOIM3-1-3	LANL	0.536	0.258	-0.278
S13GLO	EOIM3-2-1	Flight	0.417	0.355	-0.062
	EOIM3-2-2	Control	0.424	0.422	-0.002
	EOIM3-2-3	LANL	0.422	0.386	-0.036
S13GLO	EOIM3-3-1	Flight	0.507	0.515	+0.008
	EOIM3-3-2	Control	0.515	0.506	-0.009
Chemglaze Z306	EOIM3-4-1	Flight	0.955	0.960	+0.005
	EOIM3-4-2	Control	0.953	0.952	-0.001
Aluminum	EOIM3-5-1	Flight	0.394	0.330	-0.064
	EOIM3-5-2	Control	0.393	0.390	-0.003

Table 3. XPS Surface Analysis of EOIM III Flight Samples

Sample	Surface Mole % (Normalized)											
	C	O	Si	Sn	Ti	N	S	Cl	Na	F	Al	
Chemglaze A276 (TE):												
EOIM3-1-1												
Pre-flight	51	38	5.5	0.7	trace	3.1	0.4	0.2	0.5	0.6	~0.2	
Post-flight	30	51	12	1.1	0.4	2.7	0.2	trace	1.7	0.4	~3	
EOIM3-1-3 (LANL)												
Pre-exposure	50	38	7.5	0.5	trace	2.9	0.4	0.1	0.4	0.4	~0.2	
Post-exposure	23	52	14	1.2	0.6	1.2	0.5	nd	1.6	0.2	6.1	
Z306 (TE, contaminated):												
EOIM3-4-1												
Pre-flight	30	53	15	0.1	nd	1.4	0.2	nd	0.1	0.3		
Post-flight	23	56	19	0.1	nd	1.1	trace	nd	trace	0.2		
S13GLO (TE):												
EOIM3-2-1												
Pre-flight		33	43	19	0.6	0.3	2.2	0.5	0.4	0.5	0.4	
Post-flight		22	47	25	0.8	1.8	2.2	0.1	1.1	0.4	0.1	
EOIM3-2-3 (LANL)												
Pre-exposure		34	41	21	0.6	0.4	1.9	0.6	0.4	0.3	0.2	
Post-exposure		21	49	28	0.2	0.3	0.7	0.3	0.2	0.1	nd	
S13GLO (LE, contaminated):												
EOIM3-3-1												
Pre-flight		19	53	28	nd	nd	0.2	0.2	nd	nd	nd	
Post-flight		16	55	29	nd	trace	0.2	trace	trace	nd	0.1	
Anodized Aluminum (TE, contaminated):												
EOIM 3-5-1												
Pre-flight	46	37	5.7	4.8	0.4	0.3	0.3	1.7	0.3	0.2	2.4	0.4
Post-flight	11	57	11	14	0.5	0.8	0.2	0.5	0.6	0.3	2.3	2



Figure 1. Post-flight photograph of EOIM3-1-1, Chemglaze A276 LDEF TE.

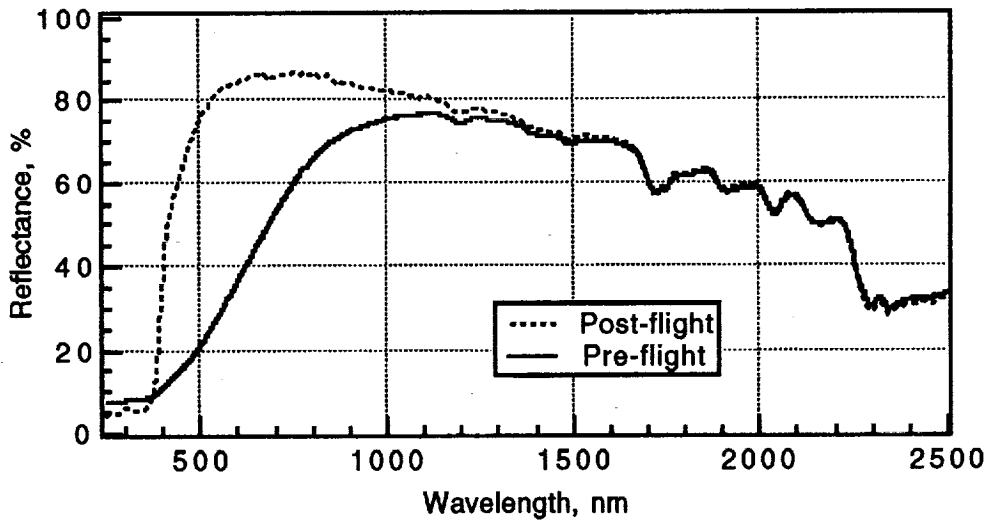


Figure 2. Reflectance spectra of EOIM3-1-1, Chemglaze A276 LDEF TE, before and after atomic oxygen exposure.

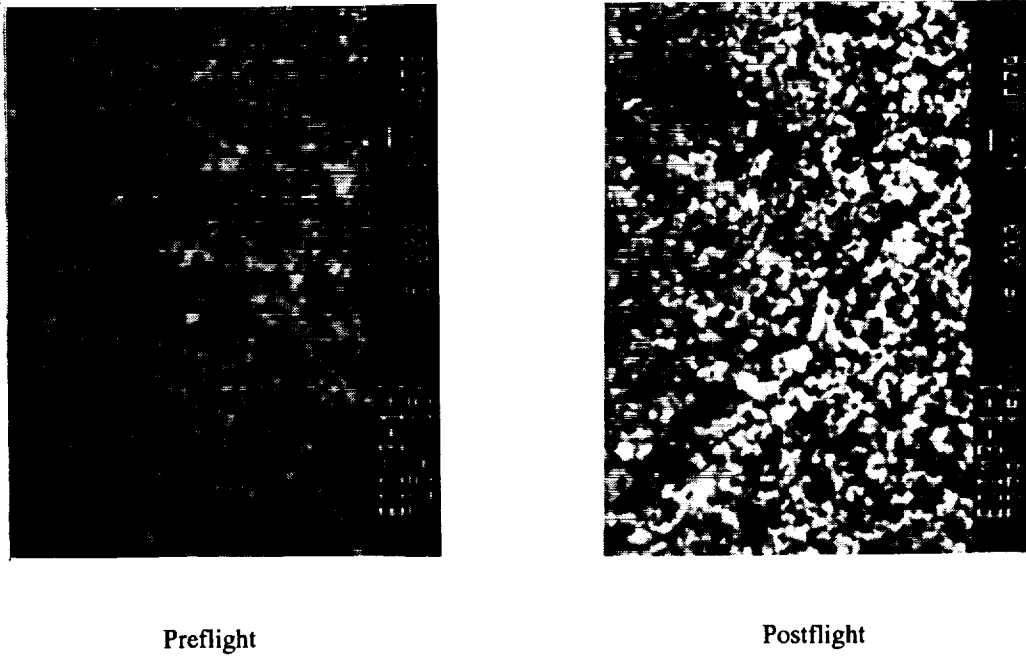


Figure 3. SEM photographs of EOIM3-1-1, Chemglaze A276 LDEF TE, before (left) and after (right) atomic oxygen exposure.

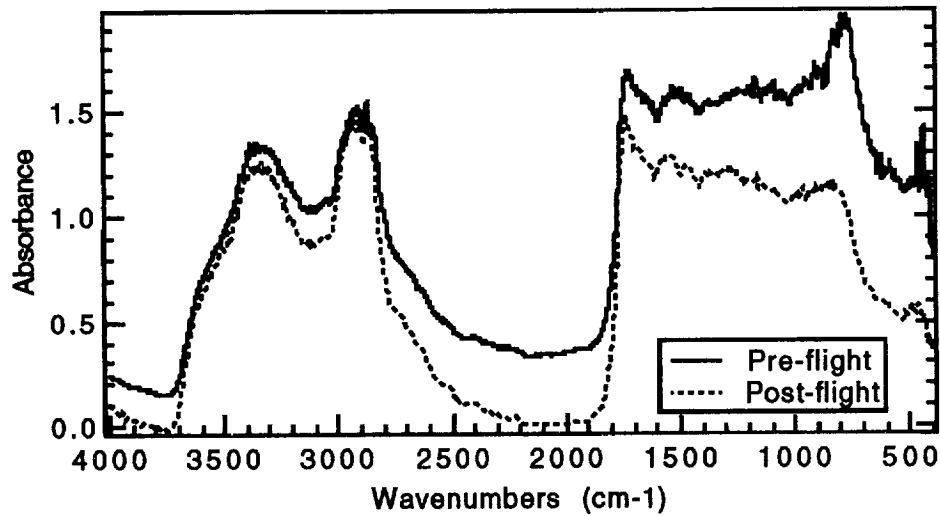


Figure 4. FTIR spectra of EOIM3-1-1, Chemglaze A276 LDEF TE, before and after atomic oxygen exposure.

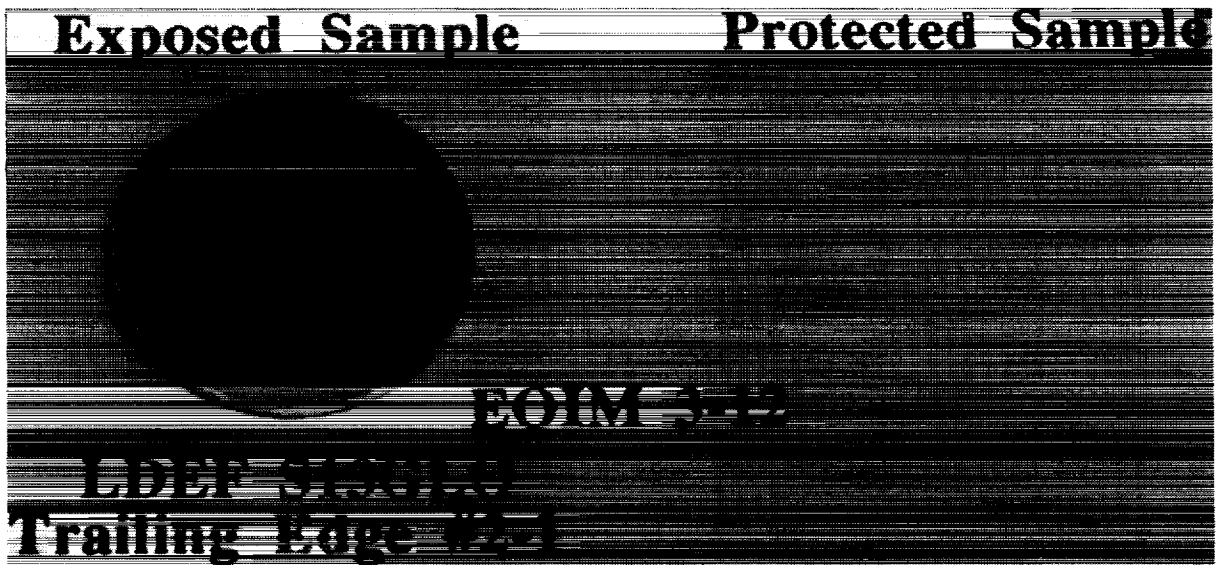


Figure 5. Post-flight photograph of EOIM3-2-1, S13GLO LDEF TE

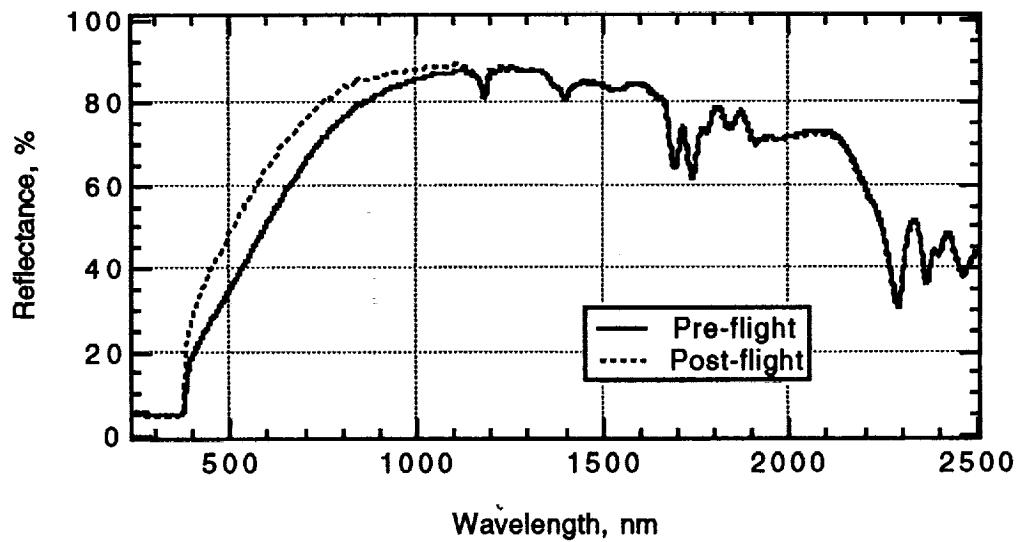


Figure 6. Reflectance spectra of EOIM3-2-1, S13GLO LDEF TE, before and after atomic oxygen exposure.

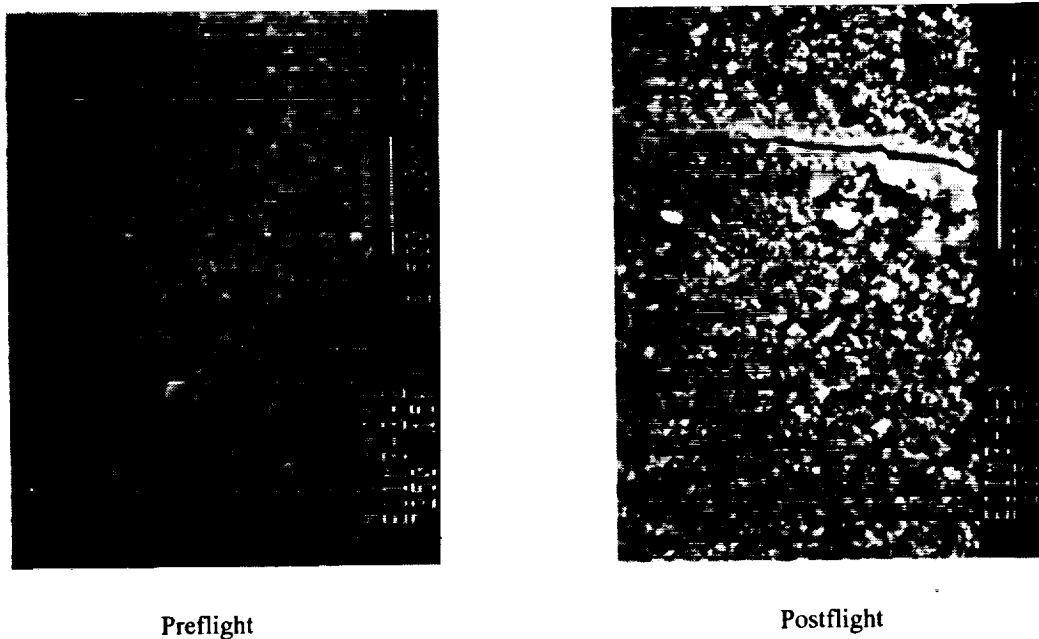


Figure 7. SEM photographs of EOIM3-2-1, S13GLO LDEF TE, before (left) and after (right) atomic oxygen exposure.

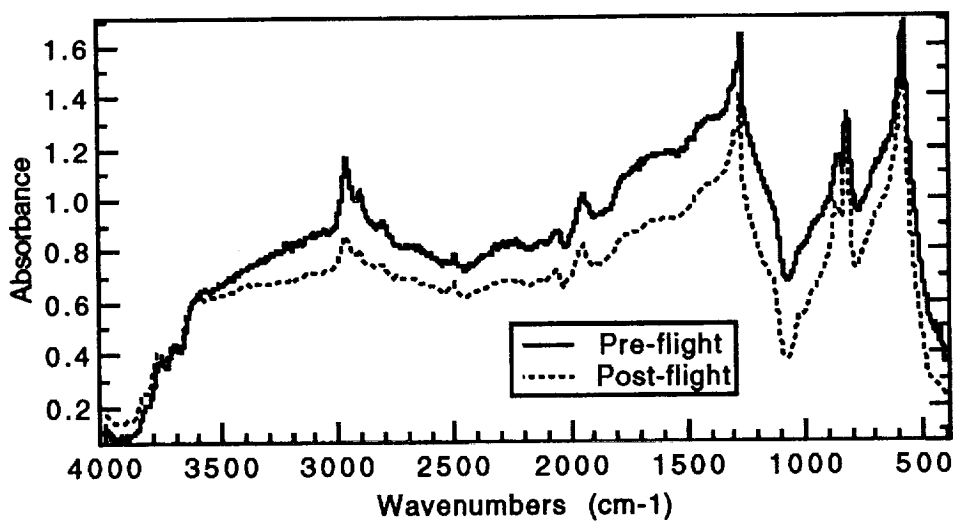


Figure 8. FTIR spectra of EOIM3-2-1, S13GLO LDEF TE, before and after atomic oxygen exposure.

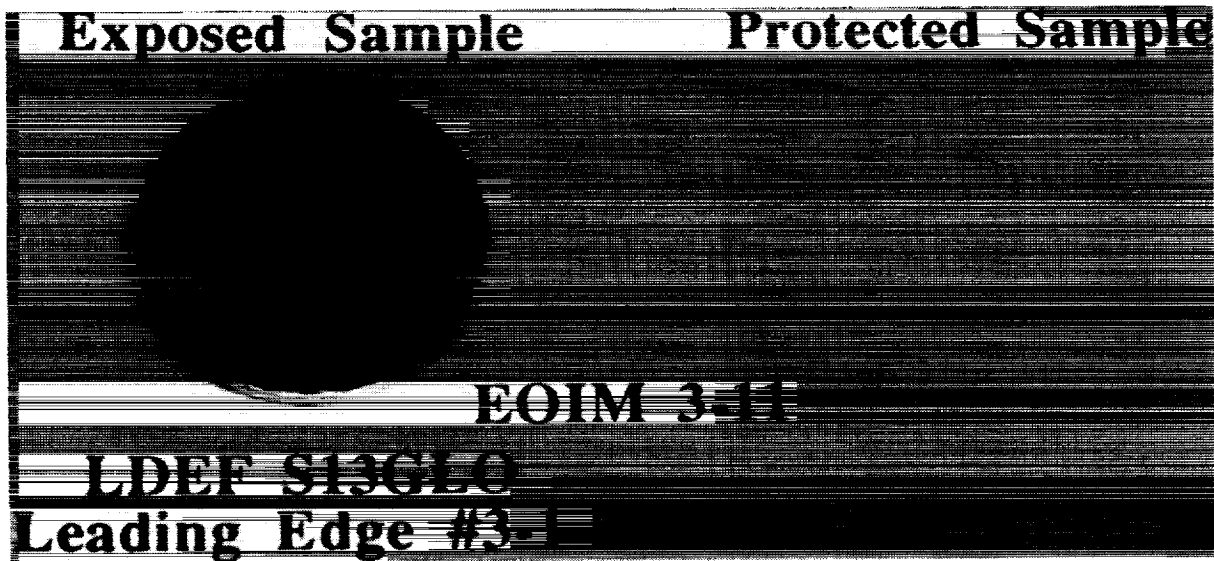


Figure 9. Post-flight photo of EOIM3-3-1, S13GLO LDEF LE (contaminated).

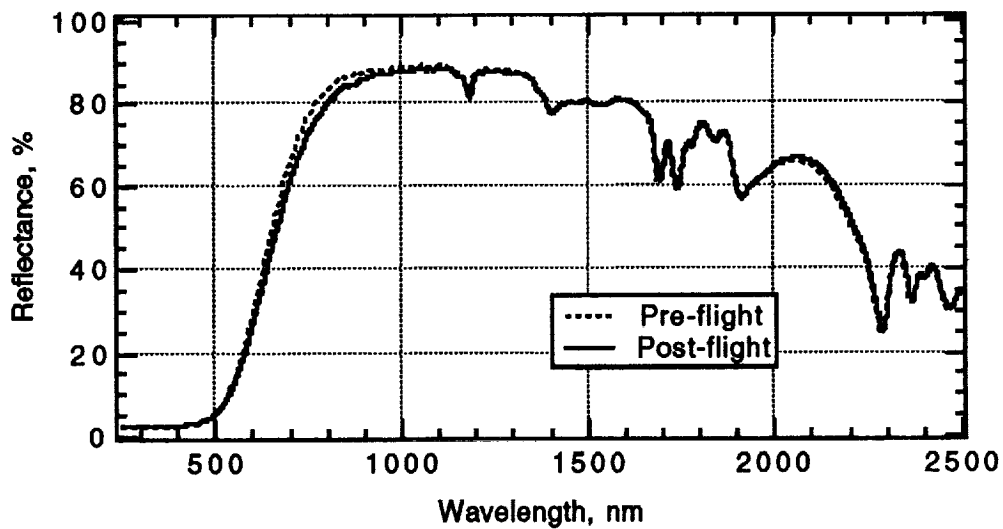


Figure 10. Reflectance spectra of EOIM3-3-1, S13GLO LDEF LE (contaminated), before and after atomic oxygen exposure.

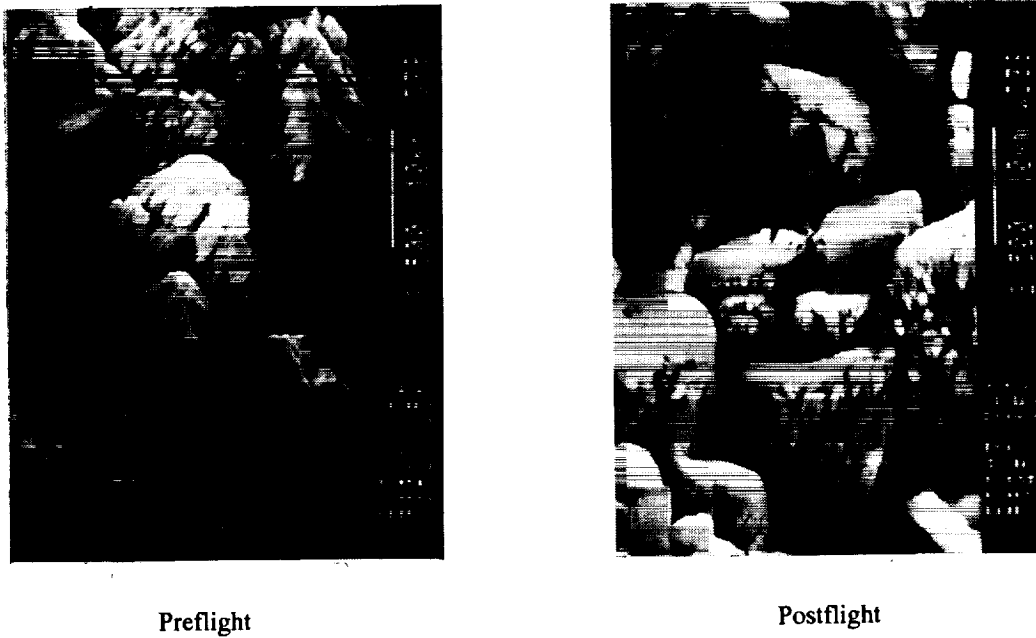


Figure 11. SEM photographs of EOIM3-3-1, S13GLO LDEF LE (contaminated), before (left) and after (right) atomic oxygen exposure.

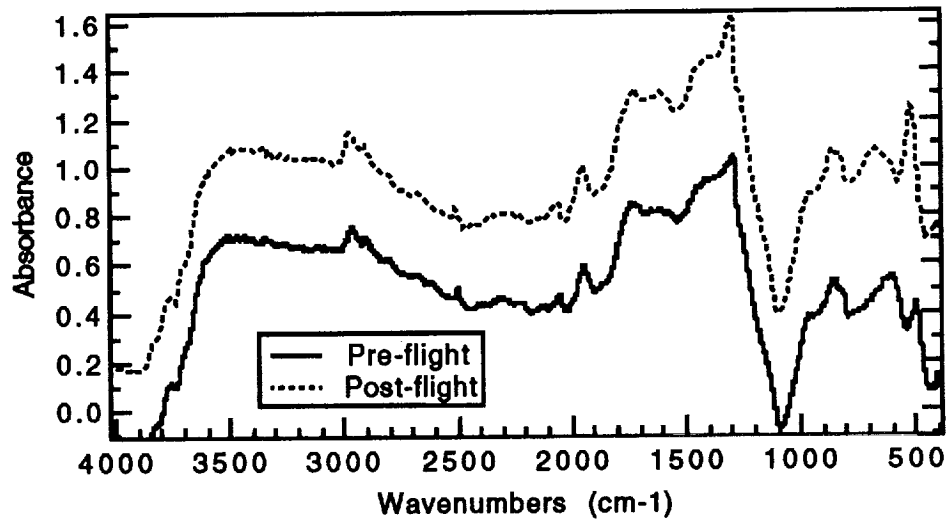


Figure 12. FTIR spectra of EOIM3-3-1, S13GLO LDEF LE (contaminated), before and after atomic oxygen exposure.

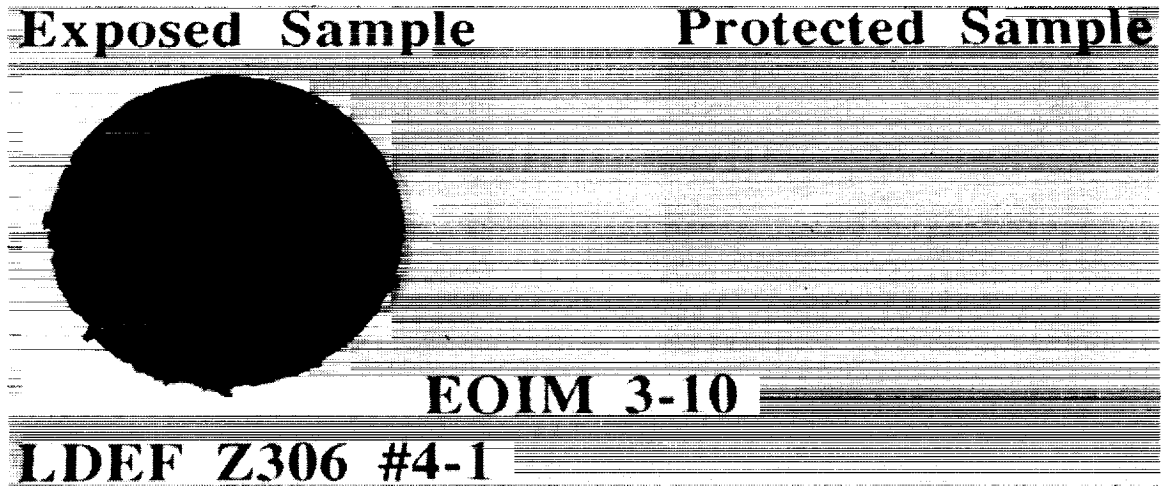


Figure 13. Post-flight photo of EOIM3-4-1, Z306 LDEF TE (contaminated).

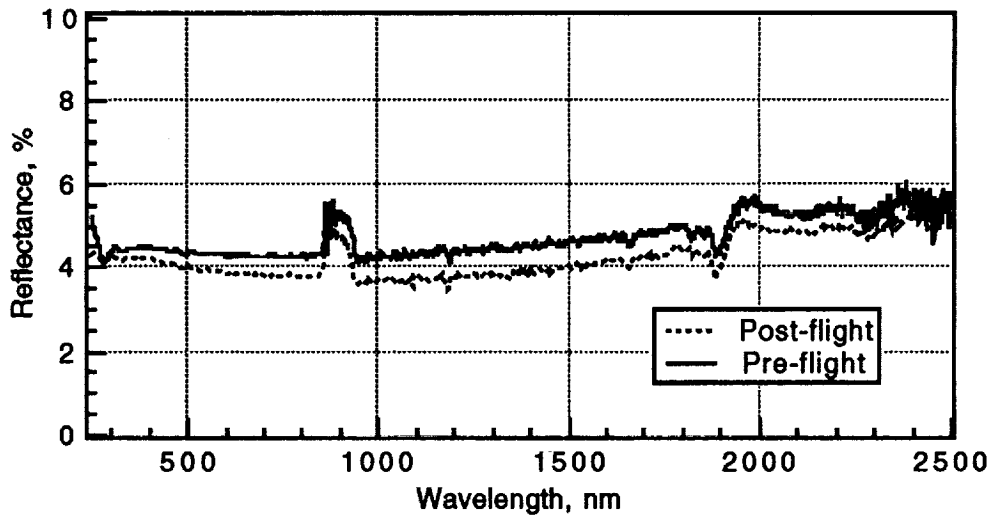


Figure 14. Reflectance spectra of EOIM3-4-1, Z306 LDEF TE (contaminated), before and after atomic oxygen exposure.

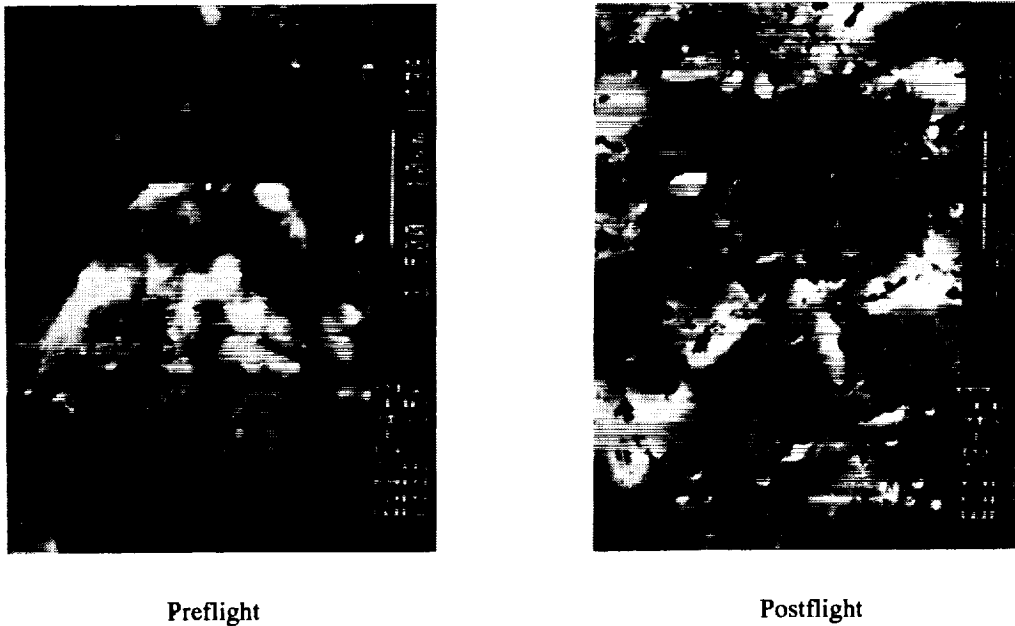


Figure 15. SEM photographs of EOIM3-4-1, Z306 LDEF TE (contaminated), before (left) and after (right) atomic oxygen exposure.

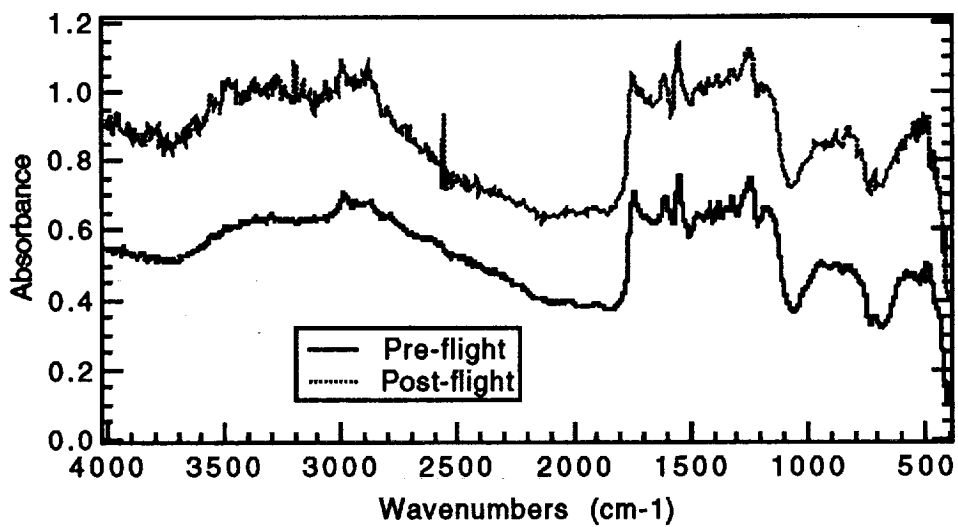


Figure 16. FTIR spectra of EOIM3-4-1, Z306 LDEF TE (contaminated), before and after atomic oxygen exposure.

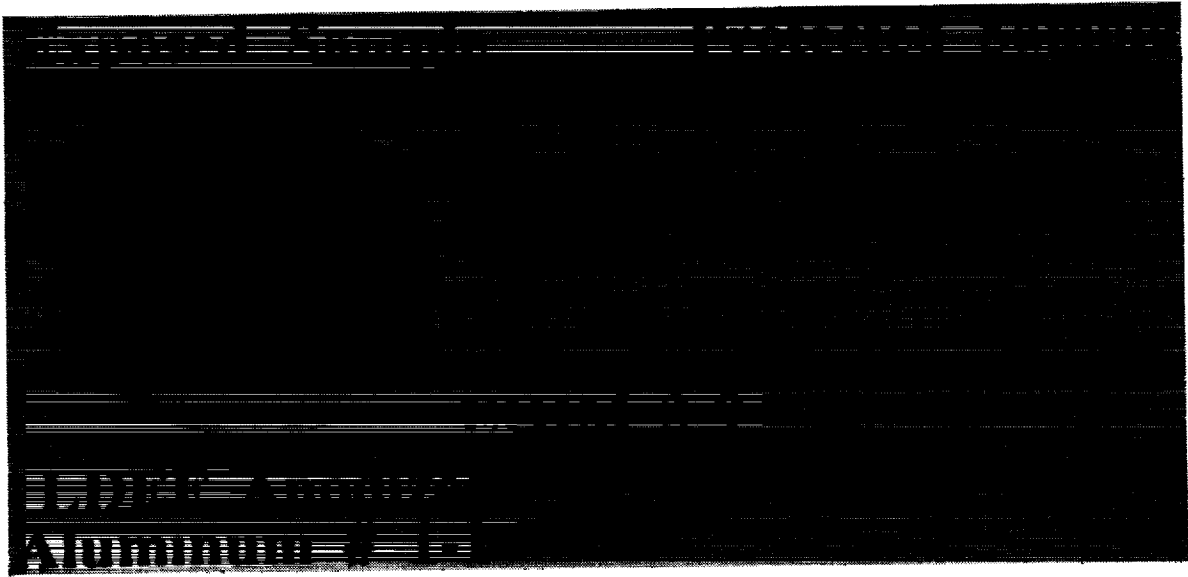


Figure 17. Post-flight photo of EOIM3-5-1, anodized aluminum LDEF TE (contaminated).

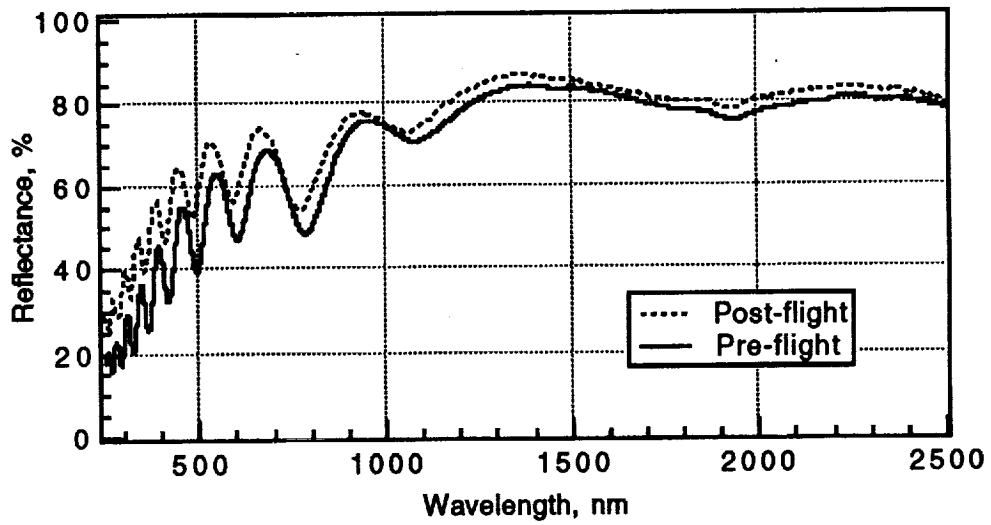


Figure 18. Reflectance spectra of EOIM3-5-1, anodized aluminum LDEF TE (contaminated), before and after atomic oxygen exposure.

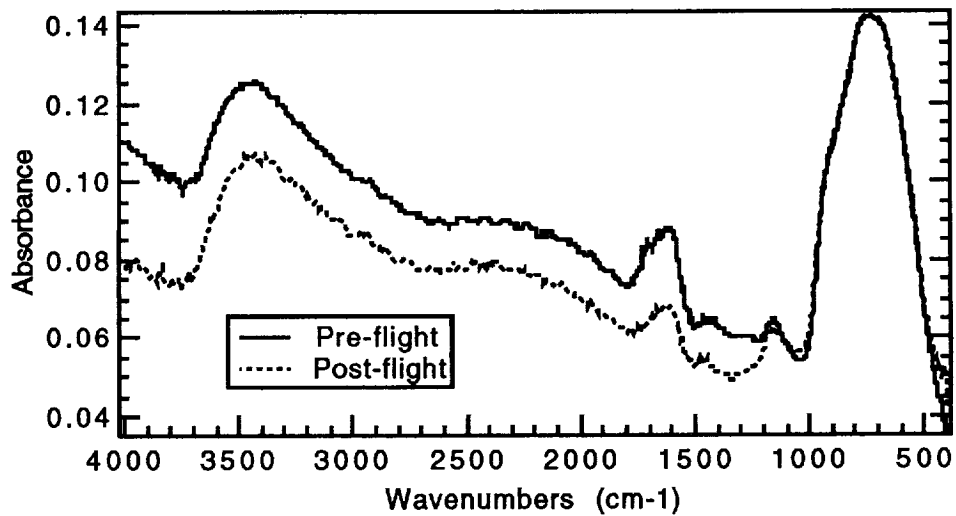


Figure 19. FTIR spectra of EOIM3-5-1, anodized aluminum LDEF TE (contaminated), before and after atomic oxygen exposure.

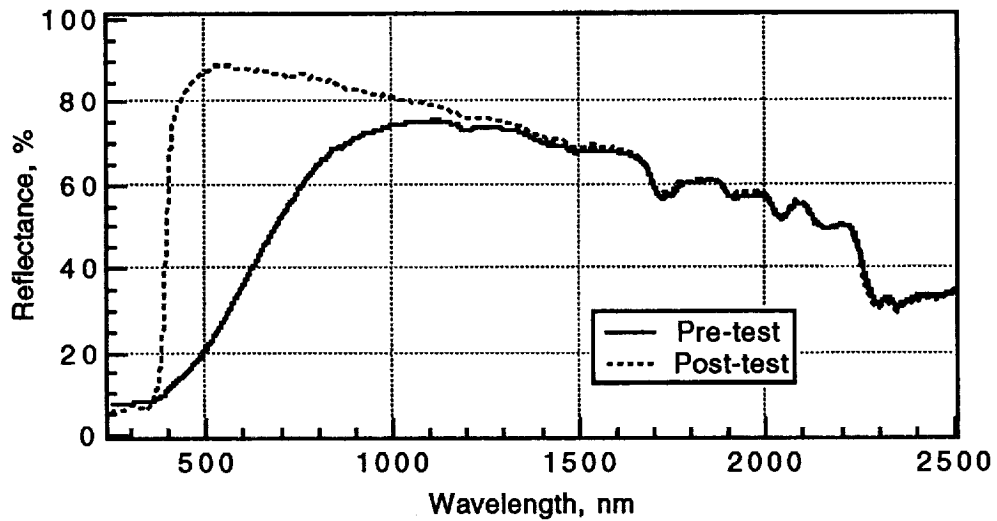


Figure 20. Reflectance spectra of EOIM3-1-3, Chemglaze A276 LDEF TE, before and after atomic oxygen exposure at LANL.

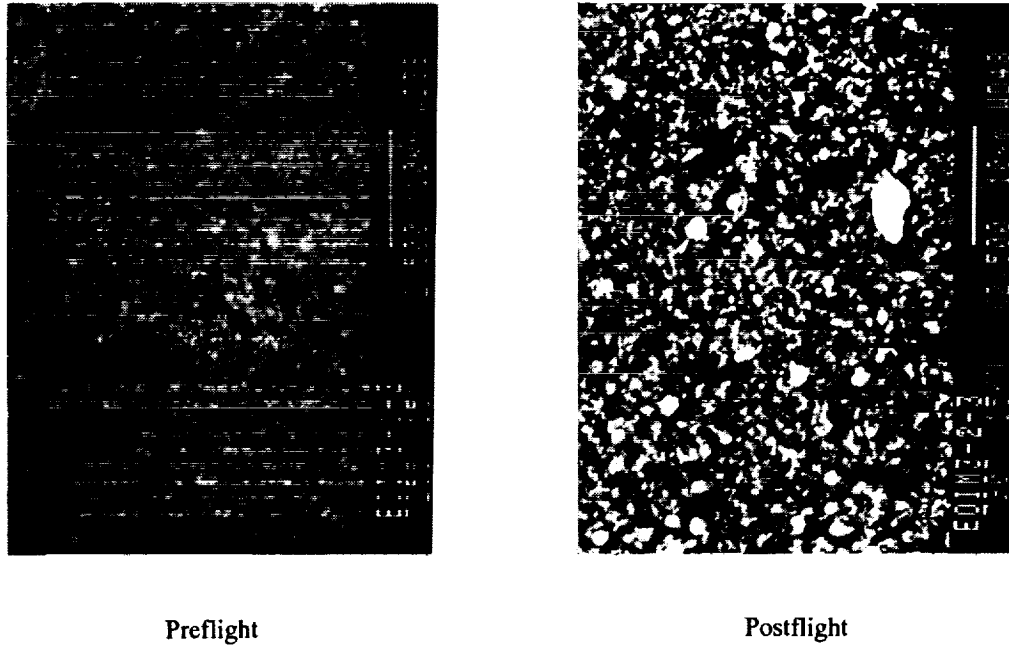


Figure 21. SEM photographs of EOIM3-1-3, Chemglaze A276 LDEF TE, before (left) and after (right) atomic oxygen exposure at LANL.

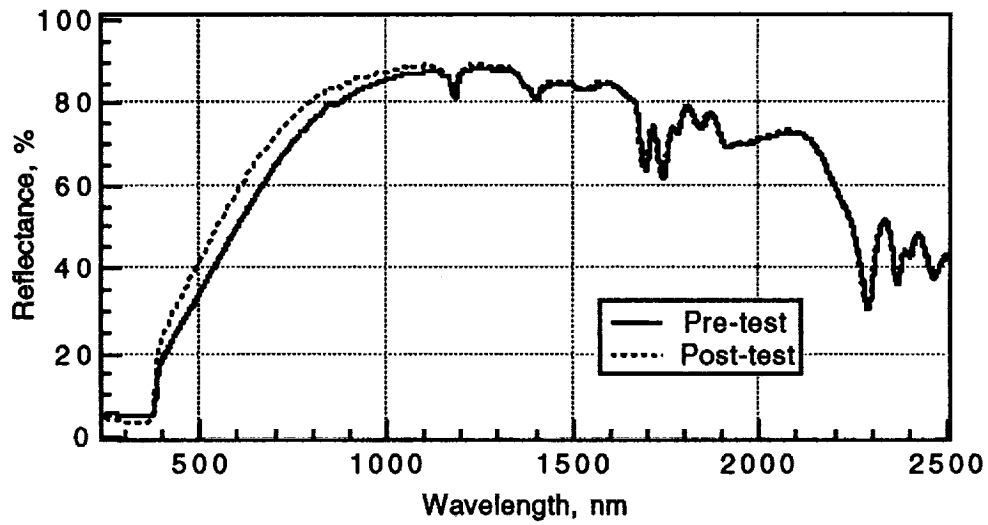
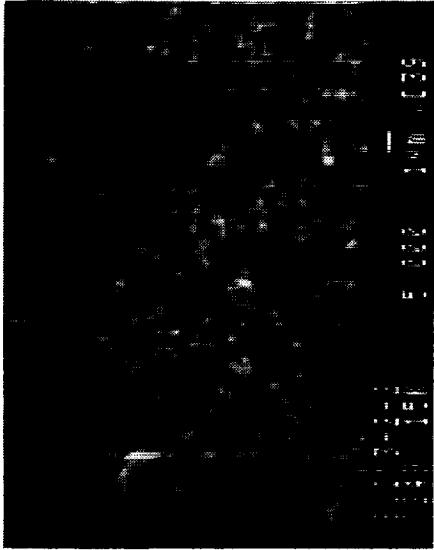
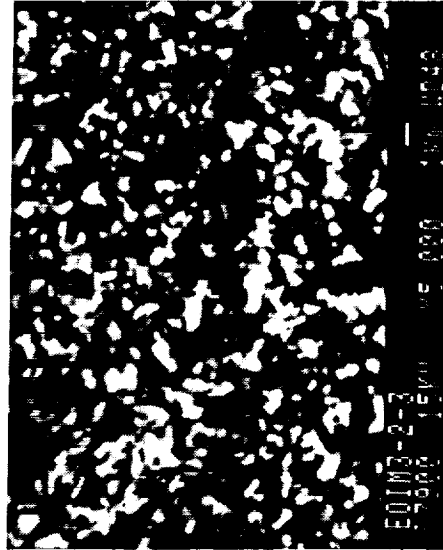


Figure 22. Reflectance spectra of EOIM3-2-3, S13GLO LDEF TE, before and after atomic oxygen exposure at LANL.



Preflight



Postflight

Figure 23. SEM photographs of EOIM3-2-3, S13GLO LDEF TE, before (left) and after (right) atomic oxygen exposure at LANL.

**ATOMIC OXYGEN DOSIMETRY MEASUREMENTS
MADE ON STS-46 BY CONCAP-II****J. C. Gregory, G. P. Miller, P. J. Pettigrew
and G N. Raikar***University of Alabama in Huntsville
Huntsville, AL 35899***J. B. Cross***Los Alamos National Laboratory
Los Alamos, NM***E. Lan***McDonnell Douglas Aircraft Corp
Huntington Beach, CA***C. L. Renschler***Sandia National Laboratory
Albuquerque, NM***W. T. Sutherland***Marshall Space Flight Center, AL 35812***ABSTRACT**

With increasing flight duration and the possibility of a permanent facility in space, long-term monitoring of material degradation due to atomic oxygen is increasing in importance. Reliance on models to determine the fluence of atomic oxygen is not only necessarily complex but also imprecise due to the strong dependence of oxygen concentration on day/night, latitude and solar activity. Mass-spectroscopy, the traditional method for determining the gas phase species densities at low pressure, is not only expensive but is limited in the area that it can monitor. Our group has developed a simple and inexpensive dosimeter to measure the atomic oxygen fluence via the change in resistance as the sensor element is gradually oxidized. The sensors consisted of thin-film circuit elements deposited on a suitable substrate. Four-point resistance measurements were used to monitor the change in resistance.

Results obtained using silver and carbon dosimeters flown on STS-46 (CONCAP II-01) will be discussed.

INTRODUCTION

In the region of Earth's atmosphere where the shuttle (and future space station) orbit, the composition of the atmosphere ceases to be dominated by diatomic molecules and is increasingly populated by atoms and ions. In particular, the number of oxygen atoms exceeds 90% of the species present in this region. As a dominant species and a major determinate of material degradation of external surfaces in space, atomic oxygen is an important long-life factor for spacecraft operating in this region. Therefore, it is essential that the spatial and temporal variations of atomic oxygen be monitored. Due to the strong dependence of atomic oxygen concentration on day/night, latitude and solar activity the reliance on models to determine the fluence of atomic oxygen is not only necessarily complex but also imprecise, due to a lack of experimental data.¹⁻⁶ The traditional method for experimentally determining the gas phase species densities at low

pressure is mass-spectroscopy. A flight MS instrument is not only expensive but also limited in the area that it can monitor. There is a need for a simple, relatively cheap atomic oxygen monitor to monitor atomic oxygen over the long-term.

To meet this need, the Material Science Laboratories, in conjunction with the Consortium for Materials Development in Space at the University of Alabama in Huntsville, is conducting a series of flight experiments. The aim is to develop an instrument that measures the atomic oxygen concentration via the change in resistance as the sensor element is oxidized. The principle of operation is based on the effect that atomic oxygen has on exposed materials. For example, silver reacts very readily with atomic oxygen to form silver oxide



(it has not been conclusively established whether Ag_2O , AgO or a mixture of both is actually formed) which can be taken to be an insulator in comparison to silver. The above reaction has been found to proceed with an efficiency of 1. That is, each atomic oxygen atom impacting with the surface reacts to form an oxide. These properties appear ideal for development of an atomic oxygen sensor relatively free of many of the problems inherent in the measurement of reactive species concentrations by mass spectrometry. In fact, it has proven to be a simple and very specific technique which dates from early sounding rocket launches undertaken in the 1970's. These experiments used silver films⁷⁻¹⁰ to obtain measurements of the atomic oxygen concentration to altitudes up to 95 km. However, due to the atomic oxygen density, these flights were capable of obtaining only one or two data points per flight.⁸

The aim of this work is to develop a dosimeter capable of measuring the hyperthermal atomic oxygen flux variations throughout a long-term space mission. This requires that the sensors be sufficiently sensitive and yet remain viable over the length of the mission. As shown later, under these circumstances the very reactivity of silver can become a problem, even at the lower atomic oxygen densities expected at higher orbits. This indicates a need to investigate other possible candidate materials. By virtue of the orbital velocity of the spacecraft, the relative kinetic energy of atmospheric atoms hitting the front surfaces of a spacecraft is about 5eV per atom (~ 500 kJ mole⁻¹). This is similar in magnitude to chemical bond energies and many examples of enhanced reactivity have been reported under these conditions. Effects have been shown to vary from heavy erosion in the case of polymers, carbon and osmium, corrosion of silver and copper, and significant changes in the optical, thermal and electrical properties of most material surfaces.¹¹⁻¹⁶

Oxidation rates obtained from two earlier flight experiments, EOIM-2 on STS-8 (1983) and experiment A0114 on LDEF (1984-1990)¹¹⁻¹⁶ indicated that carbon might provide a simple yet accurate method for measuring the atomic oxygen flux. Carbon, unlike silver, reacts to form a volatile oxide that then dissipates into space. For example,



and the carbon erodes with time, increasing the resistance across the sensor element. Results reported previously¹⁷ indicate that the reactivity of carbon to hyperthermal atomic oxygen is much lower than silver with the reaction probability of atomic oxygen atoms reduced to between 0.1 and 0.15. This effectively increases carbon sensor lifetimes by between 6 to 10 times compared to silver.

To this end, prototype dosimeters were designed using carbon and silver dosimeters, mounted on CONCAP-2 and flown on the Space Shuttle Atlantis (STS-46) in July-August 1992. The results of this experiment are reported here.

EXPERIMENTAL APPROACH

1. Dosimeters

The silver and carbon films were deposited between gold pads on 1 cm square substrates. The films were prepared and supplied by Dr. Renschler (Los Alamos), Dr. Smith/Ms. Lan (McDonnell Douglas) and Metech, PA. The specifications of the dosimeters are given in Table 1. The substrates were mounted in individual gold-coated Airpax integrated circuit mounts with Aramco 569 or 571 high temperature adhesives. Electrical connections within the mounts were made by conventional thermal acoustic bonding methods. Figure 1 shows two carbon and one silver dosimeters (preflight) in their mounts. External leads from the mounts were connected to the CONCAP measuring system.

Table 1
Dosimeter Specifications

Number of Samples	Material	Channel	Thickness	Reactivity
2	Silver	6 & 14	220 nm	1
1	vitreous carbon	24	290 nm	0.1 - 0.15
1	vitreous carbon	5	380 nm	0.1 - 0.15
1	carbon	28	28 μ m	unknown

The electrical resistance of the devices was measured during the flight exposure to provide real-time differential flux measurements, using a 4-point contact technique. In practice, however, this turned out to be a 3-point contact system. Sensitivity to contact resistance was therefore not removed.

A dosimeter lasting for multiple orbits moves in and out of the sun repeatedly as it orbits the Earth. This results in periodic changes in the temperature of the sensor elements as the element is alternatively heated and cooled. As both reaction rate and resistance are temperature-dependent, it is essential to characterize the effects of these changes. Platinum resistance thermometers (RTD's) were mounted in the base-plate to monitor changes in the temperature (in addition to controlling the hot-plate used in other experiments).

After final testing of the CONCAP-II controller and measuring system, the samples were mounted at Goddard Space Flight Center. This was done as close as possible to the flight with final changes being made at Kennedy Space Center just before closing the motorized door assembly. Figure 2 shows the preflight experiment insert plate on which the dosimeters are mounted.

2. Flight Description

The exposure was made towards the end of the STS-46 mission, with the shuttle at 123 nautical miles (228 km) altitude. The shuttle was in a nominal 28.5 deg-inclination orbit and, during the CONCAP-2 exposure, was flown at this relatively low altitude to maximize the O-atom exposure during the limited experiment time of 20 hours. The shuttle was oriented so that the normal to the cargo bay was within ± 2 deg of the velocity vector. This ensured that all the atmospheric O-atoms

struck the experimental surfaces at close to normal incidence. The gas can was positioned next to the aft bulkhead. Reflection of atoms from this bulkhead may have affected the absolute fluence of O-atoms seen by CONCAP.

Flight operations for CONCAP are given in Table 2. The experimental surfaces on CONCAP-2 were protected from ambient contamination during all ground and orbital operations by a hermetically sealing lid which was operated by the astronauts. The lid was opened as the shuttle maneuvered into the correct attitude and closed before leaving this attitude.

Table 2

Flight Operations	Experiment Elapsed Time
Orbiter in correct attitude Power to CONCAP controller MDA (lid) open at Mission Elapsed Time 5 days:22 hr:42 min	0
Hot plate on	4 hr:3 min
Temporary de-activation of hot plate	4 hr:34 min
Reactivate hot plate	5 hr:33 min
Hot plate off	15 hr:16 min
CONCAP MDA closed, controller off	20 hr:50 min

3. CONCAP-II Hardware

CONCAP-II utilizes a Get Away Special (GAS) carrier system fitted into the Space Shuttle payload bay. The 5-cubic-foot GAS canister has a hermetically sealed motorized door assembly, which protects samples and sensitive surfaces during all ground and flight operations, other than the exposure period itself. CONCAP-II has an electronic experiment controller and a data system to record resistance measurements of up to 32 samples several times per minute during exposure, as well as a hot-plate capable of maintaining samples at 320° C.

CONCAP's power supply and data acquisition/storage system are self-contained, requiring no Shuttle interface, and are adaptable for other kinds of experiments as well. The power system consists of a battery, solid state switches, and DC/DC converters to supply the heater and electronics. The system supplies 1.4 kW-hrs of power at 28 volts. The 80C86 microprocessor-based data and control system is capable of sampling up to 32 analog channels and uses a 12-bit analog to digital converter. Data blocks are stored every 60 seconds in normal mode and every second in high rate mode; time and experiment status are stored in each block as well.

RESULTS

Six dosimeters were flown. They consisted of two silver and four carbon films, (see Fig.1). All the dosimeters worked successfully with the exception of one carbon film that was mounted on the

320°C hot plate. The measured atomic oxygen flux is compared with values calculated using the MSIS-86 model of the atmosphere and preliminary results from the mass spectrometer flown on the same mission.¹⁸

1. Silver.

Figures 3 and 4 are plots of R_0/R versus elapsed experiment time, where R_0 , and R are the initial and real-time resistance's, respectively. These results amply demonstrate the extreme reactivity of silver, the samples being exhausted in less than 30 seconds following the start of data collection (there was a delay of 1 minute after the removal of the cover to prevent false starts). The presence of a passive surface layer of absorbed gas or other contaminants on the surface of a sensor element is known to yield a non-linear initial response.⁷ The programmed start-up delay prevented us from defining this response.

Following the criteria established by Henderson and Schiff,⁷ results from the two silver samples yielded AO fluxes of 1.7 and 1.64×10^{15} atoms/sec. for an atomic oxygen density of approximately 2.15×10^9 atomic oxygen atoms/cm³. These results are high compared with the average flux calculated for EIOM-3 of 1.4×10^{15} atoms/sec (and that predicted by MSIS model). While both films had identical thicknesses of 22 nm, Channel 6 was significantly more oxidized when measurements started. As thermally-accommodated atomic oxygen also readily oxidizes silver, we believe that the apparent high flux can be explained by the presence of thermally accommodated atomic oxygen scattered from the lid and other areas of the cargo bay.

These results indicate that while silver dosimeters are capable of providing a snapshot of the atomic oxygen flux they clearly demonstrate the need to use less reactive materials both for long-term dosimeters and to allow for the differentiation between hyperthermal and thermally-accommodated atomic oxygen.

2. Carbon.

Two forms of carbon were used: thin vitreous carbon films supplied by Dr. Renschler (Sandia) and a commercial thick-film composite supplied by Metech, PA.

Vitreous Carbon.

Results for the vitreous carbon are shown in Figures 5 & 6. The plots of R_0/R extend over four orbits and reveal a more complex picture than for silver. The reversal in the monotonic decrease in R_0/R at periodic intervals is the result of solar heating (and a resulting decrease in resistance). As mentioned earlier, the platinum resistance thermometers (RTD's) mounted in the baseplate were used to measure the change in temperature due to solar heating (in addition to controlling the heaters for the hot-plate). In Figure 7 the effect of solar heating can be seen, modulated by the orbital period. Since the platinum detector elements are inside the 0.25 inch thick aluminum heater plate, this effect (of the order of 10 deg.) may be less, for example, than the solar heating effects on the dosimeter elements. Using the temperature coefficient of resistance we found the temperature rise to be approximately 15 - 20 degrees.

It must be remembered that not only does this change in temperature alter the resistance, it also changes the reaction rate. As a preliminary estimate, a calculation of the temperature dependence of the reaction rate was made using

$$r = Ae^{\frac{-\Delta E}{RT}}$$

and taking the Arrhenius activation energy, ΔE , value of 1200 cal mole⁻¹ given in ref.17 and the change in temperature from the RTD's. It was found that the maximum effect of solar heating was insignificant, increasing the rate of reaction less than 3%.

Using the change in resistance, the flux for each film is given in Figures 8 and 9 together with the flux predicted by the MSIS model.¹ These results indicate that after an initial non-linear period, the flux calculated from the change in resistance mirrors the periodic behavior predicted by the MSIS model but that significant differences can be seen with respect to the day/night values obtained. These differences are supported by the preliminary mass spectrometry data (Fig. 10).

It should be noted that although the two films were approximately 90 nm different in thickness both carbon films were completely eroded in approximately the same time. We believe that this can be explained by the closer proximity of the thicker film to the hotplate, increasing the temperature of the sensor and therefore the reaction rate. This conclusion is supported by the apparent increase in flux after the hotplate is switched on, peaking at 1.8×10^{15} and 2.2×10^{15} atoms sec⁻¹ for channels 24 and 5 respectively at MET of 340 minutes.

Thick Carbon Film.

A thick ($28 \pm 5 \mu\text{m}$) carbon film supplied by Metech, PA was employed as a possible candidate as a long term dosimeter. Unfortunately, the resistance values fell into a range where the bit noise was significant. Nevertheless, after smoothing, solar effects can still be observed. Figure 11 shows the response of this sensor. The sharp drop in R_0/R , starting at 300 minutes into the mission, results from leakage from the hotplate heating the sample.

From the slope in Figure 11 (before hotplate heating and after the initial non-linear period, 50 to 250 minutes) we calculated the average flux at 3.5×10^{15} atoms sec⁻¹. This result is in very good agreement with both the MSIS and vitreous carbon data.

The hotplate heating was used to obtain a measure of the Arrhenius activation energy, ΔE , of hyperthermal oxygen atoms with this particular form of carbon. This yielded a value of approximately 2600 cal mole⁻¹. It must be noted that the temperature during this period never reached a steady-state and thus the activation energy obtained should be taken as an estimate only.

The most notable result from the use of this film is that over the entire mission the resistance changes by only 7-8% for an estimated total fluence of 1.1×10^{20} . This indicates that this sensor is capable of measuring fluences of the order of 1.5×10^{21} atoms.

Summary and Conclusions.

In this paper we report on real-time atomic oxygen flux data obtained on STS-46 using the CMDS autonomous payload system, CONCAP-II. Three different sensors; Ag, vitreous carbon, and a thick-film carbon composite were exposed to the Low-Earth orbit environment. The real-time resistance changes were measured and recorded. The following conclusions were reached:

1) The silver sensors are too reactive, having a very short life under the high flux experienced. A problem also arises because silver is oxidized by both thermally-accommodated & hyperthermal atomic oxygen, making it impossible to distinguish between them.

2) Sensors consisting of vitreous carbon lasted for approximately 4 orbits and a fluence of 2.5×10^{19} atoms. They yielded flux variations that, while generally in good agreement with the MSIS model, indicated significant diurnal differences. A result confirmed by the preliminary mass data. These results indicate the need for further work in refining the computer models.

3) Noisy data and the lack of an Arrhenius activation energy for the thick-film carbon composites limited the conclusions that could be reached in this case. However, the film was found to be very durable, yielding only a 7-8% change in resistance over 20 hrs for a fluence of 1.1×10^{20} atoms cm^{-2} .

4) A major point to come out of this study is the importance of temperature effects on resistance based dosimeters. We are still in the process of eliminating temperature effects. The final results will be reported later. However, it is apparent from the data that temperature control is a necessary feature to eliminate changes in resistance and in reaction rates resulting from solar heating or leakage from nearby instrumentation.

5) In the process of developing these sensors the lack of data on reaction rates of materials exposed to 5 eV atomic oxygen became very apparent. More work is needed in this area.

Overall, the results indicate that atomic oxygen dosimeters are capable of playing a significant role in the study and monitoring of the Low-Earth environment replacing in part the traditional method for determining the gas phase species densities at low pressure, mass-spectroscopy - a technique which is not only expensive but limited in the area that it can monitor. To conclude, our group has developed a simple and inexpensive dosimeter to measure the atomic oxygen fluence via the change in resistance as the sensor element is gradually oxidized.

Acknowledgments:

CONCAP-II-01 was sponsored by the Consortium for Materials Development in Space (CMDS), at the University of Alabama in Huntsville.

MSIS data and the preliminary EOIM-MS data was provided by Steve Koontz, JSC.

References.

- 1) Hedin, A. E., MSIS-86 Thermosphere Model. *J. Geophys. Res.* 92, 4649, 1987.
- 2) Hedin, A. E., A revised thermospheric model based on mass spectrometer and incoherent scatter data: MSIS-83. *J. Geophys. Res.* 88, 170-10, 188 1983.
- 3) Hedin, A. E., and M. J. Engebretson, Empirical model of thermospheric atomic nitrogen, *EOS Trans. AGU* 67, 322 1986.
- 4) Hedin, A. E., C. A. Reber, N. W. Spencer, H. C. Brinton, and D. C. Kayser, Global model of longitude/UT variations in thermospheric composition and temperature based on mass spectrometer data. *J. Geophys. Res.* 84, 1 1979.
- 5) Jacchia, L. G., Thermospheric temperature density and composition: New models, *Spec. Rep.* 375, Smithsonian Astrophys. Obser., Cambridge, MA 1977.
- 6) Kohnlein, W., D. Krankowsky, P. Lammerzahn, W. Joos and H. Volland, A thermospheric model of the annual variations of He, N, O, N₂, and Ar from the AEROS NIMS data, *J. Geophys. Res.* 84, 4355, 1979.
- 7) Henderson, W. R. and H. I. Schiff, A simple sensor for the measurement of atomic oxygen height profiles in the upper atmosphere. *Plant. Space Sci.* 18, 1527, 1970.
- 8) Henderson, W. R., D-Region Atomic Oxygen Measurement. *J. Geophys. Res.* 76, 3166, 1971.
- 9) Thomas, R. J. and D. J. Baker, Silver Film Atomic Oxygen Sensors, *Can. J. of Phys.* 50, 1676, 1972.
- 10) Henderson W. R., Silver Film Atomic Oxygen Sensors: Further Evidence for Utility as an Atmospheric Probe. *Can. J. of Phys.* 52, 2174, 1974.
- 11) Gregory J. C. and P. N. Peters, A measurement of the attitude stability of the LDEF satellite using a Silver/Silver Oxide detector, *J. Guid., Contr. and Dynamics, AIAA* 15, 282, 1992.
- 12) Peters, P. N., R. C. Sisk and J. C. Gregory, Oxygen Atom Velocity Distributions as viewed from a Spacecraft and their use to determine Thermospheric Temperatures, *J. Spacecraft &*

Rockets 25, 53, 1988.

- 13) Gregory J. C. and P. N. Peters, Reaction of 5eV Oxygen atoms with Polymeric and Carbon Surfaces in Earth Orbit, *Adv. in Space Res.*, 7, 231, 1987.
- 14) Gregory J. C. and P. N. Peters, A Measurement of the Angular Distribution of 5eV Atomic Oxygen scattered off a Solid Surface in Earth Orbit, *Rarefied Gas Dyn.*, 15, 644, 1986.
- 15) Peters, P. N. J. C. Gregory, and J. Swann, Effects of 5eV Atomic Oxygen Exposure on Space Optics, *App. Optics*, 25, 1290, 1986.
- 16) Raikar, G. N., J. C. Gregory, L. C. Christl, P. N. Peters, Interaction of atomic oxygen with thin films and bulk copper: an XPS, ASE, XRD and Profilometer Study, *Proc. 2nd LDEF Post-Retrieval Symp., San Diego*, NASA Conference Publication 10097.
- 17) Gregory, J. C., Interaction of Hyperthermal Atoms on Surfaces in Orbit, *Proc. of the NASA Workshop on Atomic Oxygen Effects* JPL Publication 87-14
- 18) Koontz S., *Private Communications*.

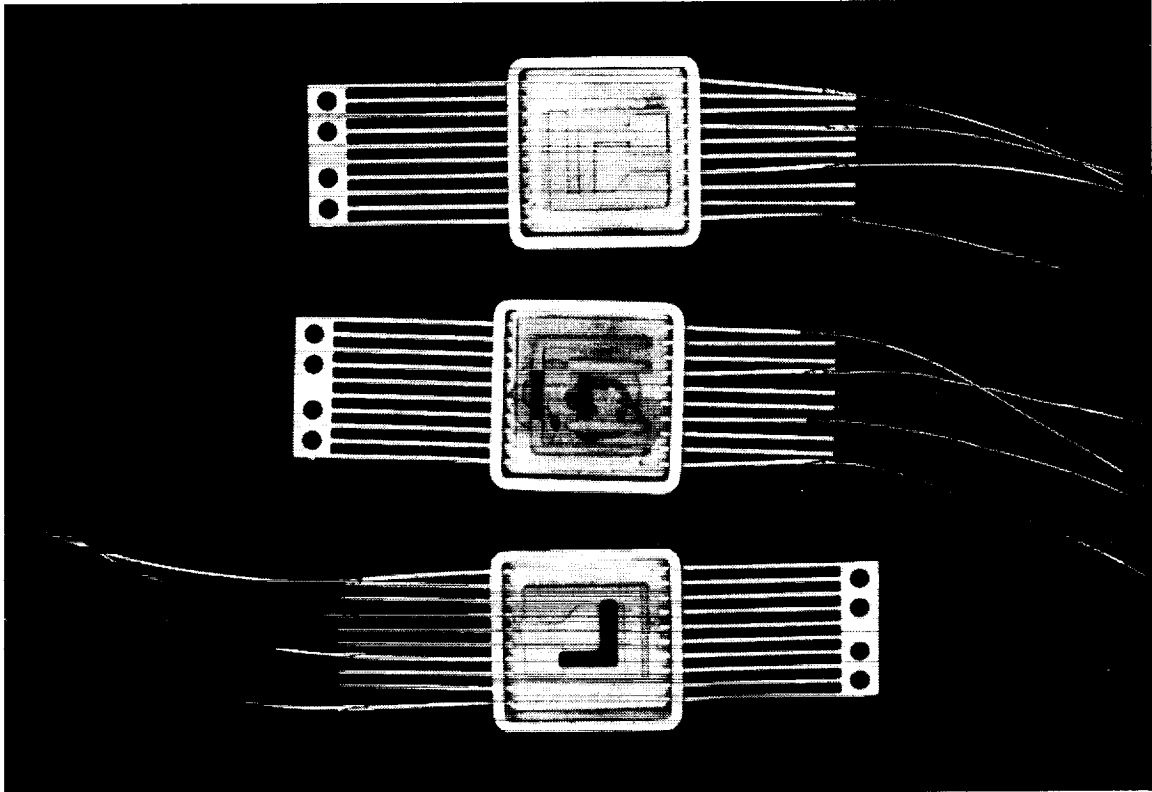


Figure 1: Three pre-flight dosimeters (two vitreous carbon, one silver) in their mounts.

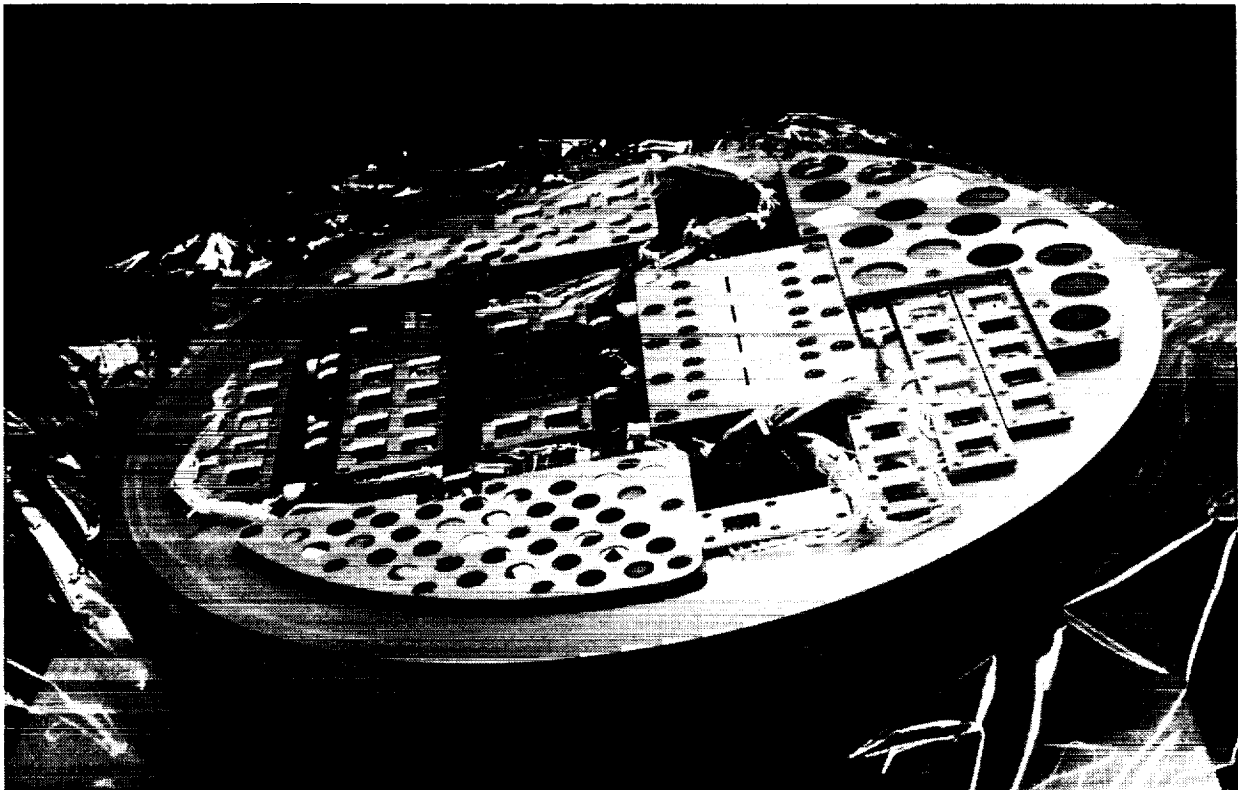


Figure 2: The experimental insertion plate on which the dosimeters were mounted.

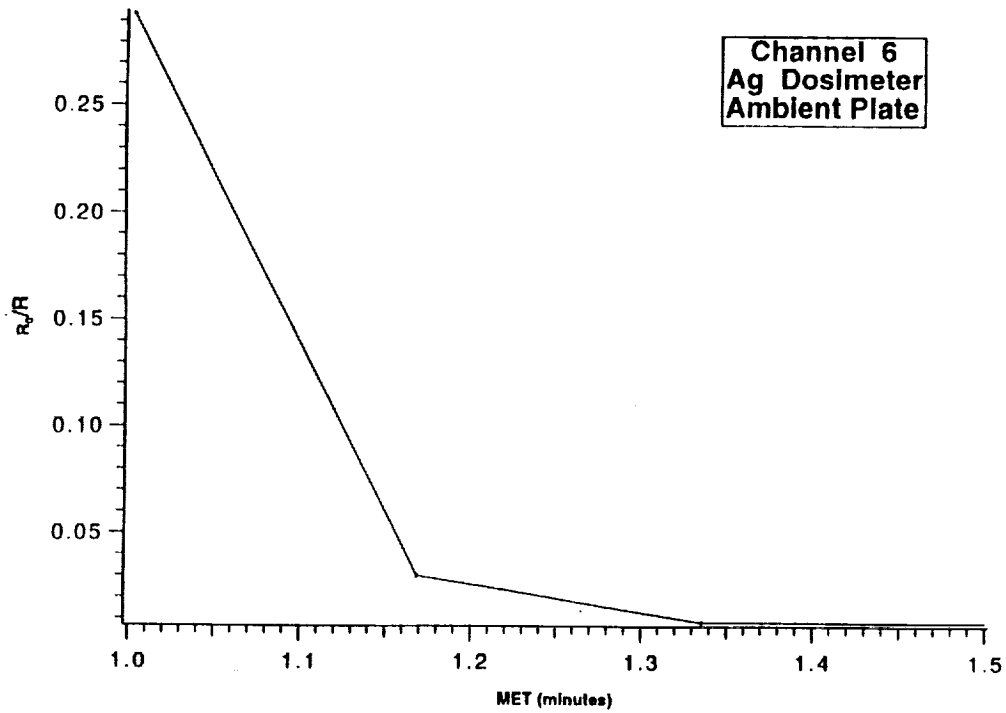


Figure 3: The change in resistance upon exposure to atomic oxygen for Silver dosimeter (Channel 6).

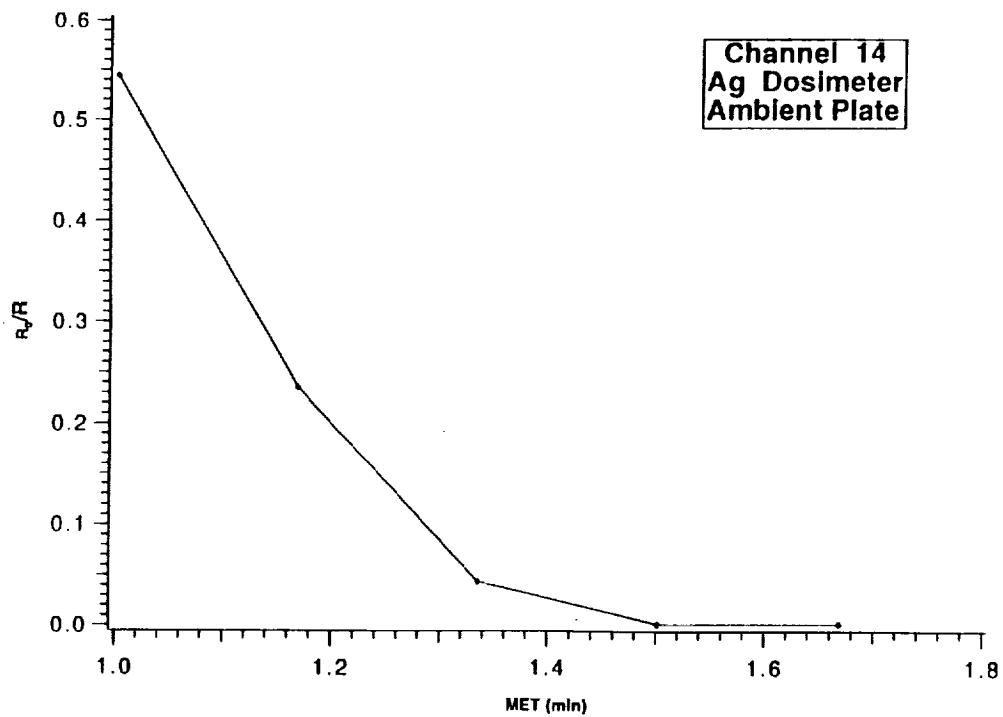


Figure 4: The change in resistance upon exposure to atomic oxygen for Silver dosimeter (Channel 14).

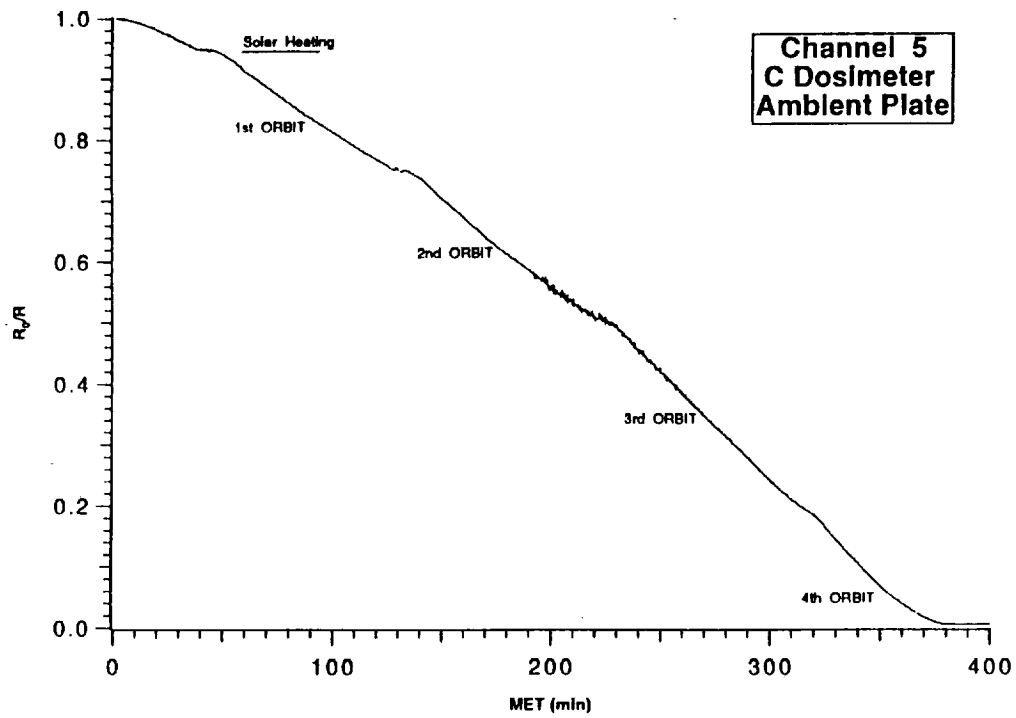


Figure 5: The change in resistance upon exposure to atomic oxygen for the vitreous carbon dosimeter (Channel 5).

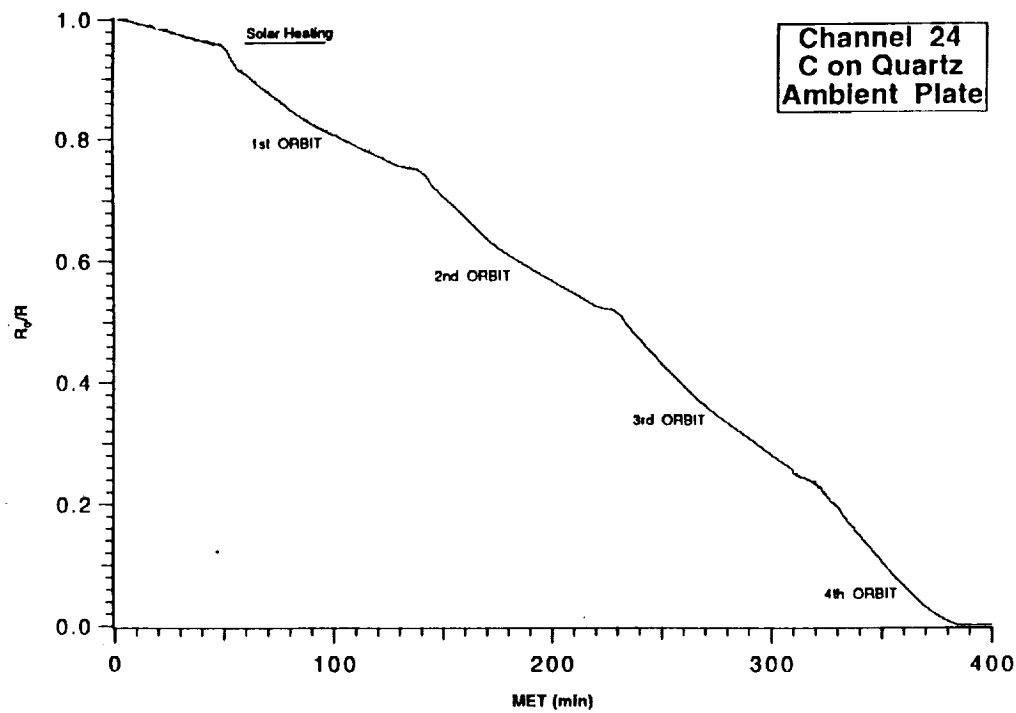


Figure 6: The change in resistance upon exposure to atomic oxygen for the vitreous carbon dosimeter (Channel 24).

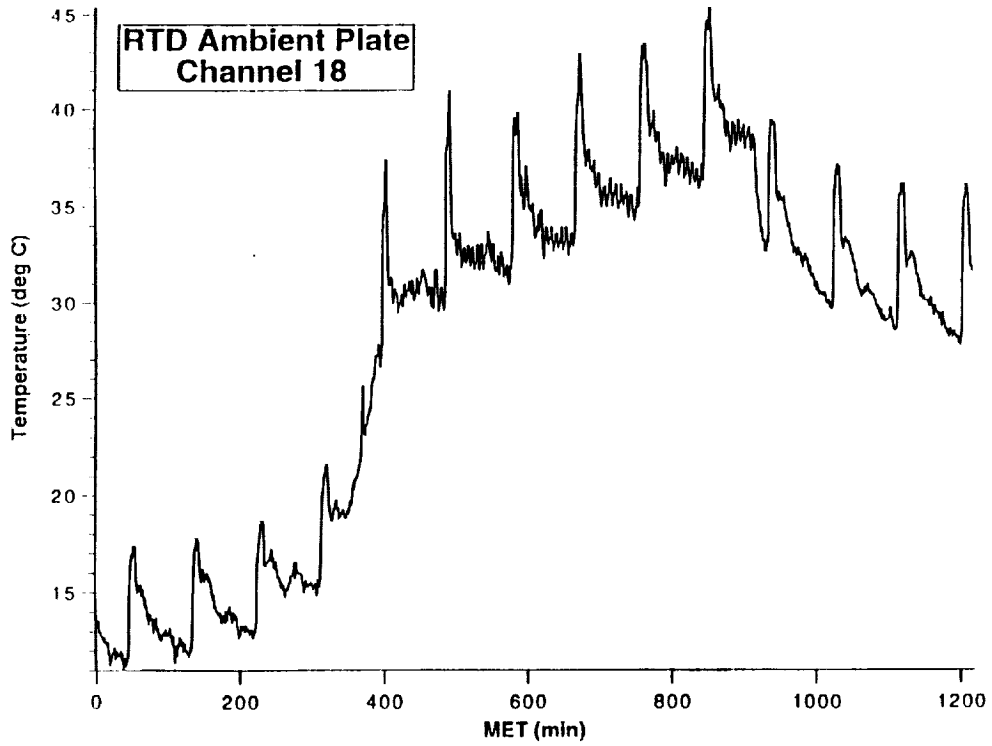


Figure 7: Temperature variations of the baseplate throughout the mission.

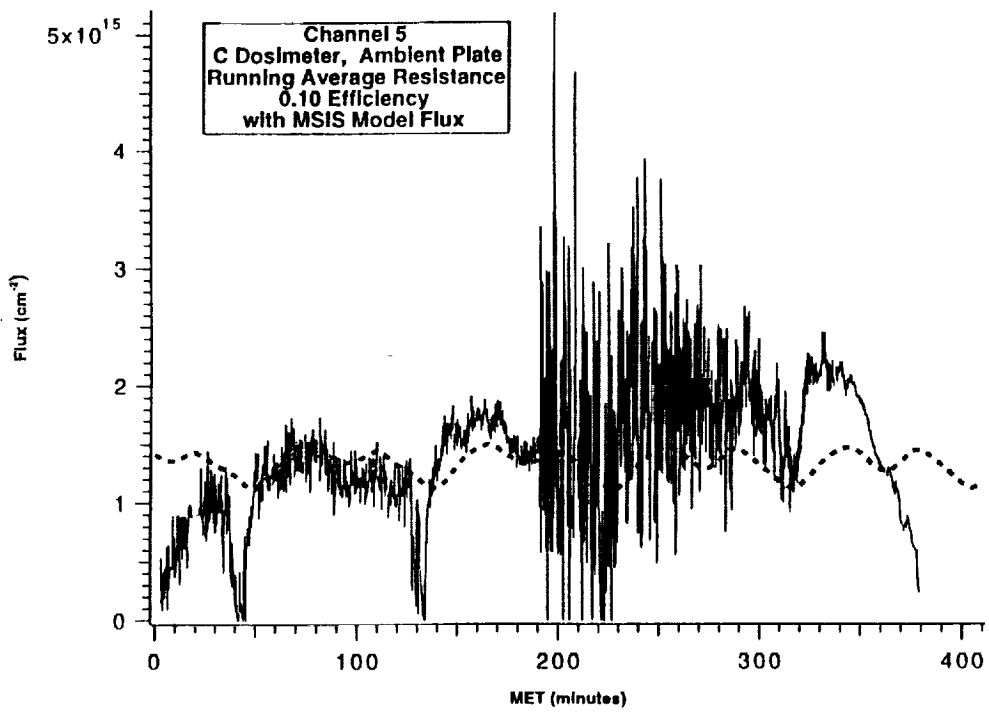


Figure 8: Variation of Atomic Oxygen Flux with time for dosimeter (Channel 5) and MSIS model.

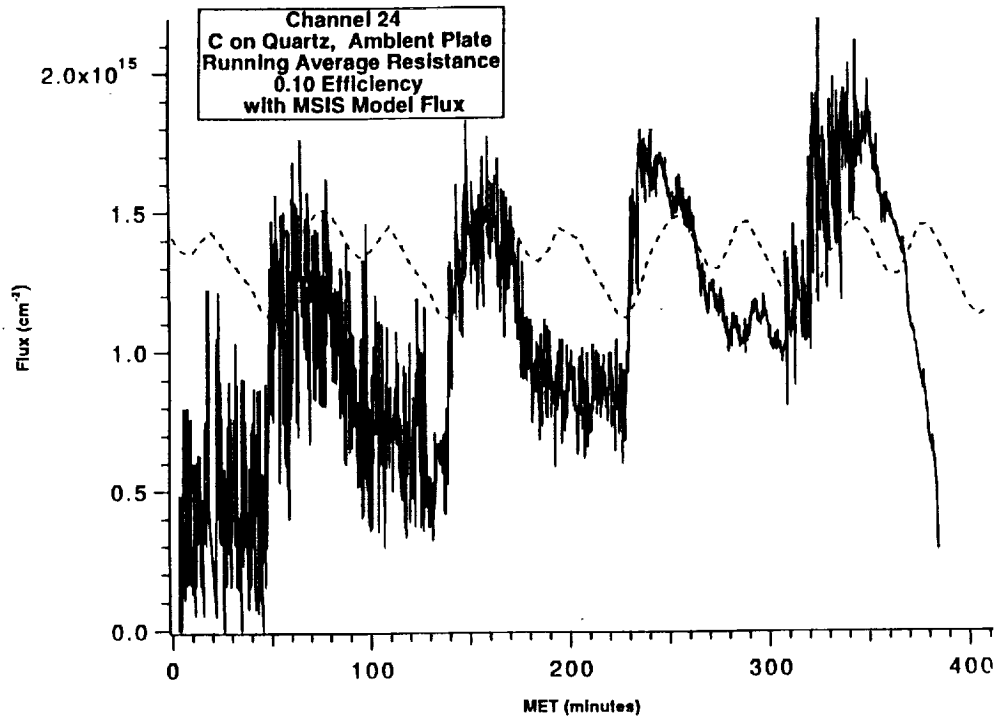


Figure 9: Variation of Atomic Oxygen Flux with time dosimeter (Channel 24) and MSIS model.

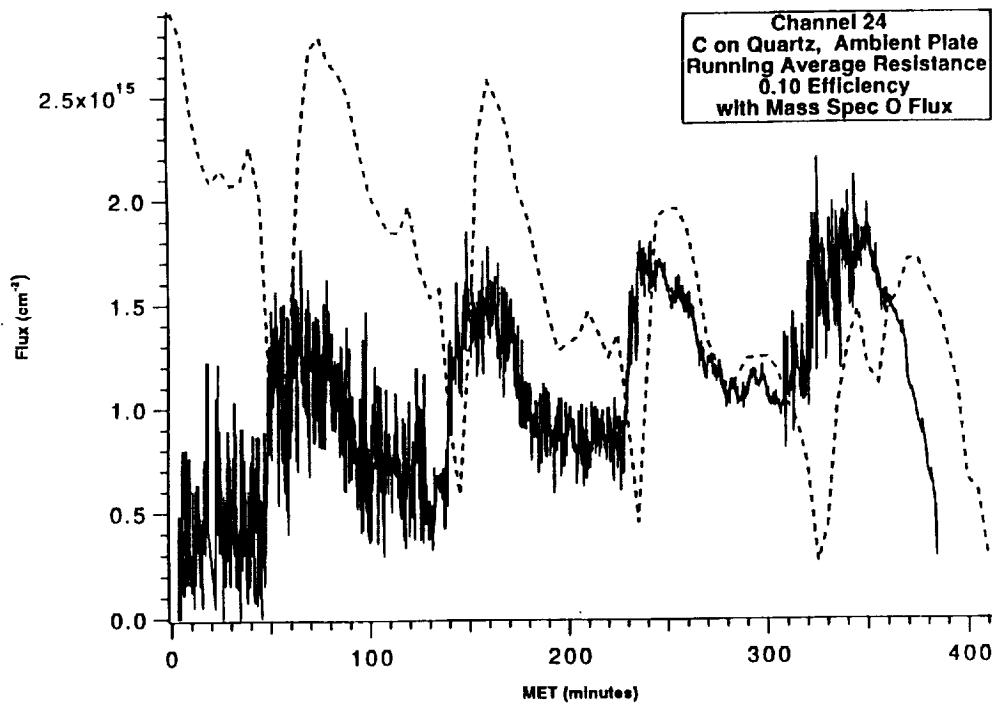


Figure 10: Variation of Atomic Oxygen Flux with time dosimeter (Channel 24) and preliminary mass-spectrometry data.

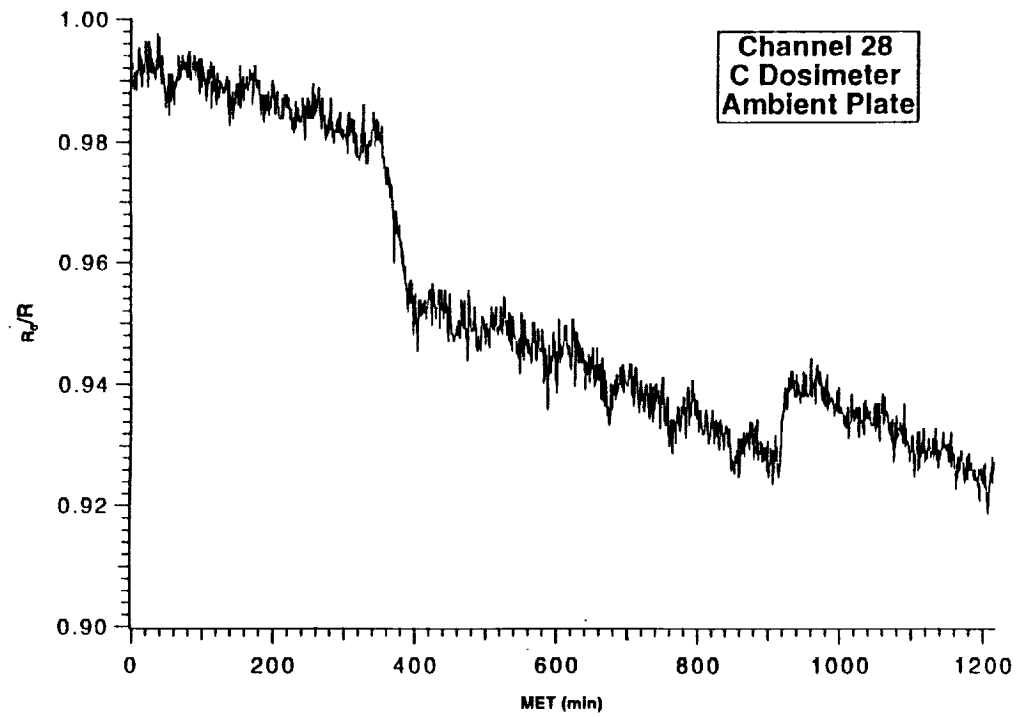


Figure 11: The change in resistance upon exposure to atomic oxygen for the thick-film carbon dosimeter (Channel 28).

**INFLIGHT RESISTANCE MEASUREMENTS ON HIGH-T_c
SUPERCONDUCTING THIN FILMS EXPOSED TO
ORBITAL ATOMIC OXYGEN ON CONCAP-II (STS-46)**

J.C.Gregory, G.N.Raikar, J.A.Bijvoet, and P.D.Nerren

Surface Science Laboratories
and

The Consortium for Materials Development in Space
The University of Alabama in Huntsville
Huntsville, AL 35899

Tel: (205) 895 6076, FAX: (205) 895 6061

W.T.Sutherland

EB25, Marshall Space Flight Center
Huntsville, AL 35812

Tel: (205) 544 7704, FAX: (205) 544 6893

A. Mogro-Campero and L.G.Turner

GE Research and Development Center
Schenectady, NY 12301

Tel: (518) 387 6031, FAX (518) 387 7597

Hoi Kwok

Department of Electrical and Computer Engineering
State University of New York, Buffalo, NY 14260

Tel: (716) 645 3119, FAX: (716) 645 5964

**I.D.Raistrick, J.B.Cross, D.W.Cooke
C.Mombourquette, R.J.Houlton, and F.H.Garzon**

Los Alamos National Laboratory
Los Alamos, NM 87545

Tel: (505) 667 4274, FAX: (505) 665 1712

R.Herschitz

Martin Marietta Astrospace Division
Princeton, NJ 08543-0800

Phone: (609) 426 2135; Fax: (609) 426 3962

ABSTRACT

In 1992, UAH conducted a unique experiment on STS-46 in which YBa₂Cu₃O₇ (commonly known as "1-2-3" superconductor) high-T_c superconducting thin film samples prepared at three different laboratories were exposed to 5 eV atomic oxygen in low Earth orbit on the ambient and 320°C hot plate during the first flight of the CONCAP-II [Complex Autonomous Payload] experiment carrier.

The resistance of the thin films was measured in flight during the atomic oxygen exposure and heating cycle. Superconducting properties were measured in the laboratory

before and after the flight by the individual experimenters. Films with good superconducting properties, and which were exposed to the oxygen atom flux, survived the flight including those heated to 320° C (600 K) with properties essentially unchanged, while other samples which were heated but not exposed to oxygen were degraded. The properties of other flight controls held at ambient temperature appear unchanged and indistinguishable from those of ground controls, whether exposed to oxygen or not.

INTRODUCTION

The effect of low Earth environment (LEO) on spacecraft has been the subject of several flight experiments over the past decade. Among these, the long duration exposure facility (LDEF) which remained in space for nearly 6 years has provided a wealth of data [1] that is invaluable from the standpoint of manufacture of long-lived spacecraft such as Space Station Freedom. Other flight experiments, such as STS-8 and 41-G [2] which studied atomic oxygen effects, provided data which was passive and there remain many unanswered questions as to the *in-situ* effects of atomic oxygen in the actual orbital environment on spacecrafts operating at altitudes between 200 and 900 km in LEO. The sticking coefficient of atomic oxygen on many materials such as silver and osmium is close to one [3]. It is important to understand the changes in the surface chemistry of many materials due to atomic oxygen and other induced environmental effects in low Earth orbit which is essential for the design of future spacecraft and many communication satellites.

A few years ago, a ceramic high temperature superconductor (HTSC), $\text{YBa}_2\text{Cu}_3\text{O}_7$, was discovered at the University of Alabama in Huntsville by M.K. Wu and J.R. Ashburn [4]. This work was partially funded by the UAH-NASA Consortium for Materials Development in Space (CMDS). Since that time, hundreds of millions of dollars have been spent on research worldwide into these ceramic systems, and although similar materials have been discovered with even higher critical temperatures than the 90 K of the UAH material, none has yet matched its combination of high- T_c and current-carrying capacity. In spite of many advances made in preparation of stable high quality devices from $\text{YBa}_2\text{Cu}_3\text{O}_7$, particularly those in thin film form, many materials processing problems remain with this material which continue to prevent its widespread use. Among the problems are those associated with very high temperature annealing required to obtain the superconducting phase with the proper quality, and the ease with which the material can lose oxygen [5,6].

Quite independently from the HTSC work, another UAH group had been studying the effect of fast atomic oxygen upon the surfaces of materials exposed in low Earth orbit. This work began in 1975 with the design of an experiment for NASA's Long Duration Exposure Facility (LDEF) and continued with flights on other carriers such as STS-8 in 1984. Under the conditions of bombardment by 5 eV atomic oxygen atoms new chemistry occurs, opening up the possibility of novel processing techniques using fast neutral beams. One of the longevity materials studied extensively on LDEF and also on the CMDS carrier CONCAP-II (STS-46) is copper and its oxides. We have shown that a pure copper surface is oxidized to a depth of 500 Å at room temperature when subjected to 5 eV atomic oxygen [7]. The stable oxide thickness at the same temperature in air is about 40 Å. Further work on CONCAP-II has shown that this oxide film may grow much thicker at 100-200°C.

Since both the conductivity and superconductivity of the cuprate class of HTSC's has been unequivocally shown to be associated with the copper oxide planes in the crystal lattice [8], a specific project was developed to probe the possibilities of low temperature

processing of these cuprate materials with fast atomic oxygen. The CMDS experiment carrier CONCAP-II was designed and built to accommodate these experiments (among others). The experiments were performed successfully in early August 1992, and some results are discussed below. High quality thin film HTSC devices were prepared by several leading U.S. laboratories including General Electric, Lockheed, LANL, and SUNY Buffalo.

The CONCAP-II-01 payload flew on space shuttle Atlantis, mission STS-46, on July 31, 1992, and was sponsored by the Consortium for Materials Development in Space (CMDS), at the University of Alabama in Huntsville (UAH). The CMDS is one of the Centers for the Commercial Development in Space funded jointly by NASA and private sector companies interested in promoting the commercialization of space. The UAH served as the integrator of CONCAP-II.

The payload contained an electronic controller and data system which monitored and recorded electrical resistance of 24 material samples of diverse composition. The system also controlled a hot plate at 320°C, the highest temperature at which material studies of this kind have been conducted in space.

OBJECTIVES

The objectives of the experiment were:

- To assess the survivability of thin film HTSC devices in the space environment at both ambient (300K) and elevated (600K) temperatures.
- To determine if fast oxygen atom bombardment may prevent loss of lattice oxygen from the HTSC's essential to performance.
- To determine if lost lattice oxygen may be replaced at relatively low temperatures by the fast O atom beam.

The first two objectives were successfully realized on STS-46. The third objective could not be achieved because of constraints on experimental complexity and shuttle operations. This objective will be sought during a re-flight of CONCAP-II in early 1994.

INSTRUMENTATION

a: CONCAP-II.01 Hardware

CONCAP-II utilized a Get Away Special (GAS) carrier system fitted into the space shuttle payload bay. The 5-cubic-foot GAS canister had a hermetically-sealed motorized door assembly (MDA) which protected samples and sensitive surfaces during all ground and flight operations, other than the exposure period itself (see figure 1). The HTSC and longevity samples contained in sample holders were mounted on the top surface "Experiment Insert Plate" and figure 2 shows the distribution of sample holders experiment and the location of electrical connectors. The experiment support equipment, including support electronics and a power supply, were mounted inside the sealed cannister.

CONCAP-II had an electronic experiment controller and a data system to record resistance measurements of up to 32 samples several times per minute during exposure, as well as a hot plate capable of maintaining samples at 320°C, the highest temperature at which materials studies of this kind have been conducted in space.

The support electronics provided for temperature control of the hot plate, multiplex sample-resistance measurements, and storage of all measured resistance, oxygen flux and temperature data. The power system included a Solid Rocket Booster (SRB) battery, solid state switch and DC/DC converter to supply the heater and monitor electronics. It supplied 1.4 kW-hrs of power at 28V. Also provided is a separate temperature recorder for all mission phases including transportation, launch and landing.

CONCAP's power supply and data acquisition/storage system are self-contained, requiring no shuttle interface, and are adaptable for other kinds of experiments as well. The 80C86 microprocessor-based data and control system is capable of sampling up to 32 analog channels and uses a 12-bit analog to digital converter. A block of data is sampled and stored every 10 seconds. There is an initial start up delay of 1 minute before data is taken to help prevent false starts. The time and experiment status are also stored in each data block. The experiment status contains information such as whether the shuttle is in the RAM-direction and whether the heater is presently on.

The experiment hardware is capable of being turned on and off up to 123 separate times and logging separate data segments for each power-on. The mission-elapsed timer is reset upon each power-on sequence. The memory can hold approximately 20.7 hours of data.

b: Processor Specifications

- Microprocessor-based (80C86) CPU running at 2.457 MHz
- Serial communications port Baud Rate: 300, 2400, or 38.4k
- Parallel port- A total of three 8 bit ports:
 - 8 bit output - 6 non-buffered outputs
 - 2 optically isolated outputs
(heater control is one output)
 - 8 bit inputs -RAM direction is one input
 - 8 bit input/output- Undefined
- Timer - Configured as a mission-elapsed timer. (Time since power on is available in hours, minutes, seconds)
- Memory-
 - I. Static ram - 4k bytes (stack/variable)
 - II. Eprom - 64 bytes (program memory)
 - III. EEprom - upto 512k bytes (Data storage-non volatile)
- Analog channels - 32 analog data channels
(4-wire resistance measurements, current source)
Four ranges: 0-200 ohms, 2.5mA
0-4k ohms, 0.125mA
0-10k ohms, 50 mA
0-20k ohms, 25 mA
- Analog to Digital Converter - 12 bit

c: Mission Description

CONCAP-II experiment was carried on mission STS-46 of space shuttle Atlantis in early August 1992. The shuttle was in a nominal 28.5° inclination orbit during the experiment exposure, and was flown at a relatively low altitude to maximize the O-atom exposure during the limited experiment time of 20 hours. The shuttle was oriented so that the normal to the cargo bay was within ±1° of the velocity vector. This ensured that most of the atmospheric O-atoms struck the experimental surfaces at close to normal incidence .

The exposure was made towards the end of the STS-46 mission, with the shuttle at 123 nautical miles (228 km) altitude. The atomic oxygen fluence was calculated using the MSIS-86 model of the atmosphere and a Johnson Space Center orbital mechanics program [9]. The experimental surfaces on CONCAP-II were protected from ambient contamination during all ground and orbital operations by a hermetically sealing lid (motorized door assembly) which was operated by the shuttle crew. The lid was opened after the shuttle had been maneuvered into the correct attitude and closed before leaving this attitude. During the time the lid was open, the average arriving flux of O-atoms was calculated to be $1.35 \times 10^{15} \text{ cm}^{-2}\text{s}^{-1}$. At this flux, each surface atom on a sample is struck by a fast O-atom about once per second. The total exposure time for CONCAP was 20 hrs for an accumulated fluence of $1 \times 10^{20} \text{ atoms cm}^{-2}$, with the 320° C hot plate energized for only about 10 hours. The following table gives the flight operations and the experiment elapsed-times.

Flight Operations	Experiment Elapsed Time
Orbiter in correct attitude Power to CONCAP controller MDA (lid) open at Mission-Elapsed Time 5 days: 22 hr: 42 min	0
Hot plate on	4 hr: 3 min
Temporary de-activation of hot plate	4 hr: 34 min
Reactivate hot plate	5 hr: 33 min
Hot plate off	15 hr: 16 min
CONCAP MDA closed, controller off	20 hr: 50 min

SAMPLE PREPARATION

The sample holders for the HTSC thin films shown in figure 3 were small, square integrated circuit mounts made of gold-plated Kovar supplied by Airpax, MD. Films were prepared at three different laboratories, General Electric, Schenectady (GE); Los Alamos National Laboratory (LANL); and SUNY, Buffalo. While prepared by different methods and deposited on several different substrates (MgO, SrTiO₃, LaAlO₃, YSZ and NdGaO₃), all were high-performance YBa₂Cu₃O₇ films with $T_c \sim 80 - 90\text{K}$ and $J_c > 1\text{MA cm}^{-2}$. All were thin, 0.14 to 0.6 μm , to maximize surface processing effects and were configured as bridges with the resistive element $\sim 100\ \text{ohm}$ (at room temperature) to match the measuring circuit performance. Details of the individual films are given in the results section below. GE films were prepared by co-evaporation, SUNY films by laser ablation, and LANL films by sputtering. No influence of preparation method on the flight measurements was observed. Figure 4 shows a representative HTSC device mounted in a flatpack.

UAH supplied each HTSC investigator with the appropriate number of flatpack device holders. The chips containing the thin film HTSC elements were installed by the individual co-investigators using either Aramco 569 or 571 high temperature adhesives. The adhesive layer was made as thin as possible to provide good heat conduction between chip and holder, and to avoid outgassing contamination. The flight measuring system needed only pins 1, 3, 7 and 10 as shown in figure 3 for the 4-point resistance measurement. Electrical connections within the mounts were made by conventional thermal acoustic bonding methods. External leads to the mounts were connected to the CONCAP measuring system. Mounting of the samples was done at Goddard Space Flight Center as late as possible before the flight and final changes were made at Kennedy Space Center prior to closing the motorized door assembly and final testing of the CONCAP-II controller and measuring system. The mask for holding the flatpacks mounted with HTSC films is shown in figure 5.

RESULTS

Two platinum resistance thermometers were used to monitor and control the heaters for the 320°C plate. Figure 6 shows the temperature profile of an RTD on the hot plate during the 20 hr CONCAP-II experiment. The heater system performed well in maintaining the temperature of the plate within the control band of $\pm 20^\circ\text{C}$. Two additional features may be noted. During periods when the plate was near ambient (0 - 50°C), the effect of solar heating may be seen, modulated by the orbital period. Since the platinum detector elements are inside the 0.25 inch thick aluminum heater plate, this effect (of the order of 10°C peak-to-peak) is much less than the solar heating effects on the HTSC elements, which also acted as thermometers. Another feature in the figure, the large spike occurring just before the sustained high temperature period, was caused by the crew shutting off the power to the CONCAP-II heaters since it was reported that the MDA (lid) had not opened. After about one hour, lid opening was verified and heater power reapplied.

Notes on General Electric HTSC thin films

Four samples were supplied, all from the same run and were 0.6 μm YBa₂Cu₃O₇ on LaAlO₃ substrates. They were post-annealed in O₂ at 30Pa and 1025K. Typical low

temperature properties were $T_C=90 \pm 1$ K, $J_C \sim 1-2$ MA cm^{-2} at 77K. On each substrate there were several bridges, but only one was monitored during flight. The four samples were mounted in two pairs: one pair at ambient temperature (~ 300 K) during the exposure and one pair at 590 K. One sample of each pair was shielded from the atomic oxygen flux and would have been at the ambient pressure of $\sim 10^{-6}$ torr in the shuttle cargo bay. The laboratory control samples were stored at room temperature in flowing oxygen.

Figures 7 and 8 show the normalized resistance versus mission-elapsed time (MET) plot of GE 1, and GE 3 (exposed) and GE 4 (covered) samples on the 320° C hot plate and the ambient plates, respectively. The effect of solar heating on the samples is evident from the periodic peaks which occur every 90 mins of shuttle cycle. Not much change in resistance is observed with the samples on the ambient plate. The sample on the hot plate showed the highest change in resistance when the heat was turned on. This can be attributed to the better quality of the film since it is known that the steeper the slope, the better the sample, which, in turn, suggests better critical current density. As can be seen from this plot, there is a slight change in resistance after \sim MET 400 (mins). This may be attributed to contact annealing. Post-flight T_C was the same as the corresponding laboratory control sample. However the GE 2 sample on the hot plate, which was covered, was totally degraded due to loss of lattice oxygen. The following table shows the T_C values of the samples before and after the flight.

Sample	T_C (Before)	T_C (After)
GE 1 (Hot Plate, Exposed)	91 ± 1 K	91 ± 1 K
GE 2 (Hot Plate, Covered)	90 ± 1 K	Non-superconducting
GE 3 (Ambient plate, Exposed)	90 ± 1 K	91 ± 1 K
GE 4 (Ambient Plate, Covered)	91 ± 1 K	91 ± 1 K
GE 5 (Laboratory Control)	91 ± 1 K	91 ± 1 K

Notes on SUNY-prepared HTSC thin films

SUNY supplied 6 samples- four of which were for R-measurement (on ambient and hot plates) and the remaining two for exposure on the ambient plate. All films were prepared by laser ablation and were the thinnest of all those flown: 0.14 to 0.16 μm . For all films flown, except sample SUNY # 6, the values of J_C and T_C obtained before the flight, and after the flight several months later, were unchanged or degraded no more than those for the ground control. SUNY #6 was mounted using a special high temperature tape to the flatpack. The flight resistance data is shown in figure 9. The resistance can be seen to steadily increase after the control temperature of 320°C had been reached. Post-flight testing showed T_C to have dropped from 84.7K to 54.5K. Since this did not occur to sample SUNY # 3, (figure 10) which was attached with high temperature epoxy, or to any other film exposed to oxygen atoms during the flight, it is suspected that a component of the tape adhesive migrated into the HTSC film at 320°C and degraded its properties. While figure 9 (SUNY # 3) shows a decrease in resistance during the high temperature phase, this may be attributed to Contact annealing. The before and after test data is given below.

BEFORE AND AFTER FLIGHT TESTING OF SUNY HTSC SAMPLES

Sample	Substrate	Testing Condition	J _c (MA cm ⁻²)		T _c (K)	
			(before)	(after)	(before)	(after)
SUNY 1	YSZ	Low temp. active	1.6	1.4	82.9	82.0
SUNY 2	SrTiO ₃	Ambient	1.07	2.21		82.9
SUNY 3	LaAlO ₃	High temp. active	-	0.84		80.32
SUNY 4	LaAlO ₃	Ambient	1.13	1.1	82.0	82.22
SUNY 5	YSZ	Low temp. active	1.6	0.0004	80.2	82.9
SUNY 6	SrTiO ₃	High temp. active	1.4	-	84.7	54.5

An *in-situ* 4-point resistance measurement as a function of temperature was performed at SUNY on two control samples in a vacuum chamber (with pressure $\sim 10^{-6}$ torr) without oxygen under identical conditions as in CONCAP-II experiment. This procedure showed that the Y-Ba-Cu-O films degraded very badly which proves that the oxygen is needed to replenish the lost lattice oxygen in these films.

Notes on LANL-prepared HTSC thin films

LANL supplied 11 HTSC thin film samples out of which only four were R-measured (2 each on the ambient and 320° C hot plates) and the rest were passive samples. Figure 11 shows a spectrum of R/R₀ vs MET on the hot plate. This sample behaved in similar fashion as GE 1 sample described above. The resistance of this sample increased by ~ 1.5 times that of ambient values. There is not much change in slope and this film is unchanged during and after the flight. T_c remained the same. The second sample on the hot plate (figure 12) behaved differently. The resistance decreased by ~ 1.2 times the ambient value. A casual inspection of the curve shows that the resistance has gradually decreased with MET and reaches a value below that of ambient. This suggests that the sample has improved, but contact annealing is not ruled out. However, T_c dropped from 79 K to 36 K after the flight, which we are unable to explain.

CONCLUSIONS

Thin film HTSC devices of state-of-the-art quality were exposed unprotected to the low Earth orbital environment while being actively monitored. These materials have major potential for revolutionizing the communication and electronics industries in the 21st century, and a major satellite program is currently underway to demonstrate device operation at superconducting temperatures on orbit (the HTSSE program [10] of the Naval Research Laboratory). On the first flight of CONCAP-II, we have demonstrated the survivability of these materials exposed unprotected at ambient.

The resistance of the thin films was measured in flight during the oxygen exposure and heating cycle using a 4-point resistance measurement. Superconducting properties were measured in the laboratory before and after the flight by the individual experimenters. Films with good superconducting properties, and which were exposed to the oxygen atom flux, survived the flight, including those heated to 320° C (600 K) with properties essentially unchanged, while other samples that were heated, but not exposed to oxygen, were degraded. The properties of other flight controls held at ambient temperature appear unchanged and indistinguishable from those of ground controls, whether exposed to oxygen or not. The main objectives have been realized on STS-46 and due to experimental constraints, we could not determine if lost lattice oxygen may be replaced at relatively low temperatures by the fast O atom beam, which we seek to test in a re-flight of CONCAP-II in 1994.

REFERENCES

1. Levine, Arlene S, Ed., (i) Proceedings of First LDEF Post-Retrieval Symposium, Kissimmee, FL, June 1991, NASA CP-3134, 1992.
(ii) Proceedings of the Second LDEF Post-Retrieval Symposium, San Diego, CA, June 1992. NASA CP-3194, 1993.
2. Visentine, James T, Ed.; *Atomic Oxygen Effects Measurements for Shuttle Missions STS-8 and 41-G*, NASA Technical Memorandum 100459, Vol.I-II, 1988
3. Gregory, J.C.; Edgell, M.J.; Cross, J.B.; and Koontz, S.L. *The Growth of Films on Metals Under the Influence of Hyperthermal Atomic Oxygen*, Proceedings of Symposium sponsored by the Minerals, Metals and Materials Society, 1990 Annual Meeting, Anaheim, Ca, Feb 1990.
4. Wu, M.K.; Ashburn, J.R; Torng, C.J.; Hor, P.H.; Meng, R.L.; Gao, L.; Huang, Z.J.; Wang, Y.Q.; and Chu, C.W.; Phys. Rev. Lett., 58, 980 (1987).
5. Simon, Randy.; *High- T_c Thin Films and Electronic Devices*, Physics Today, June 1991, P.64, and the references therein.
6. Mogro-Campero, A.; Turner, L. G.; Hunt, B. D.; Burrell, M. C; and Balz, W. E.; Appl.Phys.Lett., 52, 584 (1988).
A. Mogro-Campero, Turner, L. G.; and Kendall, G., Appl.Phys.Lett., 53, 2566 (1988), and the references therein.
7. (i) Gregory, John C; Christl, Ligia C.; Raikar, Ganesh N.; and Peters, Palmer N: *Effects on LDEF Exposed Copper Film and Bulk*,

Proceedings of First LDEF Post-Retrieval Symposium , Kissimmee, FL, June 1991, NASA CP-3134, 1992, p. 755.

(ii) Raikar, Ganesh N.; Gregory, John C; Christl, Ligia C.; and Peters, Palmer N.: *Interaction of Atomic Oxygen with Copper: An XPS, AES, XRD, Optical Transmission, and Stylus Profilometry Study.*, Proceedings of the Second LDEF Post-Retrieval Symposium, San Diego, CA, June 1992
NASA CP-3194, 1993, p. 1169.

8. Jorgensen, James D.; *Defects and Superconductivity in the Copper Oxides*, Physics Today, June 1991, p.34, and the references therein.
9. Koontz, S.L., Johnson Space Center, Private Communication.
10. Ritter, J.C; Price, G.; Nisenoff, M.; and Wolf, S., Flight Experiments Technical Interchange Meeting, Monterey, Ca, Oct 5-9, 1992, eds: Ambrus, J.H. and Frazier, J.C., NASA Headquarters, Washington, D.C.

LEGEND

- 1) Controller
- 2) Battery
- 3) DC/DC Converter
- 4) Heater Switch
- 5) Fuse Box
- 6) Vertical Mounting Plate
- 7) Suspension Plate
- 8) GAS Mounting Plate
- 12) Experiment Insert Plate
- 13) Hot Plate
- 14) Sample Mask & Holders
- 15) Reflectometers
- 16) Cable Cut-out
- 17) Primary Bumpers
- 18) Secondary Bumpers

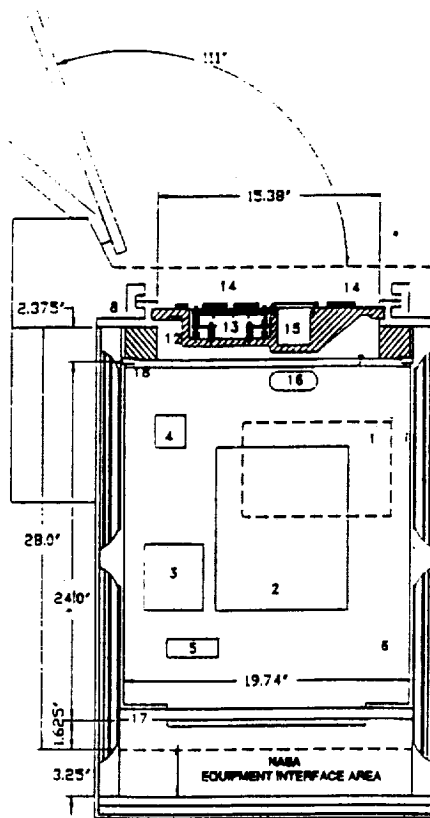


FIGURE 1: CONCAP-II.01 Experiment Accommodation.

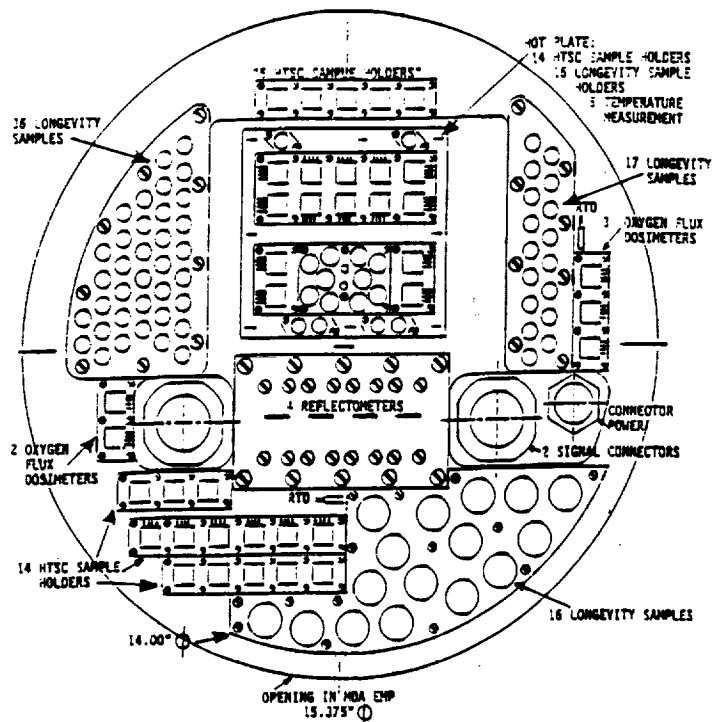
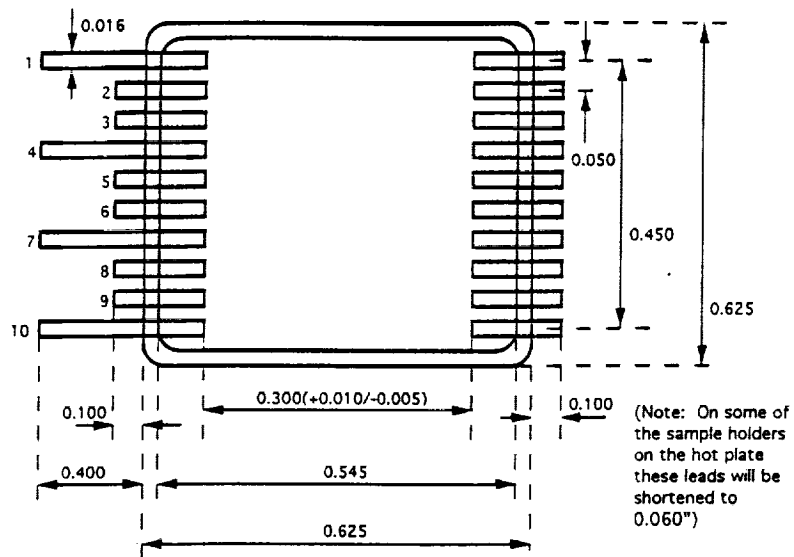


FIGURE 2: Accommodation of sample holders on Experiment Insert Plate.



Top View

FLATPACK PN AEP-2001-001

(Original leads: 0.500")
 (Depth inside: 0.115")

Figure 3: A Sketch of the "FLATPACK" Sample Holder

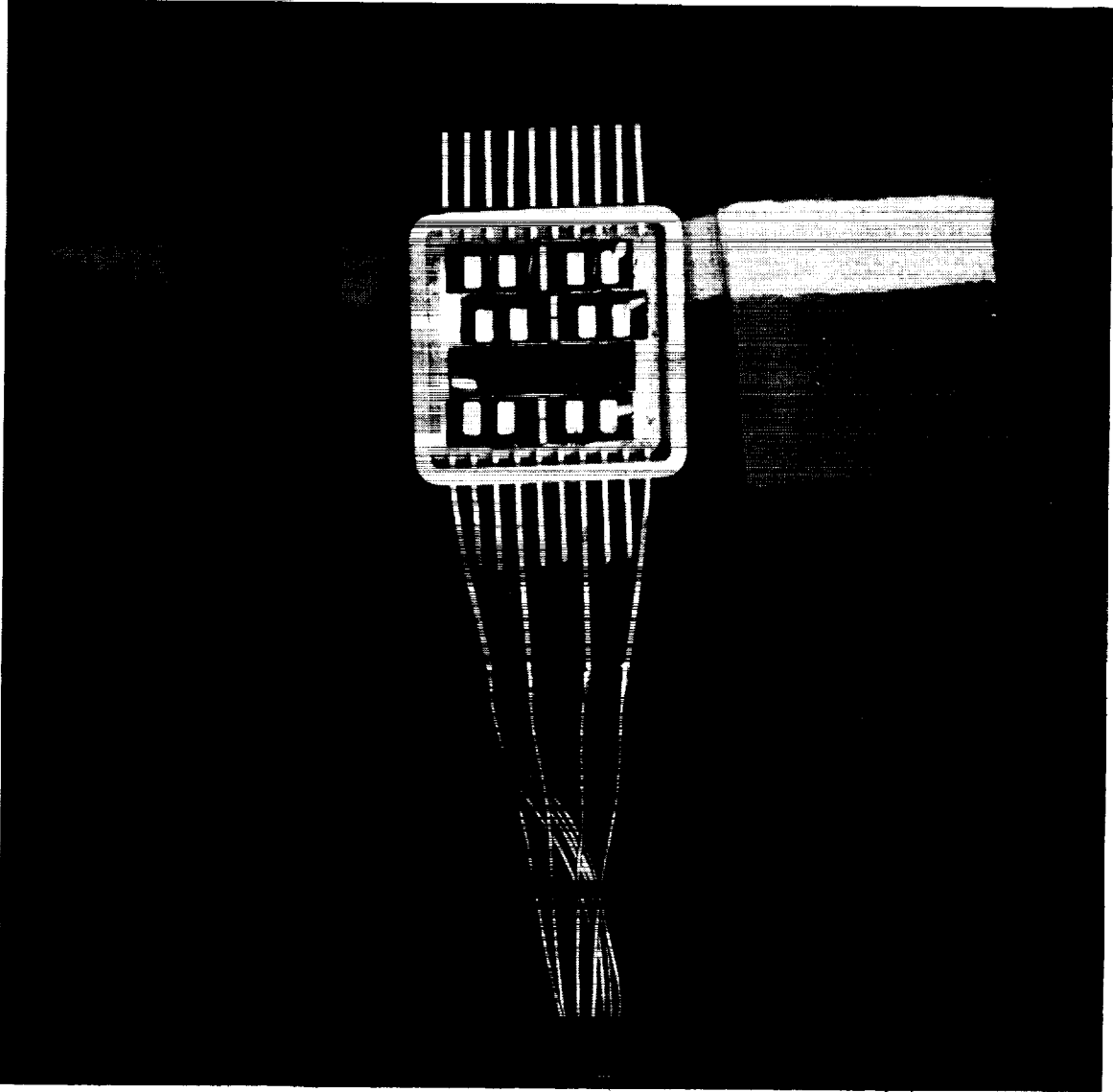


FIGURE 4: A photograph of the General Electric HTSC device mounted in a FLATPAX.

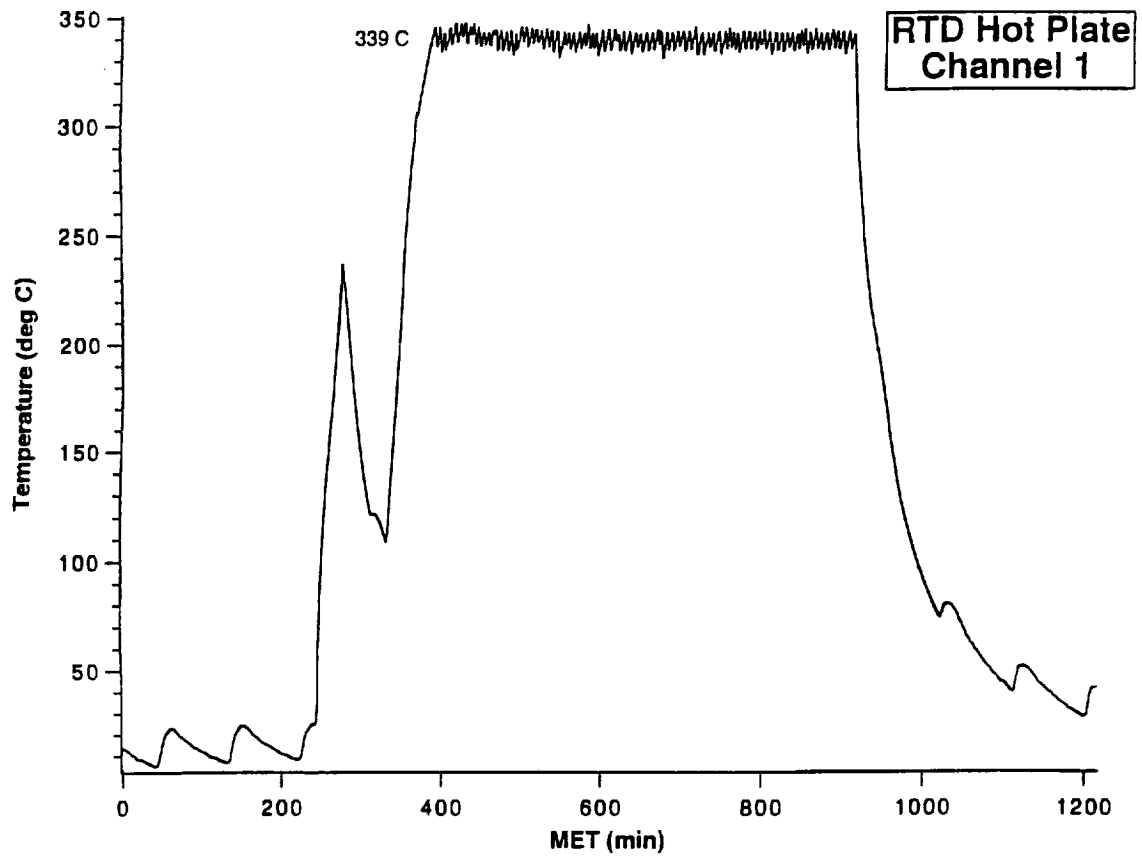


FIGURE 6: Temperature profile of the RTD on the 320°C hot plate during the 20 hr CONCAP-II.01 experiment.

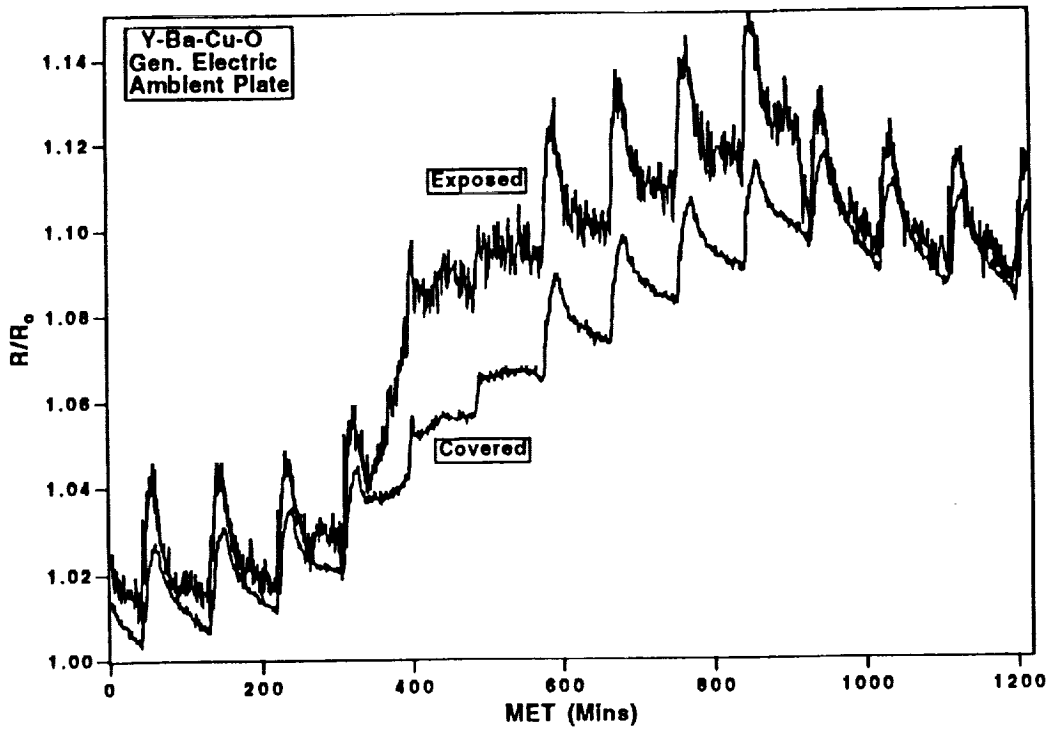


FIGURE 7: Mission Elapsed Time (Mins) versus normalized resistance of the General Electric HTSC sample #3 (Exposed) and #4 (covered) on the ambient plate.

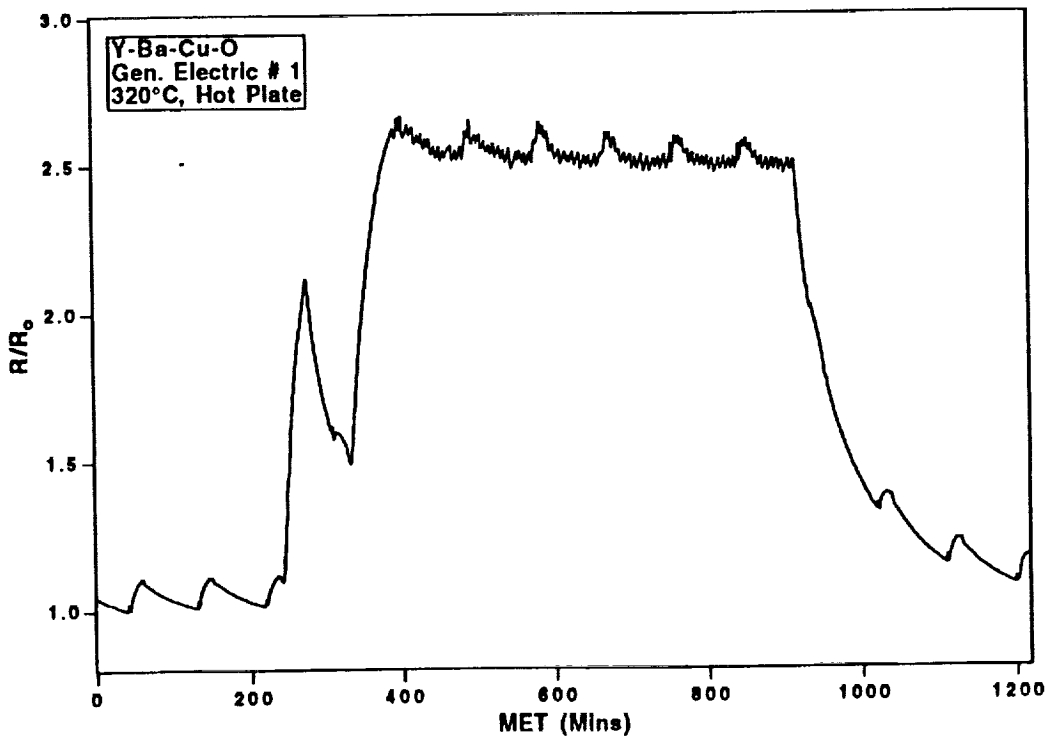


FIGURE 8 : Mission Elapsed Time (Mins) versus normalized resistance of the General Electric HTSC sample (#1) on the 320°C hot plate.

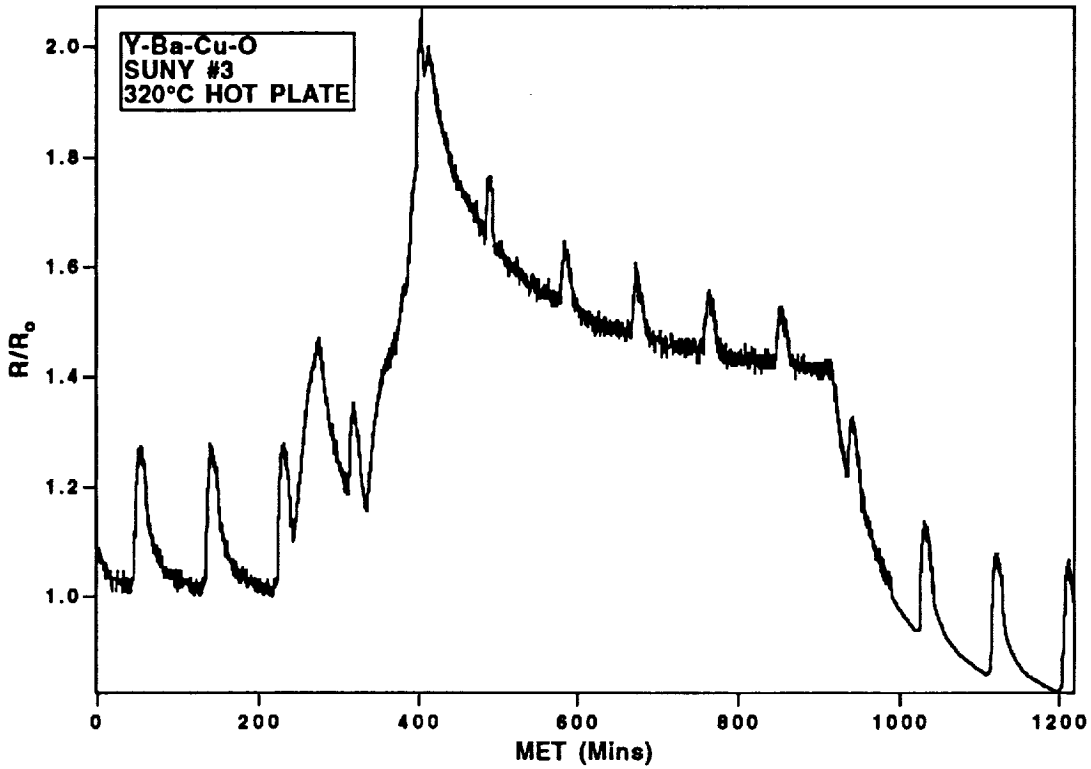


FIGURE 9: Mission Elapsed Time (Mins) versus normalized resistance of the SUNY HTSC sample (SUNY #3) on the 320°C hot plate.

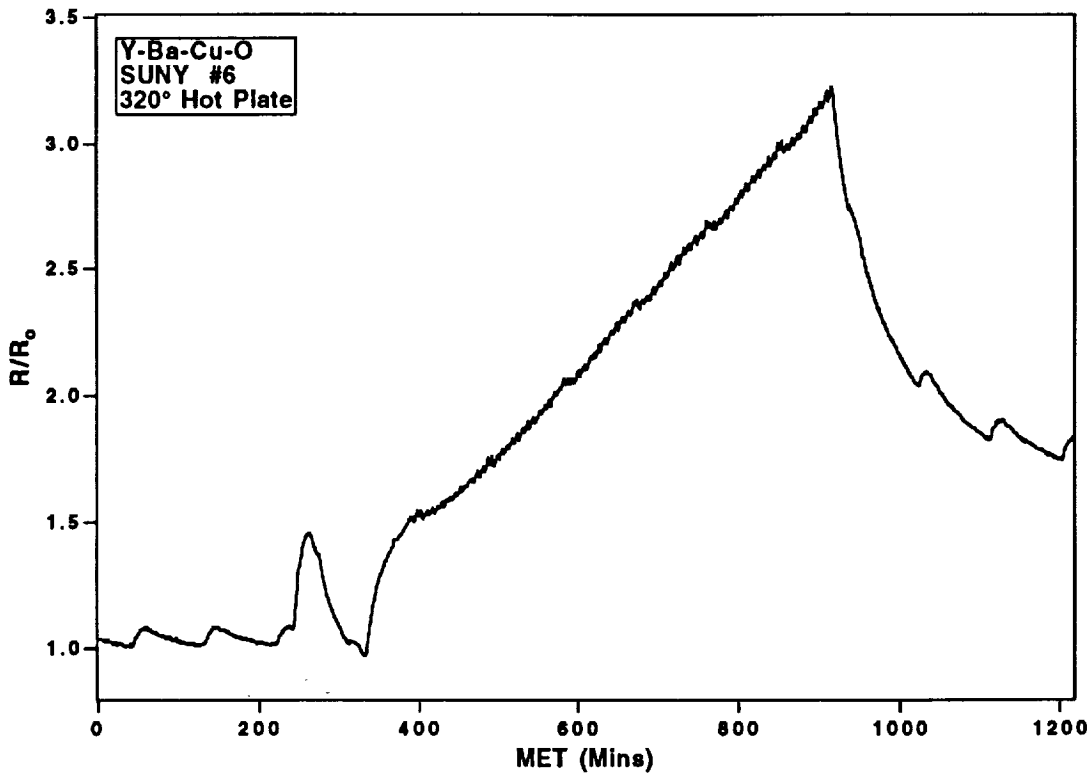


FIGURE 10: Mission Elapsed Time (Mins) versus normalized resistance of the SUNY HTSC sample (SUNY #6) on the 320°C hot plate.

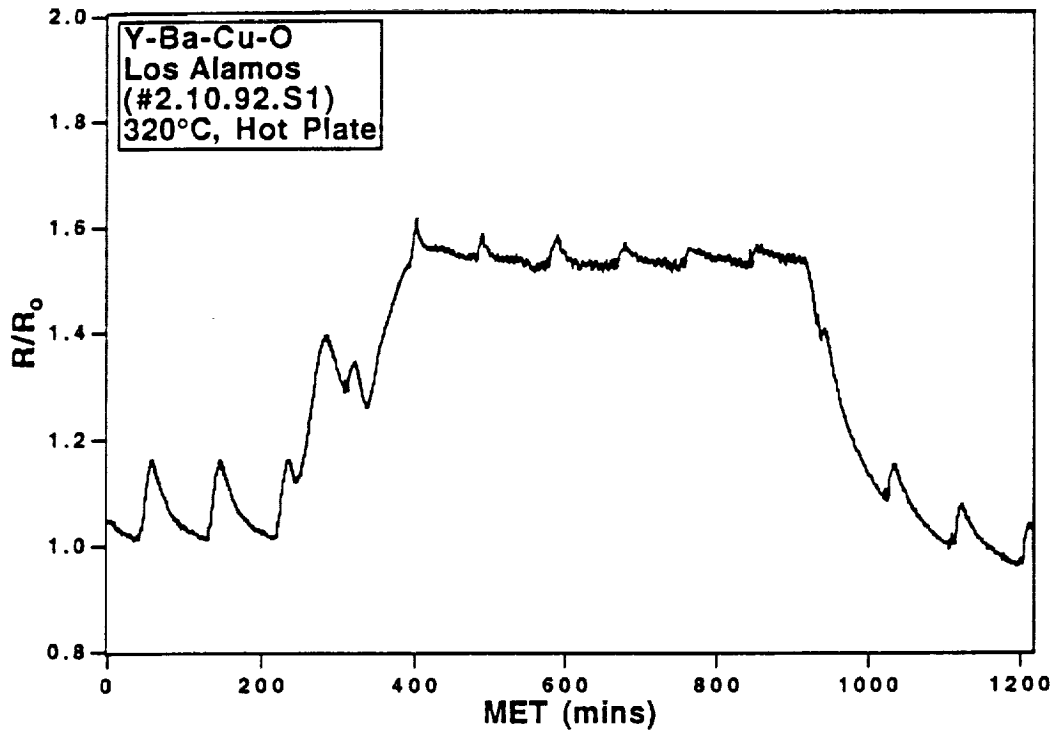


FIGURE 11: Mission Elapsed Time (Mins) versus normalized resistance of the Los Alamos HTSC sample (#2.10.92.S1) on the 320°C hot plate.

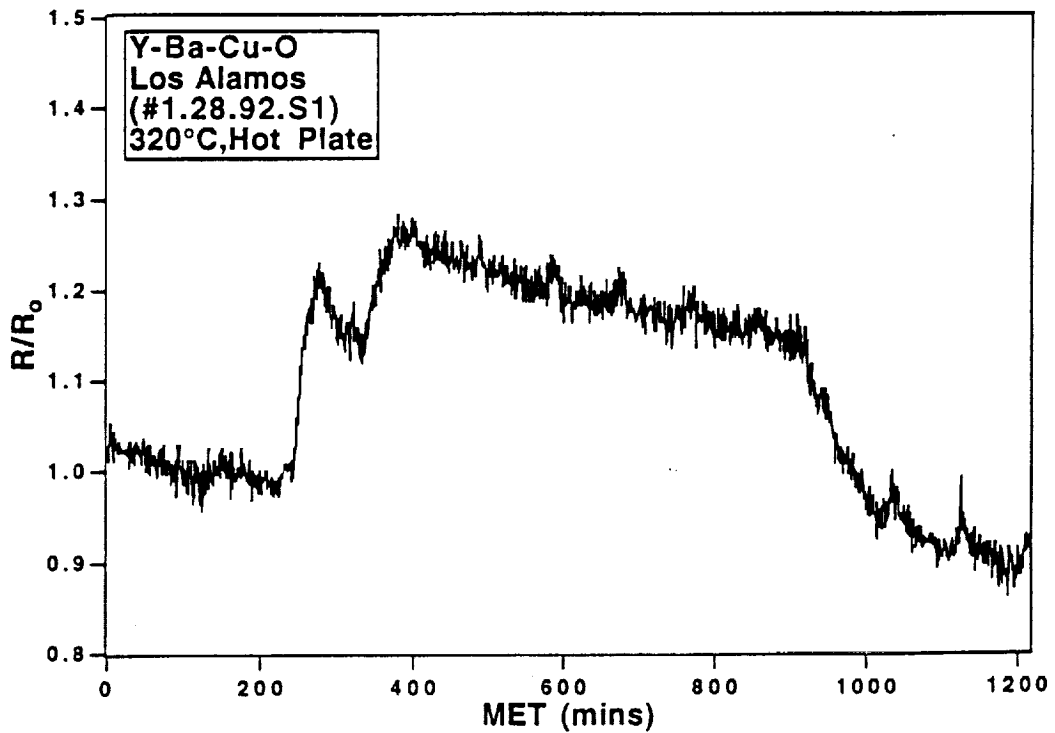


FIGURE 12: Mission Elapsed Time (Mins) versus normalized resistance of the Los Alamos HTSC sample (#1.28.92.S1) on the 320°C hot plate.

LEO DEGRADATION OF GRAPHITE AND CARBON-BASED COMPOSITES ABOARD
SPACE SHUTTLE FLIGHT STS-46*

Blaine R. Spady

R.A. Synowicki

Jeffrey S. Hale

M.J. DeVries

John A. Woollam

Center for Microelectronic and Optical Materials Research, and Department of Electrical
Engineering, University of Nebraska-Lincoln

Lincoln, NE 68588-0511

Phone: 402/472-1978, Fax: 402/472-7987

Arthur W. Moore

Union Carbide Corporation, Parma Technical Center

Parma, Ohio

Max Lake

Applied Sciences, Incorporated

Cedarville, Ohio

SUMMARY

Six different types of carbon and carbon-boron nitride composites were exposed to low Earth orbit aboard Space Shuttle flight STS-46. The samples received a nominal atomic oxygen fluence of 2.2×10^{20} atoms/cm² in 42 hours of exposure. Pyrolytic graphite and highly oriented pyrolytic graphite showed significant degradation, and the measured erosion yield was within a factor of two of published values. The erosion yield of pyrolytic boron nitride was found to be 2.6×10^{-26} cm³/atom in plasma asher exposure, over 42 times lower than that of pyrolytic graphite. This low erosion yield makes graphite plus boron nitride mixtures quite resistant to low earth orbit exposure. Evidence suggests that the graphitic component was preferentially etched, leaving the surface boron nitride rich. Degradation resistance increases with boron nitride composition. Carbon fiber/carbon composites degraded in low Earth orbit, and the carbon pitch binder was found to etch more easily than the graphite fibers which have much higher degradation resistance.

*Research Supported by NASA-Lewis Research Center Grant NAG-3-95

INTRODUCTION

High temperature radiators are necessary for rejection of waste heat generated aboard orbiting spacecraft (refs. 1,2). Radiator materials must be able to operate at temperatures up to 900 K. Other materials requirements for space radiators are high thermal conductivity and surface emittance. Furthermore, conductivity and emittance must not change with exposure to the corrosive low Earth orbit (LEO) space environment.

Atomic oxygen (AO) is the primary reactive species present in LEO (ref. 3). Oxygen atoms strike spacecraft surfaces with an average kinetic energy of 4.5 eV due primarily to the orbital speed of the spacecraft. The AO attack is directional along the spacecraft's velocity vector since the spacecraft is moving into the oxygen atoms. Ultraviolet light from the sun is also present and synergistic degradation effects are suspected.

Ion beams have been extensively used to modify the surface morphology of many materials, resulting in a "carpet-like" surface texturing (ref. 4). Surface modification of this type can significantly alter the surface emittance of a waste heat radiator.

Bulk basal plane pyrolytic graphite, as well as vapor grown carbon fibers, shows the highest thermal conductivity of all materials (ref. 5). Also, graphite can withstand temperatures up to 2800 K and has found extensive use in high temperature applications. These properties make graphite an excellent choice for radiator applications. However, it has been shown in both laboratory simulations and actual LEO exposure that graphite is readily etched by AO (ref. 6).

This paper considers the AO degradation resistance of six different types of graphite, graphite plus boron nitride mixtures, and carbon fiber/graphite composites. Their usefulness as space radiator materials has been evaluated through exposure to LEO aboard Space Shuttle flight STS-46 in July 1992.

EXPERIMENT

Six different types of materials were prepared in bulk form. Two different types of graphite were chosen, namely pyrolytic graphite (PG) and highly oriented pyrolytic graphite (HOPG) (ref. 5). Two samples consisted of carbon and boron nitride mixtures (C-BN). These two C-BN samples consisted of one hot-pressed and one as-deposited containing 40% and 60% pyrolytic graphite, respectively (ref. 7). It will be shown that the presence of boron nitride in the mixture serves to greatly decrease erosion. Boron nitride is not as good a thermal conductor as graphite, so the thermal conductivity of C-BN materials is less than that of pure graphite, but should still be quite acceptable for space radiator applications.

The remaining two samples were composites of vapor grown carbon fibers embedded in a graphite (pitch) matrix. These carbon/carbon fiber (C/C) composites were made by either liquid or gas infiltration of the graphite precursor into the fiber weave.

Sample characterization consisted of accurate measurements of mass and dimensions. Mass was measured using an ultramicrobalance with a resolution of 10^{-7} g and the physical dimensions were measured using a vernier caliper with a resolution of 25 μm . Dimension and mass measurements allow for measurement of erosion yield (ref. 6).

Scanning electron microscopy (SEM) and atomic force microscopy (AFM) were employed to measure topographic changes and quantify surface roughness. The AFM is a contact method which gives extremely fine scale measurements of surface roughness over small areas, on the order of 100 μm or less.

The bulk samples were cut into circular geometries to fit into the provided sample holder. In order to isolate the effects of the AO, the back sides of the samples were used as control surfaces.

All samples were part of the limited duration space environment candidate materials exposure-3 payload, aboard STS-46. The samples were exposed to the space environment throughout the entire shuttle flight. However, the samples received direct ram exposure to AO for only 42 hours during the 8-day mission and the oxygen fluence received during this exposure was nominally 2.2×10^{20} atoms/cm². Oxygen fluence was determined by both atmospheric modeling using the MSIS-86 thermospheric model (ref. 8) and by a mass spectrometer flown aboard STS-46 on the EOIM-3 payload. Kapton[®] mass loss measurements (ref. 9) showed the oxygen fluence to be 2.3×10^{20} atoms/cm².

RESULTS AND DISCUSSION

The PG, HOPG, and C/C composites all showed visible degradation. This is shown in Fig 1. The C-BN samples showed no visible degradation except for a slight "darkening" of the 60% C-BN sample.

SEM results for the PG, HOPG, and C/C composite made by gas infiltration showed uniform degradation. The C/C composite made by liquid infiltration showed preferential degradation of the graphite pitch surrounding the carbon fibers as shown in Fig 2. The 40% C-BN sample showed no changes in the SEM photos.

The hot-pressed 40% C-BN sample is comprised of microscopic domains of pure pyrolytic boron nitride and boronated PG; the size of the domains was found to slightly exceed 0.1 μm . Evidence on the as-deposited 60% C-BN was inconclusive of whether or not the material is a single-phase mixture of C, B, and N or a two-phase mixture of pyrolytic boron nitride domains and boronated PG domains (ref. 7). Fig 3 shows an unexposed and exposed AFM picture of the surface of the 60% C-BN sample. The figure appears to show the preferential etching of either

PG or pyrolytic boron nitride domains. A preliminary study of pyrolytic boron nitride using oxygen plasma ashers showed the erosion yield to be 2.6×10^{-26} cm³/atom. This is over 42 times lower than the published 1.1×10^{-24} cm³/atom erosion yield of PG (ref. 6). This suggests that the PG is being preferentially etched, leaving pyrolytic boron nitride domains. This behavior was observed in both the as-deposited and hot-pressed materials. Table I shows the surface roughness data for the 40% and 60% C-BN samples taken for three scan sizes with the AFM. The 1 μ m scan has the greatest percentage change between the unexposed and exposed samples; namely, 59% for the 40% C-BN, and 238% for the 60% C-BN samples. The percentage change for the 100 μ m scan was only 29% for the 40% C-BN and 36% for the 60% C-BN. This indicates the surface roughened on a sub micron scale, for which the small scans were more sensitive. From this data it can be seen that the 40% C-BN sample was more stable in LEO than the 60% C-BN sample; this is to be expected since pure pyrolytic boron nitride has a lower erosion yield than PG.

Table I. RMS Surface Roughness of 40% and 60% C-BN

SAMPLE	AFM 1 μ m scan	AFM 10 μ m scan	AFM 100 μ m scan
40% C-BN unexposed	9.88 nm	56.714 nm	108.500 nm
40% C-BN exposed	15.713 nm	70.460 nm	139.600 nm
60% C-BN unexposed	9.343 nm	15.619 nm	133.137 nm
60% C-BN exposed	31.586 nm	37.377 nm	181.667 nm

The densities (ρ) of the samples were determined from the physical dimensions and mass. The mass loss (ΔM) of each sample was the pre-flight mass minus the post-flight mass. The AO fluence (F) was nominally 2.2×10^{20} atoms/cm². The erosion yield was calculated as:

$$\epsilon = \frac{\Delta M}{\rho A F}$$

where A was the exposed area of the sample. The mass loss, density, and erosion yield for all samples are shown in Table II. The densities and erosion yields of the PG and HOPG samples were within a factor of two of published data (ref. 6). The C/C composites and C-BN samples were new materials in space so there were no published data for comparison. The erosion yields for the C-BN samples were an order of magnitude lower than either the PG or the HOPG. The gas infiltrated C/C composite erroneously lost mass due to handling, making the data unusable.

The degradation observed on pure graphite samples and the pitch in C/C composites indicates that these materials are not stable in LEO and will require protective coatings if deployed. The degradation resistance of C-BN mixtures is very encouraging. These materials

show promise as radiator materials without the need for protective overcoats due to the presence of boron nitride. The sample containing 40% carbon outperformed that containing 60% carbon. Much more work could be done studying the effectiveness of bulk mixtures of carbon and boron nitride, as well as graphite fiber composites containing boron nitride in the binding matrix. Fiber composites of this type would be advantageous since the thermal conductivity would be dominated by the graphite fibers, and atomic oxygen resistance would be enhanced by the presence of boron nitride.

Table II. Measured Density, Mass Loss, and Calculated Erosion Yield for all Samples

Material	Density (g/cm ³)	Mass Loss (mg)	Erosion Yield (cm ³ /atom)
PG	2.171	.62	.538x10 ⁻²⁴
HOPG	2.096	.77	.692x10 ⁻²⁴
40% C-BN	2.134	.08	.071x10 ⁻²⁴
60% C-BN	1.782	.21	.222x10 ⁻²⁴
C-C Liquid Infiltration	1.403	.22	1.093x10 ⁻²⁴
C-C Gas Infiltration	1.517	11.5398	*****

CONCLUSION

Six different carbon based materials were exposed to 42 hours of LEO aboard Space Shuttle flight STS-46. The PG, HOPG, and C/C composites were degraded by AO exposure, making them less desirable for space radiator applications. Measured erosion yields agreed well with published results. Samples of C-BN showed a strong resistance to atomic oxygen erosion. This resistance increased as the percentage of carbon decreased since the erosion yield of pyrolytic boron nitride is lower than that of PG by a factor of 42. In these C-BN mixtures, atomic oxygen preferentially etches the graphitic component of the material at the surface, leaving the surface boron nitride rich. C/C composites degraded easily when exposed to LEO. The graphite binder eroded similarly to bulk pyrolytic graphite; however, graphite fibers in the C/C composites were found to erode much more slowly than the surrounding pitch binder.

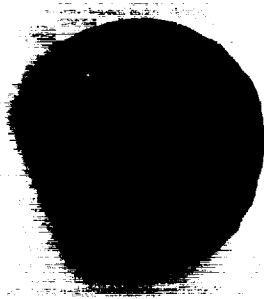
REFERENCES

1. Mirtich, Michael J., Kussmaul, Michael T., Enhanced Thermal Emittance of Space Radiators by Ion-Discharge Chamber Texturing, NASA TM-100137, March 1987.
2. Rutledge, Sharon K., Banks, Bruce A., Mirtich, Michael J., High Temperature Radiator Materials for Applications in the Low Earth Orbital Environment, NASA TM-100190, April 1987.
3. U.S. Standard Atmosphere 1976, U.S. Government Printing Office, NASA TM-X-74335, 1976.

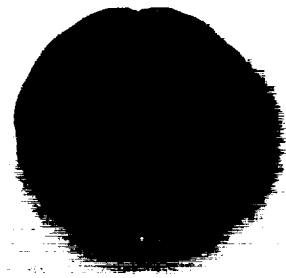
4. Banks, Bruce A., Ion Beam Applications Research- A 1981 Summary of Lewis Research Center Programs, NASA TM-81721, April 1981.
5. A.W. Moore, "Highly Oriented Pyrolytic Graphite," in Physics and Chemistry of Carbon, Volume 11, Edited by Philip L. Walker Jr. and Peter A. Thrower, Marcel Dekker, Inc., New York, 1973, pp 69-185.
6. Banks, Bruce A., Rutledge, Sharon K., and Brady, Joyce A., "The NASA Atomic Oxygen Effects Test Program," Proceedings of the 15th Space Simulation Conference, Williamsburg, VA, October (1988).
7. Moore, A.W., Strong, S.L., Doll, G.L., Dresselhaus, M.S., Spain, I.L., Bowers, C.W., Issi, J.P., Piraux, L., Properties and Characterization of Codeposited Boron Nitride and Carbon Materials, J. Appl. Phys., Vol 65, No. 12, 1989, pp 5109-5118.
8. Hedin, Alan E., "MSIS-86 Thermospheric Model," J. Geophysical Research, Vol 92, No. A5, 1987, pp 4649-4662.
9. Rutledge, Sharon K., Banks, Bruce A., DiFilippo, Frank, Brady, Joyce, Dever, Therese, and Hotes, Deborah, An Evaluation of Candidate Oxidation Resistant Materials for Space Applications in LEO, NASA TM-100122, November 1986.

Unexposed

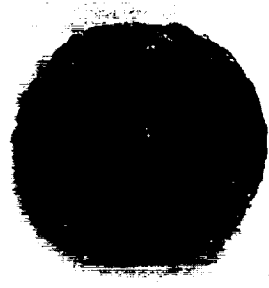
Exposed



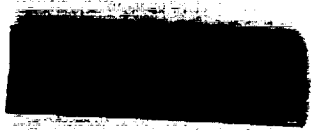
PG



HOPG



Gas Infiltrated
C/C Composite



Liquid Infiltrated
C/C Composite

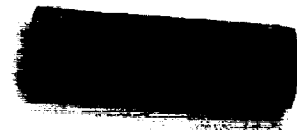
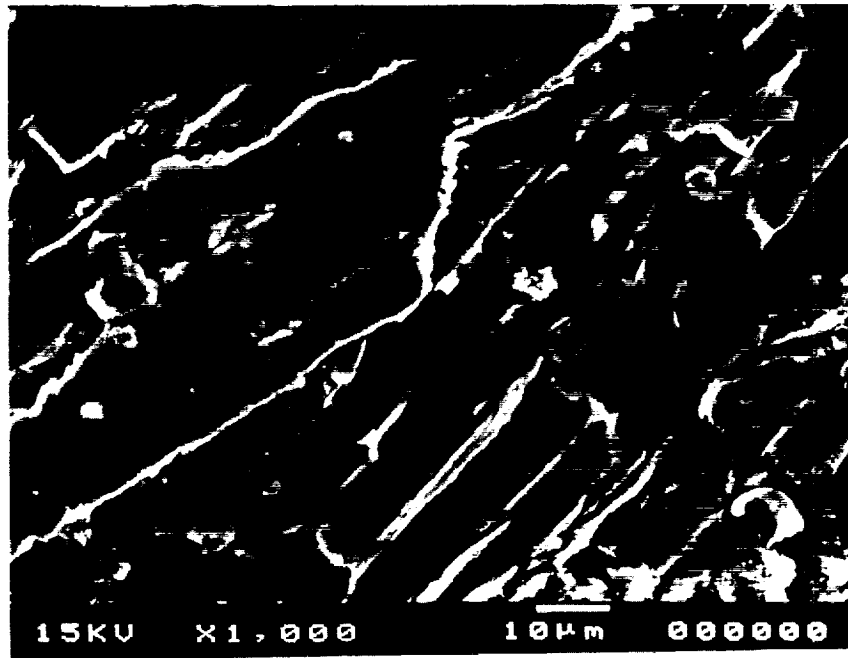
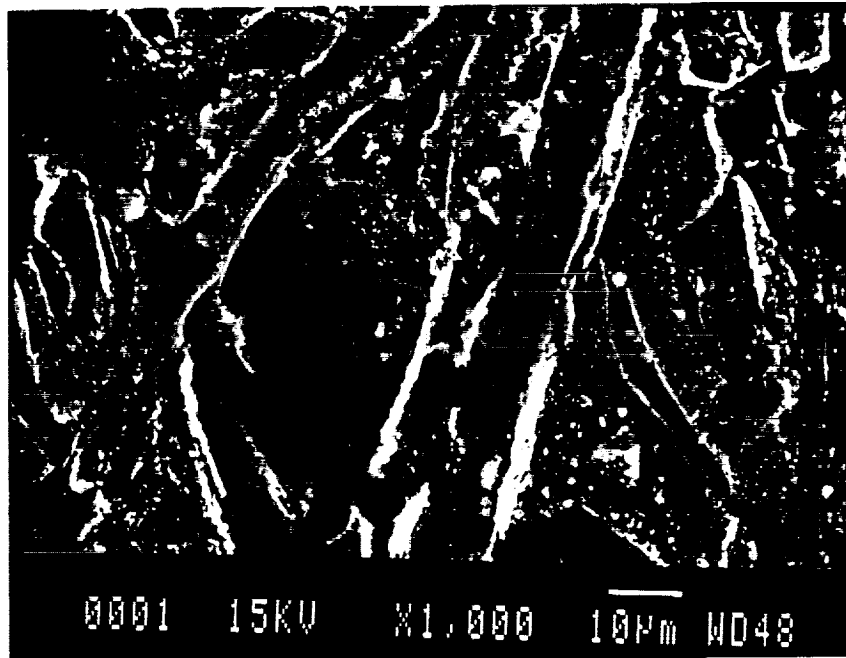


Figure 1. Visible degradation of samples after LEO exposure.



Unexposed



Exposed

Figure 2. SEM images showing preferential etching of graphite binder in the liquid infiltrated C/C composite.

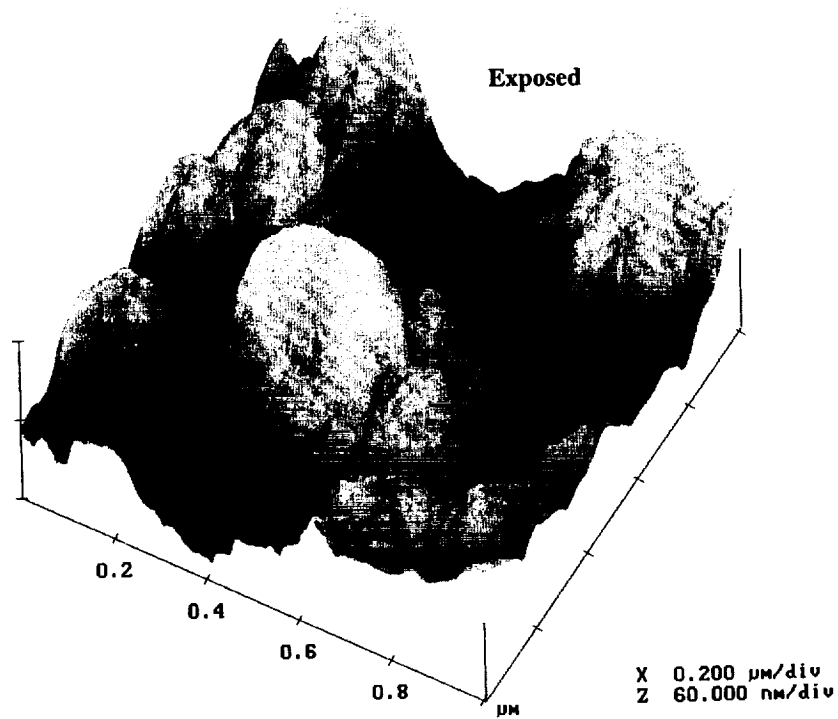
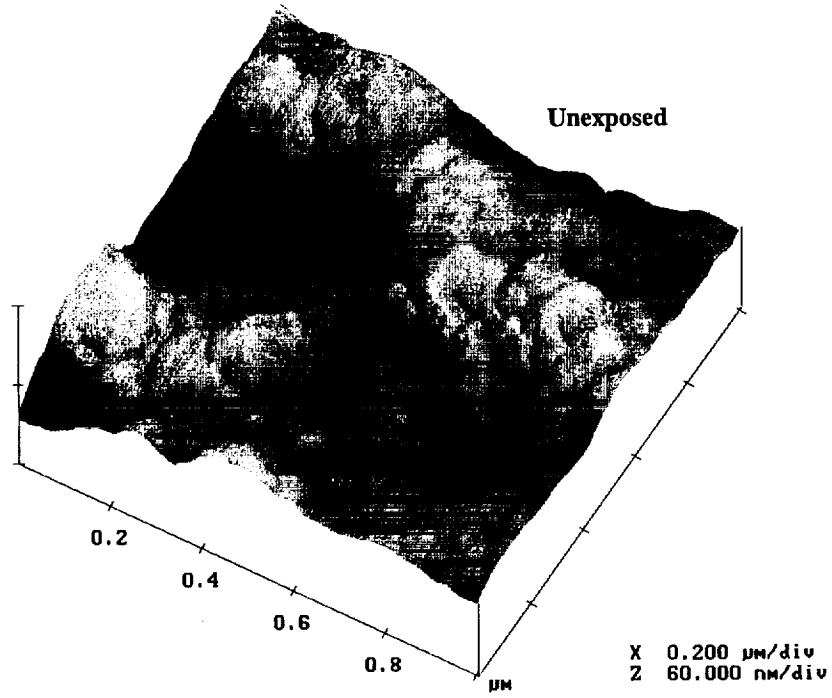


Figure 3. AFM data showing preferential etching of graphite domains in 60% C-BN.

Small, illegible text or mark at the bottom right corner.

ORBITAL ATOMIC OXYGEN EFFECTS ON MATERIALS:
AN OVERVIEW OF MSFC EXPERIMENTS ON THE STS-46 EOIM-3

Roger C. Linton
Jason A. Vaughn
Miria M. Finckenor
Rachel R. Kamenetzky
Robert F. DeHaye
Ann F. Whitaker
Marshall Space Flight Center, AL 35812

ABSTRACT

The third Evaluation of Oxygen Interaction with Materials experiment was flown on Space Shuttle Mission STS-46 (July 31 - August 8, 1992), representing a joint effort of several NASA centers, universities, and contractors.

This array of active instrumentation and material exposure sub-assemblies was integrated as a Shuttle cargo bay pallet experiment for investigating the effects of orbital atomic oxygen on candidate space materials. Marshall Space Flight Center contributed several passive exposure trays of material specimens, uniform stress and static stress material exposure fixtures, the Atomic Oxygen Resistance Monitor (AORM), and specimens of thermal coatings for the EOIM-3 variable exposure mechanisms.

As a result of 42 hours of spacecraft velocity vector-oriented exposure during the later phases of the STS-46 mission in LEO, EOIM-3 materials were exposed to an atomic oxygen fluence of 2.2×10^{20} atoms/cm². In this paper, an overview is presented of the technical approaches and results from analyses of the MSFC flight specimens, fixtures, and the AORM. More detailed results from earlier EOIM missions, the LDEF, and from laboratory testing are included in associated papers of this conference session.

INTRODUCTION

The predominant natural atmospheric constituent of Low Earth Orbit (LEO) is electrically neutral atomic oxygen. Energized to a nominal 5 eV energy by collision with orbiting spacecraft surfaces, atomic oxygen has proven to be a major factor in the degradation of a wide range of candidate spacecraft materials. Previous flight observations, including the first two EOIM flight experiments and the nearly six years of the LDEF mission, have revealed a gamut of significant material interaction effects. The flight of EOIM-3 provided an opportunity to further address AO and material compatibility issues in LEO for a comprehensive diversity of candidate space materials. The combination of active and passive exposure instrumentation and hardware provided means to isolate the effects of specific

environmental factors and material interaction parameters such as mechanical stress, temperature, and the synergism of AO and solar UV radiation.

Post-flight characterizations of these exposed materials in comparison to pre-flight measurements have provided AO erosion rates and other indicators of space environmental interaction, utilizing etch profiling, mass change, reflectance and transmittance, scattering, fluorescence, and elemental and chemical composition analyses.

EXPERIMENT DESCRIPTION

Three unheated passive exposure trays containing a total of 138 material samples, including guest samples from the Jet Propulsion Laboratory, Boeing Aerospace Corporation, and Vanderbilt University were provided by MSFC. Thermal control coatings, polymeric materials, optical materials, metal foils, composites, dry film lubricants, and others were selected as candidate materials for future space missions.

Other material specimens from MSFC were included in the three EOIM-3 heated trays, which provided stable temperature control at 60, 120, and 200 °C, for evaluation of thermal effects in interactions with atomic oxygen. Bulk, polished single crystal silver and copper, including both [100] and [111] crystal orientations, were exposed at all three temperatures for investigation of ordered oxidation effects. Other materials flown included aluminum anodizations, aluminum/lithium alloys, dry film lubricants, metals, thermal control coatings, and selected polymeric materials, including candidate Space Station seal materials. Considerations of intrinsic thermal decomposition and tray space allotments restricted the exposure of many of these materials to only one or two of the set temperature trays.

An approach to actively monitoring atomic oxygen flux stability was provided by the Atomic Oxygen Resistance Monitor (AORM). This device operated by measuring the electrical conductance of exposed carbon sensors (Fig. 2). As the carbon sensors were eroded by atomic oxygen, the decrease in conductance was proportional to the integrated fluence, and the rate of change was proportional to flux levels. The AORM experiment had six sensor units, each with an exposed carbon element. All units incorporated a protected carbon resistor element to provide temperature compensation. Three sensor units were heated to a constant temperature, in addition to having a compensating resistor. This was done to determine if constant temperature operation and resistance compensation were both required to produce unambiguous results from the AO sensors. During the EOIM-3 mission, all six of the AORM sensor units operated successfully throughout the 42 hours of atomic oxygen exposure, indicating the viability of both the heated and unheated units for use as a practical AO monitoring system.

MSFC provided Chemglaze A-276 and Z-306 coating samples for the EOIM-3 Solar Ultraviolet (SUV) Tray and the Variable Exposure Tray (VET) assemblies. These samples were covered by 90% transmissive nickel wire mesh to provide a grid pattern of unexposed material following atomic oxygen exposure for erosion etch profiling. Controlled shuttering of the SUV experiment provided continuous exposure for one set of samples and alternate exposures for selected material samples during solar illumination and shadowed phases of the EOIM-3 active mission to investigate the effects of solar UV radiation and atomic oxygen, individually and in combination. The VET experiment was similarly designed with shutters

to sequentially expose material samples to atomic oxygen for increasing intervals to evaluate induced surface recession rates as a function of cumulative AO exposure. A failed microswitch in this experiment resulted in all samples receiving full exposure during the mission.

Completing the MSFC experiment elements were two types of fixtures for investigating enhanced reactivity in stressed polymeric materials exposed to atomic oxygen. Two uniform stress fixtures were designed to maintain a constant pre-loaded mechanical stress on sheets of Kapton HN by means of a spring-loaded mechanism. Two static stress fixtures provided only an initial pre-loaded strain on Kapton HN sheets. The erosion induced by atomic oxygen across the sheet materials has been determined by mass loss measurements for comparison to unstressed material reactivity.

ENVIRONMENTAL EXPOSURE

Space environmental exposure of the pallet experiment EOIM-3 featured 42.25 hours of flight operations while the Space Shuttle cargo bay was oriented within 2 degrees of the RAM velocity vector at an altitude of 123-124 nautical miles. The cumulative atomic oxygen fluence for the entire mission, 2.2×10^{20} atoms/cm², includes a minute additional contribution (approx. 0.5%) during deployment and associated operations of the European Retrievable Carrier (EURECA).

A total of only 30.6 equivalent sun hours (ESH) of solar electromagnetic radiation for the entire mission (7.6 ESH during RAM exposure) was computed for the payload¹, although this level proved sufficient to stimulate perceptible effects in a number of UV-sensitive materials. During the eight days of Shuttle cargo bay thermal vacuum exposure, passive tray temperatures varied from -5 to +80 °C (ibid). EOIM-3 materials were subjected to presumably benign levels of ionizing radiation, and no significant impact features resulting from meteoroid or space debris have been identified on MSFC elements of the experiment.

CONTAMINATION OBSERVATIONS

Visible evidence of molecular contamination on MSFC samples and hardware resulting from exposure during the EOIM-3 mission indicated localized effects without major widespread deposition. A faint, colorless streak pattern, more clearly distinguished under black light illumination (Fig. 3), was observed on the Kapton sheet material of one of the static stress fixtures. Analysis of solvent wipes from the stress fixtures themselves revealed the presence of silicone on the static stress fixture with the contaminated Kapton, without detection of contamination from the other fixtures. Very small droplet pattern spots, in some cases revealed as liquid splash sites under visual magnification, were found on a few, selected samples, including some of the optical samples (Fig. 4).

Each of the MSFC passive trays and the two lower temperature heated trays on EOIM-3 contained one or more magnesium fluoride overcoated aluminum mirrors as optical witness samples. The inclusion of these witness samples among the optical, thermal control, and polymeric material sample trays were intended to provide a basis of comparison for localized

contamination effects from the different classes of materials. Diffuse reflectance measurements at wavelengths transmitted through air (0.25-2.5 μm) provided no significant evidence of degradation for the witness mirrors on either passive or actively heated trays.

Potentially more sensitive measurements of the optical properties at vacuum UV wavelengths (121.6 - 200 nm) indicated patterns of increased reflectance over certain wavelengths for passive tray MgF_2/Al mirrors (Fig. 5) and decreased reflectance over certain wavelengths for those from the heated trays. No significant differences in reflectance were measured between exposed and unexposed (covered) areas of the half-exposed MgF_2/Al mirrors, within experimental error. Elemental and chemical composition analyses of these and other types of mirrors, including Surface Analysis by Laser Ionization (SALI), ESCA, and Rutherford Backscattering (RBS), indicate molecular contamination common in level to the small levels of "adventitious" hydrocarbons found on all samples exposed to the atmosphere of conventional laboratories.

Contamination in the form of particulate and fibrous debris was found on all of the flight optical samples. The number and distribution of particle sizes ranged from Level 500 to Level 700, MIL-SPEC-1246, in exposed sample areas compared to an average Level 500 for unexposed sample areas. These different levels of debris were detectable with bi-directional reflectance distribution function (BRDF) measurements but did not significantly degrade the specularity of most of the affected optics.

POLYMERS

A select assortment of thin film and bulk polymeric materials were included in both the passive and actively heated trays of EOIM-3. Determinations of the atomic oxygen reaction efficiency of these materials were made on the basis of both weight loss and erosion etch depth. Individual samples were placed in vacuum, then weighed immediately after removal from vacuum. Mass change calculations were based on time dependence of weight measurements with extrapolation to zero for the "true" weight. The calculated reaction efficiencies of polymers based on weight loss are, for these samples, considered more accurate than the etch depth profiles that were compromised by stylus drag through the softer materials; the inherently stiffer Lexan polycarbonate is the major exception. These results are tabulated and discussed in comparison to results from previous EOIM flights, the LDEF, and laboratory atomic oxygen testing in the associated paper of this session reviewing polymeric materials.

Preliminary results indicate no definitive difference in erosion for the Kapton sheet material from the uniform stress fixtures compared to similar material from the passive tray exposure. Kapton erosion from the relatively lightly loaded static stress fixtures was slightly higher than passively exposed material. The extent of the role of additional atomic oxygen incident scattered from the underside of the fixtures is being investigated.

Bulk material samples of candidate Space Station seal materials, silicone S383 and Viton 747, were exposed on the 60 °C tray only. Laboratory testing of these types of materials at MSFC³ have included the effects of thermal vacuum, AO, UV, and combinations of these exposures, based on changes in seal material permeability, Shore A hardness, fluorescence, and mass. The effects of flight exposure of these materials are discussed in relation to these tests in the associated paper of this session reviewing results for polymers.

AO exposure-induced changes in the resistance of black, carbon-impregnated Kapton have proven to be a relatively reliable and accurate alternative gauge of atomic oxygen fluence in asher and beam facility testing at MSFC. The electrical properties change in inverse proportion to the loss by erosion of the carbon. The utility of this approach for LEO exposure was demonstrated by passive exposure on STS-41 as part of the ISAC experiment⁴. The flight of EOIM-3 provided the opportunity not only to expose and evaluate multiple specimens of black Kapton, but also to evaluate the function of the active AORM, based on similar principles.

THERMAL CONTROL MATERIALS

Thermal control coatings included in the complement of MSFC samples included several new formulations of polyurethane-based paints provided by Lord Chemical Corp., two formulations of the ceramic-based radiator coatings Z-93 and YB-71, a variety of aluminum anodizations prepared by different processes, and beta cloth.

Erosion of Chemglaze A-276 and Z-306 coatings, exposed through 90% transmissive nickel wire mesh on the EOIM-3 variable exposure mechanisms (VET/SUV), was comparable in magnitude to predictions based on previous EOIM and LDEF data. No significant differences in erosion were found (as expected) for VET exposure samples, since the shutters failed to activate properly. Weight loss measurements of SUV samples indicate a systematic trend with shuttered exposure for the samples exposed continuously, samples exposed only to AO, and samples exposed to AO only during the few hours when solar UV was detected. See Table 1.

Anodized 6061-T6 aluminum coatings were included in the passive trays and each of the actively heated trays. These coatings included representative samples prepared by three basic anodization processes using chromic, sulfuric, and boric/sulfuric acid, including ten minute and twelve minute processing times for the boric/sulfuric anodized samples. The measured changes in solar absorptance and infrared thermal emittance are reviewed in the associated paper for thermal control coatings¹¹.

Beta cloth has an extensive history of effective utilization in space, including the cargo bay of the Space Shuttle and the LDEF⁶. Several types of beta cloth were flown, including material with heat-rejecting thin film aluminum backing. Thermo-optical properties were basically unchanged, as expected, for this level of exposure; the predicted loss of the TFE Teflon matrix due to the EOIM-3 level of atomic oxygen is approximately one tenth of a micron.

One of the more sensitive indicators of induced environmental interaction for many thermal control coatings is fluorescence. For these materials, exposure to the space environment, including thermal vacuum, atomic oxygen, and solar UV radiation, results in changes in the spectral emission of fluorescent radiation. The flight of EOIM-3 provided an opportunity to verify the nature and degree of effects found in samples from the LDEF, from laboratory testing, and long-stored samples from earlier Shuttle flights dating to STS-5 (1982).

For each thermal coating material investigated, the fluorescence effects of EOIM-3 exposure, with a moderate fluence of atomic oxygen and a relatively minimal exposure to solar UV radiation, are identical in nature, differing mainly in degree of effect, to altered

fluorescence effects of similar materials exposed on LDEF⁷. In the laboratory, fluorescence in polyurethane-based coatings is significantly altered by a nominal exposure, in vacuum, to simulated solar UV radiation within no more than an hour of irradiation.

Common bands of fluorescent emission and similarities in response to exposure, suggesting degrees of material commonality, were found in the polyurethane paints submitted by Lord Chemical Corp., including the Chemglaze and Aeroglaze coatings, with few exceptions. Material dependent differences in fluorescence, including resolution of structure, comparative emission intensities, and additional emission band structure are found for each of the paint types. Relatively minor changes in the fluorescence of zinc orthotitanate indicate little, if any, effect on this material for the EOIM-3 level of exposure.

OPTICS

A variety of thin film and bulk optical materials were included in both the passive and actively heated trays of EOIM-3. Effects of exposure are being investigated for optical materials ranging from thin metal foil extreme UV (EUV) filters to NaCl and KBr infrared windows. A majority of the samples were thin film and bulk material optics for vacuum UV applications and a series of candidate thin film mirror coatings for X-ray applications. Characterization techniques included spectral reflectance and transmittance, fluorescence, BRDF, ellipsometry, microscopy, and chemical composition analysis. A variety of instrumented facilities were utilized to measure spectral, specular and/or diffuse reflectance and transmittance from vacuum UV through near-IR wavelengths (110-2500 nm). Chemical analyses included FTIR, X-ray fluorescence, ESCA, Auger, RBS, and SALI.

The candidate thin film reflectors for X-ray application included platinum, gold, iridium, and nickel films on optically flat substrates of the glass ceramic Zerodur, the selected substrate material for the NASA AXAF-I mirror assembly. While the x-ray reflecting layers for AXAF-I (currently iridium) are intended for extreme grazing incidence application with a thickness of only 25 nm, opaque mirrors were included with the EOIM-3 samples to simplify optically intrusive analyses such as ellipsometry.

Some of the four types of candidate X-ray mirror materials indicate some degradation in diffuse reflectance (0.25 - 2.5 μm). Iridium and gold mirrors exposed on the passive trays were not measurably changed at these wavelengths. Small changes in reflectance of the nickel mirrors at these wavelengths indicated some effects of exposure. The more significant and temperature-proportional degradation of the gold mirrors from the 120 and 200 °C heated trays provided clear evidence of a thermally dependent degradation. At vacuum UV wavelengths, the reflecting properties of the platinum mirrors were not measurably changed. One of the iridium mirrors was unaffected, while another was significantly degraded for wavelengths less than 180 nm. Analysis of the composition of this iridium mirror, using Auger and XPS techniques⁸, provided evidence for the presence of iridium oxide, IrO_2 on the mirror surface. The gold mirrors flown on the heated trays are more affected at vacuum UV wavelengths, in agreement with overlapping diffuse reflectance measurements. The optical measurements and chemical composition analyses¹⁰ indicate that the dominant mechanism affecting these mirrors is diffusion or migration of the underlying nickel to the surface of the gold layer, possibly aided in transport by atomic oxygen. There is evidence of very short wavelength degradation in the gold mirrors flown on the passive trays.

Significant changes at the vacuum UV wavelengths were also found for the nickel mirrors. Results of combined optical and chemical analyses indicate that the nickel mirrors were severely degraded by natural oxidation in the atmosphere and that additional nickel oxide was grown as a result of atomic oxygen exposure. The effects of exposure of these samples are discussed in detail in the associated optics paper in this conference session (ibid).

A luminescing phosphor of widespread utility for vacuum UV applications, sodium salicylate was found to be thinner post-flight. Visual contrast was striking under black light illumination for the exposed and unexposed areas of the partially exposed sample. Spectrofluorometer measurements of the glow stimulated by 260 nm incident light indicated only a slight change in fluorescence. Measurements of the fluorescence stimulated by vacuum UV wavelengths (120-200 nm) indicated as much as 50% loss in detected emission.

SUMMARY AND CONCLUSIONS

All of the MSFC elements of EOIM-3 functioned successfully and have provided material interaction results for a comprehensive range of candidate spacecraft materials. The six carbon sensors of the AORM functioned as designed with decreasing conductance proportional to the time integrated atomic oxygen flux (fluence) throughout the active phases of the EOIM-3 mission. Effects of mechanical stress on Kapton HN reactivity to atomic oxygen have been found to be negligible for the uniform stress fixtures, while slightly increased reactivity was found for Kapton HN in the static stress fixtures. The relative contribution of back-surface reflected atomic oxygen to the induced mass loss of Kapton HN from these fixtures is still being investigated.

Uncoated polymeric materials reacted in varying degrees of agreement with previous flight data and results from ground-based atomic oxygen testing. Reaction efficiencies for some of the polymers investigated, including Kapton and Teflon (TFE and FEP), are slightly higher than previously reported from previous EOIM flight experiments. Results indicate that coatings of hexamethyl disiloxane (HMDS) and indium tin oxide (ITO) protected the underlying Kapton from attack.

Candidate Space Station seal materials of Viton V747 and Silicone S383 were only slightly affected by the space exposure, as gauged by the small changes in Shore A hardness, helium permeability, and the thermophysical properties of solar absorptance and thermal emittance.

Thermal control ceramic-based coatings proved to be highly resistant to the EOIM-3 levels of space environment exposure. Thermo-optical properties were relatively stable for all but two of the newer formulations of the polyurethane-based coatings. No significant changes in the appearance or optical properties of the various types of anodized aluminum were detected except for the darkening of the organic dyed samples and a single chromic acid anodized aluminum sample from the 120 °C tray.

The appearance, solar absorptance, and infrared thermal emittance of beta cloth samples were basically unchanged as a result of EOIM-3 exposure.

The diversity of analytical characterization techniques proved useful in the detection and identification of environmentally induced effects for the metallic and optical samples. Mass loss/gain measurements are revealing for some samples, such as the comparative losses for aluminum/lithium 2090 alloy samples from the heated trays compared to the similar Weldalite

alloy samples from the passive trays, possibly indicating an effect of space exposure. Optical measurements do not indicate significant changes for these samples, while, for example, the changes in solar absorptance and/or thermal emittance of the silver and copper samples are obvious indicators of the expected oxidation. The thermally driven diffusion or migration of adhesion layer nickel into thin film gold samples was indicated by optical measurements but not confirmed until SALI profiles and RBS analysis showed nickel and nickel oxide on the surface and in the bulk of the gold layer. As a final example, the longer wavelength diffuse reflectance measurements of thin film nickel proved relatively insensitive to the oxidation revealed in much shorter wavelength (VUV) measurements and SALI investigations.

The exposed vacuum UV phosphor, sodium salicylate was found to be noticeably thinner, and the measured fluorescence stimulated by vacuum UV wavelengths decreased approximately 50% in the exposed area.

Molecular contamination, as indicated by ESCA sputtering depth profiles, was detected as an organic silicone approximately 7 nm. thick on selected witness samples.

ACKNOWLEDGMENTS

The candidate X-ray reflector coatings were prepared by Dr. Alan Shapiro (MSFC). Special appreciation is expressed to Ed White (MSFC) for design and fabrication support, including the stress fixtures. Others who provided substantial technical contributions include Dr. Michael Bojack (Auburn University) for Auger analysis, Dr. John Williams (Auburn University) and David Edwards (MSFC) for RBS analysis of gold/nickel samples, Dr. Chris Becker (SRI) for SALI analysis, Dr. Kijoon Chang (Alabama A&M) for providing the ellipsometer, and Perry Gray (Microcraft) for helium permeability testing and other technical support. Others from MSFC who contributed to the success of this experiment include Ralph Carruth, James Coston, Diep Trinh, Tenina Bili, Whitney Hubbs, Don Burch, and Dewitt Burns. The authors gratefully acknowledge the efforts of the JSC and KSC individuals for experiment integration and interface, with particular mention of Dr. Steven Koontz, James Visentine, and Steven Dansby of JSC.

Table 1. Space Environment Effects on SUV A-276 Paint Samples

<u>Sample</u>	<u>Environment</u>	<u>ΔMass (mg)</u>	<u>ΔThickness (Å)</u>
C-SUV	Entire mission	0.69	14,100
L-SUV	AO only in presence of UV	0.60	11,900
D-SUV	AO only, no UV	0.33	6,600

REFERENCES

1. Leger, L.J., "Evaluation of Oxygen Interaction with Materials III (EOIM-III) Flight Experiment Update," JSC memo ES5-93-118, July 2, 1993.
2. Leger, L.J., Koontz, S.L., Visentine, J., Hunton, D., "An Overview of the Evaluation of Oxygen Interaction with Materials-Third Phase (EOIM-III) Experiment: Space Shuttle Mission 46," AIAA-93-0497, January 1993.
3. Linton, R.C., Finckenor, M.M., Kamenetzky, R.R., Gray, P., "Effects of Atomic Oxygen and Ultraviolet Radiation on Candidate Elastomeric Materials for Long-Duration Missions - Test Series No. 1", NASA TM-108408, June 1993.
4. Koontz, S., King, G., Dunnet, A., Kirkendahl, T., Linton, R., Vaughn, J., "The International Telecommunications Satellite (INTELSAT) Solar Array Coupon (ISAC) Atomic Oxygen Flight Experiment: Techniques, Results, and Summary," Centre National D'Etudes Spatiales, Toulouse, France, 1992.
5. Visentine, J., comp., "Atomic Oxygen Effects Measurements for Shuttle Missions STS-8 and STS-41G, Vol. III", NASA TM-100459, Sept. 1988.
6. Linton, R.C., Whitaker, A.F., Finckenor, M.M., "Space Environment Durability of Beta Cloth in LDEF Thermal Blankets," LDEF Materials Results for Spacecraft Applications Conference, Oct. 1992.
7. Linton, R.C., Whitaker, A.F., Kamenetzky, R.R. "Fluorescence Observations of LDEF Exposed Materials as an Indicator of Induced Material Reactions," LDEF Materials Results for Spacecraft Applications Conference, Oct. 1992.
8. Williams, J.R., Bozack, M.J., Fromhold, A.T., Technical Progress Report for NASA Contract NAS8-39131, Delivery Order #3, Auburn University.
9. Kamenetzky, R.R., Linton, R.C., Finckenor, M.M., Vaughn J.A., Whitaker, A.F., "Effects of Atomic Oxygen on Polymeric Materials Flown on EOIM-3", AIAA 93-4103.
10. Vaughn, J.A., Linton, R.C., Finckenor, M.M., Kamenetzky, R.R., "Evaluation of Atomic Oxygen Effects on Metals and Optical Thin Films on EOIM-3", AIAA 93-4104.
11. Finckenor, M.M., Linton, R.C., Kamenetzky, R.R., Vaughn, J.A., "Thermal Control Materials on EOIM-3", AIAA 93-4101.
12. Franzen, W., Brodtkin, J.S., Sengupta, L.C., Sagalyn, P.L., "Ellipsometric Study of Oxide Films Formed on LDEF Metal Samples," NASA CP-3134, June 1991.

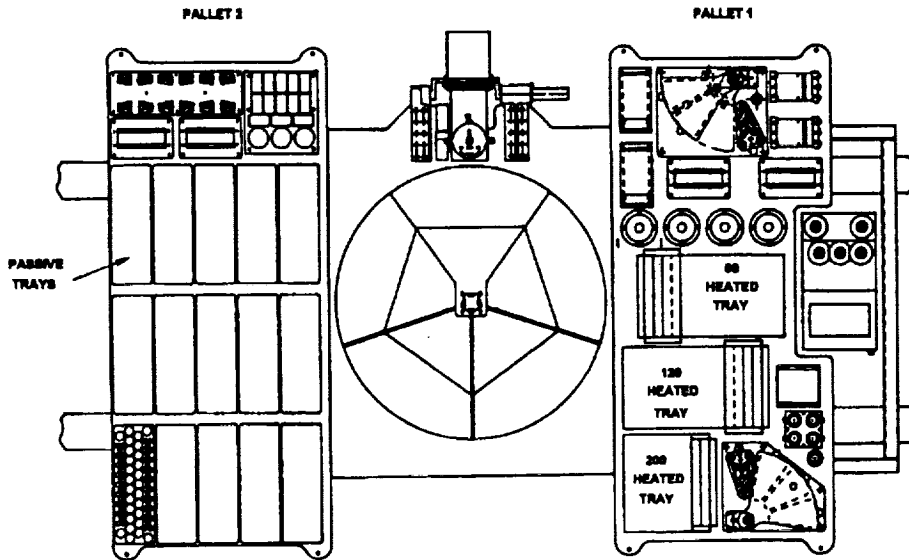
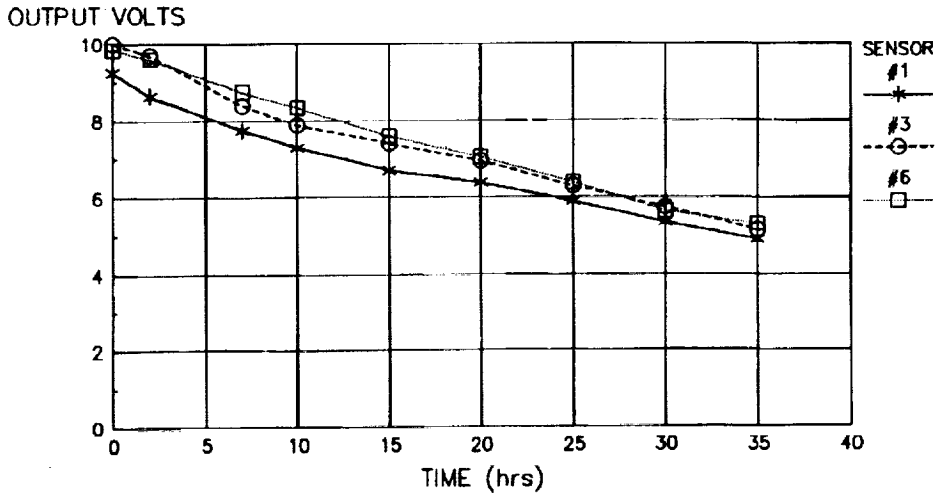


Figure 1 EOIM-3 Payload Configuration

AORM SENSOR DATA VOLTAGE OUTPUT VS. ORBITAL EXPOSURE TIME



8-6-92
Time after EOIM-3 ON

Figure 2 Effective Conductance Decrease with AO Exposure

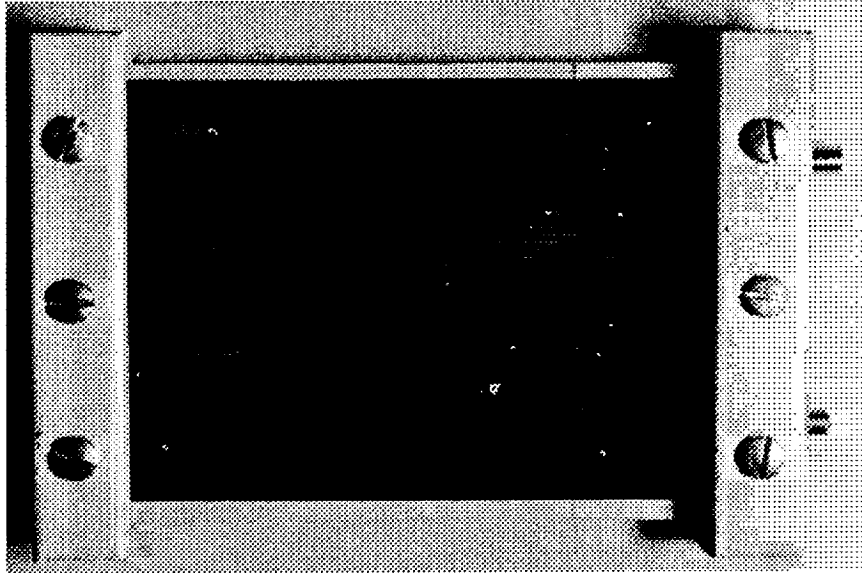


Figure 3
Contaminated Static Stress Fixture Under Black Light Illumination

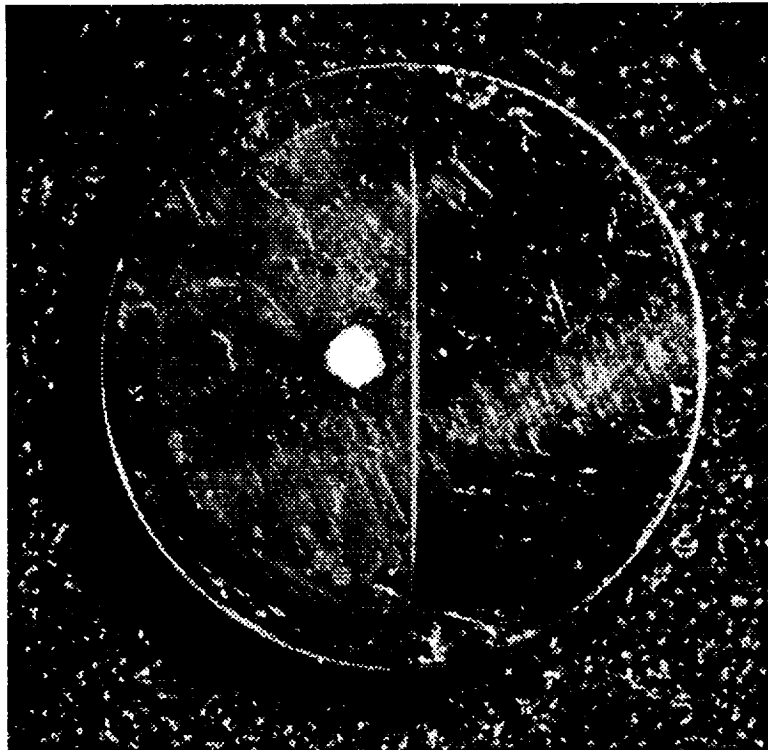


Figure 4
Contamination on Gold Mirror

MSFC Optical Witness Samples - EOIM-3
Percent Change in Vacuum UV Reflectance

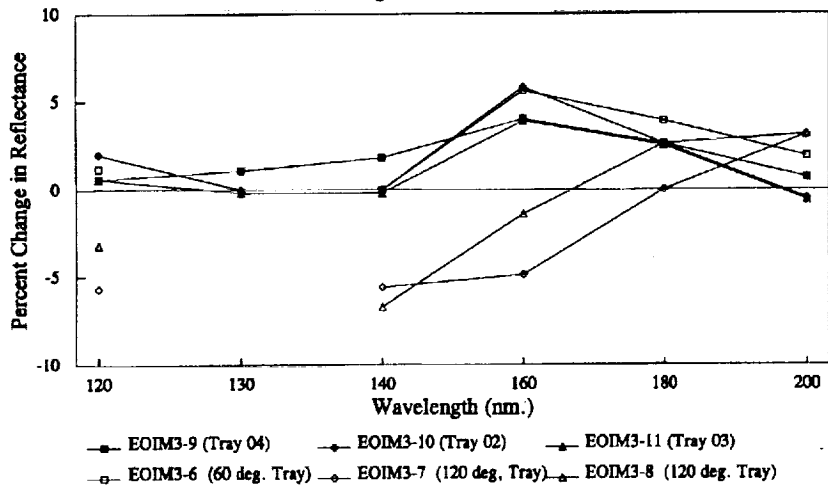


Figure 5
VUV Reflectance of MgF₂/Al/Fused Silica Mirrors
Optical Witness Samples on EOIM-3

ESCA ANALYSIS OF MSFC SAMPLES ON EOIM-3
MgF₂/ALUMINUM/FUSED SILICA GLASS OPTICAL WITNESS SAMPLE MIRRORS

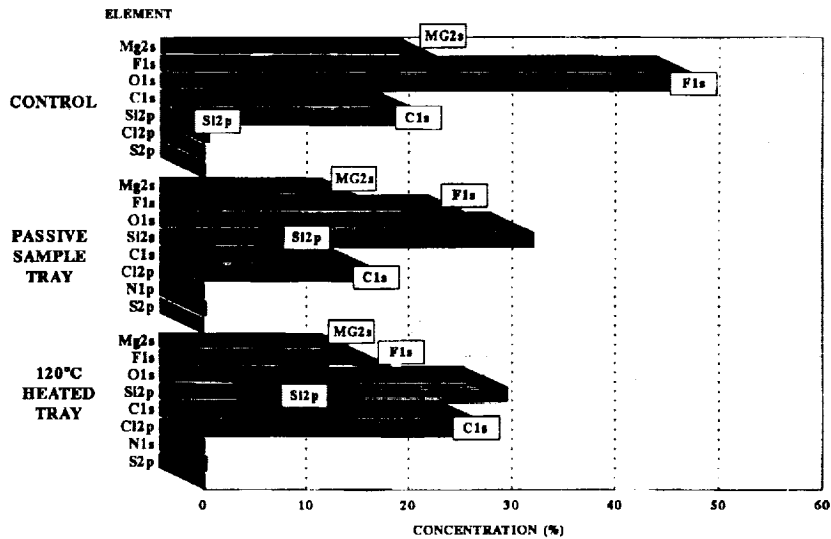


Figure 6
ESCA Analysis Results
EOIM-3 Optical Witness Samples

EFFECTS OF ATOMIC OXYGEN ON POLYMERIC MATERIALS FLOWN ON EOIM-3

Rachel R. Kamenetzky

Roger C. Linton

Miria M. Finckenor

Jason A. Vaughn

Space Environment Effects
Marshall Space Flight Center, AL 35812

ABSTRACT

Diverse polymeric materials, including several variations of Kapton, were flown on STS-46 as part of the Evaluation of Oxygen Interaction with Materials Experiment (EOIM-3). These materials were flown in the cargo bay and exposed to the space environment July 31 - August 8, 1992, including 40 hours of direct atomic oxygen impingement. The atomic oxygen exposure was approximately 2.2×10^{20} atoms/cm².

Polymeric materials flown on EOIM-3 include coated and uncoated Kapton, Tefzel ETFE, Lexan, FEP and TFE Teflon, bulk Halar and PEEK, S383 silicone and Viton elastomeric seal material. Analyses performed included thickness measurements using Dektak and eddy current methods, mass loss, resistance, permeability, hardness, and FTIR. The effects of stress and the space environment on Kapton were also evaluated.

Previous EOIM missions on STS-5 and STS-8 and the Long Duration Exposure Facility also contained polymeric material samples. Data from these previous flights are shown for comparison, as well as ground simulation of space environment effects using both thermal energy flow tubes and 5 eV neutral atomic oxygen beam facilities. Reaction efficiencies for the various atomic oxygen exposure conditions are discussed.

INTRODUCTION

Material durability in the space environment is a major concern of spacecraft designers. Over the past decade, scientists and engineers have worked to achieve a better understanding of the space environment and its effect on potential engineering materials and material processes. The Long Duration Exposure Facility (LDEF) has provided a wealth of data on long term material durability and survivability¹; however, the cost in terms of time and dollars for this type of testing is often prohibitive. As a result, spacecraft designers must often rely on data generated from short term Space Shuttle missions and ground simulations to predict long term material stability. The Evaluation of Oxygen Interactions with Materials (EOIM) flight experiments were a series of Space Shuttle exposed payloads designed to evaluate the effects of low earth orbit (LEO) exposure on materials of spacecraft design interest and, if feasible, predict long term material life.

The Space Shuttle mission STS-46 payload included the third EOIM flight experiment (fig. 1). This flight exposed a variety of materials including numerous thin film and bulk polymeric materials to the space environment July 31 through August 8, 1992. Polymeric materials in general have been shown to be highly sensitive to atomic oxygen, the predominate chemical species for LEO². The Marshall Space Flight Center (MSFC) array of polymer samples included thin films of Kapton, carbon impregnated Black Kapton, coated Kapton, Tefzel (copolymer of tetrafluoroethylene and ethylene), FEP and TFE Teflons, and Lexan. MSFC bulk polymer specimens included Halar (a copolymer of chlorotrifluoroethylene and ethylene), polyetheretherketone (PEEK), silicone S383, and Viton (a copolymer of vinylidene fluoride and hexafluoroprene).

SPACE ENVIRONMENT

The EOIM-3 payload was exposed to LEO from within the ram oriented open cargo bay of the Space Shuttle as it orbited the Earth at an altitude of 123-124 nautical miles. Although this exposure provided the majority of the total EOIM-3 atomic oxygen fluence, additional atomic oxygen was incurred during the deployment, release, and station-keeping of the European Retrieval Carrier (EURECA) such that total accumulated atomic oxygen fluence levels for the EOIM-3 flight experiment were determined to be 2.2×10^{20} atoms/cm². In addition, samples were exposed to approximately 30.6 sun hours of solar ultraviolet (UV) radiation, of which 7.6 sun hours were synergistic with atomic oxygen impingement. Thermal extremes ranged from -5 °C to 80 °C for the passively exposed trays. Particulate radiation was negligible, and there was no indication of significant micrometeoroid impact or space debris damage.

EOIM-3 FLIGHT EXPERIMENT DESCRIPTION

Thin film specimens of Kapton H, Kapton HN, Kapton with various protective coatings, Black Kapton, Tefzel, and Lexan as well as bulk polymeric Halar and PEEK specimens were exposed on MSFC EOIM-3 passive tray 04. The coated specimens consisted of plasma polymerized hexamethyl disiloxane (HMDS)/Teflon TFE over Kapton and indium tin oxide (ITO) over aluminized Kapton. Two different ratios of HMDS to TFE were used, 40:2 and 40:5. The polymer samples were configured such that many were partially shielded from atomic oxygen by way of "half-moon" aluminum covers or wire mesh (fig. 2). Thin films of Kapton H, Kapton HN (from LeRC and JSC round-robin supply), carbon impregnated Black Kapton, FEP Teflon and TFE Teflon were also exposed on the actively heated 60 °C and 120 °C trays. One inch diameter samples of bulk S383 silicone and Viton elastomeric seal material samples were also flown on the 60 °C heated tray.

In addition to the passive and heated tray polymer specimens, sheets of 2 mil thick Kapton HN were exposed in fixtures designed to maintain a constant pre-load mechanical stress (the uniform stress fixtures) by way of a spring load mechanism and on fixtures designed to provide only an initial pre-load (the static stress fixtures). Two uniform stress fixtures (fig. 3) were flown, with the Kapton specimens loaded to a pre-flight stress of 219 psi and 375 psi.

Beneath each loaded Kapton specimen, a separate Kapton sample was fixed to the base plate of the fixture to monitor reflected/scattered atomic oxygen. Two static stress fixtures (fig. 4) were flown with a "finger-tight" load placed on the Kapton specimens. Each Kapton flight specimen was coated on the backside with an aluminum grid pattern to aid in mapping thickness location measurements.

Atomic oxygen reactivity values were calculated based on changes in mass, thickness, and resistivity of the polymer films. Flight samples and ground control samples were stored in desiccators during the post flight analysis period. Kapton samples were placed under vacuum for a minimum of twenty minutes prior to taking mass measurements, with the final mass value extrapolated to time zero. All mass measurements were made using a Mettler AT250 balance. Thickness measurements were made using either a Sloan Dektak IIA probe, a Zeiss light section microscope, or a UPA Dermitron Thickness Tester D-8. Resistivity measurements were made using a Magne-Tron model M-700 four point probe. A scanning electron microscope (SEM) was used for surface morphology imaging of the film and bulk polymer specimens. Seal materials were evaluated for changes in permeability using a Varian 936-SP helium leak detector and changes in hardness using a Shore A hardness tester.

GROUND SIMULATION EXPERIMENTS DESCRIPTION

In order to better evaluate the validity of ground simulated atomic oxygen effects on materials, Halar, PEEK and FEP Teflon coated with Inconel and silver (AgFEP) polymer samples were tested for atomic oxygen sensitivity in the Princeton Plasma Physics Laboratory (PPPL) 5 eV Neutral Atomic Oxygen Facility and in the MSFC EH15 Advanced Atomic Oxygen Drift Tube Simulator (AODTS). These samples were then evaluated against their counterpart EOIM-3 flight samples. The PPPL facility produces a neutral 5 eV atomic oxygen beam via a plasma generated using a 2.45 GHz, radio frequency (RF) field that is neutralized by an inelastic collision with a tantalum plate. During the production of the atomic oxygen plasma, the system produces vacuum ultraviolet (VUV) radiation at the atomic oxygen resonant peak of 130 nm. In this particular test series, the polymers were exposed to an atomic oxygen fluence of approximately 7.2×10^{20} atoms/cm² and a VUV irradiance of approximately 8000 equivalent sun hours (ESH). The AODTS facility produces a thermal atomic oxygen plasma generated by a 14.7 MHz RF field. Samples are exposed outside of the RF field, eliminating unwanted sample heating and exposure to any plasma charged particles. In one particular test series, samples of Halar, PEEK and AgFEP were exposed to an atomic oxygen fluence of approximately 7.1×10^{22} atoms/cm². Additional samples of Halar and PEEK turned 180° from the atomic oxygen drift direction received a fluence of 2.1×10^{22} atoms/cm². In a second test series⁴, samples of S383 and Viton were exposed to 1.3×10^{22} atoms/cm² of thermal atomic oxygen in the AODTS system. Additional samples were exposed to 1714.5 equivalent sun hours (ESH) of ultraviolet radiation using a Hg-Xe 1 KWatt source followed by an accumulated fluence of 1.3×10^{22} atoms/cm² of thermal atomic oxygen in the AODTS system.

THIN FILM EVALUATION RESULTS

Atomic oxygen reactivity values for the EOIM-3 thin films are shown in table 1 along with values taken from samples flown on LDEF experiment A0171 and Shuttle missions STS-5, -8, and -41. In addition, reactivity values for samples exposed in the PPPL facility and MSFC AODTS facility are shown where available for comparison. Mass loss and resistivity measurements made on the EOIM-3 Kapton samples with protective coatings indicated that the samples were not significantly affected by atomic oxygen exposure. Reactivity values greater than 3.0×10^{-24} cm³/atom were calculated for the EOIM-3 Kapton H and Kapton HN samples. These reaction efficiencies are slightly higher than values previously reported for EOIM missions³. In general, Kapton H specimens had a slightly higher reactivity value than Kapton HN. Black Kapton samples were generally less reactive than normal Kapton, with reactivity values on the order of 2.1 to 2.5×10^{-24} cm³/atom. Reactivity values for EOIM-3 Lexan samples were somewhat higher than values generated from STS-41 flight data.

EOIM-3 TFE and FEP samples indicated reactivity values an order of magnitude lower than LDEF A0171 values, most probably due to differences in ultraviolet radiation exposure levels. By way of comparison, reactivity values of silverized Teflon tape samples exposed to atomic oxygen and 8000 ESH of VUV radiation in the PPPL facility showed a marked increase in atomic oxygen sensitivity, while samples exposed only to thermal atomic oxygen in the AODTS indicated reactivity values that were more in agreement with the flight samples exposed to low levels of UV radiation.

Samples exposed at elevated temperatures generally showed an increase in atomic oxygen reactivity. While FTIR analysis did not show any structural changes in the Teflon samples due to LEO exposure or elevated temperatures, when compared to ground controls, changes in percent transmission were noted (figs. 5 and 6).

BULK POLYMER EVALUATION RESULTS

Reactivity values for the EOIM-3 bulk Halar and bulk PEEK flight specimens as well as for LDEF A0171, STS-41, PPPL, and AODTS are shown in table 1. EOIM-3 and LDEF values are in fairly good agreement, but are somewhat higher in value than the STS-41 results for Halar and somewhat lower in value than the STS-41 results for PEEK. In both cases, PPPL values tended to be somewhat higher, while AODTS values were lower. FTIR analysis did not show any structural changes in the Halar or PEEK samples due to LEO exposure or PPPL exposure, when compared to ground controls, though changes in percent transmission were noted (figs. 7 and 8). SEM photographs (fig. 9) of the exposed region of Halar and PEEK specimens from EOIM-3, LDEF A0171, and PPPL show distinct atomic oxygen erosion characteristics. Samples exposed to thermal atomic oxygen in the AODTS facility lacked the distinctive erosion structures found in samples exposed to 5 eV atomic oxygen.

EOIM-3 S383 and Viton seal material, exposed on the 60° heated tray, were visibly unchanged. By comparison, samples exposed to ground simulated ultraviolet radiation and AODTS generated atomic oxygen were visibly changed in the exposed region. Ground tested S383 exposed to atomic oxygen appeared glossy in the exposed region. S383 samples exposed

to ultraviolet radiation followed by atomic oxygen appeared glossy and showed evidence of surface microcracking. Ground tested Viton became diffuse in appearance when exposed to ground simulated atomic oxygen. Viton samples exposed to ultraviolet radiation followed by atomic oxygen appeared grayish-white in the exposed region in contrast to the protected shiny black unexposed region.

Shore A hardness measurements (table 2) indicated a slight increase in surface hardness for both S383 and Viton samples due to the EOIM-3 low earth orbit exposure. Permeability data for the EOIM-3 S383 and Viton showed no significant change.

EOIM-3 S383 and Viton reflectance measurements from 250 nm to 2500 nm are shown in Figures 10 and 11. S383 solar absorptance and infrared emittance values (table 2) showed little change due to exposure, while the Viton flight specimen showed a 2.2 % increase in solar absorptance and a 3.5 % increase in infrared emittance (table 2). These changes are in fairly good agreement with data taken from ground exposed S383 and Viton specimens. FTIR analysis on the EOIM-3 S383 specimen (fig. 12) showed only slight structural changes, with the appearance of the early development of a carbonyl functional group (1633 cm^{-1}) and the development of O-H bonds ($3000\text{ to }3500\text{ cm}^{-1}$). This is in good agreement with FTIR spectra taken on ground tested S383. No new structures were noted for the EOIM-3 Viton specimen (fig. 13), though a general shift in transmission over the entire scan range of $700\text{ to }4000\text{ cm}^{-1}$ was noted. This transmission shift was also noted for similar samples exposed in ground testing.

Short wave blacklight observations revealed changes in fluorescence for both the S383 and Viton samples. The S383 flight sample appeared yellow/orange in the exposed region in contrast to the natural red of the unexposed region. The Viton sample appeared pea green in the exposed region, in contrast to the natural black coloring of the unexposed region. Fluorescence scans of the EOIM-3 S383 and Viton specimens (figs. 14 and 15) clearly showed distinct changes in both relative intensity and emission wavelength for the exposed sample region as compared to the unexposed region. Fluorescence scans on ground exposed S383 showed similar stimulated emission⁴. Fluorescence scans on ground exposed Viton specimens varied, dependent on exposure conditions. Ground simulated atomic oxygen exposure resulted in a grey ash on the Viton samples, interfering with good fluorescence measurements. Ultraviolet radiation exposure has quenched the fluorescent properties of the Viton in ground simulation⁴. Batch variations in Viton fluorescence have also been noted.

KAPTAN UNIFORM AND STATIC STRESS FIXTURES

The Kapton uniform stress and static stress fixtures were loaded with 2 mil Kapton HN on October 24, 1991 in preparation for the EOIM-3 flight experiment. The Kapton from all four fixtures appeared diffuse in the exposed regions in contrast to the typical transparent nature of virgin Kapton film. Because of this diffuse scatter in the exposed regions, post-flight light section microscope analysis could not be used to effectively map any thickness changes in the Kapton flight specimens. In addition, post-flight observations showed a white contaminate smear on the Kapton specimens loaded on both static stress fixtures. Efforts to map thickness changes by other methods are continuing.

The two uniform stress fixtures were flown with the Kapton specimens loaded to a pre-flight load of 1.9 pounds and 2.3 pounds. The exposed Kapton was removed from the fixtures

on July 12, 1993 at which time the measured load on the Kapton specimens was recorded as 1.4 pounds and 2.0 pounds, respectively. Mass loss measurements on the Kapton indicated reaction efficiencies of 3.2×10^{-24} and 3.3×10^{-24} cm³/atom. These values are in agreement with values generated based on mass loss for Kapton specimens exposed on the EOIM-3 passive trays (table 1). Mass loss data on the Kapton specimens removed from the two static fixtures, which were pre-loaded to a finger-tight condition, indicated in both cases an atomic oxygen reaction efficiency of 3.5×10^{-24} cm³/atom, which, despite the aforementioned contamination, is somewhat higher than the values generated from the EOIM-3 passive tray samples.

Well-defined rectangular diffuse areas were also observed during post-flight evaluation along both edges of the Kapton specimens exposed as part of the atomic oxygen monitoring packs that were attached to the base plate of each of the two uniform stress fixtures (fig. 3). Based on Kapton mass loss, measured diffuse area and an assumed reaction efficiency of 3.3×10^{-24} cm³/atom, the two fixture base plates received an atomic oxygen fluence of 3.5×10^{19} atoms/cm² and 6.0×10^{19} atoms/cm².

INTERIM CONCLUSIONS

The HMDS/TFE and ITO coatings appeared to do a good job of protecting the underlying Kapton from atomic oxygen attack. All uncoated EOIM-3 polymers showed evidence of atomic oxygen erosion. Atomic oxygen reactivity values for the EOIM-3 polymers varied in degree of agreement with values generated from previous flight data. Evaluation techniques (i.e. mass loss versus thickness change) also appear to be a factor in gauging the degree of reactivity value agreement. In general, reactivity values based on mass loss appear in fairly good agreement with LDEF A0171 values for Halar and PEEK. Reactivity values for the EOIM-3 Kapton specimens, though consistent for all the EOIM-3 specimens, are somewhat higher than values reported from previous flight experiments. The reason for the higher Kapton reactivity values is still undetermined. Polymers exposed on the heated trays had higher reactivity values than comparable samples exposed on the passive trays.

The atomic oxygen reaction efficiencies of some of these flight samples exposed on EOIM-3 are considerably less than values determined from exposure in the Princeton AO beam facility. Polymer samples exposed in the PPPL facility generally react with efficiency comparable to that experienced by similar materials in LEO, such as Kapton, black Kapton, polycarbonates, and polyethylene. Fluorocarbon materials such as Teflon have been found to be highly sensitive to the intrinsic vacuum ultraviolet (VUV - 130 nm.) radiation of most AO beam facilities, including the PPPL facility by means of synergistic reaction with the radiation and atomic oxygen. The reaction efficiencies determined from beam facility exposures of these type materials are then proportional to the irradiation levels coincident with AO. The differences in AO reaction efficiencies of EOIM-3 samples of Halar and PEEK, which are also known to be UV-sensitive, were less pronounced in comparison to the PPPL results. Polymers exposed to thermal energy atomic oxygen in the AODTS facility indicated reaction efficiencies ranging from 2 to 100 times less than polymers exposed to orbital atomic oxygen, as would be expected.

Mechanical and thermal properties of the EOIM-3 S383 and Viton seal materials were not greatly affected by the low earth orbit exposure. Seal permeability showed no significant change, while seal Shore A hardness increased only slightly for the S383 material. S383 solar absorptance and infrared emittance remained stable, while Viton showed an increase of

approximately 2% in solar absorptance and 3.5% in infrared emittance. Fluorescence scans on both the S383 and Viton specimens indicated a stimulated fluorescence emission as a result of space exposure.

EOIM-3 Kapton HN specimens exposed to the space environment on the uniform stress fixtures with a mechanical pre-load indicated reactivity values comparable to Kapton HN specimens that were exposed without a pre-load. Kapton HN samples exposed on the static stress fixtures with only a finger tight load had reactivity values slightly higher than the passive tray specimens. As a result, no definitive conclusion can be drawn as to the effect of mechanical stress on atomic oxygen reaction efficiency. However, because the Kapton HN specimens that were exposed as part of the atomic oxygen monitoring packs indicated the presence of significant atomic oxygen impingement along the fixture base plates, total EOIM-3 atomic oxygen flux values might need to be re-evaluated.

REFERENCES

1. Levine, A.S., "LDEF - 69 Months in Space First Post-Retrieval Symposium, Parts 1, 2 and 3", NASA CP 3134, Kissimmee, Florida, June 2-8, 1991.
2. Visentine, James T., "Atomic Oxygen Effects Measurements for Shuttle Missions STS-8 and 41-G, Volume III", NASA TM 100459.
3. Leger, Lubert, Koontz, S., Visentine, J., and Hunton, D., "An Overview of the Evaluation of Oxygen Interaction with Materials III Experiment", LDEF Materials Results for Spacecraft Applications Conference, Huntsville, Alabama, October 26-28, 1992.
4. Linton, R. C., Finckenor, M. M., Kamenetzky, R. R. , and Gray, P., "Effects of Atomic Oxygen and Ultraviolet Radiation on Candidate Elastomeric Materials for Long Duration Missions, Test Series No. 1", NASA TM 108408.

Atomic Oxygen Reaction Efficiency x 10 ⁻²⁴ cm ³ /atom						
Sample	STS-5 and-8	MSFC STS-41	LDEF A0171	MSFC EOIM-3	PPPL	AODTS
Halar (Bulk)		1.6 ⁽²⁾ 1.0 ⁽²⁾ 2.0 ⁽¹⁾	2.1 ⁽¹⁾	2.0 ⁽¹⁾ 2.5 ⁽²⁾	3.2 ⁽¹⁾ 3.4 ⁽¹⁾ 3.1 ⁽²⁾ 3.0 ⁽²⁾	0.034 ⁽¹⁾ 0.023 ⁽¹⁾ 0.014 ⁽²⁾
Lexan (Film)		3.6 ⁽²⁾ 1.3 ⁽¹⁾		3.6 ⁽²⁾ 4.8 ⁽¹⁾ 4.0 ⁽¹⁾		
PEEK (Bulk)		4.7 ⁽¹⁾	2.3 ⁽¹⁾	2.0 ⁽¹⁾ 2.0 ⁽¹⁾ 3.7 ⁽²⁾ 4.0 ⁽²⁾	2.8 ⁽¹⁾ 3.0 ⁽²⁾	0.11 ⁽¹⁾ 0.12 ⁽¹⁾
Tefzel (Film)		0.20 ⁽¹⁾		1.0 ⁽¹⁾ 1.1 ⁽¹⁾		
Kapton HN (Film)		3.3 ⁽¹⁾		3.3 ⁽¹⁾ 2.9 ⁽¹⁾ 4.3 ⁽¹⁾ @120 °C		
Kapton H (Film)	3.0 ⁽¹⁾			3.5 ⁽¹⁾ 3.9 ⁽¹⁾ 3.9 ⁽¹⁾ @120 °C	3.4 ⁽¹⁾	
Black Kapton (Film)		3.1 ⁽¹⁾ 2.4 ⁽³⁾		2.1 ⁽¹⁾ 2.1 ⁽¹⁾ 2.7 ⁽¹⁾ @120 °C 2.3 ⁽³⁾ 2.3 ⁽³⁾		
TFE Teflon (Film)	<0.05		0.20 ⁽²⁾ (Bulk Washers)	0.049 ⁽¹⁾ @60 °C 0.093 ⁽¹⁾ @120 °C 0.080 ⁽¹⁾ @120 °C		
FEP Teflon (Film)	<0.05		0.35 ⁽²⁾ <A0178>	0.082 ⁽¹⁾ @60 °C 0.094 ⁽¹⁾ @120 °C 0.082 ⁽¹⁾ @120 °C	6.6 ⁽¹⁾ 5.9 ⁽²⁾ <AgFEP>	0.023 ⁽¹⁾ 0.023 ⁽²⁾ <AgFEP>

Atomic Reaction Efficiency

- (1) Based on change in mass
- (2) Based on change in thickness
- (3) Based on resistivity measurement

Table 1
Atomic Oxygen Reaction Efficiencies of Polymers

Sample	Shore A Hardness	Permeability (cc/s He)	Solar Absorptance	Thermal Emittance
S383 Control	70.13 ± 0.18	2.90	0.750	0.92
S383 Flight	71.68 ± 0.27	2.81	0.751	0.91
Viton Control	76.29 ± 0.12	2.43	0.938	0.86
Viton Flight	76.86 ± 0.13	2.53	0.959	0.89

Table 2
EOIM-3 Seal Materials Data

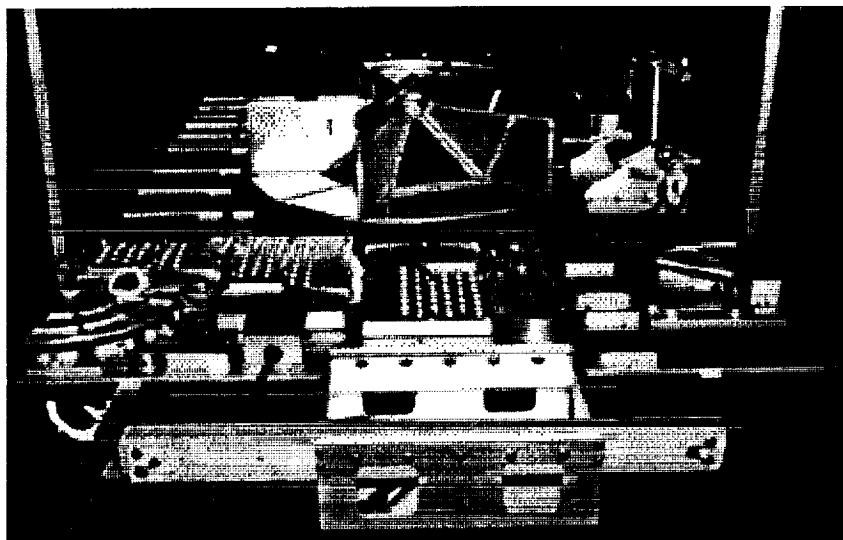


Figure 1. Photograph of EOIM-3 experiment pallet.

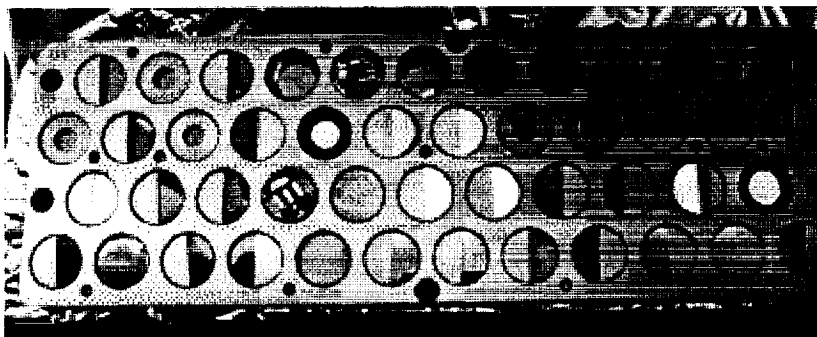


Figure 2. EOIM-3 passive tray 04 polymer samples.

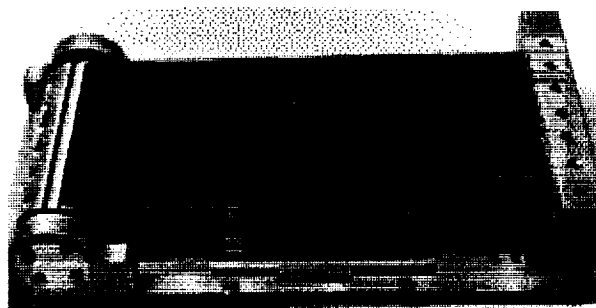


Figure 3. Post-flight photograph of MSFC uniform stress fixture showing loaded Kapton specimen. The Kapton specimen under the loaded specimen was used to evaluate atomic oxygen scatter / reflection.

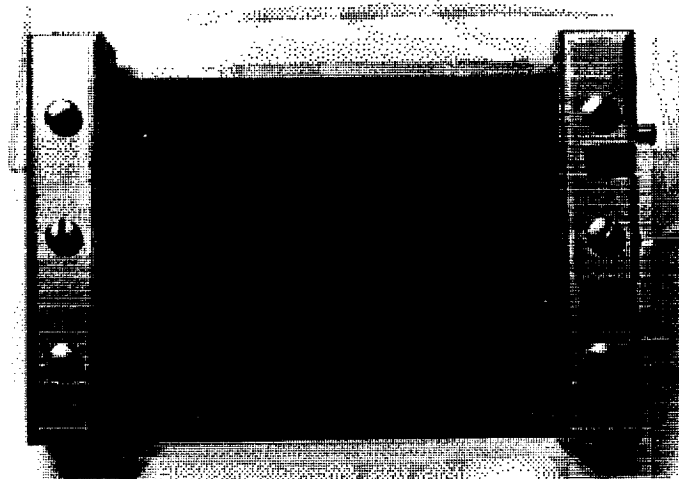


Figure 4. Post-flight photograph of MSFC static stress fixture showing loaded Kapton specimen.

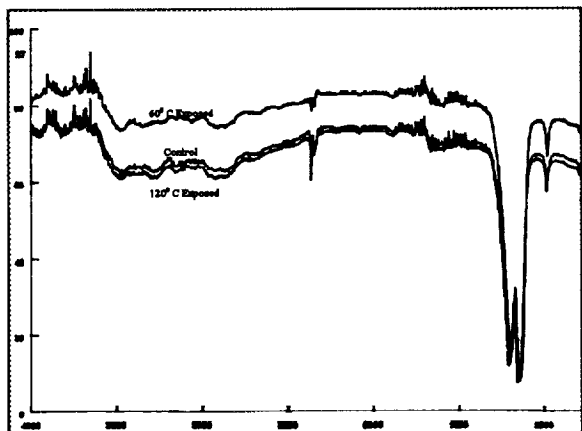


Figure 5. FTIR of EOIM-3 FEP Teflon showing percent transmission as a function of wavenumber (cm^{-1}).

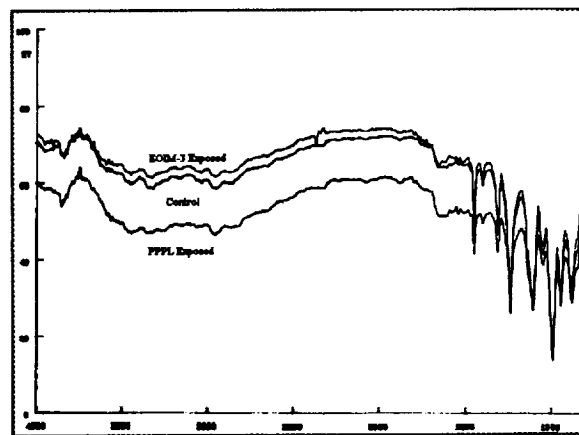


Figure 7. FTIR of EOIM-3 and PPPL exposed Halar showing percent transmission as a function of wavenumber (cm^{-1}).

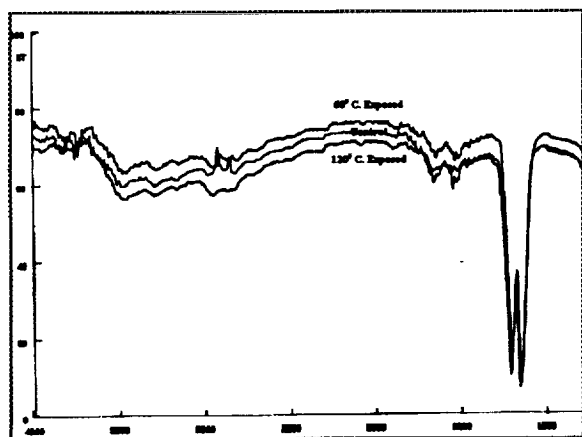


Figure 6. FTIR of EOIM-3 TFE Teflon showing changes in percent transmission as a function of wavenumber (cm^{-1}).

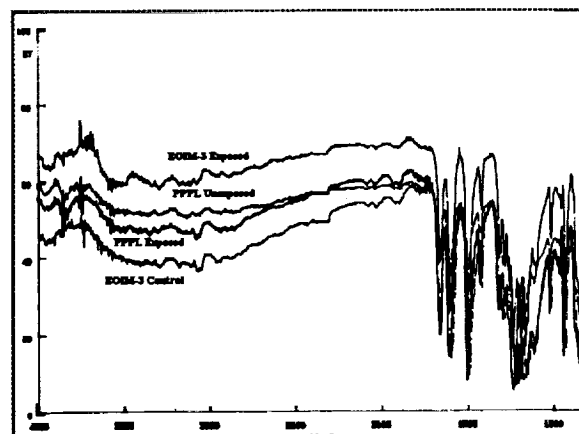


Figure 8. FTIR of EOIM-3 and PPPL exposed PEEK showing percent transmission as a function of wavenumber (cm^{-1}).

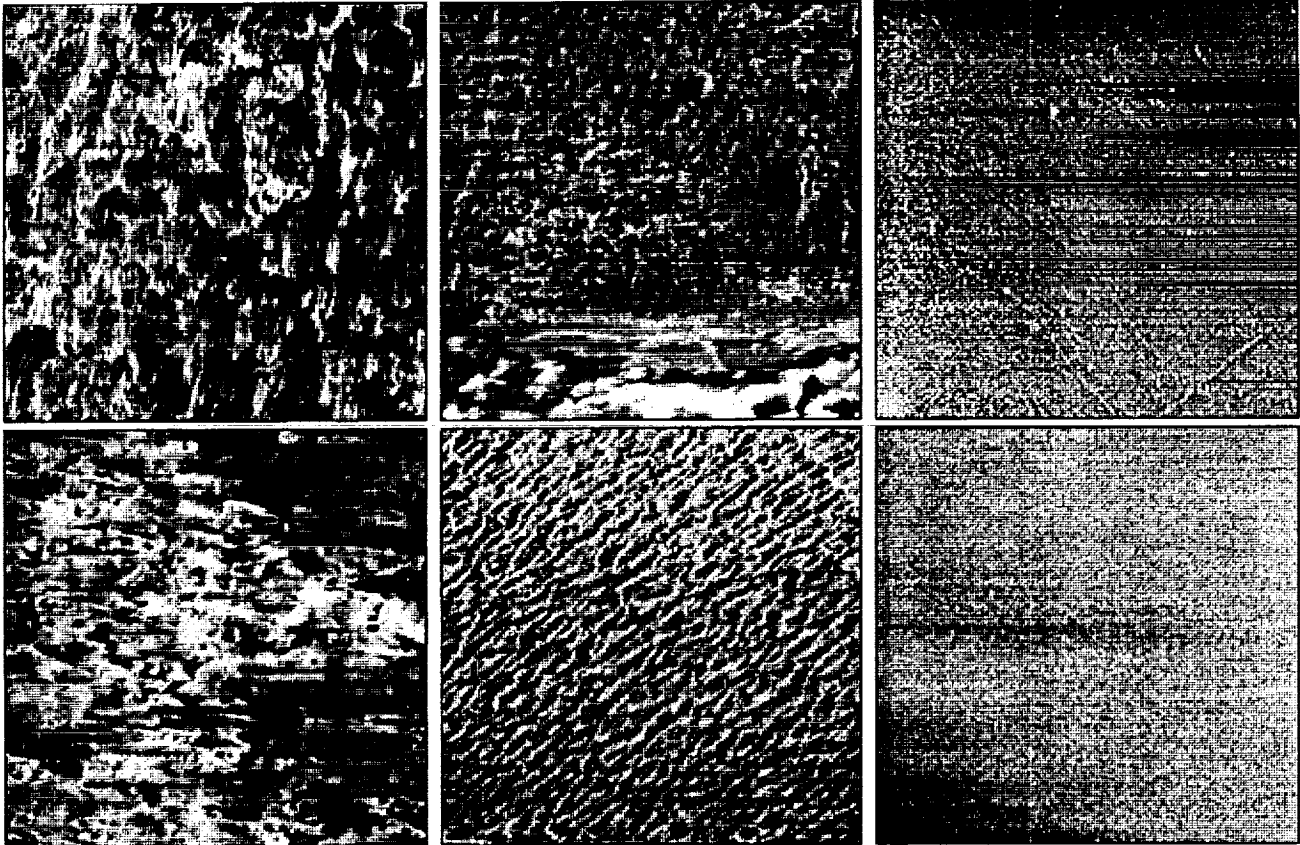


Figure 9. SEM photographs, 500 x, of exposed Halar (top row, left to right) from LDEF AO171, PPPL, EOIM-3 and exposed PEEK (bottom row, left to right) from LDEF AO171, PPPL, and EOIM-3.

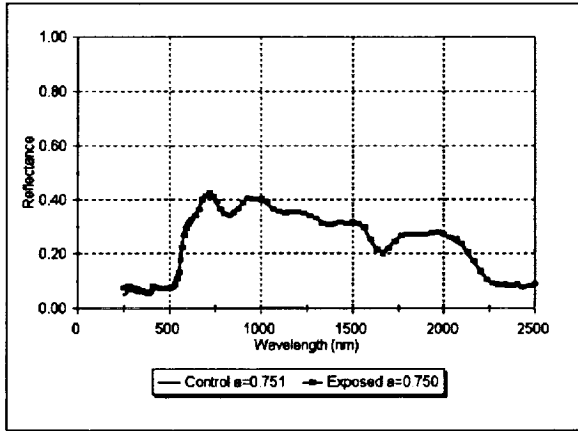


Figure 10. EOIM-3 S383 integrated reflectance as a function of wavelength.

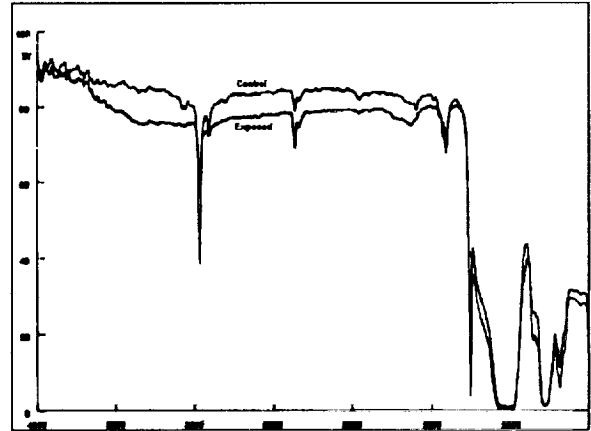


Figure 12. FTIR of EOIM-3 exposed S383 showing percent transmission as a function of wavenumber (cm^{-1}).

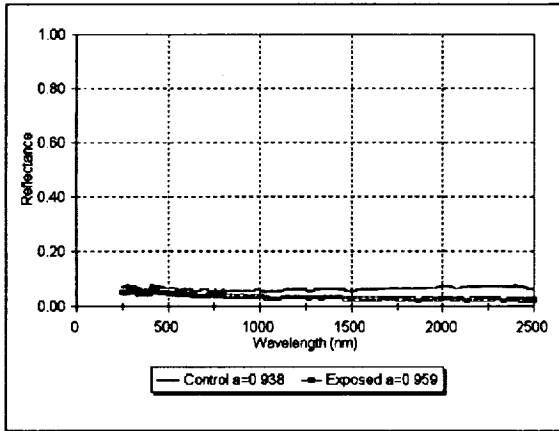


Figure 11. EOIM-3 Viton integrated reflectance as a function of wavelength.

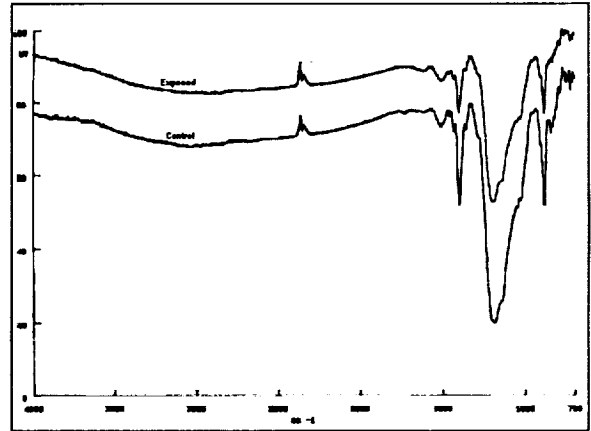


Figure 13. FTIR of EOIM-3 exposed Viton showing percent transmission as a function of wavenumber (cm^{-1}).

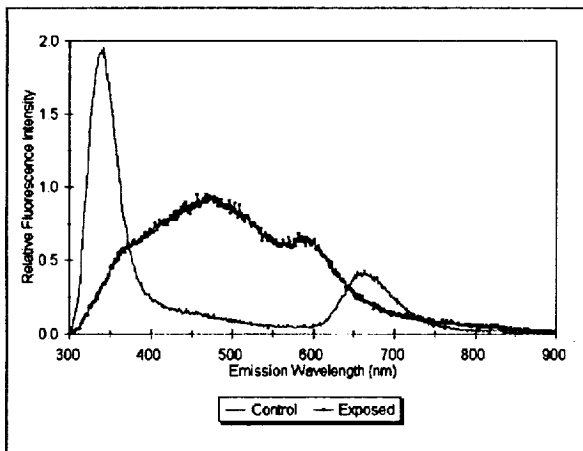


Figure 14. EOIM-3 S383 fluorescence scan showing the stimulated relative fluorescence emission as a function of emission wavelength due to low earth orbit exposure.

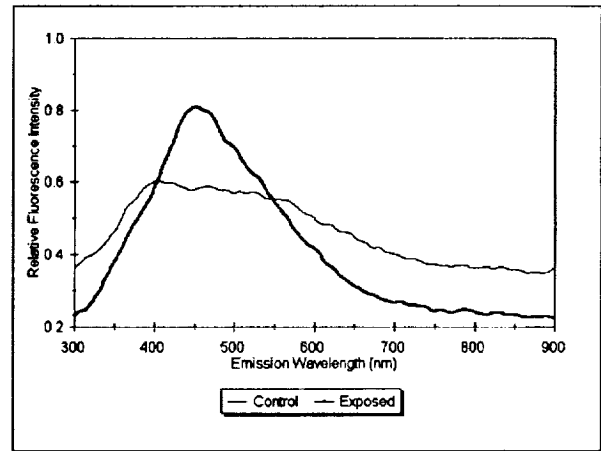


Figure 15. EOIM-3 Viton fluorescence scan showing the stimulated relative fluorescence emission as a function of emission wavelength due to low earth orbit exposure.

THERMAL CONTROL MATERIALS ON EOIM-3

Miria M. Finckenor
Roger C. Linton
Rachel R. Kamenetzky
Jason A. Vaughn
EH15 Space Environment Effects
Marshall Space Flight Center, AL 35812

ABSTRACT

Thermal control paints, anodized aluminum, and beta cloth samples were flown on STS-46 as part of the Evaluation of Oxygen Interaction with Materials Experiment (EOIM-3). The thermal control paints flown on EOIM-3 include ceramic and polyurethane-based paints. Passively exposed samples are compared to actively heated samples and controlled exposure samples. Optical property measurements of absorptivity, emissivity, and spectrofluorescence are presented for each paint.

Several variations of anodized aluminum, including chromic acid anodize, sulfuric acid anodize, and boric/sulfuric acid anodize were flown on the actively heated trays and the passive exposure trays. The post-flight optical properties are within tolerances for these materials. Also flown were two samples of yellow anodized aluminum. The yellow anodized aluminum samples darkened noticeably.

Samples of aluminized and unaluminized beta cloth, a fiberglass woven mat impregnated with TFE Teflon, were flown with passive exposure to the space environment. Data from this part of the experiment is correlated to observations from LDEF and erosion of the Teflon thin film samples also flown on EOIM-3 and LDEF.

INTRODUCTION

Materials must be tested for durability in the space environment before being approved for use on spacecraft, particularly long-term missions. Thermal control materials, such as paints and anodizations, must maintain their optical properties within certain parameters over the life of the vehicle despite the harsh environment. Ground simulators are available for testing these materials, but it is always beneficial whenever possible to expose materials to the actual space environment for analysis. This is primarily done on short flights on the Space Shuttle, with the samples on a pallet in the cargo bay.

The Evaluation of Oxygen Interaction with Materials Experiment, third flight, or EOIM-3 flew on the Space Shuttle mission STS-46 July 31 - August 8, 1992. A pallet in the Shuttle cargo bay (Fig. 1) carried numerous materials samples and fixtures which were exposed to the space environment. The Space Shuttle flew in a bay-forward position for 42 hours near the end of the mission for direct atomic oxygen impingement, exposing the experiment to a fluence of approximately 2.2×10^{20} atoms/cm². Thermal control coatings were among the 250 samples

exposed to atomic oxygen, ultraviolet radiation, particulate radiation, thermal cycling, hard vacuum, and micrometeoroid/space debris impacts. These samples have been evaluated for optical property changes caused by space environment exposure, as well as other material property changes.

SPACE ENVIRONMENT

The low Earth orbit environment consists of atomic oxygen, ultraviolet radiation, particulate radiation, thermal cycling, hard vacuum, and micrometeoroid/space debris particles. The majority of the atomic oxygen exposure was during the EOIM-3 part of the STS-46 mission, when the Space Shuttle flew with the cargo bay oriented into the RAM direction at an altitude of 123-124 nautical miles. Additional atomic oxygen exposure of approximately 1×10^{18} atoms/cm² occurred during the European Retrieval Carrier (EURECA) deployment, release, and station-keeping. Solar ultraviolet exposure consisted of 30.6 sun hours, with 7.6 sun hours synergistic with the atomic oxygen exposure. Particulate radiation was negligible for the short mission. Thermal cycling of the experiment was measured with thermocouples of varying emissivity (Ref. 2). Passive tray temperatures varied from -5 to +80 °C for the mission. To prevent molecular contamination due to the thermal cycling in the vacuum of space, material samples were baked in a vacuum oven for 24 hours prior to flight to evolve any outgassing products. Micrometeoroid/space debris particles impacts were limited to a few small impacts less than 0.25 mm in diameter.

EXPERIMENT DESCRIPTION AND ANALYSIS

Three trays containing a total of 138 samples were passively exposed to the space environment. These trays included samples of thermal control paints, anodized aluminum, and beta cloth. Active exposures were performed with three separate trays held at temperatures of 60, 120, and 200 °C during the atomic oxygen exposure. MSFC also contributed paint samples to the Solar UV trays and the Variable Exposure Trays, which varied the exposure to the ultraviolet radiation and atomic oxygen, respectively.

The Solar UV Experiment consisted of three trays. One tray was open to atomic oxygen and ultraviolet radiation during the entire mission. One tray was shuttered to only expose the samples to atomic oxygen in the presence of ultraviolet radiation. The third tray was shuttered to expose samples only to atomic oxygen with no UV exposure. The Variable Exposure Tray Experiment was intended to expose four trays to 10, 20, 30, and 40 hours of atomic oxygen. However, a microswitch failed, exposing all four trays to the entire 42 hours of atomic oxygen exposure. These paints were flown with 90% transmission nickel screens in place. This provided a grid of unexposed paint to measure erosion depth across the sample.

Samples remained in a desiccator prior to optical property measurement to eliminate any humidity effects. Diffuse solar absorptance measurements were made using a Beckman DK-2 spectrophotometer and an AZ Technology laboratory portable spectrophotometer (LPSR) on both the control and flight samples. Where the samples were partially shielded from the space

environment with a "half-moon" anodized aluminum cover, measurements were made on both the exposed and unexposed areas. Infrared emittance measurements were made with a Gier-Dunkle DB100 emissometer. A Mettler AT250 balance was used for mass measurements. Spectrofluorescence measurements were obtained using a SLM Aminco SPF-500C dual monochromator spectrofluorometer with a narrow-band excitation of 260 nm wavelength. Changes in fluorescence properties are described as quenching, stimulated emission of a new or altered color, emission wavelength shift, or enriched emission of the same color. In this paper, quenching simply refers to observed fluorescent intensity decreases rather than any imputed mechanisms of spectral change. Previous studies of the effects of space environment exposure on fluorescence properties can be found in Reference 3.

THERMAL CONTROL PAINTS

Thermal control paints exposed on the passive tray include Chemglaze A-276, Aeroglaze A-3200, Aeroglaze IC5755-60, Aeroglaze K-3210, IITRI YB-71, IITRI Z-93 with PS7 and Kasil 2130 potassium silicate binders, Chemglaze Z-306, Aeroglaze Z-3306, Aeroglaze Z-3901, other zinc oxide and zinc orthotitanate formulations, and doped silica black ceramic paint. The paints, unless otherwise noted, flew only on the passively exposed tray. Table 1 contains the optical property data measured on the flight and control samples.

Chemglaze A-276 is a glossy white titanium dioxide paint with a polyurethane binder. Samples of A-276 flew on the passively exposed tray and each of the Solar Ultraviolet and Variable Exposure Trays. It showed typical increased diffuseness with all exposures due to the erosion of the binder. Dektak measurements of the samples flown with 90% transmission nickel screens show an average thickness loss of 14,000 Å for samples exposed to 2.2×10^{20} atomic oxygen atoms/cm². Fluorescence measurements showed little difference between the actively controlled tray samples and the passive tray samples, but the control sample fluoresced more strongly in the blue-violet wavelengths (Fig. 2).

Aeroglaze A-3200 glossy white paint was similar to the A-276 in increased diffuseness. No color change was observed in either visible light or black light illumination. Fluorescence quenching did occur, similar to that of the A-276 paint sample.

Aeroglaze IC5755-60 flat black paint faded somewhat due to space exposure with black speckles remaining (Fig. 3). Black light illumination showed stimulated fluorescence in the green wavelengths, similar to the fluorescence of Chemglaze Z-306.

Aeroglaze K-3210 glossy white paint was similar to the A-276 in increased diffuseness. Significant quenching of fluorescence was observed in the blue wavelengths (Fig 4).

IITRI YB-71 paint with zinc orthotitanate pigment and potassium silicate binder flew on the 60 °C and 120 °C heated trays as well as the passive exposure trays. No color or surface morphology changes were noted, though paint flaking did occur where the sample fixture may have rubbed the material during flight. Samples passively exposed to the space environment did not change in fluorescence properties.

IITRI Z-93 zinc oxide paint was flown with two variations. The potassium silicate binder PS7 is no longer being manufactured by Sylvania, and Kasil 2130, also a potassium silicate binder, has been proposed as a substitute. Z-93 with the PS7 binder flew on the 60 °C and 120 °C heated trays as well as the passive exposure trays. No color change or surface

texturing was observed. Z-93 with the Kasil 2130 binder flew only on the passively exposed tray and also did not change in color or texture. Slight quenching of fluorescence was noted for both binder variations.

Chemglaze Z-306 is a black carbon and titanium dioxide paint with a polyurethane binder that typically becomes more diffuse when exposed to atomic oxygen due to binder erosion. Exposure to the space environment stimulated green fluorescence by apparently spectrally shifting the broad middle emission band (Fig. 5).

Aeroglaze Z-3306 flat black paint became a darker velvety black due to atomic oxygen erosion. Spectrofluorescence measurements show quenching of ultraviolet and red emission bands and a shift in the broad middle fluorescence band to longer wavelengths. This is in agreement with black light observations of stimulated color emission.

Aeroglaze Z-3901 aluminum-colored paint did exhibit a slight color change. This paint also exhibited a significant change in emittance, from 0.29 to 0.36. Nearly all fluorescence in the flight sample was quenched compared to the control sample.

A development paint of zinc oxide pigment with potassium silicate binder was tested. This paint varies from Z-93 in that the zinc oxide is of a finer particle size and the pigment-to-binder ratio (PBR) is adjusted for a lower solar absorptance. This sample exhibited no color change or surface texturing due to space environment exposure. Flaking of the paint did occur where the sample fixture may have abraded the material during flight. Slight quenching of fluorescence was noted.

Another development paint of zinc orthotitanate with potassium silicate binder was formulated in a similar fashion to the zinc oxide sample, with finer particle size and higher PBR. It also did not exhibit any color or surface changes. Black light fluorescence did not appear to have changed.

Doped silica black ceramic paint, also under development, did not appear affected by exposure to the space environment. It remained a diffuse black color.

ANODIZED ALUMINUM

A variety of anodizations were tested in the space environment. Chromic acid anodized, sulfuric acid anodized, and boric/sulfuric acid anodized samples were flown on all three temperature controlled trays as well as the passively exposed tray. The substrates were aluminum alloy 6061-T6. There were two variations on the boric/sulfuric acid anodization with 10 and 12 minute processing time. The post-flight optical properties (Table 1) are within thermal design tolerances for these materials, with the exception of the chromic acid anodized aluminum flown on the 120 °C heated tray. Possible contamination effects on this sample are being studied. No color changes were noted for any flight sample. Ellipsometry and other analyses are underway to determine if any changes in the oxidation layer occurred due to space environment exposure.

Also flown on the passively exposed tray were two samples of yellow organic dye chromic acid anodized aluminum. Organic-dyed anodized aluminum samples may be used as a gauge of incident solar UV radiation and for comparison to ground-based environmental exposure tests. Similar material samples have been observed to darken significantly after ultraviolet radiation exposure in the laboratory and to fade considerably as a result of lab

atomic oxygen exposure in the absence of ultraviolet radiation. Samples exposed to UV radiation in the laboratory and subsequently exposed to thermal energy atomic oxygen indicate less darkening. For the reported levels of atomic oxygen exposure and UV radiation during the EOIM-3 mission, the samples are darker than predicted from laboratory exposure to comparable levels of UV radiation and then atomic oxygen. Figure 6 is of a half-exposed yellow chromic acid anodized aluminum sample, with the exposed half noticeably darkened. Figure 7 shows the decrease in reflectance in the visible wavelengths of the exposed flight sample as compared to the control sample.

BETA CLOTH

Beta cloth is a fiberglass mat impregnated with TFE Teflon for flexibility and reduction in particle generation. It is generally used in multi-layer insulation thermal blankets to provide a refurbishable, thermally compatible cover and protect the underlying aluminized Mylar or aluminized Kapton layers from atomic oxygen attack. Three different types of beta cloth were flown on EOIM-3.

Two types of "plain" beta cloth were exposed. Chemical Fabrics Corporation (Chemfab) provided samples of Chemglas 250, which meets Rockwell specification #MB0135-027 and is used in the Space Shuttle cargo bay liners. Samples of beta cloth were taken from an unexposed section of the LDEF Experiment #S1005, the Transverse Flat-Plate Heat Pipe Experiment and flown. These beta cloth samples were flown with 5 layers of double aluminized Kapton with Dacron netting spacers underneath. No degradation of the multi-layer insulation was observed. Microscopic analysis of the Teflon erosion was found to be typical of short-term exposure to atomic oxygen.

These samples were measured for solar absorptance with the aluminized Kapton multi-layer insulation as a standardized backing. The control Chemglas 250 beta cloth sample α_s was 0.200, while the flight sample α_s was 0.197. The control and flight S1005 beta cloth samples had a measured solar absorptance of 0.207 and 0.204, respectively. Infrared emittance was 0.90 for all control and flight samples.

Samples of Chemglas 250F-80 aluminized beta cloth were flown with the aluminized side down. Aluminized beta cloth is being proposed for long-term spacecraft and eliminates the need for a light block layer in a thermal blanket. The solar absorptance of the aluminized beta cloth control sample was 0.357 on the non-metallized side. The two flight samples had measured solar absorptance of 0.363 and 0.366. Infrared emittance was 0.90 for all control and flight samples.

The optical property results, however, should not be misinterpreted as full approval of beta cloth for use on long-term spacecraft. These flight samples were exposed on a short duration LEO mission to a very low dose of ultraviolet radiation in presence of atomic oxygen. Laboratory tests of some types of beta cloth in an ultraviolet radiation only environment indicate yellowing attributed to a silicone additive used for increased flexibility of the cloth. Solar absorptance of aluminized beta cloth increased from 0.31 to 0.36 following exposure to 400 equivalent sun hours (ESH) of ultraviolet radiation. Solar absorptance of plain beta cloth increased in solar absorptance 0.02 and 0.03 following UV exposures of 400 and 700 ESH, respectively. This yellowing has been observed to decrease, if not disappear, following subsequent atomic oxygen exposure.

INTERIM CONCLUSIONS

Preliminary analysis of the ceramic binder paints indicate good durability in the space environment with respect to optical properties. Erosion of the paints with a polyurethane binder were as predicted. Increased diffusivity of the Chemglaze A-276 and Z-306 paints were similar to those exposed to atomic oxygen on the Long Duration Exposure Facility and earlier short duration Shuttle missions. The Aeroglaze IC-5755-60 flat black paint faded noticeably due to space environment exposure, while the Z-3901 paint experienced a significant change in emittance.

Anodizations performed well with the exception of the yellow organic dye chromic acid anodized aluminum and the chromic acid anodized aluminum flown on the 120 °C heated tray. Possible contamination effects are under investigation. The remaining anodizations were within thermal design tolerances for solar absorptance and infrared emittance. Beta cloth also performed well, maintaining its optical properties in the presence of atomic oxygen.

REFERENCES

1. Leger, Lubert, Koontz, S., Visentine, J., and Hunton, D., "An Overview of Evaluation of Oxygen Interaction with Materials III Experiment", LDEF Materials Results for Spacecraft Applications Conference, Oct. 26-28, 1992.
2. Leger, Lubert, "Evaluation of Oxygen Interaction with Materials III (EOIM-III) Flight Experiment Update," Memo #ES5-93-118, July 1993.
3. Linton, R.C., Whitaker, A.F., and Kamenetzky, R.R., "Fluorescence Observations of LDEF Exposed Materials as an Indicator of Induced Material Reactions", LDEF Materials Results for Spacecraft Applications Conference, Oct. 1992.

Sample	Environment	Control α_s	Exposed α_s	$\Delta \alpha_s$	Control ϵ_{IR}	Exposed ϵ_{IR}	$\Delta \epsilon_{IR}$
A-276	Passive	0.276	0.283	+0.007	0.89	0.91	+0.02
	AO + UV	0.276	0.275	-0.001	0.89	0.91	+0.02
	AO only	0.276	0.273	-0.003	0.89	0.90	+0.01
A-3200	Passive	0.273	0.280	+0.007	0.90	0.90	0.00
IC5755-60	Passive	0.971	0.938	-0.033	0.90	0.92	+0.02
K-3210	Passive	0.269	0.264	-0.005	0.90	0.90	0.00
YB-71	Passive	0.129	0.131	+0.002	0.88	0.89	+0.01
	60 °C	0.136	0.129	-0.007	0.88	0.88	0.00
	120 °C	0.136	0.135	-0.001	0.88	0.88	0.00
Z-93/PS7 Binder	Passive	0.182	0.180	-0.002	0.91	0.91	0.00
	60 °C	0.172	0.156	-0.016	0.91	0.91	0.00
	120 °C	0.172	0.160	-0.012	0.91	0.91	0.00
Z-93/Kasil 2130	Passive	0.139	0.138	-0.001	0.89	0.89	0.00
Z-306	Passive	0.938	0.965	+0.027	0.91	0.94	+0.03
	AO + UV	0.938	0.967	+0.029	0.91	0.94	+0.03
	AO only	0.938	0.969	+0.031	0.91	0.94	+0.03
Z-3306	Passive	0.960	0.991	+0.031	0.90	0.92	+0.02
Z-3901	Passive	0.234	0.252	+0.018	0.29	0.36	+0.07
Doped Silica	Passive	0.969	0.964	-0.005	0.91	0.91	0.00
Zinc Oxide	Passive	0.170	0.162	-0.008	0.91	0.91	0.00
Zinc Orthotitanate	Passive	0.118	0.116	-0.002	0.91	0.91	0.00
Boric/Sulfuric Acid Anodized Aluminum 10 min.	Passive	0.238	0.240	+0.002	0.31	0.31	0.00
	60 °C	0.238	0.241	+0.003	0.31	0.31	0.00
	120 °C	0.238	0.240	+0.002	0.31	0.31	0.00
	200 °C	0.238	0.244	+0.002	0.31	0.30	-0.01
Boric/Sulfuric Acid Anodized Aluminum 12 min.	Passive	0.254	0.253	-0.001	0.46	0.44	-0.02
	60 °C	0.254	0.253	-0.001	0.46	0.46	0.00
Chromic Acid Anodized Aluminum	Passive	0.357	0.366	+0.009	0.70	0.70	0.00
	60 °C	0.357	0.375	+0.018	0.70	0.70	0.00
	120 °C	0.357	0.431	+0.074	0.70	0.70	0.00
	200 °C	0.357	0.360	+0.003	0.70	0.70	0.00
Sulfuric Acid Anodized Aluminum	Passive	0.474	0.473	-0.001	0.85	0.85	0.00
	60 °C	0.474	0.487	+0.013	0.85	0.86	+0.01
	120 °C	0.474	0.481	+0.007	0.85	0.85	0.00
	200 °C	0.474	0.466	-0.008	0.85	0.85	0.00
Yellow Organic Dye/Chromic	Passive	0.458	0.483	+0.025	0.79	0.79	0.00

Table 1. Optical Properties of Thermal Control Coatings

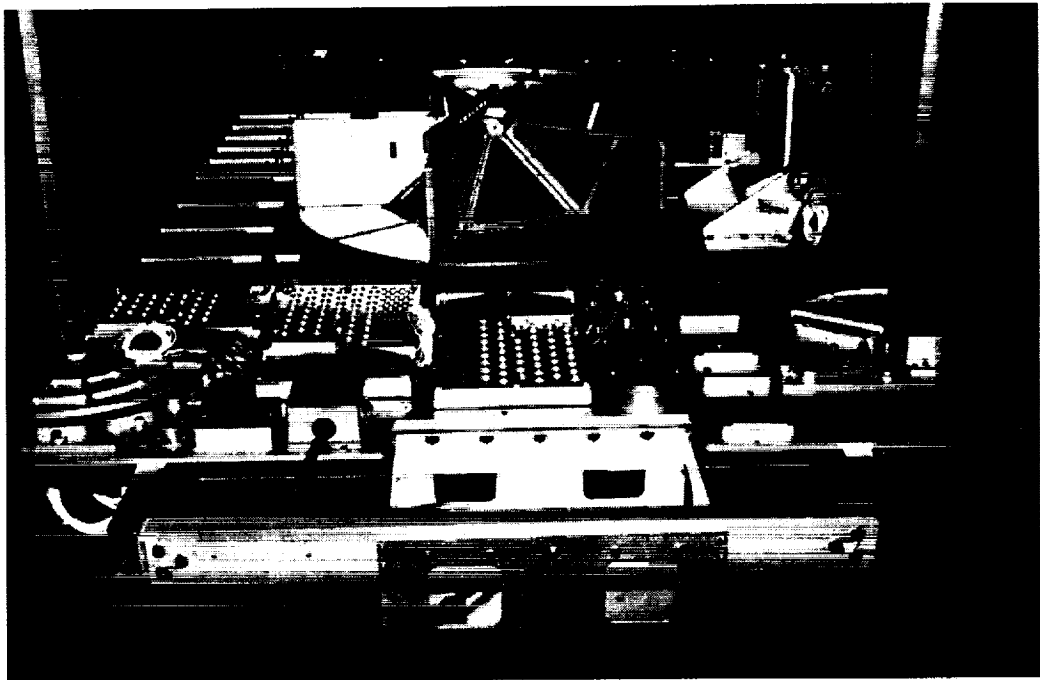
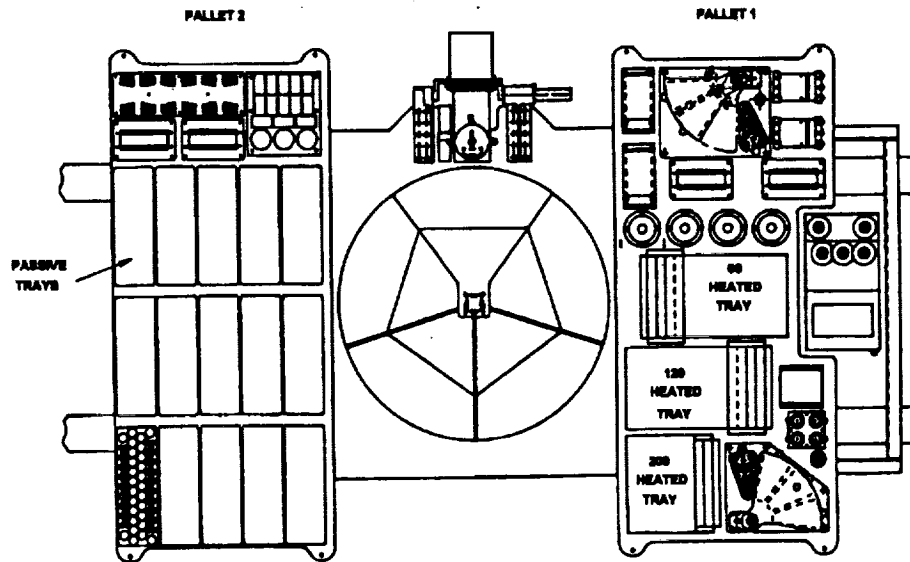


Fig. 1 EOIM-3 Pallet



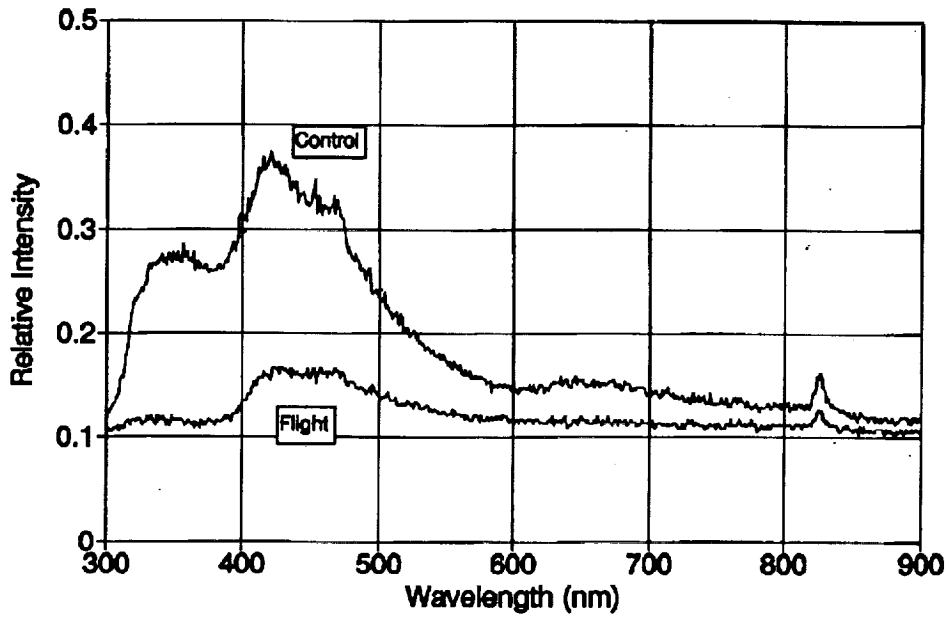


Fig. 2 A-276 Spectrofluorescence

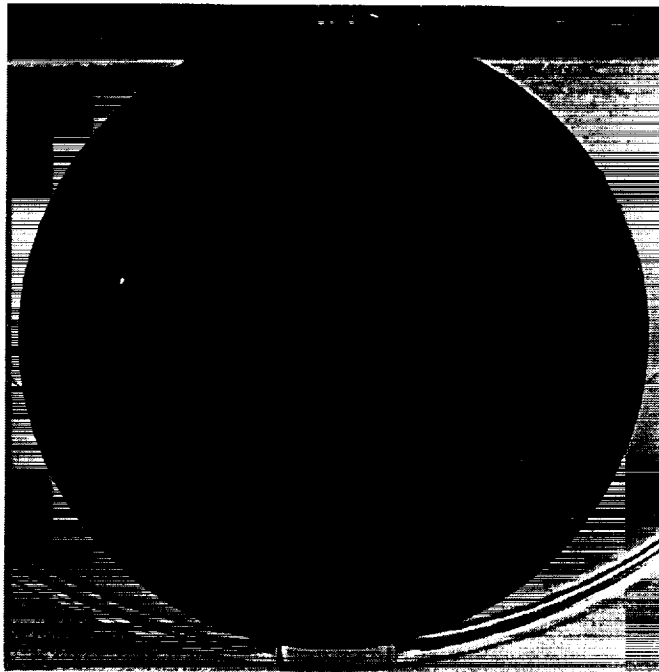


Fig. 3 IC5755-60C Paint

C-3

PRECEDING PAGE BLANK NOT FILMED

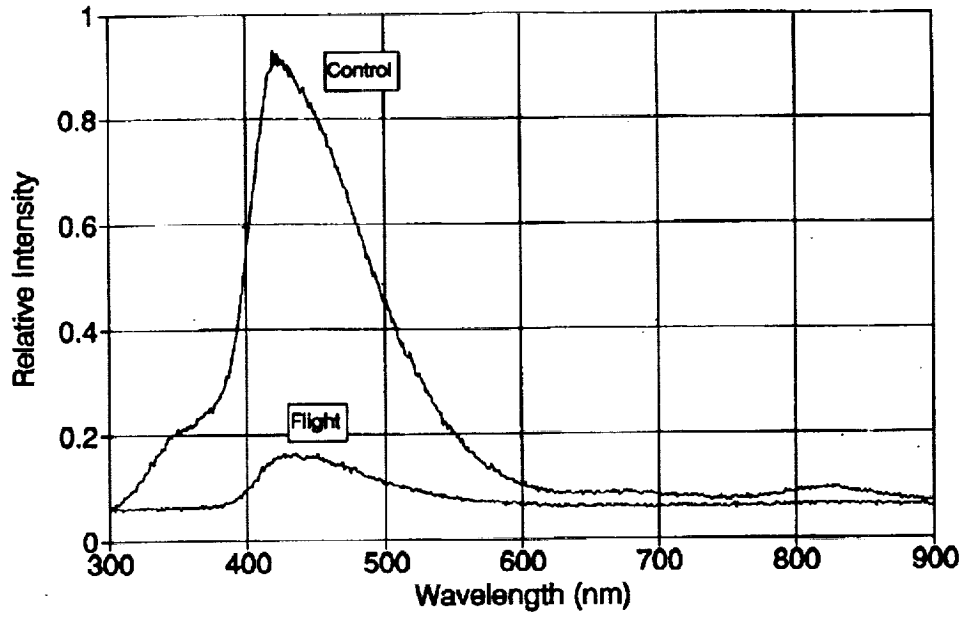


Fig. 4 K-3210 Spectrofluorescence

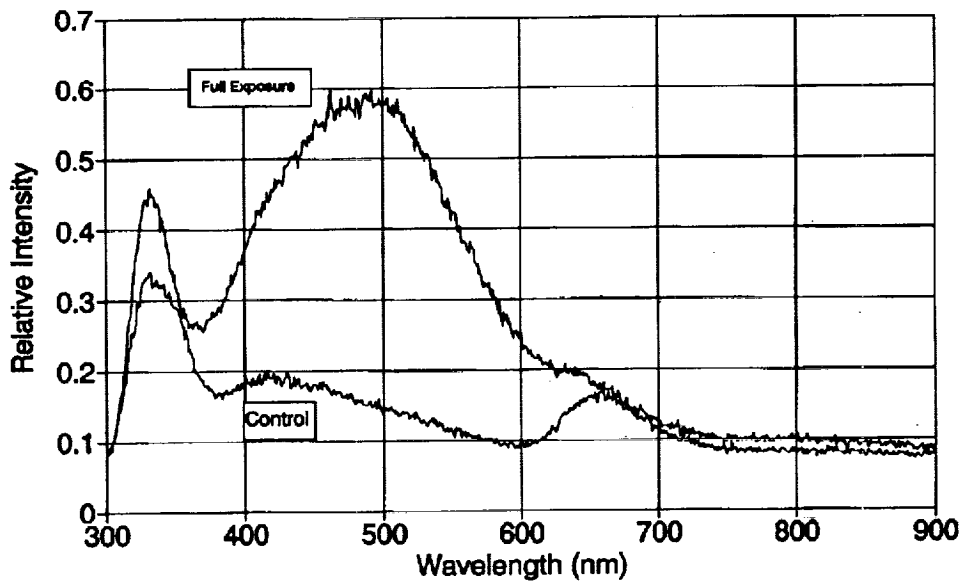


Fig. 5 Z-306 Spectrofluorescence

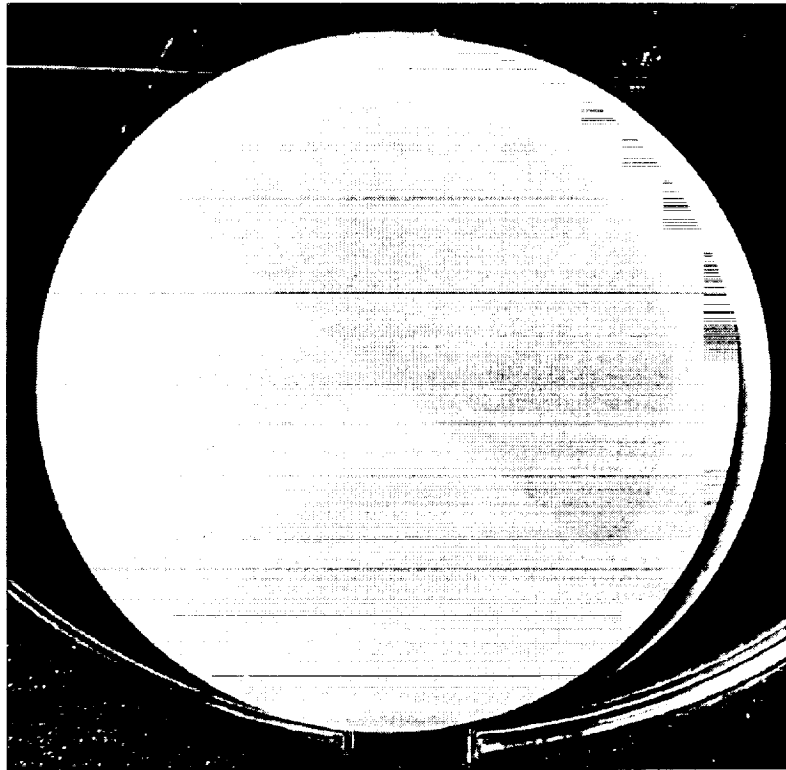


Fig. 6 Yellow organic dye chromic acid anodized aluminum

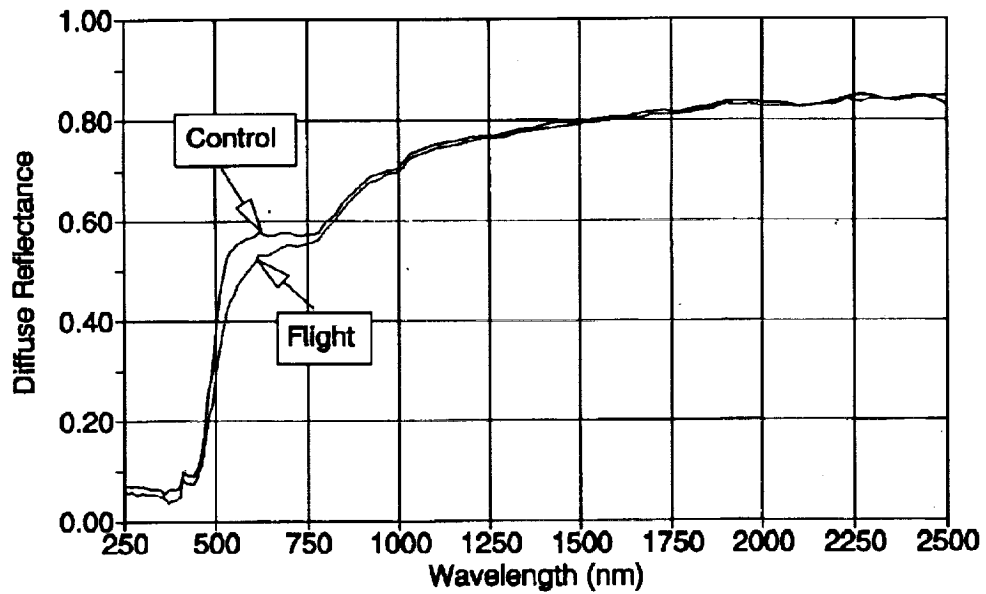


Fig. 7 Diffuse reflectance, control and flight
Yellow organic dye chromic acid anodized aluminum



**SOLID FILM LUBRICANTS AND THERMAL CONTROL COATINGS FLOWN ABOARD THE
EOIM-3 MDA SUB-EXPERIMENT**

Taylor J. Murphy*, Kaia E. David*, and Hank W. Babel**
McDonnell Douglas Aerospace
Huntington Beach, CA 92647
Phone: (714) 896-3311/Fax: (714) 896-5034

ABSTRACT

Additional experimental data were desired to support the selection of candidate thermal control coatings and solid film lubricants for the McDonnell Douglas Aerospace (MDA) Space Station hardware. The third Evaluation of Oxygen Interactions With Materials Mission (EOIM-3) flight experiment presented an opportunity to study the effects of the low Earth orbit environment on thermal control coatings and solid film lubricants. MDA provided five solid film lubricants and two anodic thermal control coatings for EOIM-3. The lubricant sample set consisted of three solid film lubricants with organic binders, one solid film lubricant with an inorganic binder, and one solid film lubricant with no binder. The anodize coating sample set consisted of undyed sulfuric acid anodize and cobalt sulfide dyed sulfuric acid anodize, each on two different substrate aluminum alloys. The organic and inorganic binders in the solid film lubricants experienced erosion, and the lubricating pigments experienced oxidation. MDA is continuing to assess the effect of exposure to the low Earth orbit environment on the life and friction properties of the lubricants. Results to date support the design practice of shielding solid film lubricants from the low Earth orbit environment. Post-flight optical property analysis of the anodized specimens indicated that there were limited contamination effects and some atomic oxygen and ultraviolet radiation effects. These effects appeared to be within the values predicted by simulated ground testing and analysis of these materials, and they were different for each coating and substrate.

INTRODUCTION

There exists a fair body of data on the effects of low Earth orbit (LEO) environment on general classes of materials and some simulated LEO environment tests on solid film lubricants and thermal control coatings, but there are little data in the literature on LEO exposure of dry film lubricants and no data for the anodic thermal control coating processes developed by MDA for the international Space Station. In the case of lubricants, the unknown parameter of LEO effects forces LEO-exposed hardware to be conservatively designed, incorporating protective shielding, assuming a higher friction value than the lubricant typically provides, and reducing the predicted service life of the hardware. Hardware with thermal control coatings are similarly affected by the lack of data on LEO effects. Designers must incorporate large uncertainties in the end of life (EOL) optical properties, which control the final temperature of the hardware. The end result of accommodating the unknown effects is consumption of space, power, and weight allocations, which are precious resources on spacecraft. Developing a better understanding of LEO effects

**Engineer/Scientist, Materials and Processes; Member, AIAA*

***Senior Manager, Materials and Processes*

on solid film lubricants and anodic thermal control coatings would result in the efficient consumption of these allocations.

LEO Effects on Solid Film Lubricants

Most solid film lubricants consist of an organic binder and a lubricating pigment, such as molybdenum disulfide (MoS_2). The only data available for use in predicting LEO environmental effects on solid film lubricants are (1) the observed effects of LEO environment on materials similar to the organic binder; and (2) the effects of a simulated LEO environment on sputtered MoS_2 .

Based on available data, LEO effects on organic binders are expected to be erosion due to the synergistic effects of AO and ultraviolet (UV) radiation. In general, organic materials that do not contain fluorine or silicone exhibit AO reaction efficiencies on the order of $2.5\text{--}3.0 \times 10^{-24} \text{ cm}^3/\text{atom AO}$.¹ AO flux for the Space Station is estimated to average $5 \times 10^{21} \text{ atoms/cm}^2\text{-yr}$, yielding erosion rates on the order of 0.013 to 0.015 cm/yr (0.0005 to 0.0006 in./yr) for organic materials oriented normal to the Space Station velocity vector. The applied thickness of most solid film lubricants is between 0.013 and 0.026 cm (0.005 and 0.010 in.).

The effects of AO on the MoS_2 pigments may be estimated using data from simulated LEO environment tests. It was found that sputtered MoS_2 exhibited the following effects when exposed to an AO fluence of $5 \times 10^{24} \text{ atoms/cm}^2$ with 1.5 eV energy:²

1. Creation of MoO_3 and MoO_2 , in estimated amounts of 45% and 15%, respectively, from the MoS_2 present at the surface.
2. Creation of a layer consisting of sulfides and oxides, approximately 90 Å thick, which inhibits adsorption of AO.
3. Creation of SO_2 , which degasses from the specimen.
4. Relatively high coefficients of friction (0.2), until the protective layer is worn off and a fresh MoS_2 surface is exposed (within 10 cycles).

Estimates of the effects of LEO environment on a solid film lubricant's performance based on the above information are rough at best. MDA's objectives in this experiment were (1) to determine the chemical and physical changes of several different types of solid film lubricants exposed to LEO and (2) to assess the effect of exposure on lubrication properties.

Anodic Thermal Control Coatings

As has been discussed in previous papers, anodic coatings were selected for the MDA Space Station aluminum hardware over organic based thermal control coatings because of their demonstrated resistance to LEO environmental effects.³ Sulfuric acid anodizing (SAA) was selected in part because of the ease of

controlling the optical properties during manufacture of large hardware.⁴ Some SAA thermal control coatings had been shown to exhibit minimal increases in solar absorptance (α_s) on exposure to ground-based UV radiation.⁵ Other SAA thermal control coatings exhibited severe degradation on exposure to simulated UV radiation.⁶ Low absorptance SAA thermal control coatings have been reported in the literature to degrade between 0.1 and 0.2 on UV exposure.⁶ In the mid-1960s, LaRC tested cobalt-sulfide dyed SAA coatings with very high absorptances. This coating showed excellent absorptance retention after UV exposure.⁷ Intermediate-absorptance coatings in the range of 0.4 to 0.7 have received little attention. These are the coatings planned for use on the Space Station program.

There are numerous factors that influence anodic coating optical property degradation in the LEO environment. Processing parameters such as the anodizing temperature, time, current density, electrolyte concentration, and sealing medium can affect degradation from UV radiation. Alloy, temper, and some processing parameters can affect the retention of dyes in the pore structure on exposure to AO. Coating thickness can affect the amount of cracking on exposure to thermal cycling and meteoroid and orbital debris impacts. Contamination that exists around a spacecraft can affect the optical properties of exposed surfaces, but has also been shown to affect some types of coatings more than others.⁴ This contamination can also contribute to an increase in absorptance because of the interaction with the natural environments.

New coating processes and variants are generally evaluated individually for AO and UV effects. However, to determine their acceptability for LEO, combined AO, UV, and contamination environmental testing for each variant is recommended. Flight testing is an important part of this evaluation. MDA flew two non-dyed (clear) SAA coatings and two cobalt sulfide (CoS) dyed (black) SAA coatings on the EOIM-3 mission as a part of a larger set of ground and flight tests in a program to verify the acceptability of these coatings for use on Space Station hardware.

SAMPLE DESCRIPTION

All MDA EOIM-3 samples were vacuum-baked prior to installation into sample carrier trays.

Lubricant Samples

Five different solid film lubricants were studied in this test. The sample set is described in Table 1. Three were MoS₂-type lubricants with phenolic, polyimide, and inorganic binders. One other consisted of niobium diselenide (NbSe₂) and a phenolic binder, and the last one utilized tungsten disulfide (WS₂) with no binder. Each lubricant was applied by the lubricant vendors on aluminum 6061-T6 substrates. During flight, some of the lubricant samples had a mesh screen placed over them, as noted in the table.

Anodic Samples

The anodic thermal control coating samples and pre-flight data are listed in Table 2. Aluminum sheet and plate material were cut into 0.875-in. diameter discs prior to anodizing. The anodizing for all the samples was performed in the Chemistry Laboratory pilot process line at the MDA Huntington Beach

Table 1. MDA Lubricant Sample Set

Lubricant	Lubricating pigment	Binder and cure	Sample size		
			Pass. tray	60°C tray	120°C tray
Lubricant 1	MoS ₂ and graphite (proprietary)	Phosphoric acid based (proprietary) Cure 204°C (400°F)	1 in. (S)	1 in.	1 in.
Lubricant 2	MoS ₂ /Sb ₂ O ₃	Polyimide Cure 0.5 hr at 149°C (300°F), then 1 hr at 302°C (575°F)			0.5 in. (S)
Lubricant 3	Niobium Diselenide (NbSe ₂)	Phenolic Air Dry Cure	1 in.	1 in.	1 in.
Lubricant 4	MoS ₂	Modified phenolic Cure 1 hr at 191°C (375°F)	1 in.	1 in.	1 in.
Lubricant 5	WS ₂	—	1 in. (S)	1 in.	1 in.

Note: The symbol (S) denotes samples flown with a mesh screen cover.

Table 2. Pre-Flight Optical Properties of the MDA Anodic Samples, 200°C Trays

Coating	Substrate	Coating thickness (mils)	Absorptance (Lambda-9)	Absorptance (MS-251)	Emittance (DB-100)
Clear SAA	2219-T851	0.6	0.47	0.49	0.86
Clear SAA	7075-T73	1.1	0.45	0.45	0.88
CoS Dyed SAA	6061-T6	1.0	0.79*	0.79	0.86
CoS Dyed SAA	7075-T73	0.5	0.84*	0.82	0.82

* Not measured—typical values shown

facility. The temperature-controlled 11-liter lead tank was used as the cathode. The anodizing procedure for the anodized samples is shown in Table 3.

TEST DESCRIPTION

The EOIM-3 Mission flew on the 31 July 1992 STS-46 flight, which orbited at an altitude of 230 km (124 nautical miles) and an inclination of 28.5 deg from the equator. The experiment was deployed on 6 August 1992 and was exposed for 42 hours. The exposure environment is described as follows:⁸

AO fluence = 2.3×10^{20} atom/cm² (annualized flux = 5×10^{22} atom/cm²-yr).

UV exposure = 25 equivalent sun hours.

Passive tray temperature = 10 to 50°C (50 to 120°F), with excursions to 80°C (176°F) prior to deployment.

MDA lubricant samples were located on the passive trays and on the 60°C (140°F) and 120°C (248°F) trays, as indicated in Table 1. All MDA anodic thermal control samples were located on 200°C (392°F) trays. After de-integration from the flight hardware, the samples were placed in individual nonmetallic sample holders.

Table 3. Anodizing Procedure

Anodizing parameters	Non-dyed sulfuric acid anodize	Cobalt sulfide dyed sulfuric acid anodize
Pre-treatment: Solvent wipe with 1,1,1-Trichloroethylene	Yes	Yes
Anodizing parameters: Bath concentration Bath temperature Current density Anodize time	150 g/l 30±2°C (86±4°F) 10 ASF 45±2 min	150 g/l 30±2°C (86±4°F) 16 ASF 60±2 min
Cobalt acetate (dye Step 1) parameters: Cobalt acetate concentration pH (acetic acid used to balance pH) Temperature Time	N/A*	200 g/l 6.0±0.1 45±3°C (110±5°F) 15 min
Ammonium sulfide (dye Step 2) parameters: Ammonium sulfide concentration Temperature Time	N/A*	30 g/l 24±3°C (75±5°F) 10 min
Hot water seal parameters: Temperature Immersion time	100°C (212°F) 20 min	95°C (205°F) 5 min

* N/A = Not applicable

Early results from analysis of other EOIM-3 specimens revealed the presence of a layer of silicone oxide approximately 20 Å thick on AO-stable materials.⁸ It is believed that the contamination was caused by outgassing of an unidentified material.

ANALYSIS

Lubricant Tests

Table 4 summarizes the analyses conducted on each lubricant sample. Scanning Electron Microscopy (SEM) studies at 50 to 5000× magnification were conducted on control and post-flight solid film lubricant samples using the International Scientific Instruments Model DS 130S Dual Stage SEM. Energy dispersion x-ray analysis (EDX) was performed on discrete portions of the samples to determine differences in inorganic materials on the unexposed and exposed surfaces. Fourier transform infrared spectroscopy (FTIR) analysis, using a Nicolet Magna 550 FTIR spectrometer and a Nic-Plan microscope, was conducted on selected specimens in an effort to gauge the amount of binder erosion experienced. This was accomplished by comparing the height of the carbon-hydrogen bands and the energy peaks of the binder materials on the unexposed and exposed areas of each sample. Electron Spectroscopy for Chemical Analysis (ESCA) was performed at the NASA-JSC White Sands Test Facility on selected samples using a Perkin-Elmer PHI 5600 ESCA/Auger instrument and calibrated using a set of copper, silver, and gold standards for binding energy and etching rates. Concentrations of compounds were determined using the peak areas of the elements in energy states of interest from high resolution spectra plots. Also using the Perkin-Elmer PHI 5600 instrument, a depth profile was obtained to determine the depth of the oxygen-

Table 4. Analyses Performed on Each Sample

Lubricant	Passive tray	60°C tray	120°C tray
1	SEM EDX FTIR ESCA	SEM EDX FTIR ESCA	SEM EDX FTIR ESCA
2	-	-	SEM EDX FTIR
3	SEM EDX FTIR	SEM EDX FTIR	SEM EDX FTIR
4	SEM EDX FTIR ESCA	SEM EDX FTIR ESCA	SEM EDX FTIR ESCA
5	SEM EDX	SEM EDX	SEM EDX

affected layer using argon gas ions accelerated to 4 keV and scanned on the surface. At discrete intervals, etching was suspended and an analysis of the surface was conducted. Etch rates were developed by comparing etch time with the time required to etch through a 1000 Å thick layer of Ta₂O₅ on tantalum foil. Because the etch rates of the lubricants could not be guaranteed to be similar to the Ta₂O₅ etch rates, etch depth is expressed as a factor of the etch depth on the lubricant control samples.

Anodic Coating Tests

The control, pre-flight, and post-flight anodic coating samples were measured for solar absorptance using the Gier-Dunkle Model MS251 Solar Reflectometer (referred to in this report as the MS251), and for infrared emittance using the Gier-Dunkle Model DB100 Infrared Reflectometer (referred to in this report as the DB100). The MS251 uses a xenon lamp with a 100-mm diameter integrating sphere and measures solar reflectance in a wavelength range of approximately 300 to 2000 nm. The DB100 uses a rotating heated cavity with a hard black anodize coating which can measure infrared reflectance from 5 to 14 μm.

The control, pre-flight, and post-flight clear SAA samples and the control and post-flight cobalt sulfide dyed SAA samples were also measured for solar absorptance using the Perkin-Elmer Lambda 9 spectrophotometer (referred to in this report as the Lambda 9). The Lambda 9 uses tungsten and deuterium lamps with a 150-mm diameter integrating sphere and measures solar reflectance in a wavelength range of 250 to 2500 nm. Data from the Lambda 9 are analyzed using a technique to account for wavelengths smaller than 250 nm and larger than 2500 nm. The final result is expected to yield values closer to the "true" solar reflectance than the MS251.

Surface morphology and chemistry of control and post-flight samples were studied using SEM and EDX similar to that used for the lubricant samples.

RESULTS

Results of Lubricant Specimens

Lubricant 1

Comparison of the SEM photographs of the exposed and unexposed surfaces of the passive tray sample (Figure 1) shows a “worm-eaten” preferential erosion of particular materials that is typical of the exposed material on all three tray samples. EDX analysis revealed no gross difference between materials in the eroded and non-eroded areas. EDX indicated that the eroded material was MoS₂, but because the EDX was conducted at a high power, the analysis may have detected the material lying underneath the eroded material. Erosion appears to be slightly more extensive in the passive tray sample than in the heated tray samples (Figure 1b and Figure 2).

There is a transition zone between the unexposed and the exposed areas on the two heated samples, which is evidenced by a light region on the SEM photographs. EDX analysis of these areas indicates a higher level of aluminum than in other areas, suggesting the lubricant had been rubbed off either by the sample carrier or by other means. Otherwise, there is little discernible difference between the three specimens.

FTIR plots of the exposed and unexposed areas of the samples were too noisy to determine any significant difference.

ESCA detected trace amounts (under 40 Å) of silicone and fluorine on the samples. ESCA detected MoO₃ only on the sample on the 120°C tray. The presence of MoO₃ on the other tray samples may have been masked by MoS₂ peaks, which are situated close to the MoO₃ peaks. On the surface of the 120°SDC sample, 30% to 50% of the molybdenum detected was in the form of MoO₃. Analysis of MoO₂ using this technique was inconclusive because the oxygen present in the binder masked the MoO₂ peaks. The depth of the oxygen-affected layer was estimated to be the depth at which the oxygen concentration remained

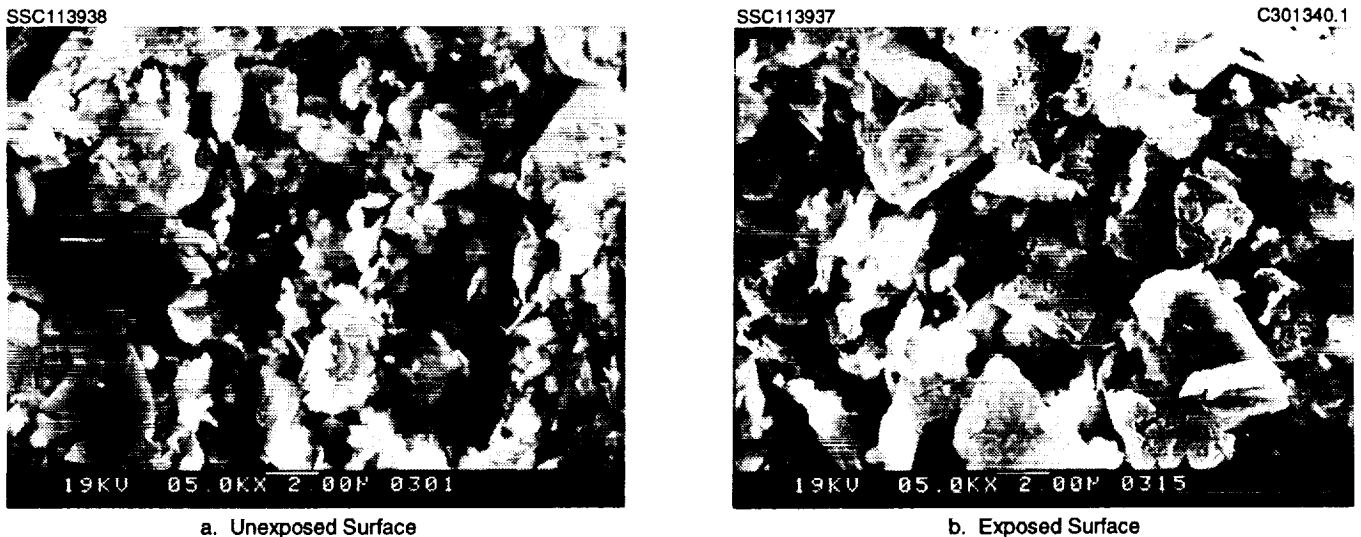


Figure 1. SEM photographs of lubricant 1 passive tray sample.



a. Exposed Surface on 60°C Tray



b. Exposed Surface on 120°C Tray

Figure 2. Lubricant 1 exposed surfaces on heated trays.

more than 50% of the difference between the maximum oxygen concentration and the background oxygen concentration. Table 5 contains the results of the depth analysis. The 120°C sample had the thickest oxygen layer.

Table 5. Oxygen-Affected Layer Thickness for Lubricant 1

Sample location	Depth of oxygen-affected layer*
Passive Tray	4.5–5.0
60°C Tray	6.8–7.5
120°C Tray	7.0–8.0

* Expressed as a multiple of control sample oxygen layer depth.

Lubricant 2

The only specimen of this lubricant was on the 120°C tray. The specimen had a screen installed over it. In the SEM photo (Figure 3), the exposed areas are distinctly lighter in shade than the unexposed areas. SEM photos also show a semitransparent material, presumably the polyimide binder, on the unexposed surfaces (Figure 4). The exposed samples appear to be missing this material. EDX analysis indicates no discernible difference in materials present in the unexposed and exposed areas.

FTIR analysis of the exposed and unexposed surfaces indicated no difference in binder concentration.

Lubricant 3

There is no discernible difference between the three tray samples in the SEM photographs. On all the samples, the exposed area is lighter than the unexposed area on all samples (Figure 5). There is a semi-transparent material, assumed to be the phenolic binder, on the unexposed surfaces. The exposed surfaces lack this material (Figure 6). EDX analysis shows very little difference between the materials in the exposed and unexposed areas, and very little difference between the samples themselves.

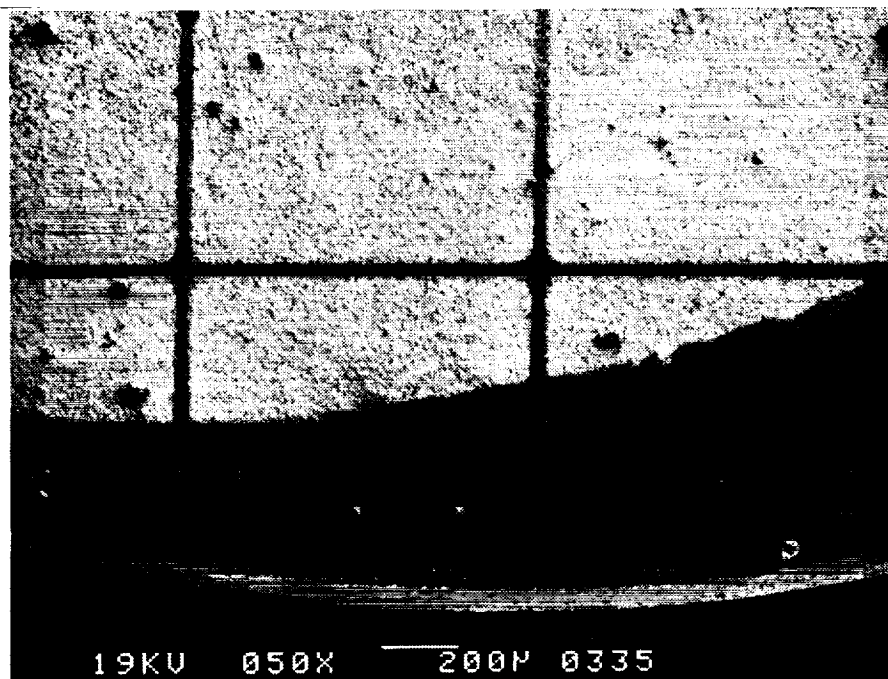
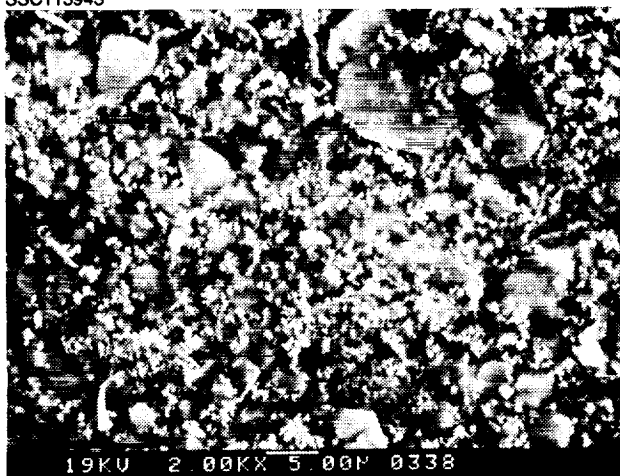
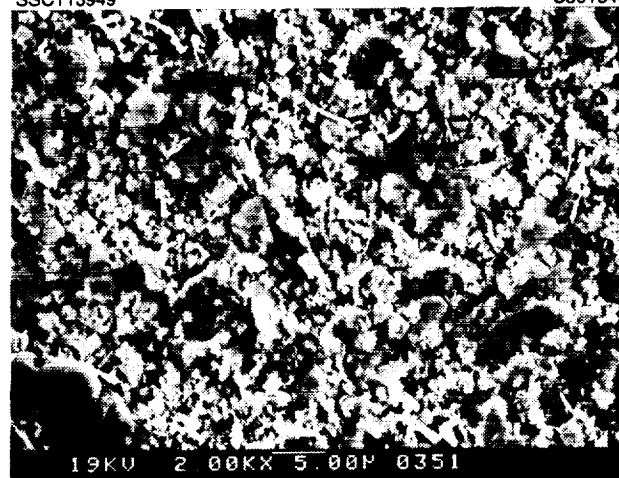


Figure 3. SEM photograph of unexposed, exposed surface of lubricant 2.



a. Unexposed Surface



b. Exposed Surface

Figure 4. SEM photograph of lubricant 2.

FTIR analysis of the surfaces of each specimen indicates no distinguishable binder on the exposed surface of the 120°C specimen, slight indication of binder on the exposed surface of the 60°C specimen, and a stronger indication on the exposed surface of the passive sample (Figure 7).

Lubricant 4

There is no discernible difference between the three specimens in the SEM photographs. The exposed area is lighter than the unexposed area on all samples. There is a semitransparent material, assumed to be the phenolic binder, on the unexposed surfaces (Figure 8a). The exposed areas appear to have some binder left (Figure 8b). The binder that is left does not exhibit the preferential erosion observed on the Lubricant 1 samples. Rather, the exposed binder appears receded, indicating a uniform erosion of material. EDX of

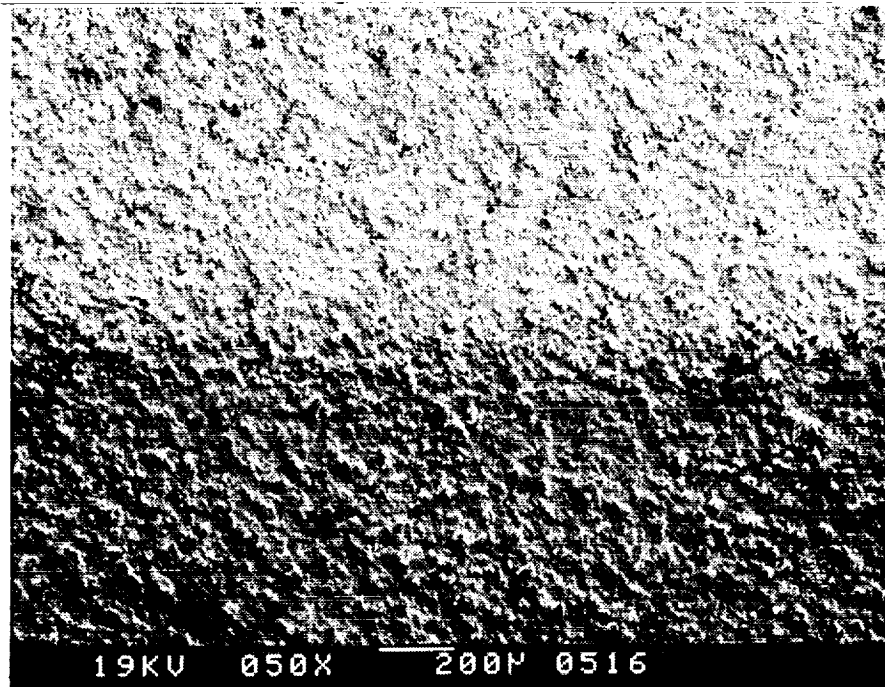
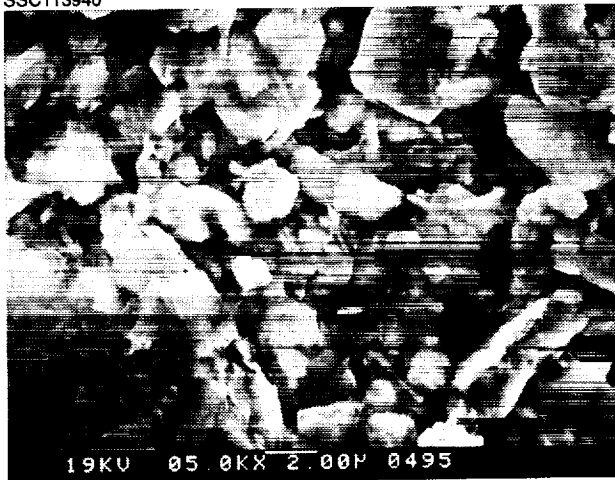
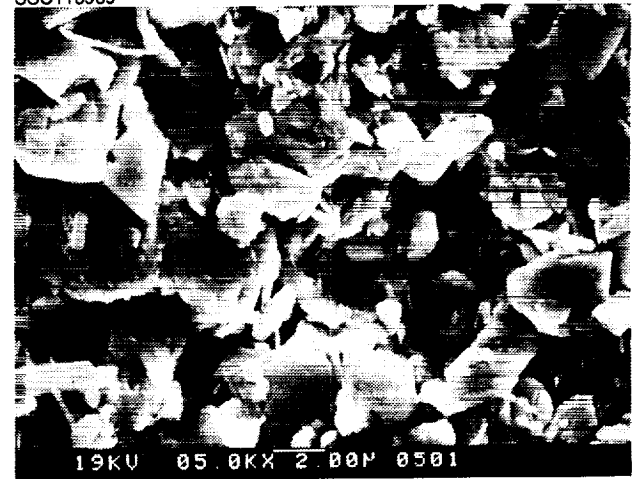


Figure 5. SEM photograph of transition from unexposed to exposed area on lubricant 3 60°C sample.



a. Unexposed Surface



b. Exposed Surface

Figure 6. SEM photographs of unexposed, exposed surfaces of lubricant 3 passive tray sample.

exposed and unexposed areas are virtually identical, and comparison of the three samples reveal no substantive difference. FTIR did not detect a significant difference in binder concentration from unexposed to exposed areas on the samples.

ESCA revealed trace amounts of silicone and fluorine on the samples. MoO_3 was detected on all three samples. Table 6 shows the estimated amounts of MoO_3 (as a percentage of the molybdenum detected) and the depth of the oxygen-affected layer. The highest concentration of MoO_3 was found on the passive sample, followed by the 60°C and 120°C samples, but the thickest oxygen layer was found on the 120°C sample.

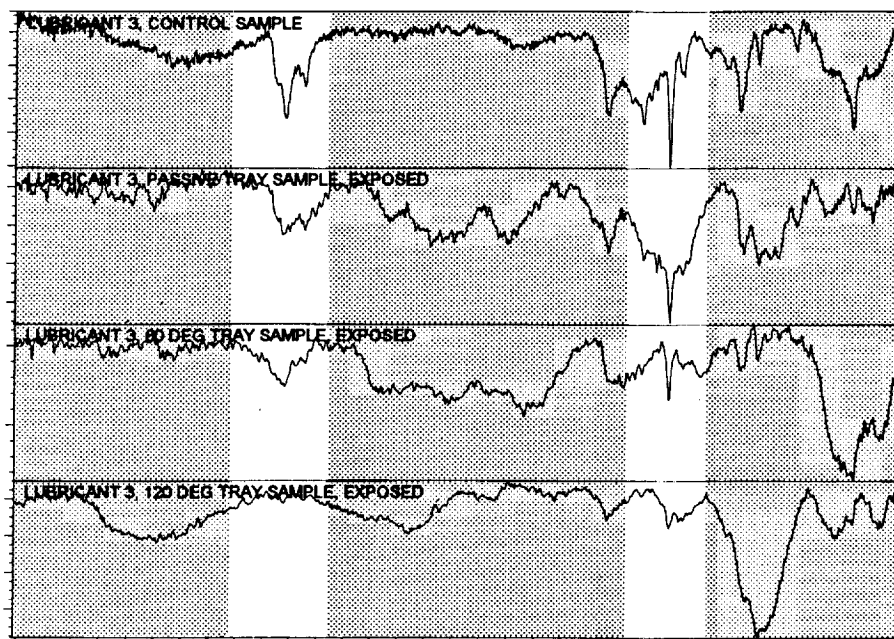
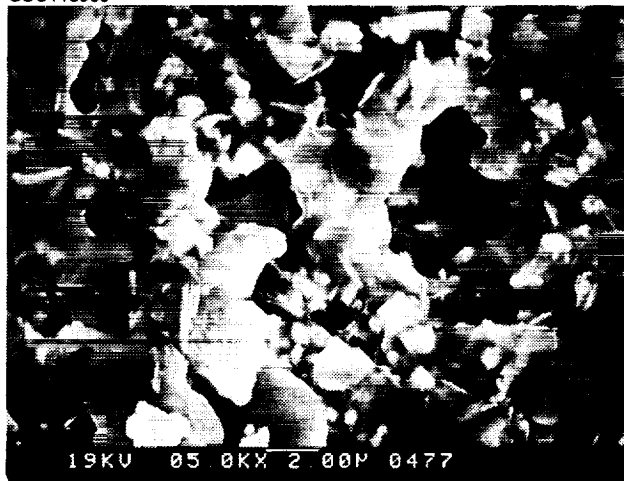


Figure 7. FTIR plots of lubricant 3 samples with phenolic peaks highlighted.

SSC113950



a. Unexposed Surface

SSC113951

C301347



b. Exposed Surface

Figure 8. SEM photographs of unexposed, exposed surfaces of lubricant 4 60°C tray sample.

Table 6. Oxygen Affected Layer Thickness for Lubricant 4

Sample location	Depth of oxygen-affected layer *	MoO ₃ /Mo (%)
Passive	5.0-7.0	56-76
60°C	4.8-7.4	38-58
120°C	5.6-8.6	30-50

* Expressed as a multiple of control sample oxygen layer depth.

Lubricant 5

There is little discernible difference between the unexposed and exposed areas of any of the samples in the SEM photographs. Each sample had bright, gray, and dark shaded regions on the SEM photographs (Figure 9). The gray areas fill in between thin, long, dark features. White features are randomly scattered. EDX analysis indicates that the bright and dark shades have high levels of aluminum, while the gray areas are high in tungsten and sulfur, leading to the conclusion that the gray areas are the air-impinged tungsten disulfide solid film lubricant. Stereo photographs indicate that the dark aluminum areas are physically lower than the lubricant.

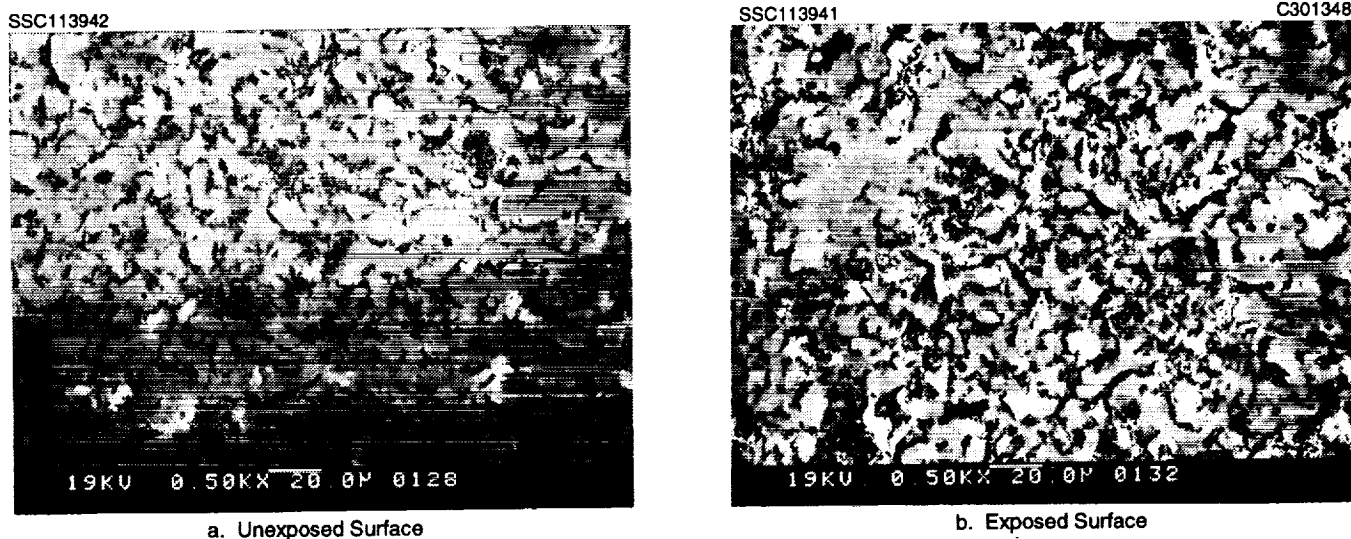


Figure 9. SEM photographs of unexposed, exposed surfaces of lubricant 4.

The passive sample had a screen placed over it. The shadow of the screen is barely visible (Figure 10). The 60°C specimen had the strongest shade contrast between the darker unexposed area and the lighter, exposed area. The areas are separated by a bright transition band (Figure 11). X-ray mapping of the transition indicates that neither an abundance nor a dearth of aluminum or tungsten is responsible for the transition.

Discussion of Lubricant Analyses

All the lubricants with binders experienced some form of erosion from exposure. The data did not indicate that temperature consistently influenced the amount of erosion experienced. SEM photographs revealed preferential erosion on discrete features on the inorganic binder lubricant, while the organic binder lubricants exhibited an even, recession-type erosion of the binder. The inorganic and organic binder lubricants had oxygen-affected layers of similar thickness. Surface MoO₃ concentrations on the inorganic and organic binder lubricants were similar to each other and to the concentrations detected on the simulated LEO-exposed sputtered MoS₂, even though the laboratory AO energy was lower and fluence higher than the EOIM-3 exposure (1.5 eV and 5×10^{24} atoms/cm² compared with 5 eV and 2×10^{20} atoms/cm², respectively).

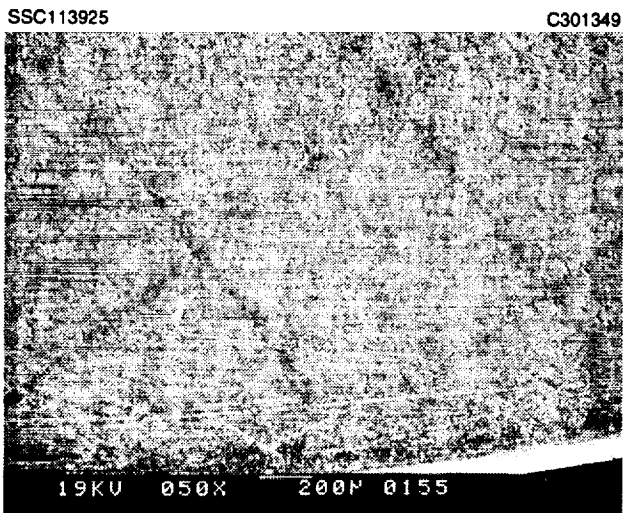


Figure 10. SEM photograph of lubricant with shadow from mesh screen.

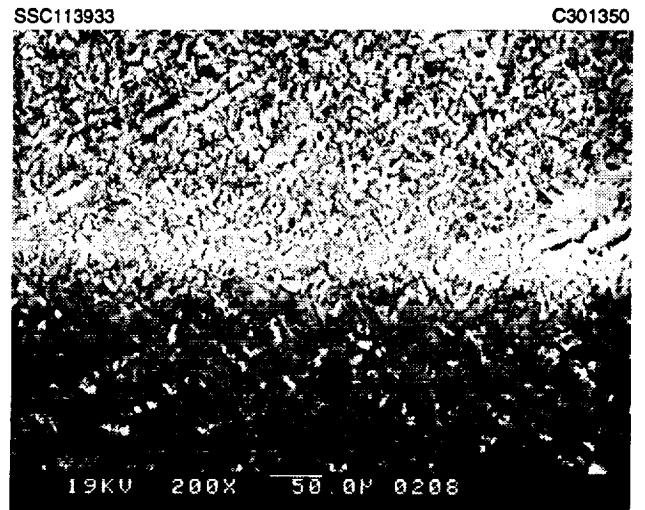


Figure 11. SEM photograph of transition from unexposed to exposed surfaces of lubricant 5.

Results of Anodic Coating Studies

The post-flight optical property results for the anodic coatings are shown in Table 7. After 42 hours of exposure in the LEO environment, the non-dyed SAA on 7075-T73 showed very little change in absorptance. The increase in absorptance of 0.01 is within the error of the measurement device. The increase in absorptance for the 2219-T851 sample ($\Delta\alpha = 0.03$), which is slightly more significant, can be attributed to UV degradation and contamination. UV degradation of anodic coatings is generally logarithmic with most of the degradation occurring in the first 200 hours.³ When the degradation is attributed solely to UV degradation, and a logarithmic degradation is assumed, the 30-year predicted degradation is below 0.10. This is well within the 30-year absorptance degradation of 0.20 that was predicted for this coating.³ The effect appeared to be confined to the wavelength range below 850 nm. Lambda 9 reflectance spectrums for the pre-flight and post-flight measurements are shown in Figure 12. The confinement of absorptance effects to this narrow wavelength range may be attributed to the presence of silicone, which was detected in a 4-keV beam energy EDX study of the 2219-T851 flight sample. In addition, the affected wavelength range includes wavelengths at which the incident energy from the sun has the highest potential to induce rupture of chemical bonds.⁹ It is not clear from the data available why the 2219 substrate degraded more than the 7075 substrate.

Table 7. Post-Flight Optical Property Changes

Coating	Substrate	$\Delta\alpha$	$\Delta\epsilon$
Clear SAA	2219-T851	0.03 ^a	0.00
Clear SAA	7075-T73	0.01 ^a	0.00
CoS Dyed SAA	6061-T6	-0.20 ^b	0.00
CoS Dyed SAA	7075-T73	0.08 ^b	0.00

Notes: Emittances measured using the Gier-Dunkle DB100. Differences in absorptance or emittance of less than 0.02 are not considered significant.

a. Absorptances measured using the Lambda 9.

b. Absorptances measured using the MS251.

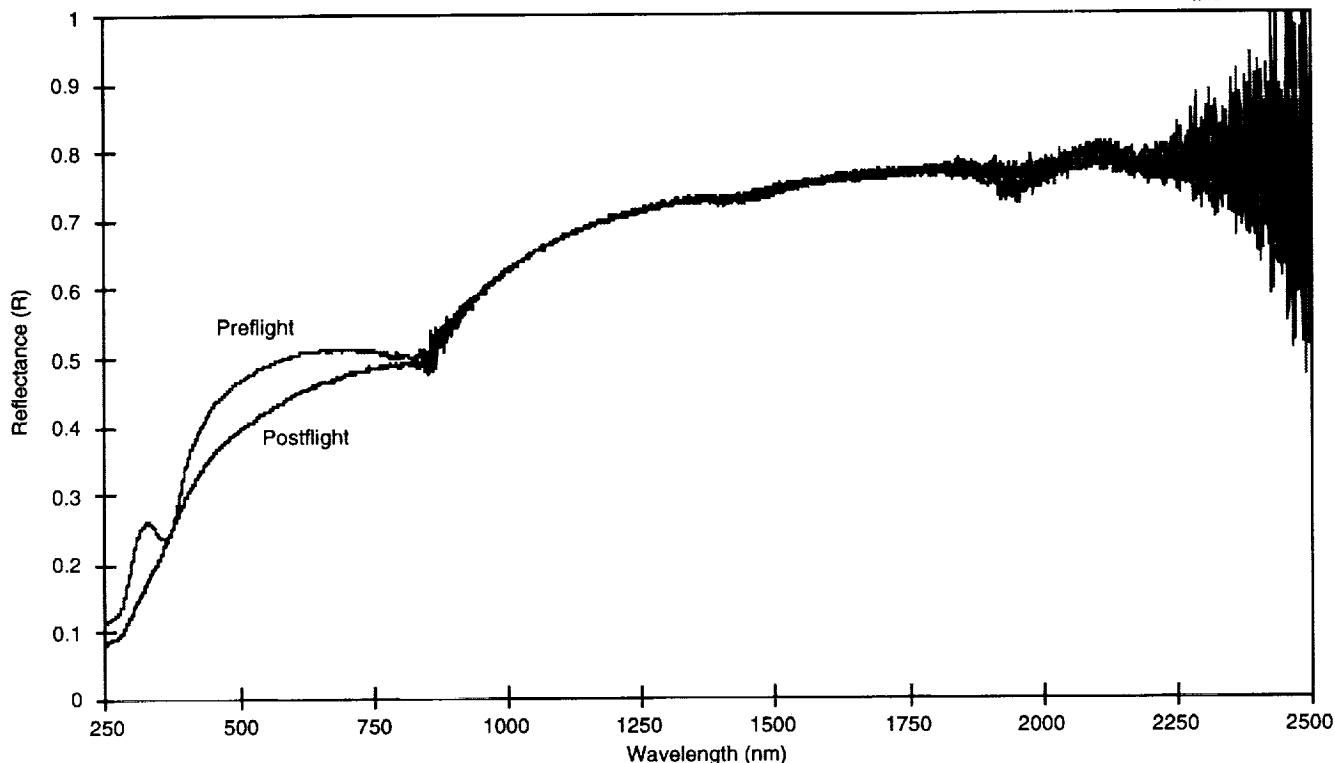


Figure 12. Pre- and postflight solar reflectance spectra for non-dyed sulfuric acid anodized 2219-T851 aluminum.

Because of the lack of available manufacturing facilities with production cobalt sulfide dye capability, environmental compliance issues, and concerns about optical property consistency, the cobalt sulfide dyed SAA process is no longer baselined for MDA Space Station hardware. However, EOIM-3 data are useful in evaluating cobalt sulfide as a potential backup coating.

Both the black cobalt-sulfide dyed SAA samples showed changes in absorptance. The cobalt-sulfide dyed SAA on 6061-T6 aluminum appeared to fade dramatically, and the absorptance was reduced by about 0.20. This effect is attributed to AO removal of the dye, which was confirmed when ground asher AO exposures of the EOIM-3 ground control samples at MDA exhibited similar fading. The results of the asher test are shown in Table 8. The asher was run at a vacuum of 2 torr and a power of 100 W and reached a maximum temperature of 57°C (135°F) during the run. The total fluence of the test was approximately 2.8×10^{21} atoms/cm², as calculated using Kapton HN polyimide standards. The test exposure was nearly ten times that experienced by EOIM-3 samples.

The results of ground AO exposure of the CoS dyed 6061-T6 are similar to those observed on orbit. The similarity suggests that the temperature of the sample and the velocity and directionality of the AO did not influence the removal rates. The bleaching effect on the 6061-T6 substrate observed on both ground exposed and flight exposed samples may be attributable to AO removal of the dye and is unexpected because the dye is inorganic. Because the CoS dyed 6061-T6 was a recent alloy addition to the Space Station program, CoS dyed 6061-T6 was not subjected to AO testing at MDA prior to the EOIM-3 flight. However, other alloys with CoS dye were not similarly affected by AO testing. A possible pH imbalance in the first dye bath during processing of the flight 6061-T6 samples may have contributed to the bleaching. Testing of additional samples is necessary to confirm AO bleaching of the cobalt sulfide dye on the 6061-T6 substrate.

The cobalt-sulfide dyed SAA on 7075-T73 aluminum did not fade during flight exposure, but acquired a slight yellowish sheen, which was not observed on the ground AO sample. The absorptance increased by 0.08. The yellowish sheen on the 7075-T73 sample and the increase in absorptance may have been caused by contamination. This explanation is supported by the ground AO sample exhibiting an increase of only 0.03. The contamination appeared to have a greater effect on cobalt sulfide dyed SAA on 7075-T73 than it had on the non-dyed SAA on 2219-T851 or 7075-T73.

SUMMARY

Analysis of solid film lubricants exposed to LEO on EOIM-3 revealed effects similar to those observed in laboratory simulated environment tests on sputtered MoS₂. On organic binder lubricants, the binders were eroded evenly, while on inorganic binder lubricants, preferential attack was evident. The unbonded lubricant did not exhibit erosion per se, but SEM photographs show the exposed surfaces to be lighter in shade, much like the exposed surfaces on the other lubricants. MoO₃ was detected on the inorganic and organic binder lubricants analyzed by ESCA. Concentrations were of the same magnitude of those detected on sputtered MoS₂ specimens exposed to simulated AO.

The non-dyed sulfuric acid anodic coatings flown on the MDA EOIM-3 sub-experiment behaved as expected when exposed to the LEO environment. Degradation did not occur with SAA on the 7075-T73 substrate. With the 2219-T851 substrate, minimal increases in absorptance were found. The environmental resistance of the cobalt sulfide dyed sulfuric acid anodic coatings may be dependent on the dye process or the substrate. CoS-dyed SAA on 6061-T6 was severely bleached by AO, while CoS-dyed SAA on 7075-T73 was not bleached by AO exposure, but it experienced a significant increase in absorptance. On 7075-T73, the black CoS-dyed SAA coating appeared to be more susceptible to absorptance increases due to contamination than the non-dyed SAA coating. EOIM-3 data indicate that CoS dyed SAA may not be stable in LEO and would not be suitable for applications where stable optical properties are required. It is no longer viewed as a backup high absorptance anodize coating. Non-dyed sulfuric acid anodize, as produced for MDA Space Station hardware, appears to be resistant to the low Earth orbit environment.

Opportunities to test the effects of LEO exposure on the tribological properties of solid film lubricants are being pursued. The clear SAA process will be tested for LEO effects on the other aluminum alloys being used on Space Station; the baseline high-absorptance anodize coating is also being tested for LEO effects.

ACKNOWLEDGMENTS

The authors wish to thank Huong Le, Vic Kerlins, Alan Babrocky, Charles Smith, and Carl Oda, of MDA-Huntington Beach, for their assistance in the measurement and interpretation of the data. Dr. Steve Hornung of NASA White Sands Test Facility provided superior support in the analysis of the lubricant samples.

REFERENCES

1. L.J. Leger, J.T. Visentine, and J.A. Schlieseng, "A Consideration of Atomic Oxygen Interaction with Space Station." AIAA Paper 85-0476, AIAA 23rd Aerospace Sciences Meeting, Reno, Nevada, 14–17 January 1985.
2. J.A. Martin, et al., "MoS₂ Interactions with 1.5 eV Atomic Oxygen." Materials Research Society, 1988 Fall Meeting, Boston, Massachusetts, 28 November–3 December 1988, Los Alamos National Laboratory document LA-UR-88-1977.
3. K.E. David and H.W. Babel, "Optical Property Degradation of Anodic Coatings in the Space Station Low Earth Orbit." Presented at the AIAA Materials Specialist Conference, Dallas, Texas, 16–17 April 1992.
4. C.A. Jones, et al., "Environmental Effects on Passive Thermal Control Materials on the Space Station Freedom." Presented at the 44th Congress of the International Astronautical Federation, Graz, Austria, 16–22 October 1993.
5. D. Duffy, Engineering Trade Study Report on Durable/Long-Life Radiator Coatings, for NASA Lyndon B. Johnson Space Center, NAS9-17530, November 1987.
6. J.H. Weaver, "Effects of Vacuum-Ultraviolet Environment on Optical Properties of Bright Anodized Temperature Control Coatings." Air Force Materials Laboratory Technical Report, AFML-TR-67-421, May 1968.
7. W.R. Wade and D.J. Progar, "Effects of a Simulated Space Environment on Thermal Radiation Characteristics of Selected Black Coatings." NASA Technical Note, TN D-4116, September 1967.
8. D.E. Brinza, "Early Results From the JPL Experiments on the Evaluation of Oxygen Interactions with Materials (EOIM-3) Experiment Aboard STS-46." Presented at the EOIM-3 BMDO Flight Experiment Workshop, 22 June 1993.
9. S. Wernick, et al., *The Surface Treatment and Finishing of Aluminum and Its Alloys*—5th ed. Vol 2, 1987 (Finishing Publications Ltd: Teddington, Middlesex, England).

Evaluation of Space Environmental Effects on Metals and Optical Thin Films on EOIM-3

Jason A. Vaughn, Roger C. Linton, Miria M. Finckenor,
and Rachel R. Kamenetzky

EH15 Space Environmental Effects Branch
George C. Marshall Space Flight Center
Marshall Space Flight Center, AL 35812

ABSTRACT

Metals and optical thin films exposed to the space environment on the Third Flight of the Evaluation of Oxygen Interactions with Materials (EOIM-3) payload, onboard Space Shuttle mission STS-46 were evaluated. The materials effects described in this paper include the effects of space exposure on various pure metals, optical thin films, and optical thin film metals. The changes induced by exposure to the space environment in the material properties were evaluated using BRDF, specular reflectance (250 nm to 2500 nm), ESCA, VUV reflectance (120 nm to 200 nm), ellipsometry, FTIR and optical properties. Using these analysis techniques gold optically thin film metal mirrors with nickel undercoats were observed to darken due to nickel diffusion through the gold to the surface. Also, thin film nickel mirrors formed nickel oxide due to exposure to both the atmosphere and space.

INTRODUCTION

The harsh environment in low Earth orbit (LEO) affected the optical and mechanical properties of many of the spacecraft materials flown on the Long Duration Exposure Facility (LDEF),^{1,2} returned in 1990 after 69 months of space exposure. Ground simulators are being developed to simulate various aspects of the space environment to evaluate candidate materials. Because it is difficult to combine some of the environments to study synergistic effects on materials, it is always beneficial to expose materials to the space environment to understand short-comings of ground simulators and verify that these simulators correctly reproduce effects caused by actual space exposure.

Various pure metals, optical thin films, and optically thin film metals were exposed to the space environment as part of the Evaluation of Oxygen Interaction with Materials Experiment, third flight, (EOIM-3) on board the STS -46 shuttle flight. The STS-46 shuttle flight started July 31, 1992 and concluded Aug. 8, 1992. It included the electrodynamic testing of the Tether Satellite System (TSS-1), the deployment of the European Retrieval Carrier (EURECA), and the exposure of the EOIM-3 payload to the Space Shuttle velocity vector. The EOIM-3 experiment pallet carried numerous material samples and fixtures into space and exposed them to the space environment for a total of 42 hrs in the velocity vector. The space shuttle flew at an altitude of 197 km (123 nautical miles) near the end of STS-46

mission exposing the EOIM-3 experiment to a directed atomic oxygen fluence of 2.2×10^{20} atoms/cm² with a total of 7.6 equivalent sun hours (ESH) of synergistic near and far ultraviolet radiation. During those 42 hours the EOIM-3 experiment received the majority of its atomic oxygen exposure. However, a small amount of atomic oxygen exposure was received during the deployment and release of the EURECA.

EOIM-3 also received simultaneous exposure to solar ultraviolet radiation, thermal cycling, particulate radiation, and micrometeoroid/space debris impacts. EOIM-3 received 30.6 equivalent sun hours (ESH) during the STS-46 mission with 7.6 ESH exposure simultaneous with direct atomic oxygen impingement. Due to the short duration and orbit of the STS-46 mission the particulate radiation dose was negligible. During the STS-46 mission the EOIM-3 pallet experienced about 120 sun to shadow cycles which include those cycles during EURECA and TSS deployment. Molecular contamination due to thermal cycling was minimized by vacuum baking all materials for 24 hours prior to flight. Post-flight analysis did not reveal any detectable evidence of micrometeoroid/space debris hits greater than 0.25 mm diameter.

EOIM-3 DESCRIPTION AND ANALYSIS PROCEDURE

The EOIM-3 experiment tray, shown in Fig.1, consisted of fifteen passive trays, three trays heated to 60°C, 120°C and 200 °C, respectively, and various active experiments. Marshall Space Flight Center supplied to the EOIM-3 experiment three passive trays which contained a total of 138 samples, several individual samples to be integrated into the heated trays, and three active experiments. The optical thin films and optical thin film metals were found primarily on the passive trays. The pure metals (bulk sheet stock or shim stock) and

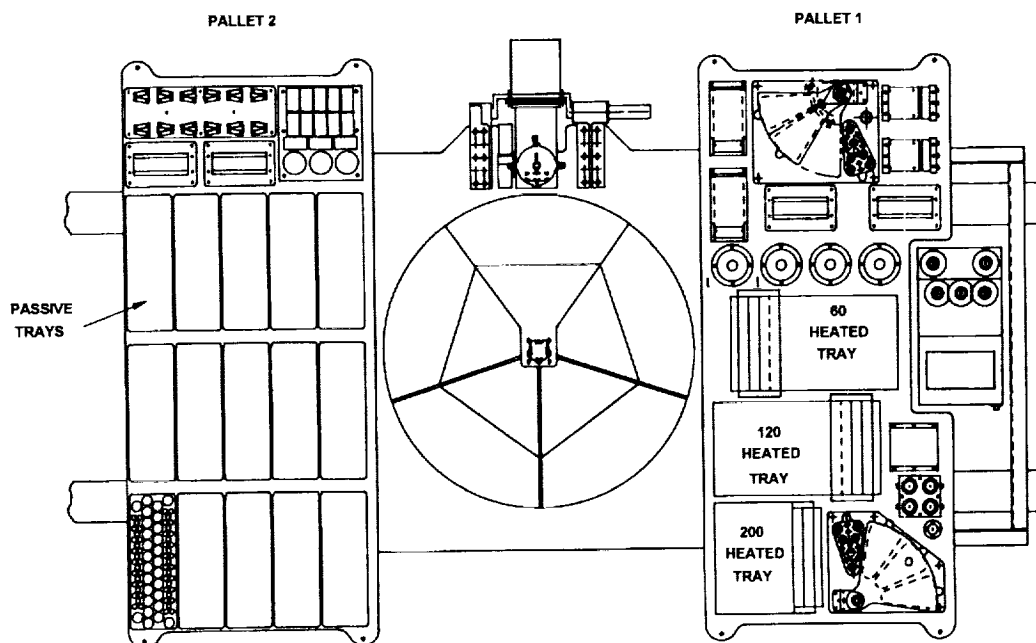


Fig. 1 Schematic of EOIM-3 Experiment

some metallic thin films presented in this paper were flown on the heated trays. The active experiments, the thermal control coatings, and polymer materials that MSFC provided on the EOIM-3 experiment are presented in detail in other papers found in these proceedings.

Most of the samples provided by MSFC for integration on the heated and passive trays were nominally 2.54 cm dia., except for the pure metals which were 1.27 cm dia. The optical thin film metals and the optical thin films found on both the heated and passive trays were covered with a half moon aluminum cover. This provided a control surface that was exposed to both the same thermal and vacuum environments as the exposed portion of the samples. The samples were weighed and optically pre-characterized prior to flight.

Following EOIM-3 de-integration from the orbiter, the samples were kept in desiccators until optical property and mass data could be measured. Optical property data were measured at MSFC using an AZ Technology laboratory portable spectroreflectometer (LPSR) and a Gier-Dunkle DB100 emissometer, and the mass properties were measured using a Mettler AT250 balance. Both the optical thin film metals and the optical thin films were examined using a TMA Quickscan scatterometer to calculate the Bi-directional Reflectance Distribution Function (BRDF) for both the unexposed and exposed region of each sample. Using this function the RMS roughness changes could be examined. To complete the reflectance analysis of the samples, spectral vacuum ultraviolet (VUV) reflectance measurements (120 nm to 200 nm) were made. After completing the series of reflectance measurements, numerous other more destructive analysis techniques were used, including surface analysis by laser ionization (SALI), proton induced x-ray emission spectroscopy (PIXE), rutherford backscatter spectroscopy (RBS), fourier transform infrared reflectance spectroscopy (FTIR), and electron spectroscopy for chemical analysis (ESCA).

PURE METALS

Numerous 99.9999% pure metals were flown on both the 60°C and 120° C heated trays. Included in these pure metals were copper, gold, nickel, niobium, silver, tantalum, tungsten, and vanadium. Silver and tungsten were also flown on the 200 ° C tray. Also included on EOIM-3 were two aluminum/lithium alloys: 2090 Al/Li and Weldalite®. All the pure metals had an exposed area of 0.71 cm². The aluminum/lithium alloys were 2.54 cm dia. samples, but the 2090 alloy was half covered while the Weldalite sample was covered with a "D" ring. A "D" ring was a 2.54 cm dia cover with a small straight edge at one edge of the sample. The goal of the "D" ring was to provide a step edge for monitoring the presence of oxide growth or perhaps erosion due to atomic oxygen with maximized exposure area.

Table I lists the results of both changes in mass and optical properties for all the pure metals flown by MSFC on EOIM-3, following exposure to the space environment. The two metals expected to be most affected by the space environment were copper and silver since both have a history of atomic oxygen effects from LDEF^{1,2} and earlier EOIM flights³. Both the copper and the silver demonstrated the largest changes in solar absorptance (α) of the pure metals which was attributed to oxidation. However, it appears that the short exposure received by EOIM-3 did not produce an oxide layer thick enough on the copper sample to be

Table I Pure Metals Mass Loss and Optical Property Summary

Sample Material	Δm (mg) (± 0.02)	$\Delta m/A$ (mg/cm ²) (± 0.03)	α_i (± 0.01)	α_r (± 0.01)	ϵ_i (± 0.01)	ϵ_r (± 0.01)
Copper						
60°C Tray	-0.03	- 0.042	0.49	0.56	0.01	0.03
120°C Tray	-0.07	- 0.098	0.47	0.52	0.02	0.03
Gold						
120°C Tray	+0.01	+ 0.014	0.19	0.18	0.02	0.02
Nickel						
60°C Tray	-0.05	- 0.071	0.33	0.34	0.02	0.02
120°C Tray	-0.05	- 0.071	0.33	0.31	0.02	0.02
Niobium						
60°C Tray	-0.05	- 0.071	0.33	0.34	0.03	0.03
120°C Tray	-0.03	- 0.042	0.33	0.34	0.03	0.03
Silver						
120°C Tray	+0.23	+ 0.323	0.11	0.80	0.01	0.46
Tantalum						
60°C Tray	-0.05	- 0.071	0.38	0.39	0.03	0.02
120°C Tray	-0.01	- 0.014	0.38	0.37	0.03	0.02
Tungsten						
60°C Tray	-0.15	- 0.210	0.46	0.48	0.02	0.02
120°C Tray	-0.02	- 0.028	0.46	0.46	0.02	0.02
200°C Tray	-0.04	- 0.051	0.46	0.55	0.02	0.01
Vanadium						
60°C Tray	-0.42	- 0.589	0.68	0.70	0.06	0.05
120°C Tray (pre-ox.)	-0.04	- 0.051	0.64	0.66	0.06	0.06
Al/Lithium						
60°C Tray	-0.51	- 0.155	0.15	0.14	0.05	0.05
120°C Tray	-0.53	- 0.162	0.15	0.14	0.05	0.05
Weldalite						
Passive	-0.15	- 0.090	0.13	0.15	0.05	0.05
Trays	-0.17	- 0.102	0.13	0.13	0.06	0.05

detected by either mass changes or infrared emittance changes or the oxide layer was lost due to flaking. The pure silver sample on the 120 °C heated tray developed a dark black silver oxide layer which is represented in the mass gain and large change in emittance (ϵ). All other pure metal samples seemed to change uniformly in reflectance proportional to the change in solar absorptance over the entire wavelength range measured.

Two vanadium samples were flown. One was pre-oxidized prior to flight and the other was cleaned of any oxidation layer. The pre-oxidized vanadium sample had a blue tint prior to flight and the other a yellow/gold tint. Upon retrieval neither sample changed much in appearance, as indicated by the solar absorptance data, but the sample which was not pre-oxidized saw a large decrease in mass. Because the sample decreased in mass and did not demonstrate any change in emittance, it is unlikely that an oxide layer was produced. The decrease in mass is most likely a result of out gassing or water desorption from the surface, but more tests are planned to understand this result.

Two different types of aluminum-lithium materials were flown on EOIM-3 by MSFC: a 2090 aluminum-lithium alloy and Weldalite®. The 2090 Al/Li alloy samples were flown on the 60 °C and 120 °C trays, while the Weldalite samples were flown on the passive trays. Both aluminum-lithium alloys lost significant amounts of mass. The 2090 alloy samples which were flown at elevated temperature lost the most weight. The loss in weight with these materials is most likely attributed to lithium loss from the samples caused by atomic oxygen exposure. The amount of lithium lost seems to be a function of temperature. More tests are underway to examine the effects of atomic oxygen exposure on these materials.

OPTICAL THIN FILM METALS

Several optical thin film metals were flown on EOIM-3 by MSFC. Included were gold, iridium, platinum, and nickel thin films, 750 Å thick with a 100 Å chrome undercoat which were flown on the passive trays. Also, samples of these same thin films 250 Å thick with a chrome undercoat and without a chrome undercoat were flown, but they are still under investigation and will not be presented in this paper. Other gold thin film mirrors ($\approx 1000\text{Å}$) with nickel undercoat were flown on all three of the heated trays. All thin film samples flown on both the passive and heated trays were half exposed during flight, providing a control surface to compare to both exposed and pre-flight measurements.

Table II Optical Property Summary for Metallic Thin Films

Sample	α_c	α_o	ϵ_c	ϵ_o
Gold				
Passive Tray	0.20	0.21	0.07	0.07
60 °C	0.17	0.17	0.03	0.03
120 °C	0.17	0.17	0.06	0.06
200 °C	0.18	0.23	0.05	0.04
Platinum				
Passive Tray	0.24	0.25	0.06	0.07
Iridium				
Passive Tray	0.24	0.25	0.11	0.12
Nickel				
Passive Tray	0.31	0.31	0.05	0.08

Table II is a summary of the optical properties data, solar absorptance (α) and infrared emittance (ϵ), measured for the four different thin film metals. The measurements made in the control region of the sample are indicated with subscript "c" and the measurements made in the exposed region are indicated with an "e". Two interesting observations made from the optical property data were the increase in solar absorptance of the gold sample, which was flown on the 200°C tray, and a small increase in the nickel sample in emittance. The change in emittance on the nickel sample could be within the resolution of the instrument; however, data will be presented later that confirm the presence of a thin oxide layer.

The gold sample from the 200 °C tray was visibly dark in the exposed region. Figure 2 is a comparison of the diffuse reflectance curves taken by the LPSR showing the 200 °C gold sample to have a much higher solar absorptance. Two different theories are possible to explain the unexpected darkening: 1) Diffusion or migration through micropores of the nickel substrate through the gold activated by the heat and atomic oxygen or 2) Contamination from a foreign source. FTIR and SALI measurements were made on both the exposed and unexposed regions of this sample. FTIR and SALI results from this sample indicated only trace amounts of hydrocarbons or surface contaminants on either the exposed or unexposed portions of the sample, which was later confirmed by ESCA analysis. SALI measurements did indicate nickel oxide present on the surface of the sample in the exposed region and only trace amounts of nickel in the unexposed. This result indicates the nickel diffused or migrated through the gold during space exposure due to the elevated temperature of the samples. RBS measurements on the gold thin film flown on the 120 °C tray indicated trace amounts of nickel in the bulk and on the surface. Attempts to reproduce the diffusion

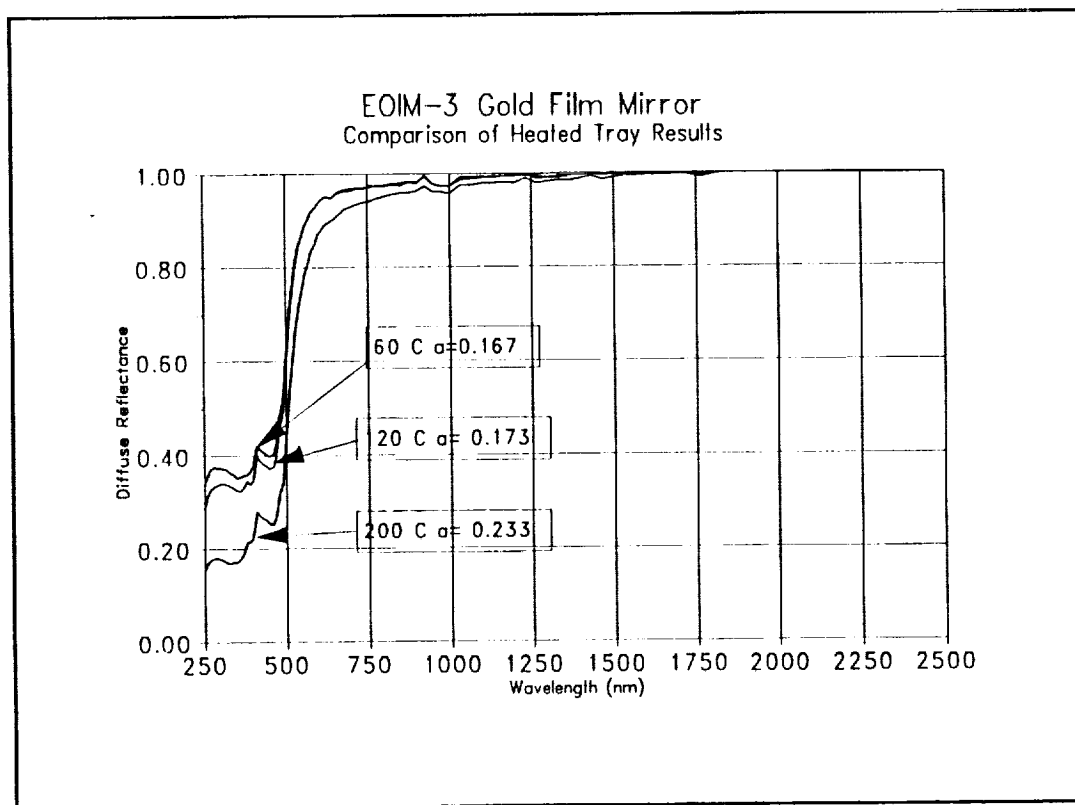


Figure 2 Comparison of Reflectance Data of Gold Thin Films on Heated Trays

Sample	Gold	Gold (60°C)		Gold (120°C)		Gold (200°C)	
	Control	Control	Exposed	Control	Exposed	Control	Exposed
Contam-ination Layer	NONE	7Å	13Å	10Å	15Å	-	-
Nickel Layer	10Å	25Å	65Å	35Å	90Å	-	250Å

Table III Nickel Depths on Gold Mirrors from the 60°C, 120°C, and 200°C Trays

process in the lab by heating a gold sample to nearly 200 °C were successfully verified using RBS, but the sample did not darken as did the flight sample. The darkening of the sample is due to the oxygen exposure as verified by ESCA analysis.

All three gold mirrors with nickel undercoats and a control were analyzed in both the exposed and unexposed regions using SALI and ESCA. The gold mirrors flown on the 60 °C, 120 °C and control gold mirrors were analyzed using ESCA with sputtering capabilities for depth analysis, and the 200 °C mirror was analyzed using SALI. Results showing the depth of nickel found on the surface in both the control and exposed sides of the flight mirrors are shown in Table III. The control mirror had no detectable contamination layer while all gold mirrors had very small contamination layer on the order of 10 to 15 Å. Thin nickel layers were detected on the surface of all four gold mirrors. The control mirror had a 10 Å layer on the surface of the mirror possibly from cross deposition during the evaporation process. ESCA verified the presence of nickel in both the unexposed and exposed regions of the 60°C and 120°C mirrors similar to the SALI analysis on the 200 °C mirror which suggests that the nickel diffuses through the gold driven by the sample temperature. Because the exposed region has thicker nickel layer in the exposed region, it is believed that the oxidation reaction between the nickel and the atomic oxygen is producing the darkening. This hypothesis is supported by the stoichiometric breakdown from the ESCA analysis which found oxygen in only the exposed region of the gold mirrors exposed in both the 60 °C and 120 °C trays.

Vacuum ultraviolet (VUV) reflectance data measured at MSFC indicated no significant change within experimental error in measurements on the unexposed, exposed side of the gold passive tray sample, the platinum sample, or the iridium sample. A typical VUV reflectance data set is shown in Fig. 3. This figure shows reflectance data measured for the platinum thin film mirror for which no significant changes in the reflectance were found. However, VUV reflectance data for the nickel sample, which is shown in Fig. 4, showed consistent change in VUV reflectance over all wavelengths from pre-flight measurements, as well as, unexposed and exposed measurements after flight. The sample remained in atmosphere for nearly six months prior to flight. The change in VUV reflectance and emittance data shown in Table II is a strong indication of nickel oxide growth caused by both atmospheric exposure as well as space environmental exposure.

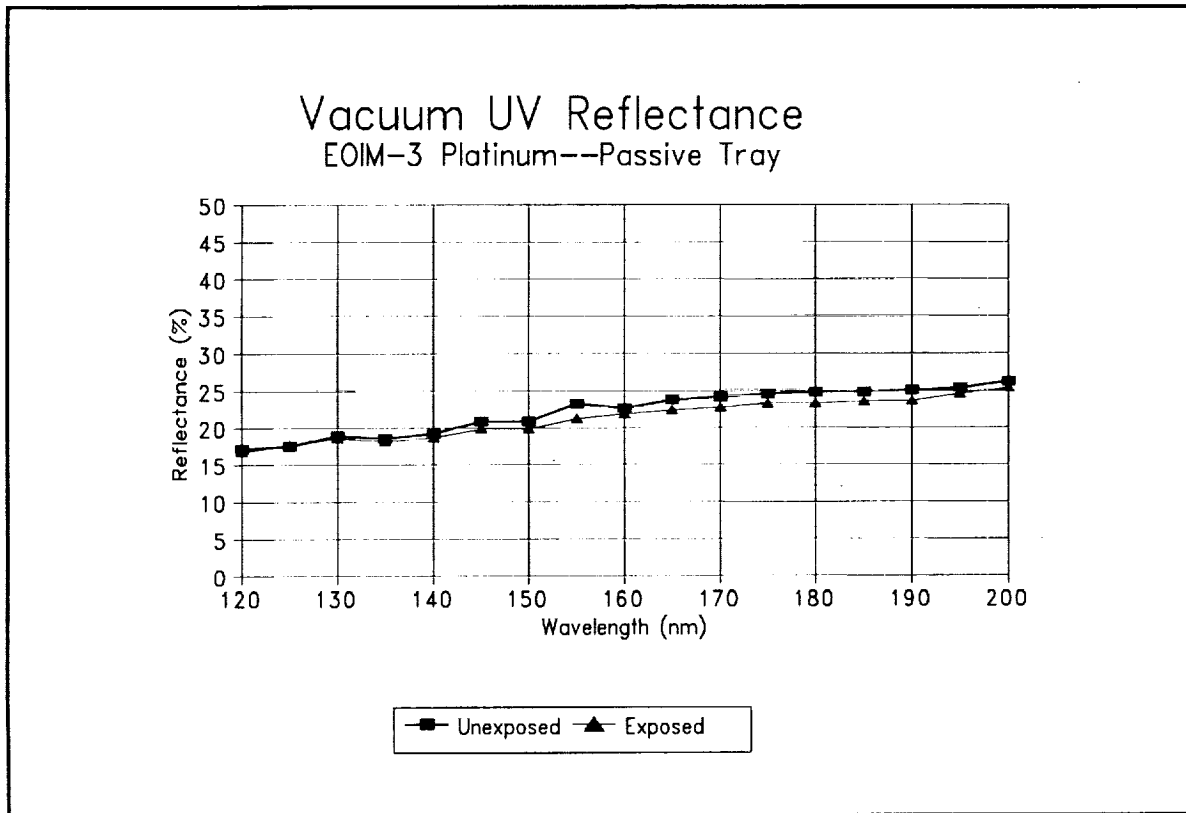


Figure 3 VUV Reflectance Data for Platinum Thin Film Mirror

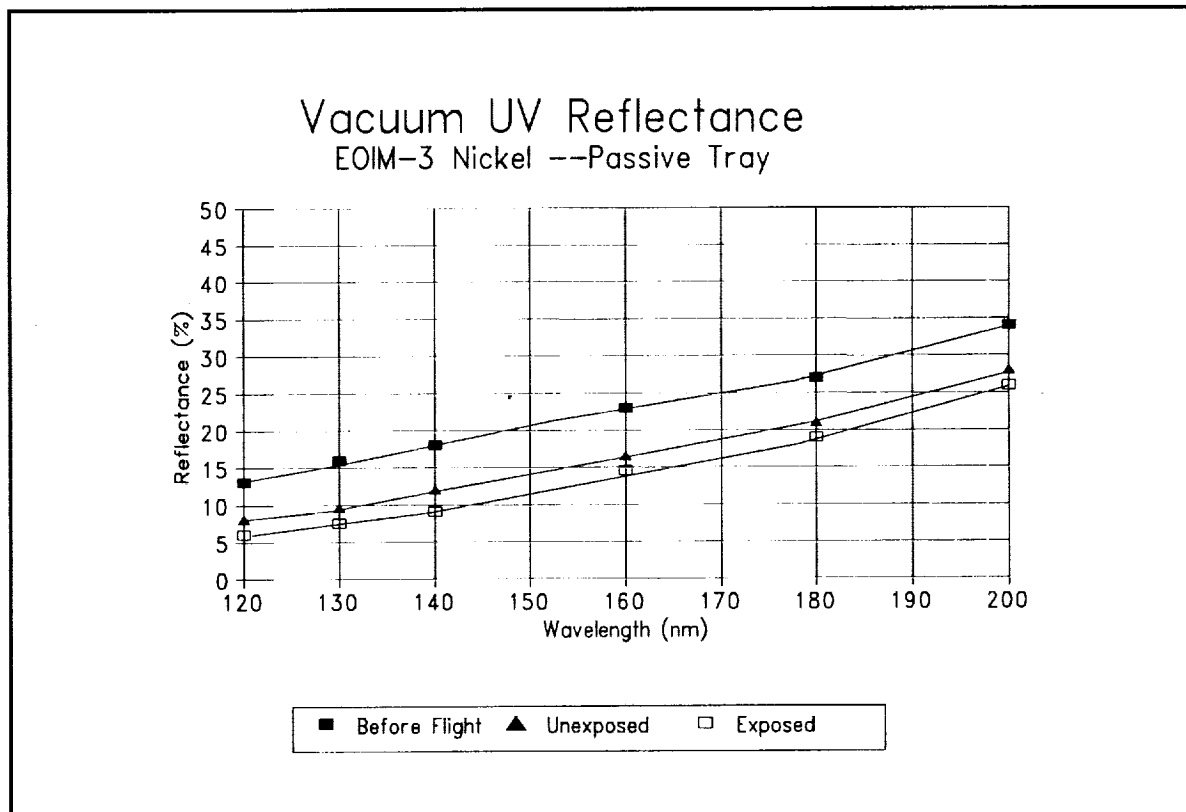


Figure 4 Vacuum Ultra Violet Reflectance Data for Thin Film Nickel

Ellipsometer measurements were made to investigate the presence, if any, of an oxide layer on all the metal thin films, particularly the nickel sample. Only a single layer substrate program which measures the substrate index of refraction (N_s) and the substrate extinction coefficient (K_s) was available for use. The results of these measurements are presented in Table IV.

Measurements of both N_s and K_s were made in both the unexposed and exposed region of the samples. The measured reflectance shown in Table IV was taken from the data file of the TMA quick scan scatterometer which is used to make BRDF measurements using the same 632.8 nm laser as the ellipsometer. Using the N & K values measured at 70° by the ellipsometer as input to a computer model designed to calculate the reflectance of the sample, comparisons of the calculated and measured reflectance were made. The computer model solves the basic Fresnel equations for the variables N , K , the incident angle, and the thickness of the coating. This model can be used for multi-layer thin film calculations. Any change indicated between the calculated reflectance and the measured reflectance would tend to indicate some anomaly with the surface.

Sample	N_s	K_s	Measured Reflectance (632.8 nm)	Calculated Reflectance (632.8 nm)
	70°	70°		
Platinum Unexposed	2.030	-4.643	0.741	0.736
Platinum Exposed	1.867	-4.399	0.735	0.729
Gold Unexposed	0.228	-3.458	0.939	0.932
Gold Exposed	0.224	-3.455	0.942	0.933
Iridium Unexposed	2.566	-4.162	0.654	0.658
Iridium Exposed	2.479	-4.143	0.659	0.661
Nickel Unexposed	1.819	-3.657	0.663	0.659
Nickel Exposed	1.681	-3.465	0.660	0.650

Table IV Summary of Ellipsometry Measurements on Metallic Thin Films

Most of the ellipsometer measurements shown in Table IV show no change within experimental error between the unexposed side and the exposed, and there is good agreement between the measured reflectance and the reflectance calculated using the measured values of N_s and K_s at 70° . One inconsistency which is evident in the table is the small but statistically significant difference between the measured reflectance and calculated reflectance of the exposed nickel thin film. Although the difference between the measured and calculated reflectance data is close, there is other data (the VUV reflectance data) which indicate there is a significant change on the surface. FTIR analysis showed no evidence of contamination. LDEF results indicate the presence of nickel oxide on nickel samples due to space exposure⁴.

SALI measurements on the EOIM-3 nickel thin film mirror indicated about 60 \AA of oxide on the unexposed side after flight and 100 \AA on the side exposed during flight. The SALI measurements were confirmed by calculating the reflectance at 121.6 nm and comparing it to measured reflectance data. Table V is a comparison of the calculated and measured reflectance data at 121.6 nm at an angle of incidence of 16° which is approximately the angle used to measure the reflectance at the VUV wavelength. The measured reflectance data shown in this table is from Fig. 4. The calculated reflectance from the computer model previously mentioned used the literature values for unoxidized nickel N and K ($N=1.220$ and $K=-3.330$)⁵ at 121.6 nm . The N and K for nickel oxide were assumed to be similar to those measured for typical metal oxides. By choosing the thickness which provided the best match to the measured reflectance data, the thickness of nickel oxide on the surface was determined. The pre-flight reflectance measurements indicated that 10 \AA of oxide was already present. After the EOIM-3 flight, the reflectance measurements indicated that even without exposure to the space environment the oxide thickness grew 60 \AA from just atmospheric exposure. Exposure to atomic oxygen resulted in an additional 30 \AA of oxide being produced for the short exposure experienced by the EOIM-3 experiment.

Sample Measured	Measured Reflectance (%)	Calculated Reflectance (%)	Nickel Oxide Thickness (\AA)
Pre-Flight	13.0	13.9	10
Unexposed After Flight	6.67	6.64	70
Exposed After Flight	4.95	4.91	100

Table V Comparison of Measured and Calculated Reflectance Data at 121.6 nm and 16° Angle of Incidence on nickel thin film on zerodur

OPTICAL THIN FILMS

Included in the materials flown on the passive trays by MSFC were several optical materials including magnesium fluoride/Al/fused silica (MgF_2) mirrors and CaF_2 , LiF and MgF_2 coated on beryllium substrates. Also, a luminescing phosphor which has wide spread use in VUV applications, sodium salicylate, was included in the samples. Because of the complexity of some measurements only initial results of the sodium salicylate will be touched on in this paper. In general, the CaF_2 , LiF and MgF_2 coatings on Be did not lose significant mass or change optically. Future work will concentrate on using RBS measurements to detect any changes in the surface and bulk materials due to space exposure.

Visual inspection of the sodium salicylate on a quartz substrate after flight indicated that the surface roughness of the samples had changed. The most striking change observed was found by the BRDF scatterometer in the transmission mode measuring the bi-directional transmission distribution function (BTDF) for the sodium salicylate sample in both the unexposed and exposed regions (Fig. 5). The data cannot be used to determine the surface roughness, but it does indicate that the sample has lost material. Mass loss data indicated a 1.27 mg decrease in mass. Because sodium salicylate is used for its luminescing capabilities in many VUV applications, fluorescence measurements were also done. The spectrofluorometer at MSFC has been used in the past to study the fluorescence changes in

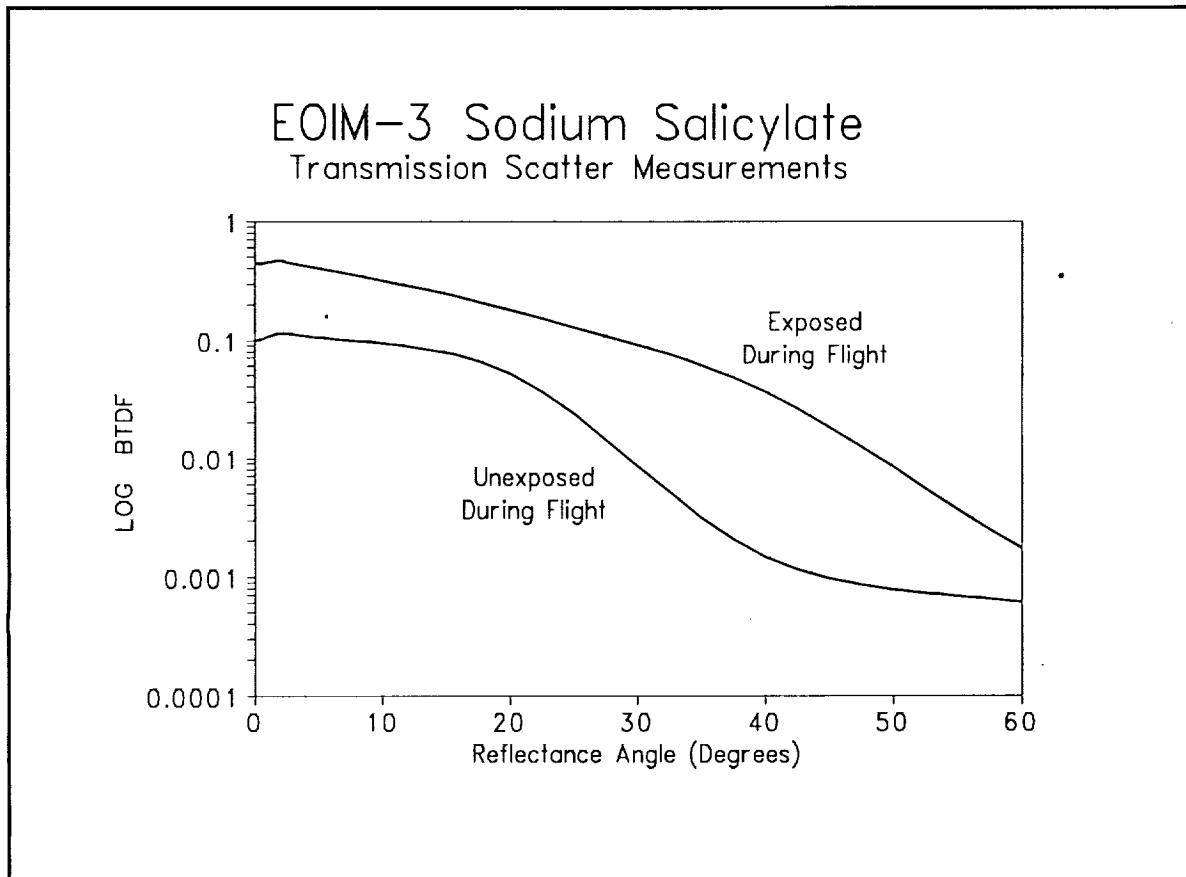


Figure 5 BTDF Measured for Sodium Salicylate

thermal control coatings⁶ with success. Spectrofluorometer measurements of sodium salicylate exposed to 260 nm light indicated only a slight change between the unexposed and exposed sides of the sample. However, when the fluorescence of the sample is measured at the vacuum ultraviolet wavelengths (120 nm to 200 nm) there is a consistent 50 % decrease in luminescence between the exposed and unexposed portion of the sample. This is consistent with the decrease in mass and transmission measured by the BTDF. Attempts to reproduce the loss of sodium salicylate were done in the laboratory by exposing samples to both 5 eV atomic oxygen and thermal atomic oxygen. While the samples did not lose mass as expected, the samples did turn yellow. After further investigation the yellowing was not due to contamination but was caused by intense VUV (130 nm) radiation from the atomic oxygen resonance line. This result did not provide any evidence to identify the cause of the thinning of the sodium salicylate but work is still continuing.

Preliminary Conclusion

General observation of all pure metals, optical thin metal films, and optical thin films indicates little or no contamination as reported by other EOIM-3 investigators. This result is backed up by numerous FTIR measurements on many samples.

Initial observations of the pure metal samples flown on EOIM-3 indicated most were unaffected by the short space exposure received. The copper and silver samples changed as expected. However, the vanadium and aluminum-lithium alloys indicated a decrease in mass by desorption of vanadium and lithium from the surfaces, respectively. Further work is required to confirm this observation.

Most of the optical thin metal films flown on EOIM-3 did not change due to the short duration space exposure. The gold thin film exposed to atomic oxygen on the 200 °C tray changed significantly in solar absorptance. ESCA, SALI, RBS, and FTIR data indicated that the darkening was not due to contamination but to diffusion or migration of the nickel substrate through the gold which was then oxidized by the atomic oxygen. The nickel thin film sample continuously grew oxide on the surface from the time it was first introduced into the atmosphere. Also, the oxide film grew when exposed to atomic oxygen during space exposure.

Sodium salicylate, which is used as a VUV phosphor, indicated some thinning in the exposed region of the sample confirmed by mass loss results, BTDF data, and VUV fluorescence measurements. More work is required to identify the cause of the thinning.

Acknowledgements

The authors wish to thank the following people for the contributions made to this paper. Mr. Dave Edwards of Space Environmental Effects Branch at MSFC and Dr. John Williams of Auburn University for the RBS measurements and analysis of the optical thin films. Dr. Kijoon Chang of Alabama A&M University for the use of his ellipsometer. Dr. Chris Becker of Stanford University for the SALI measurements and analysis of the optical thin films. Dr. N. Carl Miller at Raytheon for his ESCA analysis of the optical thin films.

Mr. Ed White of the Space Environmental Effects Branch at MSFC for his laboratory support. Mr. Alan Shapiro for providing the optical thin film metals samples and zerodur.

References

- ¹ Levine, A.S., "LDEF--69 Months in Space: First Post-Retrieval Symposium Parts 1,2, and 3", NASA CP 3134, Kissimmee, Fl, June 2-8, 1991.
- ² Levine, A.S., "LDEF--69 Months in Space: Second Post-Retrieval Symposium Parts 1,2,3 and 4", NASA CP 3194, San Diego, CA, June 1-5, 1992.
- ³ Visintine, J.T., ed., "Atomic Oxygen Effects Measurements for Shuttle Missions STS-8 and 41-G ", NASA TM 100459, Vol. 1-3, Sept. 1988.
- ⁴ Franzen, W., Brodtkin, J.S., Sengupta, L.C., and Sagalyn, P.L., "Ellipsometric Study of Oxide Films Formed on LDEF Metal Samples", NASA CP 3134, Part 2, pp. 1005-1021, June 2-8, 1991.
- ⁵ Palik, Edward D., ed., Handbook of Optical Constants of Solids, Academic Press, Inc., pp. 317-323, 1985.
- ⁶ Linton, R.C., Whitaker, A.F., and Kamenetzky, R.R., "Fluorescence Observations of LDEF Exposed Materials as an Indicator of Induced Material Reactions", Published in the Proceedings of LDEF Materials Results for Spacecraft Applications Conference, Oct. 1992.

ANALYSIS OF SELECTED SPECIMENS FROM THE STS-46 ENERGETIC
OXYGEN INTERACTION WITH MATERIALS-III EXPERIMENT

Johnny L. Golden, Roger J. Bourassa, Harry W. Dursch and H. Gary Pippin

Boeing Defense & Space Group
P. O. Box 3999 M/S 82-32
Seattle, WA 98124-2499
(206) 773-2846, FAX (206) 773-4946

INTRODUCTION

The Energetic Oxygen Interaction with Materials III (EOIM-III) experiment was flown on the STS-46 mission, which was launched on July 31, 1992 and returned August 8, 1992. Boeing specimens were located on both the NASA Marshall Space Flight Center (MSFC) tray and the Ballistic Missile Defense Organization (BMDO) tray integrated by the Jet Propulsion Laboratory (JPL). The EOIM-III pallet was mounted in the Space Shuttle payload bay near the aft bulkhead.

During the mission, the atomic oxygen (AO) exposure levels of specimens in these passive sample trays was about 2.3×10^{20} atoms/cm². The specimens also received an estimated 22 equivalent sun hours of solar exposure (ref. 1). In addition, it appears that the EOIM-3 pallet was exposed to a silicone contamination source and many specimens had a thin layer of silicon based deposit on their surfaces after the flight (ref. 2).

The specimens on the MSFC tray included seven solid film lubricants, a selection of butyl rubber (B612) and silicone (S383) o-rings, three indirect scatter surfaces, and Silver/ Fluorinated Ethylene Propylene (Ag/FEP) and Chemglaze A276 specimens which had previously flown on trailing edge locations of the Long Duration Exposure Facility (LDEF). The specimens on the JPL tray included composites previously flown on LDEF and two indirect scattering surfaces. The indirect scattering surface specimens from both trays provided minimal information and will not be discussed in this paper. The o-ring specimens were exposed to the low Earth orbit (LEO) environment under a variety of selected tensile or compressive load conditions. The Chemglaze A276 polyurethane paint specimens from the LDEF had all been previously exposed to several thousand equivalent sun hours (ESH) of solar radiation during the LDEF flight. Selected composite and Ag/FEP specimens were also chosen because of their prior solar exposure. Additional composite and Ag/FEP specimens from the LDEF which had not been directly exposed to high solar fluences were also chosen for reflight. The intent of the environmental exposure for the composite and Ag/FEP specimens was to see if the prior solar exposure enhanced their recession rates when subsequently exposed to atomic oxygen.

RESULTS & ANALYSIS

Solid Film Lubricants

The eight solid film lubricants selected for test are shown in table 1. Weight measurements were made before and after flight under tightly controlled environmental conditions by NASA MSFC. Weight change results are also shown in table 1.

Table 1. Solid Film Lubricants and Their Weight Changes After The EOIM-III Flight.

NAME	DESCRIPTION	WEIGHT CHANGE
Tiolube 29	Inorganic Coating	<0.03 mg/cm ²
Tiolube 460	MoS ₂ filled Organic Coating	-0.10 mg/cm ²
PS212	Chromium Carbide/Ag/Fluoride Eutectic Self-Lubricating Composite Coating	<0.03 mg/cm ²
Torlon 4301	Poly(amide-imide) Wear Resistant Polymer	+6.76 mg/cm ²
Delrin 100AF	PTFE filled Acetal Resin	-1.64 mg/cm ²
NPI 425	MoS ₂ /Sb oxide filled Polyimide Coating	-0.10 mg/cm ²
Garlock DU	PTFE/Pb filled with Tin Bronze	<0.03 mg/cm ²
Vitro-Lube (NPI 1220)	Ceramic Bonded MoS ₂ /Graphite/Ag With MoS ₂ /Graphite Phenolic Topcoat	-0.10 mg/cm ²

The outer ring of each lubricant specimen was covered by the lip of the aluminum sample holder. This provides unexposed material on each specimen to compare with the space exposed surface. Visual examination of the lubricants closely followed the weight change results. The two specimens with the significant weight changes both darkened with environmental exposure, as is shown in figure 1 for Torlon 4301 and in figure 2 for Delrin 100AF. For comparison, the appearance of PS212 changed very little (see figure 3).

Surface profilometry was used in an attempt to measure surface erosion at the exposed to unexposed interface on the flight specimens. Erosion was undetectable by this method.

X-ray photoelectron spectroscopy (XPS) was used to characterize the surfaces of all lubricants before and after exposure on EOIM-III. Samples of the information obtained are shown in figures 4 - 9. Comparison of the Garlock DU control specimen in figure 4 with the flight specimen (which indicated minimal weight change) in figure 5 shows that the lead (Pb) signals have increased significantly, presumably due to some erosion of the PTFE fraction. For the Tiolube 460 lubricant (which exhibited a slight weight change with exposure), comparison of the control specimen measurement in figure 6 to the flight specimen in figure 7 indicates that there has been a significant loss of carbon signal because of atomic oxygen erosion. Based on the spectrum of figure 7, the Tiolube 460

material also contains lead (Pb) and antimony (Sb). One final comparison involves the lubricant Torlon 4301, which gained significant weight with exposure on EOIM-III. Comparison of the control specimen in figure 8 with the flight specimen in figure 9 indicates a reduction in the carbon 1s signal for the flight specimen, but with no corresponding signal increases (such as for oxygen) to explain the weight increase observed for this material.

O-Rings

Fifteen specimens of butyl and silicone rubbers were flown as part of our investigation on EOIM-III. The specimens were exposed to the LEO space environment while subjected to various levels of tensile or compressive loading. Examples of the two tensile load specimen holders, as well as the compressive loading specimen holders, are shown mounted in the experiment tray (preflight) in figure 10. Stainless steel mesh covers the specimens in the tensile loading fixtures to ensure that the o-rings stayed with the experiment through sample recovery.

Scanning electron microscopy (SEM) images of the o-ring surfaces were made postflight. Figures 11 and 12 show comparison of the surfaces of butyl and silicone rubber o-rings that were held under compression during environmental exposure at 1000X and 3000X, respectively. General AO erosion is visible on the butyl rubber surfaces while no apparent erosion occurred on the silicone rubber. The silicone rubber was similarly unaffected in the tensile loading configuration. The butyl rubber, however, showed erosion patterns affected by the amount of tension applied. Figure 13 shows two butyl o-rings at 500X, the first loaded in tension by stretching it to 60% above its original diameter, the second to 100% above its original diameter. The 100% tension specimen has developed a cracking erosion pattern perpendicular to the direction of stress. Figure 14 shows a comparable erosion pattern at 80% tension. Also shown in figure 14 is the pattern of uneroded surface resulting from the AO shielding provided by the stainless steel mesh covers.

Visual examination of the two o-ring materials confirmed the erosion of butyl rubber surfaces because of the apparent loss of surface gloss. No visible effect was noted for silicone rubber o-rings. However, examination of the silicone rubber under ultraviolet illumination, as shown in figure 15, indicated that some chemical change, as evidenced by fluorescence, had occurred on the silicone surface with environmental exposure.

Graphite/Epoxy Composite

Two specimens of T300/934 graphite/epoxy composite that had previously flown on the Long Duration Exposure Facility (LDEF) were chosen for reflight on EOIM-III. The specimens were from LDEF experiment M0003-10. One of the specimens, 5C1A, had been exposed to 10,500 equivalent sun hours (ESH) of solar exposure and 2.3×10^5 atomic oxygen atoms/cm² during the LDEF mission. The other specimen, 5C2A, was shielded from environmental exposure during the LDEF flight and only exposed to

vacuum. During the EOIM-III test, both materials were exposed to 2.3×10^{20} oxygen atoms/cm².

SEM images of the surfaces of the two composite specimens are shown and 500X and 1000X magnifications in figures 16 and 17, respectively. The specimen exposed only to space vacuum during the LDEF flight eroded much faster than the LEO exposed specimen, as indicated by the quantity of carbon fiber revealed.

ESCA analyses revealed the reason for the AO erosion behavior. The LEO exposed LDEF specimen had approximately 25 atomic % silicon on its surface, before or after EOIM-III exposure. The composite specimen exposed only to vacuum during the LDEF flight had approximately 2.2 atomic % silicon on its surface. The test objective, to determine the effect of previous solar exposure on AO erosion rate, was not accomplished. However, silicon contamination from previous exposure was observed to provide some protection against AO erosion.

Ag/FEP

Specimens of Ag/FEP thermal blanket material from LDEF experiment A0178 were taken from trailing edge locations. This material had been subjected to between about 8200 and 9600 equivalent sun hours of solar ultraviolet radiation and about 33,000 thermal cycles. One specimen was taken from the edge of a blanket and had been subjected to less solar exposure. Particular specimens were then selected from this set of specimens and flown on EOIM III to provide atomic oxygen exposure to this material. The goal was to determine if the prior UV exposure would cause the material to degrade at a faster rate than new specimens. Surface contamination, deposited during the shuttle flight and remaining from the LDEF flight, masked any such effect.

The specimens were each characterized by surface analysis using ESCA. Table 2 shows the results of this examination. The relative CF and CF₃ peak intensities compared to the CF₂ peak intensity, were determined before and after the EOIM III flight and for ground control material. Significant relative increases in the CF and CF₃ peak intensities were observed for all flight specimens in comparison with the ground control material. The specimen from the edge of B-5 which is listed as "shielded" from solar UV was actually exposed to some direct and some reflected solar UV. Carbon 1s ESCA spectra of the pre-EOIM III flight F-2 specimens show substantial contamination on the LDEF specimen. The post-EOIM III F-2 flight specimen shows that the level of atomic oxygen exposure on EOIM III removed substantial contamination from the previously flown material.

The CF₃/CF₂ carbon 1s peak intensity ratio is lower for each LDEF specimen reflown on EOIM III in comparison with each corresponding LDEF specimen (taken from the same blanket) not reflown. This indicates the oxygen is removing some of the surface FEP material previously altered by solar exposure. Figures 18 and 19 show the comparison between surface conditions on blanket F2 after the LDEF flight and after the subsequent EOIM III flight.

Table 2. Ag/FEP ESCA measurements showing CF and CF₃ relative to CF₂ peak intensities with environmental exposure.

Specimens	Peak Intensities		Exposures	
	CF	CF ₃	UV(Hrs)	AO(Atoms/cm ²)
Ground control Specimens				
	0.045	0.07		
LDEF Specimens				
B-5	0.45	0.67	8200	9.6x10 ¹²
C-5	0.46	0.65	8200	1.5x10 ¹⁷
F-2	0.87, 1.06	0.40, 0.50	9600	1.5x10 ¹⁷
E-2	0.47, 0.69	0.90, 0.73	9600	1.5x10 ¹⁷
LDEF Specimens reflown on EOIM-III				
B-5	1.0, 0.89	0.18, 0.19	8200	2.3x10 ²⁰
B-5(Shielded)	0.94, 0.88	0.15, 0.25	-	2.3x10 ²⁰
F-2	0.89, 1.0	0.17, 0.20	9600	2.3x10 ²⁰

Polyurethane Thermal Control Paint Chemglaze A276

Four specimens of white polyurethane thermal control coating, Chemglaze A276, were taken from LDEF tray clamps (ref. 3). Two of these specimens were flown on EOIM-III. The other two specimens were used as ground control specimens to monitor any non-flight induced changes. The environmental conditions of exposure and the optical properties of the coating surfaces before and after EOIM-III flight are shown in Table 3 for both the flight and ground control specimens. The visual appearance of the A276 specimens is shown in figure 20. As expected, the AO erosion from the EOIM-III flight was sufficient to remove much of the solar ultraviolet (UV) radiation-damaged polyurethane resin in the paint surface, exposing white pigment and recovering some of the reflectivity exhibited by the control.

Table 3. Pre- and Postflight Exposure and Optical Properties for LDEF Chemglaze A276 Coating Specimens Flown on EOIM-III.

Sample	EOIM-III Preflight				EOIM-III Postflight			
	UV (ESH)	AO (atoms/cm ²)	α_s	ϵ	UV (ESH)	AO (atoms/cm ²)	α_s	ϵ
F1-6	8500	1.5x10E17	0.52	0.86	8500	2.3x10E20	0.35	0.88
D6-1	7100	7.3x10E16	0.48	0.88	7100	2.3x10E20	0.30	0.90
C5-2	9400	6.8x10E8	0.53	0.86	Not Flown		0.52	0.86
B2-4	9600	1.5x10E17	0.54	0.87	Not Flown		0.52	0.87
Control	-	-	0.28	0.87	Not Flown			

An interesting comparison can be made between the EOIM-III flight specimens and LDEF data for A276, plotting solar absorptance as a function of atomic oxygen fluence, shown in figure 21. The EOIM-III specimens, after sequential exposure to UV radiation then AO, follow the trend observed for LDEF specimens. The UV damaged portion of the polyurethane paint is the extreme surface of the resin fraction, and AO erosion of the surface resin provided some recovery of the coating's solar absorptance. AO erosion also increased thermal emissivity slightly.

SUMMARY

The significance of the EOIM-III flight for the materials investigated here was that short-term atomic oxygen exposure did produce some observable effects. However, the usefulness of short-term exposure can be significantly limited by contamination. Contamination on the graphite/epoxy composites of this investigation essentially precluded the intended evaluation of UV radiation effects on AO erosion rates. Regardless of contamination effects, the exposure levels on STS-046 provide only an indication of the changes in materials caused by the LEO space environment. Long-term exposure or accelerated exposure techniques are needed to provide more confidence in materials performance life predictions with space environmental exposure.

ACKNOWLEDGEMENTS

Appreciation is extended NASA for the opportunity to conduct valuable experiments such as EOIM-III. A special thanks is extended to Shirley Chung of JPL and Miria Finckenor of MSFC for their extensive efforts in the integration and de-integration analyses of the materials discussed herein.

REFERENCES

1. S. Y. Chung, D. E. Brinza, A. E. Stiegman, J. T. Kenny, and R. H. Liang, Flight and Ground-Test Correlation Study of BMDO SDS Materials: Phase I Report, JPL Publication 93-31, December 1993.
2. C. R. Maag, D. E. Williams, E. N. Borson, J. J. Palou, Induced Payload Contamination as Observed on Three Successive Flights of the Space Shuttle. Third LDEF Post-Retrieval Symposium.
3. J. L. Golden: Results of Examination of the A276 White and Z306 Black Thermal Control Paint Disks Flown on LDEF. First LDEF Post-Retrieval Symposium, NASA CP-3134, Vol. 2, p. 975, 1992.

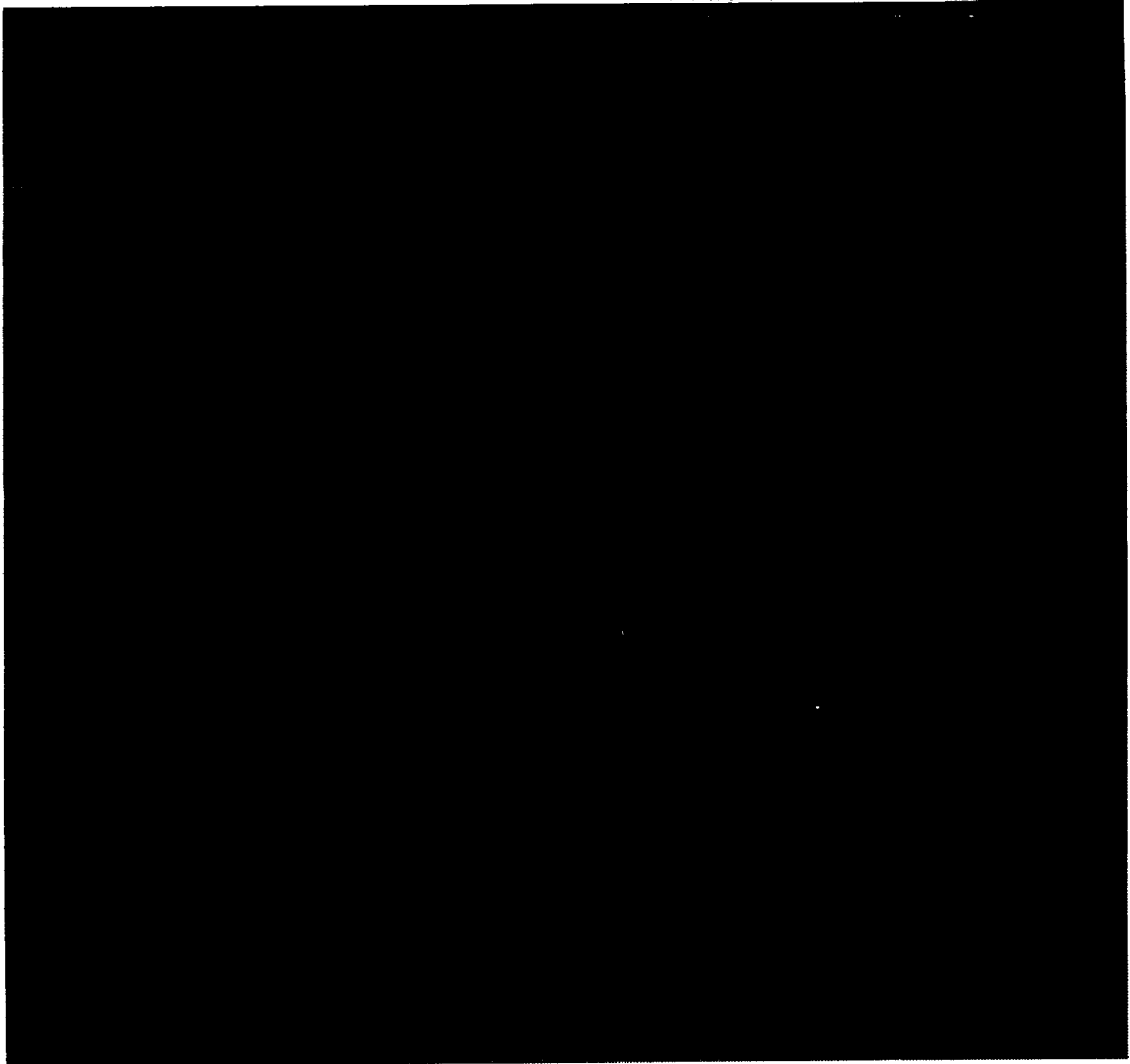


Figure 1. EOIM-III postflight view of solid film lubricant Torlon 4301.

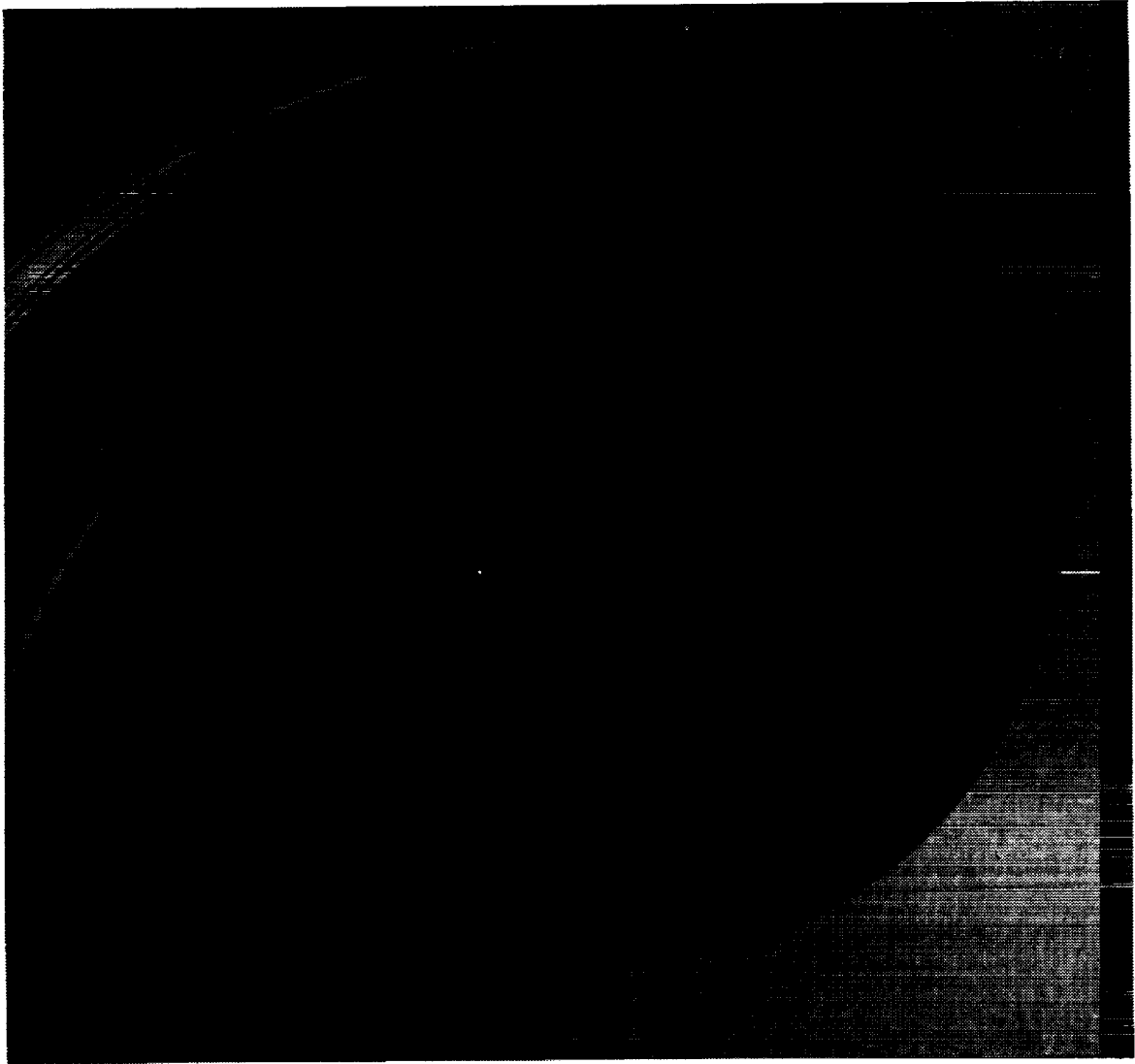


Figure 2. EOIM-III postflight view of solid film lubricant Delrin 100AF.



Figure 3. EOIM-III postflight view of solid film lubricant PS212.

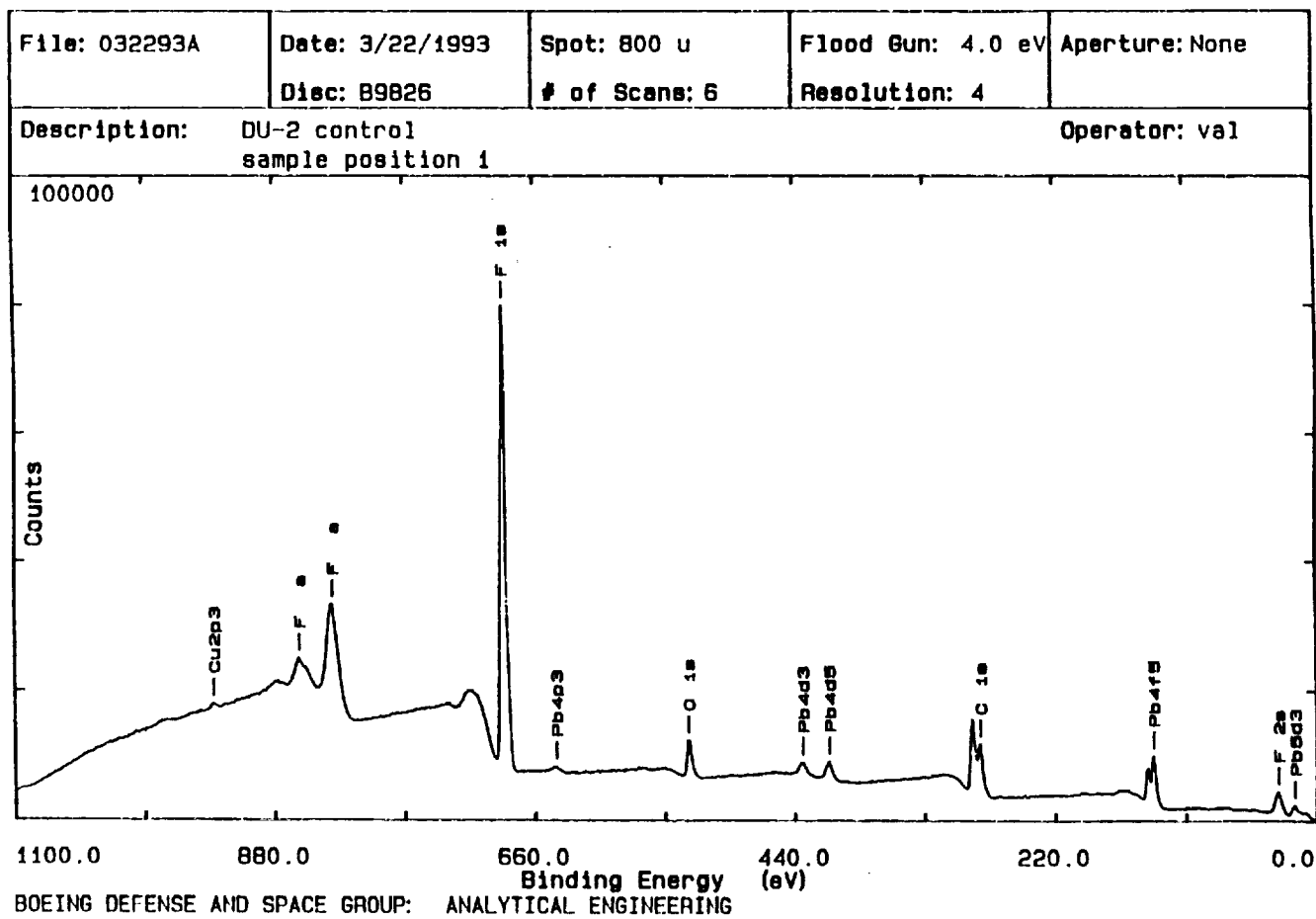


Figure 4. X-ray photoelectron spectroscopy of solid film lubricant Garlock DU control specimen.

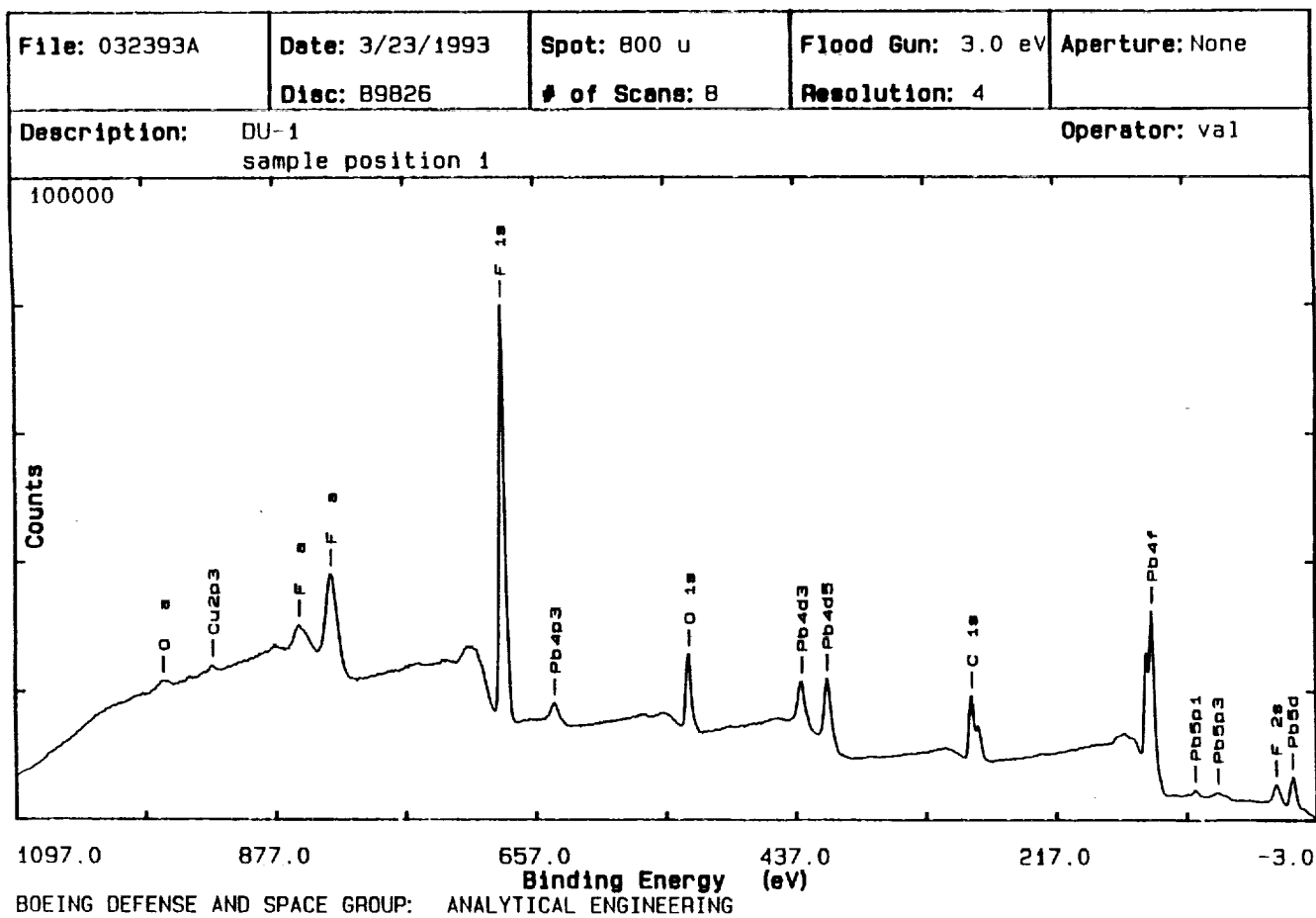


Figure 5. X-ray photoelectron spectroscopy of solid film lubricant Garlock DU flight specimen.

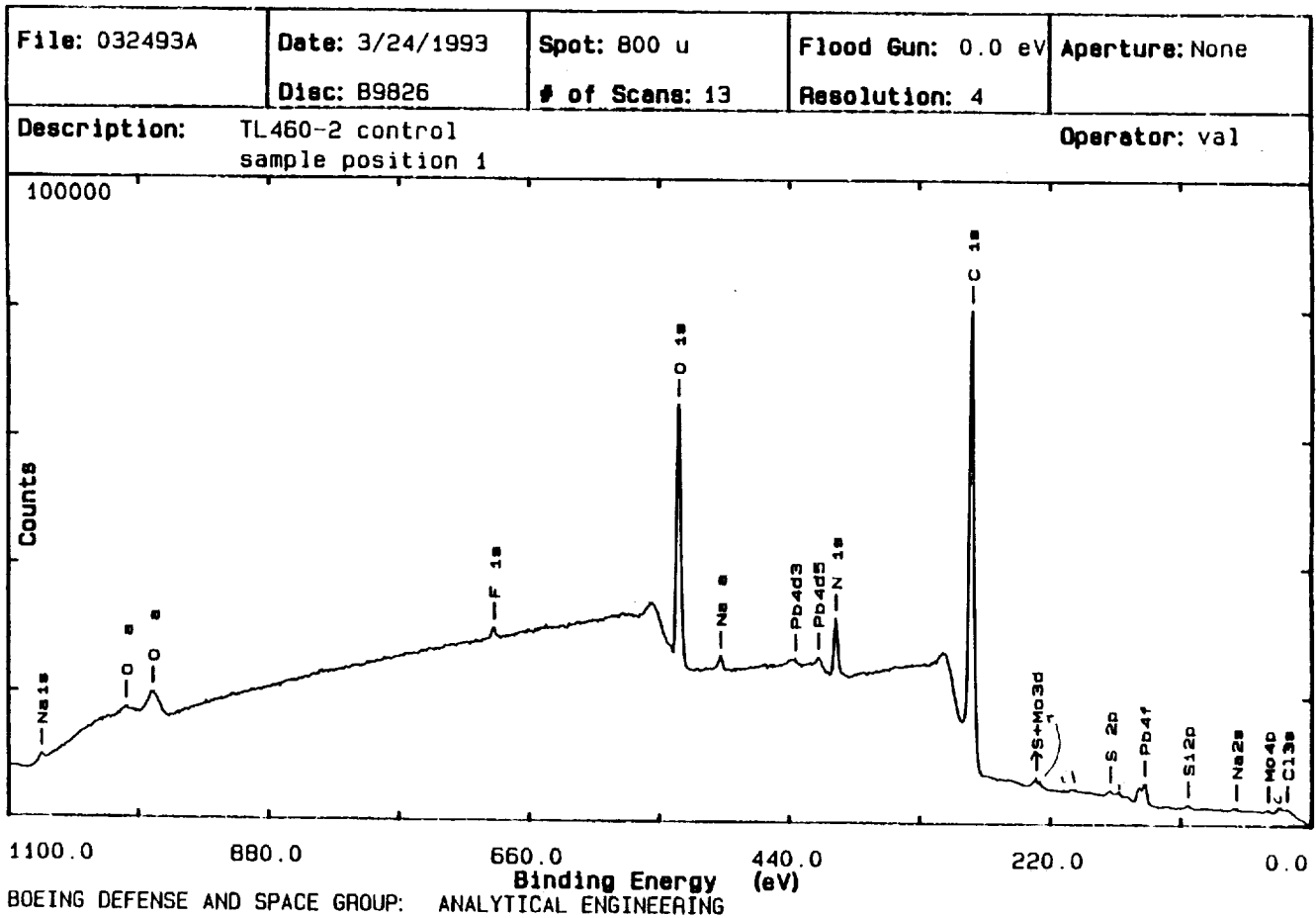


Figure 6. X-ray photoelectron spectroscopy of solid film lubricant Tiolube 460 control specimen.

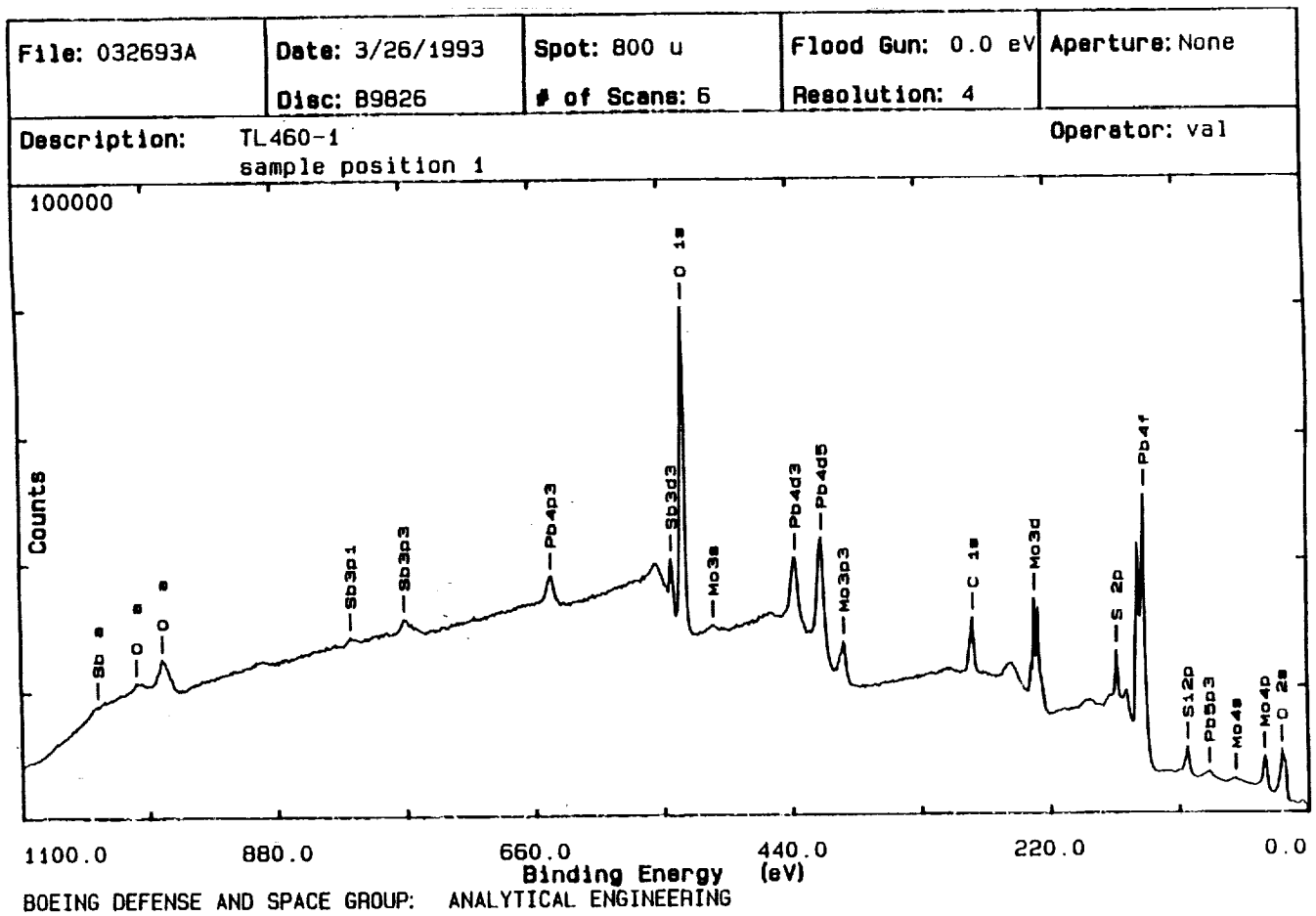


Figure 7. X-ray photoelectron spectroscopy of solid film lubricant Tiolube 460 flight specimen.

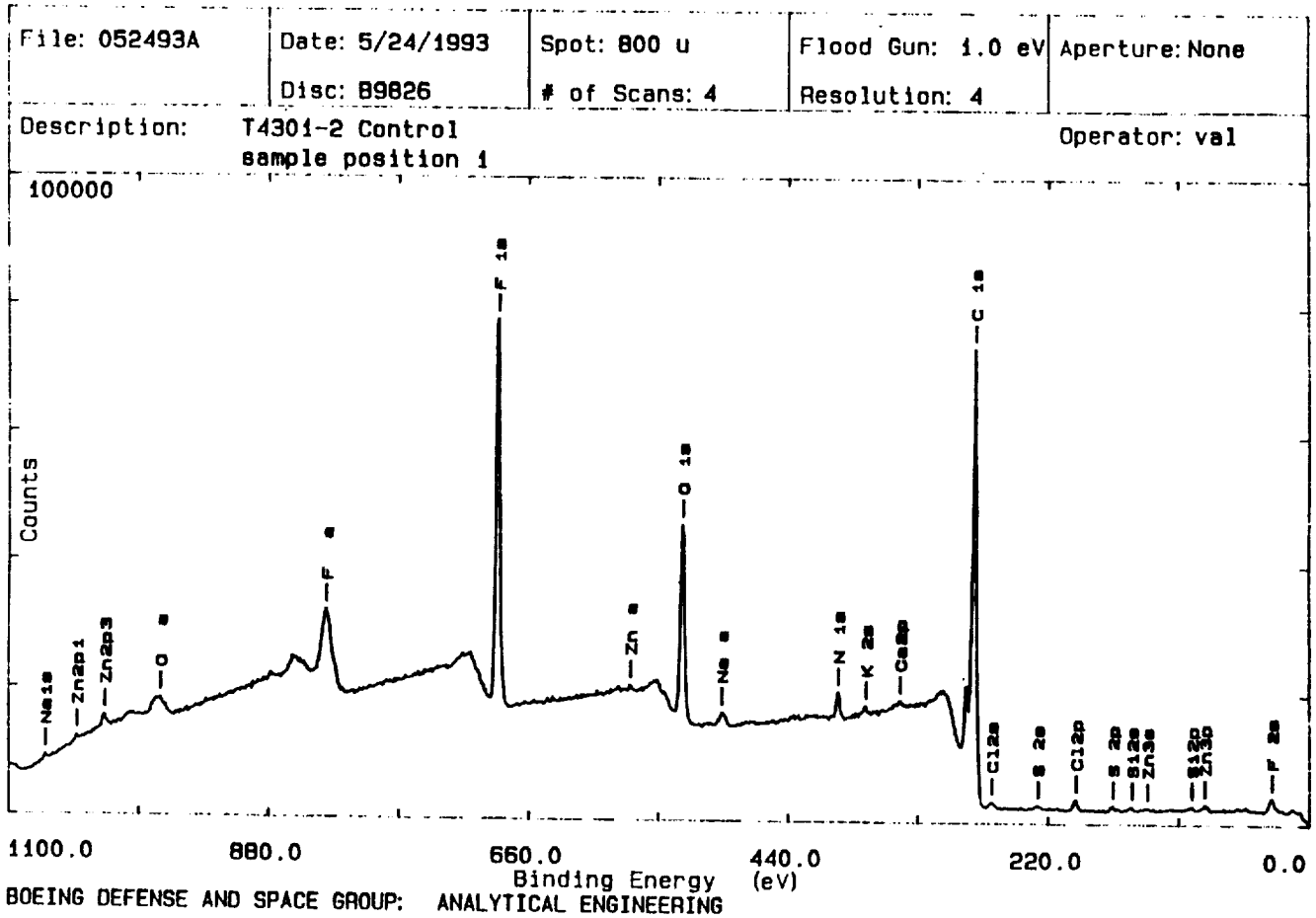


Figure 8. X-ray photoelectron spectroscopy of solid film lubricant Torlon 4301 control specimen.

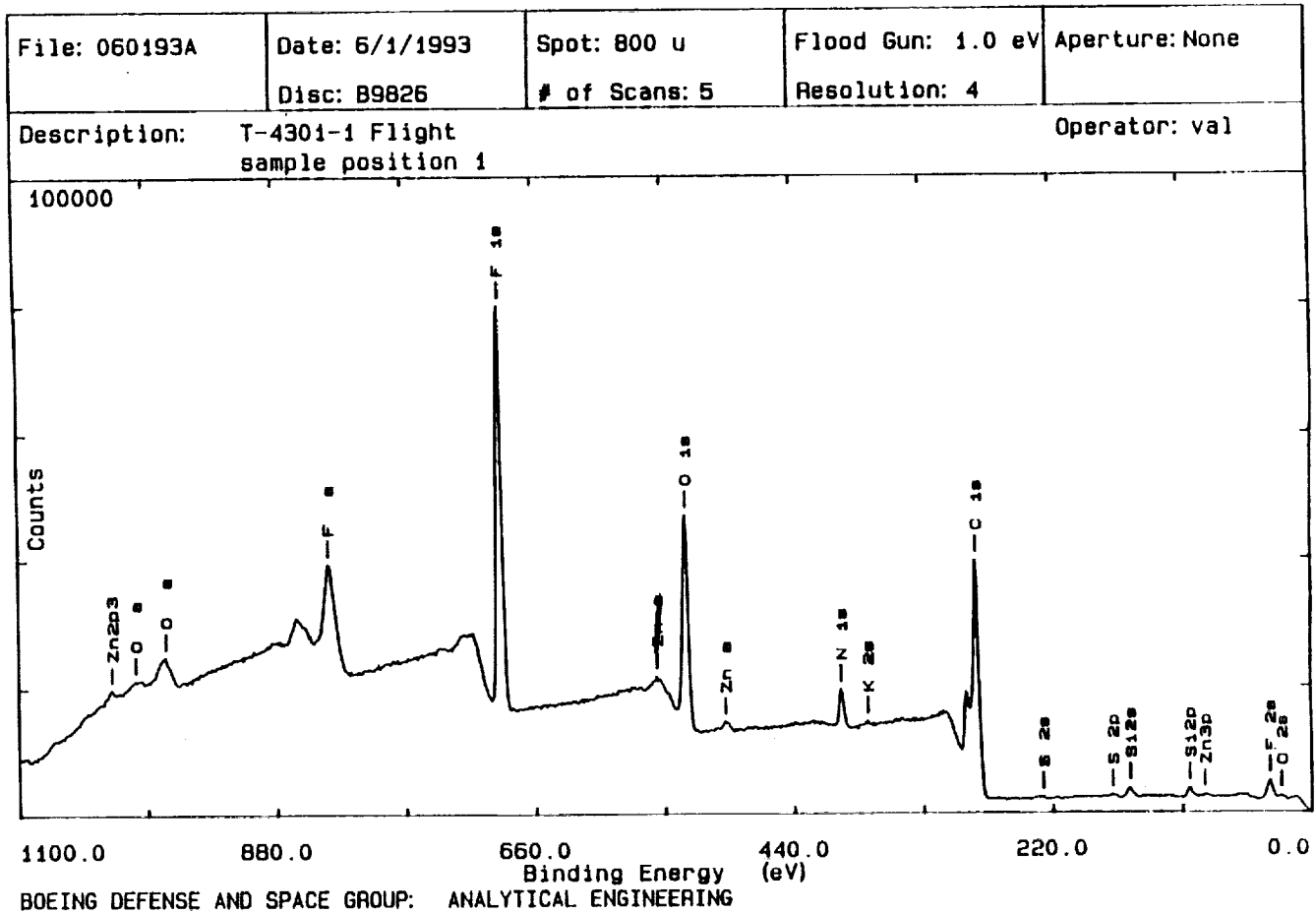


Figure 9. X-ray photoelectron spectroscopy of solid film lubricant Torlon 4301 flight specimen.

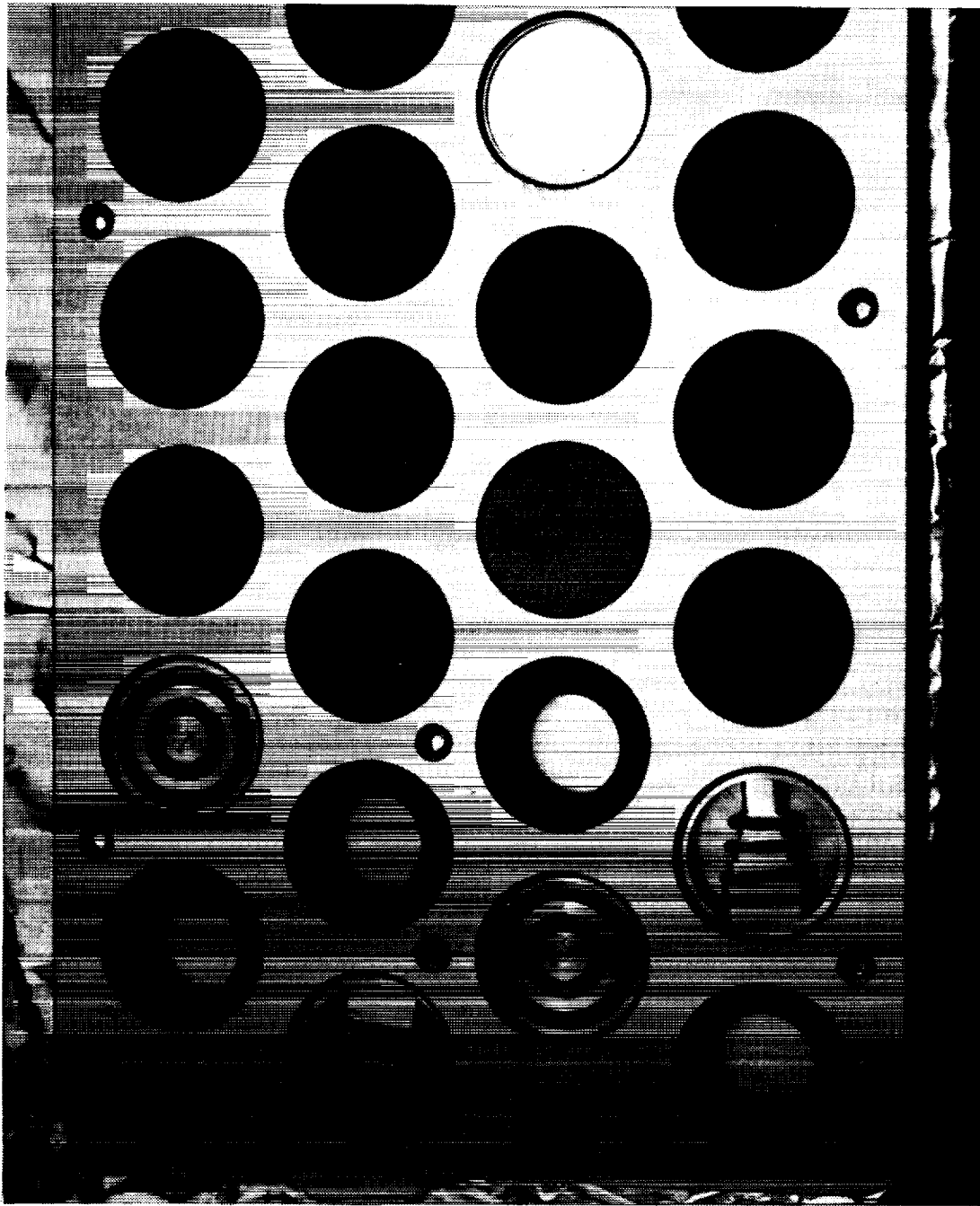


Figure 10. EOIM-III preflight view of the tensile and compressive o-ring fixtures in the experiment tray.

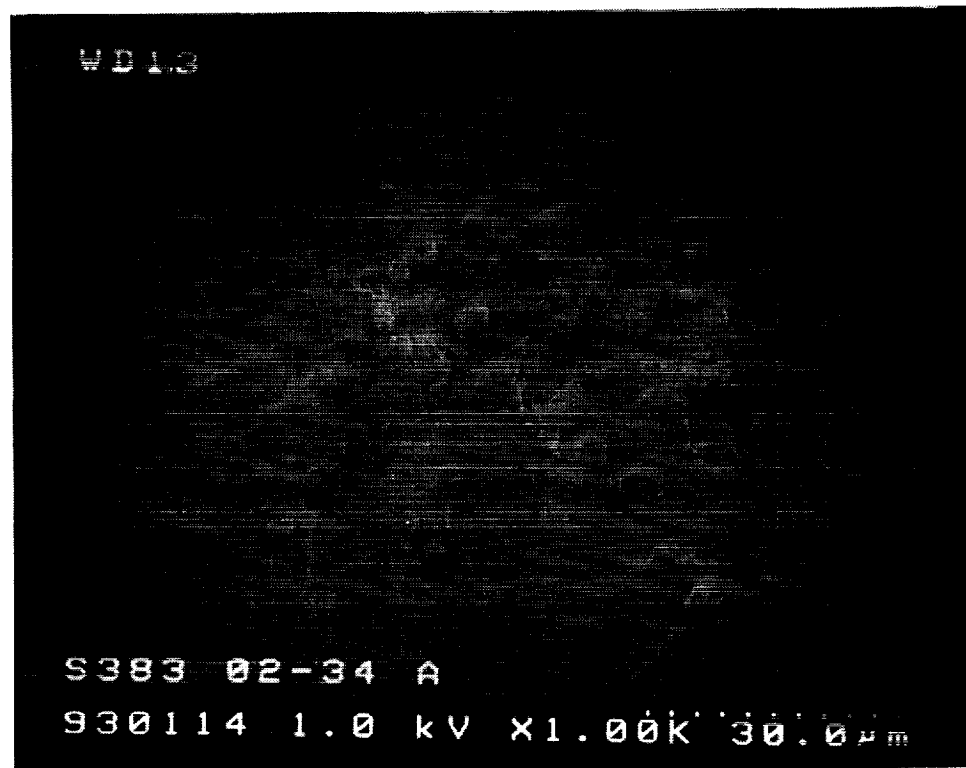
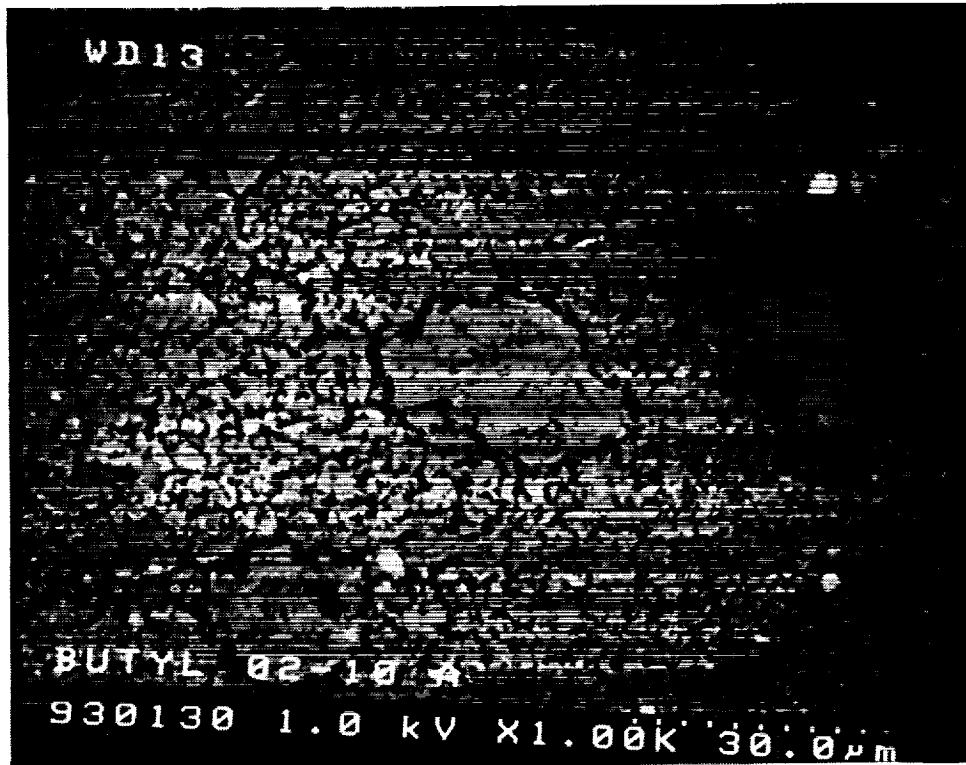


Figure 11. Scanning electron microscope images of o-rings postflight at 1000X magnification. The images are of specimens flown under compression. The top image is of a butyl rubber specimen, the bottom image is of a silicone (S383).

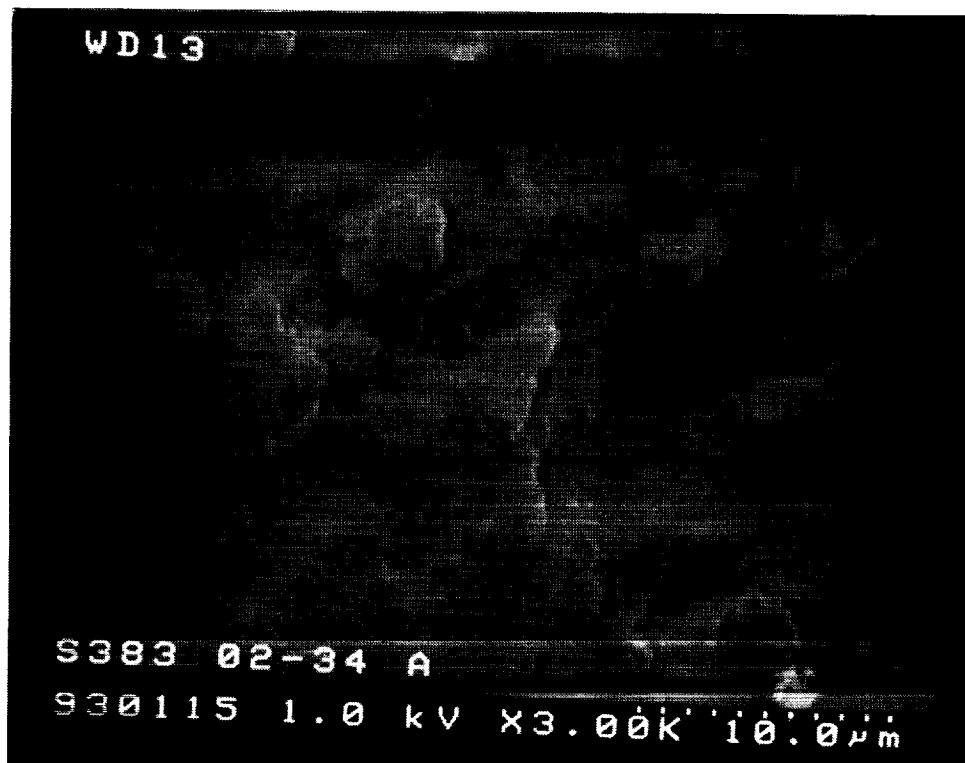
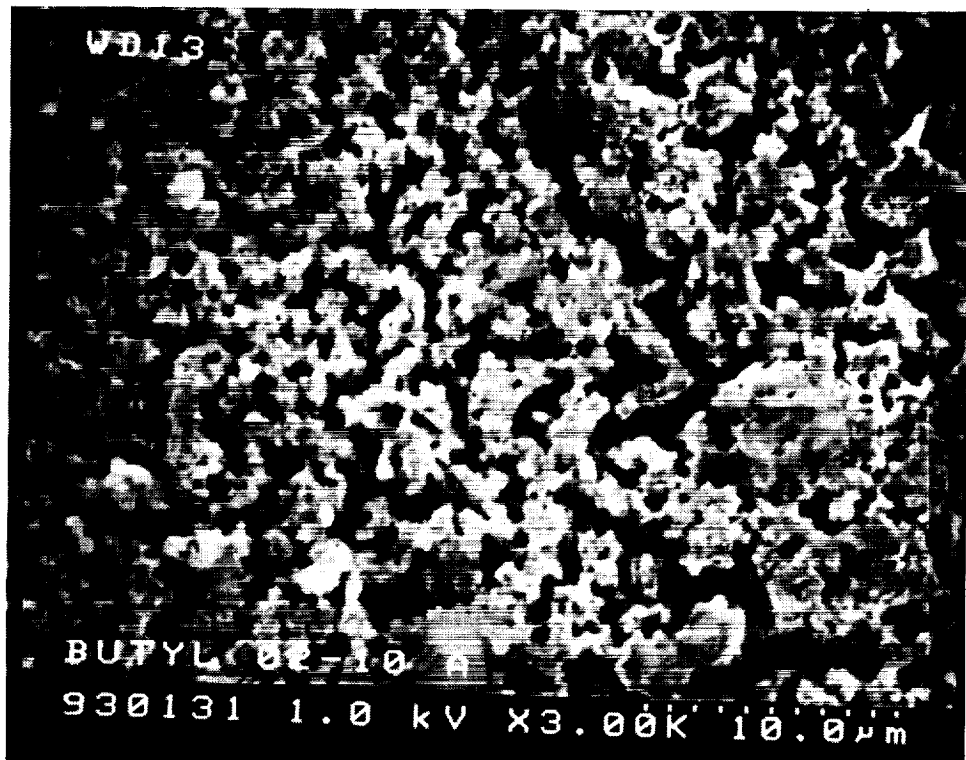


Figure 12. Scanning electron microscope images of o-rings postflight at 3000X magnification. The images are of specimens flown under compression. The top image is of a butyl rubber specimen, the bottom image is of a silicone (S383).

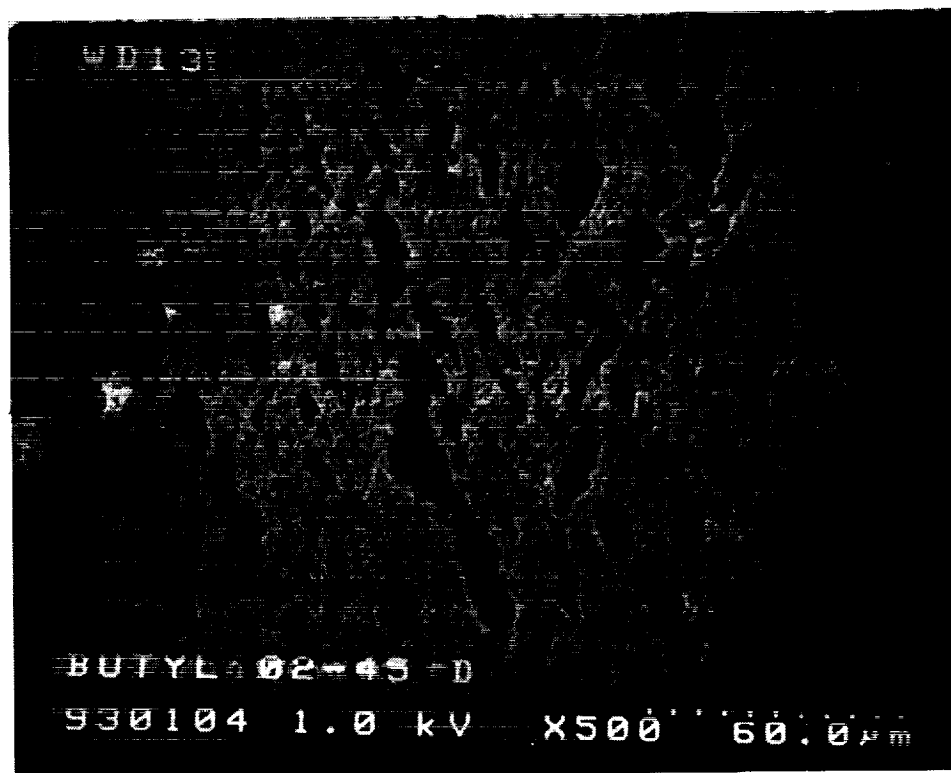
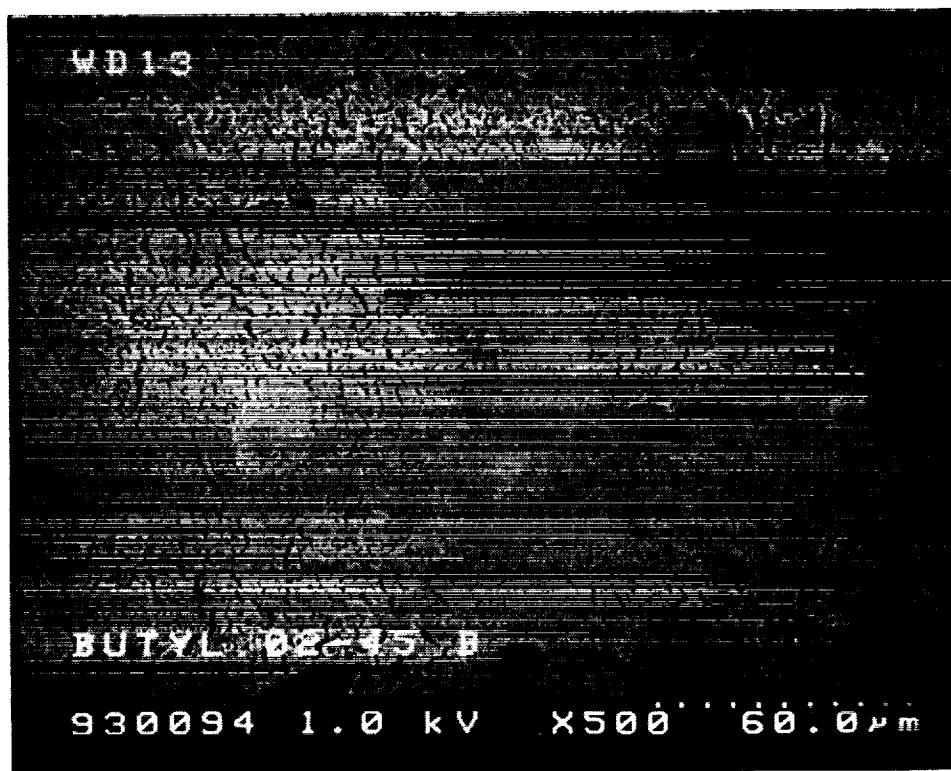


Figure 13. Scanning electron microscope images of butyl rubber o-rings postflight at 500X magnification, showing the effect of tension on atomic oxygen erosion. The top image is of a specimen flown under 60% tension. The bottom image is of a specimen flown under 100% tension.

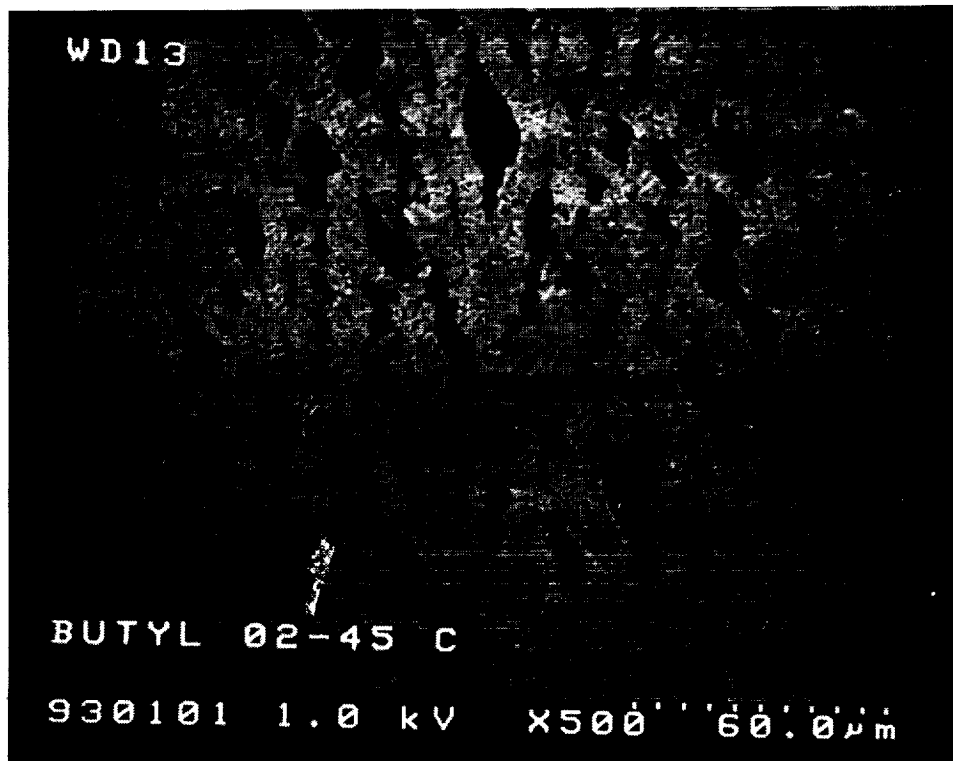


Figure 14. Scanning electron microscope images of a butyl rubber o-ring postflight at 100X and 500X magnification. This o-ring was flown under 80% tension.



Figure 15. Fluorescence behavior of the silicone rubber o-ring postflight.

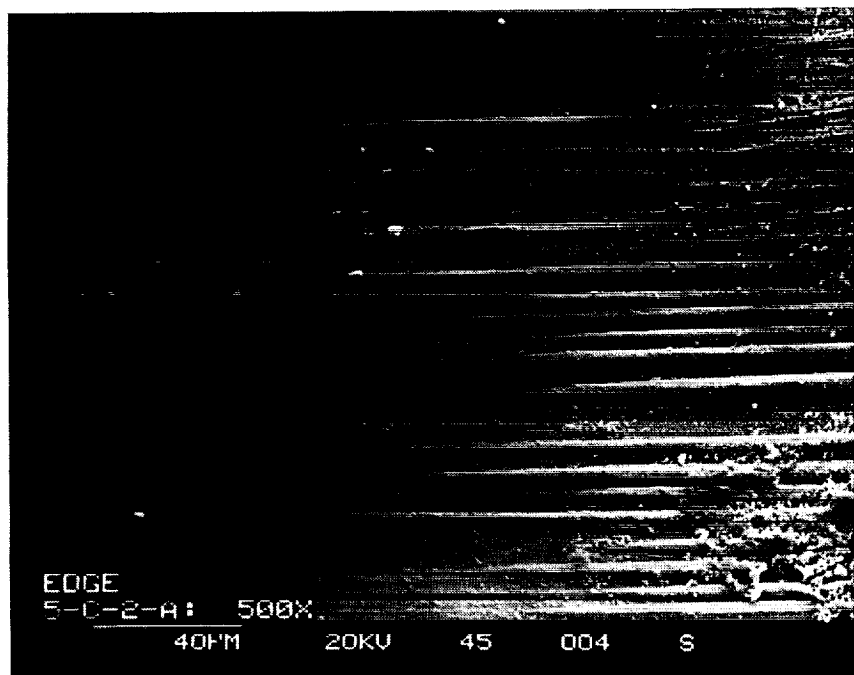
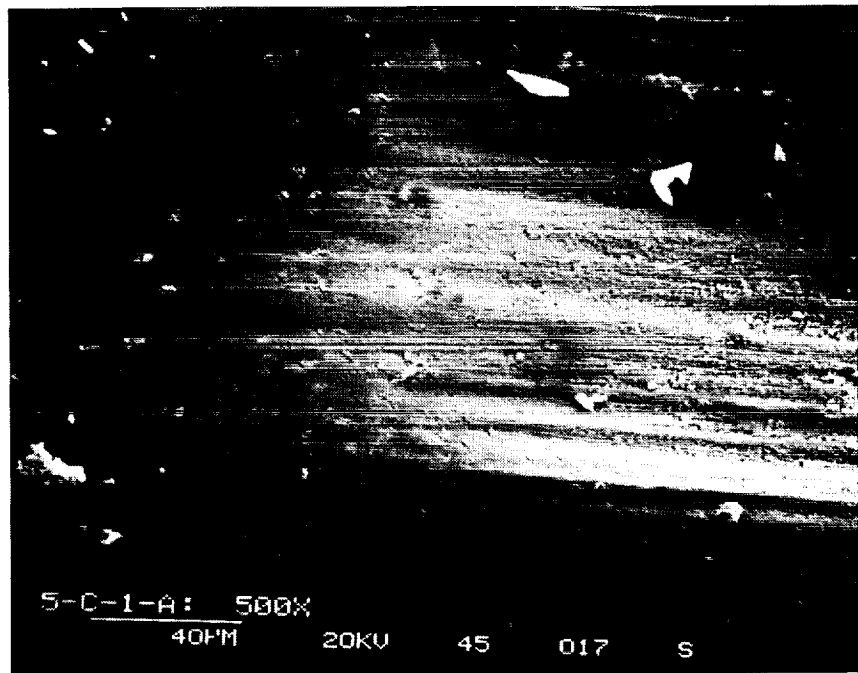


Figure 16. Scanning electron microscope images of two graphite/epoxy composite specimens at 500X magnification. The specimens were each flown on LDEF and then the EOIM-III experiment. The top image is of a specimen directly exposed to space on LDEF. The bottom image is of a specimen shielded by other specimens on LDEF.

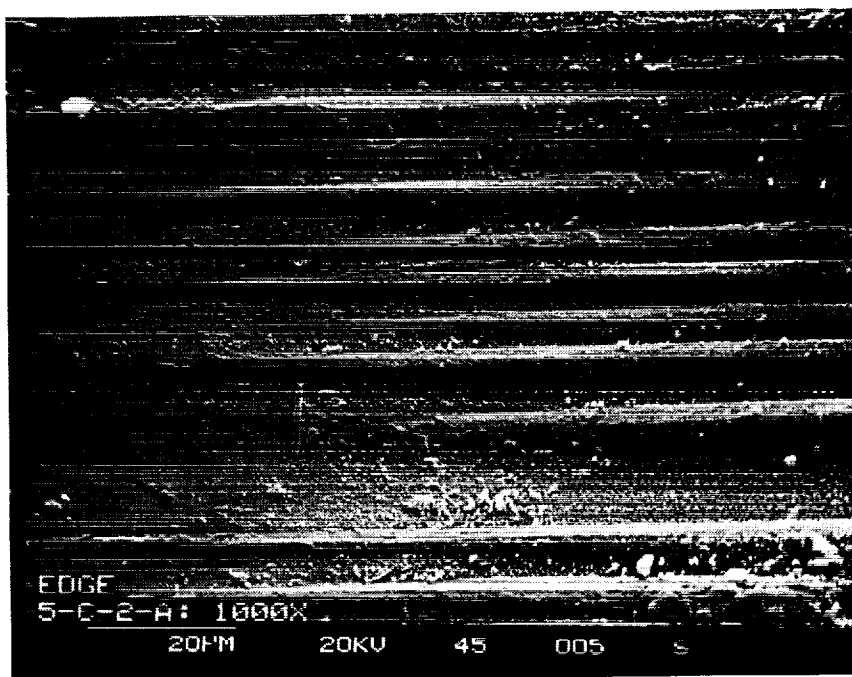
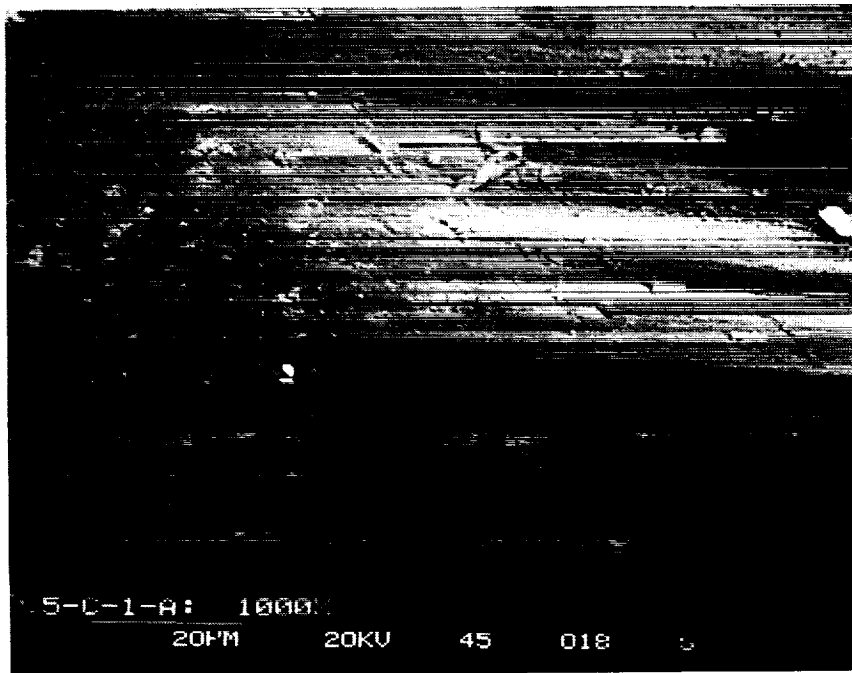


Figure 17. Scanning electron microscope images of two graphite/epoxy composite specimens at 1000X magnification. The specimens were each flown on LDEF and then the EOIM-III experiment. The top image is of a specimen directly exposed to space on LDEF. The bottom image is of a specimen shielded by other specimens on LDEF.

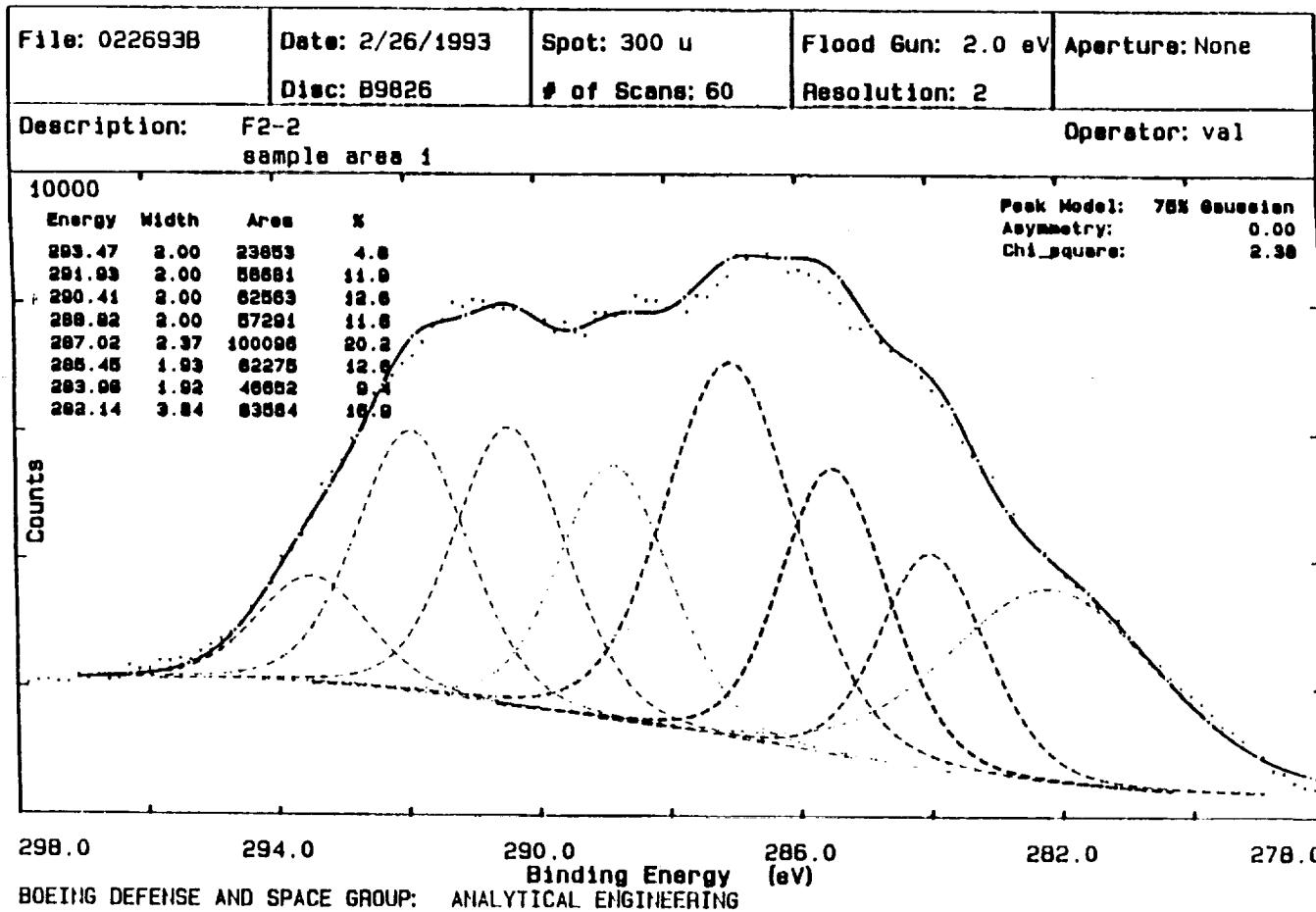


Figure 18. ESCA measurement of Ag/FEP specimen from LDEF tray F2, analyzing the carbon 1s binding energy region.

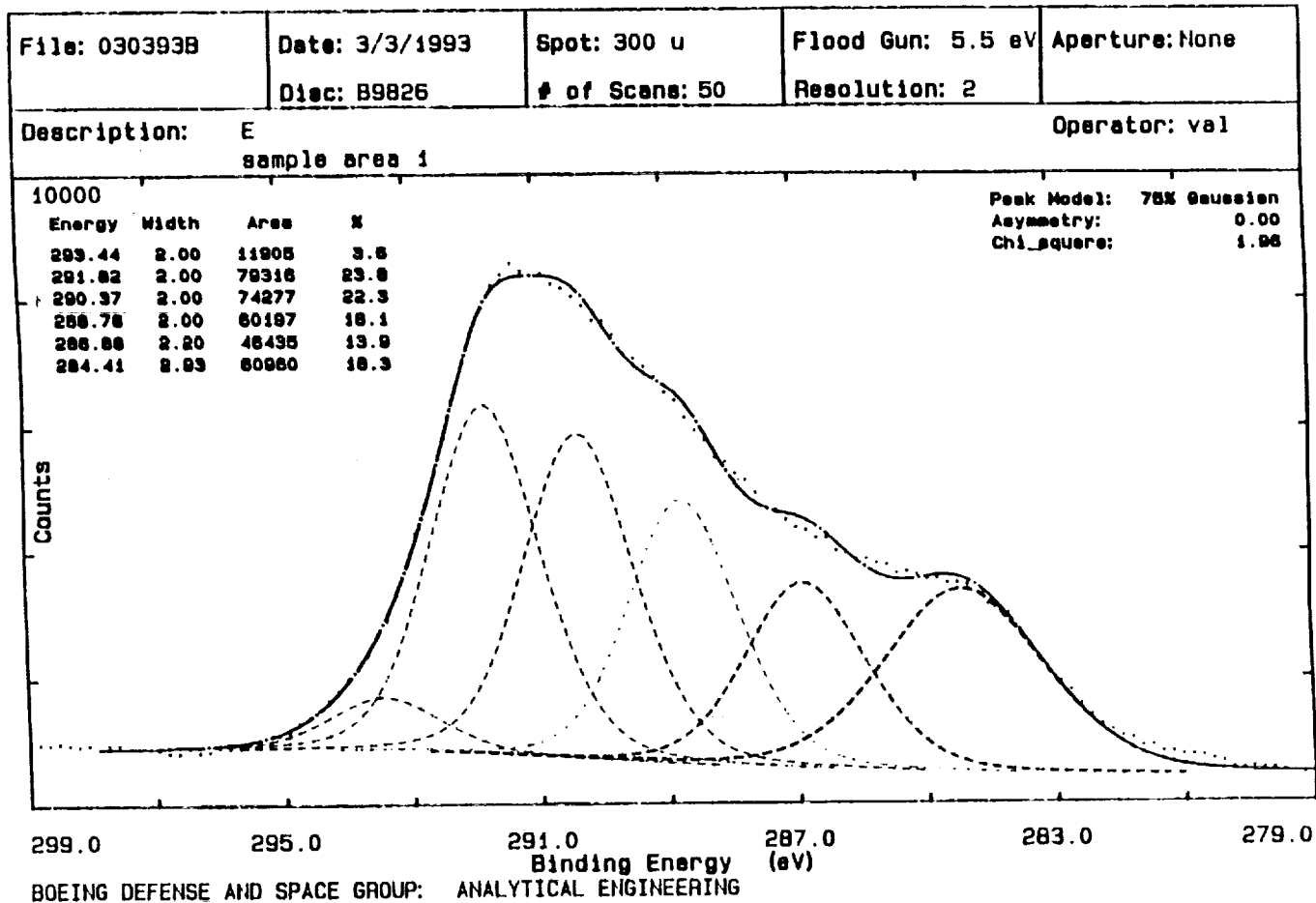


Figure 19. ESCA measurement of Ag/FEP specimen from LDEF tray F2, reflown on EOIM III, analyzing the carbon 1s binding energy region.

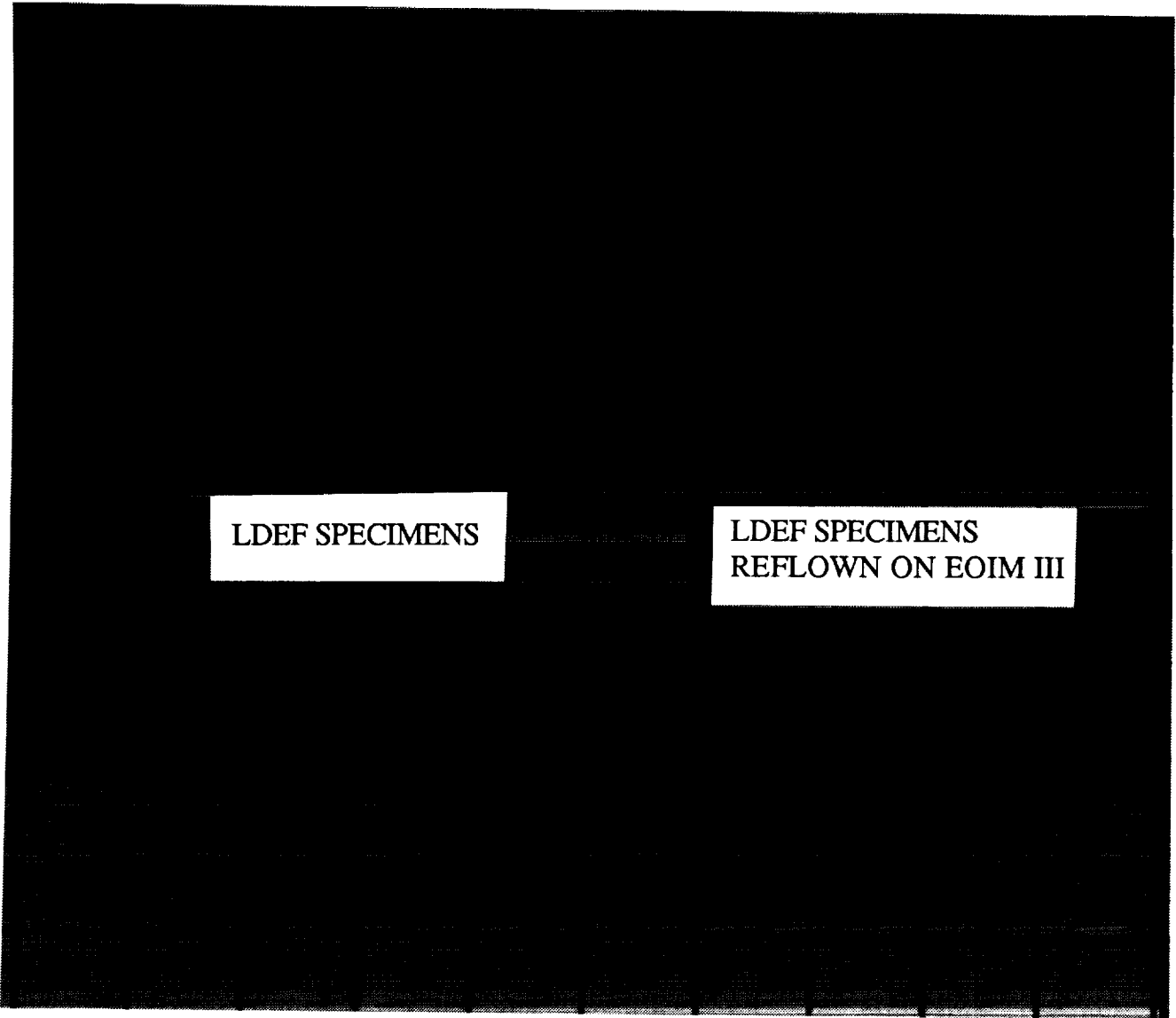


Figure 20. Chemglaze A276 polyurethane paint specimens previously flown on LDEF, shown with and without environmental exposure on EOIM-III.

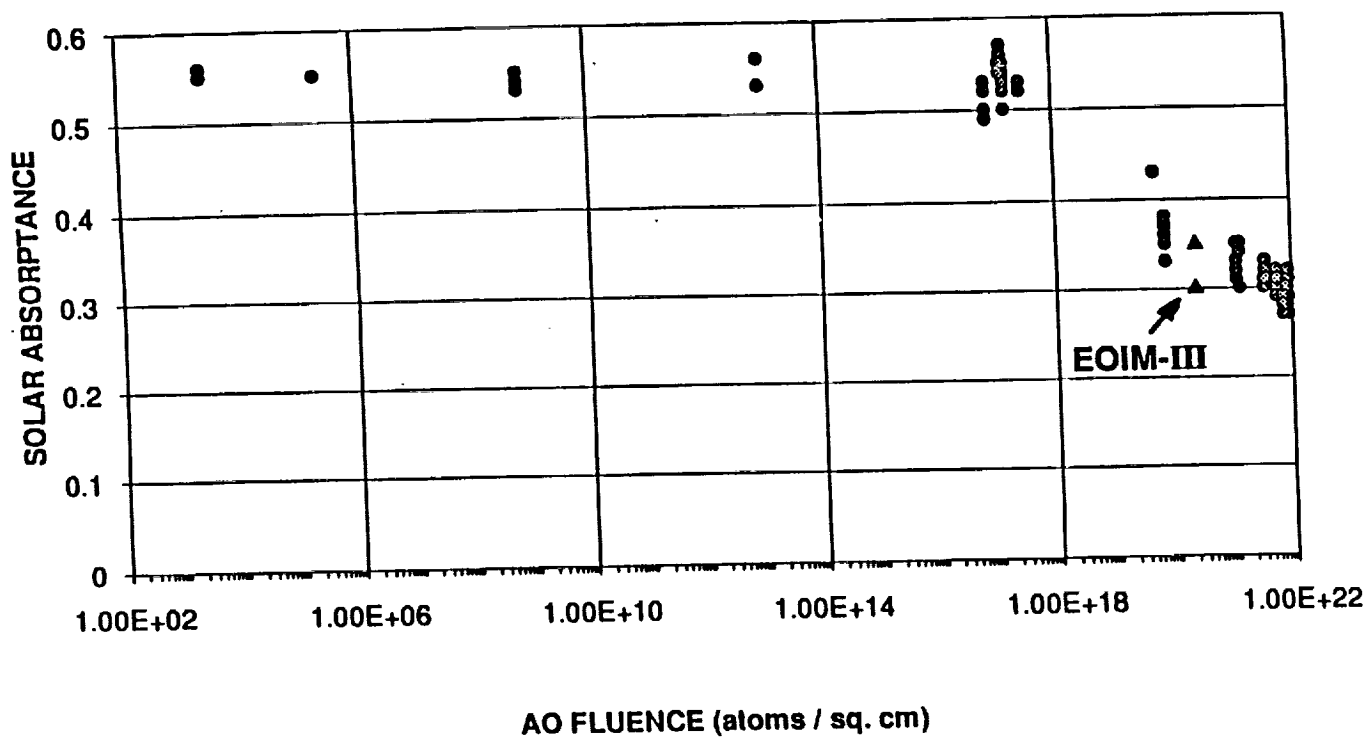


Figure 21. Comparison of solar absorbance results for EOIM-III specimens of Chemglaze A276 to those obtained for overall LDEF mission, as a function of atomic oxygen fluence. The LDEF data is shown by the filled circles and the EOIM-III data is shown by the filled triangles.

**MOLECULAR BEAM SCATTERING FROM ¹³C-ENRICHED KAPTON AND
CORRELATION WITH THE EOIM-3 CAROUSEL EXPERIMENT**

Timothy K. Minton

Jet Propulsion Laboratory

Mail Stop 67-201

4800 Oak Grove Dr.

Pasadena, CA 91109

Phone: 818/354-8580, FAX: 818/393-6869

Teresa A. Moore

Division of Chemistry and Chemical Engineering

California Institute of Technology

Pasadena, CA 91125

Phone: 818/354-6128, FAX: 818/393-6869

SUMMARY

Mass spectra of products emerging from identical samples of a ¹³C-enriched polyimide polymer (chemically equivalent to Kapton) under atomic oxygen bombardment in space and in the laboratory were collected. Reaction products unambiguously detected in space were ¹³CO, NO, ¹²CO₂, and ¹³CO₂. These reaction products and two others, H₂O and ¹²CO, were detected in the laboratory, along with inelastically scattered atomic and molecular oxygen. Qualitative agreement was seen in the mass spectra taken in space and in the laboratory; the agreement may be improved by reducing the fraction of O₂ in the laboratory molecular beam. Both laboratory and space data indicated that CO and CO₂ products come preferentially from reaction with the imide component of the polymer chain, raising the possibility that the ether component may degrade in part by the "evaporation" of higher molecular weight fragments. Laboratory time-of-flight distributions showed 1) incomplete energy accommodation of impinging O and O₂ species that do not react with the surface and 2) both hyperthermal and thermal CO and CO₂ products, suggesting two distinct reaction mechanisms with the surface.

INTRODUCTION

Recently, a protocol¹ has been written with the objective of providing "guidelines for materials testing in ground-based atomic oxygen environments for the purpose of predicting the durability of the tested materials in low Earth orbit (LEO)." The validity of testing under this protocol, or any other set of criteria, rests on the proven ability of the ground-based test facility to produce results that can be related in a straightforward manner to atomic-oxygen-induced effects on

materials in LEO. Both space- and ground-based studies on identical materials are required to evaluate ground-based test methods aimed at predicting materials durability in space. Such a ground-space correlation study, which involved materials exposure on the EOIM-3 flight experiment, has been reported.²

Proven agreement between laboratory and space experiments also adds value to the results of scientific experiments in the laboratory. It is much easier to perform sophisticated experiments in the laboratory than in space. Laboratory experiments therefore have the potential to reveal more information than space experiments about the interaction mechanisms of hyperthermal oxygen atoms with materials in LEO. The extent to which the laboratory results can lead to inferences about O-atom interactions in LEO depends on the ability of the laboratory experiment to predict effects seen in the actual LEO environment.

The EOIM-3 carousel experiment provided an ideal "calibration point" for powerful molecular beam/surface scattering experiments that can be conducted at the Jet Propulsion Laboratory (JPL). This report contains new data, both from EOIM-3 and from our laboratory at JPL, on the interaction of hyperthermal O atoms with an isotopically-labeled, Kapton-like polyimide surface. The molecular beam experiment provides the capability to examine the identity of products that emerge from the surface, as well as their directions and velocities. These diagnostic capabilities permit the interaction dynamics of fast O atoms with a surface to be inferred. The EOIM-3 carousel experiment yields information only on the identity of the scattered species; nevertheless, this information provides a common point of reference for assessing the value of the laboratory results. The new laboratory results agree qualitatively with the space observations and point the way to a clearer understanding of O-atom interactions with materials in LEO.

EXPERIMENTS

Reactive Scattering in Space

A key active experiment on EOIM-3 was the carousel experiment. This experiment has been described in detail in other papers in this session and will be briefly reiterated here with emphasis on the JPL role in the experiment. Five different materials were mounted on a carousel such that the surface normal of each material was 45° with respect to the direction of O-atom attack during exposure to atomic oxygen. The carousel could be rotated to place an individual material in view of a mass spectrometer detector whose nominal viewing axis was 90° with respect to the direction of O-atom impingement. One goal of the carousel experiment was to study the mass spectra of reactive products emerging from the surfaces and use the identity of the volatile products to help infer the reaction mechanisms of fast O atoms in space with the various surfaces. A cover was rotated over the viewed material part of the time to allow for the observation of the differences between the effect of direct O-atom attack and that of scattered O atoms.

JPL supplied one of the carousel materials, a ^{13}C -enriched polyimide polymer that is chemically equivalent to Kapton HN, which is manufactured by E. I. DuPont de Nemours and Co., Inc. ^{13}C -enrichment permits the observation of carbon monoxide (CO) reactive product, which would otherwise be obscured by the high background at a mass-to-charge ratio (m/z) of 28 due to molecular nitrogen in the residual atmosphere in LEO. In addition, detection of ^{13}CO and $^{13}\text{CO}_2$ proves unambiguously that products of the reaction of the impinging O atoms with the ^{13}C -enriched polyimide are being observed.

Because the ^{13}C -enriched polyimide is chemically equivalent to Kapton, we will henceforth refer to it as ^{13}C -enriched Kapton. Figure 1 illustrates the key steps in the synthesis of ^{13}C -enriched Kapton. All the carbons in one precursor, the ether, were carbon-13. Thus, the resulting polyimide film had in its repeat unit a biphenyl ether block containing twelve carbon atoms that were isotopically labeled as ^{13}C and an imide block containing ten unlabeled carbon atoms.

Figure 2 shows representative mass spectra taken with the mass spectrometer viewing the ^{13}C -enriched Kapton sample when the cover was off and when the cover was on. These data indicate that the net mass spectrum for direct reaction of O atoms with ^{13}C -enriched Kapton cannot be obtained simply by subtracting the cover-on spectrum from the cover-off spectrum. Even when the cover is on, a small peak from $^{13}\text{CO}_2$ can be seen; therefore, scattered O atoms must be reacting with the sample. If the cover were off, some of these reactions might not occur. Without substantial modeling of O-atom inelastic scattering from various surfaces on the EOIM-3 tray, it is difficult to know exactly how to represent the space data. The true mass spectrum for direct O-atom attack probably lies somewhere between the cover-off spectrum and the spectrum that is the difference of cover on and cover off.

Reactive Scattering in the Laboratory

We have initiated a study of the reaction of hyperthermal O atoms with a Kapton surface in the laboratory with the use of a crossed molecular beams apparatus.^{3,4} This apparatus (see Fig. 3) allows beam/surface scattering experiments similar to the EOIM-3 carousel experiment, but it is much more powerful because it permits determination of the velocities and directions of scattered products that emerge from a surface. The atomic oxygen beam source is basically a copy of the source designed by Physical Sciences, Inc. (PSI),⁵ where CO_2 laser detonation of oxygen gas is used to produce a pulsed beam of fast O atoms with translational energies near 5 eV. Our source utilizes a home-built piezoelectric pulsed molecular beam valve⁶ to inject O_2 gas into the conical nozzle and a 5 J/pulse Alltec CO_2 laser to induce breakdown in the gas. The pulse repetition rate of the source was 1.8 Hz. For the scattering experiments described herein, the central portion of the hyperthermal beam was selected with a 3 mm dia. aperture (or "skimmer"), placed 80 cm from the apex of the conical nozzle, and allowed to impinge on a target, 92 cm from the apex of the nozzle, that was mounted on the end of a manipulator. Based on Kapton erosion measurements, we estimate the atomic oxygen flux at the target to be on the order of 10^{14} atoms/cm²/pulse. A quadrupole mass spectrometer with a triply differentially pumped ionizer can be rotated about the interaction zone on the surface and can detect inelastically and reactively scattered products that

emerge from the surface in a particular direction. The distance from the surface to the ionizer of the detector is 34.5 cm, and the detector viewing angle is 3° . The mass spectrometer has been carefully designed with apertures that permit any products entering the ionizer to pass through into another differentially-pumped region. The probability of species, which pass through without being ionized, scattering back into the ionizer is therefore extremely low. Thus, measurements of the time-of-flight (TOF) distributions of species entering the detector give a true reflection of their kinetic energies. The target can be lowered out of the beam and the detector can be positioned directly along the beam axis in order to characterize the O-atom beam. When viewing the beam directly, a very small .12 mm diameter aperture is used on the front of the detector to prevent gas buildup in the ionization region.

Two samples of Kapton film, one ^{13}C -enriched and the other DuPont Kapton HN, were mounted on the end of the manipulator such that either sample could be placed in the beam path without breaking vacuum. The temperature of the sample mount was maintained at 340 K. Although the pressure in the source chamber rose to $\sim 5 \times 10^{-4}$ Torr during the pulse, the pressure in the main scattering chamber remained $\leq 2 \times 10^{-7}$ Torr during the entire experiment. The source chamber was evacuated with a 10" Varian VHS-10 oil diffusion pump, which had a water baffle that was cooled with a refrigerated liquid to 250 K. The main scattering chamber was evacuated with two 10" CTI-10 cryopumps and a liquid nitrogen cryopanel that covered the bottom of the chamber. Even with cryopumping of the main chamber and scrupulous cleaning of the samples with ultraclean ethanol prior to mounting in the chamber, a contamination layer accumulated on the samples. Although some contamination was probably being deposited constantly during exposure and thus erosion of the surface, a steady-state condition could be reached where we were certain that we were observing products of a reaction with the actual sample material and not a contamination layer on it. As will be seen below, the use of a ^{13}C -labeled sample proved that a reaction was occurring with the material. Two different means were used to rid the sample of contamination and reach steady state, as determined by observation of reactive TOF signals at CO and CO₂ product masses. One method was simply to expose the target to oxygen atoms for a long time, $> 10,000$ pulses. To reach steady state faster, we exposed the surface to a beam of 20 keV electrons during O-atom exposure. The electron gun was oriented such that the electron beam was roughly normal to the target surface when the O-atom beam incident angle was 45° . We found that about 5 minutes of electron exposure at fluxes between 1 and $10 \mu\text{A}/\text{cm}^2$ cleaned the surface sufficiently that subsequent reactive signals were identical to those seen after more than 10,000 pulses of the atomic oxygen beam alone. Because both methods led to identical reactive signals, it appeared that the short electron exposure did not alter the chemical reactions occurring at the surface. All the laboratory data presented in this report were collected after "cleaning" the surface with the electron beam.

Figure 4 shows TOF spectra collected with the mass spectrometer directly viewing the beam. Time zero is when the pulsed valve is triggered to open. At this time, oxygen gas begins to enter the conical nozzle. The spike about $250 \mu\text{s}$ later corresponds to the firing of the CO₂ laser. This can be considered the actual time zero for the formation of the hyperthermal beam pulse. The spike comes from photoelectrons produced in the detector by ultraviolet light emanating from the laser-induced plasma. The pulse of hyperthermal species arrives at the detector around $200 \mu\text{s}$ after the laser fires. Thermal O₂, which is not processed by the laser, takes more than 2 ms to travel 126.5 cm to the ionizer. These and all TOF distributions presented here include the ion flight time, which

is the time required for an ion to travel from the ionizer to the Daly-type ion counter. The ion flight time for a singly-charged ion of mass m has been found experimentally, and it can be expressed in μs by the formula $\alpha(m)^{1/2}$ where the parameter α is a function of ion energy and other mass spectrometer parameters and is equal to 2.24.

It can be seen from Fig. 4 that the fast species in the beam consist of both atomic and molecular oxygen. In fact, for the set of experiments discussed in this report, the O_2 content was roughly twice the O-atom content. The relative O-atom content in the hyperthermal beam pulse is very sensitive to the actual operating conditions of the source. We have observed O-atom fractions from 25-70% in beams produced in our laboratory. The ion content in a similar beam has been measured at PSI to be about 1%, which should be considered an upper limit for our beam. With the ionizer off, there is a tiny signal at $m/z = 16$ (or 32) whose integral is more than three orders of magnitude lower than the signal with the ionizer on. Given that the detection efficiency should be approximately four orders of magnitude higher for ions, the ion fraction in the beam is probably much less than 1%.

Because we measure the arrival time and mass of species that travel a known distance from the source to the ionizer, we can derive the energy distribution of the species in the beam pulse (assuming that the width in the measured TOF distributions is determined by particles traveling at different velocities with a single point of origin in the nozzle cone). We need only take into account the fact that the mass spectrometer is a number density detector while the translational energy distribution is proportional to flux. We thus use the relationship $P(E) \propto t^2 N(t)$. Figure 5 shows the translational energy distribution of the O-atoms in the beam and the fit this distribution gives to the beam TOF distribution. The average energy of this beam was 4.7 eV, and its width (FWHM) was 2.5 eV. Figure 6 shows the analogous energy distribution and fit for the O_2 molecules in the beam. The O_2 component had a much higher average energy (8.7 eV) and energy spread (5.5 eV) than the O-atom component.

The hyperthermal beam, just described, was directed at Kapton and ^{13}C -enriched Kapton surfaces, and scattered products were monitored with the mass spectrometer detector. The angle of incidence was 45° with respect to the surface normal, and the detector axis was also 45° . Thus, the total included scattering angle was 90° , similar to the EOIM-3 carousel experiment. The beam pulse provided the timing for the experiment; no additional chopping was used. TOF distributions of scattered products were collected at $m/z = 16(\text{O}^+)$, $18(\text{H}_2\text{O}^+)$, $28(^{12}\text{CO}^+)$, $29(^{13}\text{CO}^+)$, $30(\text{NO}^+)$, $32(\text{O}_2^+)$, $44(^{12}\text{CO}_2)$, and $45(^{13}\text{CO}_2)$. Typical accumulation times for each TOF distribution were 1200 beam pulses. The time resolution was limited by our multichannel scaler to $2 \mu\text{s}/\text{channel}$. All data were collected before a total O-atom fluence of 2×10^{18} atoms/cm² was accumulated on either surface, so the familiar "shag-carpet" morphology was not fully developed.

LABORATORY SCATTERING RESULTS

TOF distributions for O and O_2 scattering from the ^{13}C -enriched surface are shown in Figure 7. Time zero in these distributions corresponds to the firing of the laser, so the observed arrival

time includes the flight time of the beam pulse to the surface and the flight time of scattered products from the surface to the detector. For reference, the respective beam TOF distributions are shown (dashed lines) to illustrate the slowing of the impinging species as a result of energy transfer at the surface. While the O-atom distribution is the result of inelastic scattering from the surface, the O₂ TOF distribution may have an additional contribution from O-atom recombination at the surface. It is difficult to quantify the amount of O-atom recombination without a careful study of the distributions of the scattered molecular and atomic oxygen as a function of exit angle. Nevertheless, the O₂ (and O) exhibits a behavior that is typical for inelastic scattering of energetic species from a surface.⁷⁻¹¹

Regardless of whether O-atoms or O₂ molecules scatter from the surface, we see two components in the TOF distribution -- a hyperthermal component and a roughly thermal component. These two components can be understood in terms of two limiting cases of inelastic scattering.⁷⁻¹¹ The first is direct inelastic scattering, where an incoming atom or molecule bounces off the surface after a single collision. In this case, the interaction is too fast to allow for thermal equilibration with the surface and only a fraction of the initial kinetic energy is lost to the surface. The second case is trapping desorption, where the incoming atom or molecule becomes trapped long enough to come into thermal equilibrium with the surface and later desorbs at thermal energies. Both TOF distributions show a large direct inelastic component, demonstrating clearly that much of the initial energy is not accommodated on the surface. In these particular TOF distributions, the trapping desorption component appears to be enhanced relative to the direct inelastic component because 1) there is an untrue enhancement of the signal at long times due to inelastic scattering of thermalized O atoms and O₂ molecules that effuse out of the source chamber through the skimmer, and 2) species traveling more slowly through the ionizer have a greater probability of being ionized than faster species (the flux $I(t)$ is proportional to $N(t)/t$). Therefore, we estimate that the trapping desorption component is less than 20% for both O and O₂ inelastic scattering. It is important to note that the relative fraction of trapping desorption may vary considerably depending on the initial and final scattering angles.¹¹ The average fractional energy transfer for direct inelastic scattering is also dependent on the initial and final scattering angles. Surface roughness may reduce the fraction of direct inelastic scattering; however, we have observed large direct inelastic scattering components in our laboratory even when O-atoms scatter from the very rough surface of a graphite polysulfone composite material. Finally, for comparison we note that an earlier surface energy accommodation study¹² with roughly 5 eV O atoms impinging on metal and glass surfaces implied a significant amount of direct inelastic scattering with the reported energy accommodation coefficients of approximately $0.6 \pm 50\%$.

Figure 8 shows TOF distributions of carbon dioxide products emerging from the surfaces of Kapton HN and ¹³C-enriched Kapton after being struck by the hyperthermal beam pulse. Again, time zero corresponds to the firing of the laser. On the left is signal from Kapton HN, and on the right is signal from ¹³C-enriched Kapton. As can be seen, the ¹²CO₂ signal from plain Kapton is distributed between ¹²CO₂ and ¹³CO₂ when the reaction occurs with ¹³C-enriched Kapton. The fact that the sum of the signals at the two isotopes from ¹³C-enriched Kapton add up to the signal at the one isotope from plain Kapton HN indicates that the signals must originate from reactions with the actual sample materials and not contamination on them.

Two key observations stand out in the carbon dioxide TOF distributions. First, the $^{12}\text{CO}_2$ signal from ^{13}C -enriched Kapton is higher than the $^{13}\text{CO}_2$ signal even though there are more C-13 carbons in the polymer chain. This observation suggests that volatile CO_2 is coming preferentially from reactions with the imide component of the polymer repeat unit. Second, there are two components in the TOF distributions. It is clear from the bimodal distributions that two kinds of interactions lead to CO_2 products. The faster signal corresponds to products that are ejected from the surface at hyperthermal energies (~ 0.7 eV), and the slower signal corresponds to reaction products that leave the surface at velocities given by the surface temperature. The fast products may come from a direct reaction (Eley-Rideal mechanism¹³) on the surface with carbonyl groups that are part of the polyimide polymer or that accumulate on the surface during O-atom bombardment, or perhaps CO_2 residing on the surface is knocked off by collision-induced desorption. The slow products, on the other hand, are probably the result of a surface reaction that follows initial adsorption of the impinging O atoms on the surface (Langmuir-Hinshelwood mechanism¹³).

We see an analogous behavior for the CO reactive products (Fig. 9). The signal is generally lower, and the relative magnitude of the hyperthermal component is larger.

Figure 10 shows TOF distributions collected at two other product masses, corresponding to H_2O and NO . As expected, there is not much difference between the two forms of Kapton at these unlabeled masses. The shape of the NO^+ TOF distribution is uncertain because the raw data contained a relatively large contribution from inelastic scattering of O_2 , which could still be detected at $m/z = 30$ with the mass spectrometer resolution employed. We therefore estimated the contribution from O_2 to the $m/z = 30$ TOF distribution and subtracted it to arrive at the distribution shown in Fig. 10.

These preliminary data show some interesting features that suggest preferential attack at the imide group in the polymer and two types of interaction mechanisms with the surface, giving rise to thermal and hyperthermal products. A complete understanding of these data will require a detailed study of the TOF distributions at many masses as a function of incident angle, final angle, surface temperature, incident energy, and incident species. For example, the hyperthermal, or direct-reaction, signal may depend strongly on incident energy and exit angle and only weakly on surface temperature, whereas the thermal, or indirect-reaction signal may have a cosine angular distribution regardless of incident kinetic energy, and only a change in surface temperature would affect arrival time.

The observation of more CO and CO_2 products from reaction with the imide component of the polymer raises questions about the fate of the ether component. It appears from our data that the ether component may degrade partly through release of volatile species other than CO or CO_2 . If these volatile species are higher-molecular-weight hydrocarbon fragments, then they could pose a contamination threat on a spacecraft. Future experiments should include a careful search over a wide mass range in order to identify any heavier volatile products that might be evaporating from the surface.

COMPARISON OF LAB AND SPACE RESULTS

The laboratory TOF distributions can be integrated to arrive at a mass spectrum that can be compared with the EOIM-3 carousel mass spectrum from ^{13}C -enriched Kapton. Figure 11 shows two representations of the flight data with the laboratory mass spectrum in the middle. There are four peaks in the flight mass spectrum that can be compared with our laboratory mass spectrum of reactive products: $m/z = 29(^{13}\text{CO}^+)$, $30(\text{NO}^+)$, $44(^{12}\text{CO}_2^+)$, and $45(^{13}\text{CO}_2^+)$. The water peak ($m/z = 18$) is too large and variable in the flight data to be meaningful, and the $m/z = 28$ peak in the flight data is dominated by N_2 , which is in the ambient LEO environment.

The lab data show more $^{12}\text{CO}_2$ than $^{13}\text{CO}_2$, and the same may be true in the space data. The main difference between the lab and flight data is the relatively high ratio of $^{13}\text{CO}_2$ to ^{13}CO products in the lab as compared with space. The apparently high CO_2 signal in the lab might arise from the high O_2 component in the hyperthermal beam (the fraction of O_2 in the EOIM-3 environment is $< 5\%$). Perhaps O_2 adds to radical sites on the surface and/or dissociates on impact, leading to O-atom reactions on the surface. In either case, the level of surface oxidation would increase and thus favor the more highly oxidized form of carbon, i.e., CO_2 .

Although the lab and flight results are preliminary, they do appear similar. Further laboratory studies with a beam much reduced in molecular oxygen may show even better agreement with the space data. It is important to have a common point of agreement between the lab and flight experiments in order to lend credence to the laboratory experiments as representative of the interactions that take place in LEO. Our laboratory experiment is much more sophisticated than the EOIM-3 carousel experiment and can therefore reveal much more about the interaction mechanisms of hyperthermal O atoms with Kapton (or any other material); however, the value of these and future lab results to the space environment and effects community will ultimately be judged by their "calibration" with space experiments.

ACKNOWLEDGEMENTS

The research described in this report was carried out by the Jet Propulsion Laboratory, California Institute of Technology, under contract with the National Aeronautics and Space Administration (NASA). The sponsoring NASA agency was the Materials and Structures Division, Office of Aeronautics and Exploration Technologies. Partial support was also provided by the Space Environmental Effects Program of the Ballistic Missile Defense Organization (BMDO) Innovative Science and Technology Directorate. The authors wish to thank Dr. David Brinza, who conceived and planned the EOIM-3 carousel experiment with the isotopically-labeled Kapton, and Dr. Andre Yavrouian for synthesizing the ^{13}C -enriched Kapton. The assistance of Dr. Mark Hanning-Lee in obtaining the space data presented here is also appreciated.

REFERENCES

1. Minton, T. K.: Protocol for Atomic Oxygen Testing of Materials in Ground-Based Facilities; Version Number 1. JPL Publication 94-02, April 1, 1994.
2. Chung, S. Y.; Brinza, D. E.; Minton, T. K.; Stiegman, A. E.; Kenny, J. K.; and Liang, R. H.: Flight- and Ground-Test Correlation Study of BMDO SDS Materials; Phase I Report. JPL Publication 93-31, December 1993.
3. Lee, Y. T.; McDonald, J. D.; LeBreton, P. R.; and Herschbach, D. R.: Molecular Beam Reactive Scattering Apparatus with Electron Bombardment Detector. *Rev. Sci. Instrum.* **40**, 1402 (1969).
4. Brinza, D. E.; Coulter, D. R.; Chung, S. Y.; Smith, K. O.; Moacanin, J.; and Liang, R. H.: A Facility for Studies of Atomic Oxygen Interactions with Materials. *Proceedings of the 3rd International SAMPE Electronics Conference*, p. 646 (1989).
5. Caledonia, G. E.; Krech, R. H.; and Green, B. D.: A High Flux Source of Energetic Oxygen Atoms for Material Degradation Studies. *AIAA J.* **25**, 59 (1987).
6. Proch, D. and Trickl, T.: A High-Intensity Multi-Purpose Piezoelectric Pulsed Molecular Beam Source. *Rev. Sci. Instrum.* **60**, 713 (1989).
7. Rettner, C. T. and Ashfold, M. N. R.: *Dynamics of Gas-Surface Interactions; Advances in Gas-Phase Photochemistry and Kinetics Series.* (Royal Society of Chemistry, Cambridge, 1991).
8. Rettner, C. T.; Schweizer, E. K.; and Mullins, C. B.: Desorption and Trapping of Argon at a 2H-W(100) Surface and a Test of the Applicability of Detailed Balance to a Nonequilibrium System. *J. Chem. Phys.* **90**, 3800 (1989).
9. Rettner, C. T.; Barker, J. A.; and Bethune, D. S.: Angular and Velocity Distribution Characteristic of the Transition between the Thermal and Structure Regimes of Gas-Surface Scattering. *Phys. Rev. Lett.* **67**, 2183 (1991).
10. Saecker, M. E.; Govoni, S. T.; Kowalski, D. V.; King, M. E.; and Nathanson, G. M.: Molecular Beam Scattering from Liquid Surfaces. *Science* **252**, 1421 (1991).
11. King, M. E.; Nathanson, G. M.; Hanning-Lee, M. A.; and Minton, T. K.: Probing the Microscopic Corrugation of Liquid Surfaces with Gas-Liquid Collisions. *Phys. Rev. Lett.* **70**, 1026 (1993).
12. Krech, R. H.; Gauthier, M. J.; and Caledonia, G. E.: High Velocity Atomic Oxygen/Surface Accommodation Studies. *J. Spacecraft and Rockets* **30**, 509 (1993).
13. Atkins, P. W.: *Physical Chemistry* (Freeman, New York, 1986) 3rd ed., pp. 782-3.

¹³C - Enriched Kapton

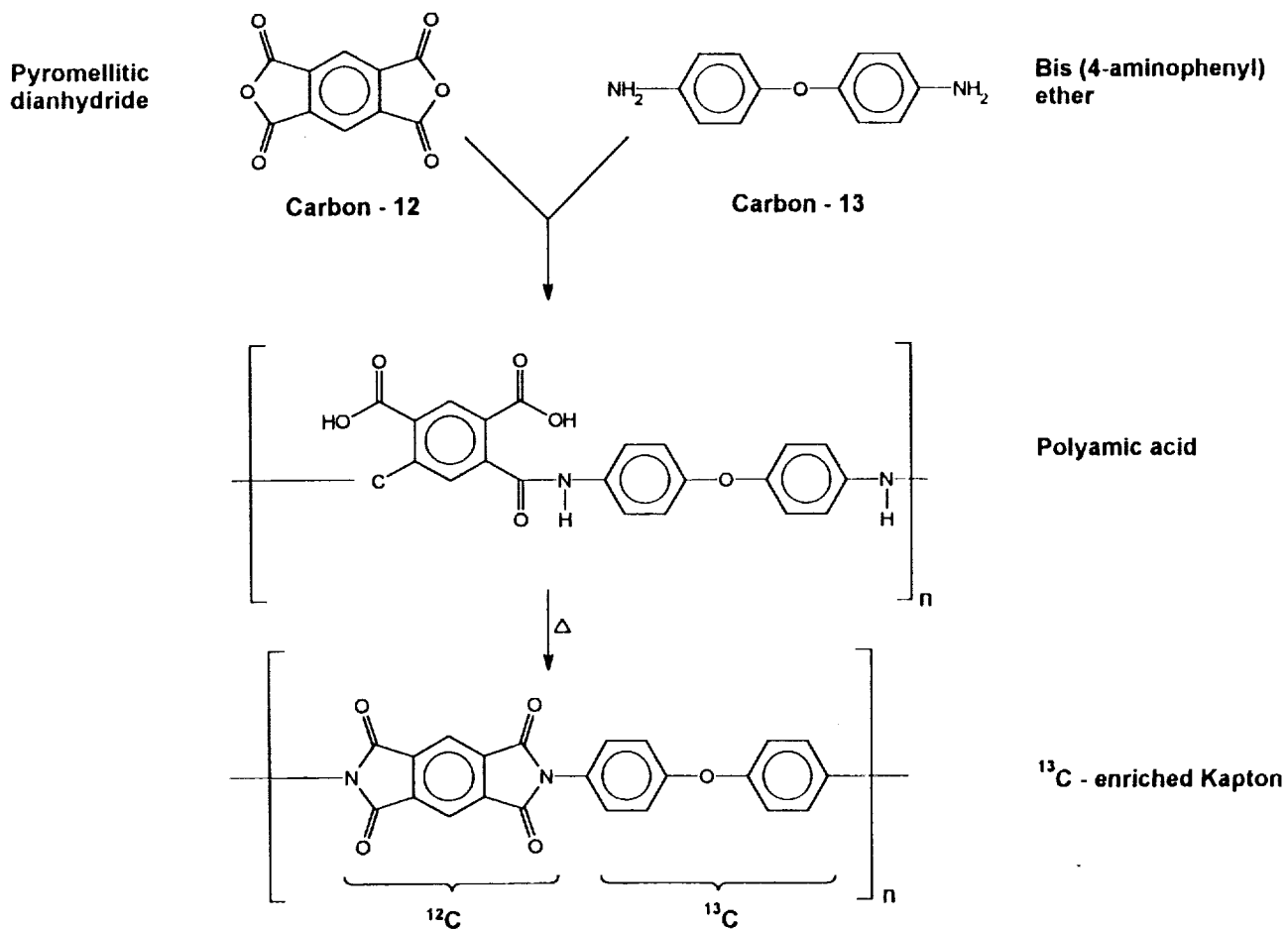


Figure 1. Key steps in the synthesis of ¹³C-enriched "Kapton."

EOIM-3 ^{13}C -enriched "Kapton"

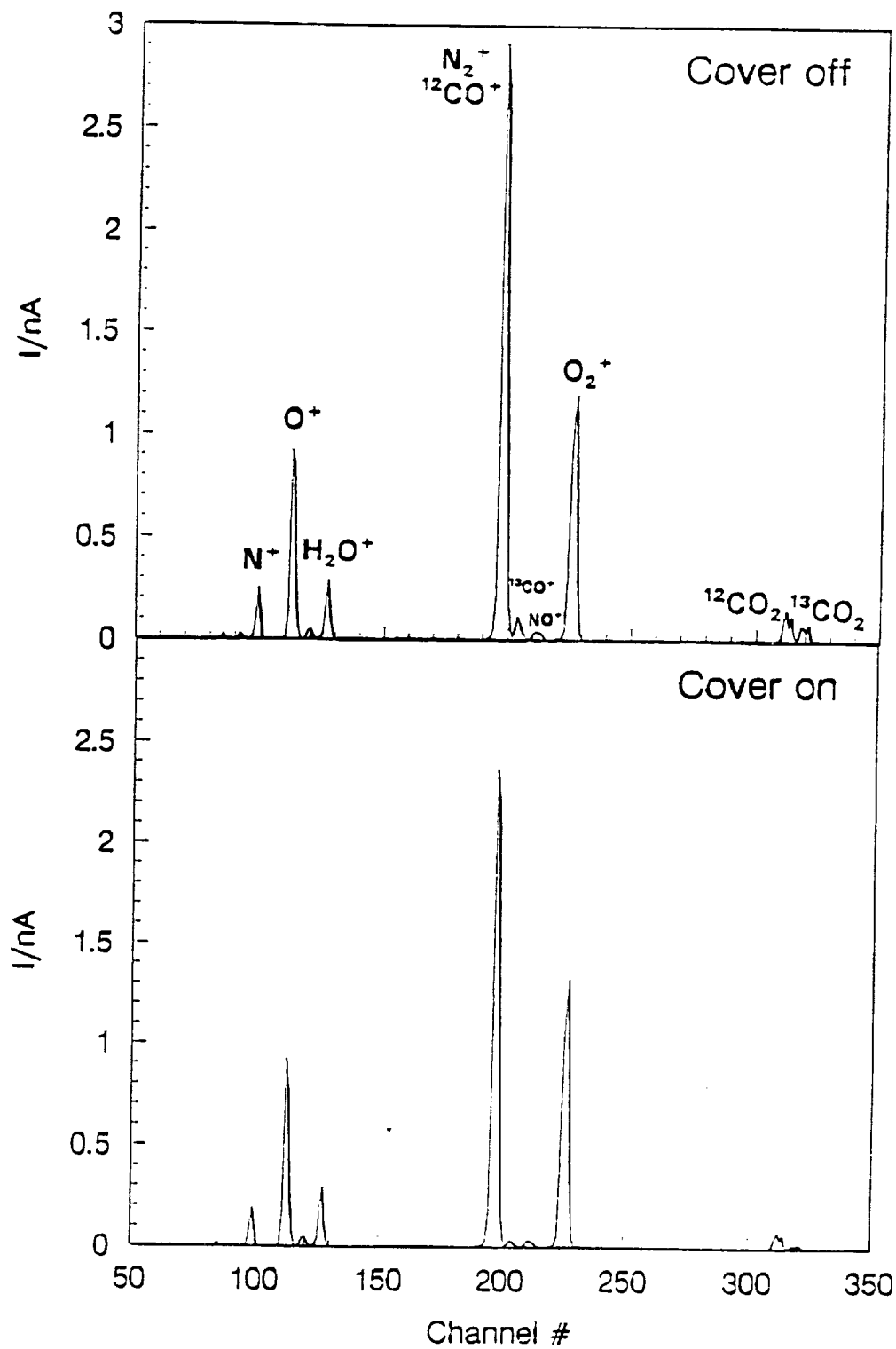
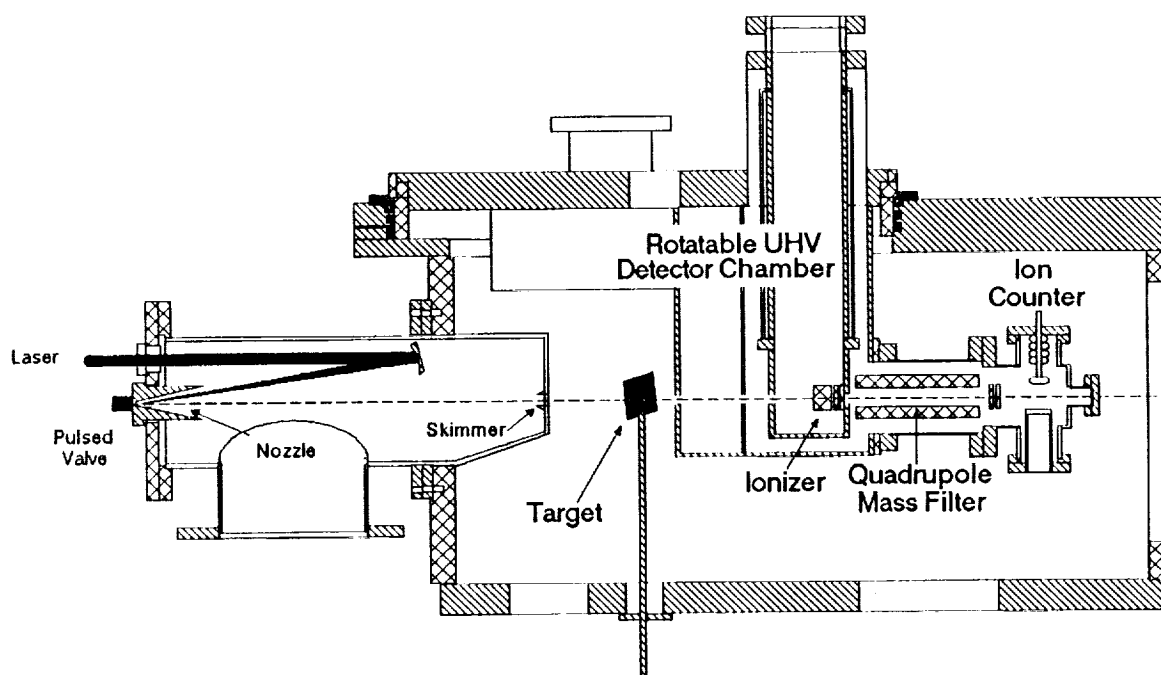


Figure 2. Mass spectra taken with EOIM-3 mass spectrometer viewing ^{13}C -enriched Kapton on the carousel.

JPL Crossed Molecular Beams Apparatus



Hyperthermal Beam – Surface Studies

Figure 3. Schematic diagram of molecular beam apparatus.

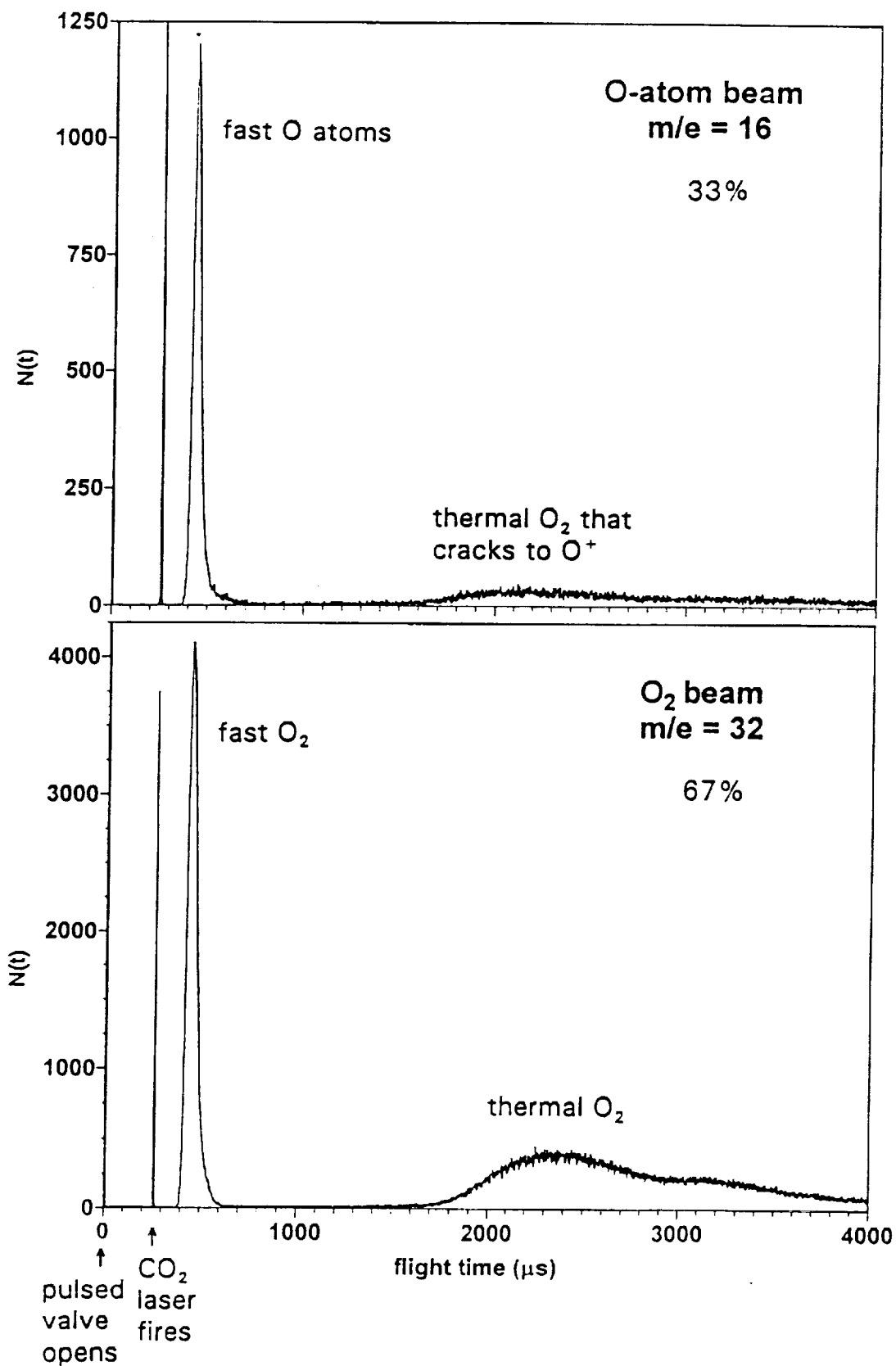


Figure 4. Time-of-flight distributions of the molecular beam collected at two masses.

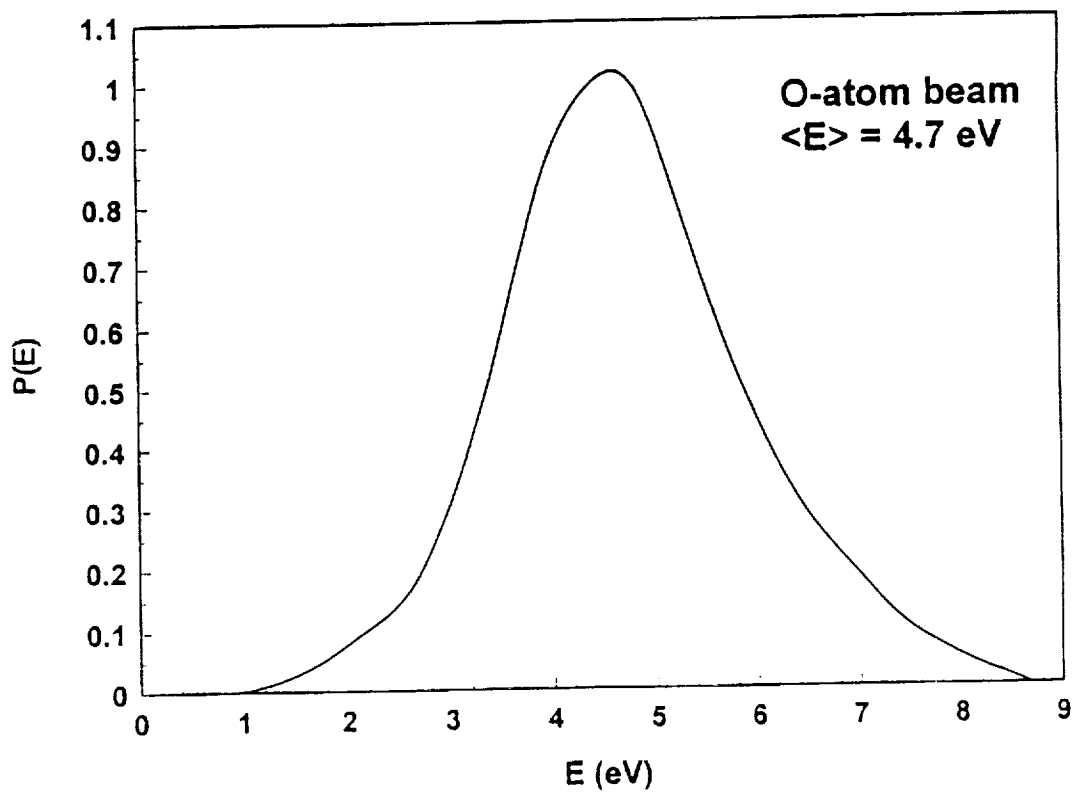
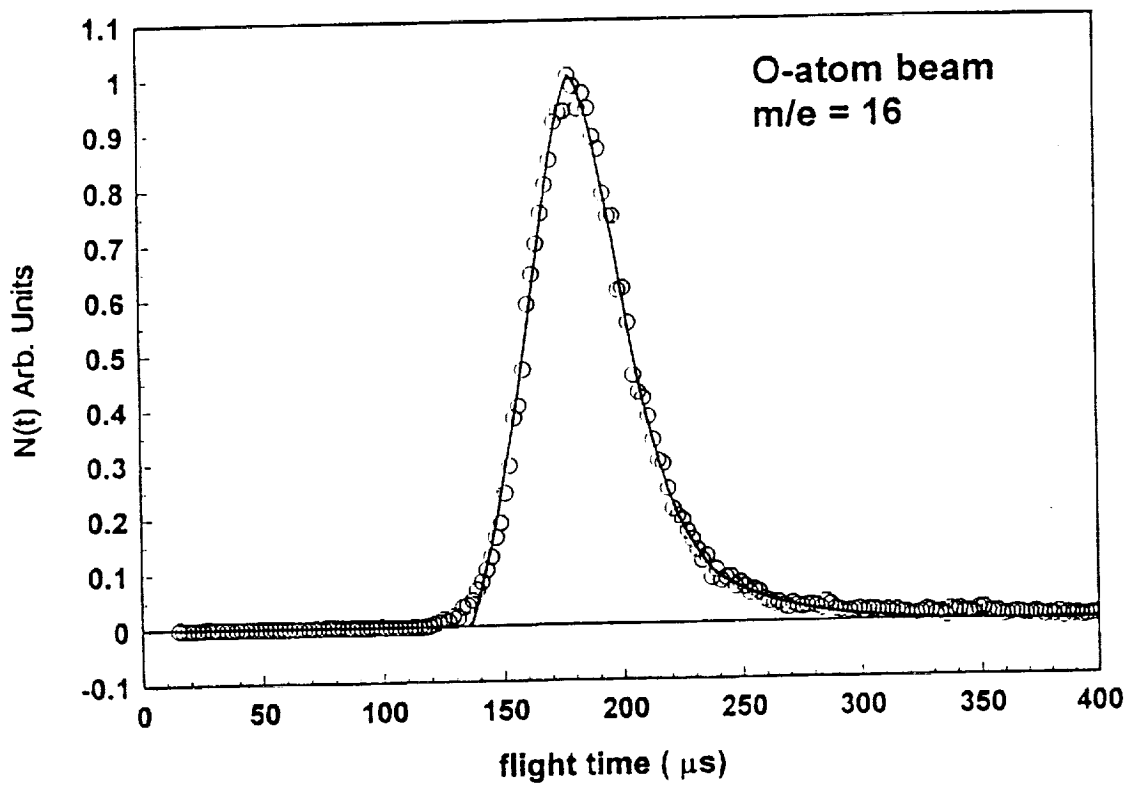


Figure 5. Time-of-flight and translational energy distributions of the O-atom component in the molecular beam.

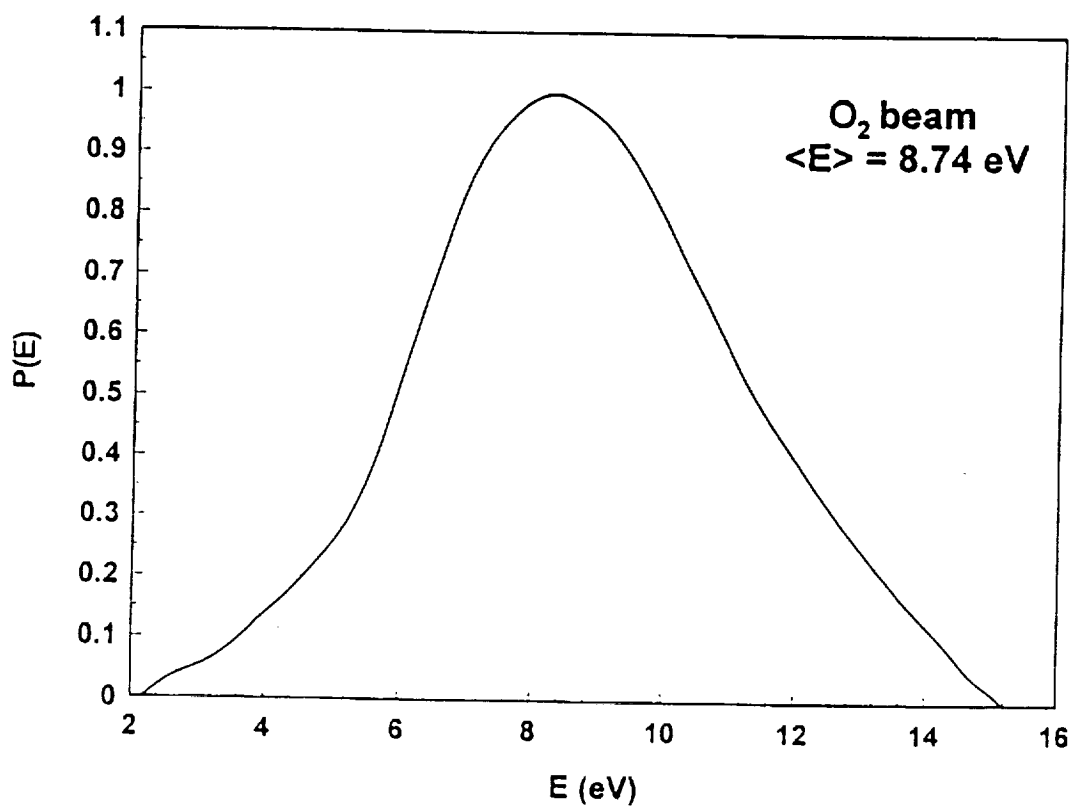
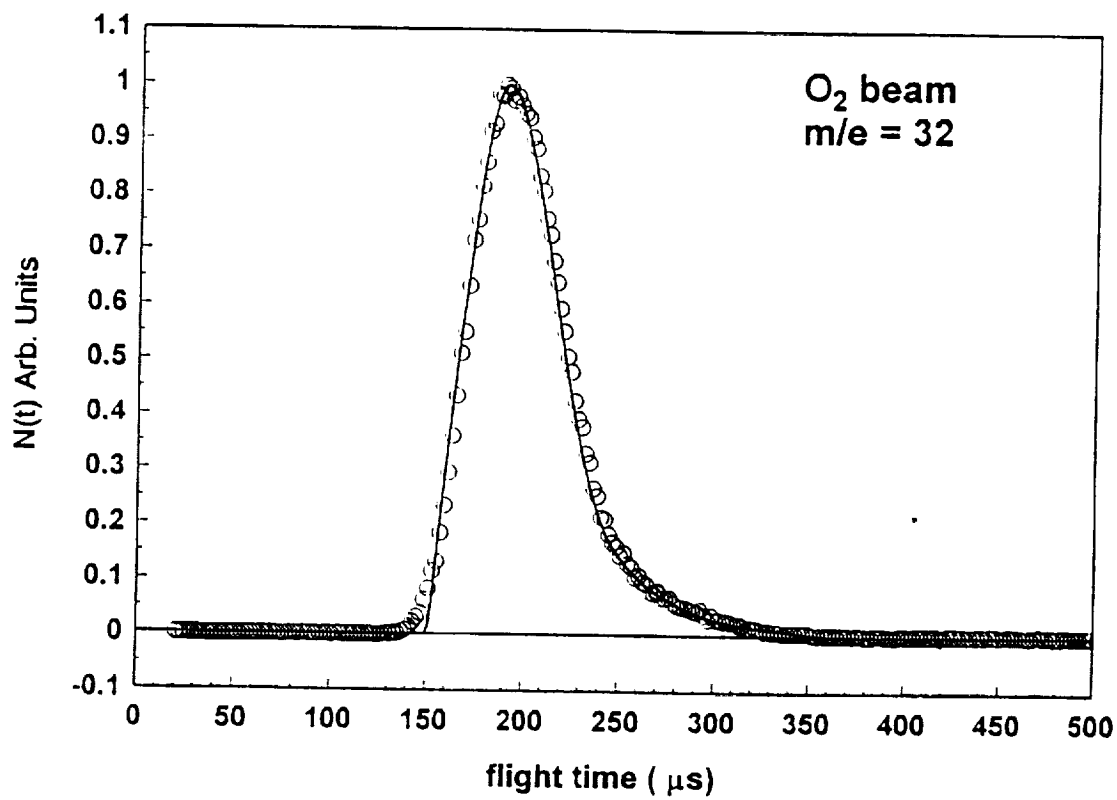


Figure 6. Time-of-flight and translational energy distributions of the fast O₂ component in the molecular beam.

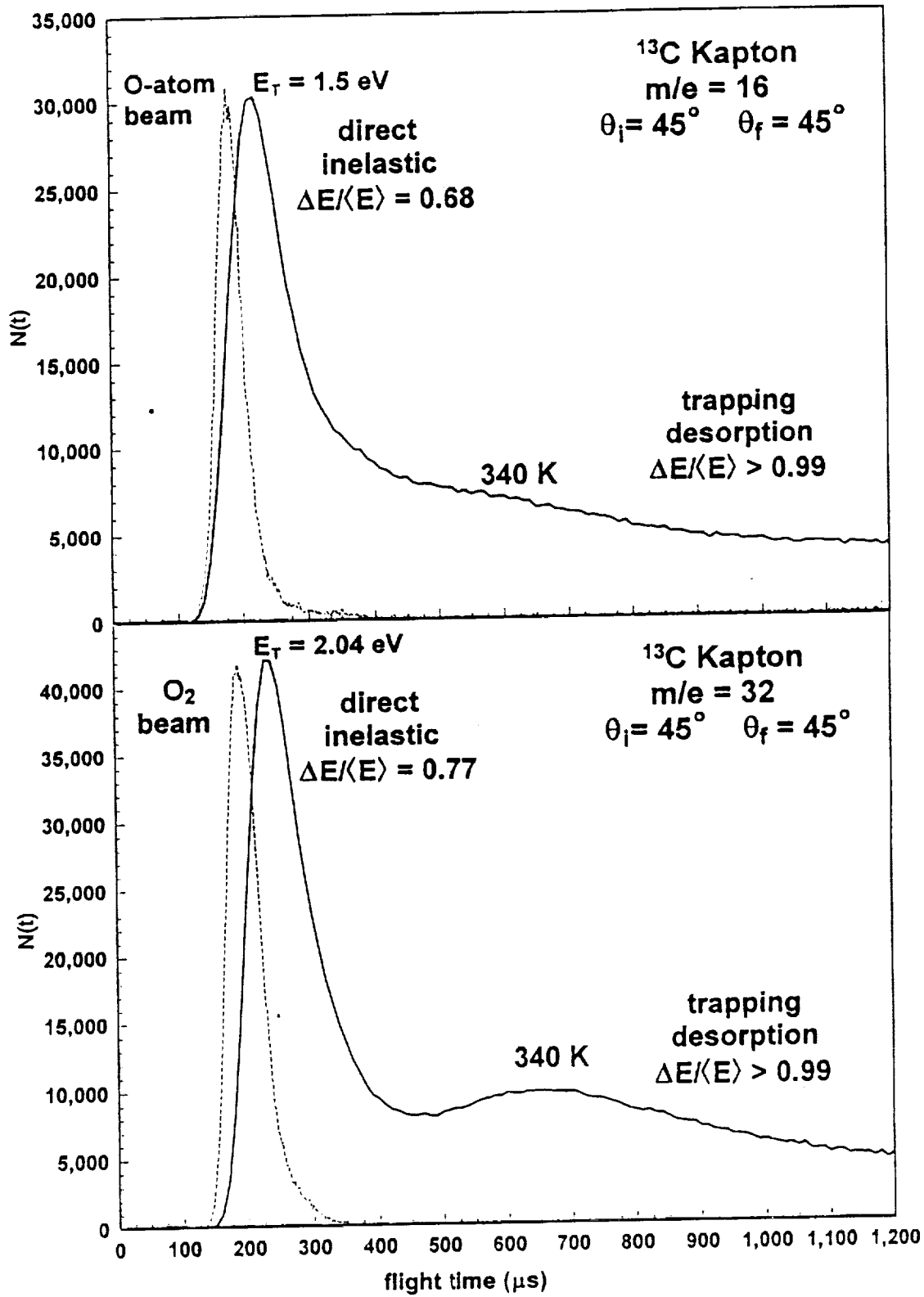


Figure 7. Time-of-flight distributions of O and O₂ scattered from a ^{13}C -enriched Kapton surface.

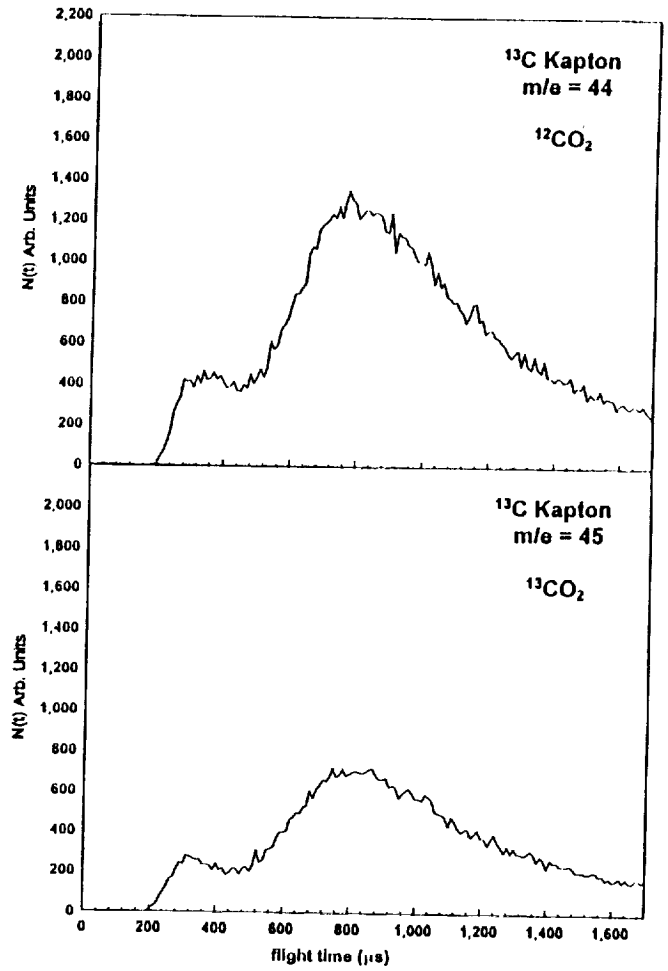
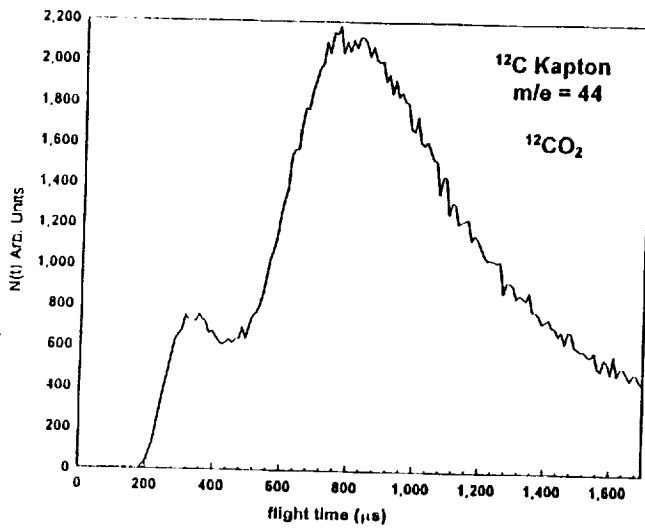


Figure 8. Time-of-flight distributions of CO_2 products emerging from Kapton HN (^{12}C Kapton) and ^{13}C -enriched Kapton surfaces.

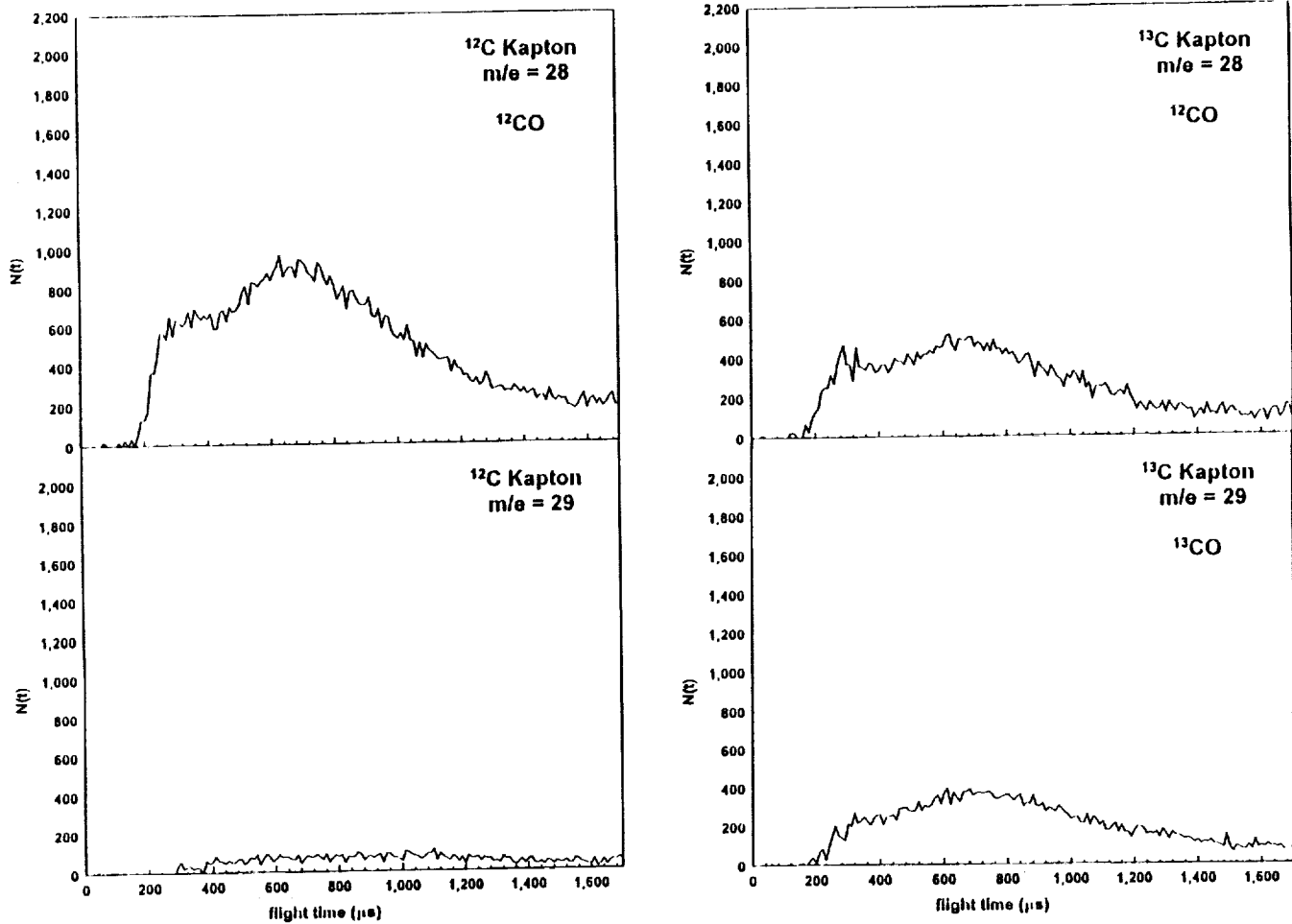


Figure 9. Time-of-flight distributions of CO products emerging from Kapton HN (^{12}C Kapton) and ^{13}C -enriched Kapton surfaces.

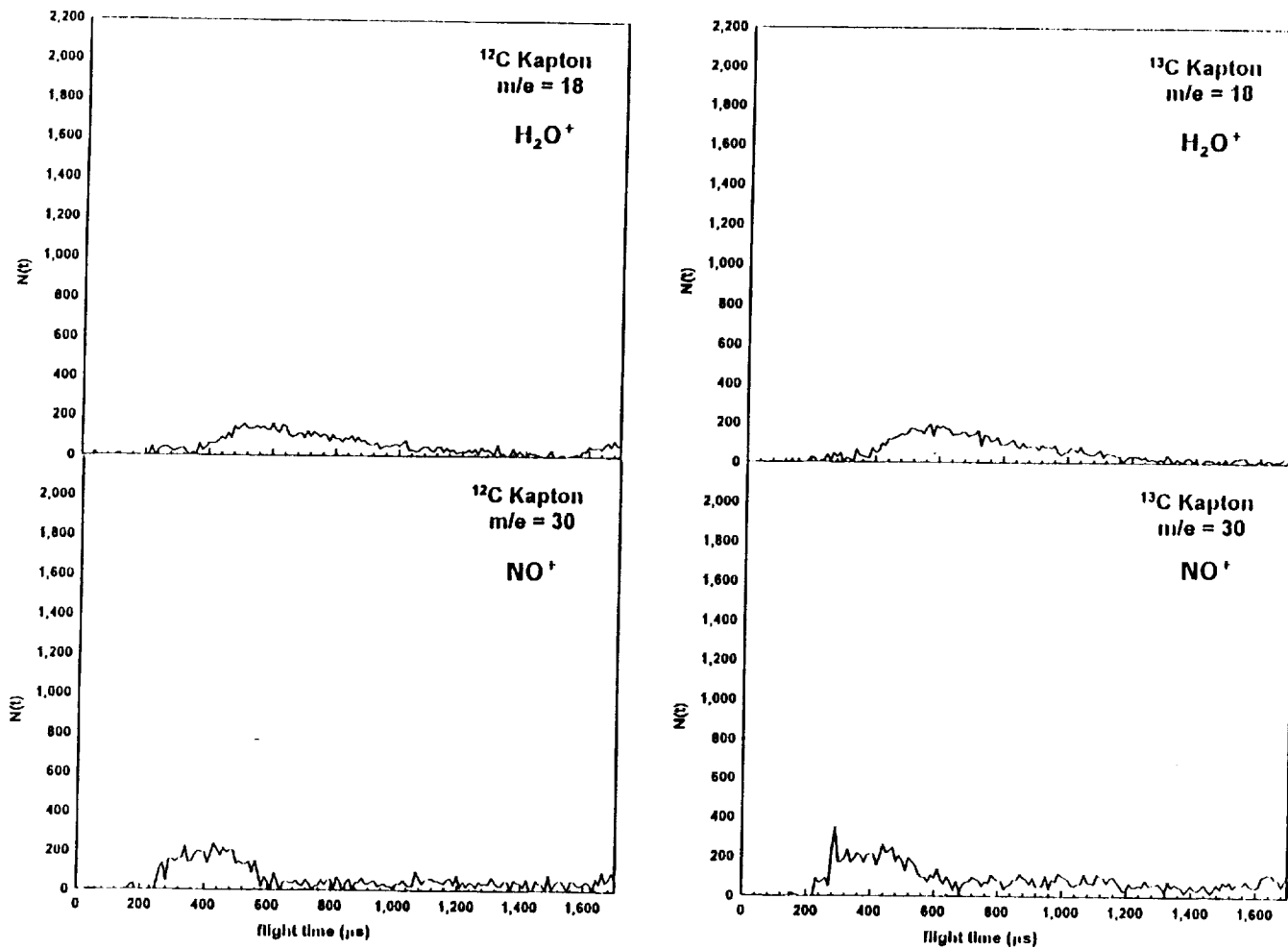


Figure 10. Time-of-flight distributions of H_2O and NO products emerging from Kapton HN (^{12}C Kapton) and ^{13}C -enriched Kapton surfaces.

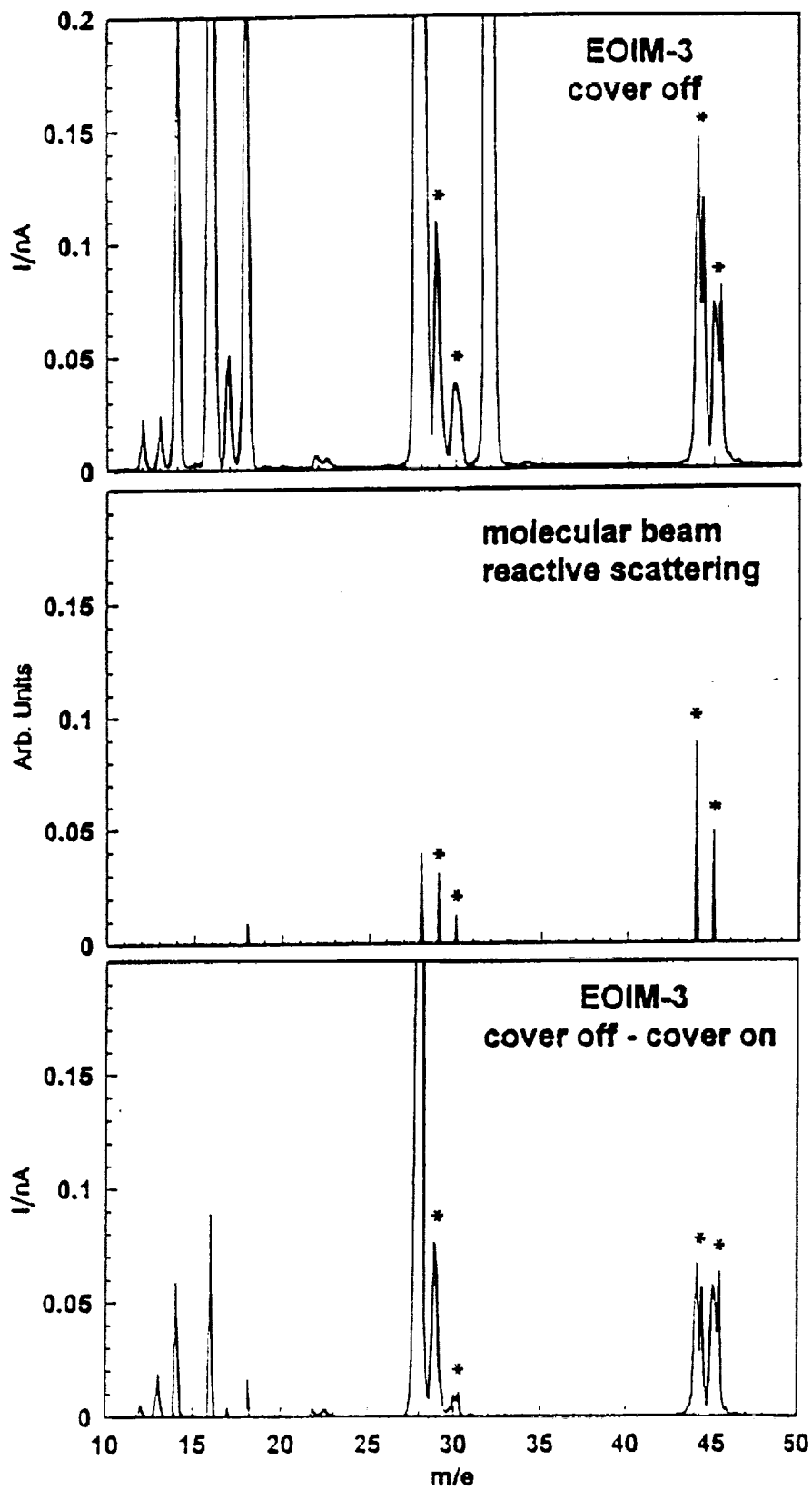


Figure 11. Comparison of mass spectra collected in space (top and bottom panels) and in the laboratory (center panel).

BMDO MATERIALS TESTING IN THE EOIM-3 EXPERIMENT

Shirley Y. Chung, David E. Brinza, Timothy K. Minton, and Ranty H. Liang
Jet Propulsion Laboratory
Mail Stop 67-201
4800 Oak Grove Drive
Pasadena, CA 91109
Phone: 818/354-4005, Fax: 818/393-6869

SUMMARY

The NASA Evaluation of Oxygen Interactions with Materials-3 (EOIM-3) experiment served as a testbed for a variety of materials that are candidates for Ballistic Missile Defense Organization (BMDO) space assets. The materials evaluated on this flight experiment were provided by BMDO contractors and technology laboratories. A parallel ground-based exposure evaluation was conducted using the Fast Atom Sample Tester (FAST) atomic-oxygen simulation facility at Physical Sciences, Inc. The EOIM-3 flight materials were exposed to an atomic oxygen fluence of approximately 2.3×10^{20} atoms/cm². The ground-based exposure fluence of $2.0 - 2.5 \times 10^{20}$ atoms/cm² permits direct comparison with that of the flight-exposed specimens. The results from the flight test conducted aboard STS-46 and the correlative ground-based exposure are summarized here. A more detailed correlation study is presented in the JPL Publication 93-31 entitled "Flight- and Ground-Test Correlation Study of BMDO SDS Materials: Phase I Report." In general, the majority of the materials survived the AO environment with their performance tolerances maintained for the duration of the exposure. Optical materials, baffles, and coatings performed extremely well as did most of the thermal coatings and tribological materials. A few of the candidate radiator, threat shielding, and structural materials showed significant degradation. Many of the coatings designed to protect against AO erosion of sensitive materials performed this function well.

INTRODUCTION

NASA provided a tray to the BMDO SEE Program for conducting O-atom exposure aboard NASA's EOIM-3 Platform flown on Shuttle Atlantis as part of the STS-46 mission. A group of 82 strategic materials of relevance to the BMDO was tested to determine material performance and reliability under hyperthermal atomic oxygen (AO) exposure characteristic of a low-Earth-orbit (LEO) space environment. The experimental data obtained from this program have allowed an assessment of the performance and longevity characteristics of a number of important materials that had not previously been flight qualified. The experiment was a cooperative effort between JPL and nineteen co-investigators from industry and government organizations, who provided test materials for both the flight and ground-based elements. The industry and government partners performed the bulk of the

laboratory evaluations of material properties to determine the effect of interaction of the materials with the AO environment on functional properties. The data was provided to JPL for insertion into the BMDO Space Environment and Effects (SEE) database. JPL identified a flight opportunity, organized the test, integrated the materials into the space flight mission, and directed the ground-based exposure. JPL also performed some pre- and post-exposure characterization of the materials.

EXPERIMENT

Materials and Sample Identification

Engineering materials relevant to the BMDO SDS Program were selected for studying AO exposure effects (see Table 1). The BMDO EOIM-3 Passive Tray design provided space for 82 disk-shaped samples: 27 one-inch diameter disks and 55 one-half-inch diameter disks. Six samples of each selected material were provided by the co-investigators. The six samples included a sample for flight, one for ground-based testing, a control sample, and three spares. A four-character code was used to identify each sample. The code identifies the sample diameter, the co-investigator's company or agency, the material number (for co-investigators who provided more than one material), and the sample type. The code was scribed onto the sample containers.

Sample Handling

At JPL, material samples were handled by personnel wearing vinyl, lint-free Class 100 clean room gloves. Samples were maintained in individual Fluoroware containers consisting of polypropylene wafer shippers with polyethylene springs. The containers protected the samples from damage and contamination during shipping and storage. The containers were cleaned with Soxhlet-extracted cloths wet with an azeotrope of 1,1,1-trichloro-ethane (75%) and ethanol (25%). Both the cloths and the solvent were supplied by Thermal Analytical, Inc. and certified by them to have a low non-volatile residue (NVR) of 4 ppm and 2 ppm, respectively. A final rinse with the solvent was used after wiping.

During shipping, the containers, with or without samples inside, were double-bagged in 3M-2110E antistatic reclosable bags. Handling and shipping instructions were provided to each co-investigator to standardize the packaging and shipping methods and to minimize the risk of contamination or damage to the samples.

JPL Sample Characterization

Photography

All specimens were photographed at JPL in a Class 100 clean room. Initially, the samples were photographed in their as-received condition prior to any thermal vacuum conditioning or characterization. For a direct comparison, close-up photographs of each flight-exposed sample adjacent to its control were taken. A third set of photographs was taken of each ground-exposed sample side-by-side with its control.

Electron Spectroscopy for Chemical Analysis

The surface chemistry of each control sample was analyzed with the use of Electron Spectroscopy for Chemical Analysis (ESCA), also known as X-ray Photoelectron Spectroscopy (XPS). The spectra were collected in a low-resolution mode of operation. This procedure ascertained material surface cleanliness and chemical composition.

Weight Measurement

The difference in sample weight before and after exposure provided a method to determine AO effects. A weight loss may indicate erosion. Weight increases may also be observed and could indicate water absorption, contamination, or a more complex interaction such as oxidation.

The flight, ground, and control samples were weighed before and after thermal vacuum conditioning. To minimize moisture absorption effects, the materials were conditioned in a 50% relative humidity chamber at room temperature for 24 hours prior to weighing, per ASTM E-595 procedures. A saturated calcium nitrate solution was used to maintain the humidity.

Weight measurements were made on a Mettler AE 163 Balance, which has a 0.01 mg sensitivity. The weighing procedure consisted of removing a sample from the humidity chamber and placing it in the balance immediately. The weight was recorded when the reading stabilized, which typically was less than one minute. After weighing, the sample was promptly returned to its Fluoroware container.

Thermal Vacuum Conditioning

Materials were subjected to a thermal-vacuum conditioning to remove any surface molecular contamination and to reduce the potential of outgassing during space flight or during ground-based testing. The thermal-vacuum conditioning environment was 65°C at 10^{-6} torr for a minimum of 48 hours per NASA Johnson Space Center (JSC) requirements.

Materials were vacuum-baked in two separate lots. Lot one contained only optical and non-polymeric materials. Lot two contained the balance of the samples including polymeric materials. Each sample set included the flight, ground, and control specimens.

A residual gas analyzer (RGA) monitored the outgassing products during the thermal-vacuum conditioning. Mass numbers greater than 60 (indicating possible hydrocarbon contaminants) were detected at the beginning of the conditioning at a pressure of 3×10^{-6} torr. There was an order of magnitude decrease of all mass peaks in the RGA by the end of the bake-out.

A Temperature-controlled Quartz Crystal Microbalance (TQCM) monitored the progress of the outgassing during the bake-outs. The amount of outgassing products deposited on the TQCM crystal at 0°C was measured and found to decrease gradually with time.

Post-thermal-vacuum ESCA results showed no significant evidence of contamination. The sensitive ultra-clean optics served as witnesses for contamination. They showed evidence of slight amounts of hydrocarbon accumulation on the surface ($\sim 10\text{-}20 \text{ \AA}$), which should be removed with a fluence of $<10^{17}$ O atoms/cm² exposure and therefore were not considered to be detrimental.

FLIGHT EXPERIMENT

Atomic Oxygen Environment

The AO fluence for EOIM-3 has been estimated to be $2.2 - 2.5 \times 10^{20}$ atoms/cm². Three methods provided estimates of the EOIM-3 atomic oxygen fluence. The first method used the Mass Spectrometric and Incoherent Scatter (MSIS-86) Thermospheric model along with the National Oceanic and Atmospheric Administration's (NOAA's) reported solar 10.7 cm (F10.7) flux and magnetic indices (A_p , K_p), and the estimated densities for various atmospheric species, including AO. The fluxes were computed with the MSIS-86 model. Fluences were calculated by multiplying number densities by orbiter velocity and integrating for the exposure periods. Depending on the period for which the solar and magnetic indices were sampled, the estimated AO fluence varied from 2.0×10^{20} atoms/cm² to 2.2×10^{20} atoms/cm². The second AO fluence estimate was based on the erosion of Kapton polyimide film. Numerous Kapton samples were located on various passive trays on the EOIM-3 pallet. Erosion was determined by mass loss, Scanning Electron Microscopy (SEM), and profilometry measurements. Based on a reaction efficiency of 3.0×10^{-24} cm³/O atom, the EOIM-3 fluence was calculated to be between 2.3×10^{20} atoms/cm² and 2.5×10^{20} atoms/cm². The weight losses varied with sample location and gave rise to the calculated fluence range. The third AO fluence estimate was based on data from the Air Force Phillips Laboratory mass spectrometer. The on-board spectrometer provided a mission fluence estimate of $2.2 \pm 0.4 \times 10^{20}$ atoms/cm².

Solar UV Environment

NASA JSC provided the EOIM-3 solar UV exposure estimate. Their estimate is based on integration of the sun angle, orbiter attitude, and ephemeris over the entire mission. The estimate does not account for shadowing from payloads and orbiter structure but is thought to be accurate within $\pm 20\%$. The estimate is 22 equivalent solar hours' (ESH) exposure.

Thermal Environment

The EOIM-3 pallet provided twelve temperature sensors as part of the state-of-health and engineering data system. One of the temperature sensors was mounted on an aluminized Kapton film bonded on a thin aluminum disk. During the EURECA operations, the payload bay was held in a solar inertial attitude for approximately 12 hours. The Kapton film reached a temperature in excess of 70°C during this period. Later, during the EOIM-3 exposure phase of the mission, the same sensor temperature cycled between $+20^{\circ}\text{C}$ and $+45^{\circ}\text{C}$. The BMDO Passive Tray (N-11) temperature excursions were damped considerably as compared to the aluminized Kapton specimen temperature excursions. The peak temperature during the solar inertial phase reached $+55^{\circ}\text{C}$, and temperatures cycled between $+5^{\circ}\text{C}$ and $+20^{\circ}\text{C}$ during the EOIM-3 exposure period.

Flight Contamination

After the mission, surface chemical analyses revealed a small percentage of silicon present on all flight samples. Materials readily eroded by atomic oxygen contained 2-3 atom percent silicon on the surface. The more stable or resistant materials contained 9-12 atom percent silicon on the surface. The stoichiometry indicated that a thin film of SiO_2 had formed on these specimens. For the stable materials, which had received a heavier accumulation of silicon, this film was on the order of 20 \AA thick. The extent of contamination witnessed on EOIM-3 was lower than that experienced on parts of LDEF. The amount of contamination (silicates and hydrocarbon compounds) found on LDEF trays varied from a few monolayers to as much as $20 \mu\text{m}$, depending on tray location and substrate characteristics (Ref. 1).

The Naval Air Warfare Center (NAWC) polycrystalline diamond on silicon (5M1A) flight sample contained a visibly distinct "crescent" feature on the surface near the tray retaining lip. ESCA showed the crescent region to be completely free of silicon. The rest of the sample surface had nearly 10 atom percent silicon. The sample contained a gold strip which was visible in tray photographs. The strip oriented the crescent area with respect to the tray and the orbiter. From a geometrical analysis of the crescent feature and the height of the retainer lip, it was determined that the contamination source was located in the aft portion of the orbiter and could not extend more than 30° above the plane of the BMDO EOIM-3 tray top surface. The contamination source was either at the top of the aft bulkhead surface or extended along the entire aft bulkhead surface.

It is not clear whether the forward surfaces of the OMS pods were in the field-of-view of the NAWC sample. Since a silicone-based waterproofing agent is applied to the shuttle thermal protection system (TPS) tiles, the tiles are a potential source of silicone contamination. The aft bulkhead is covered with a multi-layer insulation blanket with an outer layer of Beta-cloth. Beta-cloth is a woven glass fabric encapsulated in a fluorocarbon resin. In the manufacturing process, the glass fabric is treated with a silicone oil prior to encapsulation to improve the handling characteristics of the material. In the thermal vacuum environment of space, this silicone oil can slowly diffuse from within the fabric, migrate to the surface, and desorb. Yellowing of the Beta-cloth liner is commonly observed and is associated with environmental aging of the silicone film. Silicone oil could outgas and be transported via line-of-sight to all EOIM-3 surfaces.

GROUND-BASED EXPERIMENT

Seventy-seven material samples, identical to those flown on the BMDO EOIM-3 passive tray, plus ten witness samples, were exposed to atomic oxygen in the ground-based facility located at Physical Sciences, Inc. (PSI) in Andover, MA (Ref. 2). Although the passive tray contained 82 samples, three samples, 5P5, 1K8, and 1K9, were one-of-a-kind, and two were Kapton and magnesium fluoride control samples. While no spare samples of magnesium fluoride existed, numerous Kapton witness samples accompanied the ground-based materials during exposures to provide a good measurement of the Kapton-equivalent fluence. In addition, germanium-coated Kapton samples, which do not erode significantly upon exposure to atomic oxygen, were included in the ground-based test as monitors of the contamination levels in the chamber and in the O-atom beam. PSI weighed the samples before and after exposure. The samples were exposed in two batches. After exposure, samples were returned to JPL. Photographs were taken of the exposed and control samples together. The control samples had been in storage at JPL. Survey ESCA analyses were carried out on the exposed samples. The samples were then returned to the co-investigators for further analyses and comparison to the flight samples.

Environment

Four Kapton witness specimens were exposed in each batch. Based on the weight loss of these samples and a Kapton reactivity of 3.00×10^{-24} cm³/atom, the average fluences of each batch were 2.46×10^{20} atoms/cm² and 1.97×10^{20} atoms/cm², respectively. The fluence variation across the sample pallet for the first batch was 2.30 - 2.78×10^{20} and that for the second batch was 1.88 - 2.13×10^{20} . Both batches were exposed for the same amount of time, 25 hours, at a 3 Hz pulse rate. The fluence difference for the two batches provides an idea of the ability to control the fluence from test to test without an in situ monitor. The target fluence was 2.0×10^{20} atoms/cm², which was the best estimate of the EOIM-3 mission fluence at the time of the ground-based exposure. Subsequent estimates adjusted the EOIM-3 flight fluence upward to $\sim 2.5 \times 10^{20}$ atoms/cm². Given the uncertainties in the EOIM-3 fluence and in the ability to predict an actual ground-based exposure fluence, the ground-based exposures can be considered to be equivalent to the EOIM-3 fluence.

Ground-Based Facility Contamination

Survey ESCA analyses were performed on all samples subjected to ground-based exposure. The objectives of the analyses were to determine if the surface chemistry was the same for both ground and flight samples and to assess the contamination generated by the facility on the samples that were exposed in the ground-based facility.

Germanium-coated Kapton (Ge/K) witness samples accompanied both batches of samples. ESCA analyses of these witness samples were performed at JPL before shipping them to PSI. Although the germanium coating can oxidize, it has been shown to erode negligibly, if at all. Therefore, Ge/K can serve as a valid witness for contamination that is deposited on a surface and does not erode away.

The first exposure batch contained a Ge/K sample that sampled the ambient environment of the vacuum chamber. It was placed out of the direct line of sight of the O-atom beam. The only changes observed were in the relative amounts of carbon and oxygen on the surface. The increase in atom percent of O is likely the result of increased oxidation on the surface from scattered O-atoms in the chamber. There is no evidence for contamination arising from the ambient chamber environment.

One Ge/K sample (5P7C) served as the witness sample in the beam for the first batch. Two spots were examined after exposure. Again, the relative oxygen content of the surface increased, presumably as a result of oxidation. In addition, there is evidence for contamination arising from the exposure. In particular, the surface acquired silicon (Si), fluorine (F), copper (Cu), and sodium (Na). The fluorine is generated from laser ablation of the Teflon poppet in the pulsed valve in the source, and the copper comes from ablation of the adjacent copper nozzle. The origins of the Si and Na are unclear.

The Ge/K witness in the beam for the second exposure batch showed similar results. For this sample, three areas on the surface were examined by ESCA after the exposure, thus providing a good indication of the variability of the surface. Although the fluorine contamination appears to be lower for the second batch, examination of the test samples shows that both batches had similar fluorine contamination levels. It appeared that sample surfaces acquired an extra 3 to 20 atom percent F as a result of the exposure. The wide variability suggests that the measurement is strongly dependent on the area of the surface that is examined. Contamination from the other three elements, Si, Cu, and Na, did not appear to be so severe, as they were typically present at atom percentages of 5 or less.

RESULTS

The materials, the thermal-vacuum conditioning and the sample handling procedures were chosen to minimize any risk of contamination on the samples. The result was a nominally clean atomic oxygen exposure experiment. The measured mass loss of Kapton agrees with estimates based on the MSIS-86 predictions. Different erosion rates for various materials were observed, as expected. It is

important to recall that the total amount of silicone contamination is considered to be small, but it was sufficient to affect the optical performance of some of the optical test samples.

The BMDO samples that were exposed in a ground-based atomic oxygen testing facility experienced an **average** flux of O-atoms about twice that encountered on EOIM-3. The nominal O-atom velocity and the velocity distribution were close to on-orbit O-atom velocities. The O-atom fluence to which all the samples were exposed was the same as the EOIM-3 fluence within the uncertainties associated with measurement of the ground and space fluences for the respective exposures (~20 percent). Although low levels of contamination were observed on most of the witness samples, these levels should have no bearing on conclusions reached about the correlation of the ground- and space-based exposures. Any differences observed between the EOIM-3 flight samples and the identical samples that were exposed at PSI should reflect a fundamental difference between the nature of the FAST-1 and LEO environments and not an experimental artifact associated with the ground-based test.

The 82 samples flown by BMDO on the EOIM-3 experiment cover a broad range of material types for a number of specific applications. There was a broad range of atomic oxygen effects from "no effect" to highly deleterious. EOIM-3 experienced a much lower atomic oxygen fluence (2.3×10^{20} atoms/cm²) than LDEF's 9.0×10^{21} atoms/cm² (Ref. 3). Given this diversity, only a limited number of general conclusions can be drawn. One of these, which is consistent with previous atomic oxygen testing, is that carbon-containing materials, such as graphite, organic polymers, and carbon fiber composites, are extremely susceptible to erosion, while metals and refractory inorganics are not. For example, structural materials show significant erosion of bare carbon-carbon and P-100 fiber-reinforced MR56-2 bismaleimide composites. A significant result derived from the BMDO experiments, however, is that protective coatings aimed at protecting these potentially important classes of materials from atomic oxygen work very well. The tungsten-coated and titanium-carbide-coated carbon-carbon composites were resistant to erosion, unlike the bare materials. Similarly, plasma-sprayed alumina effectively protected PEEK composites, while epoxy-terminated silane materials were ultimately protected by the formation of silicon dioxide coating. Interestingly, for some materials such as the Martin Black and boron carbide on graphite optical baffles, removal of carbon occurred without any significant compromise in their primary performance characteristics as indicated by the invariance of their reflectance and BRDF parameters.

Within the specific classes of materials, some generalized comments can also be made. As mentioned previously, the optical baffle materials showed no performance changes even though erosion was observed. Some classes of materials showed no significant change when exposed to atomic oxygen, due to the chemical nature (i.e., relative inertness) of their composition. Among these are the optical materials including the Naval Air Warfare Center reflectors and the mirrors and coatings provided by other co-investigators, which with a few minor exceptions noted elsewhere, showed no degradation either in their physical or performance characteristics. Similarly, silicon carbide optical substrates showed no changes, though a small amount of oxidation was observed. Of the optical materials investigated, the most notable changes were observed for some of the protective coatings such as the diamond films. Likewise, ceramic copper oxide high temperature superconductor materials tested were also unaffected by AO.

Good results were obtained for a majority of the thermal control materials. Coatings for thermal control applications, including ceramic coatings on various composite substrates (7 samples), and several classes of coating materials (4 samples), such as Kapton-based materials showed no significant change in their performance parameters. Their measured absorptivity and emissivity did not change as a function of atomic oxygen exposure. Of the three thermal control blankets, the Beta-cloth and the glass fiber/Teflon composite were unaffected, but the Kapton HN showed the expected erosion.

The advanced radiator, threat shielding, and structural materials showed the most significant degradation. This was especially obvious for unprotected materials with a large organic chemistry component such as bare carbon-carbon composites. Two tribological materials, MoS₂/Ni and MoS₂/SbO₃, were also tested, with the latter giving the superior performance in the space environment.

Overall, the ground and flight correlation was excellent with the exception of fluorocarbons and the plasma-sprayed Beta-alumina on carbon/carbon composite samples. Details about individual materials and their correlative functional properties can be found in JPL Publication 93-31 (Ref. 4). In general, many of the materials tested showed a good resistance to atomic oxygen degradation. As a number of these have no prior flight history, this should facilitate their integration into future flight hardware. More importantly, the ability to duplicate the essential responses of the space-exposed materials with ground-based testing has provided a valuable step toward reliable ground-based testing. The results obtained from both the flight- and ground-based exposures provided input for a ground-based testing protocol (Ref. 5). This protocol provides a framework for more consistent and reliable ground-based testing in the future. Finally, all data collected in these experiments will be incorporated into a database that will be available to design engineers.

ACKNOWLEDGEMENTS

The authors appreciate the support received for this work from Lt. Col. Michael Obal, who obtained funding for this activity as part of the Space Environment and Effects Program of the Ballistic Missile Defense Organization (BMDO) Innovative Science and Technology Directorate's (DTI's) Materials and Structure Program. We also acknowledge Dr. Lubert J. Leger, Branch Chief, Materials Directorate at NASA Johnson Space Center, for providing space on the Evaluation of Oxygen Interactions with Materials Experiment-3 (EOIM-3) platform for this BMDO Experiment.

REFERENCES

1. Blue, M.D.: Degradation of Optical Components in Space. LDEF Materials Results for Spacecraft Applications. NASA Conference Publication 3257, October 1992.
2. Caledonia, G.E., Krech, R.H., and Green, B.D.: A High Flux Source of Energetic Oxygen Atoms for Material Degradation Studies. AIAA J. **25**, 59 (1987).

3. Gregory, J.C.: On the Linearity of Fast Atomic Oxygen Effects. LDEF Materials Results for Spacecraft Applications. NASA Conference Publication 3257, October 1992.
4. Chung, S.Y., Brinza, D.E., Minton, T.K., Stiegman, A.E., Kenny, J.K., and Liang, R.H.: Flight- and Ground-Test Correlation Study of BMDO SDS Materials: Phase I Report. JPL Publication 93-31, December 1993.
5. Minton, T.K.: Protocol for Atomic Oxygen Testing of Materials in Ground-Based Facilities; Version Number 1. JPL Publication 94-02, April 1994.

Table 1. BMDO EOIM-3 passive tray materials list.

Material ID Code	Material
1A1	MoS ₂ -Ni lubricant on steel, Ovonic
1A2	MoS ₂ -Ni lubricant on steel, Ovonic
1A3	MoS ₂ -SbO _x lubricant on steel, Hohman
1A4	MoS ₂ -SbO _x lubricant on steel, Hohman
1B1	SiO ₂ -doped Al ₂ O ₃ /SiO ₂ multilayer on fused SiO ₂
1B2	TiN (1000 Å) on fused SiO ₂
1K3	Four coatings* on Al/PVDF: A: Ni/PbTe B: Ni/Si/SiO ₂ C: Ni/SiO ₂ D: Ni/ZnS/PbF ₂ /ZnS
1K4	Four coatings* on Al/PVDF: A: Mo/Si/SiO ₂ B: Ni/TiO ₂ /Al ₂ O ₃ /TiO ₂ C: Mo/TiO ₂ /Al ₂ O ₃ /TiO ₂ D: Bare
1K8	Al ₂ O ₃ /Carbon foil on sapphire, Al holder
1K9	SiO _x /Carbon foil on sapphire, Al holder
1L1	TiC-coated carbon/carbon
1L2	Glass fiber/Teflon composite
1M9	CVD diamond brazed to a ZnS window
1M10	(SiC/SiO ₂) ⁶ /Si, MWIR-tuned reflector
1M11	(Si ₃ N ₄ /Al ₂ O ₃) ⁶ /Ag/fused silica, beam splitter
1M12	Al ₂ O ₃ /Al half-coated on β-SiC
1M13	Uncoated HIP I-70 beryllium, broadband reflector
1M14	(Si ₃ N ₄ /Al ₂ O ₃) ² /Al/Si, MWIR-tuned reflector
1M15	AlN/SiH/CVD diamond/ZnS
1M16	(Si/SiO ₂) ⁴ /Al/Si, MWIR-tuned reflector

* A=upper right, B=lower right, C=lower left, D=upper left.

Table 1. BMDO EOIM-3 passive tray materials list (continued).

Material ID Code	Material
1N4	Beryllium (black-etched) on beryllium foam
1N5	Boron (plasma sprayed) on beryllium
1N6	Martin Black on aluminum
1P2	Tungsten/graphite cloth/carbon foam
1P5	Solar cell
K	Kapton HN
MgF ₂	MgF ₂ on Al mirror, glass substrate
5C1	T300/934 composite, LDEF trailing edge
5C2	T300/934 composite, adjacent to 5C1 on LDEF
5C4	Polyethylene ring/anodized aluminum cover on silver oxide coated aluminum base
5C5	Polyethylene ring/anodized aluminum cover on anodized aluminum base
5D1	3M Y9469 acrylic transfer tape
5E1	HRG-3/AB epoxy silane (HAC)
5E2	HRG-3/AB epoxy silane (vendor)
5F1	Diamond film on silicon wafer
5F2	Diamond film on silicon wafer
5G1	β -cloth, graphite interwoven
5H1	SiC/Al composite, CaZrO ₃ coating
5H2	SiC/Al composite, Al ₂ O ₃ coating
5H3	IM7/PEEK, Al ₂ O ₃ coating
5H4	IM7/PEEK, BN/Al ₂ O ₃ coating
5K5	Vendor aluminum electrode/PVDF film
5K6	Y-Ba-Cu-O High temperature superconductor, oxygen deficient
5K7	Y-Ba-Cu-O High temperature superconductor, fully oxygenated

Table 1. BMDO EOIM-3 passive tray materials list (continued).

Material ID Code	Material
5L3	β -alumina (.002") coated aluminum
5L4	Silicon carbide ceramic
5L5	Carbon/carbon composite
5L6	Calcium zirconate coated carbon/carbon
5L7	β -alumina on carbon/carbon
5L8	Copper indium diselenide-photovoltaic
5L9	Niobium beryllide, high temperature alloy
5L0	P75/magnesium vacuum cast composite
5M1	CVD diamond on silicon
5M2	(SiC/SiO ₂)(SiH/SiO ₂) ⁵ /Si, MWIR-tuned reflector
5M3	(Si ₃ N ₄ /SiO ₂) ⁶ /Si, MWIR-tuned reflector
5M4	(AlN/Al ₂ O ₃) ⁶ /Si, visible-wavelength-tuned reflector
5M5	(Si/SiO ₂) ⁵ /Si, MWIR-tuned reflector
5M6	(SiH/SiO ₂) ⁵ /Si, MWIR-tuned reflector
5M7	(BN/SiO ₂)(SiH/SiO ₂) ⁵ /Si, MWIR-tuned reflector
5M8	Unprotected aluminum on silicon, broadband reflector
5N1	Beryllium, diamond turned, on beryllium
5N2	Beryllium, conv. polished, on beryllium
5N3	Beryllium/silicon/silicon carbide
5O1	P-100 fiber/MR 56-2 composite
5P1	Two coatings on Vit-C/SiC substrate upper: Si/Al ₂ O ₃ lower: Si/Al ₂ O ₃ /enhanced MLD
5P3	CVD TiC/graphite cloth/carbon foam
5P4	Alumina on aluminum substrate

Table 1. BMDO EOIM-3 passive tray materials list (continued).

Material ID Code	Material
5P6	Al ₂ O ₃ /graphite composite
5P7	Germanium/Kapton
5P8	Indium tin oxide/Teflon/VDA/Kapton
5P9	Microsheet/Ag/Y966/Al
5P0	(Si/SiO ₂)/(TiO ₂ /SiO ₂)/Kapton
5Q1	Aluminum, textured
5Q2	Aluminum, textured
5Q3	Beryllium, textured, 100 μm, on aluminum
5Q4	Beryllium, textured, 100 μm, on aluminum
5Q5	Beryllium, black etched, on beryllium
5Q6	Beryllium, black etched, on beryllium
5Q7	Boron carbide on graphite
5Q8	Boron carbide on graphite
5Q9	Magnesium oxide on beryllium
5Q0	Magnesium oxide on beryllium

STS-46 PLASMA COMPOSITION MEASUREMENTS
USING THE EOIM-3 MASS SPECTROMETER

Donald E. Hunton, Edmund Trzcinski and Roger Gosselin
Geophysics Directorate/GPID
Phillips Laboratory
Hanscom AFB, MA 01731
Phone: 617/377-4057; Fax: 617/377-7091

Steve Koontz, Lubert Leger and Jim Visentine
NASA Johnson Space Center/ES-5
Houston, TX 77058
Phone: 713/483-8913; Fax: 713/483-2162

ABSTRACT

One of the active instruments incorporated into the Evaluation of Oxygen Interactions with Materials - 3 experiment was a quadrupole mass spectrometer. The primary objectives for this instrument, which was built by the Air Force Phillips Laboratory and was a veteran of the STS-4 flight in 1982, were to quantify the flux of atomic oxygen striking the test surfaces in the EOIM-3 payload and to detect surface reaction products from the materials in the carousel. Other speakers in this session have covered the results of these experiments.

Prior to the 40-hour-long dedicated EOIM-3 mission segment at the end of the STS-46 flight, we used the mass spectrometer to make measurements of ion and neutral gas composition in the shuttle environment. We collected about 25 hours of data during a variety of mission events, including Eureka deployment at high altitude and many tethered satellite system operations.

POINT DEFECT FORMATION IN OPTICAL MATERIALS
EXPOSED TO THE SPACE ENVIRONMENT

J. L. Allen, N. Seifert, Y. Yao, R. G. Albridge, A. V. Barnes, N. H. Tolk
Center for Molecular and Atomic Studies at Surfaces
Department of Physics and Astronomy
Vanderbilt University
Nashville, TN 37235

A. M. Strauss
Department of Mechanical Engineering
Vanderbilt University
Nashville, TN 37235

R. C. Linton, R. R. Kamenetzky, J. A. Vaughn, and M. M. Finckenor
NASA Marshall Space Flight Center
MSFC, AL 35812

ABSTRACT

Point defect formation associated with early stages of optical damage was observed unexpectedly in two, and possibly three, different optical materials subjected to short-duration space exposure. Three calcium fluoride, two lithium fluoride, and three magnesium fluoride samples were flown on Space Shuttle flight STS-46 as part of the Evaluation of Oxygen Interactions with Materials - Third Phase experiment. One each of the calcium and magnesium fluoride samples was held at a fixed temperature of 60°C during the space exposure, while the temperatures of the other samples were allowed to vary with the ambient temperature of the shuttle cargo bay. Pre-flight and post-flight optical absorption measurements were performed on all of the samples. With the possible exception of the magnesium fluoride samples, every sample clearly showed the formation of F-centers in that section of the sample that was exposed to the low earth orbit environment. Solar vacuum ultraviolet radiation is the most probable primary cause of the defect formation; however, the resulting surface metallization may be synergistically altered by the atomic oxygen environment.

INTRODUCTION

The space environment offers many observational advantages over ground-based experiments. However, the low earth orbit (LEO) environment in which the space shuttle and other space systems operate has proven to be very harsh, having adverse effects on most exposed systems.¹⁻⁴ Because optical systems play a key role in many space experiments, a thorough understanding of the degradation of optical materials in a space environment is very important. To address this issue, the Vanderbilt University Center for Molecular and Atomic Studies at Surfaces (CMASS), in collaboration with NASA Marshall Space Flight Center, flew samples of calcium fluoride (CaF₂), lithium fluoride (LiF), and magnesium fluoride (MgF₂) on Space Shuttle flight STS-46 as part of the Evaluation of Oxygen Interactions with Materials - Third Phase (EOIM-III) experiment. As a result of the short duration space exposure during this flight,

point defect formation associated with the early stages of optical damage was unexpectedly observed in the CaF₂ and LiF samples. The space exposure also caused some effects in the MgF₂ samples that might be associated with F-center formation.

CaF₂, LiF, and MgF₂ are popular choices for lens and window materials in a wide variety of optical and infrared (IR) experiments, because of their excellent optical transmission properties from vacuum ultraviolet (VUV) to medium IR wavelengths (0.1 - 10 μm). It has been known for some time that ionizing radiation incident on alkali-halide and alkaline-earth-fluoride crystals creates hole defects, which may be highly mobile and lead to color center formation (F-center/H-center pairs), a process which is understood to be a precursor to darkening, surface metallization, erosion, and other optical damage phenomena.⁵⁻⁸ A single halogen ion vacancy that has trapped an electron is known as an F-center; an F₂-center is a pair of adjacent F-centers.

These defects give rise to optical absorption bands with well-characterized peak wavelengths. Table 1 summarizes the positions of the F- and F₂-band absorption maxima for the three materials studied.⁵⁻⁸

Table 1. *F-band absorption peak wavelengths.*⁵⁻⁸

Material	Peak wavelength (nm)	
	F - band	F ₂ - band
CaF ₂	370	370, 520
LiF	250	450
MgF ₂	260	370, 400

The CaF₂, LiF, and possibly the MgF₂ samples flown by CMASS/NASA on EOIM-III showed absorption peaks consistent with F-center formation as a result of the space exposure. The effects of space radiation on a wide variety of optical materials have been studied for many years in laboratory simulations and space experiments.⁹ While changes in optical absorption were seen in these studies, F-center defect formation due to space exposure has not been previously reported.

EXPERIMENT

The EOIM-III payload, which has been previously described in detail,¹⁰ contained a wide variety of experiments designed to meet its primary objective: production of benchmark atomic-oxygen-reactivity and induced-environment data. The experiment hardware included several passive sample carriers whose temperatures were allowed to vary with ambient temperature of the cargo bay. The hardware also contained three heated sample trays that were maintained at constant temperatures of 200, 120, and 60°C, during the EOIM-III Flight Operations portion of the flight.

As mentioned above, the CMASS/NASA experiment included a total of eight samples on the EOIM-III flight. Three more control samples (CaF₂-2, LiF-1, and LiF-3) were kept in the laboratory. All the samples are single crystal, parallel plane windows purchased from Infrared Optical Products, Inc. Table 2 summarizes the pertinent information about each flight sample. All of the 25-mm diameter samples were mounted in the EOIM-III trays with a 0.5 mm thick aluminum mask that covered approximately half of the sample surface. The three 12.5-mm samples were cut from original 25-mm diameter samples in order to facilitate post-flight Auger Electron Spectroscopy analysis of the samples. Two of these samples (LiF-4 and MgF₂-3) had to

be ground and polished after cutting. Unfortunately, this process increased the optical absorption and made the spectra dependent on sample orientation in the spectrophotometer with decreased reproducibility. However, as discussed below, the bulk defect formation due to space exposure was still observed in LiF-4.

Table 2. *List of flight samples.*

Sample	Nominal Diameter (mm)	Nominal Thickness (mm)	Mask	Tray
CaF ₂ -1	25	3	Yes	60°C
CaF ₂ -3	25	3	Yes	Passive
CaF ₂ -4	12.5	3	No	Passive
LiF-2	25	4	Yes	Passive
LiF-4	12.5	4	No	Passive
MgF ₂ -1	25	1	Yes	60°C
MgF ₂ -2	25	1	Yes	Passive
MgF ₂ -3	12.5	3	No	Passive

The EOIM-III experiment was flown on the STS-46 mission of the Space Shuttle Atlantis, July 31 - August 8, 1992.¹⁰ For the EOIM-III Flight Operations portion of the flight, the shuttle was maintained at an altitude of 123-124 nautical miles (nmi), or 228-230 km, for an exposure period of 42.25 hours with the cargo bay normal aligned (within +2°) with the orbital velocity vector (ram direction). During this period, the EOIM-III payload received an atomic oxygen fluence of $2.3 \pm 0.1 \times 10^{20}$ atoms/cm².¹¹

The STS-46 flight also included the European Space Agency Recoverable Satellite (EURECA), that was deployed and checked out at an altitude of 231 nmi (428 km) for an exposure period of 11.27 hours during which the cargo bay was pointed toward the sun. An additional 5.28 hours of exposure at 231 nmi occurred during EURECA release with the cargo bay in the ram direction. Atomic oxygen fluences during the 231 nmi exposure were 2-3 orders of magnitude less than those received during the 123-124 nmi exposure. However, it is very important to note that most of the EOIM-III samples, including the CMASS/NASA samples, were uncovered during the EURECA experiments. Consequently, they received a significant solar UV/VUV radiation dose, greater than that received during the rest of the mission. The solar UV/VUV flux as a function of energy was calculated using known orbit and solar parameters¹² and will be discussed below.

The optical absorption measurements were performed using a Hewlett-Packard 8452A Diode Array Spectrophotometer controlled by a PC Turbo AT microcomputer. This spectrophotometer system allowed either the optical transmittance or optical density (absorbance) of a given sample to be measured in an open air environment as a function of wavelength in the range 190 nm to 820 nm with a resolution of 2 nm. The transmittance is defined as $T = I/I_0$, where I is the light intensity transmitted through a parallel plane sample and I_0 is the intensity of the beam normally incident on the sample. The optical density is defined as $\alpha = \log(1/T)$ where "log" indicates the common (base 10) logarithm. Both the pre- and post-flight optical density spectra of all the samples were taken in the following manner.

Before each sample was placed in the spectrophotometer, a "blank" optical density spectrum was taken of the air. Then the optical density spectrum of the air and the desired sample was taken. Because of the definition of optical density, the air blank spectrum was point-by-point subtracted from the spectrum of the air and sample in order to correct for the presence of the air

in the spectrophotometer optical path. The pre-flight optical density measurements were subtracted from the post-flight measurements in order to obtain the change in optical density due to the space exposure. This procedure facilitates easier recognition of the F-bands. In the figures shown below, the air-corrected optical density spectra are shown in part (a) of the figures, and the change in optical density due to the space exposure are shown in part (b). One pre-flight spectrum was taken for each of the fixed temperature samples: CaF_2 -1 and MgF_2 -1. All other spectra shown and discussed below are averages of at least three different spectra.

It should also be noted that almost all of the pre- and post-flight spectra for all samples had narrow spikes at approximately 580, 600, and 658 nm (the Balmer- α line). All three spikes are features of the spectrophotometer deuterium light source and not of the samples. Because they are not features of the samples, the data points associated with the 580 nm and 658 nm features were removed from the spectra presented below to better facilitate plotting and curve fitting of the spectra. With one exception (sample CaF_2 -1), the 600 nm spike usually disappeared when the pre-flight spectra were subtracted from the post-flight spectra, so the data associated with this feature were not removed from the spectra.

RESULTS

The optical density spectra for sample CaF_2 -1 are shown in figure 1. The optical density spectrum for the masked area is essentially the same as the pre-flight spectrum; it is within the variance seen between different spectra taken on the same day. The exposed surface shows an increased optical density in the UV in addition to an overall increase over the entire spectral range. The feature at 370 nm indicates F-center formation in the exposed side of the sample. This feature is absent in the masked and pre-flight spectra. As discussed above, the spike evident in Figure 1(b) at approximately 600 nm is not a real feature of the sample and can be ignored.

Similar to CaF_2 -1, the optical density spectra for sample CaF_2 -3 show a feature at 370 nm in the exposed side spectrum that is absent in the masked and pre-flight spectra. However, both the masked and exposed optical density are greater than the pre-flight optical density, and in particular, the masked optical density is greater than the exposed. Closer examination of the sample surface revealed that a large portion of the masked area was covered by very fine scratches due to the pre-flight diameter-cutting procedure. These scratches render that region of the sample slightly less transparent than the exposed region due to increased scattering of the light incident on the sample. This increased scattering could certainly be the cause of the increased optical density over the entire spectral range of the masked region of the sample. It should also be noted that CaF_2 -1 was held at a fixed temperature of 60°C during the space exposure while the temperature of CaF_2 -3 was allowed to vary with the ambient environment.

Four different sets of pre- and post-flight optical density spectra were taken for sample CaF_2 -4, and all the post-flight data show a feature at 370 nm that is absent in the pre-flight data. The post-flight optical density is slightly greater than the pre-flight, with the increase qualitatively similar to CaF_2 -1.

The absorption features at the UV end of the spectra shown in figure 1(a) are typical of all the CaF_2 samples. Because the optical density is greatly varying with wavelength in this region near the air/ CaF_2 UV cutoff, the features seen in the corresponding region in figure 1(b) may not be real, even though their magnitudes are of the same order as the F-band observed. However, the F-center appears in a relatively flat, well-behaved section of the exposed-side spectrum, and clearly does not appear in either the pre-flight or masked spectra. Therefore, the observed F-band in CaF_2 is real.

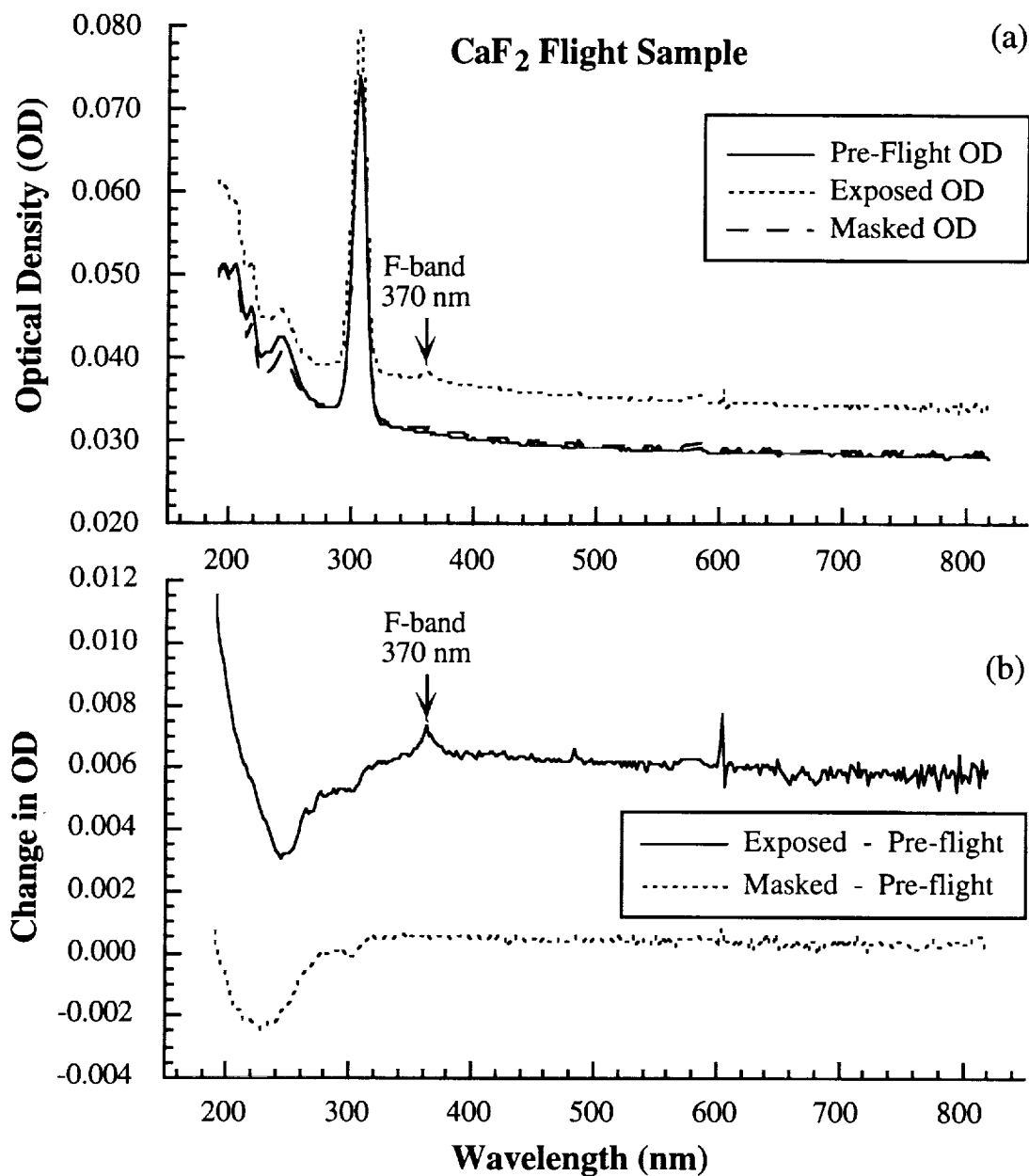


Figure 1. (a) Pre-flight and post-flight optical density (OD) spectra of the exposed and masked areas of sample CaF₂-1. (b) The change in optical density due to the space exposure determined by the difference between the post- and pre-flight spectra from figure (a). The post-flight spectra show the formation of an F-band at 370 nm only on the exposed side of the sample. Sample temperature was held at 60°C during space exposure.

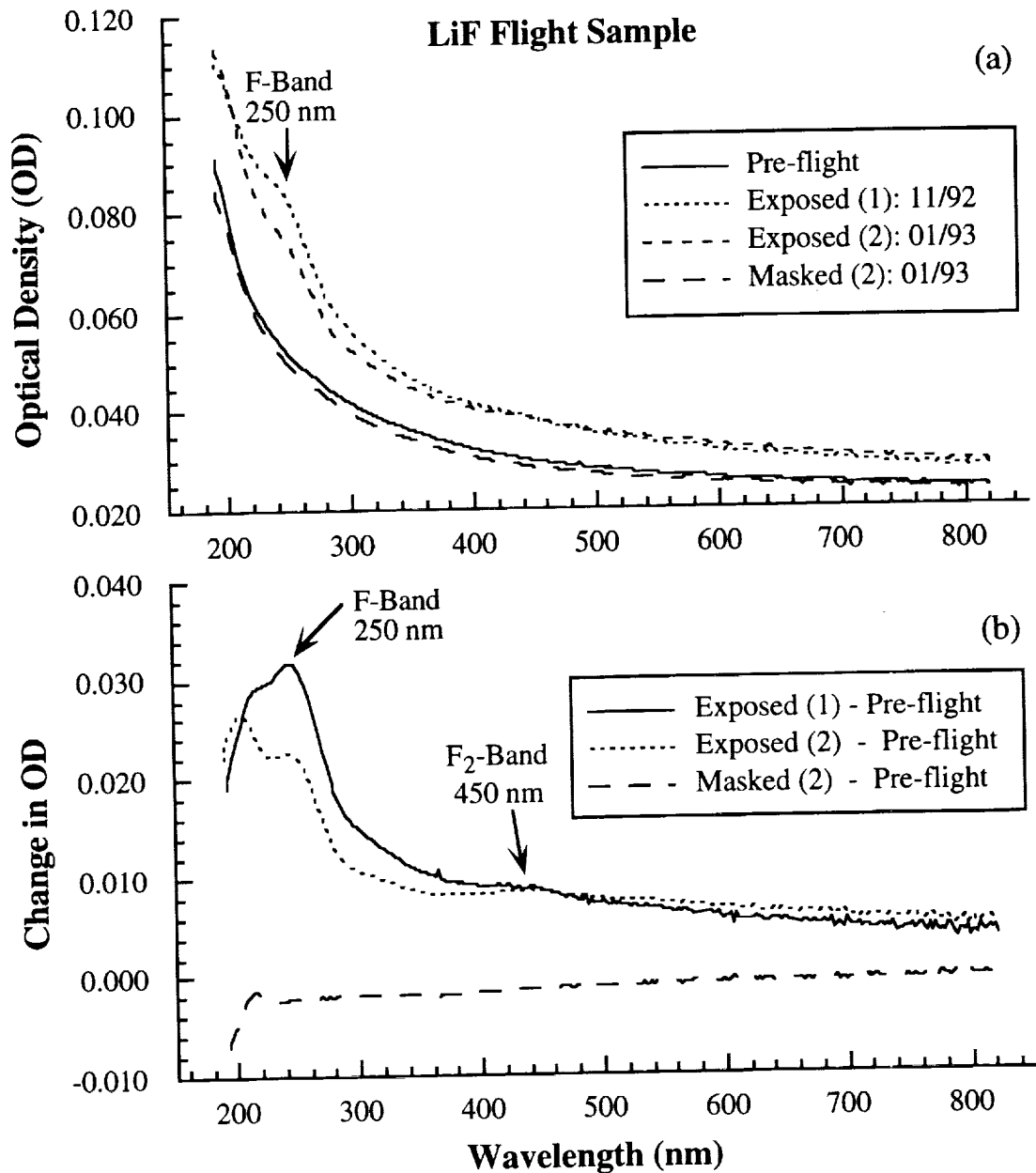


Figure 2. (a) Pre-flight and post-flight optical density (OD) spectra of the exposed and masked areas of sample LiF-2. (b) The change in optical density due to the space exposure determined by the difference between the post- and pre-flight spectra from figure (a). The post-flight spectra show the formation of an F-band at 250 nm and an F₂-band at 450 nm only on the exposed side of the sample. Sample temperature varied with the ambient environment during space exposure.

The optical density spectra for sample LiF-2 are shown in figure 2. The exposed side of the sample shows an increase in optical density as compared to the pre-flight spectrum, while the masked-side spectrum is essentially the same as the pre-flight spectrum. The exposed side shows a prominent F-band at 250 nm, and a small F₂-band is evident at 450 nm. The post-flight spectra taken on different dates clearly show that the F-band is slowly disappearing with time. The absorption peak at 210 nm has been seen before in other experiments where LiF is subjected to

electron bombardment.¹³ A similar F-band envelope in LiF subjected to proton bombardment has been determined to be a complex combination of defect bands involving the presence of impurities and the formation of Li colloids in the crystal.¹⁴

The pre- and post-flight spectra for sample LiF-4 varied greatly with sample orientation in the spectrophotometer and had poor reproducibility. This fact is most probably due to the grinding and polishing described above. In spite of the poor quality of the spectra, an F-band at 250 nm due to space exposure was evident for all sample orientations.

The optical density spectra for sample MgF₂-2 are shown in figure 3. All post-flight spectra for sample MgF₂-1 are very similar to those displayed for MgF₂-2. The exposed side of each sample shows an increased optical density as compared to the pre-flight spectra. Both show a small feature at 230 nm that may be associated with the F-band, which is known to have a peak wavelength of 260 nm in MgF₂ (see table 1). As shown in figure 3(b), the MgF₂-2 exposed side spectrum has a shoulder at approximately 260 nm. This indicates that F-centers may have been formed in that region of the MgF₂ samples exposed to the space environment, but the concentrations are too close to the spectrophotometer detection threshold (approximately 10¹³ F-centers/cm³) to offer conclusive evidence.

Also, the masked side optical density for MgF₂-1 is greater than that of the pre-flight from 200 to approximately 320 nm and is less than the pre-flight for greater wavelengths. The masked optical density for MgF₂-2 is less than the pre-flight optical density at all wavelengths. This difference in the masked side optical densities of the two samples is not yet understood, but it could be at least partially due to a variation in the spectrophotometer lamp intensity and/or room conditions between or during measurements. Both samples were cut from the same crystal, but temperatures of the samples during exposure differed; MgF₂-1 was held at a fixed temperature of 60°C during space exposure while the temperature of MgF₂-2 was ambient.

As mentioned above, sample MgF₂-3 was ground and polished prior to the flight. As with LiF-4, the spectra varied greatly with sample orientation in the spectrophotometer and had poor reproducibility. Consequently, evidence of F-band formation in this sample was inconclusive.

Note that in all cases, the areas of the samples exposed to the LEO environment during the flight show an increased optical density over the entire spectral range. This is evidence for surface metallization although this assumption has not yet been verified by an independent technique. Also, all samples show a greater increase in optical density in the UV portion of the spectra, indicating all of the materials suffered some degree of UV darkening. It also is important to note that none of the samples show any visible signs of darkening or damage.

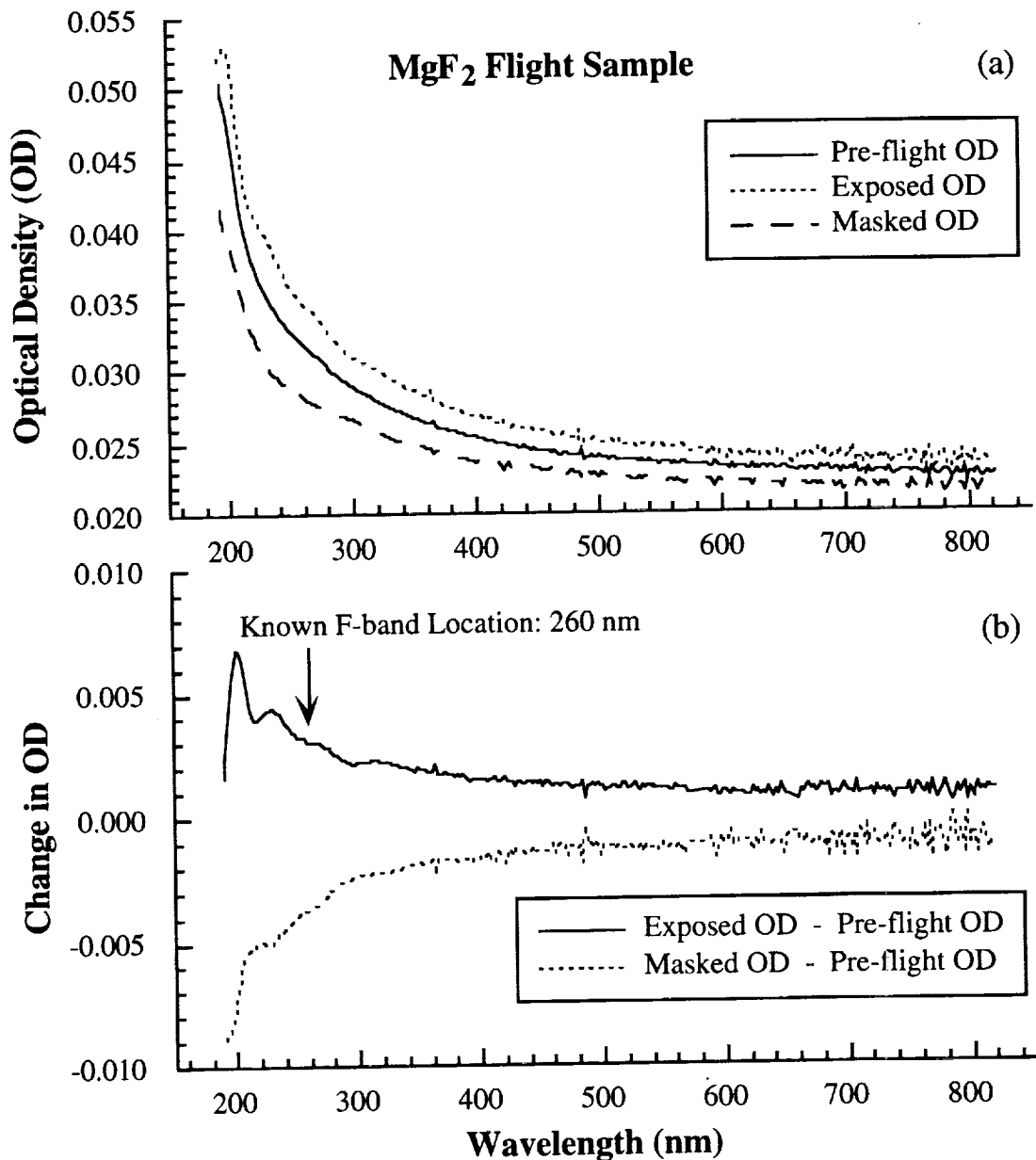


Figure 3. (a) Pre-flight and post-flight optical density (OD) spectra of the exposed and masked areas of sample MgF₂-2. (b) The change in optical density due to the space exposure determined by the difference between the post- and pre-flight spectra from figure (a). The post-flight spectra show absorption features that could be associated with F-center formation only on the exposed side of the sample. Sample temperature varied with the ambient environment during space exposure.

DISCUSSION

F-center formation in alkali-halide crystals such as LiF has been studied in detail for many years, and the shape of the F-band in optical absorption spectra is well-known to be Gaussian, or nearly Gaussian.^{8, 15} An order of magnitude estimate of the average F-center concentration in sample LiF-2 can be made using the following form of the modified Smakula formula for a Gaussian band shape:^{8, 16}

$$Nf = 0.87 \times 10^{17} \frac{n}{(n^2 + 2)^2} \mu_m W$$

where N is the number of defects per cubic centimeter, f is the oscillator strength, n is the index of refraction in the spectral region of the band, μ_m is the absorption coefficient at the band peak expressed in cm^{-1} , and W is the full width at half maximum of the band expressed in electron volts.

The absorption coefficient is defined as $\mu = (1/d) \ln(1/T)$, where d is the sample thickness and "ln" indicates the natural (base e) logarithm. Consequently, the absorption coefficient is related to the optical density, as measured by the spectrophotometer, by $\mu = 2.303 \alpha/d$.

The F-band peaks and full widths for sample LiF-2 were determined from fits of multiple Gaussians with a second order polynomial background to the difference between the exposed and pre-flight optical density spectra (as shown in figure 2b). The F-band has a constant peak wavelength and width at a given temperature,⁵⁻⁸ so only the peak height should change as a function of time. Therefore, the final fit of each spectrum was made with the center wavelength and width of the F-band fixed at the average value achieved from initial fits. The oscillator strength is nearly unity for F-bands^{15, 17} and the index of refraction of LiF is 1.420 at the peak wavelength of the F-band.¹⁸ Therefore, the average F-center concentrations in sample LiF-2 due to space exposure can be calculated using the Smakula formula above. For the 0.4 cm thick LiF-2 sample, the results of the curve fits are tabulated in table 3.

Table 3. *F-center concentrations in sample LiF-2.*

Parameter	Spectrum 11/92	Spectrum 01/93	Spectrum 08/93
λ_0 (nm)	245.7	245.7	245.7
μ_m (cm^{-1})	0.1031	0.0757	0.0721
W (eV)	0.953	0.953	0.953
N (cm^{-3})	$7.53 \cdot 10^{14}$	$5.53 \cdot 10^{14}$	$5.28 \cdot 10^{14}$

These concentrations are about 5 orders of magnitude smaller than the typical concentrations induced by low-energy electron bombardment.¹³ If we assume 100 eV is needed to create each stable F-center,¹⁹ then the energy absorbed by sample LiF-2 in the formation of the F-band was approximately 7.53×10^{16} eV/ cm^{-3} for the 11/92 spectrum.

The interactions of low-energy electrons, protons, and heavy particles with an alkali-halide crystal are confined to the near surface bulk of the crystal. If the energy of the incident particles is high enough to allow F-center formation, the resulting F-center distributions will greatly vary

with depth in the crystal. Bombardment of alkali-halide crystals by photons with energies well above the band gaps will produce similar distributions. However, photons with energies near the excitonic absorption edge, where the sample is still largely transparent, will deposit their energy fairly uniformly throughout the sample bulk, leading to a relatively uniform F-center distribution.

When alkali halides, such as LiF, are bombarded by electrons with energies of a few hundred eV, clusters of lithium atoms form on the sample surface.^{9, 13, 20} This surface metallization is observed as a very broad absorption band that first appears near the F₂-band and shifts to longer wavelengths as the clusters increase in size. The absorption spectra for sample LiF-2 do not exhibit a broad metal peak, but any lithium clusters that might have formed on the surface of LiF-2 would have been most likely altered by exposure to atomic oxygen during the flight or air during the post-flight retrieval. Therefore, absence of a broad metal peak does not rule out electron bombardment as the cause of the F-center formation.

However, typical LEO electron densities range from 10⁵ to 10⁶ cm⁻³ with an average energy of 0.1 eV.²¹ Electrons and protons in the keV energy range were present in the EOIM-III flight environment,^{*} but fluxes were several orders of magnitude lower than the calculated UV/VUV fluxes. Therefore, electron, proton, and other ion fluences were far too small to be primary causes of the F-center formation observed. Even though the samples were exposed to significant atomic oxygen fluxes, the collisional energies are most probably far below the threshold for physical sputtering,²² and are too low to cause the ionization necessary for F-center formation.

The band gap energy of pure LiF is 13.6 eV,¹⁸ and it is possible to create the vacancies and interstitials that lead to F-centers in LiF crystals by irradiating them with ultraviolet light with energies down to the excitonic region of the absorption spectrum⁸, which begins at approximately 11 eV for LiF.²³ The laboratory experiments discussed below also indicate that photons with energies as low as Lyman- α (121.5 nm - 10.2 eV) can form F-centers in the LiF samples of this study. As mentioned above, preliminary solar UV/VUV fluxes/fluences were calculated for the STS-46 flight by using a detailed calculation to estimate the accumulated direct solar flux on the EOIM-III payload.¹² The results for photons with energies sufficient to cause F-center formation in LiF are tabulated in Table 4.

Table 4. *STS-46 solar UV exposure history for photon energies great enough to cause F-center formation in LiF.*¹¹

Mission Days	Sun Hours	Solar UV Flux (mW/cm ²)	
		121.5 nm	119-10 nm
0 - 2.0	5.8	7.1·10 ⁻⁴	3.3·10 ⁻⁴
3.0 - 4.0	6.8	7.5·10 ⁻⁴	3.7·10 ⁻⁴
4.0 - 5.8	10.4	7.5·10 ⁻⁴	3.6·10 ⁻⁴
5.8 - 6.0	0.3	7.5·10 ⁻⁴	3.6·10 ⁻⁴
6.0 - 7.0	4.4	7.7·10 ⁻⁴	3.7·10 ⁻⁴
7.0 - 8.0	2.9	7.8·10 ⁻⁴	3.8·10 ⁻⁴

The total integrated fluence from these data, normalized to the exposed volume of sample LiF-2, is 1.0·10¹⁹ eV/cm³. This is approximately a factor of 130 greater than the estimated energy needed to form the F-band observed in the 11/92 absorption spectrum for this sample. It also should be noted that during the EOIM-III operation period at 123-124 nmi a significant change in solar activity occurred.¹⁰ Since the calculated solar exposure is based on typical solar

^{*} Donald Hunton, private communication

radiation behavior in LEO, it is very likely the EOIM-III samples were subjected to a significantly higher solar UV/VUV radiation exposure than was calculated. Experience with electron bombardment of alkali halides has shown that production efficiency of stable F-centers is a few percent. Given this fact, the fluence and F-center concentrations discussed above are very consistent. Therefore, solar UV/VUV exposure is the most likely cause of the observed F-band in sample LiF-2, and consequently, in all the CMASS/NASA samples.

For photon energies above approximately 12 eV (103 nm), LiF has an average absorption coefficient of approximately $0.5 \cdot 10^6 \text{ cm}^{-1}$ [23] which corresponds to an absorption length (or penetration depth) of 200 Å. Consequently, F-centers produced in LiF by photons with energies above 12 eV would be limited to the near surface bulk, and average concentrations of 10^{14} F-centers/cm³ would actually represent local concentrations on the order of 10^{19} F-centers/cm³. Such concentrations are sufficient to produce coloration that is noticeable to the unaided eye. No visible signs of any coloration or damage was evident in any of the CMASS/NASA samples flown on EOIM-III. Also, it is well known that the solar UV spectrum is dominated by Lyman- α and longer wavelengths. Therefore, the F-centers observed in the CMASS/NASA samples are most likely due to solar UV photons with energies below 12 eV. If this is indeed the case, then the F-centers will be distributed somewhat uniformly throughout the bulk of the samples. Measurements of the actual F-center spatial distributions will clarify this issue, and experiments are currently being set up to perform such measurements on the samples.

To test the hypothesis that solar UV/VUV exposure caused the F-center formation in all the CMASS/NASA samples, UV/VUV exposures were performed in the laboratory using deuterium lamps. Control samples CaF₂-2 and LiF-3 were masked in an identical fashion as the flight samples, placed in a vacuum chamber, and exposed to approximately 100 solar equivalent hours. With the same spectrophotometer used for the flight samples, optical absorption spectra were taken of samples CaF₂-2 and LiF-3 both before and after the laboratory UV/VUV exposure. Figure 4 shows the change in optical density due to the UV exposure as a function of wavelength for samples CaF₂-2 (figure 4a) and LiF-3 (figure 4b). The spectra are similar to the applicable flight sample spectra, and F-bands in the exposed area of each control sample can clearly be seen. Also, as with the flight samples, no visible darkening, coloration, or damage is evident in these samples.

The deuterium lamps used for these experiments have MgF₂ windows which transmit very little light at wavelengths shorter than Lyman- α (121.6 nm).²⁴ Therefore, the small F-band evident in sample LiF-3 justifies the inclusion of photon fluxes at Lyman- α in the above analysis associated with Table 4. The differences between the control and flight sample spectra are most probably due to the fact that a deuterium lamp does not exactly duplicate the solar spectrum, especially in the spectral range of interest. However, the fact that F-centers were formed in the control samples by photons limited to Lyman- α wavelengths or longer is significant, because photon fluxes in this region dominate the solar UV spectrum. Consequently, this laboratory experiment provides very strong evidence that solar UV radiation was the primary cause of the F-center formation in the flight samples.

The formation of F-bands in optical materials exposed to the space environment has prompted the re-examination of optical absorption spectra from previous shuttle flight experiments. Figure 5 shows pre- and post-flight optical density spectra for a LiF sample flown on STS-4, which was of similar duration to STS-46. The post-flight spectrum clearly shows an F-band at 250 nm, and the calculated F-center concentration is approximately $5 \cdot 10^{14}$ F-centers/cm⁻³, a concentration very similar to that observed in EOIM-III sample LiF-2.

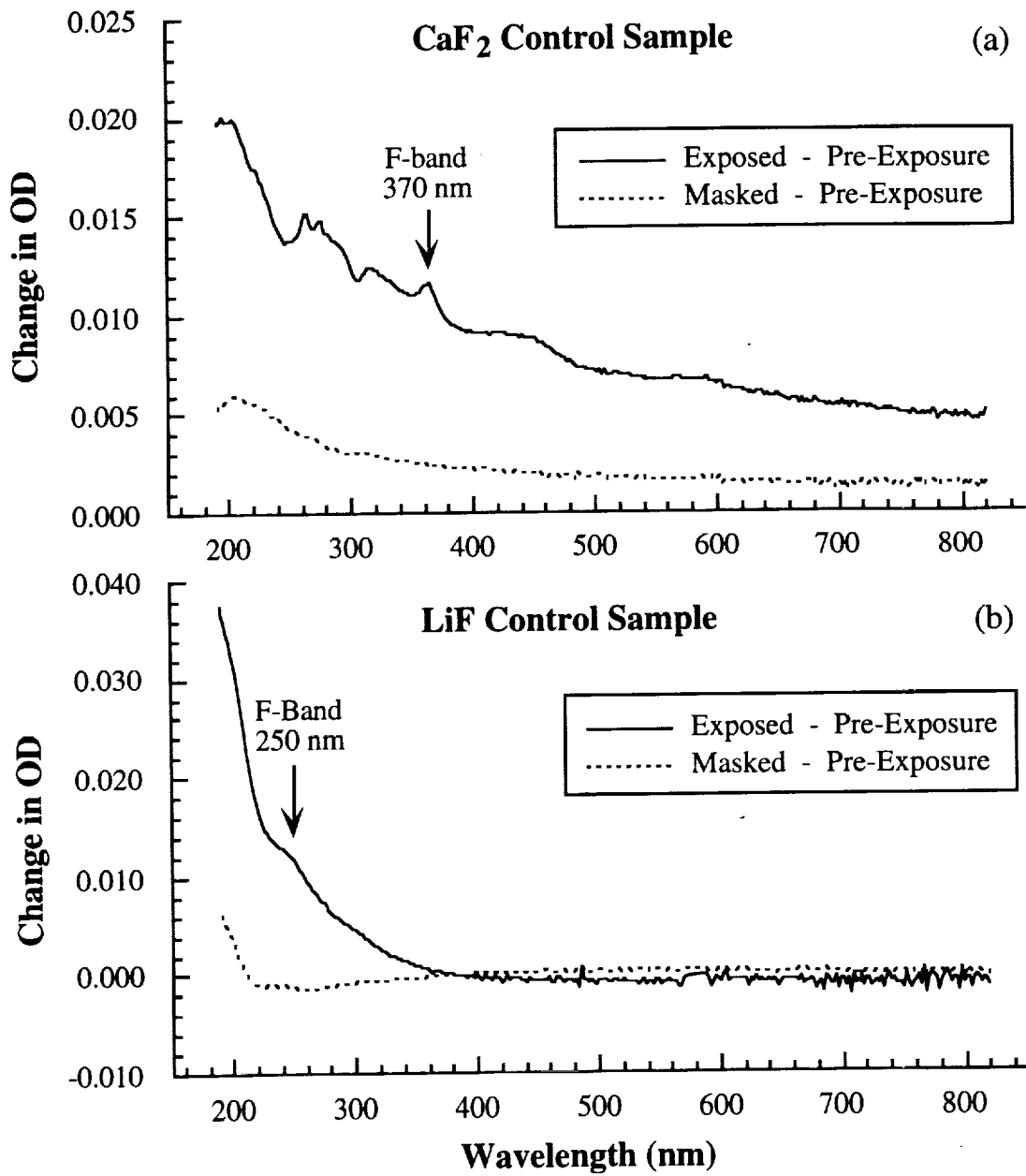


Figure 4. The change in optical density due to VUV exposure in the laboratory of control samples (a) CaF₂-2 and (b) LiF-3. The laboratory VUV exposures show similar defect formation as that observed in the EOIM-III flight samples.

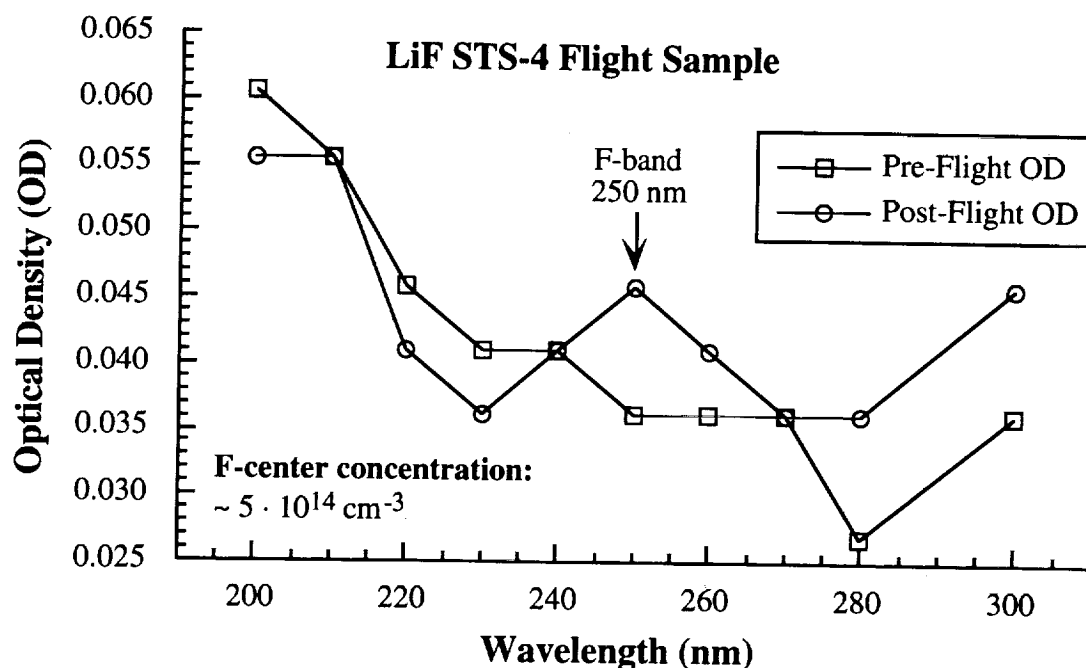


Figure 5. Pre- and post-flight optical density spectra for a LiF sample flown on space shuttle flight STS-4. The spectra show that F-centers were formed due to the space exposure.

CONCLUSIONS

Pre- and post-flight optical absorption measurements of CaF_2 and LiF samples flown by CMASS/NASA on EOIM-III clearly indicate F-center formation in these samples due to space exposure. The space-exposed MgF_2 samples show some UV absorption features that could be associated with F-center formation, but the evidence is less compelling than with the CaF_2 and LiF samples. All samples also exhibited UV darkening as well as increased optical density throughout the entire spectral range of measurement. This overall darkening is evidence for surface metallization with subsequent oxidation due to the atomic oxygen environment, although this assumption has not yet been verified by an independent technique.

The F-center formation in the LiF samples was much more pronounced than in either the CaF_2 or MgF_2 samples. This is consistent with previous laboratory experiments,²⁵ and what is known about the ability to produce F-centers in alkali halides as compared to alkaline-earth fluorides.⁷ Estimates of the F-center concentration in sample LiF-2 and the energy available in solar VUV radiation to create the F-centers are consistent. Laboratory experiments to simulate solar UV exposure caused F-center formation in control samples similar to that observed in flight samples. Because of these results and what is known about the EOIM-III radiation environment, solar VUV radiation exposure is most likely the primary cause of the F-center formation. Re-examination of STS-4 flight experiment data shows F-center formation in LiF similar to that observed on EOIM-III.

These results represent the initial set of post-flight examinations being planned for these samples; the next tests to be performed are currently being determined. Emphasis will be placed on determining F-center spatial distributions and detailed studies of how F-center formation is affected by crystal impurities. This information is not only of fundamental scientific interest in

understanding microscopic defect dynamics, but also could lead to schemes for radiation hardening of optical materials against darkening and damage.

It has been established that point defect formation leads to darkening and damage of optical materials. The results presented here show that the precursors to darkening and damage can be quantitatively studied in materials exposed to the space environment before any visible darkening or damage occurs. This further emphasizes the importance of careful selection and development of optical materials for space experiments.

ACKNOWLEDGMENTS

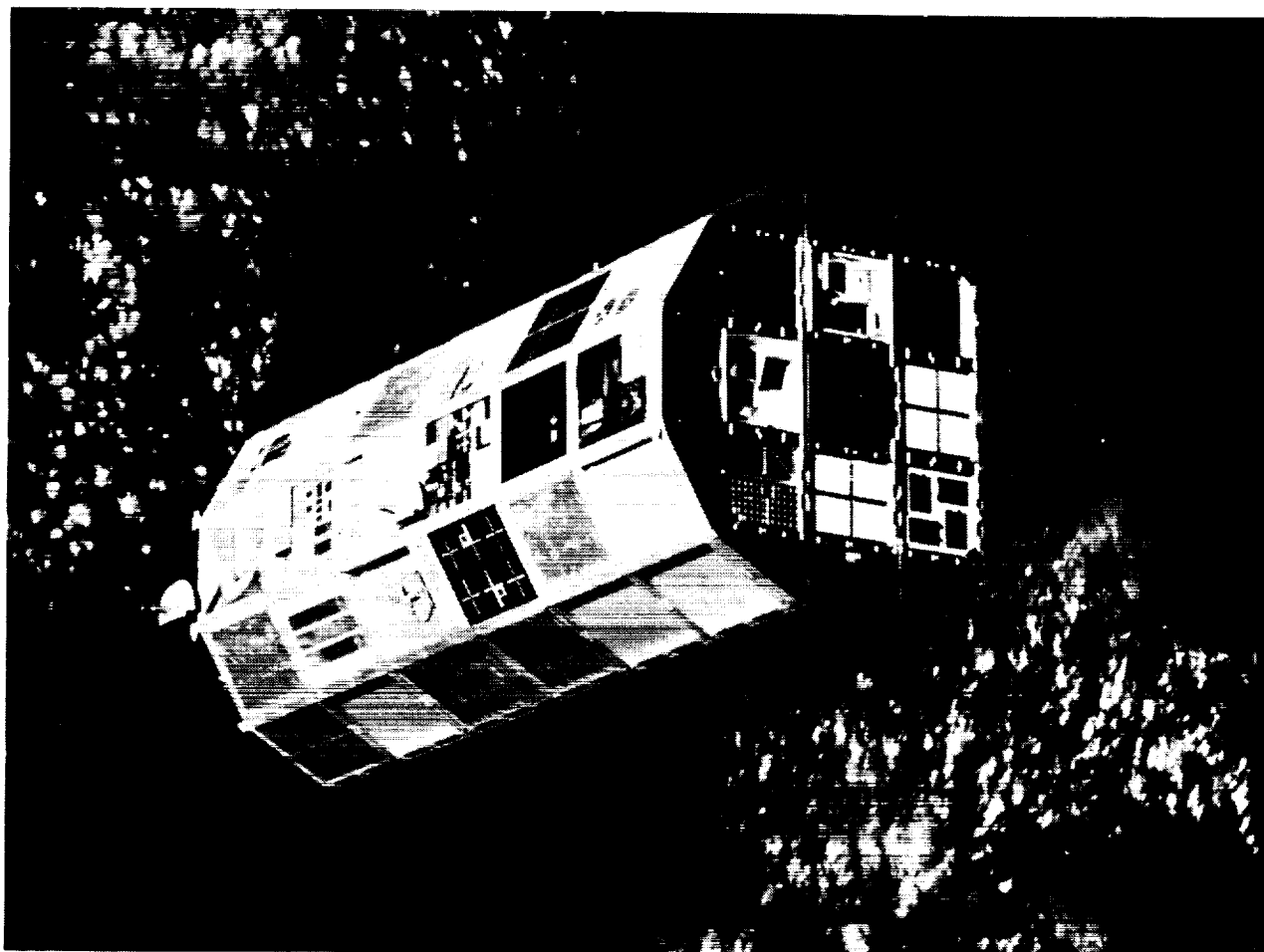
The authors wish to thank L. Reinisch for the use of his spectrophotometer, and P. Gray for his assistance in performing the laboratory UV exposure experiments. The authors also wish to thank S. Espy, I. Urazgil'din, W. Heiland, and P. Nordlander for helpful discussions. This work was supported in part by the National Aeronautics and Space Administration through the Tennessee Space Grant Consortium, NASA Contract No. 4-20-630-3581, and the Office of Naval Research under Contracts No. N00014-87-C-0146, No. N00014-91-C-0109, and Grant No. N00014-91-J-4040.

REFERENCES

1. L. J. Leger, "Oxygen Atom Reaction with Shuttle Materials at Orbital Altitudes - Data and Experiment Status," AIAA paper AIAA-83-0073, AIAA 21st Aerospace Sciences Meeting, January 10-13, 1983, Reno, NV.
2. J. T. Visentine, L. J. Leger, J. F. Kuminecz, and I. K. Spiker, "STS-8 Atomic Oxygen Effects Experiment," AIAA paper AIAA-85-0415, AIAA 23rd Aerospace Sciences Meeting, January 14-17, 1985, Reno, NV.
3. L. J. Leger, J. T. Visentine, and J. A. Schliesing, "A Consideration of Atomic Oxygen Interactions with Space Station," AIAA paper AIAA-85-0476, AIAA 23rd Aerospace Sciences Meeting, January 14-17, 1985, Reno, NV.
4. P. N. Peters, J. C. Gregory, and J. T. Swann, "Effects on optical systems from interactions with oxygen atoms in low earth orbits," *Appl. Opt.* **25** (8), 1290 (15 April 1986).
5. W. B. Fowler, editor, *Physics of Color Centers*, Academic Press, New York, 1968.
6. A. Van Den Bosch, " γ -Radiolysis of LiF," *Rad. Eff.* **19**, 129 (1973).
7. Y. Farge and M. P. Fontana, *Electronic and Vibrational Properties of Point Defects in Ionic Crystals*, North-Holland Publishing Company, Amsterdam, 1979.
8. F. Agullo-Lopez, C. R. A. Catlow, and P. D. Townsend, *Point Defects in Materials*, Academic Press, London, 1988.
9. See several of the articles and their associated references in "Damage to Space Optics and Properties and Characteristics of Optical Glass," *Proceedings of SPIE, Volume 1761*, edited by J. A. Breckinridge and A. J. Marker III (1992).
10. L. J. Leger, S. L. Koontz, J. Visentine, and D. Hunton, "An Overview of the Evaluation of Oxygen Interaction with Materials - Third Phase (EOIM-III) Experiment: Space Shuttle Mission 46," AIAA paper AIAA 93-0497, AIAA 31st Aerospace Sciences Meeting, January 11-14, 1993, Reno, NV.
11. L. J. Leger, "Evaluation of Oxygen Interactions with Materials III (EOIM-III) Flight Experiment Update," NASA Johnson Space Center Memorandum ES5-93-118, July 2, 1993.

1993. The latest atomic oxygen fluence data was relayed to EOIM-3 community by S.L. Koontz, June 1994
12. S. L. Koontz, L. J. Leger, S. L. Rickman, J. B. Cross, C. L. Hakes, and D. T. Bui, "Evaluation of Oxygen Interactions with Materials III - Mission and Induced Environments," presented at the *Third LDEF Post-Retrieval Symposium*, Williamsburg, VA (November 8-12, 1993).
 13. N. Seifert, H. Ye, D. Liu, R. G. Albrige, A. V. Barnes, N. Tolk, W. Husinsky, and G. Betz, "Simultaneous measurements of transmission optical absorption and electron stimulated Li desorption on LiF crystals," *Nucl. Instrum. Meth. Phys. Res.* **B72**, 401 (1992).
 14. R. A. Wood and P. D. Townsend, "An investigation of the structure of the F-band and envelope in LiF," *Nucl. Instrum. Meth.* **B65**, 502-506 (1992).
 15. J. H. Schulman and W. D. Compton, *Color Centers in Solids*, Pergamon Press, Oxford, 1963.
 16. B. Henderson and A. E. Hughes, editors, *Defects and Their Structures in Nonmetallic Solids*, Plenum Press, New York, 1976.
 17. J. J. Markham, *F-Centers in Alkali Halides*, Academic Press, New York, 1966.
 18. P. Klocek, editor, *Handbook of Infrared Optical Materials*, Marcel Dekker, Inc., New York, 1991.
 19. A. E. Hughes and A. B. Lidiard, AERE-R13319, Harwell Report HL89/1047, 1989.
 20. Q. Dou and D. W. Lynch, "Electron-Irradiation-Induced Structural and Compositional Changes on Alkali Halide Surfaces," *Surf. Sci.* **219**, L623 (1989).
 21. "Space Station Natural Environment Definition for Design," Johnson Space Center, Houston, TX, JSC 30425, Jan. 1987.
 22. R. Behrisch, editor, *Sputtering by Particle Bombardment II*, Springer-Verlag, Berlin, 1983.
 23. R. -P. Haelbich, M. Iwan, E. E. Koch, editors, "Optical Properties of Some Insulators in the Vacuum Ultraviolet Region," *ZAED Physik Daten* (August 1, 1977).
 24. J. H. Moore, C. C. Davis, and M. A. Coplan, *Building Scientific Apparatus: A Practical Guide to Design and Construction* (2nd edition), Addison-Wesley Publishing Co., Inc., Redwood City, CA, 1989.
 25. D. H. Heath and P. A. Sacher, "Effects of a Simulated High-Energy Space Environment on the Ultraviolet Transmittance of Optical Materials between 1050 Å and 3000 Å," *Appl. Opt.* **5** (6), 937 (June 1966).

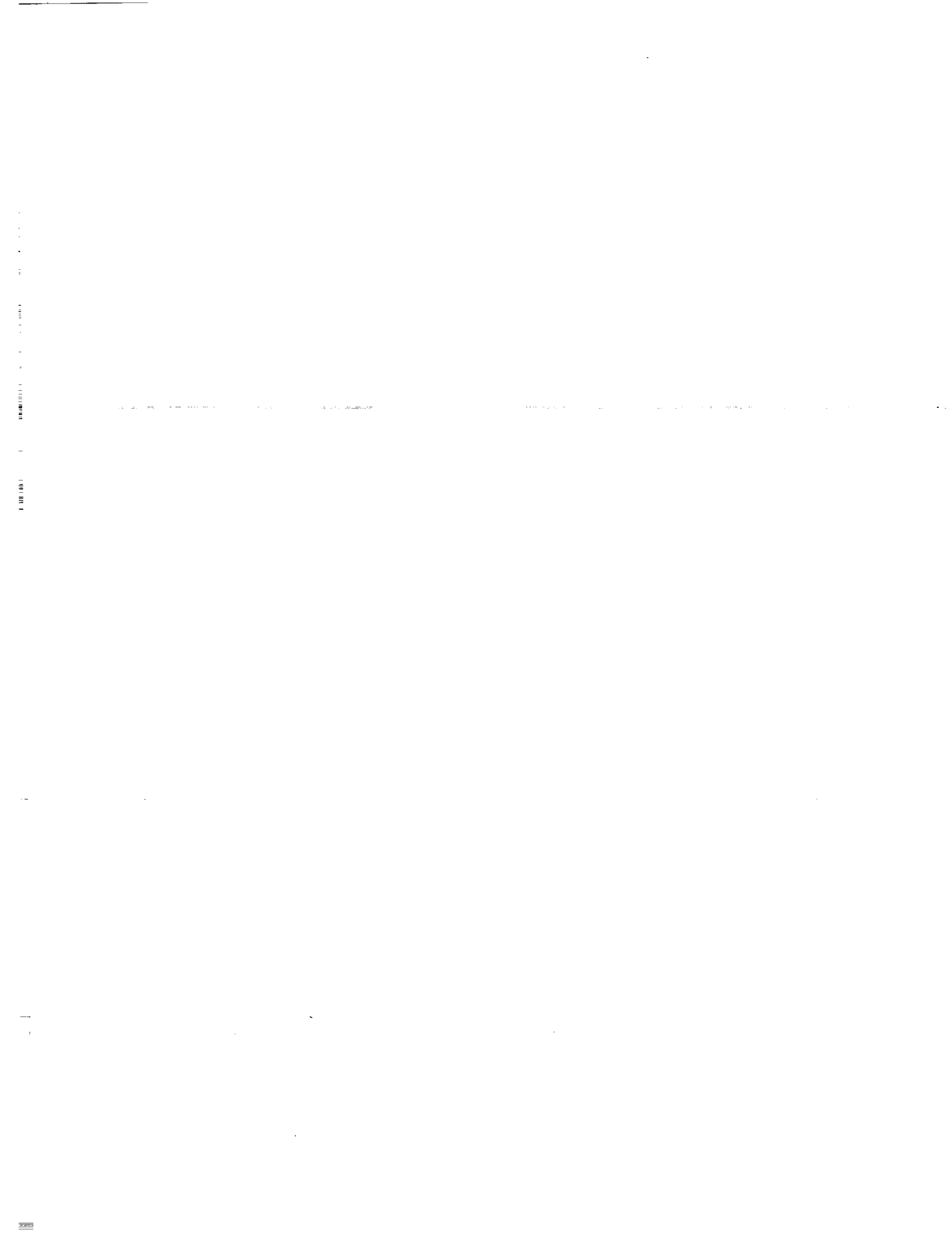
SYSTEMS



84-04319

PRECEDING PAGE BLANK NOT FILMED

1147



LDEF Systems Special Investigation Group Overview*

Jim Mason

NASA Goddard Space Flight Center
Greenbelt, MD 20771
Phone: 301-286-7256; Fax: 301-286-1600

Harry Dursch

Boeing Defense & Space Group
Seattle, WA 98124
Phone: 206-773-0527; Fax: 206-773-4946

INTRODUCTION

The Systems Special Investigation Group (Systems SIG), formed by the LDEF Project Office to perform post-flight analysis of LDEF systems hardware, was chartered to investigate the effects of the extended LDEF mission on both satellite and experiment systems and to coordinate and integrate all systems related analyses performed during post-flight investigations. The Systems SIG published a summary report in April, 1992 titled "Analysis of Systems Hardware Flown on LDEF - Results of the Systems Special Investigation Group" that described findings through the end of 1991. The Systems SIG, unfunded in FY 92 and FY93, has been funded in FY 94 to update this report with all new systems related findings. This paper provides a brief summary of the highlights of earlier Systems SIG accomplishments and the describes tasks the Systems SIG has been funded to accomplish in FY 94.

PREVIOUS ACCOMPLISHMENTS

The hardware of interest to the Systems SIG included an enormous diversity of components. The management of this hardware was facilitated by the division into four major engineering disciplines: mechanical, electrical, thermal, and optical. In order to assist the post-flight testing and analysis of LDEF hardware, the Systems SIG developed a set of standardized test plans for each of these four discipline areas (ref. 1). These plans were designed to be used by either the Systems SIG or the experimenters in their testing and analysis of systems hardware. These test plans are available through the LDEF Archive Office and have been used in assisting in the post-flight inspection of the retrieved Hubble Space Telescope hardware.

* The Boeing Defense & Space Group activities have been funded by NASA Langley Research Center on NAS1-18224 Task 15 and NAS1-19247 Tasks 2 and 8.

Beginning with on-site support of the de-integration of LDEF at Kennedy Space Center (KSC), Systems SIG personnel have supported the testing of active system related testing of experiments either at KSC, experimenter facilities, or at Boeing Defense & Space Group (BD&SG) facilities. BD&SG was funded by the Systems SIG to provide the necessary personnel and facilities required to meet the Systems SIG objectives.

To distribute the ongoing results of all LDEF related investigations to the spacecraft community, the Systems SIG authored and distributed a semi-quarterly newsletter titled "LDEF Newsletter". Because of the newsletter's popularity, the LDEF Project Office assumed responsibility for the continuation of this activity.

An LDEF Optical Experiment Database was created (using Filemaker Pro database software) that provides for quick and easy access to available experimenter optics related findings. The database contains a file for each of the LDEF experiments that possessed optical hardware. Each file contains various fields that identify the optical hardware flown, describes the environment seen by that hardware, summarizes experimenter findings and lists references for additional information. This database has been updated by Materials SIG funding to include findings from the 2nd LDEF Post-Retrieval Symposium held June 1992.

In April 1992 the Systems SIG distributed a report titled "Analysis of Systems Hardware Flown on LDEF - Results of the Systems Special Investigation Group" (ref. 2). This 300 page report summarized the major Systems findings through 1991. The report contained sections describing LDEF and the LDEF mission, brief summaries of the various LEO environments seen by LDEF, all major findings discussed by the four engineering disciplines, paper copy of the Optical database, and over 140 references for further details. This document is also available by contacting the LDEF Archival Office.

FY 1994 SYSTEMS SIG TASKS

The LDEF Systems SIG has been funded to accomplish the following tasks in FY94: 1) Collect and review all new LDEF systems related data generated by the various LDEF experimenters, 2) Update the April 1992 Systems SIG report and the Optics database, 3) Support the development of the LDEF Database and Archival effort, and 4) Identify specific concerns from ongoing spacecraft programs and address these concerns with LDEF data. The following paragraphs describe these tasks in more detail.

Task 1 - Collection and Review of All New LDEF Systems Related Data. Data to be reviewed includes the 2nd and 3rd LDEF Post-Retrieval Symposiums and the LDEF Materials Results for Spacecraft Applications Conference. In addition, a literature search will be performed and LDEF principal investigators contacted to obtain additional relevant information.

Task 2 - Updating the Summary Report and the Optics database. The results from Task 1 will be used to update the Summary Report and Optics database with new findings and lessons learned. The updated report will then be distributed to the spacecraft community using the LDEF Newsletter distribution list. Updated electronic copies of the Optics database will be distributed to the approximately 150 personnel currently possessing the database. Both the new report and database will also be available from the LDEF Archival Office.

Task 3 - LDEF Contamination Study. The objective of this task, performed by NASA Goddard Space Flight Center personnel, is to compile and analyze LDEF contamination data. The compiled data will then be used to model portions of LDEF in an attempt to determine the accuracy of contamination modeling of orbiting spacecraft. A final report summarizing the results of this task will then be released. A summary of the contamination report will be included in the update Systems report described in Task 2.

Task 4 - Support Development of the LDEF Database and Archival Effort. All LDEF systems hardware and data will be identified and located with this information forwarded to the LDEF Archival Office.

Task 5 - Determine On-going Spacecraft Concerns and Address with LDEF Data - The Systems SIG will identify specific issues on programs such as Hubble Space Telescope, Space Station, Earth Orbiting Satellite, Tropical Rainfall Measurement Mission, and Ballistic Missile Defense Organization (BMDO) missions and attempt to address these concerns with information generated from LDEF data. This information will be forwarded on to the Space Environments and Effects (SE&E) Program.

REFERENCES

- 1) Dursch, H.W et. al., "*LDEF Systems Special Investigation Group Investigation Plan*", Boeing Defense & Space Group, February 1990.
- 2) Dursch, H. W. et. al., "*Analysis of Systems Hardware Flown on LDEF - Results of the Systems Special Investigation Group*", NASA CR 189628, April 1992.

SYSTEM RESULTS FROM FRECOPA

Christian DURIN CNES - CT/AQ/EQ/QM
18, Avenue E. BELIN, 31055 TOULOUSE Cedex (France)
Phone : (33) 61 28 14 39, Fax (33) : 61 27 47 32

Lucinda BERTHOUD
Jean-Claude MANDEVILLE
CERT-ONERA/DERTS
2, Avenue E. BELIN, 31055 TOULOUSE Cedex (France)
Phone: (33) 61 55 71 17, Fax: (33) 61 55 71 69

INTRODUCTION

The work carried out over the past three years on FRECOPA and the LDEF has enabled a large quantity of information to be collected, part of which has already been exploited. As far as CNES is concerned, the major spin-offs of this mission mainly focus on the orbital environment and the behavior of materials in such an environment.

With respect to the environment, we shall develop the lessons learned from expert appraisals on impacts by microparticles, which are the main feature observed in this area. As for the materials, the results show a variety of behavior when subjected to the space environment and even now constitute a wealth of information for the designing and validation of future mechanical systems. Apart from these direct spin-offs, there are repercussions on in-flight and ground testing, the calibration of test benches and improvements to simulation models.

FRECOPA SYSTEM RESULTS

The FRECOPA system includes all materials and mechanisms used on FRECOPA with the exception of technological experiments flown in the three canisters. All these elements were exposed to a low orbit space environment for the 5.7 years of the mission while the specimens inside the canisters were only exposed during the first 10 months. These materials were not designed for such a long mission, yet their overall performance appears very satisfactory, as does the condition of the experiment itself. The most notable damage observed was as follows:

Impact by microparticles

Two types of support were found to show signs of impact: thermal blanket screens in teflonized woven glass fabric and aluminum screens protecting the box seals. 90 impacts over 50 microns in size were counted in one m². The largest impact perforated the 0.8 mm thick aluminum screens, projecting a cloud of debris into the experiment (as seen in fig. 1). The position of the crater on the edge of the experiment explains why such an impact caused no internal damage. Another crater on the same screen was at the edge of the perforation.

The impacts observed on the fabric of the flexible screens perforated the fabric but remained local because of the very nature of the fabric. No tearing was observed (as seen in fig. 2). The chemical analyses carried out on these craters did not clearly identify the nature of the impact-causing

particles. Either particle velocity was very high and the particles vaporized on impact, or the nature of the substrate (aluminum) masked the nature of the particle, as much debris is also of aluminum - the most commonly used metal on satellites.

Erosion and ageing

All the materials directly exposed to the space environment showed noticeable ageing. Deterioration parameters for FRECOPA are vacuum, U.V. radiation and the numerous thermal cycles to which the structure is subject. Organic materials (adhesives, thread, velcro, anodic protection, fabric used for the thermal blankets etc.) change color, thus revealing their ageing, but do not always show any catastrophic variation in their physical characteristics. Two important cases should however be noted.

The first concerns the flexible thermal blankets of teflonized woven glass fabric combined with an aluminized Mylar film. The environment damaged this fabric considerably, with erosion of approximately 12 microns, thus revealing glass fibers (as seen in fig. 3). A large network of cracks was also visible. The decline in the fabric's mechanical resistance explains this damage, which then allowed U.V. rays to go through the fabric and deteriorate the Mylar on the inner side of the screen. The Mylar then yellowed and became extremely fragile, which meant it was impossible to disassemble or test for mechanical characteristics. This thermal protection proved too little therefore with respect to the actual length of the mission.

The second case of erosion concerns the Delrin parts ensuring the mechanical link when the canisters were shut. The upper, exposed surface of these circular parts revealed erosion of approximately 30 microns (as seen in fig. 4). As the canisters only opened and shut once in orbit, there were no functional consequences. However, if such a mechanism were needed to operate several times, the play induced by ageing could be problematic.

Contamination

Numerous traces of contamination are visible on FRECOPA. Not only are there contaminants induced by outgassing or the deterioration of experiment materials (glass fabric), but external contaminants too. Here again, two phenomena were observed which show the complexity of the problem.

The shadow of one of the canisters was observed on the sides of the experiment. This shadow results from the deposit of contaminants on their surfaces then their polymerization when exposed to U.V. rays. In this particular case, the outgassing products were spread uniformly over all the surfaces which were cold when the structure was in shade. As the sun rose on the most quickly illuminated side, the contaminants were polymerized and as the box carrying structure formed a partial screen, its shadow is seen on the side of the experiment. On the opposite side of the experiment, surface temperature rose due to conduction and as the sunlight reached those surfaces later, outgassing products had time to vaporize and be deposited on other cold surfaces still in shade. The other traces observed were found on both the backside of the experiment (facing LDEF's interior) and along the experiment sides. This time, there was a contamination flux from inside the satellite moving out towards FRECOPA's backside. The shadow of a nut and bolt could clearly be seen on the rear structure of the FRECOPA experiment, as could that of an electric wire (as seen in fig. 5). We think these objects protected the surfaces from the contaminating flux. On the sides of the experiment, rivets played the same role and similarly-protected areas may also be seen there. These multiple traces prove the existence of several different fluxes over time (as seen in fig. 6). The search for sources of contamination shows that they are located on the front of the satellite. The interstices between the various experiments allowed contamination through, and no doubt both atomic oxygen (AO) and U.V. radiation too.

Intermetallic adherence

This phenomenon proves a very controversial subject. The appearance of intermetallic welding requires special conditions as regards pairs of materials, temperature, pressure and mechanical stress (vibration). For FRECOPA, taking both launch and mission parameters into account, two metallic parts were seen to stick together, the parts in question being a steel spring and an aluminum plate. They were used in AO experiments 138-1 and -6. The spring pressed against the aluminum plate which held in place a sample to be exposed to the environment. The force needed to separate the materials was slight and could not be measured. Electronic microscopy revealed a transfer of matter, in that aluminum was found on the spring (as seen in fig. 7). The parameters mentioned above encouraged such a phenomenon but the state of the surface of the two materials themselves is an important parameter. Intermetallic adhesion was thus observed, with a transfer of matter which could, in the case of mechanisms, cause operating problems.

The positive points of this experiment are as follows:

Thermal blankets

Despite visible ageing, they showed good mechanical resistance to the large number of thermal cycles suffered by the structure. The system of attachment using Velcro strips either sewn or glued to the structure allowed sufficient flexibility to avoid the loss of fabric functionality by tearing. This choice of material also enabled impacts to be contained locally, avoiding propagation and destruction of the blanket itself.

Mechanisms and electronics

The canisters opened and closed because both the mechanisms and control electronics worked correctly. No anomalies were found in these components during the technical evaluation, and they worked on the ground with results similar to those recorded during flight.

Materials

All the materials used (structure), kinematic chain, adhesive, Velcro, surface treatment performed well and validated certain technological choices made. Ageing was apparent in certain components, but there was little change in mechanical or physical/chemical properties as a result.

THE SYNERGY OF AGEING FACTORS

The origin of ageing is not always easy to determine. For FRECOPA experiment, located on LDEF's trailing edge, the factors identified as causing ageing were predominantly U.V. radiation, thermal cycling and exposure to vacuum. However, ageing can only be understood in the context of the synergy between all environment parameters. For example, the erosion observed in the thermal blankets is attributed to the effects of thermal cycling and U.V. radiation. Looking at surface morphology, it is possible to think that atomic oxygen also played a role. Indeed, when LDEF was retrieved the trailing edge was exposed to a low atomic oxygen fluence. The dose received was only for a short period of time but with a higher fluence value because at a low altitude. It could thus have interacted with FRECOPA materials already weakened by 5.7 years of exposure to the environment.

Another example of interaction between several different environment parameters is shown by deterioration caused by AO and U.V. radiation following impacts on the structure by

microparticles. Not only is there the effect of the impact itself, but also the physical and/or chemical interaction of radiation fluxes. Materials not intended, and therefore not designed, to be exposed to such constraints found themselves on the front line and thus suffered considerable ageing. This typical phenomenon was found on the LDEF in the multilayer thermal blankets (Teflon, silver, Inconel and paint), where the inner silver layer had been oxidized following the penetration of a particle. As far as FRECOPA is concerned, the thermal blankets of teflonized woven glass fabric were eroded and allowed U.V. rays through. The latter damaged the Mylar layer on the inner side of the screens. The criticality of such synergy between impact/AO/U.V. radiation depends on whether the damage caused by the particle remains local or spreads throughout the material.

THE IMPACT PHENOMENON

As seen above, impacts linked with AO or U.V. exposure can cause great damage. As far as the damage related to the impact itself is concerned, the result depends on several different parameters. The nature of both the particle (shape, chemical origin, size, velocity) and substrate is important. On FRECOPA, particles were observed to have pierced aluminum screens 0.8 mm thick, but that multilayer materials used as detectors stopped certain particles more easily. The concept of this kind of protection may avoid damage from part of the microparticle population whilst not adding greatly to the structure's mass.

Such perforating impacts raise the problem of equipment located on "preferable" surfaces. These items of equipment can be directly damaged by the projectile and/or the debris created by the particle crossing through the surface. The velocity of such secondary impacts is less but their geographical dispersion, and thus their zone of interaction, greater.

It is not only important to study the fluxes themselves, as FRECOPA has allowed, but also to determine the nature of orbiting particles. The one parameter currently increasing in the space environment is the number of debris-type particles generated by human activity in space. The determination of sources (ageing of materials, impacts, propulsions, outgassing etc.) should permit such proliferation to avoid densities incompatible with space missions, and particularly manned missions. There is a close relationship between materials, their use and impacts. Knowledge of the environment is closely linked to the collection of particles in the different orbits used for their analysis. The human factor can then be distinguished from the natural factor and protective means and materials better-suited in terms of impacts and ageing can then be proposed so as to limit the generation of debris.

In-flight experiments also provided further knowledge about the Earth's natural environment. Particles of human origin were identified on FRECOPA whereas because of the experiment's rear position on the satellite, only impacts of a natural origin should have been observed. This means that the presence of debris is no longer limited to circular orbits but also elliptical ones.

USE OF RESULTS

Results may be used at several levels. Firstly, they enable ground simulation facilities to be improved by comparing flight samples and accelerated ageing results obtained in a laboratory setting, particularly ageing from U.V. radiation, AO, or impact simulations in which chemical analyses have allowed us to correlate the presence of an element (Fe) with particle velocity. This also leads to an improvement in test benches, making them more lifelike, although this does of course make them more complex too. These tests will never replace real-time in-flight experiments but they help us evaluate ageing problems more quickly. With this in mind, on-orbit tests with telemetry of results

have the further advantage of avoiding possible changes in atoms when the materials come in contact with the Earth's environment ("healing" phenomenon by the recombination of free radicals).

The second point is the choice of materials for future missions taking into account their exposure. As seen above, this choice is also linked to the problem of satellite design. Engineers must build into their way of thinking problems relating to geometry (secondary impacts, shadows, contaminations etc.) and the possibility of avoiding defect propagation (choice of multilayers to limit the penetration of impacts, choice of materials to limit the extension of defects).

The last way of using results is as input data for numerical simulation codes which are used to set the parameters for several factors and thus broaden our knowledge of ageing. This is the case for hydrocodes which can model impact phenomena and lead to a better understanding of their dynamics. Structural calculations also use the results from on-orbit experiments to determine behavior at the end of the structure's lifetime.

On the other hand, the application of results from this experiment to other orbits may be problematic, as numerous environment parameters change with altitude and inclination. However, results could be used on a case-by-case basis as an envelope for designing the specific satellite.

CONCLUSIONS

As described above, the main spin-offs from the LDEF/FRECOPA mission concern:

* impacts

- nature of microparticles
- impact morphology
- resulting damage and propagation
- global fluxes for the orbit and mission considered

* ageing of materials

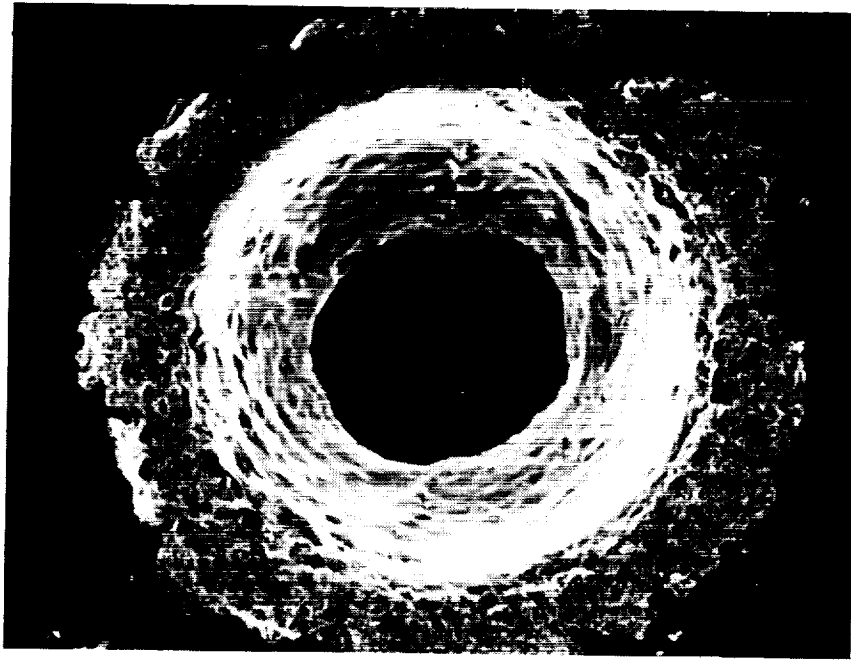
- erosion phenomena
- contamination
- the effect of U.V. radiation and atomic oxygen
- thermal cycling

These lessons enable the actual orbital environment to be better taken into account and materials optimized with respect to designing. This knowledge must be extended to other orbits used. An improved characterization of the fluxes of microparticles and their nature would enable an improvement to be made in the measures needed to prevent the proliferation of debris in space. The utility of such scientific missions is evident and it is on the wealth of knowledge gained as a result that reliability, availability, maintainability, and safety aspects of future missions depends.

REFERENCES

- Ref. Å French Cooperative Passive Payload (FRECOPA)
System Results
Ch. DURIN - CNES
First Post Retrieval Symposium
Kissimmee Florida, June 1991
- Ç Results of the "Post flight" analyses on system materials for LDEF/FRECOPA experiment
Ch. DURIN, I. ALET - CNES
Materials in a space environment
Cannes France, Sept. 1991
- É System Related Testing and analysis of FRECOPA
Ch. DURIN
LDEF Materials Workshop'91
NASA La RC, November 1991
- Ñ New Results from FRECOPA Analysis
Ch. DURIN - CNES
Second Post Retrieval Symposium
San Diego California, June 1992

a



b

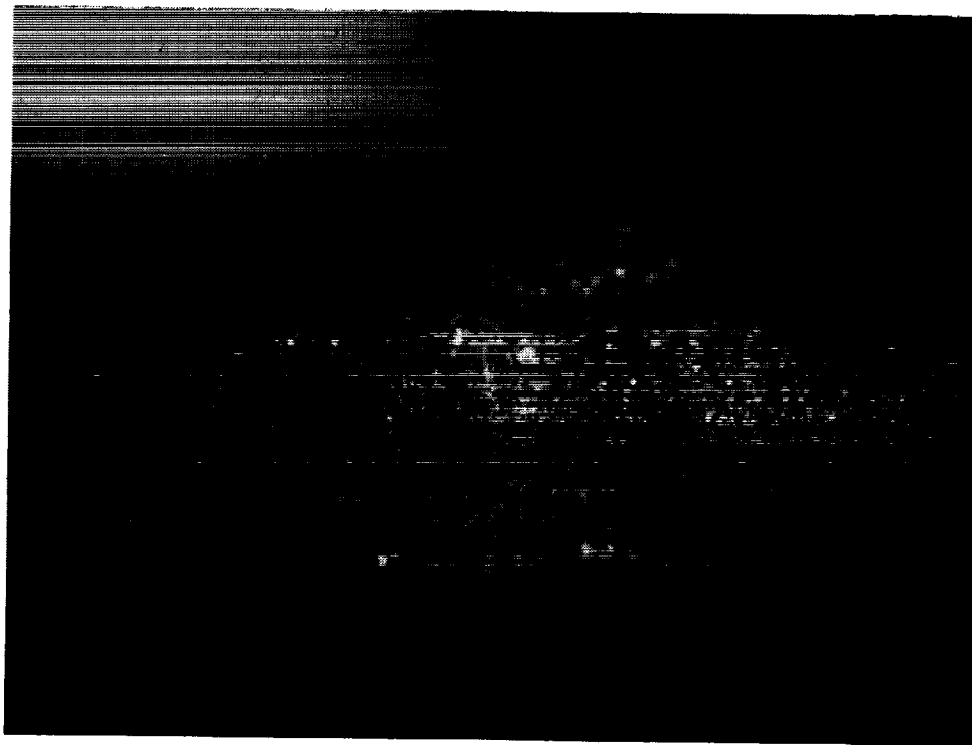


Figure 1 - The biggest crater on FRECOPA tray (a)
cloud of debris on the structure (b)

SCALE : $100\ \mu\text{m}$

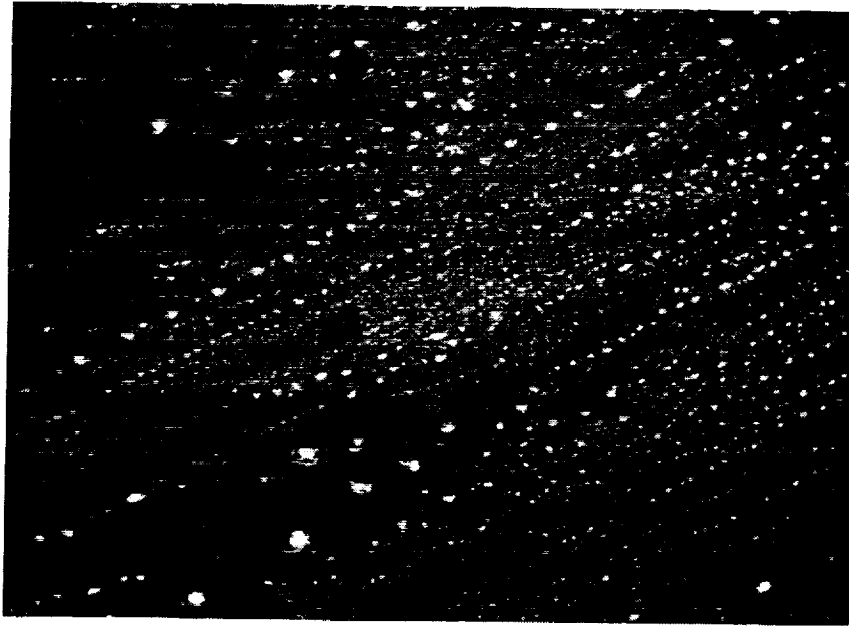


SCALE : $10\ \mu\text{m}$

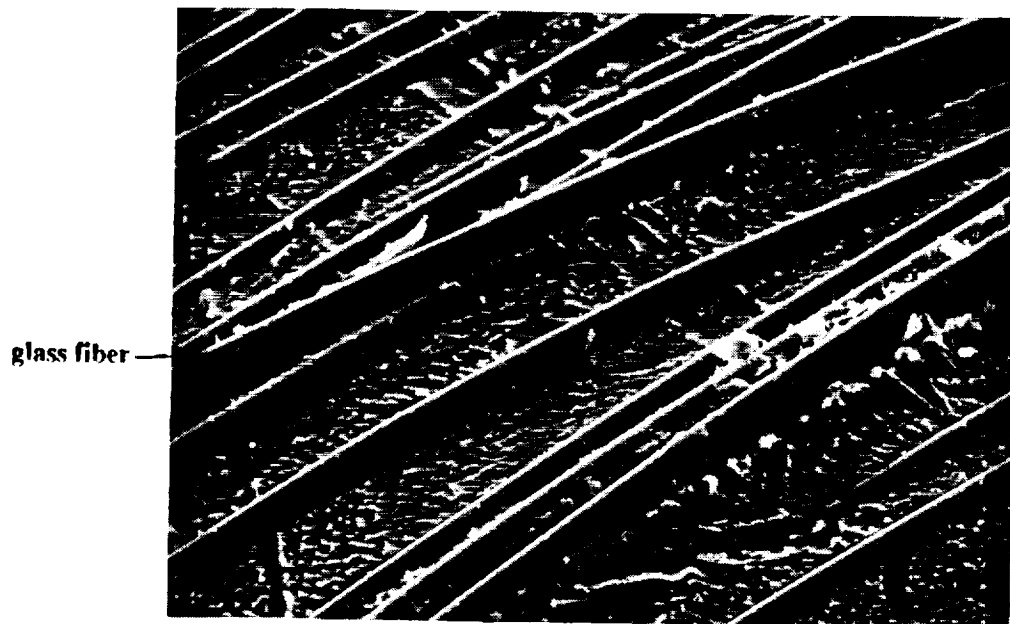


Figure 2 - Impact morphology on thermal blankets

scale 10 μm ———



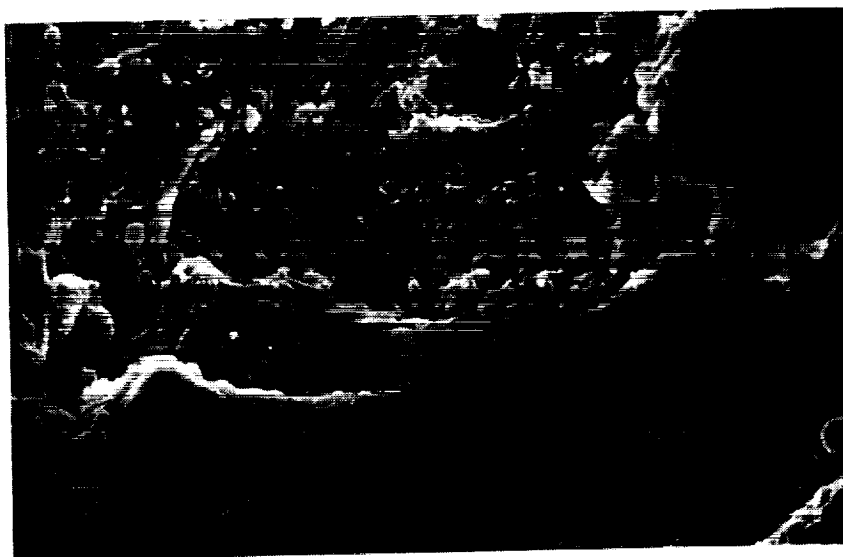
Reference sample



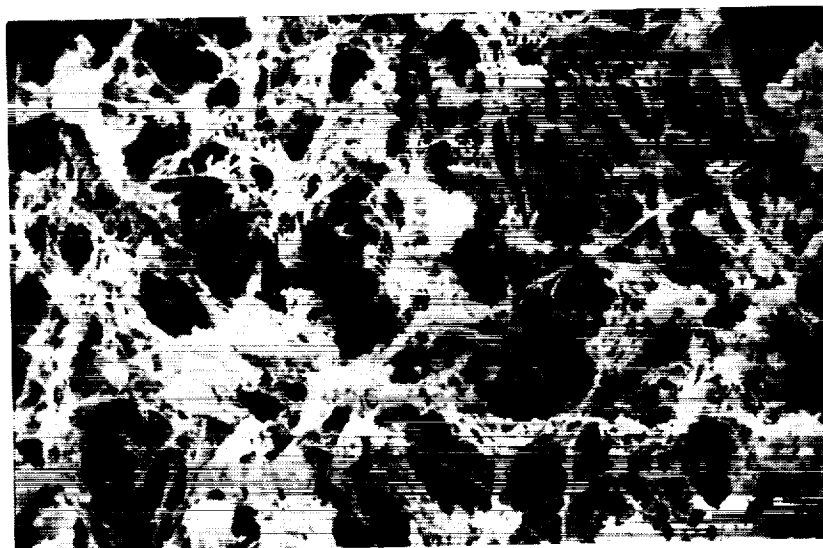
Flight sample

Figure 3 - Surface degradation on thermal blankets

SCALE: 10 μ m



Reference sample



Flight sample (exposed area)

Figure 4 - Erosion on Delrin samples

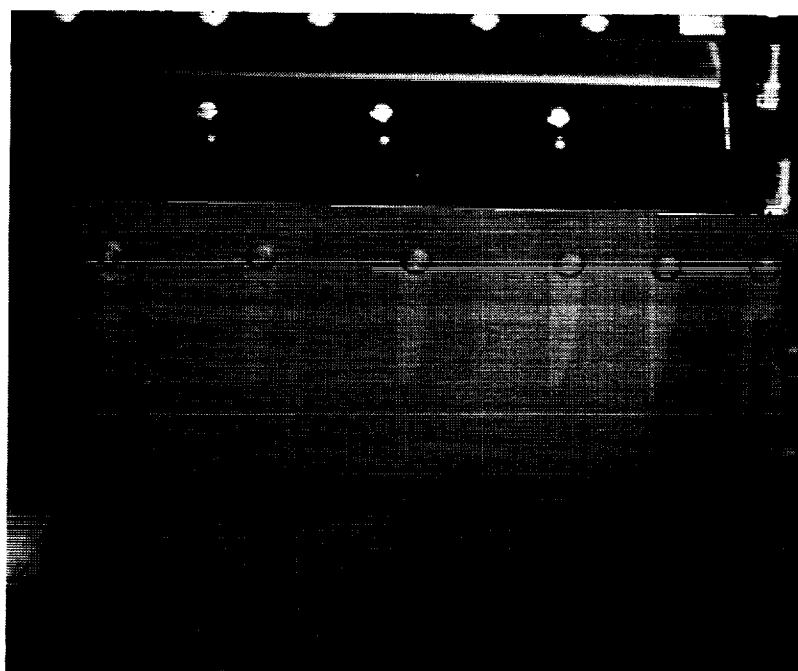
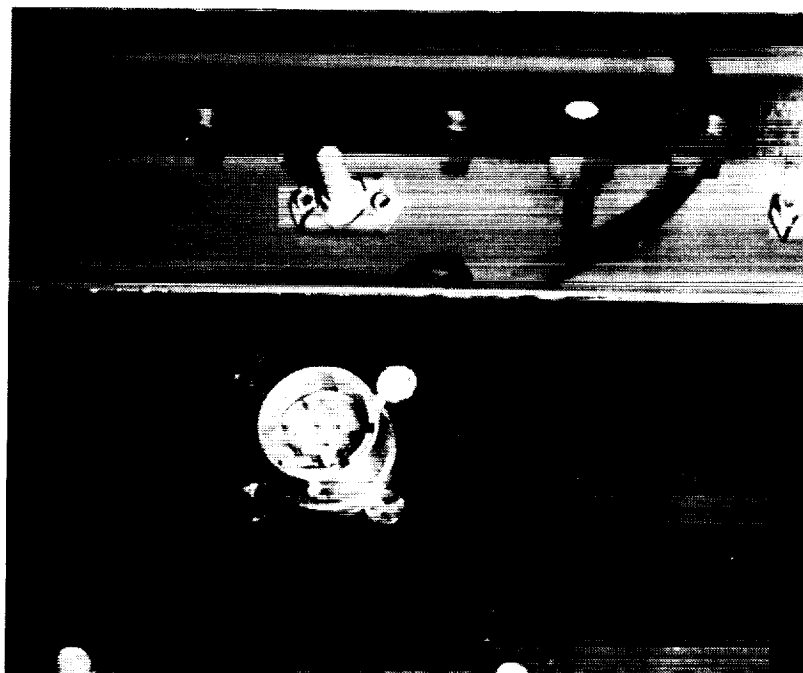


Figure 5 - Bolt, wire and rivet shadows on the back of the tray

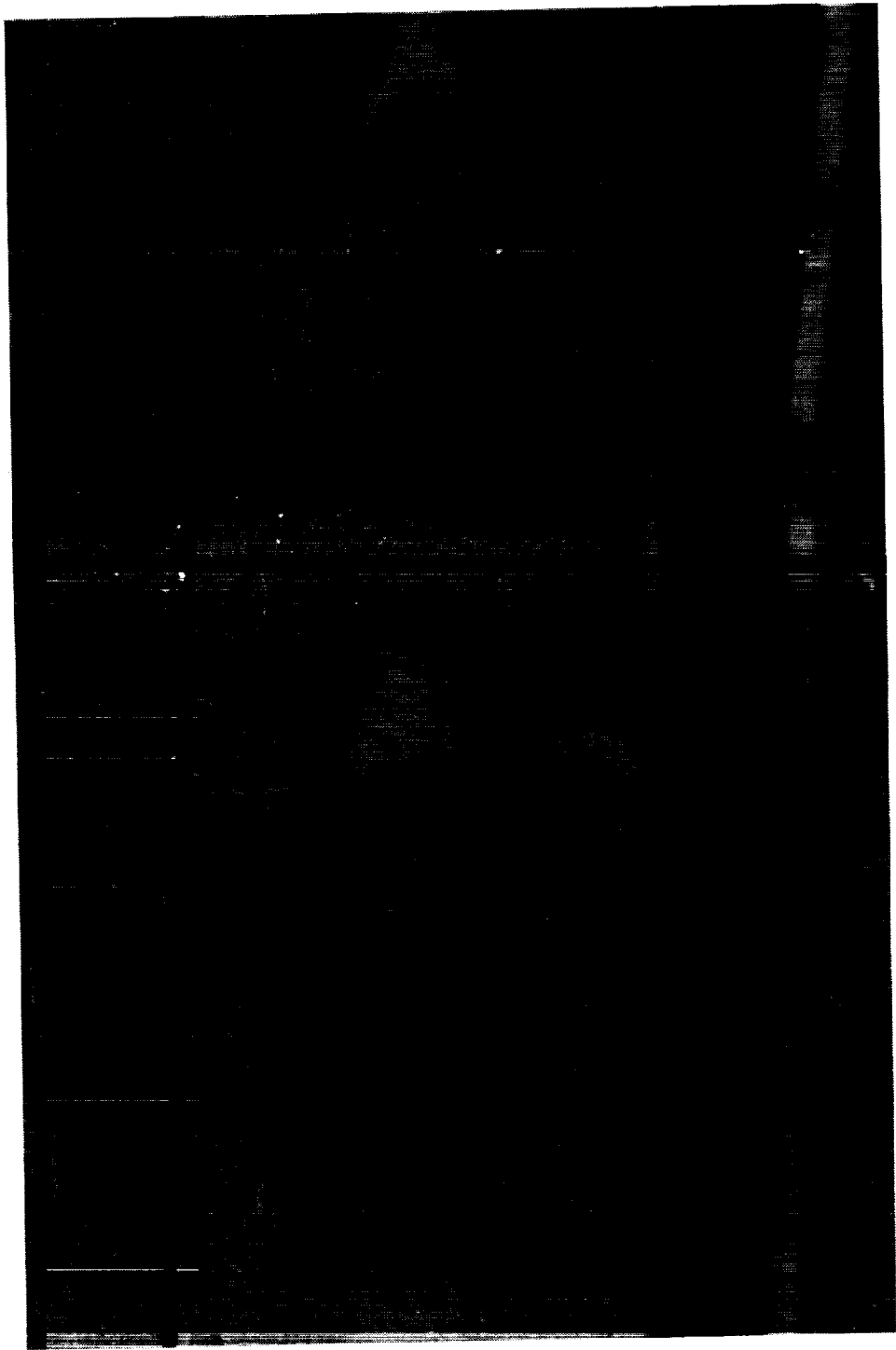


Figure 6 - Multi shadows around rivets

Aluminium

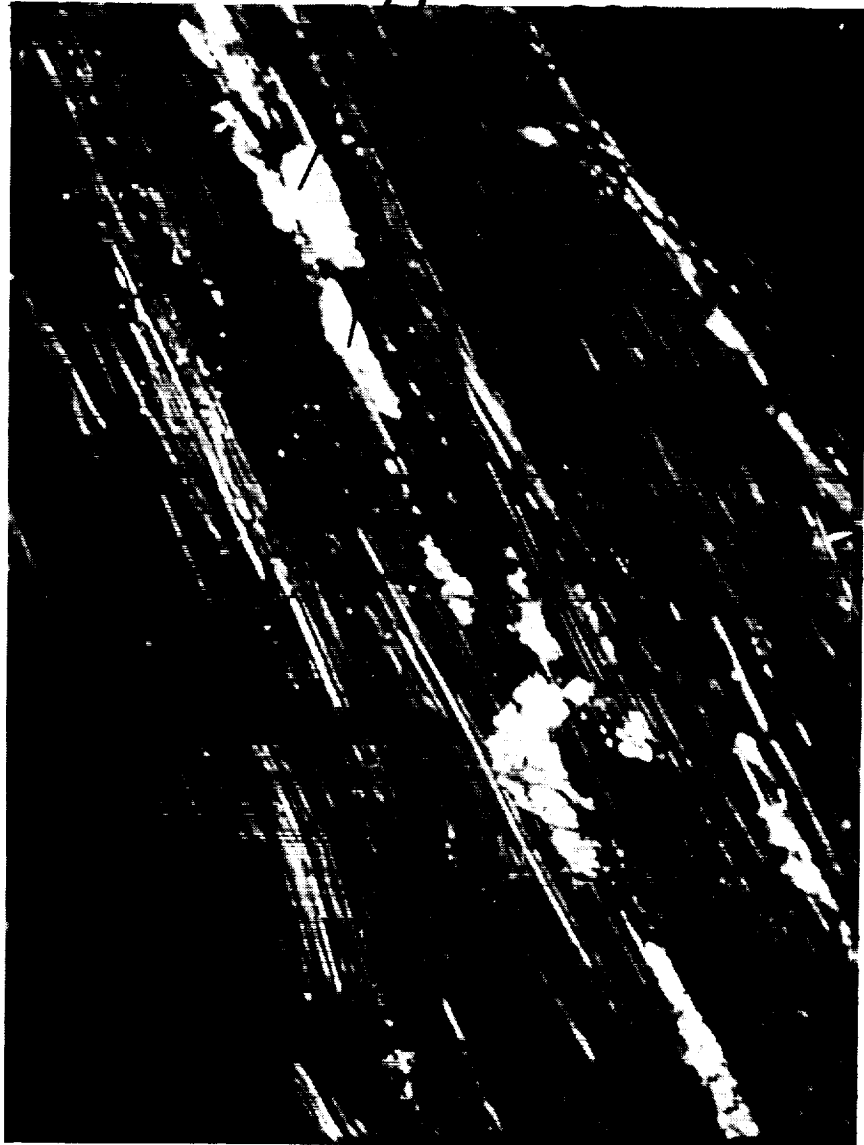


Figure 7 - Aluminium transfer on steel spring

SPACE ENVIRONMENTAL EFFECTS ON SOLAR CELLS:
LDEF AND OTHER FLIGHT TESTS*

Peter Gruenbaum and Harry Dursch
Boeing Defense & Space Group
P.O. Box 3999, MS 82-32
Seattle, WA 98124-2499
Phone: (206) 773-8437 / FAX: (206) 773-4946

SUMMARY

This paper summarizes results of several experiments flown on the Long Duration Exposure Facility (LDEF) to examine the effects of the space environment on materials and technologies to be used in solar arrays. The various LDEF experiments are compared to each other as well as to other solar cell flight data published in the literature. Data on environmental effects such as atomic oxygen, ultraviolet light, micrometeoroids and debris, and charged particles are discussed in detail.

The results from the LDEF experiments allow us to draw several conclusions. Atomic oxygen erodes unprotected silver interconnects, unprotected Kapton, and polymer cell covers, but certain dielectric coatings can protect both silver and Kapton. Cells that had wrap-around silver contacts sometimes showed erosion at the edges, but more recently developed wrap-through cells are not expected to have these problems. Micrometeoroid and debris damage is limited to the area close to the impact, and microsheet covers provide the cells with some protection. Damage from charged particles was as predicted, and the cell covers provided adequate protection. In general, silicon cells with microsheet covers showed very little degradation, and solar modules showed less than 3% degradation, except when mechanically damaged. The solar cell choices for the Space Station solar array are supported by the data from LDEF.

INTRODUCTION

Several experiments were flown on the LDEF to examine the effects of the space environment on materials and technologies to be used in solar arrays. Although a great deal of work has gone into analyzing these experiments and drawing conclusions, the experiments were conducted by a variety of organizations and published in separate papers. In this paper, the published data are summarized and the various LDEF experiments are compared to each other as well as to other solar cell flight data published in the literature. This information can provide designers of new solar arrays with data on specific environmental effects that might apply to their spacecraft's orbit without requiring extensive literature searches.

This paper begins with a description of the various experiments flown on LDEF, as well as other flight data mentioned. A section on how solar cell measurements are made follows. Data on environmental effects such as atomic oxygen, ultraviolet light, micrometeoroids and debris, and charged particles are then covered. Finally, future flights are described and conclusions are drawn.

*This paper was supported by NASA Langley Research Center and Goddard Space Flight Center under contract NAS1-19247.

FLIGHT EXPERIMENTS

Table 1 presents a list of the experiments on LDEF that involved solar cells or solar arrays. Experiment S0014, the Advanced Photovoltaic Experiment (APEX) had active on-orbit monitoring of some of its cells for the first 325 days of the 69 month mission, and covered a large variety of cell types[1]. Experiment A0171, the Solar Array Materials Passive LDEF Experiment (SAMPLE) contained a variety of experiments with no active sampling. Unfortunately, due to the unexpected length of the mission, some of the polyimide substrates were eroded by atomic oxygen, and several pieces of the experiment were lost. SAMPLE was used to test different types of cells[2] and different types of cell covers[3]. Similar experiments were flown on M0003-4[4], and complete results are expected to be published soon. Two other experiments had solar modules to power non-solar experiments: the LDEF Heat Pipe Power System (S1001)[5], and the Space Plasma High Voltage Drainage Experiment (A0054)[6]. These experiments were useful because they provide data from actual working modules. Calculations of atomic oxygen fluence and solar ultraviolet irradiation exposure for the LDEF mission are given for each experiment in Table 2.

Other data discussed in this paper come from Space Shuttle flights STS-5 and STS-41, LIPS, Hughes, Space Systems/Loral, CRRES/HESP and the Hubble Space Telescope.

Table 1. List of solar cell experiments on LDEF.

Principal Investigator	Type of Cells	Number of Cells	Experiment/Description
NASA LeRC - D. Brinker	Si, GaAs	155	S0014 - Advanced Photovoltaic Experiment (APEX) [1]
NASA MSFC - A. Whitaker L. Young	Si	4 modules & 5 cells	A0171 - Solar Array Materials Passive LDEF Experiment (SAMPLE) [2]
NASA LeRC - D. Brinker	Si	20	A0171 - Solar Array Materials Passive LDEF Experiment [1]
JPL - P. Stella	Si	30	A0171 - Solar Array Materials Passive LDEF Experiment [3]
NASA GSFC - E. Gaddy	Si	45	A0171 - Solar Array Materials Passive LDEF Experiment
Wright Pat AFB - T. Trumble	Si, GaAs	70	M0003-4 - Advanced Solar Cell and Coverglass Analysis [4]
NASA GSFC - S. Tiller	Si	4 arrays	S1001 - LDEF Heat Pipe Power System [5]
MBB - L. Preuss	Si	3	S1002 - Evaluation of Thermal Control Coatings and Solar Cells
TRW - J. Yaung	Si	12	A0054 - Space Plasma High Voltage Experiment [6]

Table 2. Atomic oxygen fluence and solar UV radiation exposure for solar cell experiments on LDEF.

Experiment/Description	Atomic Oxygen Fluence (atoms/cm ³)	Solar ultraviolet irradiation (equivalent sun hours)
S0014 - Advanced Photovoltaic Experiment (APEX)	8.99x10 ²¹	11,200
A0171 - Solar Array Materials Passive LDEF Experiment (SAMPLE)	7.15x10 ²¹	9,400
M0003-4 - Advanced Solar Cell and Coverglass Analysis	8.99x10 ²¹ (leading) 1.32x10 ¹⁷ (trailing)	11,200 (leading) 11,100 (trailing)
S1001 - LDEF Heat Pipe Power System	4.59x10 ²⁰	14,500
S1002 - Evaluation of Thermal Control Coatings and Solar Cells	1.32x10 ¹⁷	11,100
A0054 - Space Plasma High Voltage Experiment	8.43x10 ²¹ (leading) 2.31x10 ⁵ (trailing)	10,700 (leading) 10,500 (trailing)

SOLAR CELL MEASUREMENT

Solar cell efficiencies are measured from a current-voltage curve, where the voltage is swept from zero to its highest value at open circuit conditions (V_{oc}) and the current is measured from its highest value at short circuit conditions (I_{sc}) down to zero. Since the power of the cell is the voltage times the current, there is a value of voltage and current where the power is at its maximum. At this maximum power point, the fill factor (FF) is defined as

$$\begin{aligned} \text{Max. power} &= V_{mp} I_{mp} \\ &= FF V_{oc} I_{sc} \end{aligned}$$

where V_{mp} and I_{mp} are the maximum power point voltage and current. A sample current-voltage curve is shown in Figure 1.

It is difficult to extract relevant information by measuring V_{mp} and I_{mp} , whereas V_{oc} , I_{sc} , and FF correspond directly to physical properties of the cells. By comparing the V_{oc} , I_{sc} , and FF of a cell before and after a flight, it is often possible to diagnose the physical cause of any change. I_{sc} is proportional to the number of photons converted into electron-hole pairs that are successfully collected. If there is a drop in I_{sc} and a slight drop in V_{oc} , then this is caused by non-optimum light collection, and implies that there was added darkening or shading. If there is a drop in FF only, then the series resistance has increased, which means that a structure that is used to carry current -- such as cell gridlines or cell interconnects -- has been damaged. If there is both a drop in FF and V_{oc} , then shunt resistance has decreased, which means that a new conductive path has been created between the positive and negative contacts of the solar cell. This generally occurs when the semiconductor junction has been physically damaged, which can be caused by a micrometeoroid/debris impact or by high energy protons. Figure 2 shows a circuit schematic for series and shunt resistance.

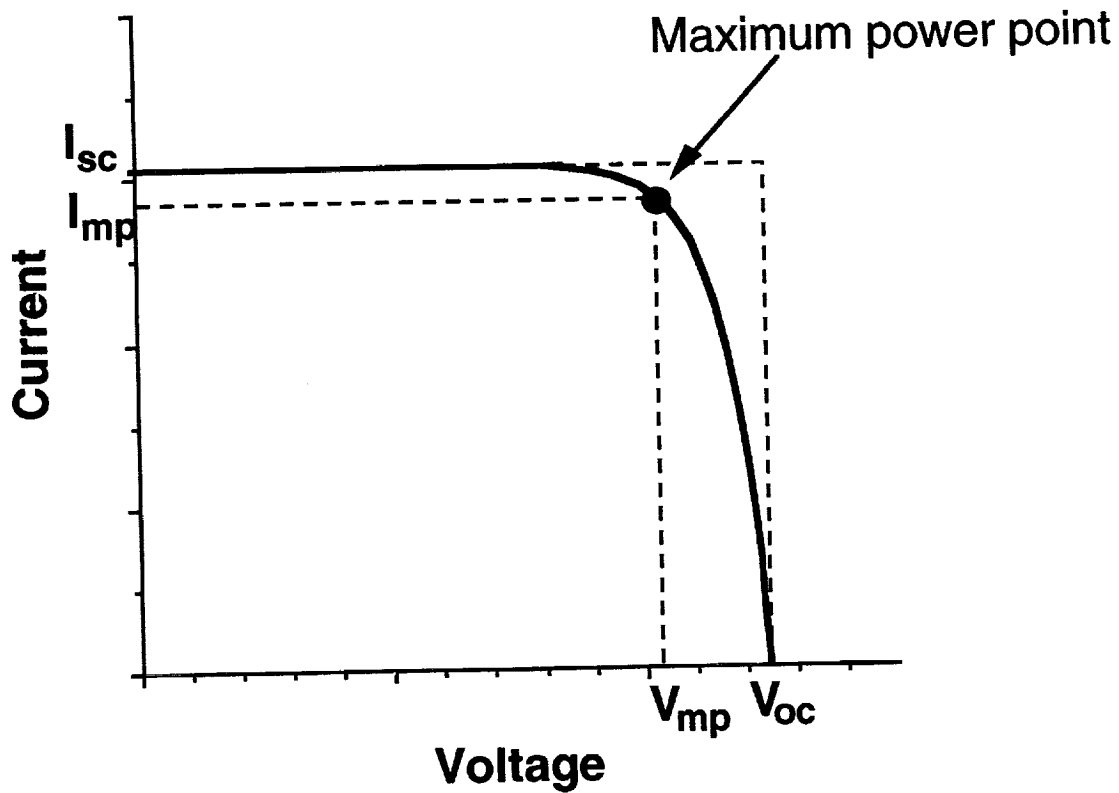


Figure 1. A sample solar cell current-voltage curve.

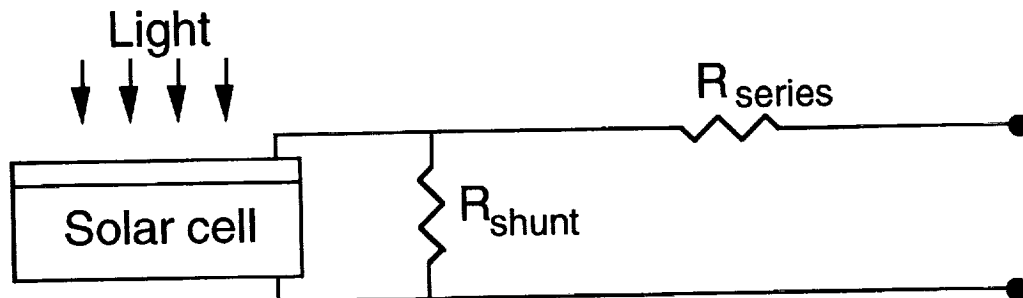


Figure 2. A circuit schematic showing the effects of series and shunt resistance.

ENVIRONMENTAL EFFECTS

Atomic Oxygen

Atomic oxygen is known to erode several materials that are often used in solar cell panels. In particular, the metal interconnects, the metal on the solar cells, the solar cell covers, and parts made of Kapton have all experienced atomic oxygen erosion. This section discusses each of these effects in detail.

Of particular importance is silver, which often is used as an interconnect material. Considerable data is available on these interconnects. On LDEF, silver ribbon was eroded when the flat side was to ram, but not when it was perpendicular to ram[1]. An Intelsat experiment on

Space Shuttle flight STS-41 investigated the erosion of silver interconnects[7]. From this experiment, an erosion rate for silver interconnects was calculated to be of $1.0 \mu\text{m}$ per 10^{20} atoms/cm². Intelsat also found that the back of the interconnect loop was oxidized due to atomic oxygen reflection. Silver that was coated with silicon nitride, silicon dioxide, and aluminum oxide was adequately protected. An earlier experiment on Space Shuttle flight STS-5 showed that coatings of aluminum, gold and palladium were inadequate to protect the silver[8]. Other silver results from Space Shuttle flights are discussed in reference [9].

The SAMPLE experiment on LDEF contained interconnects of rolled copper that were protected by Kapton, and no noticeable degradation was observed[2]. Similarly, measurements of the LDEF thermal blanket grounding straps showed that although copper oxidized in the LDEF orbit, the copper oxide was limited to less than 600 \AA [10].

Certain cells carried on the LDEF SAMPLE and APEX experiment were "wrap-around" cells. Since it is simpler to make a module where both the positive and negative contacts of the cell are on the back side, the front contact of these cells wrapped around the cell edges and then continued on to the back, where contact is made. On the SAMPLE experiment, significant loss of silver on the edges of these cells was observed[2]. This corresponded to a loss in fill factor from an increased series resistance. When the current-voltage curves were measured while the edge of the wafer was bridged over, the fill factor and efficiency returned to near their beginning-of-life values. The modern version of the wrap-around cell is called "wrap-through," and there is a hole in the center of the cell where the front contact wraps through to the back. Since the center of the cell is well-protected by the coverglass, wrap-through cells are not expected to have this problem.

On the APEX experiment, the silicon cells made by Applied Solar Energy Corporation showed FF degradation for both the wrap-around cells (2% loss) and their conventional cells (6-18% loss)[1]. In this experiment, the wrap-around edges were protected, and the reason for the drop in fill factor is unknown.

Atomic oxygen can also affect the solar cell covers. The combined effects of atomic oxygen and ultraviolet light on LDEF will be discussed in a later section. LDEF experiment M0003-4 studied the effects of atomic oxygen on magnesium fluoride (MgF_2), which is sometimes used as an anti-reflection coating on solar cell covers[4]. Data suggests that MgF_2 loses fluorine and converts to MgO , which has a higher index of refraction, and therefore lessens the antireflective properties. Similarly, ThF_2 also appears to lose fluorine. These effects are still being studied.

LDEF experiments using Kapton with coatings of SiO_2 and Al_2O_3 show that these coatings adequately protect the Kapton from atomic oxygen[11]. However, cracks in the coating will lead to undercutting of the Kapton. Kapton used in the solar array on Space Station Freedom will see an atomic oxygen exposure that sweeps across various angles as the array tracks the sun. Laboratory and computer simulations show that this is expected to affect the undercutting profile[12].

Ultraviolet Light

Although ultraviolet light does not generally affect solar cells, it can reduce the amount of light that strikes the cell by either darkening an optical material or by creating and/or fixing films of contamination. In addition, ultraviolet light and atomic oxygen can combine to create a stronger effect; the combined effects on solar cell covers will be discussed in a later section.

Adhesives (DC 93-500, DC Q3-6576 and DC 3-6527) were used on Vertical Junction solar cells that were flown on the Living Plume Experiment (LIPS); they showed a small degradation as predicted, and no measurable difference among the adhesive types[13]. Trailing edge glass samples on LDEF showed significantly reduced transmission due to a film of contamination[14]. However, any atomic oxygen exposure seems to reduce this contamination film down to a thickness that is optically insignificant.

Micrometeoroids and Debris

One of the major sources of damages to solar cell panels is micrometeoroid and debris impacts[15]. Solar cells on SAMPLE with various cell covers showed that polymer cell covers provide very little protection[3]. For cells with microsheet glass covers, impacts were limited in area, and sometimes the microsheet cover prevented the particle from hitting the cell itself. When the crater diameters were about 100 μm , 2-4% degradation in short circuit current was observed. Impacts that only created small craters in the coverslide resulted in no measurable change in efficiency[2]. Also, no measurable change was found in the strength of glass samples struck by debris on another LDEF experiment[16].

If the cell itself was damaged, the loss in current was proportional to the damaged area[1]. In some instances, there was a loss in fill factor from increased series resistance due to breakage of the cells' grids. Cells impacted by micrometeoroids and debris can exhibit any of the three damage mechanisms discussed in the introduction: loss of optical conversion due to damaged covers, increase in series resistance due to grid damage, or decrease in shunt resistance due to junction damage.

Charged Particles

The high energy proton and electron environment for LDEF was very low compared to most other orbits. The effects from electrons are almost negligible, and the majority of damaging photons were absorbed in most coverglass materials. The only cells that were expected to experience a significant amount of charged particle damage were cells with no coverglass protection. Note that the Space Station environment may have higher exposure, given that its orbit's inclination is higher than that of LDEF.

Calculations were performed to predict the charged particle damage for silicon cells on LDEF[17]. Physitron calculated a $5 \times 10^6 \text{ e}^-/\text{cm}^2$ 1 MeV electron equivalent, which corresponded to a 20% degradation. This calculation matches well with measurements on silicon cells without a coverglass. Similarly, other calculations were performed by Hughes for their HS393 solar arrays in geosynchronous orbit, and they found good agreement with measurements[18].

Silicon solar cells on LDEF with no coverglass showed I_{sc} and V_{oc} damage, consistent with charged particle damage[1]. Cells without covers on SAMPLE had a 21% degradation, whereas those with covers were protected with no effect from cover type[2]. Charged particle effects are not always predictable: Space Systems/Loral found that their silicon back-surface field cells in geosynchronous orbit were damaged more by solar flares than expected, but that they showed surprisingly high annealing[19].

For gallium arsenide (GaAs) solar cells, those flown on LDEF without covers showed significant damage that varied with the cell's junction depth, which is as expected[1]. GaAs cells were very new when LDEF was launched, so more recent data is preferable. 30 days of data for a geosynchronous transfer orbit flight to test solar cells made of gallium arsenide (GaAs) and gallium

arsenide grown on germanium (GaAs/Ge) showed that coverglass thickness has a large effect[20]. Coverglass thickness of 12 mil or higher makes a significant difference in reducing the damage. The new GaAs/Ge cells performed quite well.

Combined Effects on LDEF

This section details the overall effects on the various solar cell experiments on LDEF. There were two experiments on LDEF with working solar arrays: the Heat Pipe experiment, which had a space-end array[5], and the Space Plasma High Voltage Damage Experiment, which had leading and trailing edge solar modules[6]. The Heat Pipe Experiments space-side array showed 1.5-3% overall degradation due to the combined effects of radiation, cover adhesive darkening, and micrometeoroid damage. The leading and trailing edge modules of the SP-HVDE showed less than 2% overall degradation, except for one module which was damaged by a micrometeoroid/debris impact, and showed a 10% loss. The SAMPLE experiment had several modules, many of which were lost on flight or during the Space Shuttle recovery. The one surviving complete module, Module 5, was found in the Space Shuttle cargo bay. It showed a 32% loss as an array, but this may have been due to its fall in the cargo bay[2].

Other solar cell results are listed in this paragraph. Most cells with 6 mil coverslides on SAMPLE had a degradation of 5% to 9%[2]. No degradation was measured on two types of cells on APEX: a 10 Ω -cm Si cell with a TaO₂ anti-reflection coating and a 12 mil coverslide; and a 1 Ω -cm Si cell with a 30 mil coverslide[1]. One GaAs cell flown on APEX with a 12 mil coverslide started at 16% efficient, but showed a surprisingly high 10% loss. Cells with polymer covers on APEX showed a current degradation (due to darkening) or a decrease in shunt resistance (reason unknown)[2]. Two cells were flown on SAMPLE with solar concentrators designed for 2X, although flight data showed that the concentration was actually 1.6X[2]. Over time, atomic oxygen eroded away the concentrator material, which was Kapton and Mylar, from the back side.

SAMPLE contained a very thorough experiment on solar cell covers[3]. Solar cells were covered with a variety of materials, including standard cerium-doped microsheet and a number of experimental polymer coatings. The short circuit current was measured before and after exposure to look for changes in the cover's transmission. Cells covered with cerium-doped microsheet showed the smallest change (3% loss). FEP Teflon had a darkened top surface (22% loss). Soft silicone coatings exhibited crazing and some loss near the cell edge (13% loss). Hard coat silicone showed crazing, flaking, and close to complete removal (17% loss). Cells covered with polyimide silicon co-polymer coating maintained a high current, but the reason is that it was largely removed (3% loss). GE x-76 polyimide was also significantly removed (8% loss). The conclusion of this experiment is that a quality polymer replacement has not been demonstrated, and that microsheet works quite well as a protective cover.

FUTURE FLIGHTS

The largest solar cell array to be flown in the near future is for Space Station. A description of the array is given in references [21] and [22]. The solar cells will be silicon, with a 10 Ω -cm base resistivity, 8 cm x 8 cm square, 0.0203 cm thick, with a wrap-through contact. There is a dual anti-reflection coating and a (p+) back surface field. The efficiency is 14.2%. The cover is a ceria-doped microsheet, 5 mil thick, with a UV-reflective coating. The interconnects are made of copper.

The results of LDEF suggest that these are good choices. Although this exact type of cell was not flown on LDEF, similar silicon cells performed well, and the wrap-through contact should avoid the problems that some of the wrap-around cells had on LDEF. The cover should protect the cells adequately from charged particles, and the UV-reflective coating does not contain MgF_2 [23], so there should be no problem with conversion to MgO . Copper is a good choice for interconnects, since it will not be eroded in the same way as silver.

Although the Space Station orbit will have a similar altitude to the LDEF orbit, the new inclination is planned to be 57° as opposed to 28° for LDEF. This will result in an environment with a higher charged particle exposure that is very sensitive to altitude. The 5 mil coverglass will absorb protons of energy less than 4 MeV; the number of protons with energy greater than 4 MeV is expected to be higher by a factor of 2 to 8 at a 60° inclination, depending on the altitude[24]. Only the very low energy electrons will be affected by the coverglass; the total number of electrons is expected to be higher by a factor of 2 to 10 at a 60° inclination, depending on the altitude[24].

Other recent solar technologies include the Hubble Space Telescope array, where the silver interconnects are replaced with molybdenum, except where they are welded[25]. Silver plated molybdenum and silver plated Invar are now fairly common materials for interconnects. Cells made of gallium arsenide grown on germanium are gaining acceptance as having many advantages over silicon: higher efficiency, better charged particle resistance, and better temperature coefficient (i.e., the efficiency does not drop as much as the cell temperature rises). Even higher charged particle resistance can be obtained by using cells made of indium phosphide (InP). InP cells that flew in a polar orbit with only 2 mil coverglass showed very little degradation, despite a high radiation environment[26]. Multijunction cells have the potential for extremely high efficiency[27]. New materials are also being developed for solar cell covers, including new types of teflon and new protective coatings for silicone.

Future LDEF solar cell activity includes: the organization and publication of the solar cell results from experiment M0003-4 (Advanced Solar Cell and Coverglass Analysis); further research into the MgF_2 coating effect; and completing the testing of the cells on SAMPLE. The Photovoltaic Array Space Power Plus experiment (PASP+) is scheduled to be launched in 1994. This satellite contains a large variety of new solar cell technologies, including new thin films, concentrator modules, and multijunction cells. Further flights are expected using GaAs/Ge and InP cells.

CONCLUSIONS

This survey of space environmental effects on solar cells covered a wide range of flights. The conclusions from LDEF data can be listed as follows:

- Atomic oxygen erodes unprotected silver interconnects, unprotected Kapton, and polymer cell covers. Coatings can protect both silver and Kapton.
- Cells with wrap-around silver contacts sometimes showed erosion at the edges, but modern wrap-through cells are not expected to have these problems.
- Micrometeoroid and debris damage is limited to the area close to the impact. Microsheet covers provide the cells with some protection.
- Damage from charged particles was as predicted. Covers provide adequate protection.
- In general, silicon cells with microsheet covers showed very little degradation.
- Solar modules showed less than 3% degradation, except when mechanically damaged.
- LDEF data supports solar cell choices for Space Station.

ACKNOWLEDGEMENTS

Many papers were used as references in this survey paper. However, the majority of the data comes from excellent and thorough work under the guidance of L.E. Young and A. Whitaker of NASA Marshall Space Flight Center, D. Brinker of NASA Lewis Research Center, and P. Stella of the Jet Propulsion Laboratory. In addition, R. Burgess of the Boeing Company laid the groundwork of this paper with his contributions to NASA Contract Report 189628 ("Analysis of Systems Hardware Flown on LDEF -- Results of the Systems Special Investigation Group," April 1992).

REFERENCES

1. D. Brinker, J. Hickey, D. Scheiman, "The Effect of the Low Earth Orbit Environment on Space Solar Cells: Results of the Advanced Photovoltaic Experiment (S00014)," LDEF Second Post-Retrieval Symposium, June 1992, pg 1291.
2. L.E. Young, "Impact of LDEF Photovoltaic Experiment Findings Upon Spacecraft Solar Array Design and Development Requirements," LDEF Materials Results for Spacecraft Applications Conference, Oct 1992, pg. 201.
3. P. Stella, "LEO Effects on Candidate Solar Cell Cover Materials," LDEF Second Post-Retrieval Symposium, June 1992, pg 1303.
4. T.M. Trumble, "Experiment M0003-4, Advanced Solar Cell and Coverglass Analysis, an Overview," LDEF First Post-Retrieval Symposium, June 1991, pg 1255.
5. R. McIntosh, C. McCreight, P. Brennan, "Long Duration Exposure Facility (LDEF) Low Temperature Heat Pipe Experiment (HEPP), LDEF First Post-Retrieval Symposium, June 1991, pg 1431.
6. J.Y. Yaung, B.K. Blakkolb, W.C. Wong, L.E. Ryan, H.J. Schurig and W.W.L. Taylor, "LDEF Space Plasma-High Voltage Drainage Experiment Post-Flight Results," LDEF Second Post-Retrieval Symposium, June 1992, pg 1343.
7. S. Koontz, G. King, A. Dunnet, T. Kirkendahl, R. Linton, and J. Vaughn, "The International Telecommunications Satellite (INTELSAT) Solar Array Coupon (ISAC) Atomic Oxygen Flight Experiment: Techniques, Results and Summary," to be published.
8. A. Dunnet and R.D. Kirkendahl, "Assessment of Atomic Oxygen Erosion of Silver Interconnects on Intelsat V1 F-3," Proceedings of the European Space Power Conference, September 1991, pg 701.
9. M.R. Reddy, N. Srinivasamurthy, B.L. Agrawal, "Effects of the Low-Earth-Orbit Environment on Solar Array Materials," ESA Journal, vol 16, no. 2, 1992, pg 193.
10. A. de Rooij, "Some Results of the Oxidation Investigation of Copper and Silver Samples Flown on LDEF," LDEF First Post-Retrieval Symposium, June 1991, pg 479.
11. S. Rutledge, R.M. Olle, and J.M. Cooper, "Atomic Oxygen Effects on SiO_x Coated Kapton for Photovoltaic Arrays in Low Earth Orbit," 22nd IEEE Photovoltaics Specialists Conference, 1991, pg 1544.
12. B. Banks, S. Rutledge, K.K. de Groh, B.M. Auer, M. Mirtich, L. Gebauer, C.M. Hill, R.F. Lebed, "LDEF Spacecraft, Ground Laboratory, and Computational Modeling Implications of Space Station Freedom's Solar Array Materials and Surfaces Durability," 22nd IEEE Photovoltaics Specialists Conference, 1991, pg 1434.
13. R.L. Statler and D.H. Walker, "The Space Performance of Silicon Vertical Junction Solar Cells on the LIPS-III Satellite," IEEE AES Magazine, Dec 1989, p. 13.
14. S.P. Hotaling, "Analysis of Leading Edge and Trailing Edge Cover Glass Samples Before and After Treatment with Advanced Satellite Contamination Removal Techniques," LDEF Materials Results for Spacecraft Applications Conference, Oct. 1992, pg. 419.

15. H.W. Dursch, W.S. Spear, E.A. Miller, G.L. Bohnoff-Hlavacek, J. Edelman, and R. Burgess, "Analysis of System Hardware Flown on LDEF -- Results of the Systems Special Investigation Group," NASA Contract NAS1-19247, April 1992, p. 139.
16. D. Wiedlocher and D. Kinser, "Cratering in Glasses Impacted by Debris or Micrometeorites," LDEF Second Post-Retrieval Symposium, June 1992, pg 529.
17. C.J. Rives, J.L. Azarewicz, and L. Massengill, "LDEF Solar Cell Radiation Effects Analysis," NASA report NASA-CR-191776, January 1993.
18. S.W. Gelb and L.J. Goldhammer, "In-Orbit Performance of Hughes HS 393 Solar Arrays," 22nd IEEE Photovoltaics Specialists Conference, 1991, pg 1429.
19. J.F. Murray, R.E. Neff, H.E. Pollard, "Space Environment Effects on a Rigid Panel Solar Array," 22nd IEEE Photovoltaics Specialists Conference, 1991, pg 1540.
20. J.S. Powe, E.L. Ralph, G. Wolff, and T.M. Trumble, "On-Orbit Performance of CRRES/HESP Experiment," 22nd IEEE Photovoltaics Specialists Conference, 1991, pg 1409.
21. C. Winslow, "Space Station Freedom Solar Array Design Development," IEEE AES Systems Magazine, January 1993, pg. 3.
22. R.J. Christie, C.Y. Lu, and I. Aronoff, "Applicability of Long Duration Exposure Facility Environmental Effects Data to the Design of Space Station Freedom Electrical Power System," AIAA 30th Aerospace Sciences Meeting & Exhibit, January 1992.
23. Rancourt et. al., "Silicon Solar Cell and Nanometer Cut-On Filter for Use Therein," United States Patent 4,293,732 (Oct. 6, 1981).
24. Stassinopoulos, E.G. and Raymond, J.P. , "The Space Radiation Environment for Electronics," Proceedings of the IEEE, Vol. 76, No. 11, Nov. 1988, p. 1423.
25. R.C. Linton, R.L Gause, R.J. Harwell, R.F. DeHaye, H.D. Burns, Jr., and J.M. Reynolds, "Results of Protective Coating Studies for the Hubble Space Telescope Array," 34th International SAMPLE Symposium, May 1989, p. 1190.
26. M. Yamaguchi, T. Hayashi, A. Ushirokawa, K. Takashi, S. Ikegami, and H.Arai, "Analysis of Space Flight Data of InP Solar Cells In EXOS-D Orbit," 22nd IEEE Photovoltaics Specialists Conference, 1991, pg 1576.
27. P.E. Gruenbaum, V.T. Dinh, and V.S. Sundaram, "Gallium Antimonide Infrared Solar Cells with Improved Efficiency and Manufacturability," Solar Energy Materials and Solar Cells, Vol 32, 1991, pg 61.

A FINAL LOOK AT LDEF ELECTRO-OPTIC SYSTEMS COMPONENTS

M. D. Blue

Georgia Tech Research Center
Georgia Institute Of Technology
Atlanta, Georgia 30332

Phone: (404)894-3642, Fax: (404)894-6285

SUMMARY

Postrecovery characteristics of LDEF electro-optic components from the GTRI tray are compared with their prelaunch characteristics and with the characteristics of similar components from related experiments. Components considered here include lasers, light-emitting diodes, semiconducting radiation detectors and arrays, optical substrates, filters, and mirrors, and specialized coatings. Our understanding of the physical effects resulting from low earth orbit are described, and guidelines and recommendations for component and materials choices are presented.

INTRODUCTION

As the LDEF program was developing in the early 1970's, the ability of optical systems to survive in the space environment had been demonstrated by successes with interplanetary probes such as Mariner II in 1962. Ground-based testing had been the method used to simulate the expected major effects of the space environment, while the consequences of any unexpected effects were assumed minor. Confirmation of these assumptions was difficult to obtain, particularly for effects related to the near-earth environment. The availability of the LDEF satellite provided an opportunity to expose a set of state-of-the-art components to the space environment and look carefully for unexpected degradation effects in both familiar and novel materials and devices. This report summarizes the results of this experiment, discussing both the components which were unchanged, and the components whose properties were altered during the nearly six years in space.

Figure 1 shows the position of the tray containing the components on the LDEF satellite. This location, on the rear portion of the satellite, resulted in a lower fluence of atomic oxygen and fewer micrometeorite impacts than was the case for the leading edge trays. Five of the six subtrays were covered with a sunscreen (with $\approx 50\%$ transmission) which provided some temperature stability in the event of an undesired orbit. The environmental parameters for this tray position, as determined from data supplied by NASA, are presented in Table 1.

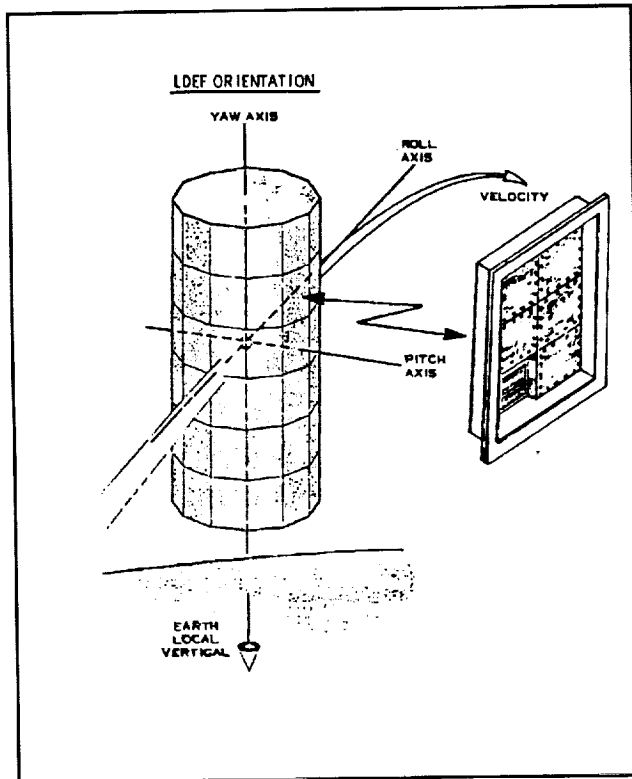


TABLE I. THE LDEF ENVIRONMENT FOR THE COMPONENT SET

Maximum Temperatures From NASA Estimates For The First Year
66°C (105°F)
Atomic Oxygen Fluence
1.1×10^{13} atoms/cm ³
Radiation Dose At The Tray Position Of Figure 1. From NASA Reports
< 300 Rads(Si)

Figure 1. Location Of The Active Optical Systems Components Experiment On The LDEF.

The total radiation dose for components protected by the sunscreen was less than 300 krads which is well below the value where degradation is observed in many materials and components. No effects of radiation on component properties were found with the exception of the silicon CCD array. The location of the tray on the rear of the satellite minimized effects from micrometeorite impact as well as effects of atomic oxygen. The oxygen flux represents less than one oxygen atom per 100 surface atoms, a negligible amount.

The components typically were mounted in such a manner as to simulate a minimum level of protection to be expected in a realistic application except that, in a few cases, no protection was provided merely to satisfy our curiosity.

OPTICAL COMPONENTS

In addition to the windows, filters, and mirrors in the GTRI tray, similar optical components from several other experiments were carried on the LDEF. Common results were found for optical substrates, filters, and mirrors covering wavelength regions from the ultraviolet to the infrared. Most components survived space exposure quite well, and space-induced degradation was not a major factor for most optical component properties. Some of our results have been published.^{1,2}

Window materials including SiO_2 , MgF_2 , Al_2O_3 , CaF_2 , and LiF , were returned from space with a thin brown or yellow-brown contamination layer.³ The contamination layer or layers could usually be removed by cleaning. Infrared spectroscopy of all window materials except SiO_2 indicated the presence of methyl and methylene bands. Their absence on SiO_2 indicates substrate selectivity for the deposition of contaminant.⁴ Optical filters on the GTRI tray were coated with a slight contamination layer, but did not show measurable transmittance changes attributable to this contamination.

The results of these and other measurements^{3,4,5,6} reveal that the contamination layer absorbs strongly in the ultraviolet region, but has negligible absorption in the visible and infrared regions: a result independent of the location of the contamination on the satellite. The spectral transmission of the substrate materials is similar to results for transparent substrates subjected to heavy doses of radiation.⁷

KRS-5 windows used on pyroelectric radiation detectors degraded⁸ as did KRS-5 and KRS-6 uncoated material and filter substrates from the University Of Reading experiment (unpublished work). When these two materials were used as substrates for multi-layer dielectric stack filters, delamination occurred.

Thin-film dielectric-multilayer narrow-band filters and mirrors showed a band shift, increase in band width, and reduced throughput or reflectance after return from the space environment.^{1,2,9} Figures 2 and 3 show the results for an optical narrow-band filter from the GTRI set, and a long-wave infrared filter from the Reading University set. Both filters show the three effects mentioned above. The band shift is small, but may be important for certain space-borne systems. These effects appear to be result of temperature cycling expediting the realignment and compaction of the deposited dielectric layers which tend to decrease the average film thickness and shift the peak transmittance toward the blue. Similar effects occur in a laboratory environment, although at a lower rate in most cases. Interdiffusion between layers increases bandwidth, and lowers transmittance. Deterioration of cement used to attach filter substrates together can also lower transmittance.

Among the effects considered but not found important in the deterioration of the GTRI set of filters and mirrors were surface contamination, atomic oxygen flux, and radiation dose.

The substrates, filters, and mirrors aboard LDEF provided a rich source for information about the effects of space exposure, stability of various types of substrates, coatings, and films, and performance of these optical elements in various configurations and constructs. Additional information on this topic may be found in the other 1993 NASA symposium papers on this topic and in the references.

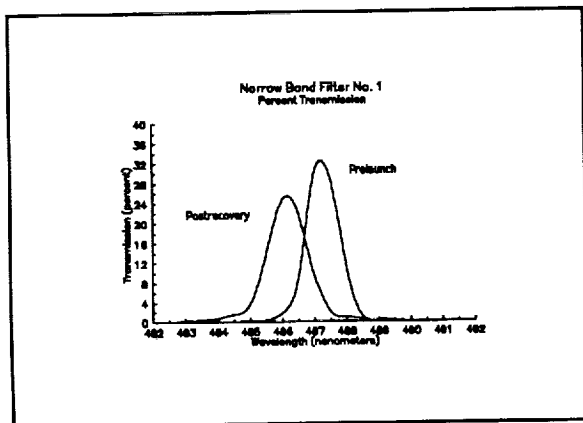


Figure 2. Prelaunch And Postrecovery Transmittance Of A Narrow-Band Filter From The GTRI Set.

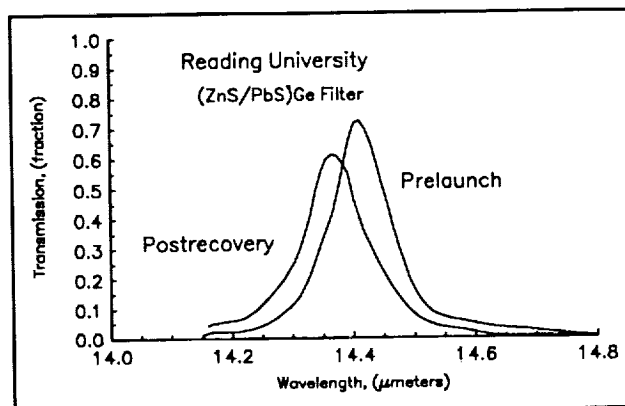


Figure 3. Prelaunch And Postrecovery Transmittance For A Narrow-Band Filter From The Reading University Set.

OPTICAL RADIATION DETECTORS

The LDEF carried a variety of radiation detectors which were of interest in the 1970-1980 time frame. All detectors were maintained at ambient temperature. Regarding their survivability in space, postrecovery measurements support the general conclusion that their detection properties were not degraded. However, degradation unrelated to direct intrinsic loss of detector sensitivity, such as degradation of detector assembly windows or loss of electrical contact can occur. These effects are of a mechanical origin and do not contradict the general conclusion that the detector element survives. The assortment of detectors supporting our conclusions included a group of pyroelectric detectors, Si, PbS, PbSe, InSb, HgCdTe, GaAsAlP, and two Pd₂Si Schottky-barrier IRCCD imaging-array chips.

The only exceptions to this typical result concern TGS (triglycine sulphate) material used in pyroelectric detectors and CCD readout structures. TGS detectors either failed or

deteriorated for both the control and the space-exposed samples. This material is to be avoided. The results for the set of pyroelectric detectors have been described by Robertson.⁸

CCD structures can be damaged by the natural radiation in space. Silicon CCD readout or scanning circuitry is associated with image frame sensors. As will be discussed further, CCD's are arguably examples of the most radiation-sensitive semiconductor devices.

Six silicon large-area photovoltaic (pv) detectors were mounted so that the sensitive photosurface was exposed to the space environment. After recovery, small scars from the apparent impact of micrometeorites could be observed by eye.

Properties measured for these detectors included spectral noise density, responsivity, and reverse leakage current. Only one detector showed any increase in leakage current, and the amount was less than 2 microamperes per cm². Figure 4 shows the prelaunch and postrecovery capacitance for one of the detectors. Despite the micrometeorite impacts and the lack of radiation protection, the detectors survived without notable change in properties.

The postponed launch date of the LDEF permitted addition of two Pd₂Si arrays to the collection of radiation detectors in 1983. Two different chips were used. The first chip contained process test devices, while the second chip contained a Schottky-barrier 32X63 IRCCD imaging array. Postrecovery characterization compared the recovered chips with a control from the same silicon wafer.

Radiation produces three different types of permanent degradation in CCD arrays. First, radiation effects can increase the thermal generation rate of minority carriers which increases the dark current and shortens the storage time of the device. Second, because of a tendency for some charge to be left behind in each transfer step from gate to gate, there is an inherent charge transfer loss in CCD's. This transfer loss or transfer inefficiency is enhanced by radiation and works to degrade image resolution. Finally, irradiation of a CCD causes a shift in the range of bias voltages in the propagation and transfer gates over which satisfactory operation can be obtained.

A major damage mechanism in these devices is the production of positive charge which can be trapped in the SiO₂ insulator or at the semiconductor-insulator interface. Because the amount of energy required to create a hole-electron pair in SiO₂ silicon is 18 eV, the total received dose must be corrected to include only the radiation with energy above this value. This correction is negligible for LDEF. For 18 eV/pair, it can be calculated that 7.6 X 10¹² pairs/cm³ are created per rad(Si) dose. The calculated received dose was 68 krads(Si).

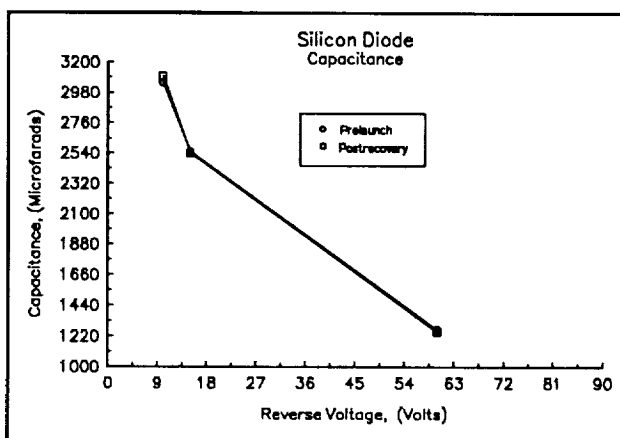


Figure 4. Prelaunch and Postrecovery Capacitance for a Large-Area Silicon Photodiode.

This calculated dose is about two orders of magnitude greater than originally expected because of (1) the extended time in orbit, and (2) a higher radiation flux than originally expected. In a more realistic setting, these arrays would be mounted inside a cryogenic assembly and mechanical structure at the focal plane of a telescope, all of which would provide extensive radiation protection.

From the thickness of the oxide and area of the electrodes, the volume of insulator and, therefore, the number of hole-electron pairs per electrode created by the radiation can be calculated. Most of the charge pairs recombine quickly (about 95%) and most of the defects produced by the remainder would be expected to be removed by the annealing resulting from the periodic temperature cycling experienced by the LDEF along its orbital path. A reasonable assumption is about 1% if the irradiation dose results in permanent trap creation. As a result, the expected number of traps per electrode is estimated to be 1.5×10^6 . These traps cause transfer inefficiency. Injection of additional charge to fill these traps is one means of improving operation.

For these devices, a charge injection equivalent to 2×10^6 electrons per pixel restored most of the lost transfer efficiency. This number is to be compared to the estimated trap density. The reasonable agreement obtained suggests that the received radiation dose is the major source of the reduced device performance.

The construction of these chips represents technology over ten years old. Since these arrays were produced, alternative insulating systems were produced which provide greater radiation hardness. Newer devices also have shorter gate lengths and greater transfer efficiency which suggests better performance in a radiation environment. As mentioned above, additional radiation protection would be afforded by the required cryogenic support and necessary mechanical structures.

MISCELLANEOUS COMPONENTS

In the category of miscellaneous components, we examined lasers, flashlamps, LED's, black paints in the extreme-IR region, and an electro-optic modulator.

Our interest in black paints was stimulated by interest in sensor technology in the extreme-IR region (20-1000 μm) and the lack of measurements on dielectric properties of materials in this wavelength region. In particular there was a lack of information in the early 1970's regarding black surface finishes necessary for stray light rejection in radiometer systems. Moreover, the stability of the materials in a space environment was also unknown, and was of considerable interest. Some of the results of our normal reflectance measurements¹⁰ for coatings on aluminum substrates are shown in Figures 5 and 6 where wavelength is plotted on a logarithmic scale to better display the short-wavelength reflectance.

Measurements at cryogenic temperatures (near the temperature of liquid helium) indicate increased reflectance of five percent to ten percent at wavelengths where the coatings become partially transparent (wavelengths beyond 100 μm) and negligible differences at shorter wavelengths where the films are strongly absorbing.

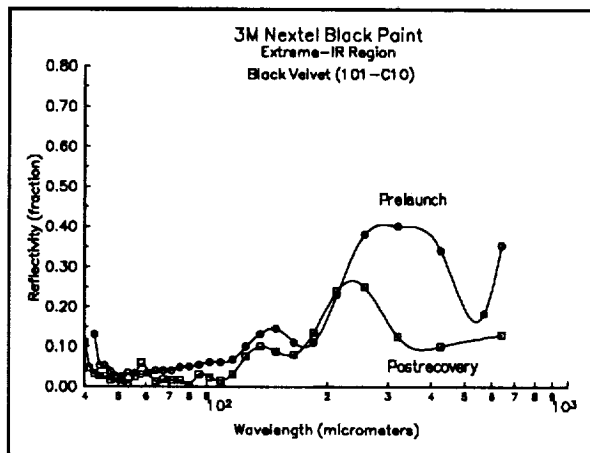


Figure 5. Prelaunch and Postrecovery Normal Reflectance Of 3-M Black Velvet Paint From 40 μm to 600 μm at room temperature. Postrecovery data indicate reduced reflectance.

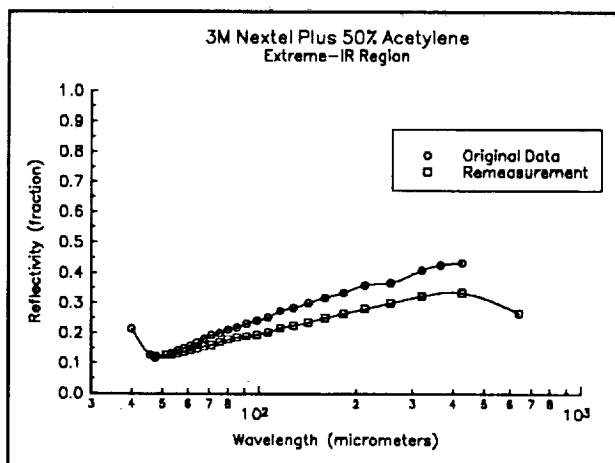


Figure 6. Original And Remeasured Normal Reflectance For A Sample Of 3-M Paint Containing 50% Acetylene. Period between Measurements Was approximately 13 Years.

Figure 6 represents results for one of our special coatings designed to improve performance at the longer wavelengths. This sample provides an indication of the effect of storage in a laboratory for thirteen years on normal reflectance, and also provides an indication of any calibration problems arising as a result of instrument modifications during the years between measurements. Samples from this set showed slightly increased or slightly decreased reflectance (Fig. 6), but do not exhibit the striking changes that appear in the spectra of the space-exposed samples. The reflecting-layer model of Smith¹¹ was used to analyze the reflectance data. While the assumptions in this model limit its applicability at wavelengths beyond 250 μm , the short wavelength spectra could be reproduced and the interference fringes could be roughly reproduced without allowing the dielectric properties to vary with wavelength. The results suggest that the imaginary component of the refractive index of the coatings increased by about 0.15.

The data could not be fitted with a change in surface roughness or coating thickness, indicating that surface roughening or loss of material from erosion or other effects of space dust and debris were not responsible for the change in properties.

These results suggest that increased absorption may be related to loss of volatile components in the coating binder, and degradation of the pigment and binder by UV radiation providing an increased density of absorption sites in the paint films. While these effects could occur during natural ageing, space exposure may accelerate them.

Less spectacular effects were found for the lasers, flashlamps, LED's, and modulator. The extended time in orbit is believed the cause of the inability of our gas lasers (HeNe and CO₂) to operate, although they arrived in otherwise excellent condition.

Two or three years is the maximum time these lasers will operate without replacing the laser gas mixture. However, no changes in the characteristics of the YAG laser rods, the semiconducting laser-diodes, or the LED's could be found.

Figure 7 shows the prelaunch and postrecovery characteristics of a recovered LED compared with the original and remeasured characteristics of a stored LED. The original and later measurements are in excellent agreement. The stored LED continues to have greater radiation output than the space-exposed unit. The space exposed units could be distinguished from stored units because of the small indentation on the plastic domes, a result of the impact of small micrometeorites which left their mark on soft surfaces on all components.

Other components in this category, such as the modulator and flashlamp, did not show any changes in performance. For the modulator, transmittance, half-wave retardation voltage, and frequency response were measured. For the flashlamp, spectral output was measured.

All members of this set of miscellaneous components survived without change except for the black paints and the sealed gas lasers. The lasers require periodic refills wherever their location.

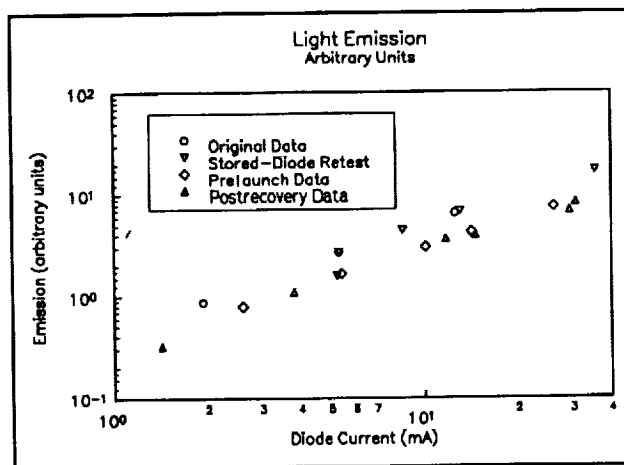


Figure 7. Light-emitting Diode Output vs Drive Current. Note That The Control Diode Has Slightly Greater Output Than The Flight Unit.

CONCLUSIONS

A review of results from several different experiments is required in order to arrive at any general conclusions regarding effects of space exposure on optical materials and components. Some general conclusions for a group of experiments related to optical and

electro-optical components are listed in Table II. The LDEF, with its planned six to eighteen months in space, was not expected to provide a test of radiation hardness. With the extended stay in orbit, comparison with predicted effects is more meaningful. The results are in agreement with expectations for these materials.

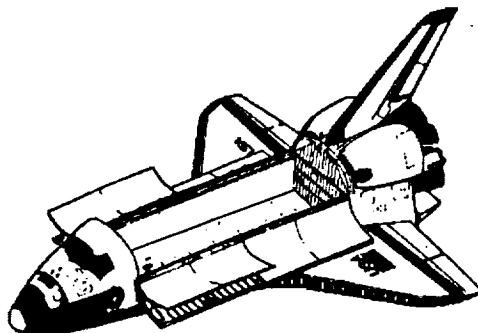
TABLE II. GENERAL CONCLUSIONS

<p>(1) Radiation effects for LDEF materials and components do not differ from ground-testing results. Results are consistent with previous radiation-effects studies.</p> <p>(2) Radiation creates additional absorption sites which increase the attenuation for radiation from the UV to the Far-IR. Black paints become increasingly black and thus, more effective.</p>

TABLE III. CONCLUSIONS REGARDING OPTICAL MATERIALS

<p>STABLE SUBSTRATE MATERIALS</p> <p>Si, SiO₂, Al₂O₃, Quartz, ULE Glass</p> <p>POOR SUBSTRATE MATERIALS</p> <p>KRS-5, KRS-6</p> <p>SUSPECT SUBSTRATE MATERIALS</p> <p>Fluorides such as MgF₂, CaF₂</p>

Table III lists conclusions relating to materials. Other investigators at this symposium have reached similar conclusions. Multilayer dielectric-stack narrow-band filters and mirrors prepared using substrate materials listed as poor or suspect in Table III are expected to suffer greater degradation in performance than similar components fabricated from materials listed as stable. Simply put, covalently-bonded materials should be more stable over time in the low-earth environment than ionically-bonded materials.



REFERENCES

1. Blue, M. D. and Roberts, D. W.: Effects Of Space Exposure On Optical Filters, *Applied Optics*, 31, No. 21, 4305-4309 (1992).
2. Blue, M. D.: Degradation Of Optical Materials In Space, GTRI Report, April 30 (1993), Available from NASA LDEF Program Office.
3. Harvey, Gale A.: Effects Of Long-Duration Exposure On Optical System Components, LDEF-69 Months In Space, NASA Conf. Pub. 3134, 1327-1340 (1992).
4. Harvey, Gale A.: Effects Of Long-Duration Exposure On Optical System Components, NASA Conf. Pub. 3134, 179-196 (1992).
5. Preuss, Ludwig: Evaluation of LDEF Experiment S 1002, LDEF-69 Months In Space, NASA Conf. Pub. 3134, 1405-1417 (1992).
6. Linton, R. C., Kamenetzky, R. R., Reynolds, J. M., and Burris, C. L.: Atomic Oxygen Stimulated Outgassing, LDEF-69 Months In Space, NASA Conf. Pub. 3134, 763-767 (1991).
7. An example is the following. Suzuki, H., Iseki, T., and Yamamoto, A.: Effect Of Reactor Irradiation On The Physical Properties Of Fused Quartz, *Bull. Tokyo Inst. of Tech.*, No. 21, 83-88 (1974).
8. Robertson, James B.: Effect Of Space Exposure On Pyroelectric Infrared Detectors, LDEF Materials Workshop '91, NASA Pub. 3161, 501-506 (1991).
9. Donovan, Terry, Klemm, Karl, Johnson, Linda, and Scheri, Rick: Effects Of Low-Earth Orbit On The Optical Performance Of Multilayer Enhanced High-Reflectance Mirrors, Third LDEF Post-Retrieval Symposium, November 9-12 (1993).
10. Blue, M. D., and Perkowitz, S.: Space Exposure Effects On Optical-Baffle Coatings At Far-Infrared Wavelengths, *Appl. Optics*, 31, 4305-4309 (1992).
11. Smith, S. M.: Specular Reflectance Of Optical Black Coatings In The Far-Infrared, *Appl. Opt.* 23, 2311-2326 (1984), *and* The Specular Reflection Of IR-Opaque Coatings, *Int. J. Infrared Millimeter Waves* 5, 1589-1595 (1984).

EFFECTS OF THE LDEF ORBITAL ENVIRONMENT ON THE REFLECTANCE OF OPTICAL MIRROR MATERIALS

Howard Herzig

NASA Goddard Space Flight Center
Optics Branch, Code 717
Greenbelt, MD 20771-0001
Phone: 301/286-2085, Fax: 301/286-1694

Charles M. Fleetwood, Jr.
Optical Research Section, Code 717.1
Greenbelt, MD 20771-0001
Phone: 301/286-5861, Fax: 301/286-1694

ABSTRACT

Specimens of eight different optical mirror materials were flown in low earth orbit as part of the Long Duration Exposure Facility (LDEF) manifest to determine their ability to withstand exposure to the residual atomic oxygen and other environmental effects at those altitudes. Optical thin films of aluminum, gold, iridium, osmium, platinum, magnesium fluoride-overcoated aluminum and reactively deposited, silicon monoxide-protected aluminum, all of which were vacuum deposited on polished fused silica substrates, were included as part of Experiment S0010, Exposure of Spacecraft Coatings. Two specimens of polished, chemical vapor deposited (CVD) silicon carbide were installed in sites available in Experiment A0114, Interaction of Atomic Oxygen with Solid Surfaces at Orbital Altitudes, which included trays in two of the spacecraft bays, one on the leading edge and the other on the trailing edge. One of the silicon carbide samples was located in each of these trays.

This paper will compare specular reflectance data from the preflight and postflight measurements made on each of these samples and attempt to explain the changes in light of the specific environments to which the experiments were exposed.

INTRODUCTION

The scientific community has long been aware that the orbital space environment presents a unique set of ambient conditions for their flight instruments. There has been a determined effort, going back to the early Space Shuttle flights, to establish the ability of candidate materials to withstand this environment. Particular concern about some thin film coatings used for reflective optical elements led to the investigation by Gull and coworkers on the short-term, low earth orbit effects, as part of a series of experiments known as the Evaluation of Oxygen Interaction with Materials (EOIM).¹ Their

selection of coatings was part of the contingent which was exposed during the second mission of this experiment, flown on Shuttle mission STS-8 from August 30 to September 5, 1983. During the following year, the opportunity to evaluate long-term effects on these coatings, as well as others, presented itself with the deployment of the Long Duration Exposure Facility (LDEF), with an intended flight duration of one year. However, due to changes in Shuttle schedule priorities, it was almost six years before the spacecraft was retrieved.

Eight optical coating materials were included in the complement furnished by the Goddard Space Flight Center (GSFC), most of which have application in the vacuum ultraviolet (VUV) portion of the electromagnetic spectrum and several which find primary use in instruments for the visible and near-UV regions.

EXPERIMENT DESCRIPTIONS

Seven test samples, all of which were vacuum deposited thin films on 25 mm diameter by 2.5 mm thick, polished fused silica substrates, were mounted in an aluminum tray with machined recesses to accommodate these samples as well as those provided by others. The tray was covered with an aluminum plate having circular openings concentric with those in the tray but of slightly smaller diameter so as to retain the samples while permitting their exposure to the orbital environment. The entire assembly was mounted in a container known as the Experiment Exposure Control Canister (EECC), which is an automated experiment container capable of opening and closing during the flight. This collection is part of LDEF experiment S0010, Exposure of Spacecraft Coatings. The moving section of the EECC system, which contains the sample platform, translates out of a sealed container to expose the samples in a manner similar to the opening of a drawer. Thus the system provides a means for maintaining a clean, low pressure or inert gas environment while closed during ground operations and delaying the exposure of the experiment until the spacecraft is in orbit.

The timer control circuitry for the EECC was set so that the drawer was in the open position for 10 months, so that despite the extended orbital period for the spacecraft, the materials in this experiment were only exposed to the space environment for the period of time originally intended. It was noted that the canister was still under partial vacuum just prior to its being opened to retrieve the samples. The system was mounted on the leading edge of the spacecraft, so that the normal to the sample surfaces was about 10° from the ram vector.

The thin films exposed as part of the EECC experiment were aluminum, gold, iridium, osmium, platinum, magnesium fluoride-overcoated aluminum, and aluminum overcoated with reactively deposited silicon monoxide (SiO_2). The source of each sample and the nominal film thicknesses are provided in Table I.

It was mentioned earlier that eight optical materials were furnished by GSFC for this flight. In addition to the seven already mentioned as being mounted in the EECC, two specimens of polished, chemical vapor deposited (CVD) silicon carbide, provided by Choyke of the Westinghouse Research and Development Center², were installed in sites available in another experiment package, A0114 (Interaction of Atomic Oxygen With Solid Surfaces at Orbital Altitudes), which included trays in two of the spacecraft bays, one on the leading edge and the other on the trailing edge. One of the SiC

samples was located in each of the trays and they were exposed for the full duration of the flight. The samples, which were 16-mm long, 12-mm wide, and 0.25-mm thick, were masked by the tray's cover plate so as to shield 1/2 of their surfaces from the environment, the protected half serving as a control. The edges of the cutouts in the cover plate delineating the two halves of the samples were beveled to minimize shadowing effects from obliquely incident flux.

EXPERIMENTAL RESULTS

The wavelength range selected for reflectance measurements of a particular sample being studied depended on the typical usage of that coating and whether the measurement could provide some insight into the nature of the changes observed. Wavelengths varied from as low as 58 nm up to 20 micrometers. Reflectances at wavelengths below 100 nm were measured using a 2-m glancing incidence vacuum monochromator with a duoplasmatron light source. Measurements from 100 to 200 nm were made with a gaseous discharge light source mounted to a 1-m normal incidence vacuum monochromator. Each monochromator was fitted with a reflectometer of the type described by Hunter³ in which the sample reflectances were measured at a 15° angle of incidence. Preflight near-UV and visible region reflectances were measured in a prism spectrophotometer equipped with an integrating sphere attachment, which provided the reflectance relative to a vacuum deposited aluminum standard. This instrument has since been replaced with a grating spectrophotometer with an absolute reflectance accessory, which may account for some of the reflectance differences between preflight and postflight measurements, since the absolute reflectance of the aluminum standard used with the original instrument was not documented at that time. This will be addressed where appropriate in the following discussion of the experimental results. A Fourier transform spectrometer was used to make IR reflectance measurements in the 2-20 micrometer wavelength region.

The recovered EECC experiment package was delivered intact to the NASA Langley Research Center, home installation of the principal investigator, where the canister was vented and preliminary visual examination of the specimens was conducted prior to their removal from the trays. Those noticeably changed were the osmium and gold samples.

Osmium

The appearance of the osmium sample was typical of what we had seen on previous low earth orbit exposures¹. The film had become sufficiently transparent so that the identification number scribed on its back surface was visible from the front. Subsequent reflectance measurements, made after the samples had been removed from their tray and returned to GSFC, were essentially a duplication of earlier results and are shown graphically in Figure 1. As before, the postflight reflectance spectrum is characteristic of vacuum deposited chromium, again indicating that the osmium had disappeared, presumably by oxidation to its relatively volatile tetroxide, leaving behind the chromium binder layer.

Gold

Preliminary examination of the gold sample prior to removal from the EECC tray revealed an area that appeared to be lighter in color than the rest of the surface. This area was kidney-shaped, its longest dimension was about 2/3 that of the sample diameter, and it was somewhat eccentric while still including the sample center within its bounds. After retrieval of the sample and return to GSFC, it was microscopically examined in greater detail using Nomarski differential interference contrast at magnifications from as low as 3X to as high as 1,000X. This examination revealed that the surface outside the kidney-shaped area was considerably rougher than that inside. This was later verified using a Wyko TOPO-2D two-dimensional surface profiler. The measured RMS roughnesses of the outer and inner areas were 1.42 and 0.62 nm, respectively, compared to 0.43 nm for the control sample, which had been coated at the same time and was stored in the laboratory for the duration of the flight.

Normal incidence reflectance measurements at the center and edge of the sample over the wavelength region from 58 to 200 nm indicated substantial degradation of the coating. These data, presented in Figure 2, show that the reflectance of central area, within the kidney-shaped zone, decreased fairly uniformly over the entire spectral region, whereas that of the area outside this zone showed an additional decrease in the region above 100 nm, suggesting multiple degenerative phenomena.

In an attempt to understand the mechanisms of the observed degradation, reference was made to the work of others studying the modifications of material surface properties due to interaction with ambient atomic oxygen in low earth orbit, in particular, the work of Peters, et al⁴, which included a study of gold films. They studied the physical removal of films by momentum imparted from collisions with incident atoms rather than chemical reactions, which represents the situation for gold since it sputters with relatively high yields and is not reactive with oxygen. Based on their sputtering yield of 5×10^{-5} for 5-ev oxygen atoms incident on gold, and a reported⁵ oxygen fluence in the order of 10^{21} atoms/cm², we have estimated that several monolayers of gold could have been sputtered during the exposure period.

They also observed that etching in orbit is very sensitive to certain contaminants overlying the reactive materials, including silicones, which are not effectively removed by oxygen atoms. The presence of silicone contamination on our gold sample is a distinct possibility, since considerable amounts of contaminant found to contain silicone material were visible on the drawer guides and other external surfaces of the EECC and the position of the gold sample was immediately adjacent to one edge of the drawer.

On the basis of this information, one possible scenario for the observed degradation of the gold film involves creep of the silicone molecules onto its surface, moving from the tray cover toward the exposed center of the sample, where the contaminant layer would be expected to be thinnest. This layer would retard the sputtering action of the oxygen atoms most effectively at the periphery of the sample where its thickness is greatest, giving rise to a contaminated outside zone and an etched central portion. The displacement of the etched area away from the drawer edge could be explained by the directional source of the contaminant.

As part of the process of preparing the gold samples, the deposition monitor's reflectance was measured

over the spectral range of 350-750 nm. Since gold coatings have application in the visible and IR as well as in the VUV, these measurements were repeated for the flight and control samples upon retrieval of LDEF, although instrumental geometry limited these to the centers of the samples. As we pointed out above, preflight and postflight measurements in this spectral region were made with different instruments. This may explain the difference between the preflight reflectance curve of the deposition monitor and the postflight reflectance of the control sample, as shown in Figure 3, although a portion or all of the change may be due to adsorption of ambient contaminants on the surface of the latter. More importantly though, the flight sample suffered substantial degradation, especially above 500 nm, when compared to the control, which is consistent with the visual appearance of its surface.

Platinum and Iridium

Both the platinum and iridium samples fared comparatively well, as shown in Figures 4 and 5. The largest of the changes exhibited by the Pt are about 2%, which is in the order of magnitude of the measurement accuracy and, therefore, it may be considered essentially unchanged. The Ir sample experienced losses of about 6% or less in the measured spectral range, which is very similar to the changes seen in the short term exposure in the EOIM experiment on STS-8, referred to previously. It appears that whatever is affecting the reflectance of the Ir, be it oxidation or some other phenomenon, occurs within a short time of its initial exposure to the orbital environment, after which the film seems rather stable. Surface roughness comparison with its control sample did not show any roughening of the flight specimen.

Aluminum

The bare, vacuum-deposited aluminum sample, unprotected by any dielectric overcoating, seems to have suffered significant reflectance degradation only in the wavelength region below 250 nm, presumably due to the oxidation of the aluminum to aluminum oxide, which is absorbing in the UV. As seen in Figure 6, the reflectance is essentially unchanged through the visible portion of the spectrum, although there is a slight decreasing trend, amounting to no more than a few percent toward the longer wavelengths. Since the oxidation of aluminum occurs rapidly upon its exposure to the atmosphere, after which its reflectance is relatively stable, the additional losses experienced, compared to the relatively small changes in the control sample, can probably be attributed to the greater reactivity of the atomic oxygen in low earth orbit relative to that of atmospheric, molecular oxygen. The reflectance losses observed are almost identical to that for the sample from the same deposition batch flown as part of the EOIM-II shuttle-borne experiment, indicating that these changes occurred early in the flight, i.e., within the first few days. The close agreement between preflight and postflight reflectance measurements in the visible tend to refute the earlier suggestion that instrumentation differences may have been responsible for some of the change observed for the gold sample.

Al + MgF₂

Magnesium fluoride-protected aluminum mirrors, commonly used in the vacuum ultraviolet (VUV) because of their high reflectance down to 110 nm, were flown as part of both the EOIM-II and LDEF contingents. Those in the former experiment were essentially unchanged with the exception of those samples which were obviously contaminated by discharges from other sources in the shuttle environment. The LDEF sample, on the other hand, which showed no visible evidence of having been contaminated, experienced significant reflectance degradation in the wavelength region around 150 nm, as seen in Figure 7. Studies have shown⁶ that the presence of a thin absorbing film on the surface of an Al+MgF₂ mirror with a nominal MgF₂ thickness of 25 nm causes reflectance degradation in the wavelength vicinity of 200 nm, where the MgF₂ thickness corresponds to a 1/4-wave and the electric field at the mirror surface is at a maximum, thus resulting in the greatest sensitivity to thin contaminant layers. The substantial change in the 150 nm region suggests a plasma resonance absorption in aluminum enhanced by surface roughness⁷, and although interferometric comparison of the flight and control samples indicated no significant difference in surface roughness, additional investigation of the surface is needed before a final assessment can be made.

Al + SiO_x

Al + SiO_x films are produced by overcoating the evaporated aluminum with silicon monoxide (SiO) at low deposition rates and relatively high pressures of oxygen or air, in order to produce films with low indices of refraction and negligible absorptance in the solar spectral region. During this reactive evaporation process, the ratio of evaporated SiO and oxygen molecules arriving simultaneously at the substrate surface is carefully controlled to obtain highly transparent films of a higher oxide.

The reflectance spectrum of the LDEF flight mirror sample so produced is compared with that of its control sample in Figure 8. Although this coating is not normally used at wavelengths as low as 160 nm, measurements were made in this region in an attempt to understand the nature of the environmentally induced changes. For the same reason, reflectances were also made in the 2 to 20- μ m region and are plotted in Figure 9.

Examination of the data below 750 nm reveals a shift in the reflectance curve toward the shorter wavelengths, resulting in substantial increases below 300 nm. This effect is very much like that ascribed to UV irradiation of the films, a technique used to eliminate undesired UV absorptance of reactively deposited silicon oxide^{8,9}. The infrared measurements show that the reduction in UV absorptance, while it may indicate a change in oxidative state, is not the result of the conversion of the SiO_x into SiO₂, since it did not produce a new absorption band at 12.5 μ m, but may also be due to removal of dislocations and the production of a better defined stoichiometric order throughout the film¹⁰.

Silicon Carbide

The reflectance changes exhibited by the two SiC samples, which were exposed for the full duration of the flight, are shown in Figs. 10 and 11. The exposed portion of the leading-edge sample suffered a drastic drop in reflectance over the wavelength range of 60-160 nm, whereas the losses of the trailing-edge sample were less than half as much over the same region. An analysis of these samples is being continued by the supplier, but a candidate mechanism for the gross loss observed is oxidation caused by direct exposure to the ram for an extended period, based on the similarity of the reflectance cutoff to that of silicon dioxide.

The recently published work of Seely et al.¹¹ supports this contention. They simulated the effects of exposures of up to 7.5 years in low earth orbit by bombarding SiC with oxygen atoms in the laboratory. Their analysis indicated that the reflectance reductions were due to an increase in thickness of a surface layer of SiO_x (where x is ~ 1.5) from 0.8-1.8 nm to 3.5-4.5 nm. Their measurements, which were consistent with x-ray photoelectron spectroscopy of the exposed mirrors, indicated that most of the growth in thickness of the SiO_x layers occurred during the first several years of simulated space exposure.

Examination of their calculated reflectance spectrum of a bombarded SiC mirror shows that the predicted values fall between those of the leading- and trailing-edge specimens in our flight experiment. Several possible explanations for the variance exist, including deviation of the assumed optical constants of the SiC substrate in their analysis from actual values, and a possible enhancement of the oxidation process in space due to simultaneous exposure to solar UV radiation.

DISCUSSION

It is clear from the results for these optical mirror materials that they reinforce the data obtained from the EOIM experiments. It has been shown that the low-earth-orbit environment can be a harsh setting for mirrors, particularly those that have proved useful in VUV applications. The mechanisms by which the optical materials degrade may not be fully understood and will require further analysis, but the indications are that atomic oxygen plays a significant role, either as a sputtering agent, as an oxidant, or both. The situation is complicated by evidence of contamination of various spacecraft and sample surfaces, some of which appear to be due to outgassing of sources within the structure. There is also an indication of unexpected thin layers of metallic species on specimen, as well as spacecraft, surfaces.¹²

In spite of remaining uncertainties about the mechanisms of the observed changes, the results strongly suggest the need for protecting optical surfaces against the external low-earth-orbit environment, particularly ram direction effects, although the degradation of some materials is not limited to surfaces in that orientation. The deterioration of the SiC mirror mounted on the trailing edge, while not as severe as that of its leading-edge counterpart, supports that contention, as do the results with Os oriented 180° to the ram vector in one of the earlier EOIM experiments.¹³ The smaller, but significant, degradation of the masked portions of the LDEF SiC samples indicates the need for careful consideration in the design of optical instrumentation to protect the sensitive surfaces.

REFERENCES

1. Gull, T.R., Herzig, H., Osantowski, J.F., and Toft, A.R., "Low Earth Orbit Environmental Effects on Osmium and Related Optical Thin-Film Coatings," *Appl. Opt.* **24**, 2660-2665 (1985).
2. Samples provided by W.J. Choyke, Department of Physics, University of Pittsburgh, Pittsburgh, PA through W.D. Partlow, Westinghouse Research and Development Center, Pittsburgh, PA.
3. Hunter, W.R., "On the Cause of Errors in Reflectance vs Angle of Incidence Measurements and the Design of Reflectometers to Eliminate the Errors," *Appl. Opt.* **6**, 2140-2150 (1967).
4. Peters, P.N., Gregory, J.C., and Swann, J.T., "Effects on Optical Systems from Interactions with Oxygen Atoms in Low Earth Orbits," *Appl. Opt.* **25**, 1290-1298 (1986).
5. Visentine, J., "Excerpt from internal correspondence at NASA/Johnson Space Center," in *LDEF Spaceflight Environmental Effects Newsletter*, W. Kinard, ed. (LDEF Corp., Silver Spring, Md., 1990), Vol. 1, No. 3, pp. 8-9.
6. Osantowski, J.F., "Contamination Sensitivity of Typical Mirror Coatings - A Parametric Study," *Proc. SPIE Int. Soc. Opt. Eng.*, **338**, 80-86 (1983).
7. Stanford, J.L. and Bennett, H.E., "Enhancement of Surface Plasma Resonance Absorption in Mirrors by Overcoating with Dielectrics," *Appl. Opt.* **8**, 2556-2557 (1969).
8. Bradford, A.P. and Hass, G., "Increasing the Far-Ultraviolet Reflectance of Silicon-Oxide-Protected Aluminum Mirrors by Ultraviolet Irradiation," *J. Opt. Soc. Am.*, **53**, 1096-1100, (1963).
9. Herzig, H., Spencer, R.S., and Zaniewski, J.J., "Effect of UV Irradiation on the Reflectance of Silicon-Oxide-Protected Aluminum in the Far-UV," *Appl. Opt.* **17**, 3031-3032 (1978).
10. Bradford, A.P., Hass, G., Heaney, J.B., and Triolo, J.J., "Solar Absorptivity and Thermal Emissivity of Aluminum Coated with Silicon Oxide Films Prepared by Evaporation of Silicon Monoxide," *Appl. Opt.* **9**, 339-344 (1970).
11. Seeley, J.F., Holland, G.E., Hunter, W.R., McCoy, R.P., Dymond, K.F., and Corson, M., "Effect of Oxygen Atom Bombardment on the Reflectance of Silicon Carbide Mirrors in the Extreme Ultraviolet Region," *Appl. Opt.* **32**, 1805-1810 (1993).
12. Ritter, J., Phillips, G., King, S., and Haskins, P., "Beryllium 7 discovered in LEO atmosphere," in *LDEF Spaceflight Environmental Effects Newsletter*, W. Kinard, ed. (LDEF Corp., Silver Spring, Md., 1990) Vol. 1, No. 3, pp. 7-8.
13. Park, J.J., Gull, T.R., Herzig, H., and Toft, A.R., "Effects of Atomic Oxygen on Paint and Optical Coatings." Presented at the American Institute of Aeronautics and Astronautics Shuttle Environment and Operations Meeting, Washington, DC, 31 October - 2 November 1983.

Table 1. Optical Thin-Film Samples for the LDEF/EECC		
Film Material	Source	Nominal Film Thicknesses (nm)^a
Al	GSFC	70
Au	GSFC	10Cr + 10Cr/Au + 80Au
Os	ARC ^b	5-10 Cr + 20 Os
Ir	ARC	5-10 Cr + 17.5 Os
Pt	ARC	5-10 Cr + 20 Pt
Al + MgF ₂	GSFC	70 Al + 25 MgF ₂
Al + SiO _x	GSFC	70 Al + 180 SiO _x

^aChromium was used as a binder layer where indicated to improve adhesion between the top film and substrate. The GSFC process for Au includes an intermediate layer of codeposited Cr and Au to enhance adhesion further.

^bActon Research Corporation, Acton, Massachusetts

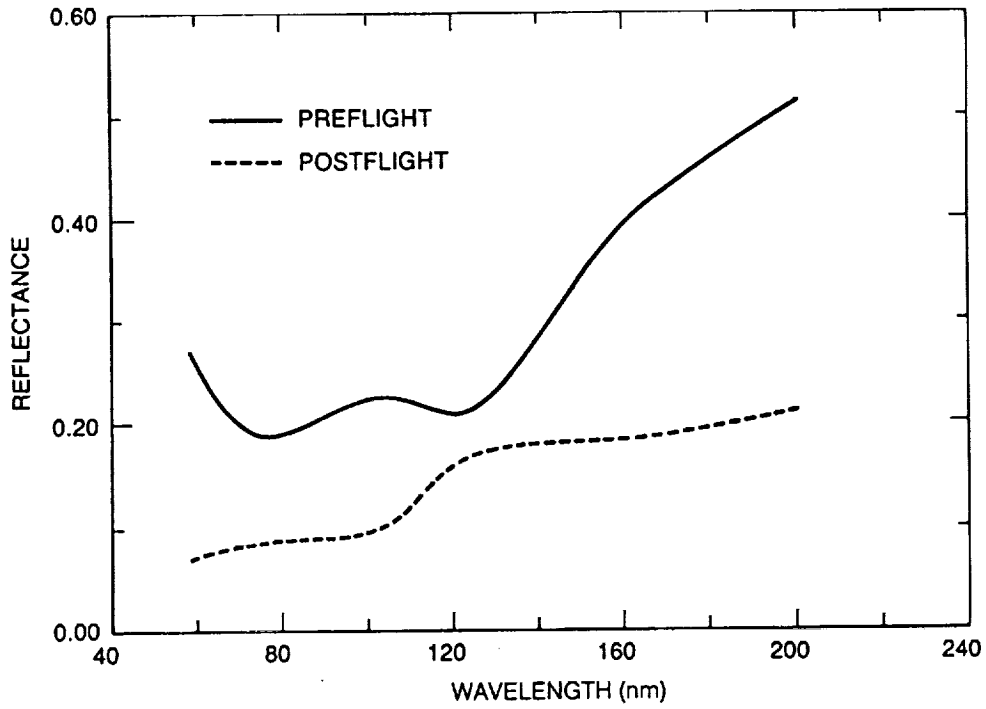


Figure 1. Effect of long duration, low earth orbit exposure on the VUV reflectance spectrum of an osmium film.

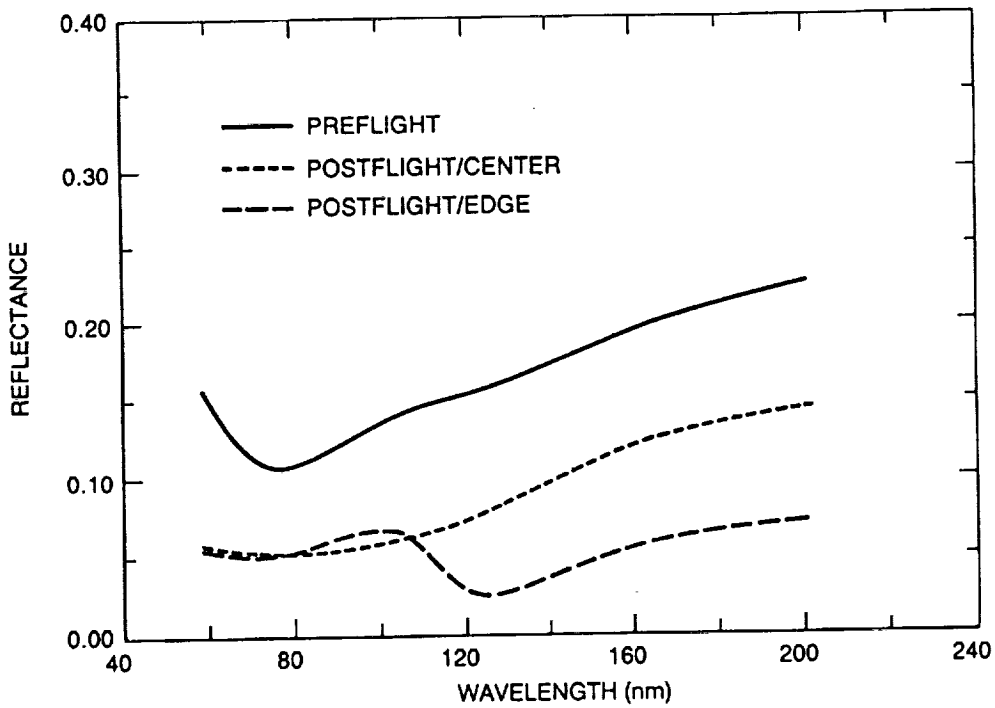


Figure 2. Effect of long duration, low earth orbit exposure on the VUV reflectance spectrum of a gold film.

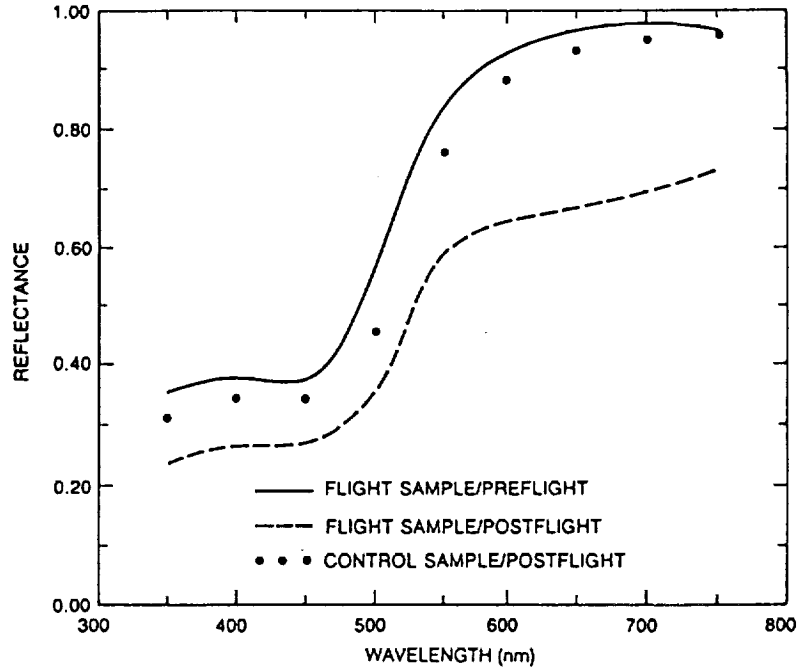


Figure 3. Comparison of visible wavelength spectra of the flight sample and a nonflight control sample of a gold film.

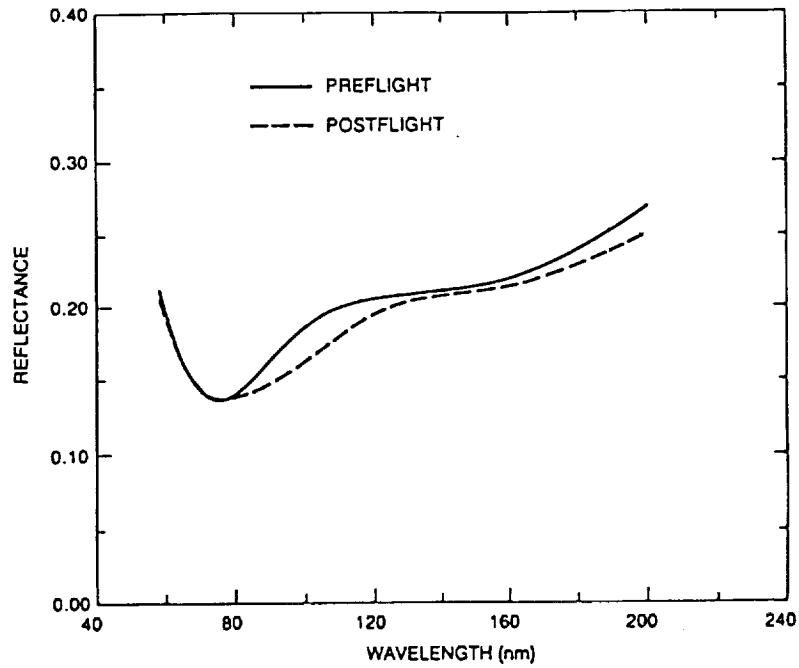


Figure 4. Effect of long duration, low earth orbit exposure on the VUV reflectance spectrum of a platinum film.

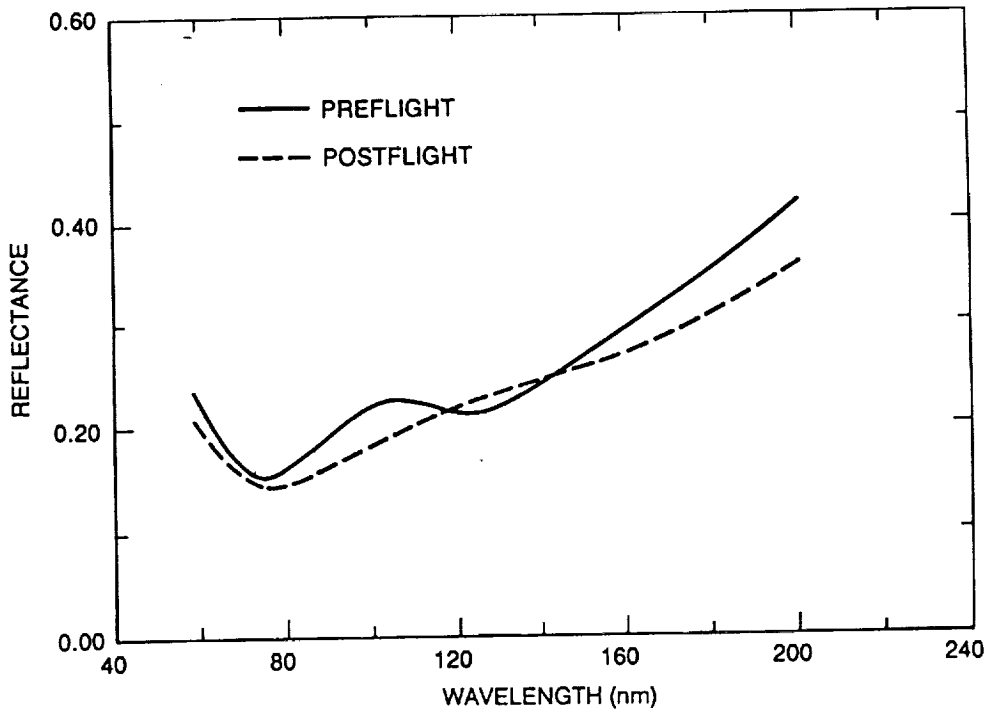


Figure 5. Effect of long duration, low earth orbit exposure on the VUV reflectance spectrum of an iridium film.

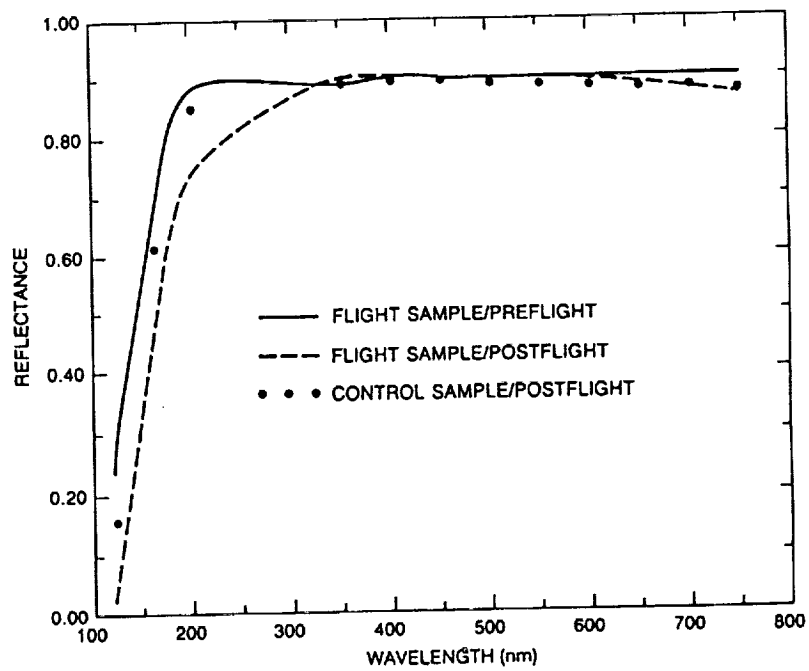


Figure 6. Comparison of VUV-through-visible spectra of the flight sample and a nonflight control sample of an aluminum film.

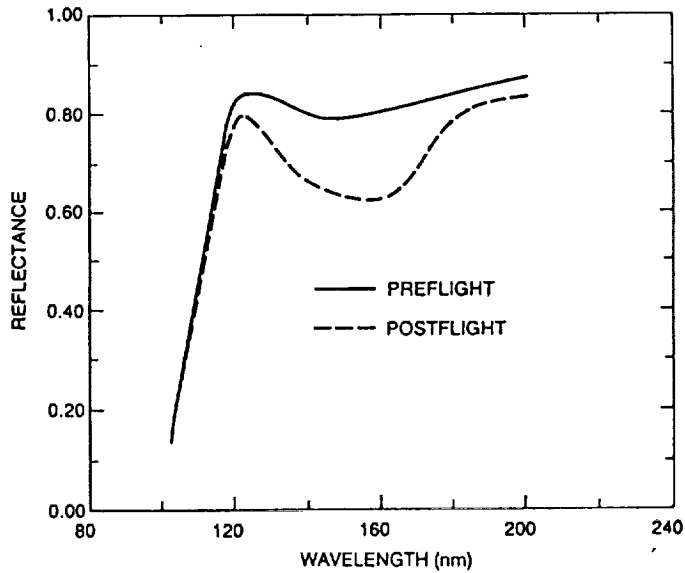


Figure 7. Effect of long duration, low earth orbit exposure on the VUV reflectance spectrum of a magnesium fluoride-overcoated aluminum film.

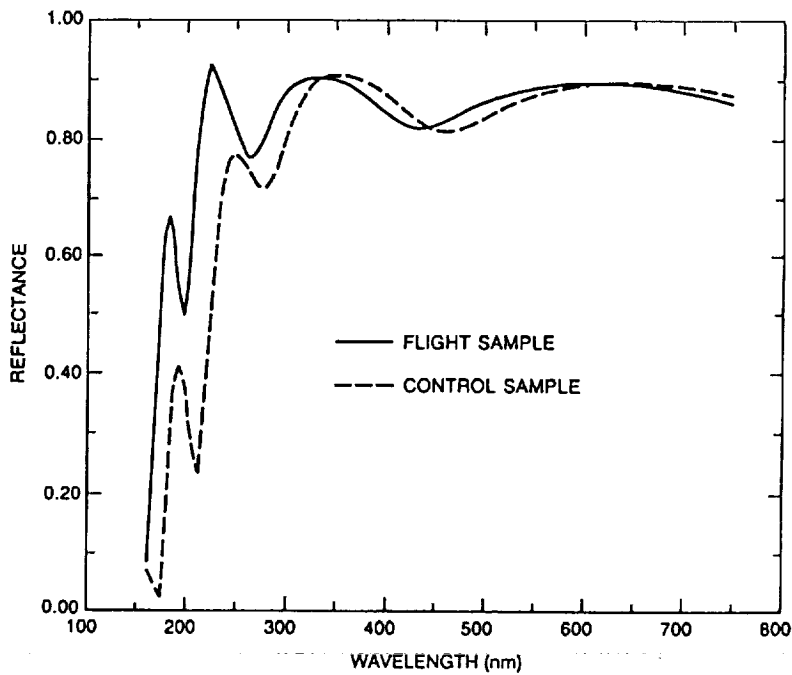


Figure 8. Comparison of VUV-through-visible spectra of the flight sample and a nonflight control sample of an aluminum film overcoated with reactively deposited silicon monoxide.

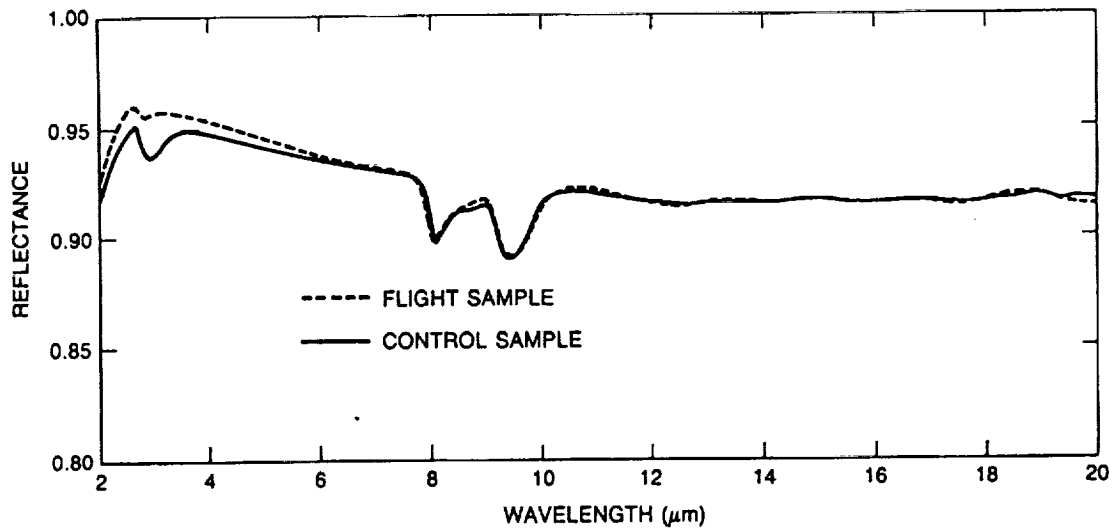


Figure 9. Comparison of infrared reflectance spectra of the flight sample and a nonflight control sample of an aluminum film overcoated with reactively deposited silicon monoxide.

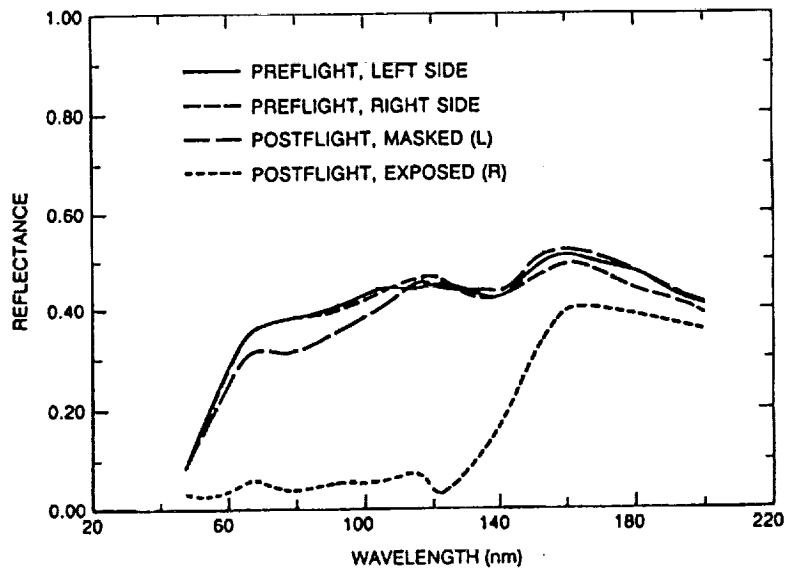


Figure 10. Effect of long duration, low earth orbit exposure on the VUV reflectance spectrum of exposed and masked portions of a CVD SiC sample mounted on the leading edge of the LDEF spacecraft.

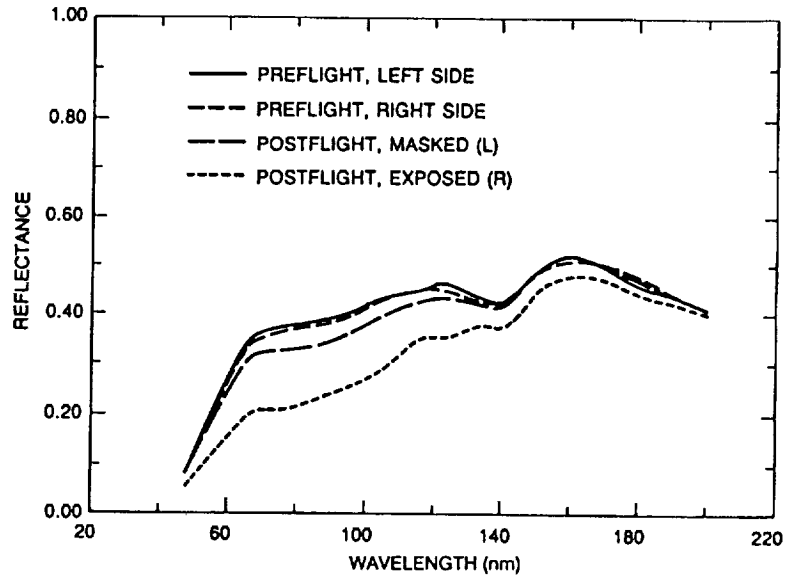


Figure 11. Effect of long duration, low earth orbit exposure on the VUV reflectance spectrum of exposed and masked portions of a CVD SiC sample mounted on the trailing edge of the LDEF spacecraft.

1
2
3
4
5
6
7
8
9
10
11
12
13
14
15
16
17
18
19
20
21
22
23
24
25
26
27
28
29
30
31
32
33
34
35
36
37
38
39
40
41
42
43
44
45
46
47
48
49
50
51
52
53
54
55
56
57
58
59
60
61
62
63
64
65
66
67
68
69
70
71
72
73
74
75
76
77
78
79
80
81
82
83
84
85
86
87
88
89
90
91
92
93
94
95
96
97
98
99
100

THE UNIVERSITY OF CHICAGO

PHYSICS DEPARTMENT

EFFECTS OF LOW EARTH ORBIT ON THE OPTICAL PERFORMANCE OF
MULTILAYER ENHANCED HIGH REFLECTANCE MIRRORS*

Terence Donovan
3481 Murdoch Drive
Palo Alto, CA 94306
Phone: 415/424-8990

Linda Johnson, Karl Klemm, Rick Scheri, and Jean Bennett
Naval Air Warfare Center Weapons Division
China Lake, CA 93555-6001
Phone: 619/939-1422, Fax: 619/939-1409

Jon Erickson and Filippo di Brozolo
Charles Evans and Associates
Redwood City, CA 94063
Phone: 415/369-4567, Fax: 415/369-7921

ABSTRACT

Two mirror designs developed for space applications were flown along with a standard mid-infrared design on the leading and trailing edges of the Long Duration Exposure Facility (LDEF). Preliminary observations of induced changes in optical performance of ZnS-coated mirrors and impact-related microstructural and microchemical effects are described in the proceedings of the First LDEF Post-Retrieval Symposium.¹

In this paper, effects of the induced environment and meteoroid/debris impacts on mirror performance are described in more detail. Also, an analysis of reflectance spectra using the results of Auger and secondary ion mass spectroscopy (SIMS) profiling measurements are used to identify an optical-degradation mechanism for the ZnS-coated mirrors.

Structural damage associated with a high-velocity impact on a (Si/Al₂O₃)-coated mirror was imaged optically and with scanning electron and atomic force microscopy (SEM and AFM). Scanning Auger and SIMS analysis provided chemical mapping of selected impact sites. The impact data suggest design and fabrication modifications for obtaining improved mechanical performance using a design variation identified in preflight laboratory simulations.²

Auger surface profile and SIMS imaging data verified the conclusion¹ that secondary impacts are the source of contamination associated with the dendrites grown on the leading-edge ZnS-coated test samples. It was also found that dendrites can be grown in the laboratory by irradiating contaminated sites on a trailing-edge ZnS-coated sample with a rastered electron beam. These results suggest a mechanism for dendrite growth.

* Financial support provided by DARPA, USAF Wright Laboratories, and NASA Langley Research Center.

INTRODUCTION

Multilayer-coated test mirrors and single-layer witness samples were flown on both the leading and trailing edges of LDEF. The samples were provided from a DARPA-sponsored program to develop dielectrically-coated high reflectance mirrors for space applications. Two types of mirrors were flown: (1) an industrial standard mid-IR design; (2) two alternative designs that promised improved stability in laboratory simulations of the space environment.² The mirrors were contained in vacuum cassettes and exposed for timed periods which varied from 90 to 270 days from the deployment of LDEF. Witness samples consisting of half-wave layers of materials included in the multilayer stacks were exposed for the flight duration. Sample designs and locations on LDEF along with exposure times and atomic oxygen fluences are listed in Table 1.

Table 1. Flight Samples, Location on LDEF, Exposure Time, and Atomic Oxygen Fluence for Experiment Number M0003-7

Sample ID ^a	Design	LDEF location ^b	Exposure (months)	Atomic Oxygen Fluence (atoms/cm ²)
L6-VI-7-46-11	(Si/Al ₂ O ₃) ³ Ag/Si	D8	3	3.1x10 ²⁰
T6-VI-7-31-4	(Si/Al ₂ O ₃) ² Ag/Mo	D4	3	9.9x10 ³
L3-II-7-61-3	Si/fused silica	D9	70	9.0x10 ²¹
T3-II-7-60-4	" " "	D3	70	1.3x10 ¹⁷
L6-VI-7-68-15	(ZnS/ThF ₄) ⁵ Ag/Mo ^c	D8	6	6.1x10 ²⁰
T6-VI-7-30-36	" " " "	D4	9	3.0x10 ⁴
L3-II-7-65-10	ZnS/fused silica	D9	70	9.0x10 ²¹
T3-II-7-64-11	" " "	D3	70	1.3x10 ¹⁷
L6-VI-7-67-239	(ZnS/Al ₂ O ₃) ⁴ Ag/Mo	D8	9	9.2x10 ²⁰

^a Sample ID provides the tray, module, sub-experiment, module location, and sample numbers

^b Row numbers: leading edge (D8, D9); trailing edge (D3, D4)

^c Industrial-standard, mid-IR design

The post-flight optical, surface/profiling, and impact-related data on test mirrors and witness samples listed in Table 1 are discussed in this paper along with an analysis of the factors found detrimental to optical performance. These results along with laboratory simulation data are used to suggest an alternative coating design and fabrication process for improved mirror performance.

(Si/Al₂O₃)ⁿAg/Si MIRROR DESIGN RESULTS

The spectral reflectance of the leading-edge (Si/Al₂O₃)³Ag/Si test sample after 90 days exposure to the effects of low-Earth orbit (LEO) is shown in Figure 1. As seen in the figure, the reflectance of the test sample is reduced less than 0.1% at the design wavelength (2.8 μm) relative to the laboratory control. The reflectance of the control was reduced by less than 0.1% after 10 years on the laboratory shelf. Profilometer measurements showed that increases in optical scatter resulted from surface debris and not

from changes in microstructure or topography. The scatter increase contributed to the small reflectance loss relative to the control.

Auger profiles of the test sample are shown in Figures 2 and 3. The depth profile (Figure 2) reveals the design; three Si/Al₂O₃ high/low index pairs, a Ag reflectance enhancing layer, and the silicon substrate. Some charging occurred during sputter etching of the third silicon layer but the thicknesses are fairly uniform. Note the small Ag peak at the outer Si/Al₂O₃ interface and a C contamination peak at the Al₂O₃/Ag interface.

An Auger surface profile is shown in Figure 3. The estimated sputter rate and time to when oxygen reaches the background level indicates approximately 36 Å of surface oxide. This is within a factor of two of what one would expect from a natural oxide layer on silicon. It is noted that the small growth rate relates to the atomic oxygen (AO) flux at the deployment altitude (476 km) and the short exposure (3 months). This thickness will have little effect at the design wavelength but could account for a slight increase in absorption at wavelengths greater than 3 μm.

Rutherford backscattering spectrometry (RBS) measurements were made on two single-layer Si witness samples that were exposed for the 70-month flight duration (AO fluence: D9 = 9.0x10²¹ atoms/cm²; D3 = 1.3x10¹⁷ atoms/cm²). An average of 20 atomic % O was found in the outer 900 Å on the leading-edge witness (L3-II-7-61-3) and relates to the long exposure and significantly higher average AO-flux levels than were experienced by the test mirror (L6-VI-7-46-11). In contrast, no surface oxidation was detected by RBS on the trailing-edge witness (T3-II-7-60-4).

One impact site was observed on the test mirror. The 10-μm-diameter x 0.6-μm-deep impact crater is shown in Figure 4a. The effective damage area was increased by the radial and spiral fractures shown in Figure 4a and delamination in the crater vicinity as shown in a scanning atomic force micrograph (AFM) in Figure 4b. An impacting particle of carbon was identified by scanning Auger microscopy; silver was detected along the spiral fracture. The Auger profile in Figure 2 suggests the Ag migrated from the reflectance-enhancing layer to the surface, thermally driven by the impact. The extended structural damage severely limits the potential performance of the mirror.

A larger, 50-μm-diameter crater was found on the Si/fused silica witness, T3-II-7-60-4. The crater is enriched in K, Cl, O, (SO₂)⁻, SiO₂, and (OH)⁻. Au and Au⁺ were also seen in the time-of-flight secondary ion mass spectroscopy (SIMS) data. K was concentrated in the crater and probably originated from a less-energetic, secondary impact. In this case, no extended structural damage was observed.

DISCUSSION OF (Si/Al₂O₃)ⁿAg/Si MIRROR DESIGN RESULTS

The (Si/Al₂O₃)³Ag/Si design is optically stable in an ionizing-radiation environment as predicted by extensive laboratory simulations² and confirmed by the LDEF flight. AO flux at the deployment altitude and for a limited exposure period has little effect on mirror performance at the design wavelength. Impacts, on the other hand, because of associated structural effects (delamination and fracture) can lead to severe mirror degradation and failure.

The design can be improved by the elimination of Ag as a reflectance-enhancing layer and the substitution of SiO₂ for Al₂O₃ as the low-index component. Ag can melt and diffuse at temperatures generated by particle impacts. Si/SiO_x multilayers were shown to be stable in a combined solar-UV/charged-particle environment in preflight laboratory simulations.² Si/SiO₂ multilayers can be

deposited directly on silicon using a reactive sputtering process. This will result in lower stress, increased adhesion, and a reduction in the possibility of delamination and fracture induced by high-velocity impacting particles.

(ZnS/Al₂O₃)⁴Ag MIRROR DESIGN RESULTS

The post-flight reflectance of the leading-edge (ZnS/Al₂O₃)⁴Ag test sample compared to a laboratory control is shown in Figure 5. The mirror was exposed for nine months beginning with the deployment of LDEF. The test sample has an absorption band centered at 3 μm which reduces the reflectance at the design wavelength of 2.8 μm. The control has no similar loss.

Surface profilometry measurements show an increase in roughness (and related scatter) compared with preflight data. The increase is due to some degradation of the coating surface, debris, and the presence of dendritic material. The scatter, degraded material, and areas of dendritic growth, however, do not account for the spectral feature.

A depth profile of this sample taken by SIMS is shown in Figure 6. Sputter etching was accomplished using O⁻ primary ions to minimize charging effects. The layers are uniform in thickness and there are no significant deviations from the quarter-wave design to account for the spectral band, suggesting the absorption is due to water contamination. Unfortunately, an analysis of H and O couldn't be obtained by sputtering with O⁻ primary ions.

(ZnS/ThF₄)⁵Ag MIRROR DESIGN RESULTS

Similar spectral bands, in this case centered at 2.9 μm, are observed in the post-flight reflectance data of both leading- and trailing-edge ZnS/ThF₄ test samples. SIMS profiling data is shown in Figure 7 for the leading-edge sample. Here, atomic concentration versus depth is plotted with sputter time converted to depth with stylus profilometry using the assumption that ZnS and ThF₄ sputter at equal rates. Sputter etching was accomplished in this case with Cs⁺ primary ions, which can be used to determine H and O. Charging is somewhat of a problem with Cs⁺, but the data is in qualitative agreement with Auger profile data¹ which also shows a relatively thin surface and thick base layers of ZnS.

SIMS depth profiles of O and H are shown in Figures 8 and 9, respectively, for this sample. Calibration in terms of atomic concentration was done using data from float-zone-refined silicon. Note the presence of H and O in the ThF₄ layers with tendency of both materials to peak at high/low index interfaces. Also, concentrations of O and particularly H tend to increase with depth into the coating. It is possible that water contamination incorporated during fabrication was ionized in the radiation environment of LDEF and moved to the film interfaces driven by a reduction in free-energy.

Thin-film design software³ and literature values^{4,5} for the optical constants of ZnS, ThF₄, and Ag were used to model the observed post-flight reflectance spectra. Two approaches were taken using the SIMS and Auger data.

In the first approach, only the thicknesses of the ZnS and ThF₄ layers were varied in the reflectance calculation. The thickness variations either were derived from experimental data (i.e., the SIMS depth profiles) or were arbitrarily chosen to try to force the calculated curve to fit the observed reflectance

spectra. With this approach it was not possible to reproduce either the spectral position or the magnitude of the absorption band centered at 2.9 μm .

The second approach used both the layer thickness variations and the water contamination observed at the interfaces in the SIMS depth profiles. Optical constants for thin layers of water⁶ were entered into the reflectance calculation along with the layer thickness variations derived from the SIMS data. The optimum water contamination (10 $\text{\AA}/\text{interface}$) was determined by iteration within the range of possible values determined by SIMS.

The calculated spectral reflectance values are compared with post-flight reflectance data in Figure 10. As seen in the figure, the SIMS data gives an excellent fit to the reflectance spectrum in the 2.9 to 4.0 μm region. This result validates preflight simulations of combined solar-UV/charged-particle radiation at the Boeing Radiation Effects Laboratory² which showed that the irradiation of water-contaminated ZnS/ThF₄ multilayers increased the optical absorption about 1% at 2.9 μm .

IMPACT DAMAGE, CONTAMINATION, AND EFFECTS OF THE SOLAR UV/ATOMIC OXYGEN ENVIRONMENT

Two types of impact damage found on the ZnS-coated mirrors were described earlier;¹ craters formed by high-velocity impacts and secondary impacts associated with copper contamination. Copper and other contaminants have been found by Auger and SIMS analysis on the leading- and trailing-edge ZnS mirrors. Cu is associated with dendrite growth on leading-edge test samples.¹ A third type of damage with crater-like features was found in the raster-pattern areas that were sputter etched during SIMS depth-profiling measurements.

Figure 11 shows one of two craters formed by high-velocity impact on leading-edge sample L6-VI-7-68-15. This crater is about 70 μm in diameter and about 3.5 μm deep and was formed by a particle approximately 10 μm in diameter. The multilayer structure is exposed, revealing melt and some undercutting of the individual layers suggesting their vulnerability to attack by solar UV/atomic oxygen. An analysis was not performed for possible residual material from the impacting particle.

Figures 12a and 12b show optical and AFM images of one of four sites found on trailing-edge sample T6-VI-7-30-36. The crater is irregular in shape and about 1 μm deep. Melted material estimated by AFM to be 2000 \AA thick is spewed in a radial fashion from the impact site. SIMS analysis in the region of two other impact sites (smaller craters) on this sample identified Cu, Al, Na, K, and siloxane contaminants. The Cu probably originated from diamond-turned Cu mirrors in the sample module.

A large number of dendrites were observed by optical microscopy during de-integration of the two leading-edge ZnS test samples.¹ Figures 13a and 13b show optical images of dendrites grown in orbit on samples L6-VI-7-68-15 and L6-VI-7-67-239. These and other dendrites are surface features that appear to result from a thermal (melt/solidification) growth process.⁷

A high-contrast SEM image and scanning Auger analysis of a dendrite described earlier¹ suggest a reaction with Cu to form a CuZn or CuZnS alloy. An Auger depth profile (Figure 14) taken in a region of dendrites gives a direct indication of a displacement reaction between Cu and ZnS. This profile also shows that O has to some extent replaced S in the ZnS. The thickness of the "alloy" and oxide is estimated from the sputter time to be about 400 \AA . A mass-resolved SIMS image of a dendrite at an Al-contaminated site on the leading-edge ZnS/ThF₄ test sample is shown in Figure 15.

No dendrites were found on the trailing-edge sample, but they could be grown in the laboratory by rastering an electron beam in the vicinity of an impact site. The electron-stimulated growth of dendrites was recorded on video tape. An SEM image of a dendrite grown by electron irradiation is shown in Figure 16. The spherical particles, shown in the figure, appeared as a result of electron irradiation. The depletion of these "clusters" in the vicinity of the dendrite suggests a diffusion-limited growth process. Nucleation and growth possibly initiated at the small damage site in the upper left branch of the dendrite shown in Figure 16.

ZnS is known to dissociate in a UV environment and react with oxygen⁸ to form the oxide. Evidence for the occurrence of this reaction in LEO is provided by RBS analysis and optical micrographs (Figure 17) of leading- and trailing-edge witness samples of ZnS exposed for the 70-month duration of LDEF. The leading-edge sample is 15 atomic % O throughout as estimated by RBS. The coating has buckled and, as seen in Figure 17a, annular features are observed at high magnification. The composition and origin of these features has not been determined. The trailing-edge sample (Figure 17b) is mostly intact but many blisters, perhaps related to locally poor adhesion, are observed at high magnification. This sample is not oxidized.

Finally, several crater-like features were found in the ion-raster patterns during profiling-SIMS measurements of sample L6-VI-7-68-15. A raster pattern with small crater-like features is shown in Figure 18a. A profilometer trace through one of the craters is shown in Figure 18b. The crater is 40 μm in diameter and about 2.4 μm deep. The "craters", which were observed after profiling, developed when a 14.5 kV, 0.1 to 0.7 mA Cs^+ primary ion beam was rastered over a square region 500 μm on a side.

DISCUSSION OF ZnS COATING RESULTS

All ZnS coatings had significant reflectance losses at the design wavelength. The reflectance losses, based on modeling of sample L6-VI-7-68-15, are attributed to deviations from the quarter-wave design thicknesses and absorption increases due to $(\text{OH})^-$ accumulation at interfaces between high and low index coating layers. It is suggested that water present as an impurity in the coatings was ionized in the charged particle (e^- and p^+) environment and the mobile ions moved to film interfaces where a reduction in system free energy can occur. Similar in-band absorption increases were observed in preflight laboratory simulations.²

Primary and secondary impact damage, surface contamination, oxidation, and extensive dendrite formation also contributed directly to the optical degradation of these mirrors.

Dendrite formation, which occurred in orbit on samples flown on the leading edge of LDEF, is attributed to displacement reactions of primarily Cu and Al contamination with Zn to form alloys. A phase change from face-centered-cubic to body-centered-cubic Cu is suggested as a possible driving force for the displacement reaction; AO could provide thermal energy for the Cu diffusion and also react with Zn^{++} , created by the UV dissociation of ZnS, to form the oxide.

The Cu and possibly Al contamination originated from secondary impacts from other mirrors in the sample modules. The electron-stimulated growth of dendrites observed in the laboratory on the trailing-edge mirror (T6-VI-7-30-36) suggests a diffusion-rate-limited growth process. Growth was observed, in the laboratory, to initiate (and presumably nucleation occurred) at secondary impact sites.

The crater-like features that developed as the result of Cs⁺ ion etching during SIMS profiling may result from displacement damage, possibly of cosmic ray origin. Further study will be required to understand the origin, extent, and effect of these features on mirror performance.

CONCLUSIONS AND SUGGESTIONS FOR FURTHER WORK

The LDEF flight established the validity of laboratory simulations in screening coated optics for applications in the space environment. Preflight laboratory simulations predicted the optical stability of silicon/oxide designs and identified a potential water-impurity problem in the ZnS designs.² Impact damage, both primary and secondary, was identified as a serious degradation mechanism for both silicon and zinc sulfide designs.

A reactively sputtered (Si/SiO₂)ⁿ/Si design is suggested as a low-stress, adherent alternative to the optically-stable but impact-damage-susceptible-(Si/Al₂O₃)ⁿAg/Si and chemically-unstable-ZnS designs flown on LDEF.

The ZnS designs suffered reflectance losses, impact damage, surface contamination, oxidation, and extensive dendrite growth, all of which contributed to degradation of the mirrors. Deviations from quarter-wave thicknesses and water contamination identified in SIMS-depth profiles successfully accounts for reflectance loss in the 3- μ m-spectral region. The dendrites are associated with displacement reactions of primarily Cu contamination with ZnS. It is suggested that the energy for the diffusion-limited-growth process was supplied by energetic (5eV) AO impacting the leading-edge test mirrors.

Finally, crater-like features that developed deep in a ZnS/ThF₄ coating during SIMS-profiling analysis should be studied in more detail to determine if they are impact related and of extraterrestrial origin. Ultimately, the effect of these craters on mirror performance should be assessed.

ACKNOWLEDGMENTS

Integration and de-integration was accomplished by the Aerospace Corporation (experiment M0003). The authors also thank T. Beirling and R. Helms of Stanford University for Auger surface profile measurements and R. Feigelson, also of Stanford University, for discussions of dendrite growth.

REFERENCES

1. Donovan, T. M.; Bennett, J. M.; Dalbey, R. Z.; Burge, D. K.; and Gyetvay, S.: Space Environmental Effects on Coated Optics. Presented at the First Post-Retrieval Symposium for LDEF, Kissimmee, Florida, 2-8 June 1991. NASA Conference Publication 3134, Part 3, pp. 1361-76.
2. Fogdall, L. B.; Cannaday, S. S.; Gellert, R. I.; Polky, J. N.; and Davies, F. W.: Natural and Induced Space Radiation Effects on Optical Coatings and Materials. Boeing Radiation Effects Laboratory Final Report submitted to the Naval Weapons Center, China Lake, California on Contracts N00123-78-C-0989 and N60530-79-C-0263, April 1981.
3. Macleod, H. A.: *Macleod Thin-Film Design Software*. Thin Film Center, 2745 East Via Rotonda, Tucson, Arizona.
4. Palik, E. D., ed.: *Handbook of Optical Constants of Solids*. Academic Press, Inc., Orlando, Fla., 1985.
5. Palik, E. D., ed.: *Handbook of Optical Constants of Solids II*. Academic Press, Inc., San Diego, Calif., 1991.
6. Rusk, A. N.; Williams, D.; and Querry, M. R.: Optical Constants of Water in the Infrared. *J. Opt. Soc. Am.*, vol. 61, (1971), pp. 895-903.
7. Langer, J. S.; Issues and Opportunities in Materials Research. *Physics Today*, vol. 45, no. 10, October, 1992.
8. Hass, G.; Heaney, J. B.; Hunter, W. R.; and Angel, D. W.: Effect of UV Radiation on Evaporated ZnS Films. *Appl. Opt.*, vol. 19, (1980), pp. 2480-81.

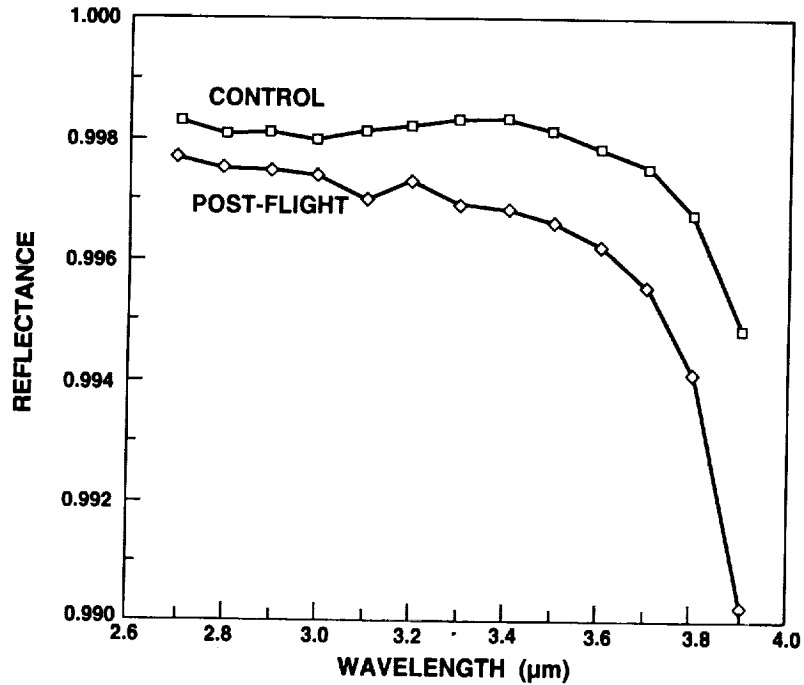


Figure 1. Post-flight reflectance of the leading-edge $(\text{Si}/\text{Al}_2\text{O}_3)^3\text{Ag}/\text{Si}$ test sample compared to a laboratory control. The reflectance loss of the test sample relative to the control is less than 0.1% at the design wavelength (2.8 μm).

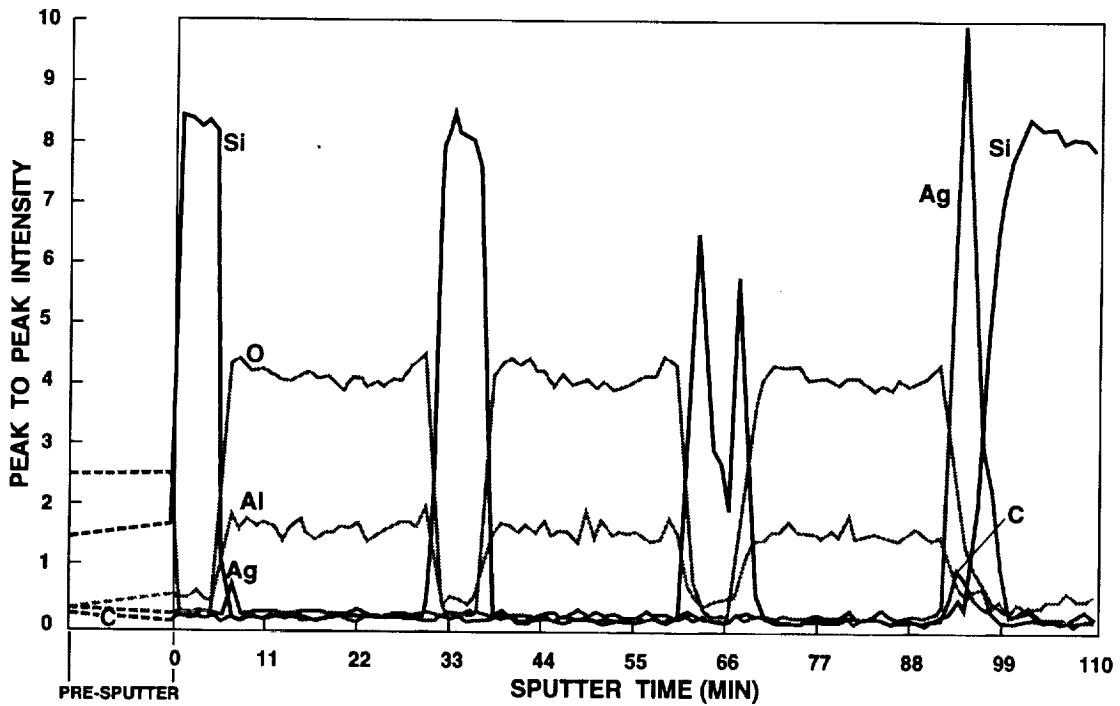


Figure 2. Post-flight Auger depth profile of the leading-edge $(\text{Si}/\text{Al}_2\text{O}_3)^3\text{Ag}/\text{Si}$ test sample showing uniform layer thicknesses. Distortion of the third Si layer peak is due to surface charging.

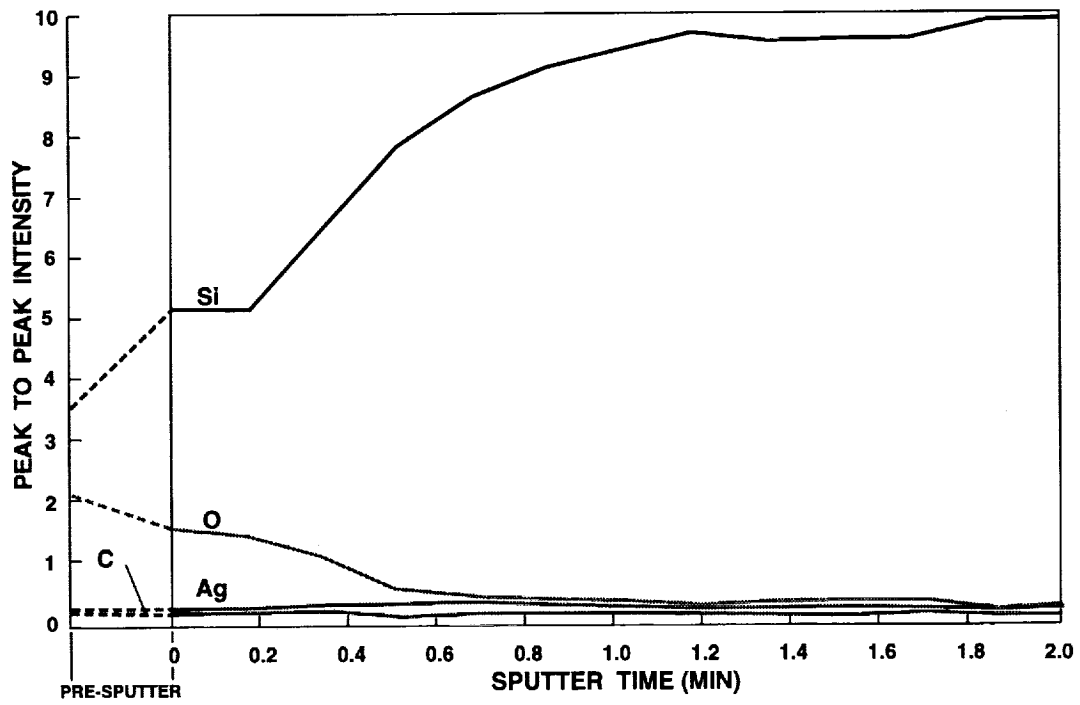


Figure 3. Post-flight Auger surface profile of the leading-edge $(\text{Si}/\text{Al}_2\text{O}_3)^3\text{Ag}/\text{Si}$ test sample. The thin surface oxide layer indicates that Si is not significantly degraded by the energetic AO encountered in LEO.



10 μm

Figure 4a. Scanning electron micrograph showing radial and spiral fractures extending from the impact crater on the leading-edge $(\text{Si}/\text{Al}_2\text{O}_3)_3\text{Ag}/\text{Si}$ test sample.

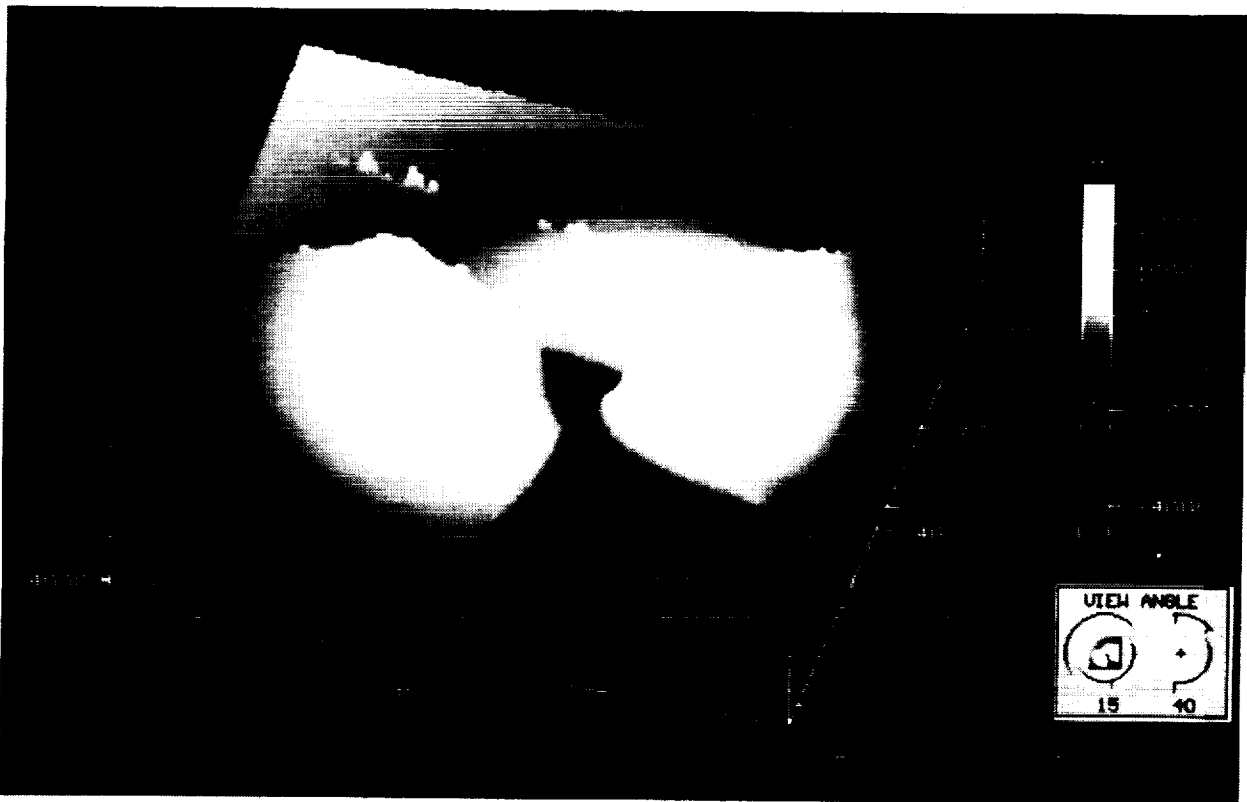


Figure 4b. Atomic force micrograph of impact site in Figure 4a showing the impact crater and film delamination surrounding the crater.

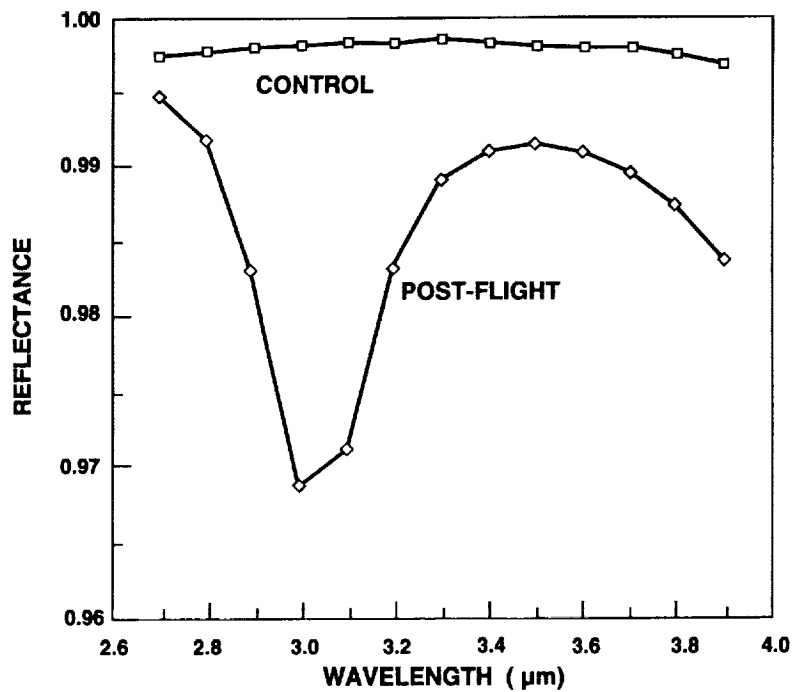


Figure 5. Post-flight reflectance of the leading-edge $(\text{ZnS}/\text{Al}_2\text{O}_3)_4\text{Ag}/\text{Mo}$ test sample compared to a laboratory control.

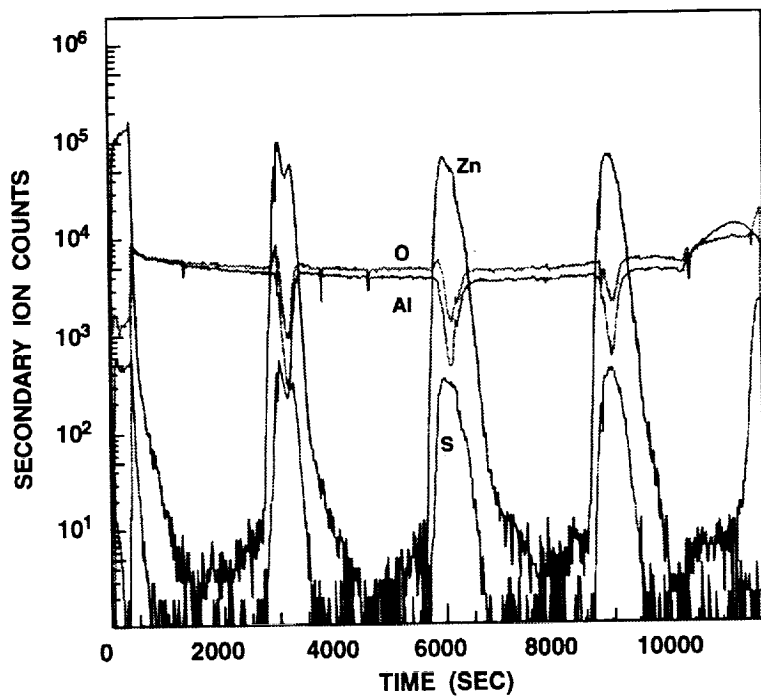


Figure 6. SIMS depth profile of the leading-edge $(\text{ZnS}/\text{Al}_2\text{O}_3)_4\text{Ag}/\text{Mo}$ test sample showing uniform layer thicknesses.

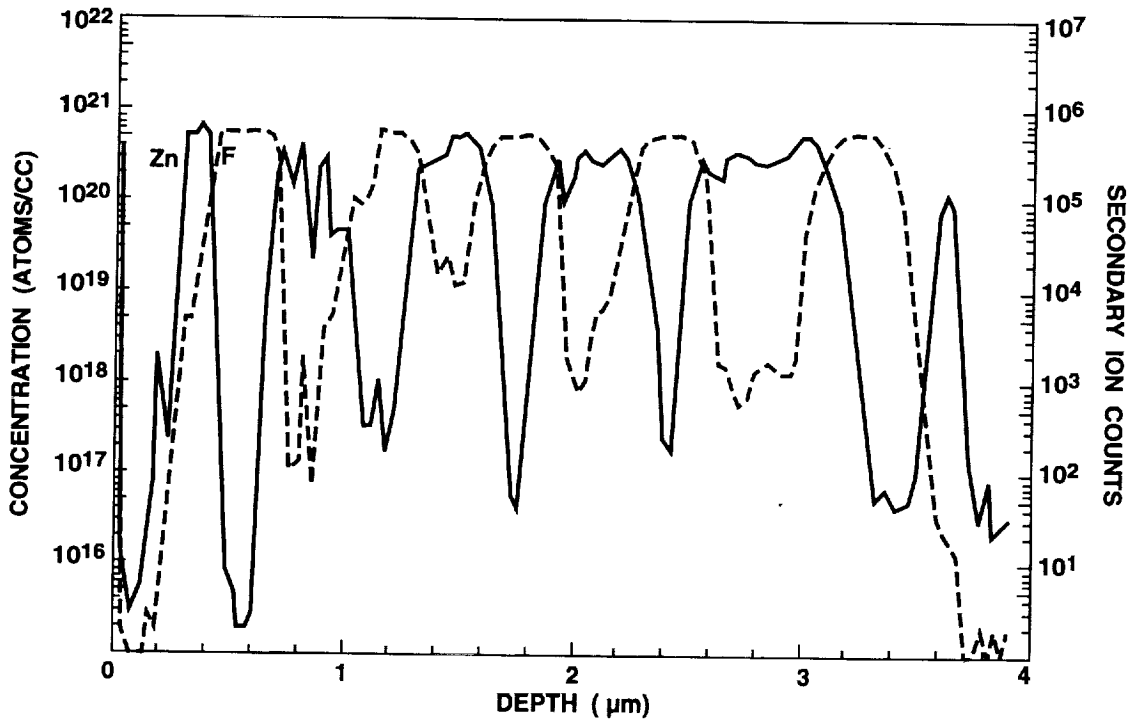


Figure 7. SIMS depth profile of the leading-edge $(\text{ZnS}/\text{ThF}_4)^5\text{Ag}/\text{Mo}$ test sample showing a thin surface layer and thick base layers of ZnS.

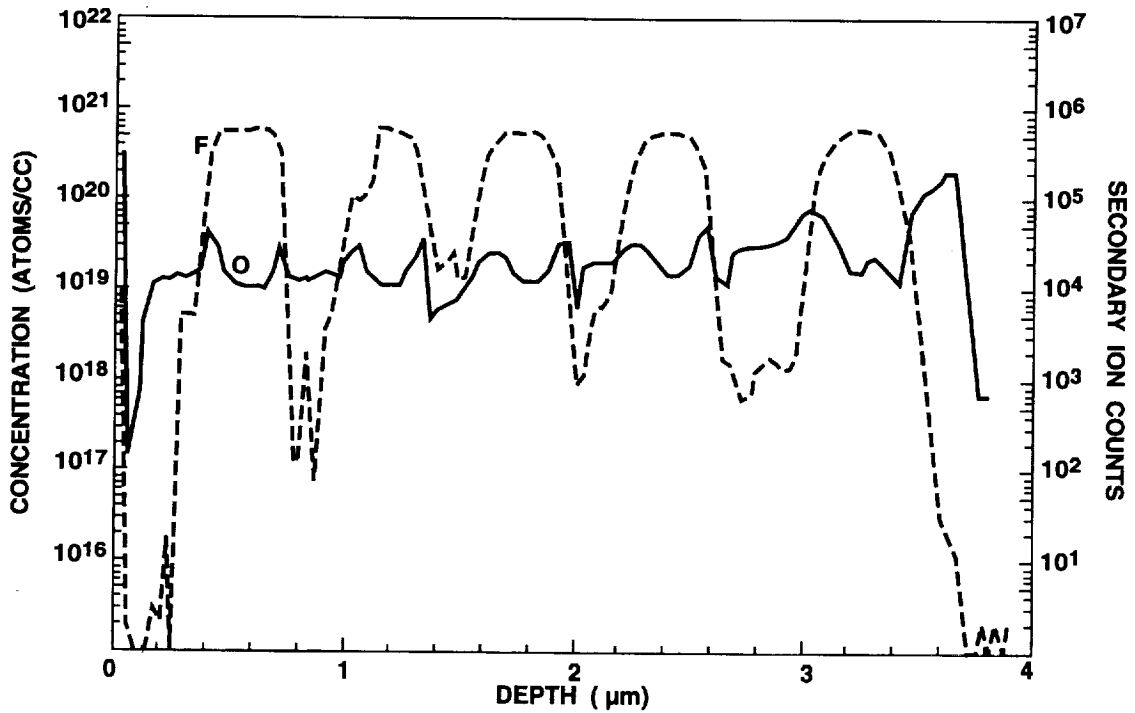


Figure 8. SIMS depth profile of the leading-edge $(\text{ZnS}/\text{ThF}_4)^5\text{Ag}/\text{Mo}$ test sample. The O concentration peaks at the interfaces and increases with depth into the coating.

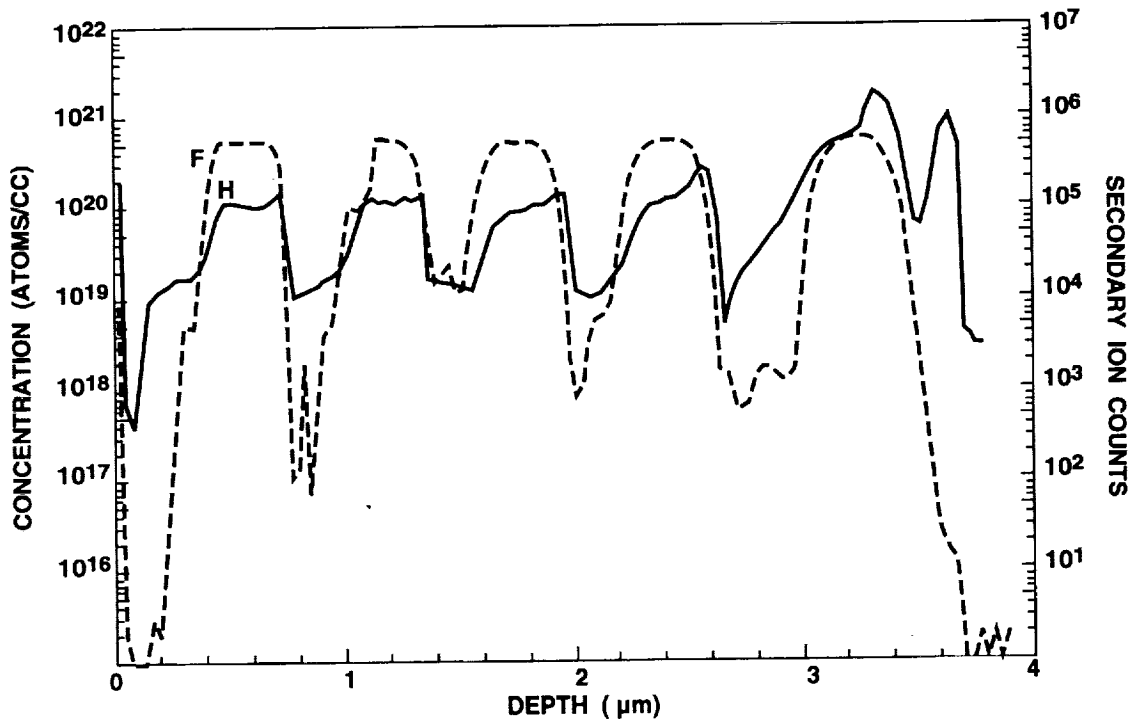


Figure 9. SIMS depth profile of the leading-edge $(\text{ZnS}/\text{ThF}_4)_5\text{Ag}/\text{Mo}$ test sample. The H concentration is high in the ThF_4 layers and increases with depth into the coating.

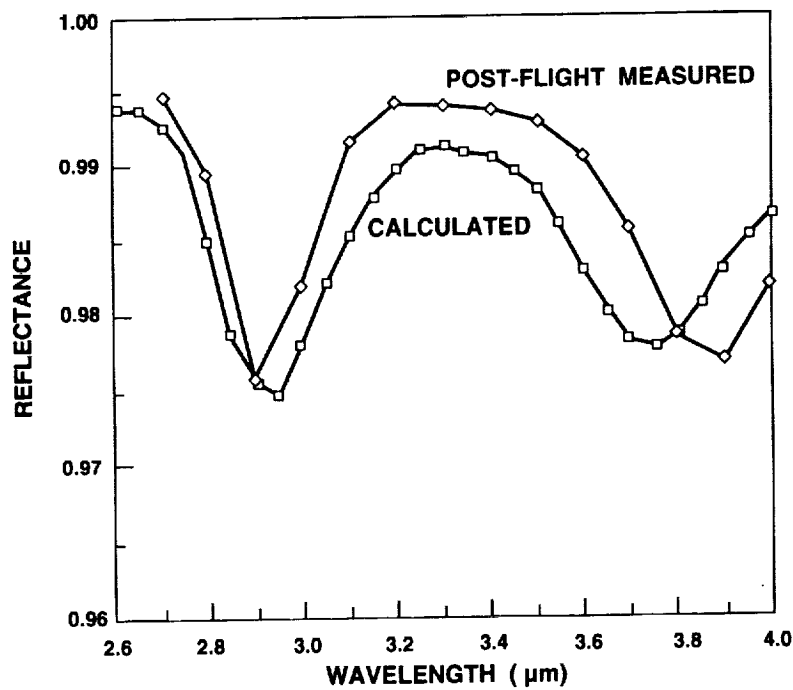
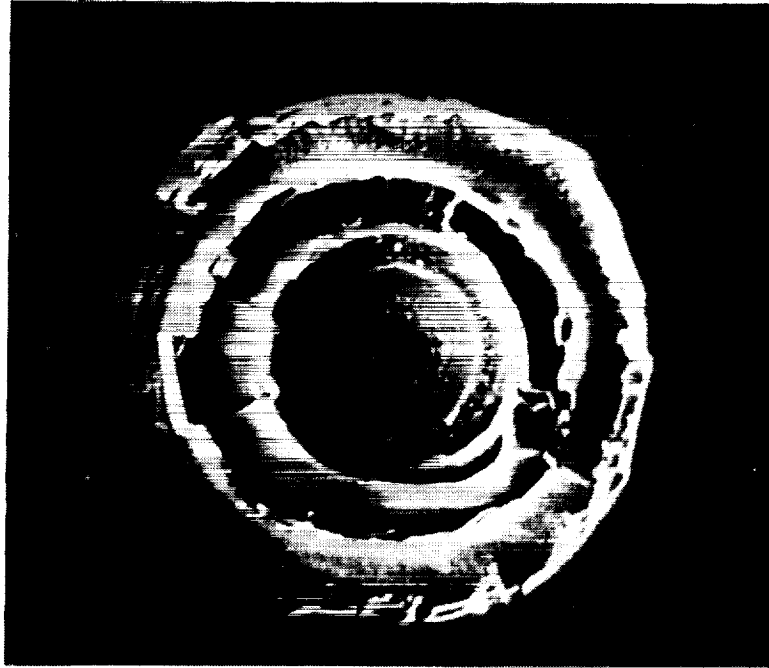
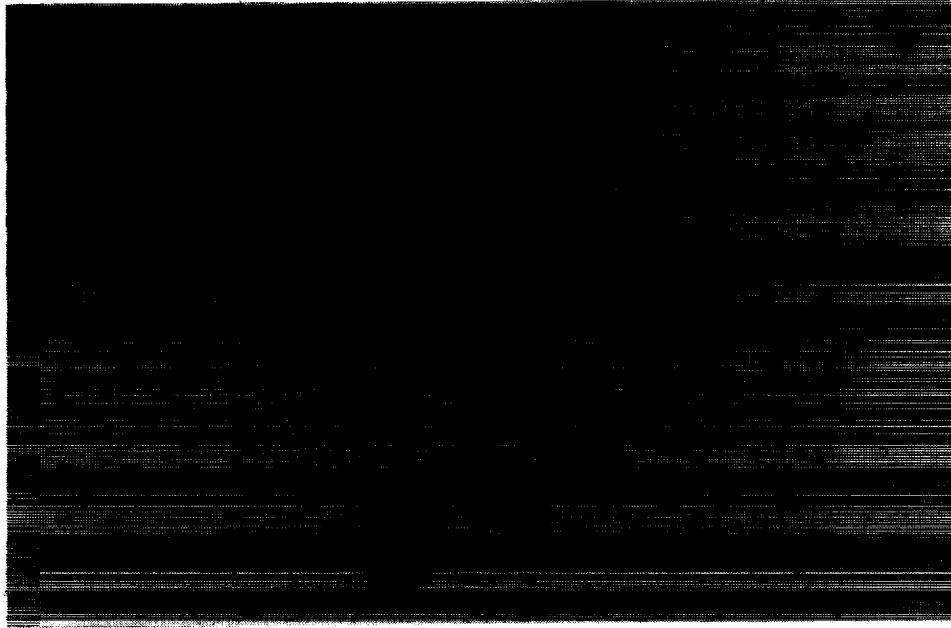


Figure 10. Measured post-flight reflectance of the leading-edge $(\text{ZnS}/\text{ThF}_4)_5\text{Ag}/\text{Mo}$ test sample compared to a calculated reflectance curve. Thin layers of water contamination at film interfaces and layer thicknesses derived from the SIMS data shown in Figures 7-9 were used to match the calculated to the measured reflectance curve.



$10\ \mu\text{m}$

Figure 11. Scanning electron micrograph of impact crater on leading-edge $(\text{ZnS}/\text{ThF}_4)^5\text{Ag}/\text{Mo}$ test sample revealing the multilayer structure and melt of individual layers.



100 μm

Figure 12a. Optical micrograph of secondary impact crater on trailing-edge $(\text{ZnS}/\text{ThF}_4)^5\text{Ag}/\text{Mo}$ test sample. (Micrograph courtesy of S. Gyetvay, Aerospace Corporation.)

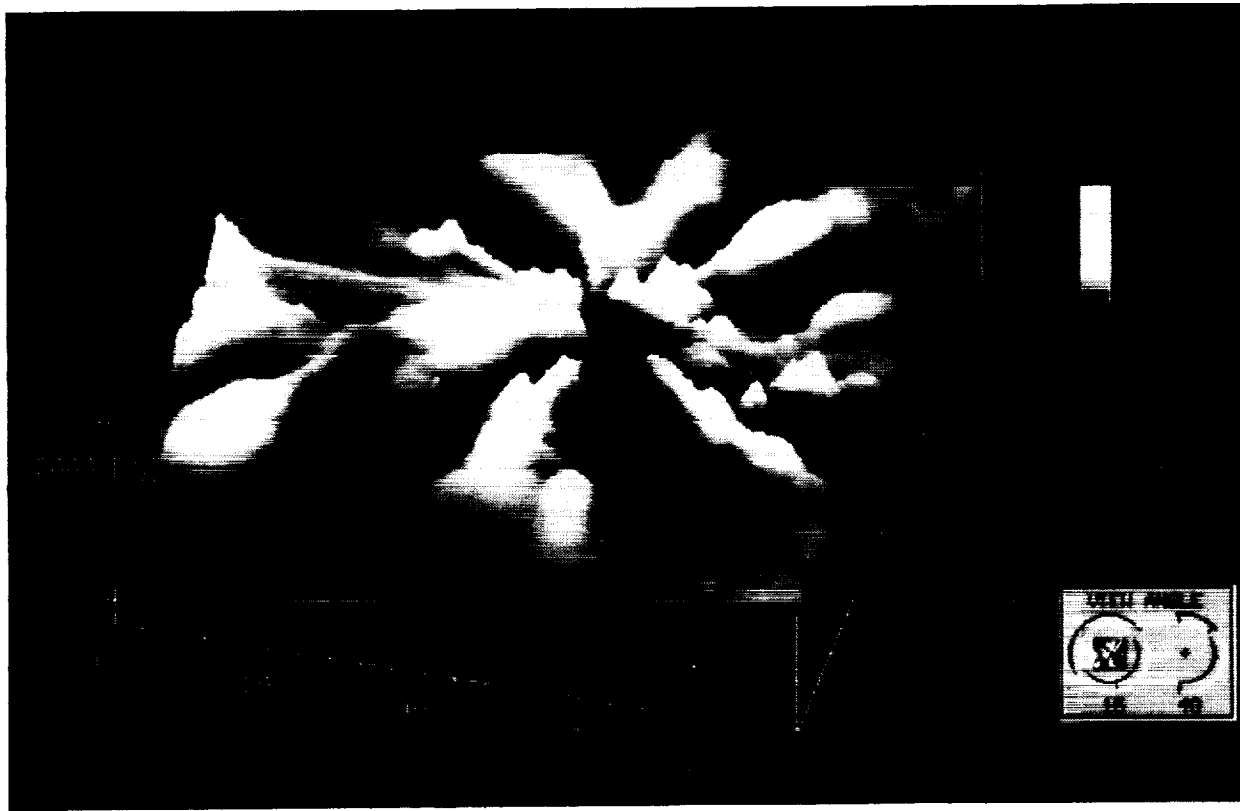
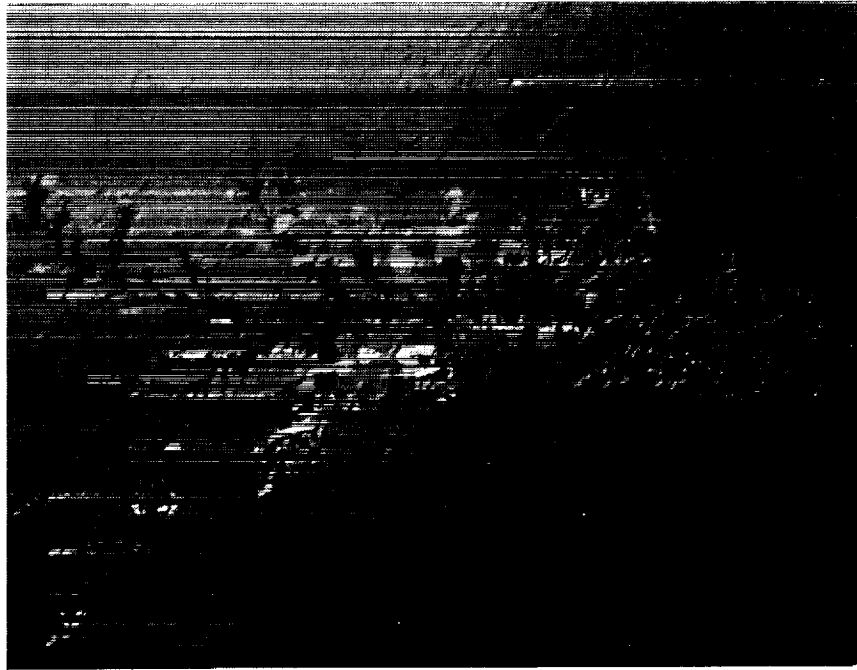
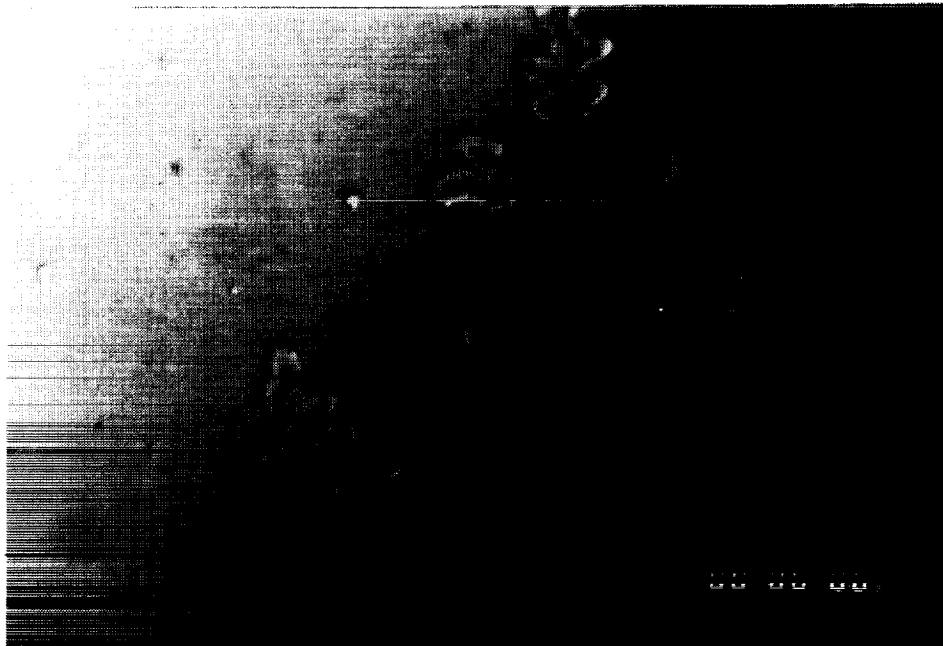


Figure 12b. Atomic force micrograph of secondary impact site in Figure 12a. The melted material around the impact site is an estimated 2000 \AA thick.



100 μm

Figure 13a. Nomarski micrograph of dendrites on leading-edge $(\text{ZnS}/\text{ThF}_4)^5\text{Ag}/\text{Mo}$ test sample, L6-VI-7-68-15. (Note the grain structure of the polished polycrystalline Mo substrate is revealed in the phase-sensitive micrograph.)



50 μm

Figure 13b. Optical micrograph of dendrites on leading-edge $(\text{ZnS}/\text{Al}_2\text{O}_3)^4\text{Ag}/\text{Mo}$ test sample, L6-VI-7-67-239. (Micrograph courtesy of S. Gyetvay, Aerospace Corporation.)

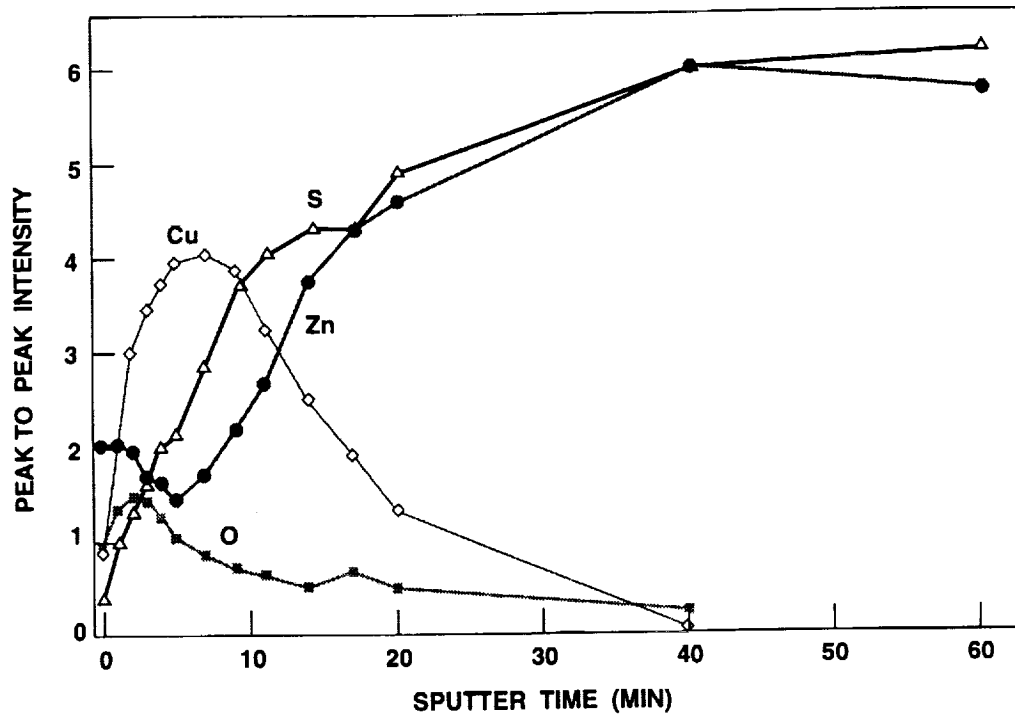


Figure 14. Auger depth profile showing Cu and O reaction with ZnS surface layer in dendrite region of leading-edge test mirror, L6-VI-7-68-15. (Auger depth profile courtesy of T. Beirling and R. Helms, Stanford University.)

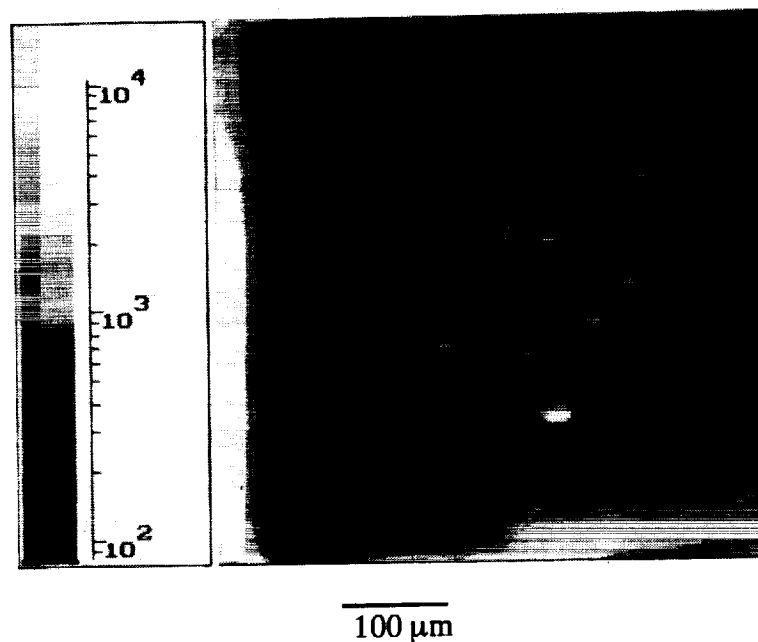
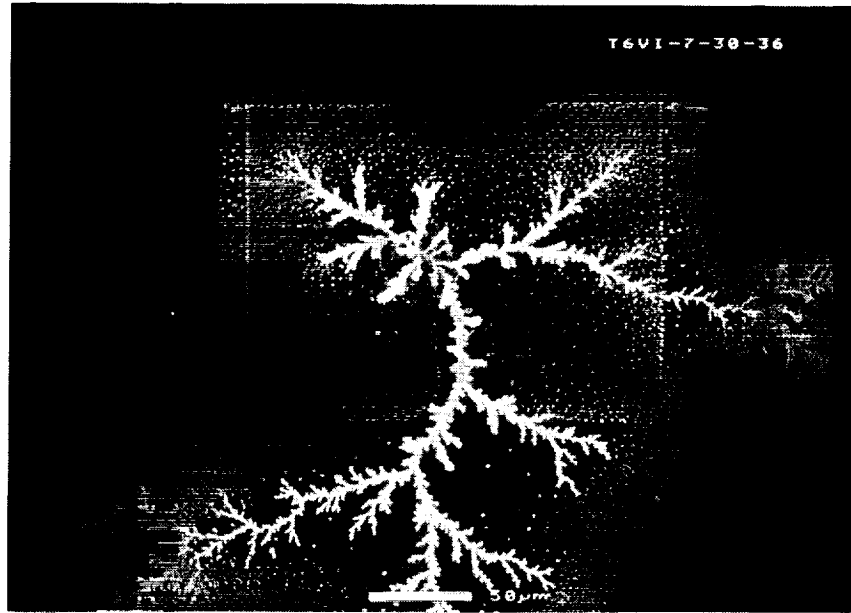


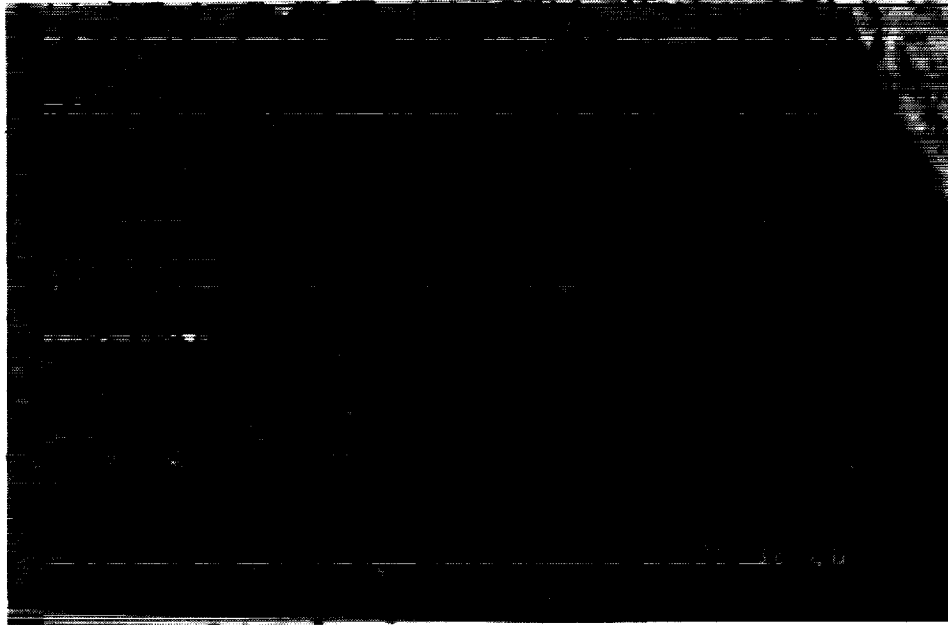
Figure 15. Mass-resolved SIMS image of a dendrite on the leading-edge ZnS-coated test mirror, L6-VI-7-68-15. The bright areas show high concentrations of Al contamination.



50 μm

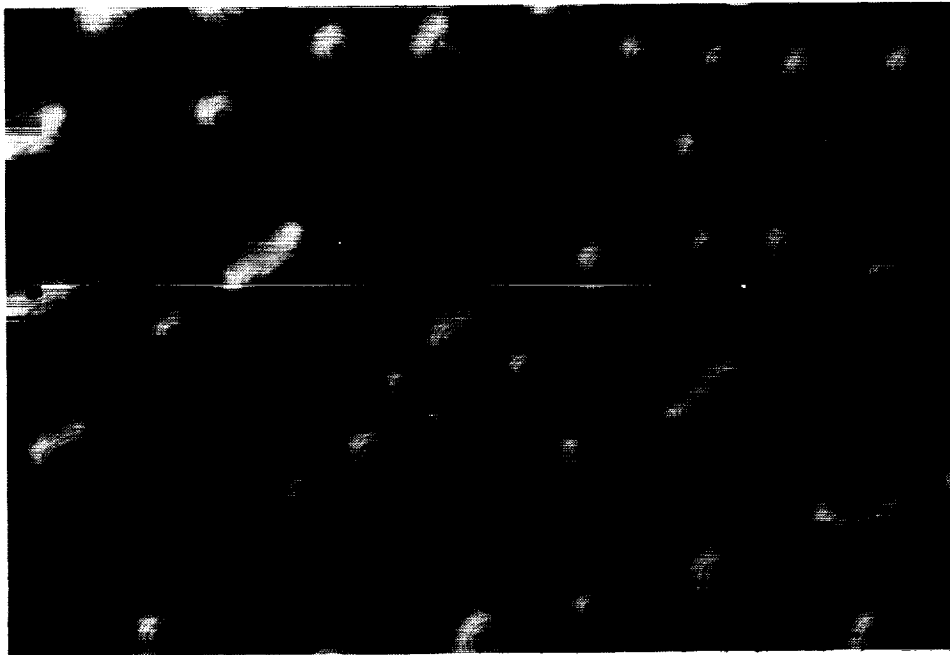
Figure 16. Scanning electron micrograph of dendrite grown in the laboratory on trailing-edge ZnS-coated test mirror, T6-VI-7-30-36. Growth was stimulated by electron irradiation in the region of a secondary impact.

d-5



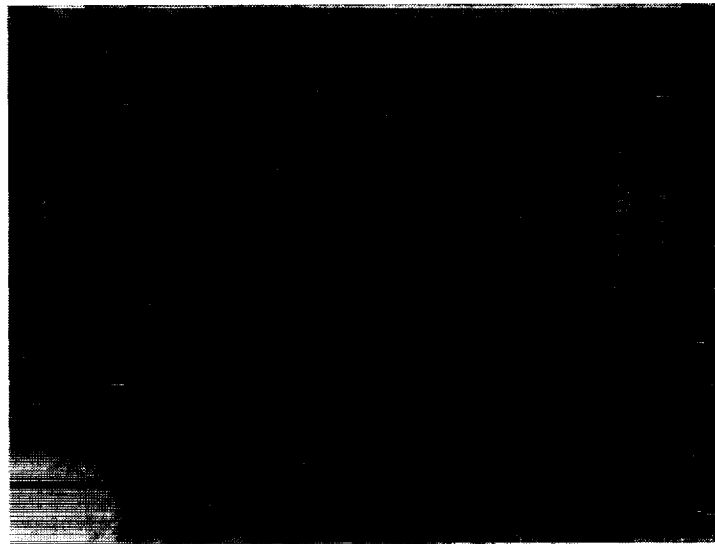
100 μm

Figure 17a. Optical micrograph of leading-edge ZnS-witness sample (L3-II-7-65-10) after 70-month exposure in LEO. The coating is buckled and annular features are observed at this magnification (168X). (Micrograph courtesy of S. Gyetvay, Aerospace Corporation.)



100 μm

Figure 17b. Optical micrograph of trailing-edge ZnS-witness sample (T3-II-7-64-11) after 70-month exposure in LEO. The coating is mostly intact but many blisters, perhaps related to locally poor adhesion, are observed. (Micrograph courtesy of S. Gyetvay, Aerospace Corporation.)



100 μm

Figure 18a. Optical micrograph of a SIMS raster pattern on the leading-edge ZnS-coated test sample, L6-VI-7-68-15. The small crater-like features located within the raster pattern developed as the sample was rastered with a Cs^+ primary ion beam. The source of the crater-like features has not been identified.

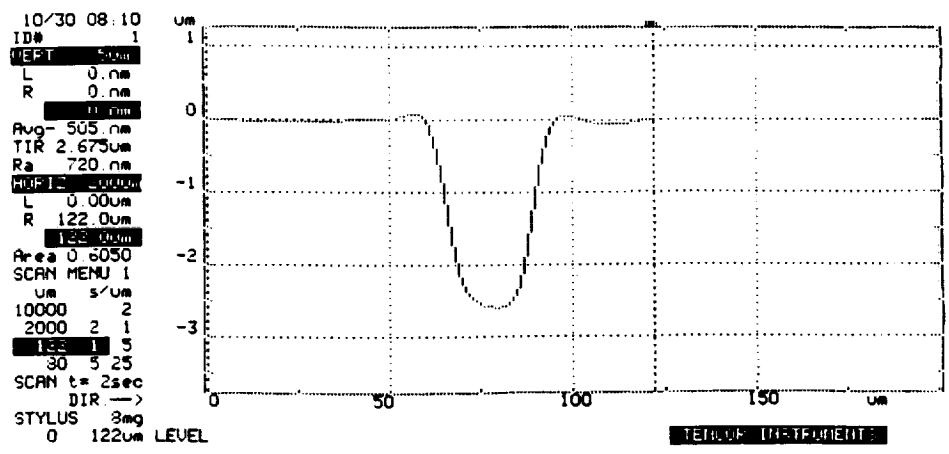


Figure 18b. Profilometer trace through one of the small crater-like features in Figure 18a.

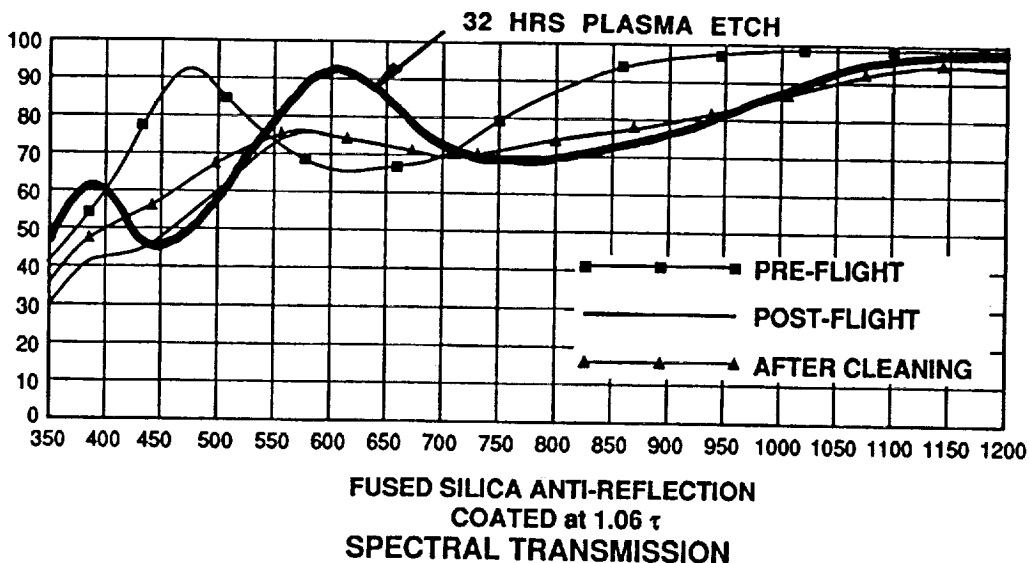
[Heavily distorted and illegible text block]

**EFFECTS OF LONG TERM SPACE ENVIRONMENT
EXPOSURE ON OPTICAL SUBSTRATES AND COATINGS
(S0050-2)**

John Vallimont, E. Steven Brandt,
Keith Havey, and Arthur Mustico
Eastman Kodak Company, Rochester N.Y.

At the time of our Second LDEF Post-Retrieval Symposium report, we had completed cleaning and measuring the post flight spectral performance of all of the samples except for the fused silica substrate with an antireflection ($\text{SiO}_2/\text{TiO}_2$) coating. As was documented in that report, after cleaning, all of the samples returned to their original pre-flight performance, with the exception of the fused silica anti-reflectance coated sample, which had significant degraded performance. All normal methods of removing the contaminant from the surface of this sample failed except for oxygen plasma etch. At the time of the previous report, we had only exposed the sample to three hours of plasma etch. We have since continued the plasma etch for a total of 32 hours, after which time, the transmission of the sample almost reached its pre-flight values. The peak areas of the transmission curves remained shifted approximately 150 nm, as can be seen in the chart below. Of interest is the fact that the control samples, which hadn't flown, did not exhibit any spectral shifting.

In summary, after the 6 yr exposure to the space environment, all of the coatings and substrates returned to their pre-flight performance after cleaning, with the exception of the anti-reflection coated fused silica sample. On this sample, the spectral transmission curves shifted approximately 150 nm.



PRECEDING PAGE BLANK NOT FILMED

LONG DURATION EXPOSURE FACILITY (LDEF) SPACE OPTICS HANDBOOK

William T. Kemp and Edward Taylor
AFMC Phillips Laboratory
Space and Missiles Technology Directorate
Kirtland AFB, New Mexico 87117-6008
Phone: 505/845-4439; Fax: 505/846-2290

Robert Champetier
Science Application International Corporation
Santa Monica, California 90401
Phone: 310/547-4205

Alan Watts and Dale Atkinson
POD Associates, Inc.
2309 Renard Place, SE
Suite 201
Albuquerque, New Mexico 87106

ABSTRACT

The overall objective of this effort is to construct a top-level space optics handbook that provides design guidelines based upon data collected from the Long Duration Exposure Facility (LDEF) experiment. The content of the handbook would cover optical coatings, surfaces, fiber optics, and fabricating process for lenses, windows and mirrors that were used on LDEF. The goal of this program (and handbook) is to ensure that the space community can derive the maximum benefit from the LDEF experiment relative to future optics designs for space applications. The summary of this handbook is "What did we learn from the LDEF experiment?"

This presentation will show the progress in the handbook, in the form of a draft, before it is published for distribution.



SPACE ENVIRONMENTAL EFFECTS OBSERVED ON THE HUBBLE SPACE TELESCOPE

Joel E. Edelman
LDEF Newsletter
Silver Spring, MD

James B. Mason
NASA Goddard Space Flight Center
Greenbelt, MD

INTRODUCTION

The Hubble Space Telescope (HST) Repair Mission of December, 1993, was first and foremost a mission to improve the performance of the observatory. But for a specialized segment of the aerospace industry, the primary interest is in the return to Earth of numerous pieces of the HST hardware, pieces which have been replaced, repaired, improved, or superseded. The returned hardware is of interest because of the information it potentially carries about the effects of exposure to the space environment for three and a half years.

Like the LDEF retrieval mission four years ago, the HST repair mission is of interest to many engineering disciplines, including all of the disciplines represented by the LDEF Special Investigation Groups (SIGs). There is particular interest in the evaluation of specific materials and systems in the returned components. Some coated surfaces have been processed with materials which are newer and still in use by, or under consideration for, other spacecraft in a variety of stages of development. Several of the systems are being returned because a specific failure or anomaly has been observed and thus there is, at the outset, a specific investigative trail that needs to be followed. These systems are much more complex than those flown on LDEF and, in two instances, comprised state-of-the-art science instruments. Further, the parts used in these systems generally were characterized more rigorously prior to flight than were those in the LDEF systems, and thus post flight testing may yield more significant results.

THE RETURNED HARDWARE

The hardware returned by the repair mission includes two complete instruments and an array of additional components which supported observatory operations. The instruments include the first Wide Field Planetary Camera (WFPC-I), a JPL instrument which was replaced by an updated version of the same instrument containing its own corrective optics, and the High Speed Photometer (HSP), a University of Wisconsin instrument which was replaced with the Corrective Optics Space Telescope Replacement (COSTAR), the Ball Aerospace/Goddard Space Flight Center corrective optics for the remaining instruments on board the HST.

Both instruments were operational at the time of their replacement, although the WFPC-I had suffered from an unusual contamination effect on its extremely cold sensor window, an effect

loosely referred to as "measles". This effect is speculated to be condensation around nucleation sites and may also be the initial phases of the kind of process that resulted in the unusual crystal-type growth features observed on LDEF and other space exposure missions. At KSC, significant degradation (blistering and peeling) of the M-1 (UV flood) mirror MgF_2 /aluminum coating was observed along part of its outer edge; the remainder of the surface, however, was visually clean, with no evident mottling, cloudiness, or particulates. This mirror was external to the WFPC-I and exposed to a deep space view. The pickoff mirror, which was located in the HST interior, was observed to be in excellent condition. Aside from several dust particles there was no visible evidence of degradation or contamination.

More than two dozen high velocity impact craters visible to the naked eye have been counted on the WFPC-I's exposed radiator surface; impact feature characteristics, similar to those documented on LDEF, were seen in this initial cursory look and include symmetrical and oblique craters, and apparent paint loss in the spall area from the impact shock wave. Contamination effects reminiscent of LDEF were also observed, including a brown line of undetermined origin on the radiator near its bolted edge, and areas of brown stain surrounding rivets; the latter is tentatively attributed to the rivet lubrication, and was present to a much lesser degree prior to launch.

One of the five detectors in the HSP had suffered a throughput drop of nearly two thirds partway through the HST mission; later in the mission there was an equally anomalous recovery. Several possible causes have been speculated but none is a leading candidate at this time.

The degraded solar arrays were replaced on orbit and one of the original two arrays returned as part of this mission; the second array was jettisoned. The original array was returned directly to the European Space Agency (ESA) from the Kennedy Space Center (KSC) and will be subjected to a program of functional testing and characterization as well as an extensive study of micrometeoroid and debris impact craters. Some delamination of the solar array bus bars was observed during the repair mission, and it was also observed that two of the hinge pins had begun to walk out of their hinges.

Other hardware returned included the three rate sensing units (RSUs), or pairs of gyros, two of which had suffered apparent failures during the HST's first three years. Two electronic control units (ECUs), which are also believed to have failed, were returned. Finally, the P-15 and P-16 fuse plugs were replaced with upgraded versions and the original plugs returned for examination.

Minimal evaluation of the returned hardware was performed at KSC at the conclusion of the Repair Mission. Following photography and the taking of contamination samples, the solar arrays were packed and shipped to ESA, and the remaining hardware was barged to GSFC, using modified containers from previous missions, the Gamma Ray Observatory (GRO) container and the LDEF Assembly Transportation System (LATS). Both containers were continuously purged.

EVALUATION PLANS

Because of the similarities between the LDEF and HST hardware investigations, a serious effort is being undertaken to assure the carryover of as many as possible of the lessons learned from the LDEF experience. On January 27, 1994, several LDEF investigators supported a planning meeting and telecon at GSFC for the evaluation of the returned HST hardware.

The Systems SIG became active in the earliest stages of the HST planning process because of the special significance of the HST hardware for systems and because of the complexity of the testing options.

The Systems SIG recommendations have followed the pattern of the LDEF Test Plan developed by the Systems SIG prior to the LDEF retrieval. The overriding philosophy remains focused on testing from the top down; that is, testing each system at the highest practical level prior to disassembling and testing individual subsystems and components. Specific areas of concern that are highlighted by the Systems SIG included electronics, lubricants, seals, mechanisms, heat pipes, solar cells, adhesives, and optical components including windows, mirrors, filters, and sensors. The Systems SIG has also emphasized the need for all results, including the raw data and any hardware for which no future use is planned, to be archived properly and adequately for future research.

Following are abstracts from the most recent drafts of the investigation plans for the evaluation at GSFC of the returned HST hardware.

Wide Field Planetary Camera (WFPC-I) Evaluation

External Inspection

The WFPC-I will be examined visually and a detailed photographic record made. Operations such as fit checks, integration, and deintegration will be recorded on videotape.

Optical

Assessment of the M1 mirror, the pickoff mirror, and the aperture window are planned for GSFC. The areas of interest are the optical characteristics, such as the reflectance, of optical components and changes caused by the on orbit environment. No end-to-end optical system tests are planned at GSFC. Because extremely cold temperatures under vacuum are required for operation of the CCD, such a test would be inordinately expensive.

Contamination

The contamination assessment will consist primarily of evaluating contaminant deposition on WFPC-I components and external surfaces, both inside and outside of the aft shroud. Activities will include a rinse of the vent baffle plate and flight handle, scraping a sample from the vent pipe, and tape lifts and swabs at various locations. Further assessments of optical elements and the detectors mounted inside the instrument enclosure will be performed at JPL.

Of particular interest is the optical window at the entrance aperture. Because this window acted as a seal between the HST and the WFPC, the inner and outer surfaces will provide accurate, independent characterizations of the instrument and telescope contamination environments, respectively.

Mechanical

The mechanical assessments at GSFC will include measurement of critical areas of the WFPC-I including the location of the pickoff mirror with respect to the "A" latch, features near the pickoff mirror and the instrument (+V3), the radiator light baffle, and the light pipe. The combination of WFPC-I metrology with that of WFPC-II will provide a complete and detailed description of the allowable radial Science Instruments physical envelope. The assessment will also include a detailed evaluation of both the side latches, blind mate connector, and guiderails. A lubricant sample will also be taken from the WFPC-I for analysis. Further assessments of mechanisms and interior mechanical components will be made at JPL.

Electrical

The electrical and electronic assessments at GSFC will consist of system testing using the Vehicle Electrical System Test (VEST). This will include Current-Voltage Test (IVT), Electrical Integration Continuity and Isolation Test (EICIT), aliveness, and functional tests. Both A and B side circuitry will be tested. Comparison of these test results with prelaunch data on WFPC-I will provide an assessment of environmental effects. Further evaluations of specific electrical components such as pc boards and solder joints will be performed after disassembly at JPL.

Thermal

The thermal assessment will include alpha and epsilon measurements of both radiators, evaluation of the thermal properties of external surfaces and MLI, Thermal Emittance Coatings (TEC) degradation, and heat pipe performance to determine the effects of long duration exposure to the low earth orbit environment. Bolt torques for the heat pipe saddles will be checked to assess the effects of thermal cycling. Heat pipe performance and TEC degradation will be evaluated after disassembly of the instrument at JPL.

Impact Craters

An assessment of micrometeoroid and debris impacts on the outside surfaces of the two radiators will be performed. Details of this plan are pending review of recommendations from the LDEF Meteoroid and Debris SIG.

Disposition

The WFPC-I will be returned to JPL for further evaluation. The Materials and M&D SIGs are expected to request sample specimens of the radiator surface for SEM evaluation, subsequent to JPL testing.

High Speed Photometer (HSP) Evaluation

External Inspection

Prior to unpacking, preliminary contamination samples will be obtained from the top of HSP. This will include rinses, tape lifts, and removal of the witness mirror from inside its protective enclosure. Additionally, a visual inspection will be performed and unique contamination features will be sampled.

During the unpacking process, photographic and video documentation will be performed. The latches will be inspected and samples of the Braycote lubricant will be taken. More contamination samples of the box exterior surfaces will also be taken, particularly in the area near the aperture.

Metrology

A survey of the HSP exterior surface will be performed including at least the following: latches, guide block, aft strip, guide block mounting bracket, and all six exterior surfaces. This survey will be performed according to an approved procedure and will use the Automated Image Metrology System (AIMS). The procedure will simply be a modification of the existing COSTAR metrology procedure.

Quarter panel measurements will be made to relate the HSP volume to the quarter panel. The B-latch gap will also be measured. Also, measurements of the aperture location will be made to verify its position.

Internal Inspection

One HSP side panel will be removed and internal wipes, tape samples, and rinses will be performed. Also, a witness mirror will be installed inside of HSP to monitor ground contributions to contamination. If appropriate, one or more flight mirrors will be removed for further analysis. The side panel will then be reinstalled onto HSP.

Electrical Testing

HSP will undergo Electrical Integration Continuity and Isolation Test (EICIT), Current-Voltage Test (IVT), aliveness, short form functional, and long form functional tests using the same Electrical GSE used before HSP was flown. This will allow comparison of the before and after performance of HSP.

Throughput Test

This would be performed in order to try to understand the factor in 3 loss in throughput that the HSP experienced during part of its time in orbit. Although some alternatives have been identified, the method for performing this test is still undetermined.

Depending on whether further electrical tests are planned with HSP at Goddard or at the University of Wisconsin, the Remote Interface Unit (RIUs) can be removed at this point. The RIUs are scheduled for refurbishment and availability for reflight.

Remove Latches

The latches will be removed for refurbishment before HSP is shipped. The latches will undergo a detailed inspection and ultimately be refurbished for reflight.

Disposition

The HSP will be returned to the University of Wisconsin.

Other Hubble Space Telescope (HST) Hardware Evaluation

Much of the testing of other HST hardware will be performed by the original vendors. Proposed plans are now under review. Work that is planned at GSFC is described briefly below. Evaluation of selected components (contamination, optics, materials, and thermal performance) are being discussed.

RATE SENSING UNIT (RSUs)

These units will be visually inspected, particularly the connector pins. Photographs and contamination samples will be taken. Electrical interface continuity and isolation tests will be performed, and the units will be returned to Allied Signal for functional testing and evaluation. It is planned that these units will be refurbished and reflown.

ELECTRONIC CONTROL UNIT (ECUs)

These units will be visually inspected, particularly the connector pins. Photographs and contamination samples will be taken. Full functional tests are desired but not planned at GSFC.

FUSE PLUGS

These units will be visually inspected and photographed. A DC milliohm and high voltage test is planned, as is resistance and current characterization at GSFC.

MULTIPLE LAYER INSULATION (MLI) SAMPLES

Both physical and chemical evaluations are being planned, in addition to thermal performance. Brittleness of some MLI specimens has been observed as a result of its handling on orbit.

FLIGHT SUPPORT EQUIPMENT

A variety of equipment used on the servicing mission, and exposed to the space environment for the duration of the mission, will be examined. Included are the Flight Support System, the instrument carriers, and the tools used by the astronauts.

HARDWARE CLEANLINESS METHODOLOGY AND CERTIFICATION

Gale A. Harvey, Thomas J. Lash, and J. Richard Rawls
 NASA Langley Research Center
 Hampton, VA 23681-0001
 Phone: 804-864-6742, FAX 804-864-7790

ABSTRACT

Inadequacy of mass loss cleanliness criteria for selection of materials for contamination sensitive uses, and processing of flight hardware for contamination sensitive instruments is discussed. Materials selection for flight hardware is usually based on mass loss (ASTM E-595). However, flight hardware cleanliness (MIL 1246A) is a surface cleanliness assessment. It is possible for materials (e.g. Sil-Pad 2000) to pass ASTM E-595 and fail MIL 1246A class A by orders of magnitude. Conversely, it is possible for small amounts of nonconforming material (Huma-Seal conformal coating) to not present significant cleanliness problems to an optical flight instrument. Effective cleaning (precleaning, precision cleaning, and ultra cleaning) and cleanliness verification are essential for contamination sensitive flight instruments. Polish cleaning of hardware, e.g. vacuum baking for vacuum applications, and storage of clean hardware, e.g. laser optics, is discussed. Silicone materials present special concerns for use in space because of the rapid conversion of the outgassed residues to glass by solar ultraviolet radiation and/or atomic oxygen. Non ozone depleting solvent cleaning and institutional support for cleaning and certification are also discussed.

INTRODUCTION

Hardware cleanliness for space flight applications is usually driven by performance requirements for optics, adhesion of potting and staking compounds and coatings, and electrical continuity or insulation of conformal coatings. The rapid, large temperature fluctuations often experienced by hardware in low earth orbit and resulting from entering and exiting the Earth's shadow, and the acceleration of outgassing in vacuum play a significant role in optical component contamination. The long-term bulk outgassing and chemical reversion (depolymerization) of silicones is a special problem (ref. 1). The polymerization of organic films and the conversion of silicone films to glass by solar ultraviolet radiation and/or atomic oxygen also play significant roles. The vacuum ultraviolet and mid-infrared spectral regions are especially sensitive regions to certain contaminations because of strong molecular absorptions in these regions. Molecular contamination can also be a concern to the electronic, pharmaceutical, and food industries.

A contamination sensitive flight instrument such as the Halogen Occultation Experiment (HALOE) instrument (ref. 2) should include the following six major cleanliness activities: 1. Selection of Materials; 2. Cleaning of parts, i.e. precleaning, precision cleaning, and ultracleaning; 3. Rough vacuum bake of parts or systems; 4. High-vacuum bake or functional test of instrument; 5. Purge or vacuum storage of instrument or contamination sensitive parts; and 6. Cleanliness verification or certification by wipes, washes, witness plates, mass spectroscopy, etc..

However, in practice, cleanliness of many instruments at Langley Research Center (LaRC) is based primarily on 1. selection of "low outgassing materials" from RP-1124 (ref. 3) and integration and testing of the instruments in clean rooms. The clean rooms do an excellent job of minimizing particle contamination, but generally do not address molecular contamination. The main pitfalls from this expediency are that some materials such as silicones and urethanes that are approved, or are suitable for very limited use in non-critical areas are used in significant amounts and in critical areas, and that handling, environments, and aging effects are overlooked. For example, clean rooms designed to greatly reduce particle contamination often use heavy outgassing materials (such as vinyl) in downflow curtains. Another common practice

is to use a solvent such as alcohol and new cleanroom wipes and gloves to wipe particles and stains from work surfaces and instrumentation. The solvent extracts plasticizers (e.g. alkyl phthalates and other esters) from the gloves and wipes and deposits this material as a thin film on the "cleaned" surface. Although nitrile and polyethylene gloves are relatively low in molecular residue, Teflon is the only really clean glove material for solvent cleaning. Unfortunately, Teflon gloves are expensive, and tear easily. Fortunately, only a small amount (~5%) of clean room work is solvent cleaning. However, much current precision cleaning is with trichlorotrifluoroethane (Freon 113), and gloves and plastic wear can easily contaminate this cleaning solvent.

The hardware that is precision cleaned at LaRC varies greatly in size, shape, and use. A general guideline used at LaRC is that if hardware is visibly dirty, or is suspected to have more than 10 mg of molecular contamination, it is pre-cleaned with soap and water, or wiped with alcohol before being run through the ultrasonic solvent parts cleaner. The ultrasonic parts cleaner does a good job of removing loose particles and cleans the parts to about 0.5 mg per square foot of molecular films. A rough vacuum bake (with an LN₂ trap) will generally reduce this by a factor of two by offgassing the lighter molecular weight (MW<300) constituents. This rule-of-thumb was obtained from several before-and-after vacuum bake surface-cleanliness-wipes of hardware.

MASS LOSS AND SURFACE CLEANLINESS

Materials selection for flight hardware is often based on mass loss (ASTM E-595, ref. 3). This selection process is generally a quick and convenient procedure to address hardware cleanliness. It has been effective for a large number of applications and has become standard practice. It does not address the identification of the outgassing products and is sometimes used to imply surface cleanliness, which is a Shuttle requirement for space flight. That is, there are two types of cleanliness: 1. material outgassing, and 2. surface cleanliness. Bulk material outgassing is indicative of potential to contaminate nearby hardware with molecular films. Surface cleanliness (the molecular films) affects adhesion, electrical and optical properties. Currently, many cleanliness evaluations are based on outgassing (ASTM E-595) alone. This is an expedient practice, but allows hardware with slow outgassing material, or that has acquired significant surface films, or that has deteriorated, to be used in contamination sensitive applications.

Heavy silicone and alkyl phthalate fluids (synthetic oils) outgas relatively slowly, but significantly, during long exposure to vacuum. Hardware processed in facilities or equipment with silicone or plastic material will accumulate films of silicones and synthetic oils until each type of outgassing product reaches equilibrium between adsorption and evaporation. The equilibrium time is days or weeks for light and volatile compounds such as alcohols and ethers (MW<200) and years for heavy silicones and phthalates (MW>300). The equilibrium time is much quicker if the hardware is in a small, confined space (e.g., an optic stored in a plastic shipping box). Some materials deteriorate with age and some silicones undergo chemical reversion (depolymerization) when exposed to chemicals such as ammonia. These processes can lead to great disparity between cleanliness inferred from ASTM E-595, and measured surface cleanliness (MIL 1246A).

Surface cleanliness can be measured by washing or wiping the surface with suitable solvents and by electron microscope techniques. Table 1 lists several examples of hardware measured at LaRC which demonstrate this disparity. The Sil-Pad-2000 is a silicone heat transfer pad used with the Measurement of Air Pollution from Satellites (MAPS) instrument, and the high voltage cable is used in a high energy laser instrument (Laser Atmospheric Sensing Experiment (LASE)). The expediency of treating cleanliness primarily by reliance on ASTM E-595 is difficult to question when non-cleanliness-related performance and schedule requirements drive most projects.

The environmental testing and development group at LaRC has initiated customized cleaning of hardware at little or no monetary or schedule costs to projects when hardware such as that listed in Table 1 is brought into the test facilities. That is, the facility personnel assume ownership of hardware as well as facility cleanliness concerns. The greater continuity in cleanliness resources and hands-on expertise in the facilities compared to the projects is part of the rationale for this practice.

VACUUM OUTGASSING

Low vacuum ($P \sim 10^{-1}$ Torr) can be used to polish-clean, and measure cleanliness of hardware for vacuum applications. The outgassing products from the hardware can be collected on a cold surface, i.e. a scavenger plate, inside the chamber during the test, and then removed, weighed, and analyzed after the test. Infrared analyses of the thin films of the outgassed residue can conveniently be performed to determine chemical composition. Table 2 and figure 1 list common outgassing products collected during vacuum cleaning and testing at LaRC. Generally the hardware is heated to accelerate the outgassing or to simulate the space environment. Dynamic pumping and LN_2 foreline traps are used to maintain chamber cleanliness under vacuum.

Mass spectrometry can be used to measure cleanliness of hardware in high vacuum ($P \sim 10^{-6}$ Torr). A mass spectrometer gives real-time outgassing history as well as chemical identification of the outgassing products. Table 3 and figure 2 list typical outgassing species and show their mass spectra. Infrared analyses of residues collected on a scavenger plate in the vacuum chamber provide complimentary chemical analyses. A polish cleaning of hardware or instruments intended for space or vacuum application can be performed. This cleaning process is designed to benignly remove molecular contamination which could migrate to contamination sensitive surfaces in vacuum and is amenable to integrated hardware and systems. A 24 hour bake at $125^\circ C$ is a typical vacuum bake process. This corresponds to roughly one year under vacuum at room temperature. Clean hardware should be maintained under vacuum, or protected from recontamination by sealing in appropriate bagging material, preferably with an ultrapure gas purge such as LN_2 boiloff.

Vacuum chamber cleanliness measurement can be used to determine the contamination potential of non-approved material in hardware. Huma-Seal conformal coating (not an approved material) was applied to electronic boxes for a high energy laser instrument. Extracted cleanroom wipes were placed at the vents of the cover of these boxes and collected about 0.3 mg of alkyl phthalates during a high vacuum test. The small amount of alkyl phthalates on these wipes, on witness plates, and on external instrument surfaces, showed that the Huma-Seal did not pose a risk of contamination to the laser instrument or to nearby hardware.

NON-CFC SOLVENT CLEANING

The standard practice in the aerospace industry is to precision clean parts in an ultrasonic cleaner using Freon 113 as the cleaning solvent. This solvent is a non-polar chlorofluorocarbon solvent which readily dissolves many organic fluids such as hydrocarbons and esters, and silicones. However, two of its most redeeming properties for cleaning purposes are that it is nonflammable and that it evaporates quickly (expediting quick cleaning). Freon 113 is one of several chemicals listed as ozone depleting substances by the Montreal Protocol and scheduled for restricted use or phaseout in the present decade.

Cleaning efficiencies of several aqueous systems were measured and compared to the present in-house cleaning. New polyester cleanroom wipes were used as the test coupons. The results are listed in Table 3. A negative cleaning efficiency means that more material is added to the test wipe than is removed by the cleaning process. The residue on the test wipes was measured by the standard practice of soaking a 225 cm^2 test wipe in 40 ml of analytical

grade isopropyl alcohol for 30 minutes, and weighing the residue after evaporation of the alcohol. The infrared spectra show significant differences in the composition of the residue left on the wipes after cleaning. Therefore, the cleaning efficiencies of column 3 in Table 4 represent a loss of some types of residue and a gain of other types of residue. A negative efficiency means that more residue is added than is removed by the cleaning process.

Four of the six aqueous cleaning procedures tested added more residue than they removed. This is probably because these aqueous cleaners are added in much larger amounts than the original residues to be cleaned, so it requires much higher dilutions in the rinse stage to remove almost all of the added cleaner.

Water is strongly polar and not a good solvent for most of the nonpolar residues, e.g. alkyl phthalates, on LaRC flight hardware to be precision cleaned. Freon 113 is a good nonpolar solvent and leaves little residue because the Freon 113 has low surface tension and drains off. Small amounts of Freon will be absorbed, and will wick along wires. This Freon is readily detected by a mass spectrometer if hardware cleaned in a Freon cleaner is placed in a high vacuum chamber within a few weeks of being cleaned (Fig. 2). This is seldom a problem since Freon is relatively inert and will eventually offgas from the hardware. These properties: nonpolarity, low surface tension, and rapid evaporation, make Freon 113 a good solvent for nonpolar residues. The low boiling temperature and small heat capacity of Freon 113 make it easy to purify or reclaim by distillation.

Since water is not a good solvent for most organic residues, a detergent and/or surfactant is needed to remove and suspend organic residue. These cleaning additives are used in many times the amount of residue to be cleaned from the hardware in order to be effective, and must be removed by a subsequent cleaning process (generally deionized water rinses). A lot of ultrapure water is needed to remove almost all of the surfactants and detergents. It was concluded from the data in Table 1 that aqueous cleaning of LaRC flight hardware could not meet the existing cleanliness requirements with the available equipment and facility resources.

Several nonpolar solvents such as hexane, benzene, toluene, acetone, and light alcohols are as good organic solvents as Freon 113 and also have low surface tension and evaporate quickly. However these solvents are flammable and some pose health concerns. LaRC has experience in ultracleaning using Soxhlet extractors and isopropyl alcohol (IPA) as the working solvent (ref. 4). Much higher cleaning efficiencies (Table 4) are attainable with a Soxhlet extractor and IPA than with Freon in an ultrasonic cleaner because the working temperature of the IPA is higher (180° F) in the Soxhlet extractor, and generally the wash time is much longer. The Soxhlet extractor uses a closed loop repetitive distillation and flush process and is generally constructed of glass. The high cleaning efficiencies obtained with Soxhlet extractors led to modification of an existing ultrasonic cleaner in order to use IPA as the working solvent. The modifications included use of covered tanks (telescoping lids) for the ultrasonification-wash tank, use of ultrapure deionized water for rinsing, and use of an organic vapor detector in the cleaning station.

The rinsing operation is often necessary because the wash solvent usually becomes contaminated soon after hardware is placed in it, and this will result in localized deposits of residue on the hardware when the alcohol evaporates. The rinse operation washes the slightly contaminated IPA off the hardware. The use of ultrapure water as a rinse fluid usually requires blow drying because of the low levels of colloidal silica in most ultrapure water, which is converted to silica during drying.

CERTIFICATION

The cleanliness requirement for hardware and instruments to be flown in the orbiter payload bay is $<10 \text{ mg/m}^2$ of molecular residue. The certification of this requirement is usually in the form of gravimetric analysis of residue washed from an accessible surface of the hardware. This measurement is usually included in a test report or as part of a quality assurance report. These measurements are sometimes performed for historical purposes only, and have long processing and distribution times.

The LaRC cleanliness measurements laboratory has adopted the practice of writing and distributing cleanliness test reports for every major vacuum test of flight hardware and for periodic cleanliness measurements of the hardware. These reports are distributed within five working days of the test, or return of the witness specimens to the lab. A handwritten report is usually given to the test conductor within 24 hours, and sometimes during the same shift, so that the results can be used in project evaluations and decision making. Chemical analyses of the residues, by infrared spectroscopy and, or mass spectroscopy are usually included in the reports. These reports are used by project personnel, facility personnel and by quality assurance personnel for functional assessments, facility assessments, and compliance with regulations.

Cleanliness activities within NASA have been institutionally supported by projects which either assigned a design engineer or test engineer from an engineering organization the responsibilities of contamination control. These contamination control engineers are sometimes left on their own to find or develop laboratory support for cleanliness measurements. Their access to hardware and responsibility usually decreases as the project hardware is integrated onto a spacecraft, or moves to a non-project owned facility. The support for tracking of cleanliness effects and for formal reporting usually follows a similar decline and has resulted in a small data base for hardware flown on the the Shuttle and exposed to the induced space environment. There is a current need for more dedicated laboratory support for hardware cleanliness measurements. These hardware and instrument cleanliness measurements are a legitimate area of responsibility of Quality Assurance.

CONCLUSIONS

There is a general overreliance on mass loss criteria (ASTM E-595) for hardware and instrument cleanliness. This is partly a result of a general lack of inhouse cleanliness measurement capability. More recognition is needed for continuity of cleanliness assessments through mission completion, for measurement and analyses capability and for reporting. There are many measurement techniques that can be used to measure cleanliness at very low or no cost.

REFERENCES

1. Raper, J. L., and Harvey, G. A., "Halogen Occulation Experiment (HALOE) Contamination Control Program," Cleanroom Technology Forum Proceedings, October 1991, pp 175-184, Canon Publications, Inc., 1991.
2. Hill, W. L., and Mitchell, S. M., "Certification of Rewaterproofing Agent for Shuttle Thermal Protection Sytems," 199th Am. Chem. Soc. Conf., Boston, MA, April, 1990.
3. Campbell, W. A. Jr., and Scialdone, J. J., "Outgassing Data for Selecting Spacecraft Materials," NASA RP 1124, Rev. 3, September 1993.
4. Harvey G.A., Raper, J. L. and Zellers, D. C., "Measuring Low-Level Nonvolatile Residue Contamination on Wipes, Swabs, and Gloves," Microcontamination, 8(11): pp 43-46, 69, 1990.

TABLE 1

CLEANING OF MATERIALS

Material	As received	After cleaning
Sil pad 2000	125 mg/ft ²	6 mg/ft ²
Silicone gasket	10 mg/ft ²	1 mg/ft ²
HV cable	400 mg/ft	1 mg/ft ²
SEDS cable	52 mg/ft	ND
RG58 cable	.1 mg/ft	ND

TABLE 2

IR ABSORPTIONS OF COMMON CONTAMINANTS

Class	Absorptions, cm^{-1}
Phthalates mw - 400	1730 (C=O), 1600 and 1575 (C_6H_4)
Urethanes	1640 (NH_2), 1615 (NH), 1540 (NH)
Silicones mw - 250 DC704 = 484	1265 (SiCH_3), 1025-1100 (SiO), 1120 (Si δ)
Hydrocarbons C ₁₈ mw - 250	1460 (CH_2 , CH_3), 1375 (CH_3)

Figure 1.- IR spectra of common contaminants.

TABLE 3

MASS FRAGMENTS OF COMMON CONTAMINANTS

Class	Mass, amu
Phthalates	149, 167
Freons	$\Delta M = 2$; $\text{C}_{135}/\text{C}_{137} = 3:1$
Silicones	$73[\text{Si}(\text{CH}_3)_2]$, 147 $[\text{Si}_2\text{O}(\text{CH}_3)_2]$
Hydrocarbons	$\Delta M = 14[\text{CH}_2]$ picket fence

Figure 2.- Mass spectra of common contaminants.

TABLE 4.- CLEANING EFFICIENCIES

Cleaning	Recovered NVR (mg/ft ²)	NVR Cleaning Efficiency (%)
New Wipe-Coventry	2.22	N/A
DI H ₂ O	2.20	0.
Bronson Surfactant	2.44	-10
Trisodium Phosphate	2.59	-17
Hurri Clean	2.27	0
Triton X-100	3.02	-36
Alconox	.96	56
Zone Defense	8.12	-370
Freon 113	.49	78
IPA 5%	2.27	0
IPA 50%	2.48	-10
IPA 95%	.48, .75, 1.30	78, 66, 40
IPA 100%	.38, .37, .50	85, 83, 77
50% IPA/50% F113	1.05	50
Soxhlet IPA 2X	.04, .09, .12	98, 96, 95



FUTURE ACTIVITIES



Tropical Rainfall Measuring Mission (TRMM), artist's concept

**FROM LDEF TO A NATIONAL SPACE ENVIRONMENT AND EFFECTS (SEE)
PROGRAM: A NATURAL PROGRESSION**

**David E. Bowles, Robert L. Calloway, Joan G. Funk, William H. Kinard,
and Arlene S. Levine
NASA Langley Research Center
Hampton, VA 23681-0001
Phone: 804/864-3095, Fax 804/864-8093**

As the LDEF program draws to a close, it leaves in place the fundamental building blocks for a Space Environment and Effects (SEE) program. Results from LDEF data analyses and investigations now form a substantial core of knowledge on the long term effects of the space environment on materials, system and structures. In addition, these investigations form the basic structure of a critically-needed SEE archive and database system. An agency-wide effort is required to capture all elements of a SEE program to provide a more comprehensive and focused approach to understanding the space environment, determining the best techniques for both flight and ground-based experimentation, updating the models which predict both the environments and those effects on subsystems and spacecraft, and, finally, ensuring that this multitudinous information is properly maintained, and inserted into spacecraft design programs.

Many parts and pieces of a SEE program already exist at various locations to fulfill specific needs. The primary purpose of this program, under the direction of the Office of Advanced Concepts and Technology (OACT) in NASA Headquarters, is to take advantage of these parts; apply synergisms where possible; identify and when possible fill-in gaps; coordinate, and advocate a comprehensive SEE program. The SEE program must coordinate and support the efforts of well-established technical communities wherein the bulk of the work will continue to be done.

The SEE program will consist of a NASA-led SEE Steering Committee, consisting of government and industry users, with the responsibility for coordination between technology developers and NASA customers; and Technical Working Groups with primary responsibility for program technical content in response to user needs. The Technical Working Groups are as follows: Materials and Processes; Plasma and Fields; Ionizing Radiation; Meteoroids and Orbital Debris; Neutral External Contamination; Thermosphere, Thermal, and Solar Conditions; Electromagnetic Effects; Integrated Assessments and Databases.

Specific technology development tasks will be solicited through a NASA Research Announcement to be released in May of 1994. The areas in which tasks are solicited include: 1) engineering environment definitions, 2) environments and effects design guidelines, 3) environments and effects assessment models and databases, and 4) flight/ground simulation/technology assessment data. The OACT anticipated FY95 funding for this program is in the \$2-\$3M range.

NASA Langley Research Center has been asked to lead this activity and the LaRC SEE Program Manager is

Mr. Don Avery
NASA LaRC, Mail Stop 367
Hampton, VA 23681-0001
Phone (804) 864-1947

The OACT program manager is
Dr. Dana Brewer
NASA HQ
Code CD
Washington, DC 20546-0001
Phone 202 358-1678

Questions regarding the status and content of the National SEE program may be directed to either of the above individuals.

LONG DURATION EXPOSURE FACILITY (LDEF) ARCHIVE SYSTEM

Brenda K. Wilson

Boeing Aerospace Operations, Inc.
3221 N. Armistead Avenue, Suite B
Hampton, VA 23666-1311

ph 804-766-8976 / fax 804-766-8977 / e-mail b.k.wilson@larc.nasa.gov

SUMMARY

The Long Duration Exposure Facility (LDEF) Archive System is designed to provide spacecraft designers and space environment researchers single point access to all available resources from LDEF. These include data, micrographs, photographs, technical reports, papers, hardware and test specimens, as well as technical expertise. Further, the LDEF Archive System is planned such that it could be the foundation for a NASA Space Environments and Effects (SEE) Archive System, with the addition of other spaceflight, laboratory and theoretical space environments and effects data and associated materials. This paper describes the current status and plans of the LDEF Archive System.

BACKGROUND

The multi-year studies of the retrieved LDEF by hundreds of investigators have resulted in a large, unique and valuable set of resources on the environments in low Earth orbit (LEO) and the effects of these environments on spacecraft and space operations. These diverse resources were generated by many organizations in the federal government, industry and academic institutions. Since the original LDEF Project Plan involved returning its payloads to their principal investigators with no project involvement in data collection and analyses, no central archival plans were made.

NASA is required to archive data from spaceflight experiments in accordance with the requirements of the National Archives. Also, NASA has an agreement with the National Air and Space Museum of the Smithsonian Institution, which gives the National Air and Space Museum the right of first refusal of NASA's spaceflight hardware.¹ NASA has the right to keep spaceflight hardware for as long as it desires, but the National Air and Space Museum must be given the first opportunity after NASA to assume responsibility for the hardware.

Other aerospace databases and data centers relate to the LDEF Archive System. These include the National Space Science Data Center (NSSDC), which has operated for 28 years as an active repository for space and Earth science data from space experiments and ground-based observations.^{2,3} Over the past four years, LDEF special investigation groups and principal investigators have developed focused databases generally oriented toward specific LDEF experiments, areas of special investigations or disciplines. These local databases reside on minicomputers, workstations and personal computers and employ a variety of database management software for data storage and retrieval. In addition, these databases are characterized by custom user interfaces and access mechanisms.

The LDEF activities have brought together a community of space environment and effects researchers and form the basis for a continuing space environments and effects program. While NASA has not maintained a comprehensive SEE program throughout its history, in recent years

the NASA Office of Advanced Concepts and Technology (OACT) and NASA Langley Research Center (LaRC) have placed emphasis upon the development of a SEE Program. Although the program is in its early stages, the following general technical discipline areas have been identified: ionizing radiation; meteoroids and orbital debris; neutral external contamination; plasmas and fields; thermosphere, thermal and solar conditions; electromagnetic effects; materials and processes; and environmental model and database integration.⁴ Technical working groups, similar to the LDEF special investigation groups, have been established in these areas.

Boeing Aerospace Operations, Inc. (BAO) has defined the structure of the LDEF and proposed SEE Archive System for the LDEF Science Office at NASA LaRC, and is in the process of identifying and assembling the detailed contents. NASA LaRC's Information Systems Division (ISD) has provided and interfaced the computing resources in the form of hardware, software and network components required to develop the Online Archive System. ISD and BAO will work to integrate the distributed LDEF data into a centrally accessible archive system. This activity also involves the LDEF principal investigators, special investigation groups and contractor organizations. The four LDEF special investigation groups, focused upon ionizing radiation, meteoroids and debris, materials and systems, were directed by the LDEF FY 1994 plan to support the development of the LDEF Archive by identifying and making available to BAO all archivable information.

ARCHIVE SYSTEM DESCRIPTION

Overview

The LDEF Archive System is comprised of two parts. The first part is the physical contents of the archive, including space flight and ground control hardware, documentation, data, photographs and publications. The second part is the electronic or online system. It is available to users via the Internet, and it takes advantage of public domain software whenever possible.^{5,6} It contains data files, both numerical and graphical image files, micrograph and photograph image files, technical report abstracts and full text files.

The elements of both components of the LDEF Archive System, physical and electronic, are categorized according to the following:

- Directory
- Project / Mission Documentation
- Experiment Documentation
- Hardware
- Data / Analysis
- Photographs
- Publications

The LDEF Archive System elements can also be viewed from the perspective of technical disciplines:

Environments and their effects:

- Ionizing Radiation
- Meteoroids and Debris
- Neutral External Contamination
- Plasmas and Fields
- Thermal and Solar

Environmental effects-related:

- Electromagnetic Effects
- Materials and Processes
- Systems

These technical discipline classifications reflect the areas of LDEF special investigations and the structure of the developing SEE Program. Figure 1 illustrates the elements of the LDEF Archive System.

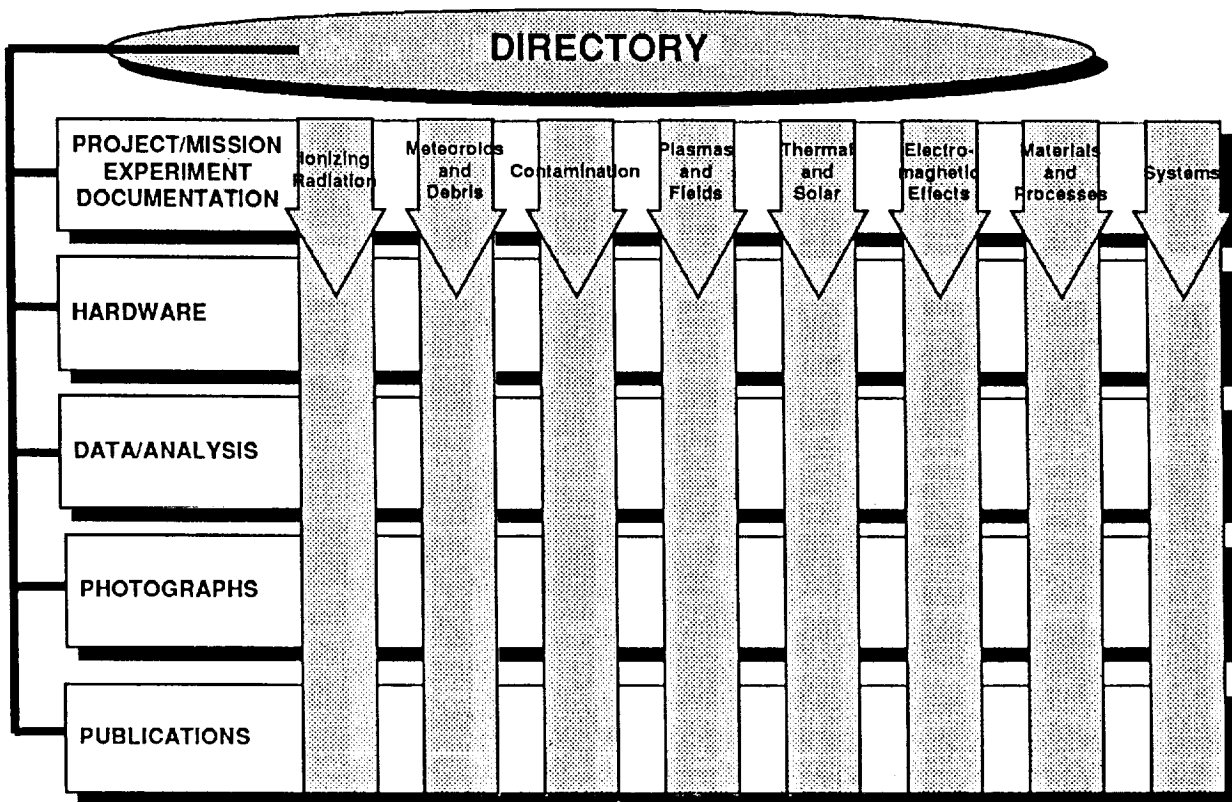


Figure 1. LDEF Archive System.

The LDEF Archive is a distributed system, and both physical and electronic segments are maintained at a host of locations. The LDEF Archive at NASA LaRC has the ultimate responsibility for the total system, and it is the location to which all hardware, data and associated materials should be sent when they are no longer maintained at investigators' facilities. The remainder of this section includes a discussion of the Online Archive System, followed by descriptions of the elements and their incorporation into the final product.

Online Archive System

The Online Archive System will provide the single point of entry to the resources of the LDEF Archive System. This concept is illustrated in Figure 2. A prototype was developed in Autumn 1993 that contained network access to the following data systems: LDEF Meteoroids and Debris Special Investigation Group Database at NASA Johnson Space Center, the Jet Propulsion Laboratory/NASA Ground Test Radiation Data Bank (RADATA) at JPL and the Materials and Processes Technical Information System (MAPTIS) at NASA Marshall Space Flight Center. It also contained access to a small set of digital images of LDEF photographs and accompanying descriptions. This prototype was demonstrated to attendees of the Third LDEF Post Retrieval Symposium in Williamsburg, VA, in November 1993.

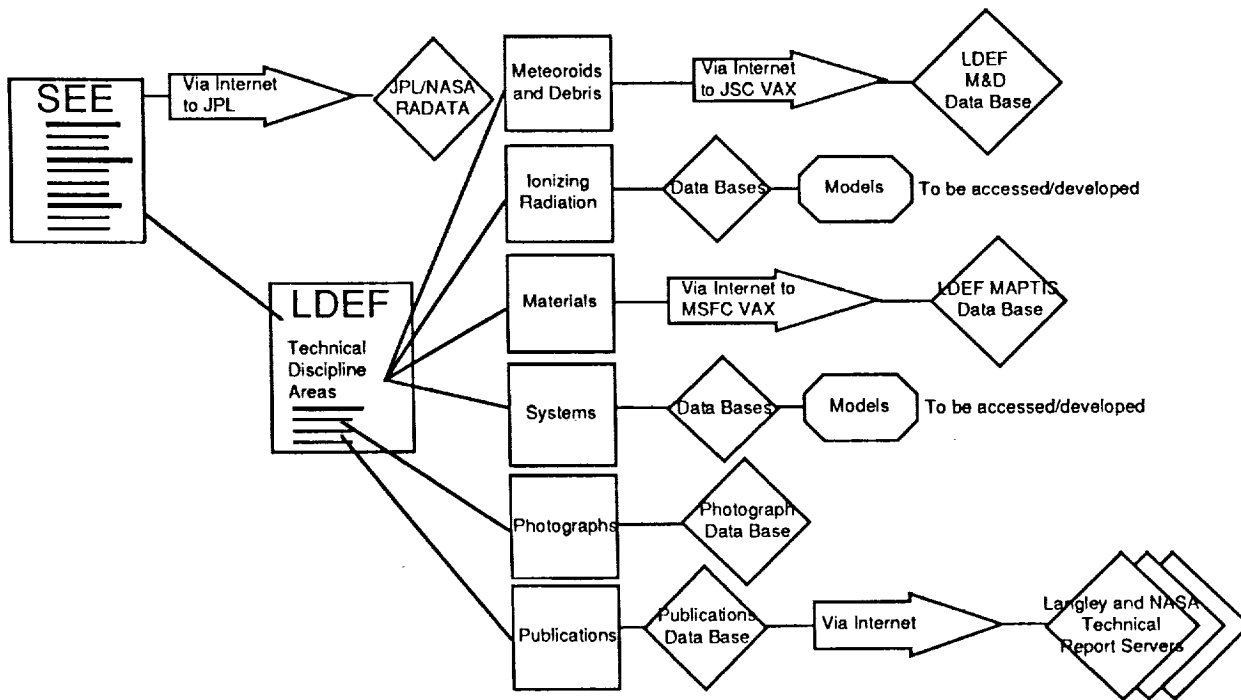


Figure 2. Online LDEF Archive System concept illustration.

The LDEF Archive System has been established on a UNIX workstation at NASA LaRC, and it is accessible via Internet. The LDEF Archive System's capability to reach out to other data systems is achieved through the use of an Internet information service referred to as the World Wide Web (WWW). WWW was initially developed by researchers at the Conseil European pour la Recherche Nucleaire (CERN) to enable information sharing among internationally dispersed teams of researchers. Built on a client / server architecture, it is a global hypermedia information retrieval system.^{7,8} Hypermedia is a form of hypertext. Hypertext is text that may be "expanded" to provide links to other text. Hypermedia extends this concept by allowing links to multimedia information, such as images, audio and animations. The hypermedia language utilized by the WWW is referred to as HyperText Markup Language (HTML), which is based on a document formatting language called the Standard Generalized Markup Language (SGML).

The client and server components of the WWW architecture communicate with each other via HyperText Transmission Protocol (HTTP). The WWW client, often referred to as a browser, makes a request for a document to a WWW server, sometimes referred to as an HTTP server. The LDEF Archive utilizes Mosaic from the National Center for Supercomputing Applications (NCSA) as the WWW client, although other WWW browsers are available.

NCSA Mosaic has been developed by the Software Development Group of the National Center for Supercomputing Applications at the University of Illinois at Urbana-Champaign.^{9,10} NCSA receives support from the University of Illinois, the state of Illinois, the National Science Foundation, other government agencies and industry. Mosaic runs on X-Windows displays, IBM and Macintosh personal computers, and it is public domain software. It is available at no cost when downloaded from NCSA via anonymous file transfer protocol (FTP). A minimal cost is charged when NCSA provides Mosaic on disks for IBM or Macintosh PCs through the mail. Information about Mosaic is available from NCSA at the following:

e-mail: mosaic@nasa.uiuc.edu.

phone: (217) 244-0072

In addition to supporting HTTP, NCSA Mosaic also supports other protocols and Internet resource services such as: the File Transfer Protocol (FTP) for retrieving files, Telnet for connecting to remote machines, and the Wide Area Information Servers (WAIS) and gopher for both searching and retrieving information.¹¹ Mosaic also provides internal and external "viewers" for displaying multimedia information including images and audio.

The LDEF Archive System also uses the LaRC-developed Program for Information Storage and Management (PrISM) data tracking software for managing experiment, photograph and hardware information that resides at the central archive site.

The LDEF Archive System and other systems, programs, projects and organizations that are part of the World Wide Web each begin with a "home page," an HTML page that provides the user with descriptive information and serves as the starting point for finding other information. A home page has a function similar to a book cover and table of contents, although it rapidly provides much more information through hyperlinks to the listed items. One can browse through the WWW by using NCSA Mosaic, in a manner similar to paging through a book. Data are presented on pages that appear on the computer monitor, and with the use of the pointer (mouse) one can browse or turn the pages. One can also go directly to a specific page of interest once the page's filename, or Uniform Resource Locator (URL), is known. Each NASA Center and Headquarters has a home page; the URL for the home page for NASA LaRC is:

<http://www.larc.nasa.gov/larc.html>

Figure 3 shows a portion of the NCSA Mosaic menu and the URL entry option.

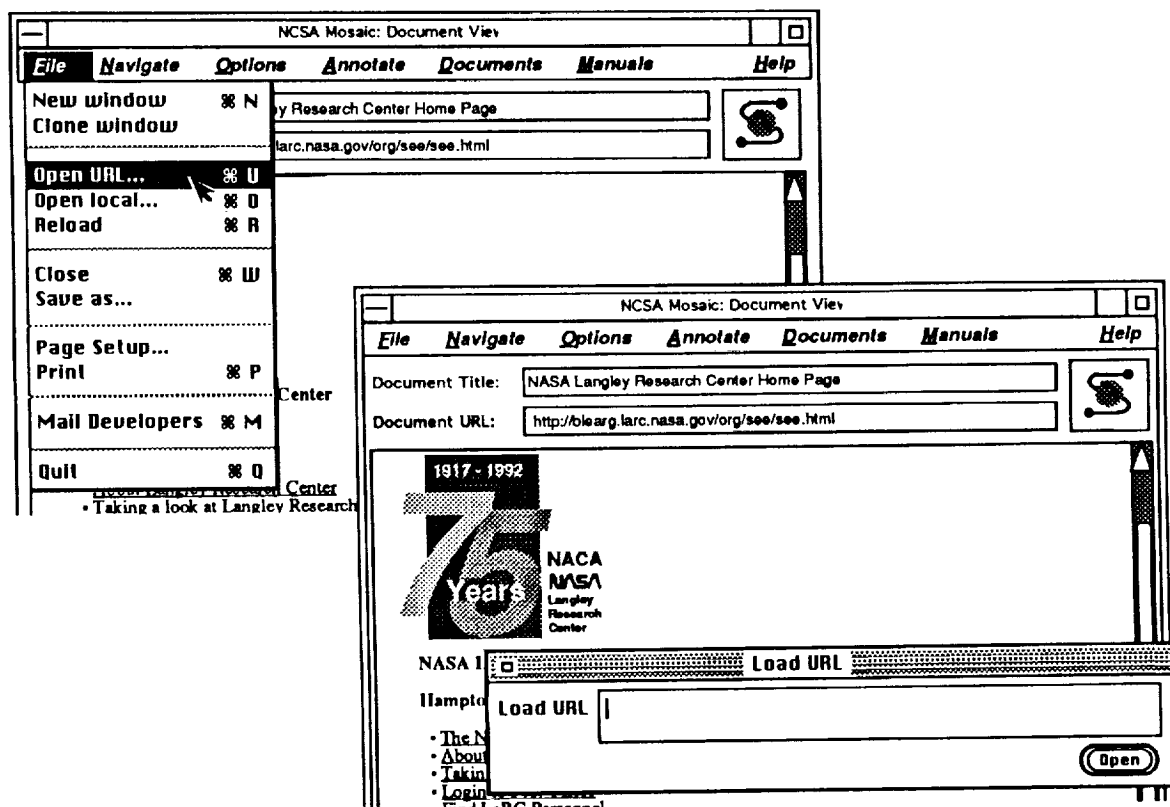


Figure 3. Uniform Resource Locator (URL) entry option.

The entrance to the LDEF Archive System is through a Space Environments and Effects Archive System home page. This is shown in Figure 4. Since the SEE Archive System is intended to access data in addition to that from LDEF, the items listed on the SEE Archive System home page can be modified as the SEE Archive System grows. The SEE Archive System will be listed on the LaRC home page; it is also available through the URL:

<http://blearg.larc.nasa.gov/org/see/see.html>

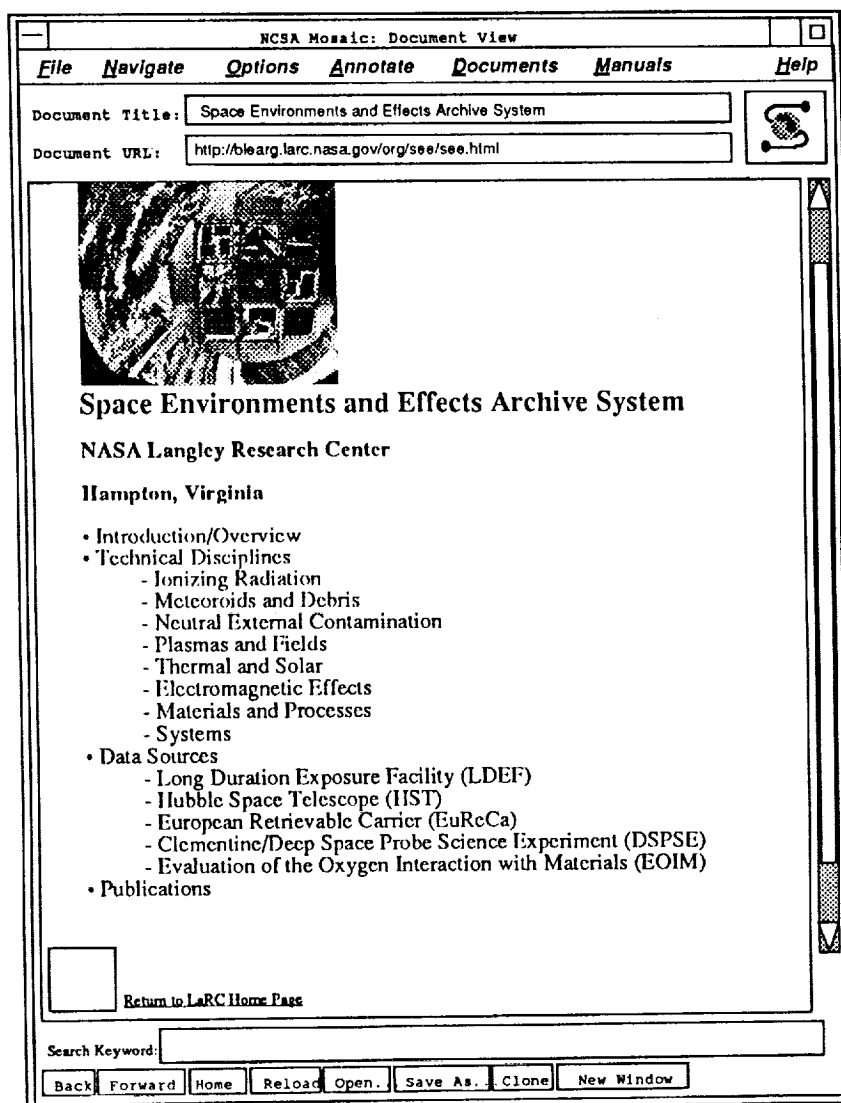


Figure 4. Space Environments and Effects Archive System home page for LDEF access.

Selection of the *Overview* hypertext will lead the user to a page of descriptive information. The *Technical Disciplines* hypertext will lead the user through the system according to the particular area of interest. The *Data Sources* hypertext will lead the user through the system according to a particular space mission or experiment of interest. A *technical discipline-oriented* and a *data source-oriented* path are illustrated in Figure 5. Both paths will lead the user to the same LDEF data area.

The LDEF Archive System home page is illustrated in Figure 6. One can reach this page through the LaRC home page, the SEE Archive System home page, or directly through the URL:

<http://blearg.larc.nasa.gov/org/see/ldef.html>

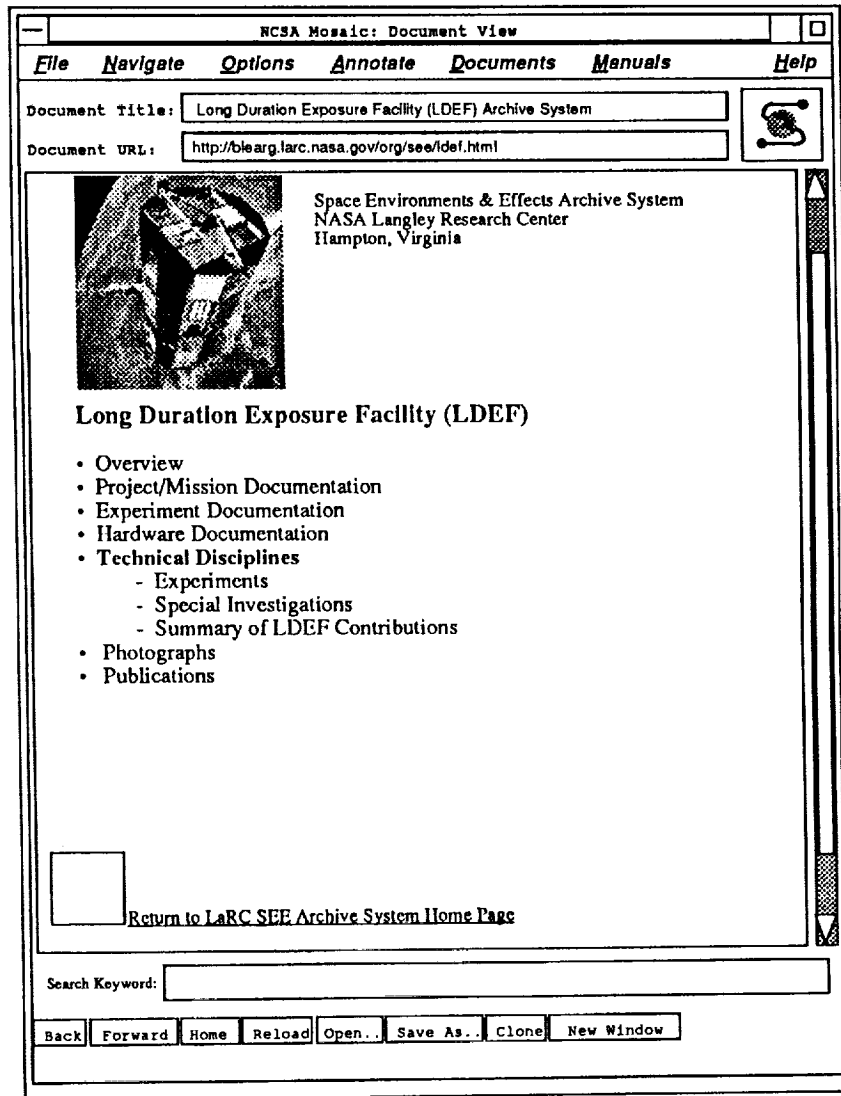


Figure 6. LDEF Archive System home page.

Portions of the LDEF Archive System can be searched through the use of the NCSA Mosaic interface to WAIS, which enables full-text searching of varied databases. WAIS employs a keyword search program from a client machine, and it searches databases that can be located on different server machines.

Physical and Online Aspects of Archive System Elements

Project / Mission Documentation

The project / mission documentation archive element contains the technical plans, design review documents, safety analyses, stress corrosion, electromagnetic interaction and structural failures testing and analyses records. It includes documentation on the Announcement of Opportunity process to acquire experiments and the memoranda between NASA and other organizations. It also will include the data recorded during flight operations at Johnson and Kennedy Space Centers. Currently the documentation is in the LDEF Archive and in the files of LDEF Project staff. The LDEF Science Office is responsible for organizing and preparing these documents and their associated descriptive information for archival. This is planned to be done in conjunction with Lockheed Engineering and Sciences Company, which has a task to author a NASA publication on the LDEF history. The documentation is organized chronologically:

- General
- Concept Development and Design Philosophy
- Facility Design and Development
- Acquisition and Project Tasks in Experiment Development
- Experiment Development Organization Tasks
- Experiment / LDEF Integration Engineering
- LDEF / Space Transportation System (STS) Integration Engineering
- Integration Operations
- Launch
- Orbit
- Retrieval
- Post-Retrieval Deintegration Operations

The Online Archive System will contain at a minimum an identification of the project / mission documents in the archive. Any LaRC-published reports on this area will be included when completed.

Experiment Documentation

The experiment documentation includes experiment number, title, location on LDEF, principal investigators, description, approach, objective, payload materials usage list and drawing list. The Archive will contain a complete set of the 1,461 LDEF as-flown experiment drawings and the 358 LDEF structure drawings. The drawings with LaRC numbers are also archived by LaRC on microfiche.

Hardware

This archive contains flight and ground specimens associated with the LDEF experiments and facility. Hardware is located at the LDEF Archive adjacent to NASA LaRC, NASA Johnson Space Center (JSC), Marshall Space Flight Center (MSFC), Kennedy Space Center (KSC) and principal investigators' laboratories. Principal investigators may retain their hardware as long as they wish. When they no longer wish to retain it, they will return the hardware to the LDEF Archive in Hampton, VA.

Data / Analysis

The results of LDEF investigations have been recorded in databases, lab journals, files, reports and publications. Many LDEF researchers have developed focused databases to review, maintain and access the LDEF resources in specific disciplines. LDEF data have also been used in the development of space environment and environmental effects models.

The data / analysis archive is organized according to technical disciplines. Two special investigation groups have created remote databases that are accessible directly from the LDEF Archive System by using the capabilities of the Mosaic browser and the WWW server. These are the Meteoroids and Debris Special Investigation Group Database at NASA JSC,¹² and the Materials Special Investigation Group Database at NASA MSFC.¹³ The M&D database at JSC is located under the M&D Special Investigations page of the LDEF Archive System; its access from the LDEF Archive System via the Mosaic interface to Telnet is illustrated in Figure 7.

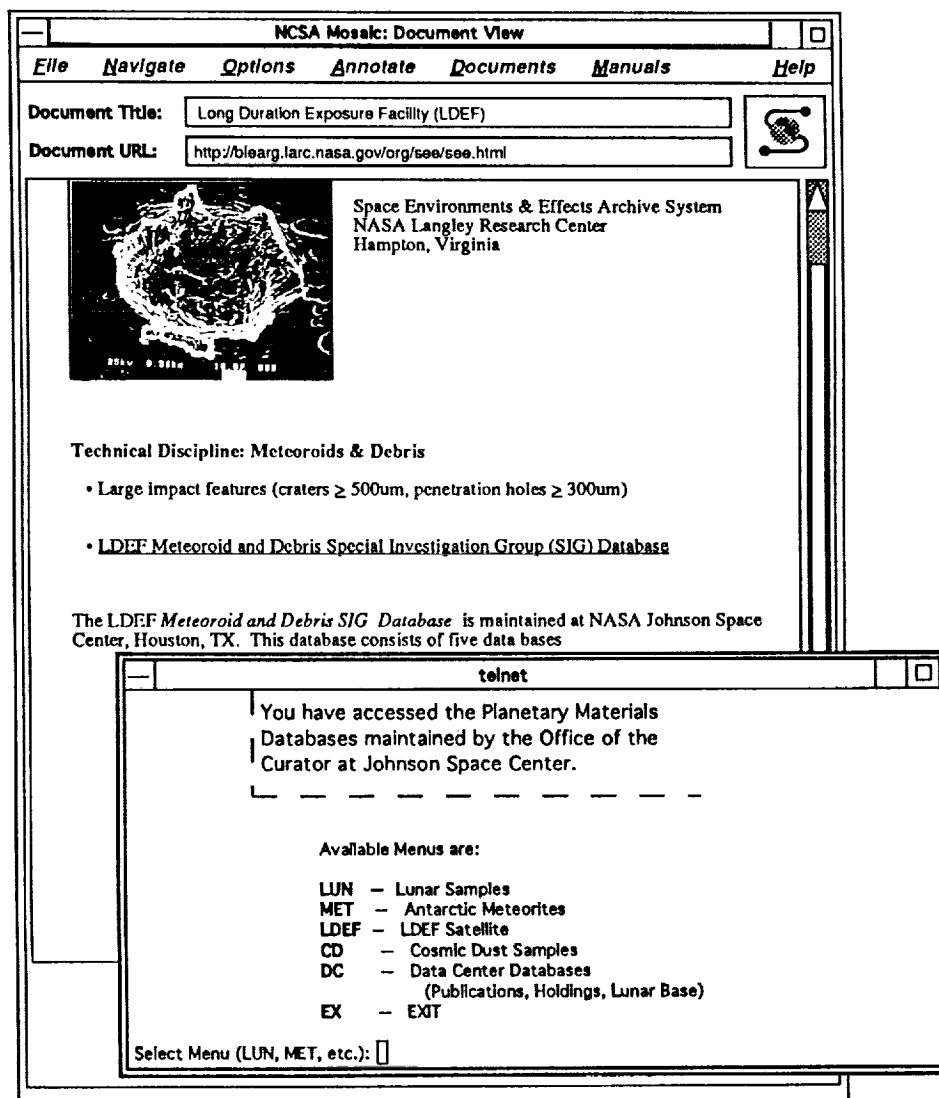


Figure 7. Access of the LDEF Meteoroids and Debris Special Investigation Group Data Base.

While the M&D database can be accessed without a password, the Materials SIG database requires that the user obtain a password from the Materials and Processes Technical Information System (MAPTIS) at MSFC prior to accessing. Also as part of Materials and Systems SIG activities, Boeing Defense and Space Group has created a set of specialized databases for use on personal computers that address optical materials, thermal control coatings, silverized Teflon, treated aluminum, and LDEF environments.¹⁴ In addition to being available on disk for use with Filemaker® Pro [Claris Corp.] software, these databases are planned to be accessible through the Online Archive System.

Principal investigators have used commercial and public domain software to create databases. PI databases using commercial software include Aerospace Corporation's M0003 Deintegration Database available for use with Fourth Dimension™ [ACTIUS, Inc.] and Paradox® [Borland International, Inc.] software. The Technical University of Munich has developed hypermedia databases using the public domain Mosaic software from NCSA. They include data, micrographs, photographs, publications and other items relative to LDEF experiments AO187-1, AO187-2, AO201 and S1003. These databases will be accessible via the LDEF Archive System.

In general, the Online Archive System will identify what databases are available, in what form, and how they are available. Through the use of NCSA Mosaic, the databases available via the Internet will be accessible from the Archive. Some of the databases that are available for use with commercial software are also planned to be network-accessible.

Photographs / Videos

More than 20,000 photographs of LDEF, LDEF experiments, samples and research efforts are currently in the collections of LaRC, KSC, JSC, MSFC and principal investigators. Individual photographic surveys were taken by NASA during the pre-launch period, STS-41C (originally STS-13) deployment flight, STS-32 retrieval flight, Edwards Air Force Base operations, and KSC operations, including those at the Demating, Orbital Processing, Operations and Checkout Facilities and the Spacecraft Assembly and Encapsulation Facility II (SAEF-II). The SAEF-II photographic records are extensive and cover the initial visual inspection period, deintegration of experiments, facility and systems. Each experiment tray was the subject of a detailed photo survey immediately following deintegration. Individual principal investigators also have extensive photographic collections, and efforts are being made to include copies of these collections in the LDEF Archive.

The Online Archive System will contain at a minimum three images for each LDEF tray location and experiment: preflight, on-orbit and post-flight. Currently only the on-orbit photo images have been entered. Graphical Interchange Format (GIF) and Tagged Image File Format (TIFF) files are part of the system. No standard digital image format exists in practice within NASA or within the broad archive community.

Lockheed Engineering and Science Company has a task from NASA LaRC to catalog LDEF photographs and videos, and to produce a document of LDEF photographs for NASA publication. The parallel activities are being coordinated in order to produce complementary products.

Publications

The LDEF Archive will contain a copy of all LDEF-related publications available. These include publications in professional journals, NASA publications, other government publications, books, newspapers and other sources.

The Online Archive System will utilize the online document retrieval services being developed by NASA LaRC's Information Systems Division, including the Langley Technical Report Server (LTRS) and the NASA Technical Report Server (NTRS).¹⁵ It will also access other technical report servers as they relate to LDEF and as they become available. The goal over the long term is to be able to provide access to the extensive publications databases and retrieval services that currently are available through a combination of government and commercial publications databases.

INTERACTION WITH USERS

The prototype of the Online LDEF Archive System was developed in Autumn 1993 and was available for review at the Third LDEF Post Retrieval Symposium in November 1993. Since that time, BAO has worked with system users who have expressed comments. It is planned that a more comprehensive draft will be available in mid-1994, and a form has been incorporated in the system to enable users to reply via e-mail regarding the system.

In the developing Space Environments and Effects Program, the technical working groups comprise the greatest technical expertise related to their discipline, and it will be these groups that are responsible for the development of space environment models, environmental effects modeling, design criteria, guides and knowledge base systems. The Space Environments and Effects Archive will be the resource upon which these groups can draw in order to build these products.

INTERACTION WITH OTHER DATA SYSTEMS AND ARCHIVES

Lessons have been learned from other archives and data systems that have similar objectives to the LDEF Archive System but that do not necessarily contain space environments and effects data. BAO participates in Internet discussion groups on museums and archives that have a total of several thousand members interested in the development of systems to catalog, access and archive diverse resources for users with varied needs and computer capabilities. It is clear that while some standards exist for cataloguing items, the technologies for data storage evolve rapidly and standards do not cover the growing range of data storage and access options. BAO has also consulted with a broad set of organizations including the NSSDC and some of its affiliated data systems, such as the Planetary Data System; the Library of Congress; the Smithsonian Institution; and organizations at LaRC active in data storage and retrieval, including the Earth Observing System Data and Information System (EOSDIS) Distributed Active Archive Center (DAAC).

Key to the development of a useful and efficient system is the definition of requirements prior to establishing formats for data storage, media and access. Also, any system must be flexible enough to adapt to changes in data storage technologies. Computer technology can advance dramatically in one year, as in the case of NCSA Mosaic.

In addition to the LDEF-related computer network-accessible systems discussed earlier, more systems are coming online that relate to the LDEF Archive System and space environments and effects. A number of NASA Centers have programs devoted to space environments and effects, and Department of Defense laboratories similarly have areas of focused SEE-related research. As appropriate, links to these systems are planned as part of the proposed SEE Archive System.

CONCLUDING REMARKS

The purpose of LDEF Archive System is to maintain LDEF data, analysis, hardware, photographs, documentation and publications as a long term resource, and to provide easy access to these distributed elements. BAO is developing the LDEF Archive System as the single point of entry into the distributed LDEF resources and areas of technical expertise maintained at different locations. When it develops into the SEE Archive System, it will be the gateway for the growing quantity of space environments and effects data distributed throughout the aerospace research community.

It is hoped that this system will lead to more data archival and technology transfer planning at the outset of space experiment planning. As more space environment and effects data are generated, it becomes increasingly important that the raw data be available for review, application and comparison. NASA-funded research results are typically made available through published papers; with the advances in personal computer capabilities and network technologies, not only the papers but the data files can be downloaded for use at the researcher's desk.

A SEE Archive System is an essential basis for the development and subsequent utilization of space environment and effects models, design criteria, guides and knowledge base systems. A SEE Archive System will be the resource in which space researchers and spacecraft designers can store and access data, and it will be the means through which data, models, design tools and hardware can be disseminated. Key to the archive's success will be the coordination with principal investigators prior to missions on the definition of requirements for data archival and access after flight. The proposed SEE Archive System was developed based on the anticipation that the structure of the SEE Program would be as illustrated in Figure 8.

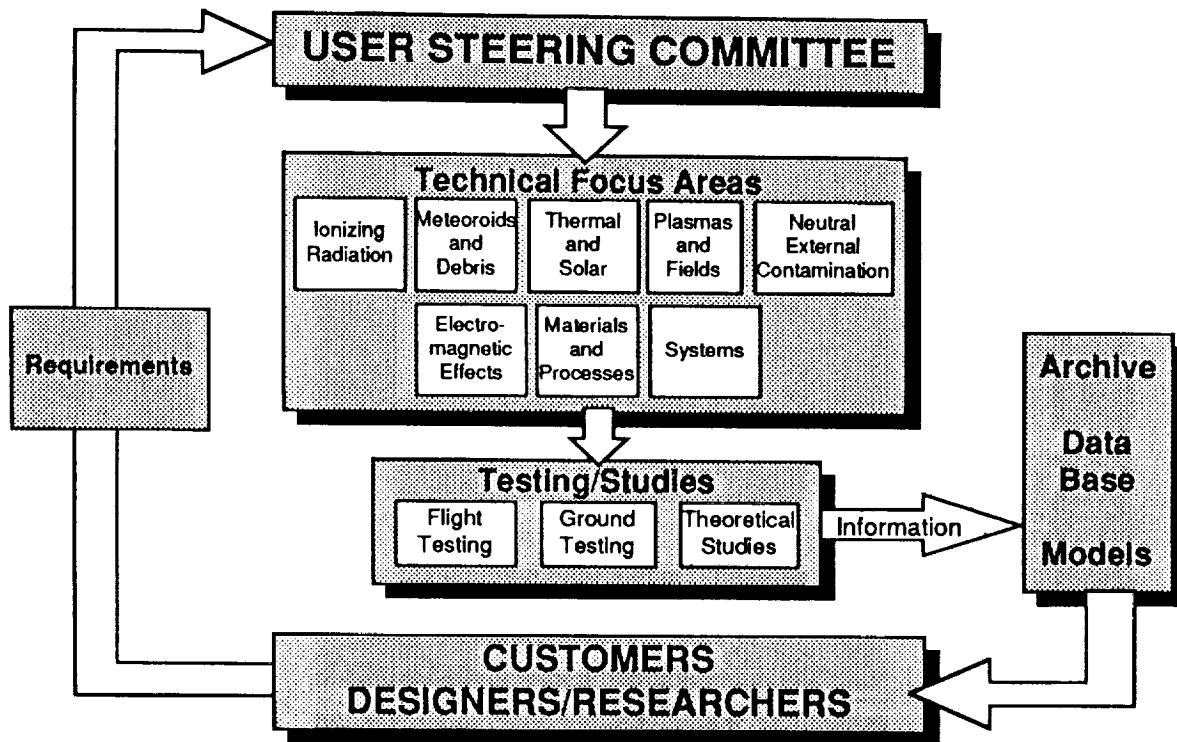


Figure 8. Space Environments and Effects Program and Archive System concept.

REFERENCES

1. *Agreement Between the National Aeronautics and Space Administration and the Smithsonian Institution Concerning the Transfer and Management of NASA Historical Artifacts*. May 12, 1988.
2. *A Guide to the National Space Science Data Center*. NSSDC 90-07, June 1990.
3. Wilson, Brenda K.: LDEF Archival System Plan. *LDEF - 69 Months In Space: Second LDEF Post-Retrieval Symposium*, NASA CP-3194, Part 4, 1993.
4. *NASA Research Announcement, Space Environments and Effects Program*. NRA 94-LaRC-1, May 16, 1994.
5. Krol, Ed: *The Whole Internet - User's Guide and Catalog*. O'Reilly & Associates, Inc., 1993.
6. Schwartz, Michael F.; Emtage, Alan; Kahle, Brewster; and Newnam, B. Clifford: A Comparison of Internet Resource Discovery Approaches. *Computing Systems*, Vol. 5, No. 4, 1992, pp. 461-493.
7. Hughes, Kevin: *Entering the World Wide Web: A Guide to Cyberspace*. Uniform resource locator: <http://www.hcc.hawaii.edu/guide.html>, October 1993.
8. Berners-Lee; Tim, Cailliau, Robert; Groff, Jean-François; and Pollermann, Bernd: World-Wide Web: The Information Universe. *Electronic Networking: Research, Applications and Policy*, Vol. 2, No. 1, Spring 1992, pp. 52-58.
9. Andreessen, Marc: *NCSA Mosaic Technical Summary*. Revision 2.1, May 4, 1993.
10. Andreessen, Marc and Bina, Eric: NCSA Mosaic: A Global Hypermedia System. *Internet Research: Electronic Networking Applications and Policy*, Vol. 4, No. 1, Spring 1994, pp. 7-17.
11. Kahle, Brewster; Morris, Harry; Davis, Franklin; Tiene, Kevin; Hart, Clare; and Palmer, Robin: Wide Area Information Servers: An Executive Information System for Unstructured Files. *Electronic Networking: Research, Applications and Policy*, Vol. 2, No. 1, Spring 1992, pp 59-68.
12. See, T.; Allbrooks, M.; Atkinson, D.; Simon, C.; and Zolensky, M.: *Meteoroid and Debris Impacts Features Documented on the Long Duration Exposure Facility: A Preliminary Report*. JSC Publication #24608, August 1990.
13. Funk, Joan G.; Strickland, John W.; and Davis, John M.: *LDEF Materials Data Bases*. NASA TM 107757, June 1993.
14. Bohnhoff-Hlavacek, Gail: Databases for LDEF Results. *LDEF - 69 Months In Space: Second LDEF Post-Retrieval Symposium*, NASA CP-3194, Part 3, 1993.
15. Nelson, Michael L., and Gottlich, Gretchen L.: *Electronic Document Distribution: Design of the Anonymous FTP Langley Technical Report Server*, NASA TM 4567, March 1994.

THE LONG DURATION EXPOSURE FACILITY (LDEF) ANNOTATED
BIBLIOGRAPHY

Arlene S. Levine
MS 404
NASA Langley Research Center
Hampton, Virginia 23681-0001
Phone 804/864-3318; Fax 804/864-8094

A major objective of the Space Act of 1958 which led to the establishment of the National Aeronautics and Space Administration (NASA) was the dissemination of science and technology. Today, under NASA administrator Daniel Goldin and the White House, there is a reemphasis on the dissemination and transfer of NASA science and technology to U.S. industry: both aerospace and non aerospace. The goal of this transfer of science and technology is to aid the U.S. industry making them more competitive in the global economy.

After 69 months in space, LDEF provided new and important information on the space environment and how this hostile environment impacts spacecraft materials and systems. The space environment investigated by the LDEF researchers included: ionizing radiation, ultraviolet radiation, meteoroid and debris, atomic oxygen, thermal cycling, vacuum, microgravity, induced contamination and various synergistic effects. The materials used as part of LDEF and its experiments include polymers, metals, glass, paints and coatings. Fiber optic, mechanical, electrical, and optical systems were also used on LDEF.

Approximately 1161 pre- and post-retrieval LDEF publications and papers have been published to date. Published LDEF papers have been written in several languages, including English, French, and German. These papers have appeared in the world's scientific journals, including *Nature*, and in three NASA published LDEF Post-Retrieval Symposium volumes. A partial list of the scientific journals containing LDEF papers is given in Table 1. A total of 132 papers appeared in the first LDEF Post-Retrieval Symposium volume (ref. 1), and 112 papers appeared in the second LDEF Post-Retrieval Symposium volume (ref. 2). The third LDEF Post-Retrieval Symposium volume is in preparation and will contain over 100 papers when it is published in late 1994 (ref. 3).

As part of the effort to disseminate and transfer LDEF science and technology, an annotated bibliographic database is being developed. This bibliography will be available electronically, as well as in hard copy. All LDEF domestic and foreign publications in the open literature, including scientific journals, the NASA LDEF Symposia volumes, books, technical reports and unrestricted contractor reports will be included in this database. The hard copy, as well as the electronic database, will be categorized by section in the scientific and technical discipline. For example, all LDEF papers dealing with ionizing radiation will appear as a stand alone database. All LDEF materials papers will also appear as a stand alone database. Within each individual subject database, there will be further divisions by category. For example, in the LDEF materials database, all polymer papers will be grouped; all metals will be grouped and further subdivided by the particular species of metal. By publishing each LDEF discipline database as a separate unit, information will be disseminated more quickly to the user community. Each LDEF

reference will include the following information: title, author(s) name, publication name, volume, date, page, abstract. and NASA RECON number.

A sample entry follows:

The Distribution of Debris Impacts Over Satellite Surfaces With Special Regard to the Long Duration Exposure Facility LDEF
Zhang, J.
Rex, D.
Zeitschrift fuer Flugwissenschaften und Weltraumforschung
Vol. 17 No. 3
1993
170-180

Examination of surfaces recovered from space indicates a high flux of small particles of natural as well as manmade origins. In this paper, a model of small orbital debris particles is presented and impact distributions resulting from this model are derived and discussed. In order to understand the observed impacts on LDEF, general relationships between particle orbits and crater distributions over the LDEF surfaces are analyzed. After comparison of modeling results with observational data, a modification of the debris model is proposed which fits the measurement favorably.
93A56043

The compilation of LDEF papers can be updated periodically and converted into Space Environment and Effects (SEE) bibliographic publications and databases (ref. 4). Thus, researchers, environment modelers, and spacecraft designers may access a readily available database of previous findings on the space environment and its effects on materials, systems, and spacecraft. The third post-retrieval symposium contained papers on EOIM-3, Mir, and EURECA. Those papers will be integrated in the respective databases for their disciplines. For example, the Benton and Frank paper on radiation results on EURECA (ref. 5) will appear in the radiation volume and database. Therefore the database will cover references from other spacecraft and experiments.

This author asks that you assist in the development of the SEE database by sending her a list of your LDEF publications and a list of SEE related publications.

References

1. Levine, A. S. (Editor): 69 Months In Space: The First LDEF Post-Retrieval Symposium. Volumes I, II, and III. NASA Conference Publication, NASA CP-3134, 1991.
2. Levine, A. S. (Editor): 69 Months In Space: The Second LDEF Post-Retrieval Symposium. Volumes I, II, III, and IV. NASA Conference Publication, NASA CP-3194, 1992.
3. Levine, A. S. (Editor): 69 Months In Space: The Third LDEF Post-Retrieval Symposium. Volumes I, II, and III. NASA Conference Publication, NASA CP-3275, 1995.

4. Bowles, David E. , Robert L. Calloway, Joan G. Funk, William H. Kinard, Arlene S. Levine, From LDEF to a National Space Environments and Effects (See) Program: A Natural Progression, NASA CP-3275, 1994.

5. Preliminary Results of Radiation Measurements on EURECA, E.V. Benton, A.L. Frank, NASA CP-3275, 1995.

Table 1. Some Journals and Proceedings Containing LDEF Papers

Journals

Advances in Space Research
Applied Optics
Geophysical Research Letters
Icarus
Journal of Geophysical Research
Journal of Materials Science
Journal of Spacecraft and Rockets
Luft und Raumfahrt
Nature
Scripta Metallurgica et Materialia
Zeitschrift fuer flugwissenschaften und Weltraumforschung

Conference Proceedings

American Astronautical Society (AAS)
American Institute for Aeronautics and Astronautics (AIAA)
Committee on Space Research (COSPAR)
Composite Materials Conference
European Space Agency (ESA) Conferences
European Symposium on Spacecraft Materials in Space
International Astronautical Conference
International Conference on Engineering, Construction, and Operations in Space
International Conference on Fourier Transform Spectroscopy
International Instrumentation Symposium
International SAMPE Conferences
International Society for Optical Engineering
LDEF Materials Workshops
LDEF Symposia
Lunar and Planetary Science Conferences, Lunar and Planetary Institute
Meteoritical Society
NASA/SDIO Space Environmental Effects on Materials Workshop
Space Flight Mechanics Conferences
Symposium on Chemical Evolution and the Origin of Life
Symposium on Shuttle Small Payloads

10

10

**The Long Duration Exposure Facility (LDEF)
Photographic Survey Special Publication**

Robert L. O'Neal
MS 404
NASA Retired
Hampton, Virginia 23681-001

Arlene S. Levine
MS 404
NASA Langley Research Center
Hampton, Virginia 23681-0001
Phone 804/864-3318; Fax 804/864-8094

Carol C. Kiser
MS 404
NASA Retired
Hampton, Virginia 23681-0001

During the construction, integration, launch, retrieval and deintegration of the Long Duration Exposure Facility (LDEF), photographic surveys were made. Approximately 10,000 photographs were taken during the various phases of the LDEF project. These surveys are of technical and scientific importance because they revealed the pre and post flight conditions of the experiment trays as well as the spacecraft. Visual inspection of the photographs reveal valuable data such as space environment's effects and the earth atmosphere's effects post-retrieval. Careful files and records have been kept of these photographs. Each photograph has a Kennedy Space Center photo number or a Johnson Spaceflight Center photo number as well as a Langley Research Center photo number. The tray number, row number, and experiment number are also noted.

Out of the 10,000 photographs taken, approximately 700 selected photographs were chosen for publication in a NASA Special Publication (SP) because they reveal the effects of space exposure to the viewer. These photographs will give researchers and spacecraft designers visual images of the effects of the space environment on specific materials, systems and spacecraft in general. One can visually see the degradation of thermal blankets, meteoroid craters, outgassing discoloration, atomic oxygen erosion, etc.

The photographs published in this NASA Special Publication (NASA SP) will appear in black and white on the printed page and in high-resolution color images on a CD-ROM. An index to all (approximately 10,000) photographs will be published as a separate appendix. In addition to the photographs, the photo numbers, location, experiment number and title, the authors will prepare a materials list for each experiment tray as well as a brief discussion of the experiment. Scanning these photographs began during the summer of 1994, and the CD-ROM and SP should be available in 1995. The following text and photographs are an example of the entries in this NASA SP.

Heavy Ions In Space (M-0001)

Naval Research Laboratory

The objective of this experiment is to provide a deep survey of intensely ionizing particles in low earth orbit. The experiment used eight thick stacks of plastic track detectors mounted in two trays on the space facing end of LDEF. Plastic track detectors record charged particles by the trails of radiation damage they leave as they pass through the detector sheets. These tracks are revealed by chemical etching the detectors in the laboratory after flight. The stacks were made up of a unique arrangement of CR-39 and Lexan sheets. Seven of the eight modules were identical and used a honeycomb lid pressure cover. In the eighth module the fiberglass lid was replaced with four thin Kapton window pressure covers to provide a lower energy threshold to ion penetration.

Preflight (Figure 1)

The four modules including the one subdivided into quadrants are shown mounted in a 4-inch deep space facing end tray. The exposed surface of each detector is Chemglaze II A-276 white paint on the aluminized Kapton top layer of a multilayer thermal blanket. The frame around each of the four modules is a "Z" shaped aluminum structure covered with a silvered teflon film secured with 3M-Y966 acrylic tape. The 3M-Y966 tape on a silvered teflon film is also used to attach the multilayer thermal blankets to the module frames.

In Orbit (Figure 2)

This photo shows extensive damage to the thermal cover of each module. It appears the tape used to attach the thermal blankets to the structure failed in tension. When the bond joint released along two sides the tension was relieved and the remaining tape continued to hold the blanket. The outside painted surfaces that were white are now discolored and are a somewhat glossy brown. The gold colored material underneath the failed covers in the three full modules are the top sheets of lexan detector stacks held in place by the aluminum "Z" shaped struc-

ture. The dark brown discolored sections visible underneath the failed cover of the fourth module is also the top layer of detector sheets underneath support straps. A light discoloration is visible on the tray flange near the American flag.

Postflight (Figure 3)

This photo was taken prior to the experiment tray being removed from LDEF. The damaged thermal blankets were removed so the experiment tray protective cover could be installed prior to tray removal. The photo shows the thermal covers on all modules to be severely damaged. The paint on the top layer that was white prior to flight is now discolored and brown in color. The thermal blankets shrunk in flight due to thermal cycling causing the taped attachment to the structure to fail along two sides. The tape used to attach the blanket apparently failed in tension leaving portions of the tape on both the frame and the top layer of the blanket.

The thermal blankets on the three large modules have curled to expose the top Lexan layer of the detector stack beneath. The curled blankets that protected the four smaller modules now expose the 5-mil thick aluminized kapton pressure covers beneath.

The damaged thermal covers shown in the two tray quadrants on the right side of the photo reveal representative cross sections of the multilayer thermal blankets. The thermal blankets top layer is a 5-mil thick aluminized Kapton film painted with Chemglaze II A-276 white paint. The blanket core is constructed of approximately twenty two (22) layers of 1/4-mil thick perforated mylar film with aluminum vapor deposited on each side. A dacron mesh separator seen in the lower right quadrant is placed between each aluminized mylar layer of core material and also between the core material and the aluminized Kapton film used for the blanket top and bottom covers.

Heavy Ions In Space (M-0001)



Figure 1

Photo No.: KSC-384C-331/6
Photo credit: KSC 1/24/84
Digitized from dup. neg. L84-7187
Location: KSC SAEF II
Subject: Tray H12
Experiment: M-0001; Heavy Ions In Space

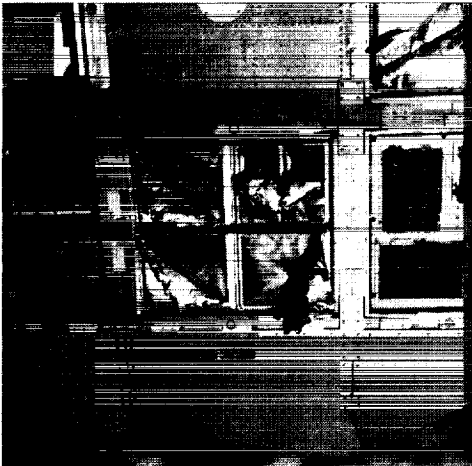


Figure 2

Photo No.: S32-75-067
Photo credit: JSC 1/12/90
Digitized from dup. neg. L90-10,373
Location: In Orbit
Subject: Tray H12
Experiment: M-0001; Heavy Ions In Space

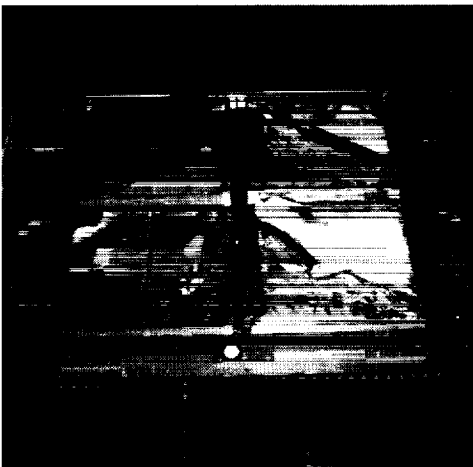


Figure 3

Photo No.: L90-1796
Photo credit: LaRC 2/6/90
Digitized from dup. neg. L90-1796
Location: KSC SAEF II
Subject: Tray H12
Experiment: M-0001

SPACE STATION

PRECEDING PAGE BLANK NOT FILMED

1271

LDEF'S CONTRIBUTION TO THE SELECTION OF THERMAL CONTROL COATINGS FOR THE SPACE STATION

Henry W. Babel
Senior Manager, M&P, Space Station Program
McDonnell Douglas Aerospace

ABSTRACT

The design of the Space Station presented new challenges in the selection and qualification of thermal control materials that would survive in low Earth orbit for a duration of up to 30 years. Prior to LDEF, flight data were obtained from Orbiting Solar Observatory (OSO) satellites, a number of Orbiter flights, and limited ground tests. The excellent data obtained from the OSO satellites were based on calorimetry and temperature measurements which were transmitted to Earth; these satellites were not recovered. For some of these flight experiments it was difficult to distinguish between changes due to contamination, atomic oxygen (AO), ultraviolet radiation (UV), particle radiation and the synergistic effects between them. The data from Shuttle flights were primarily focused on developing a better understanding of atomic oxygen (AO) effects. Although UV and AO were present, the relatively short duration of the Orbiter flights, about one week, was viewed as too short to show the effects from UV or possible synergistic interactions with AO and contamination. At the beginning of the program in 1989 there was no established design data base for AO resistant thermal control coatings for the Space Station. Then came the Long Duration Exposure Facility (LDEF). It provided the first long life data for materials exposed and recovered from space with a characterized environment. Post flight analysis proved data on the effects of contamination on optical properties in the ram (velocity) and wake directions and the erosion of Teflon and multilayer insulation (MLI) covers. The results from LDEF confirmed and, in some cases, modified the approach used for the Space Station, as well as helped to focus our development activities. These development activities resulted in a number of new technical solutions which are applicable to many spacecraft surfaces and missions. LDEF also showed the detrimental effects that could occur from silicone contamination, an issue that has not been completely resolved. An investigation was initiated in 1993 on the effects of silicone contamination and was continuing at the time this paper was prepared.

INTRODUCTION

The importance of identifying and qualifying long life thermal control coatings was established early in the evolution of the Space Station (SS) design. Satellite manufacturers have long been faced with the requirement to provide thermal control and have done so through a combination of thermal control coatings, multilayer insulation (MLI) blankets, louvers, heat pipes, and heaters. For many satellites the thermal control coatings were primarily used for radiator applications with the rest of the spacecraft enveloped in MLI blankets along with various other thermal control devices. For the size and limited life of most satellites, these design approaches were and are completely satisfactory.

However, early in the Space Station Program (SSP), it was decided that the structure would be exposed directly to the low Earth orbit (LEO) environment with a specified design life of 30 years. This decision was made because the MLI blankets and heaters would add additional weight and be power-intensive for long-life use, and because the blankets would impede astronaut access to hardware located on the structure. Figure 1(J30593S) shows a photograph of a typical satellite which is contrasted to the open and exposed truss structure of one of the SS segments.

J030593

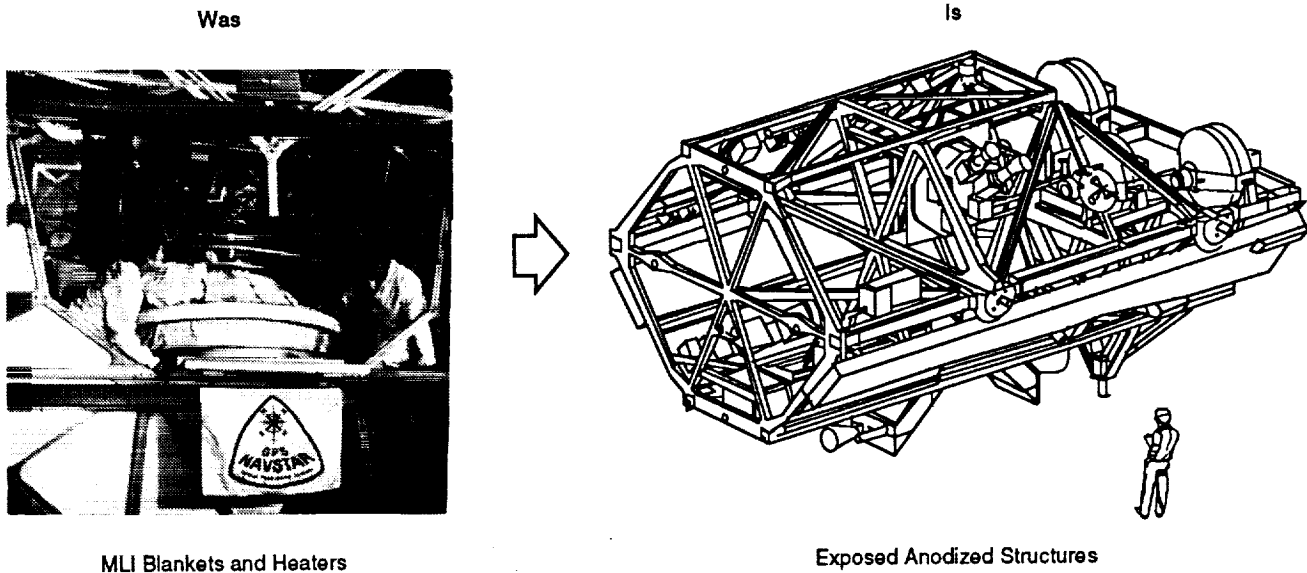


Figure 1. The open exposed truss structure contrasted to a typical satellite design where the structure is covered by MLI

For the SS, there are three general areas where temperature restrictions exist. The SS has a variety of different fluids that are required to be kept within both low and high temperature bounds. These bounds are different for each fluid. The SS reboost fuel needed to be protected from freezing, which, for the hydrazine monopropellant fuel originally planned for the SSF, occurred at around 35°F. The fuel also had an upper storage temperature limit to ensure proper performance at the time it reached the thrusters. There were requirements for the astronauts' glove touch temperature to prevent frost bite or burning from contacting a surface that was too cold or too hot. Initially, the touch temperature was used as a requirement but was later modified to account for the mass of the structure being contacted. To ensure proper functioning of the electronic hardware there are also minimum non-operating temperatures as well as maximum temperatures that should not be exceeded, usually occurring during system operation. Finally, temperature variations that would lead to unacceptable distortions of the structure had to be prevented. In selecting passive thermal control coatings, MDA had to consider each of these factors as relevant to the particular design as well as the natural and induced environmental exposure.

SPACE STATION THERMAL CONTROL DESIGN PRIOR TO LDEF RETURN

The exposed coatings on the segments have to survive a variety of different natural and induced environments. These include atomic oxygen (AO); ultraviolet radiation (UV); thermal cycling stresses during the approximate 90 minute day-night cycle; plasma coupling from the ionized residual

atmosphere present at the SS altitude (typically around 180 to 240 nautical miles); the electron, proton, and heavy nuclei radiation, and the environments induced by man, including debris impacts and contamination deposition. For the initial design of the SS, which had an orbit inclination of approximately 28.5° , analysis showed that the 30 year particle radiation was a maximum of 10^6 rads silicone. This radiation dosage was sufficiently low that it would not affect any of the structural materials or thermal control coatings with the possible exception of fluorocarbon materials. No further consideration or analysis relative to particle radiation effects was made for the coatings and structural materials. Because the structure was solar-exposed, any coating had to survive the 175,000 thermal cycles experienced in 30 years in addition to the AO and UV. A typical thermal cycle is shown in Figure 2.(J30591S) Be cautioned that this is only an example, as the temperatures for any particular structure will depend on the coating, conduction paths, materials, mass, orientation, and shading from other structures. In addition to the natural environments, the effects of impacts from man-made debris on coating spallation and damage and the effects of the natural environment on any contamination on the coatings also had to be taken into consideration.

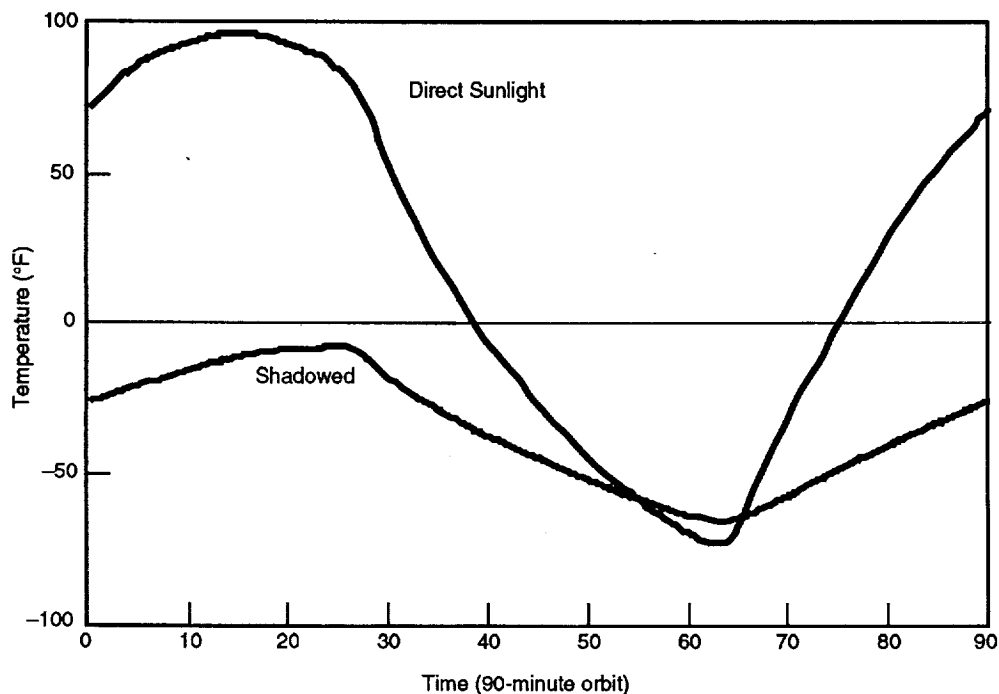


Figure 2. Typical thermal cycle experienced by a 2219 aluminum alloy truss element without shadowing from other structural elements

As for all hardware programs with defined schedules, a review was made of the available data and decisions were made based on those data augmented by additional ground and flight tests as schedules and funding constraints permitted. The SSP was started prior to retrieval and analysis of LDEF; the available data base at that time was limited. The flight data consisted of a number of Space Transportation System (STS) flights which were helping to develop an understanding of the AO effects on materials (References 1-3). In the mid 1980s there were no ground-based facilities operational that provided a good representation of LEO, although many groups were working on the development of such facilities. Plasma Ashers were primarily being used for AO screening purposes, but there was controversy among the specialists in the field as to whether they should be used since ashers do not accurately simulate several of the parameters of the LEO AO environment.

The other group of flight data had been obtained from controlled material experiments on satellites where telemetry was used to relay changes in temperature of the various samples back to Earth. Great care was exercised in these experiments to prevent contamination from masking changes induced by the

natural environment, primarily UV, AO, and at higher altitudes, particle radiation. Although the UV is the same at various orbits, particle radiation and AO are different for higher orbits. The data available from OSO orbits was of limited value for assessing the individual effects of UV, AO and particle radiation (References 4-6). Ground testing for UV had been primarily conducted in the longer wavelength, near UV region, with only a few studies using the shorter, more energetic wavelengths in the far/vacuum UV region.

The prevailing viewpoint was that most of the designs up to that point were not close to the temperature limits and did not require more rigor in the analysis or testing. This may well have been true for the satellite applications, but was not true for the SS where numerous design applications arose that were close to allowed temperature limits. There was almost a complete absence of data of synergistic effects between AO and UV, particularly in the presence of contamination. The lack of these data created high uncertainties in end-of-life properties that were selected for design. A summary of the knowledge base at the time design activities for the SS were initiated in the late 1980s is shown in Table 1.

Table 1. Summary of design and test information available at the beginning of the Space Station Program in the mid-1980's

Item	Status
AO	<ul style="list-style-type: none"> • Erosion model based on one week Orbiter flights extrapolated to 30 years • Metals and oxides didn't erode and all appeared to be acceptable except osmium and silver, which oxidized
UV	<ul style="list-style-type: none"> • Some satellite data • Ground tests data, primarily near UV • Most effects seemed to occur in first 1000 sun hours of exposure
AO + UV	<ul style="list-style-type: none"> •None except limited satellite data
Contamination + AO + UV	<ul style="list-style-type: none"> •No data
Plasma coupling	<ul style="list-style-type: none"> • No test data • Coating resistivity data used as an indicator • Data obtained in air with only a few materials tested in vacuum
Debris hits	Essentially no data on thermal control coatings
Optical properties	<ul style="list-style-type: none"> •Beginning of life—data available or easily obtainable for most coatings •End-of life—estimates based on limited data

The early configurations of the SS had composite truss tubes which required AO protection. The AO protection was provided by an aluminum cover. Chromic acid anodize had been selected to provide the desired optical properties. This selection was based on the ground test results in preparation for LDEF (Reference 7) which showed very little change in absorptance when exposed to UV. The literature data for UV effects on sulfuric acid anodized coatings was primarily for coatings with low absorptances. These coatings showed significant increases in absorptance after testing ranging from 0.1 to 0.2 (References 5, 6, and 8).

The composite tube baseline design prevailed to 1990, at which time a major restructuring of the configuration was made. An aluminum truss structure was selected for the baseline design which replaced the composite truss tubes. The use of ceramic coatings was rejected as being impractical for the large aluminum bulkheads and truss elements. The issue then was what type of coating should be

selected for the 2219-T851 truss materials. Anodic coatings were selected for study.

There were many other material areas in 1990 that had not been addressed, such as MIL covers. LDEF had been recovered during the time of the restructuring activity. From this point forward, LDEF influenced everything that was done for selecting environmentally exposed materials on McDonnell Douglas Aerospace (MDA) SS hardware.

INTEGRATION OF LDEF RESULTS

MDA contacted several of the principal investigators with trays on LDEF to obtain preliminary information that was being developed. A summary of this early information is shown in Table 2.

Table 2. Initial results obtained from LDEF

Material	Environmental Effects	Suitable for SS
Silicone Thermal Control Coatings	Contaminated LDEF; coatings darkened on wake side	No
Teflon	Erodes slowly, but faster than STS results	Yes, some orientations
MLI Kapton Cover	Completely eroded away	No
Other Organics	Erode unacceptably	No
Chromic Acid Anodize	Stable	Yes
Z-93	Stable	Yes

These results supported the judgments made based on the ground and flight data reviewed previously with one notable exception. Originally, silicone had been allowed, but based on the LDEF results, it was considered advisable to prohibit its use as a thermal control coating. Teflon also eroded faster than had been derived from the STS results, but this erosion rate could easily be taken into account by increasing the Teflon thickness. The 5-3/4 years that LDEF was in space thus provided the best information for extrapolating the expected condition after 30 years in space. The LDEF results confirmed our view that the outer surfaces of the SS should be either a metal, a metal oxide or other ceramic, or, for selected applications, fluorinated polymers such as Teflon. Based on these preliminary LDEF results, a set of ground rules were created and imposed on the effort being managed by MDA. These requirements and guidelines are listed in Table 3

Table 3. Ground rules and guidelines established for WP-2 hardware

Item	Ground Rules and Guidelines
Thermal Control Coatings	<ul style="list-style-type: none"> • Exposed surfaces—use a metal, a metal oxide or other ceramic, or in special cases, Teflon • Do not use any organics except Teflon • No silicone materials on exposed surfaces
	<ul style="list-style-type: none"> • MDA will develop an AO resistant outer cover
Lubricants	<ul style="list-style-type: none"> • Shield from AO and UV environments
Analysis	<ul style="list-style-type: none"> • Use LDEF results to calculate AO erosion including various angles of incidence to the velocity direction
Contamination	<ul style="list-style-type: none"> • Minimize use of all silicones • Include effects to determine end-of-life optical properties

There were no significant program reactions when these ground rules were established, except for lubricants. The responsible design engineers were not initially receptive to the additional weight associated with shielding all lubricated surfaces but eventually accepted this position.

MDA DEVELOPMENT ACTIVITIES AND RESULTS FOR ENVIRONMENTALLY EXPOSED MATERIALS

MDA's thermal design engineers requested that we provide nominal beginning-of-life (BOL) properties with guaranteed tolerance limits. After due consideration, we selected a 95% confidence level, i.e., plus and minus two standard deviations. This meant that the reproducibility of each of the processes selected had to be established. In addition, the thermal designers required that an estimate be provided of the end-of-life (EOL) optical properties, both nominal values and tolerances. The latter required evaluation of both natural environmental effects as well as contamination effects. Again, LDEF was a very important source of data to help make these assessments.

Anodizing

Although little data were available from LDEF for sulfuric acid anodize and none for 2219 aluminum, the use of anodic coatings in general was judged as the right approach. No optical property data existed for either chromic or sulfuric acid anodized coatings when this effort was initiated for this alloy. The initial focus of our activities was to develop controlled optical properties for the 2219-T851 aluminum truss structure. Although it was not a common aerospace practice to chromic acid anodize this alloy, studies were conducted on both chromic and sulfuric acid anodizing. The major differences in optical properties resulting from these two processes is illustrated in Figure 3. The optical properties of chromic acid anodizing (CAA) can be varied over a wider range than sulfuric acid anodized (SAA) surfaces, but CAA requires greater process control to ensure repeatability to obtain the desired optical properties. During this time period there was a great deal of discussion of the plasma coupling effects because of the voltage potential between the SS and the surrounding plasma. This potential difference was 140 volts. Limited ground test results indicated that the break down voltage of CAA was less than 140 volts while that of SAA was significantly higher than 140 volts. Based on these results and the processing studies conducted, SAA was selected as the baseline. Arbitrarily, the limit that the absorptance could increase at the EOL was set at 0.2 which was to account for environmental and contamination effects. Under laboratory conditions, short wave length UV (VUV) exposure of uncontaminated sulfuric acid anodized samples resulted in no change in absorptance although a small increase occurred after AO exposure. This was in contrast to the nonstructural, low absorptance aluminum alloys that had been tested previously which showed substantial increases in absorptance when exposed to VUV.

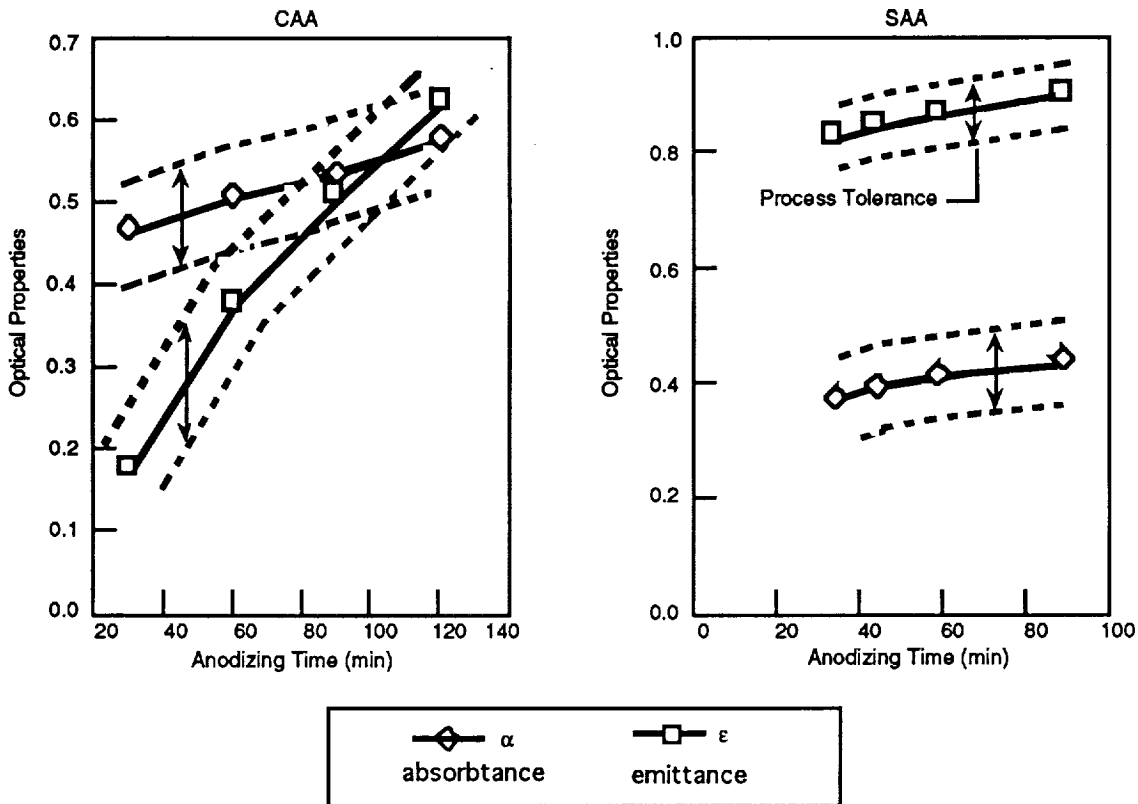


Figure 3. Difference in optical properties of CAA and SAA as a function of anodizing time

Silicone contaminated SAA 2219-T851 samples were exposed to VUV under laboratory conditions. The samples exhibited no changes in optical properties after exposure. The results were contrary to expectations since the CAA contaminated samples on LDEF had shown an increase in absorbance. After test of the SAA contaminated samples, surface analyses were conducted which verified the presence of silicone, but the amount of silicone present was not determined. The exposure tests were repeated and the same results were obtained. The thickness of the initial contamination layer was slightly less than 4000Å and only one type of silicone oil was used as a model material (Reference 9). Subsequently it was learned that some silicones will evaporate when placed in a vacuum for several hours. Since in MDA's tests, the silicone was first deposited followed by UV exposure, it is conceivable that the silicone evaporated prior to being fixed to the surface in the VUV exposure test. The tests are scheduled to be repeated with UV radiation of the sample surfaces during contamination deposition. The results of this test are expected to better model the exposures that can be expected in space.

MDA's thermal designers also requested that stable (optical properties not altered by the environments) coatings be provided that also had an absorbance/emittance ratio of approximately one. A black coating was judged most likely to provide the required properties. The LDEF results also contributed to MDA focusing on anodizing processes with and without inorganic black dyes. The process finally selected was a one-step anodizing process known as the "Duranodic process," a special type of SAA process. The trade studies and evaluations conducted that led to this selection are reported in Reference 10. BOL tolerances were tighter than for standard SAA. Contamination deposition and UV exposures showed that the absorbance of this coating was not changed just as had been found for the standard SAA.

The results from the anodizing studies showed that commercial sulfuric acid anodizing processes including the Duranodic™ process provided consistent, reproducible results. Specialized processing controls were not required. In addition, silicone contaminated samples showed no change in absorptance after VUV exposure, but as already mentioned there are reservations as to the validity of the results and additional testing is being conducted. The results obtained to date are shown in Table 4.

Table 4. Environmental exposure of clean and silicone contaminated 2219 and 7075 aluminum

Alloy	Coating and Condition	Exposure	Results
2219-T851	SAA, Clean	Near UV	No change
		VUV	No change
		AO	$\Delta\alpha = -0.03$
	SAA, Contaminated $\leq 4000\text{\AA}$	VUV	No change
7075-T7351	SAA, clean	AO	No change
		VUV	$\Delta\alpha = +0.04$
7075-T6 clad	Black SAA, clean	VUV	No change
	Black SAA, Contaminated 375A - 4000A	VUV and AO	No change

Z-93

The original baseline for the large radiators was 5-mil thick embossed silver-Teflon. With the higher Teflon erosion rates experienced on LDEF, it would have been necessary to increase the Teflon thickness from 5 to 10 mils. This led to a trade study comparing 10 mil silver-Teflon with Z-93. Because of the 1200 pound weight savings, and the excellent performance of Z-93 on LDEF, Z-93 was selected as the new baseline for the active thermal control radiators as well as for many smaller, passive radiators.

For weight economies, MDA designers selected 2219 for the approximately 70 passive radiators rather than 6061 aluminum, the latter being the substrate most commonly used for Z-93. Since 2219 has poorer corrosion resistance, an evaluation was made of whether Z-93 could be applied to anodized aluminum, a process which had not been seriously studied previously. The results were highly successful and the baseline was changed from applying Z-93 to bare 2219 to applying Z-93 to anodized 2219 aluminum. The application of Z-93 to anodized aluminum is now generally accepted. A patent was awarded to Henry W. Babel and Huong G. Le for this concept, Patent No. 5,296,285, entitled "High Emittance, Low Absorptance Coatings."

The margins associated with thermal activities required a high confidence in the optical properties used. Measurements of the absorptance of Z-93 by various instruments led to the understanding that significantly different results are obtained depending on the instrument. A comparison of three instruments is shown in Table 5.

Table 5. Comparison of Z-93 absorptance measurements with three different instruments on the same sample

Measurement Device	Absorptance Value
Gier-Dunkle MS-251	0.101
Spectrophotometer, Perkin-Elmer Lambda 9	0.134
Surface Optics Spectrophotometer and Infrared Reflectometer	0.169

The results using an infrared reflectometer that measures reflectance from 1.6 to 25.0 microns showed that there is a large drop in reflection between 2500 and 3000 nanometers and the reflection remains low above 3000 nanometers. Spectrophotometers used to measure solar absorptance have a cutoff at or below 2500 nm. The true thermal behavior of Z-93 is best approximated by the value 0.169 instead of 0.12 or 0.134. The value 0.169 was used in conjunction with tolerances in our thermal design analysis. The differences described above had not been reported previously in the open

literature. Most other coatings tested did not exhibit such differences because their reflectance did not change as dramatically as Z-93 in this region, in which there is still a significant portion of solar energy present.

MLI Cover

Post flight analysis of LDEF has provided MDA and the technical community in general with an understanding of the effects of long space exposure on MLI. The results showed that the blankets performed well after multiple small debris hits. Also the blankets continued to function even after the cover had been eroded away. Double aluminized layers were not eroded away, although significant undercutting at debris hits was evident. The conclusion that could be drawn was that MLI would be satisfactory for the Space Station Program and that the blankets could be made more durable if an AO resistant cover was developed.

The cover not only had to be AO resistant, but in addition, the thermal designers wanted a light-block (zero transmission of solar radiation) and optical properties similar to that of Beta™ cloth, i.e., high emittance and low absorptance. After conducting various screening tests, PTFE Teflon-impregnated Beta cloth was selected with vapor deposited aluminum on the back side. The tight weave used in fabricating the Beta cloth helps protect the underlying Teflon from AO erosion. The Beta cloth is to be woven without the use of a silicon or other sizing material that darkens under UV exposure. The trade studies conducted are reported in Reference 11.

To make the entire blanket AO resistant, designs were developed to protect the hook-and-pile (Velcro™ type) attachment favored by the astronauts, and MDA learned to machine sew with glass,

but had to hand sew with quartz threads in exposed areas. All these features are shown in the blanket schematic shown in Figure 4.

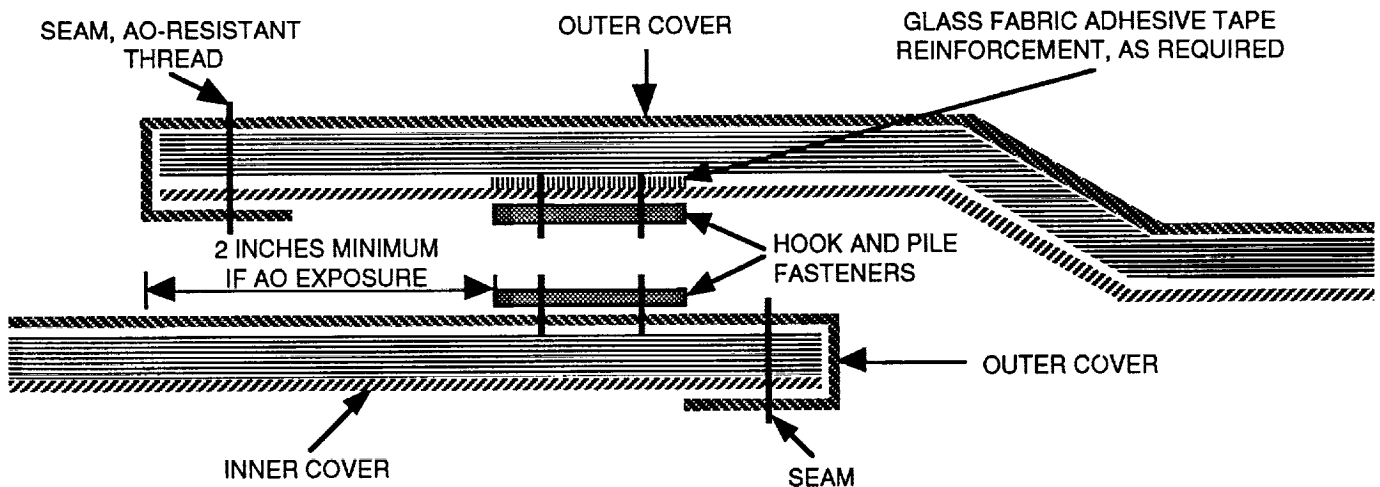


Figure 4. MLI blanket design to protect AO susceptible materials

BENEFITS THE SSP DERIVED FROM LDEF RESULTS

The results from LDEF provided a great service to the SSP. Significant economies were realized because trade studies could be limited and focused. With today's high level of technology, there are often many alternatives to consider when developing a design solution. This focus also resulted in MDA re-examining a number of commonly held perceptions and discovering that test data were lacking to support these perceptions. In a number of cases it was later shown by test that approaches previously not extensively evaluated were viable. These efforts have directly contributed to advancing the state-of-the-art of thermal control coatings for long life spacecraft. Those discussed in this paper are summarized below.

1. Z-93

a. MDA showed that the bond integrity of Z-93 to anodized aluminum was excellent.

Z-93 had not been applied in production applications to anodized aluminum.

b. MDA showed that different measuring instruments used on Z-93 result in different values of absorptance. The absorptance value to be used for design is higher than that used for previous designs with Z-93.

2. Sulfuric acid anodize

a. MDA showed that reproducible optical properties within acceptable tolerance ranges are obtainable with commercial processes. Conventional and black coatings were qualified for Space Station use.

b. MDA's ground tests results to date have shown that the absorptance of structural alloys did not increase after contamination with one model silicone material, but there are reservations whether the test procedures could have produced erroneous results. Additional testing is scheduled to better model the exposures that can be expected in space.

3. MDA developed and qualified AO resistant MLI covers with light blocks and developed MLI designs using AO resistant threads and AO protected attachment techniques.

4. MDA is continuing to develop a data base on the response of thermal control coatings to UV exposure after receiving deposits of various amounts and different kinds of contaminants.

It was found that many of the ideas above and others inspired by LDEF were sufficiently novel that patent applications have been made. One has been issued and five others are still pending.

CONCLUSIONS

At the time this paper was prepared, the Space Station configuration was being restructured to include the Russian hardware. The work described here will have SS applications independent of the final configuration selected. This technology represents basic building blocks that can be used for the SS and many other future spacecraft.

REFERENCES

1. Leger, L.J., Spiker, I.K., Kuminez, J.F., Ballentine, F.J., and Visentine, J.T., STS-5 LEO Effects Experiment: Background, Description, and Thin Film Results, AIAA paper #83-2631, Nov. 1983.
2. Leger, L. J., Visentine, J. T., and Kuminez, J. F., Low Earth Orbit Atomic Oxygen Effects on Surfaces, AIAA Paper #84-0548, Jan. 1984.
3. Atomic Oxygen Effects Measurements for Shuttle Missions STS-8 and 41G, NASA TM 100459, Vol I-III, Sept 1988. Compilation of papers; compiled by J. T. Visentine.
4. Triolo, J.J., Heany, J.B. and Hass.G, Coatings in Space Environment, SPIE Vol 121, Optics in Adverse Environments, 1977, pp 46-66.
5. Millard, J.P., Results from the Thermal Control Coatings Experiment on OSO-III, AIAA Paper No 68-794, AIAA 3rd Thermophysics Conference, Los Angeles, 24-26 June 1968.
6. Millard, J.P. and Pearson, Jr., B.D., Optical Stability of Coating Exposed to Four Years Space Environment on OSO-III, AIAA Paper 73-734, AIAA 8th Thermophysics Conference, Palm Springs, 16-18 July 1973.
7. Duckett, R.J. and Gilliland, C.S., Variable Anodic Thermal Control Coatings on Aluminum, AIAA-83-1492, AIAA 18th Thermophysics Conference, Montreal, Canada, 1-3 June, 1983.
8. Weaver, J.H, Effects of Vacuum-Ultraviolet Environment of Optical Properties of Bright Anodized Aluminum, AFML-TR-64-355, January 1965.
9. Jones, C.A., David, K.E., LeVesque II, R.J, and Babel, H.W., Environmental Effects on Passive Thermal Control Materials of the Space Station Freedom, Paper IAF-93-1.4.223, 44th IAF Conference, Graz, Austria, October 16-22, 1993.
10. Levesque, R.J., Ho, M.M., Vickers, B.D., and Babel, H.W., Black Anodize as a Thermal Control Coating for Space Station Freedom, AIAA Paper 92-2160 and MDC Paper No. 91H1111, Dallas, Texas, 16-17 April 1992.
11. Smith, C.A., Hasegawa, M.M., and Jones, C.A., Space Station WP-2 Application of LDEF MLI Results, presented at the LDEF Materials Results for Spacecraft Conference, Huntsville, Alabama, 27-28 October 1992.



SPACE STATION PROGRAM STATUS AND RESEARCH CAPABILITIES

Alan C. Holt
Space Station Program Office
NASA Johnson Space Center
Houston, TX 77058
Phone: 713-244-8316; Fax: 713-244-8294

INTRODUCTION

Space Station will be a permanent orbiting laboratory in space which will provide researchers with unprecedented opportunities for access to the space environment. Space Station is designed to provide essential resources of volume, crew, power, data handling and communications to accommodate experiments for long-duration studies in technology, materials and the life sciences. Materials and coatings for exposure research will be supported by Space Station, providing new knowledge for applications in Earth-based technology and future space missions.

Space Station has been redesigned at the direction of the President. The redesign was performed to significantly reduce development, operations and utilization costs while achieving many of the original goals for long duration scientific research. An overview of the Space Station Program and capabilities for research following the redesign is presented below. Accommodations for pressurized and external payloads are described.

SPACE STATION RESEARCH CAPABILITIES

Space Station has extensive research capabilities for pressurized payloads and unpressurized or external payloads. Resources for the payloads will include power, ranging from 10 kW in year 1998 to 50 kW in 2000, 2 crew members dedicated to payload operations in 1998 and 4 crew members in 2002, and data downlink capability of 43 megabits per sec in 1998 and 57 megabits per sec in 2001. Payload accommodations range from 13 internal, standard laboratory payload racks or mounting locations in 1998 to 33 standard payload racks in 2001, and 4 dedicated, external, attached payload sites on the station truss structure and 10 sites on the Japanese Experiment Module Exposed Facility in 2000.

The United States, European Space Agency, Japan and Russia will all provide pressurized laboratories with the capabilities for the operation of payloads which are equivalent to (or which exceed) those capabilities available for Spacelab payloads. The U.S. Lab will have 13 payload racks available for payloads early in the Space Station assembly sequence (late 1998). These International Standard Payload Racks (ISPRs) have standard interfaces for data, power and cooling which enable them to be easily located in any payload rack mounting location in the U.S., ESA and Japanese Labs. Each ISPR will be capable of accommodating up to 1400 lbs. of payload.

Three U.S. Lab payload racks will provide 12 kW of power and cooling, five payload racks will provide 6 kW of power and cooling and five payload racks will provide 3 kW of power and cooling. Nitrogen is plumbed to all of the payload rack locations. Each payload rack can transmit 43 megabits of data per second to the Ku-band downlink

system, can transmit 100 megabits per second between payloads in different racks and receive and output an analog video signal (which is digitized for downlink in the video broadband signal processor). A lower rate data transmission capability of up to 10 megabits per second is also available from each rack. Nine of the thirteen payload racks have access to a vacuum exhaust line to reach 10⁻³ torr and a vacuum resource line to maintain that vacuum level.

The ESA Attached Pressurized Module (APM) and the Japanese Experiment Module (JEM) have similar International Standard Payload Rack (ISPR) rack capabilities. The ESA APM has five payload racks with 6 kW of power and cooling and five payload racks with 3 kW of power and cooling. Nitrogen is plumbed to all of the payload rack locations. Five of these payload racks will be available for U.S. payloads. Each of these racks will have access to a high rate data line capable of transmitting up to 43 megabits of data per second to the KU-band downlink system. The Japanese Experiment Module has four payload racks with 6 kW of power and cooling and six payload racks with 3 kW of power and cooling. Nitrogen is plumbed to all of the payload rack locations; in addition, four payload racks also receive carbon dioxide and six payload racks receive helium and argon. Five of these payload racks are available for U.S. payloads. Each of the ESA APM and JEM payload racks have analog video input and output capabilities. Ten of the ESA APM payload racks and six of the JEM payload racks have vacuum exhaust and vacuum resource lines. A JEM Experiment Logistics Module will also be provided and will be located on top of the JEM. The racks in this module will be used for storage.

Russia will provide three Research Modules with the capability to accommodate the equivalent of about 10 double racks of payloads. The racks in these modules will not be built according to International Standard Payload Rack (ISPR) capabilities. The power and data transmission capabilities of these payload racks have not yet been defined. A Russian systems design review in the fall of 1994 should provide most of this data.

To facilitate Earth observations, an optical window is planned and will be installed in the ESA APM or in the U.S. Lab. The window will allow photography and other sensing apparatus to be used inside a pressurized area, which facilitates the removal of film, the changeout of instrumentation and routine maintenance. Access to an optical window also provides a capability to observe and assess unexpected events or targets of opportunity, such as hurricanes, earthquakes, large-scale flooding, and other world events.

A centrifuge of sufficient size to accommodate small animals will also be provided in 2002. Laboratory support equipment (LSE) will be provided to support the centrifuge and other payloads. The LSE will include a life sciences glove box, a microgravity science glove box, refrigerators and freezers, microscope, tools, etc.

EXTERNAL PAYLOAD ACCOMMODATIONS

Both the U.S. and Japan are providing unpressurized, external attached payload capabilities. The U.S. is providing six sites on the truss for single, large attached payloads or multiple small to medium sized payloads. Each site has a 15x6x10 ft envelope capability - 4 sites on segment S3 and 2 shared sites on segment P3 (shared between unpressurized logistics carriers (ULCs) and attached payloads). The attached payload sites have viewing directions in the zenith, nadir, ram (into the velocity vector) and wake (opposite to the velocity vector). Each U.S. attached payload site will provide up to 3 kW of power, a high rate link capability to support the transmission of up to 43 megabits of data to the Ku-band downlink system and a MIL-STD-1553B low rate data capability (200 kilobits per second). Each site can accommodate a single payload of up to

11500 lbs. or multiple payloads up to that amount using a multiple payload mounting structure.

Japan will provide an Exposed Facility (EF) with 10 sites for attaching small to medium sized payloads. Each EF attached payload site provides 3 kW of power and active cooling and low rate data up to 1 megabits per second of data from each site. Each site can accommodate 1100 lbs of payload. Two of the ten sites will provide 6 kW of power and eight sites will provide high rate data (up to 43 megabits per second) and analog video output.

The Space Station has a manipulator arm provided by Canada which can be used to install (and remove) external or attached payloads on the truss. The manipulator can also be used to temporarily position sensing packages at various station sites. These packages can remain attached to the manipulator if sensing or observing time for a package is relatively short. The Japanese Experiment Module has its own manipulator arm and an equipment airlock which provides the capability to retrieve equipment from the Exposed Facility external sites (or install equipment on the sites) and bring it into the pressurized environment in the module. Thus, materials processing samples, film or exposed samples and materials can be retrieved without the use of EVA and can be studied in near-real time.

RESEARCH PLANS AND PROGRAM STATUS

The current Space Station assembly sequence results in the U.S. Lab being installed and checked out for payload operations in late 1998. The first Utilization Flight (UF), a flight dedicated to carrying up experiment equipment and resupplies, is scheduled for early 1999. After that first utilization flight, extensive payload operations in the U.S. Lab can be initiated. The U.S. and the other partners will have percentage allocations of the onboard payload accommodations (payload racks and attached payload sites); resources such as power, crew time and data; and Shuttle and other transportation services.

The U.S. payload accommodation and resource allocation will be sub-allocated among the NASA/U.S. users such as the Office of Life and Microgravity Sciences and Applications (OLMSA), Office of Advanced Concepts and Technology (OACT), Office of Mission to Planet Earth (OMPE), Office of Space Science (OSS) and the Office of Space Flight (OSF). Each of these disciplines will have an opportunity to sponsor one or more payloads which will be flown to the station and installed in payload racks or on attached payload site in 1998 or 1999. The truss attached payload capabilities will be available beginning in late 1999.

The first Russian Research Module will be installed at the station in late 1998; the Japanese Experiment Module (JEM) will be installed in early 2000, the JEM Exposed Facility (EF) will be installed in late 2000, the ESA Attached Pressurized Module (APM) will be installed in early 2001 and two additional Russian Research Modules will be installed in late 2001. The payloads installed in these modules and on the attached payload sites will be brought up primarily on the Shuttle in the Mini-Payload Logistics Module (MPLM), which can carry up to 8 payload racks at a time, and in mid-deck lockers for payloads requiring late access (or installation) prior to launch (Launch-40 hours).

The station will have the capability to support a permanent crew of 3 from mid-1998 on. A capability to support a permanent crew of 6 will be available in mid-2002. Six

dedicated Utilization Flights are planned from early 1999 through early 2002. Some experiment logistics and resupply will also be able to be accommodated in mid-deck lockers on other Shuttle assembly flights or in unused volume in the cargo bay (assuming mass and center-of-gravity constraints are met).

The U.S., Canada, European Space Agency and Japan have all signed Inter Governmental Agreements (IGAs) and Memoranda of Understanding (MOUs) which provide guidance and direction to this major space infrastructure partnership. NASA and the partners will soon begin extensive negotiations with Russia which will result in a Russian MOU and a modified set of other partner MOUs. With the MOU guidance and a description of the station payload accommodations, station payload resources and transportation capabilities to the station, a long-term international plan for the utilization of the station will be developed (the Consolidated Operations and Utilization Plan).

CONCLUSION

The Space Station will have a wide range of research accommodations and resources. With the increased payload power capabilities, ten times greater than Spacelab and five times greater than the Russia MIR space station, and extensive opportunities for attached external payloads, Space Station will provide excellent opportunities for innovative and challenging research in new and improved materials, new applications of materials and advanced technologies in many key space and ground systems areas.

The International Space Station Alpha (ISSA) will enable significant research in a broad range of scientific and technical disciplines. It will provide our civilization with a significant next step towards the exploration and settlement of our moon and Mars and eventually our planetary neighborhood. ISSA will provide a means for many nations to unite together in a challenging and exciting, space technology and research endeavor - the benefactors will be all of mankind.

SPACE STATION AS A LONG DURATION EXPOSURE FACILITY

Adrienne Folley
McDonnell Douglas Aerospace
Space Station Division
Huntington Beach, CA 92647
Phone: (714) 896-3311 x70155
/Fax: (714) 896-2937

Jim Scheib
McDonnell Douglas Aerospace
Space Station Division
Huntington Beach, CA 92647
Phone: (714) 896-3311 x60457
/Fax: (714) 896-1935

ABSTRACT

There is need for a space platform for experiments investigating long duration exposure to space. This platform should be maintainable in the event of a malfunction, and experiments should be easily recoverable for analysis on Earth. The International Space Station provides such a platform.

The current Space Station configuration has six external experiment attachment sites, providing utilities and data support distributed along the external truss. There are also other sites that could potentially support long duration exposure experiments. This paper describes the resources provided to payloads at these sites, and cites examples of integration of proposed long duration exposure experiments on these sites. The environments to which external attached payloads will be exposed are summarized.

INTRODUCTION

Many materials and systems used in Space Station design are applications from LDEF results and other unmanned missions. The Space Station program is currently planned for a 10 year operational lifetime with the option of extending it to 15 years. As a result, the station has the potential to be a valuable resource for long duration exposure data.

This paper will discuss the current Space Station design, as it relates to space exposure science, and the importance of early data collecting in maximizing science return capabilities of the station. The accommodations for space exposure experimenters will be presented, including the baseline attached payload sites and the resources provided to users, and an Express Pallet concept, similar to the Space Shuttle's Get Away Special program.

1.0 SPACE STATION TECHNOLOGY EXPERIENCING LONG DURATION SPACE EXPOSURE

Many of Space Station's designs are applications of LDEF results, and have the potential to be valuable resources for long duration exposure data in an active spacecraft application. The environments of an active spacecraft are more complex and will impose different effects than a passive space platform on the exposed technologies applied. Early measurement and experimentation with these station-unique designs would be valuable to assessing life limits and planning maintenance approaches to maximize performance of the Station's systems and extend its lifetime.

Fig. 1 indicates the designs for which there is interest in measuring environmental effects and which will be discussed in this paper. Alternate design concepts are still being evaluated at the time this paper was published, and the figures presented are only examples. No matter what configuration may be decided upon, many elements, common to all configuration concepts, will require protective material coatings to preserve longevity by passively controlling thermal environments. Material coatings are susceptible to optical property degradation due to atomic oxygen (AO) and ultraviolet (UV) radiation sensitivity, which can result in degradation of system performance. Among those used on Space Station are:

- Sulfuric Acid Anodized aluminum structure. The anodize keeps the truss in a medium temperature range, required for EVA operations.
- Yellow Dyed Anodize on EVA handrail. This anodize provides medium-range temperatures and visibility to EVA astronauts.
- Z-93 inorganic zinc oxide based white paint¹. This thermal control paint is used on the Active Thermal Control System (ATCS) radiator panels for its low absorptivity and high emissivity.
- Silver Teflon thermal control tape. This is used on the radiators of the mobile transporter for its low absorptivity and high emissivity.

Micro Meteoroid/ Orbital Debris shielding is used on several critical Space Station elements to protect them from damage caused by micro meteoroids and by orbital debris impacts. The standard design for these elements is the aluminum Whipple shield. This will be applied for protection of the ATCS pump modules and ammonia tank modules, the pressurized mating adapter, airlock and the cryo tanks. Nextel[®], an aluminum boro-silicate fabric manufactured by 3M, is under consideration for shield design. It is much lighter and can defeat a 30% larger particle than an aluminum shield of similar design². Space Station offers the opportunity to develop advanced shielding concepts such as Nextel[®].

Space Station systems are yet another area where the LDEF program has influenced the design. LDEF showed good performance of fiber optic systems in the space environment, and recoverability of performance after an inactive state. Fiber optic systems offer data management systems increased data traffic over traditional twisted shielded pairs and will therefore be used for the high level of expected payload data and communications. The greatest losses of these systems are in the connections. However, McDonnell Douglas Aerospace (MDA) has developed several advanced connections designed to minimize signal loss, including a hermetically sealed

¹ Manufactured by the Illinois Institute of Technology Research Institute (IITRI)

² IRAD report MDC 91H0515, "Test Results for Alternative Orbital Debris Shield Concepts."

dual-side connector for the pressurized volumes. The glass fibers, light-emitting diodes and the connections are considered together as an interdependent system.

2.0 SUMMARY OF SPACE STATION ENVIRONMENTS

The Space Station is planned for a 190-250 n-mi orbital attitude similar to that of LDEF. The environments it will experience are similar to LDEF in some respects, yet much more complicated in others due to the inherent activity involved in an active, manned spacecraft. The effects of the natural environment on system performance will be compounded by contamination contributed by Station activities.

AO flux and solar radiation levels are expected to be slightly different from that experienced on LDEF. Radiation levels increase with orbital inclination, and Space Station may be orbiting at the 51.6° inclination in order to take advantage of Russian contributions to the program. LDEF flew at a 28° inclination, where there is comparatively less radiation exposure. In addition, Space Station will be periodically reboosted to maintain a nominal 250 n-mi orbit for most of its flight, whereas LDEF started at the same altitude as Space Station and drifted lower over time. This results in less AO flux for Station than that experienced on LDEF, but the additional exposure to AO from a longer life in orbit may negate this benefit.

The Space Station will fly in a Local-Vertical-Local-Horizontal (LVLH) orientation, which provides constant viewing directions not only to users, but also to various exposed station surfaces. This requires specific elements to be designed with micro meteoroid and orbital debris protection. This is key, since Space Station will experience increased orbital debris density over LDEF due to the increased space satellite traffic a decade later.

The Space Station, in contrast to LDEF, is an active spacecraft with regular interfaces with the Space Shuttle Orbiter and other activities which affect the design. The program has responded, where practicable, to minimize the contamination of exposed surfaces resulting from these activities. The responses are summarized as follows:

- Orbiter proximity operations, including mating and demating to Station, involve the Orbiter Reaction Control (RCS) System thrusters to control its trajectory. The emitted propellant is directed toward Station hardware, resulting in deposition buildup on surfaces. Of more critical concern, however, are the RCS thruster plumes directed at the large Solar Arrays, threatening structural damage. To avoid such a catastrophic event, the Solar Arrays will be oriented in a "feathered" position to the RCS jet stream, during orbiter proximity operations, minimizing loading on the array mast.
- Plasma Contactors will be installed on the center Truss Assembly to significantly reduce the ion sheath impedance and related high structure floating ground negative voltage potential occurring as the Space Station travels through the ambient plasma. This is accomplished by emitting electrons to reduce the Ion sheath impedance thereby reducing, or eliminating, the negative voltage potential on the Space Station structural members.
- Periodically, waste fluids will be vented from the internal environments. These fluids may potentially stick to external surfaces or cause ice bridges between elements. This problem can be alleviated through proper alignment of the vents in the design process.

Some operations' contamination effects may be minimized with planning, but not all operations can be controlled. The Russian Tug is planned for reboost and it is directed aft of the Space Station. However, in the space vacuum, the exhaust plume tends to expand and curl around nearly 180° back on itself; so some contamination to surfaces is expected, and must be considered in the overall assessment. Also, outgassing from all station hardware contributes to contamination of Station surfaces.

3.0 ENVIRONMENTAL IMPACTS ON SPACE STATION BASELINE DESIGN

Contamination can be reduced by careful planning, as discussed above, but not eliminated. It will compound the problems imposed by the natural space environment. Solar radiation, extreme thermal cycling, AO and contamination all work together to degrade system performance of Space Station elements. The synergistic effects of these degrading influences need to be evaluated as follow-on experiments from pure test article to application. Program requirements specify the contamination limit from all sources to be 100 Å deposition/year³.

Table 1 presents the impacts of the space environment on sensitive materials and systems used in the Space Station design. The materials were chosen based on LDEF experience and data from other unmanned programs.

Table 1: Environmental Impacts on Space Station Baseline Design

Exposed Material	Environmental Concerns
Sulfuric Acid Anodize	UV Radiation, Spacecraft Contamination, Resulting in Absorptance Increases
Yellow Dyed Anodize	AO or UV can Bleach the Coating
Silver Teflon Tape	AO Erodes the Teflon. Contamination Could Affect Optical Properties. May see Thermal Expansion Difficulties with the 10 mil Tape.
Z-93 Paint	Contamination, Impairing Optical Properties
Optical Fiber Systems	Solar Radiation Darkening Glass, Resulting in Signal Loss.
Nextel® Shielding	Upon Impact, Nextel® Sheds Particulates, Posing Potential Hazard to Crew.

- Sulfuric Acid Anodize, used on the truss to maintain medium range temperatures, is UV sensitive, and its optical properties respond by increasing absorptance. This effect is compounded by the contamination resulting from proximity operations, system vents and outgassing of surrounding elements.
- Yellow Dyed Anodize on EVA handrails will become bleached when exposed to AO or UV, thereby reducing visibility and affecting its ability to maintain medium range temperatures.

³ SSP-30426, Rev. B, July 1991, "Space Station External Contamination Control Requirements."

- Silver Teflon thermal control tape is required on the mobile transporter radiators due to the low absorptivity and high emissivity. AO degrades the Teflon in the tape, damaging its integrity. Contamination could impair the optical properties of both these elements, affecting their radiative performance. In addition, the silver Teflon tape has never been flown using a 10 mil thickness (5 mil thickness has substantial flight experience): the extreme thermal cycling of the space environment could cause cracking.
- Z-93 white paint is used on the large thermal control radiators for its low absorptivity and high emissivity. Contamination buildup on these large surfaces could impair the optical properties of the paint, reducing heat radiation efficiency.
- Inactive optical fiber systems darken due to solar radiation, resulting in signal loss. However, performance fully recovers when reactivated. Fiber optic communications on Space Station will be active and inactive, as mission requirements demand. Although system performance recovers once the system is activated, the long-term effect of these cycles is not known and warrants measurement. The greatest loss is expected in the terminations due to contamination upon assembly, many of which are designs unique to Space Station.
- Space Station offers the opportunity to develop advanced shielding concepts to defeat micro meteoroids and orbital debris. Nextel® is one option as a replacement for aluminum in the shield design. Although Nextel® can defeat larger particles than a similar aluminum shield design, it sheds particulates into the immediate environs upon impact and these glass particles can obstruct viewing and find their way into the pressurized modules, posing a health hazard to the crew. Teflon coating is an option currently under consideration for reducing the particulate shedding.

All the above are good candidates for early experimentation to determine performance stability and degradation over time. For example, several small material samples of the Sulfuric Acid Anodize, Yellow Dyed Anodize, Z-93 paint and Silver Teflon thermal control tape could be pre-integrated into the structure and deployed. Partial retrieval at six month intervals to measure progressive effects over time would augment the two-point data - initial condition and final condition - developed by LDEF and other unmanned experiments. . Optical fiber systems can be tested by appropriate instrumentation or by a small, cycleable, closed, active system pre-integrated into the structure. A sample of Nextel® shielding, with and without Teflon coating, would be valuable to assess its performance life and particulate shedding. Additionally, dopants, or coloring agents, can be added to the Nextel fabric which give it various thermal control properties, depending on the dopant used; and samples of these dopants in Nextel® should be tested in the space environment. Early data gathering and assessment will increase the accuracy of Space Station's life certification and maintenance scheduling, which could lead to pre-planned product improvements.

4.0 EARLY EXTERNAL EXPERIMENTATION OPPORTUNITIES

There are opportunities for pre-integrating experiments into the truss early so that experimental data may be derived as early as possible, making Space Station a working laboratory for external science upon deployment, and maximizing Space Station science return. Figure 2 indicates potential attachment sites that may be used in the earliest assembly stages. The Russian Universal Docking Joint and the Nadir port of Node 2 are reserved for additional pressurized modules to be manifested a few years into the Station program, and are therefore available for pre-integrated payloads prior to that time. The Russian Tug is a modified Kvant vehicle which has 3 external payload ports available on the Nadir side. The truss extension leading to the advanced Solar Power Module (SPM) may provide excellent viewing to pre integrated payloads. These locations have varying resources for payloads.

Distributed systems incorporated over much of the infrastructure offer temporary sites in the early stages of assembly whereby experiments may be pre-integrated and initiated upon deployment prior to full station operation, as determined by mission planning. There are several camera mounts, but only 4 EVA cameras, which will be used during an EVA intensive activity. Each mount has structural attachment, with guide pins and bolted attachment, and provides power and data interfaces. Similarly, the Remote Manipulator System (RMS) grapple fixtures are used for remote assembly purposes and are available thereafter, providing power and data to an on-orbit assembled payload. The Portable Foot Restraint sockets are used during EVA missions and provide only structural attachment. Utility Distribution System tray breakouts are power sources, nominally used to power the RMS. These options are offered as early opportunities only in the 1997 - 1999 time frame, when the attached payload accommodations in the outboard truss segments become active, as discussed in the next section.

These alternative payload sites can accommodate small, LDEF-type experiments which require minimal or no power and data handling capabilities. Larger payload facilities with more complex resource requirements, such as the Cosmic Dust Collection Facility proposed by JSC, can be accommodated by the baseline Attached Payload Accommodations. These external attachment sites provide Station power and fully integrated data handling resources, as well as serviceability, in a variety of integration options, as discussed in detail in the next section. The variety of experiment concepts provides the opportunity to make full use of Space Station's capabilities as an orbiting space laboratory, which not only can help assess its own designs, but also get experimenters on board as soon as possible.

5.0 SPACE STATION ATTACHED PAYLOAD ACCOMMODATIONS

Prior to the Space Station Redesign, the Space Station Freedom design included four Attached Payload ports on the US truss: two on the starboard side on the back face and two sites on the front faces of the port side. The two starboard sites were available to become active at the Manned Tended Configuration (6/97) and the two port side sites would become active by Permanent Manned Capability (6/00).

Currently, on the redesigned International Space Station Alpha (ISSA), there are up to eight attached payload port sites on the US truss (See Figure 3)⁴. These sites provide external payloads with a standard interface, viewing in all directions, adequate resources and flexibility to

⁴ The Redesign of the Space Station is a continuing process. The Figure presented is for reference only, and should not be considered the final Space Station design.

accommodate a variety of payload classes (e.g., large, complex to small, simple payloads). There are three sites on each of the starboard and port truss segments located inboard of the Solar Power Modules (SPM's). In the ISSA configuration the port sites may become available in early 1999 and the starboard sites may become available in mid 1999. An additional two attach sites may be located on the truss of the starboard SPM. However, the sites inboard of the solar arrays provide better overall accommodations (e.g., ease of access, data management, payload mass and volume), and these are considered the primary locations.

In general, attached payload accommodations are improved over the Freedom Design. Each Attached Payload port provides standard utilities and a robotically compatible attach mechanism. The Station can provide up to 3 kW of power from redundant sources to each site and a total of 6 kW aggregate for all sites. Attached payloads will still be required to provide their own thermal control. Data accommodations are provided by 1553 local bus service and a connection to a High Rate Data Link (HRDL). Access to the HRDL increases the maximum data down link capability from 400 Kbps to 43 Mbps. Attached payloads will be installed and serviced using the Space Station RMS and dexterous manipulator with EVA backup. The shortage of EVA time requires that external payloads be as robotically compatible as possible. The Space Station will provide accommodations to integrate, operate and service attached payloads on a regular basis.

The attachment mechanism for external payloads remains the standard Space Station mechanical attach structure, or Attached Payload Attach Structure (APAS). The redesigned Station configuration may offer the ability to pre-integrate the APAS to the truss for launch and the increased payload capability of 11,500 pounds. This combined with a slightly larger operational envelope allows larger payloads to be accommodated. Figure 4 demonstrates full loaded APAS's on the port side. The view of the Station is from the front, looking down on the Zenith sites. It shows two attached payload pallets between the photo-voltaic arrays and the thermal radiator, and the Inboard lower attach location is dedicated to the Unpressurized Logistics Carrier (ULC).⁵ Each site offers flexibility in experiment size, attachment concept and utilization.

6.0 SPACE STATION EXPRESS ATTACHED PAYLOAD PALLET CONCEPT

The EXPRESS Payload Program has been initiated to support the Space Station external payload program. The Expedite the Processing of Experiments to Space Station (EXPRESS) Program will provide the capability for an accelerated and simple integration process for externally mounted payloads. The goal of the EXPRESS Payload Program is to reduce the cost and time associated with the small, rapid response payload development, operation and integration. To accomplish this, small payload accommodations hardware and a streamlined integration process must be developed. Exposure science experimenters will find these smaller, standardized carriers an efficient vehicle for integrating their experiments onto the APAS in order to take advantage of the power, data and communications capabilities of the attached payload sites. Many smaller payloads may be accommodated on one APAS to maximize the use of the site. Standardization of payload interfaces and certification of payload carriers are a key feature of the EXPRESS Program.

The EXPRESS Attached Payload Program Study was sponsored by NASA to define an attached payload EXPRESS Program including carrier concept definition, integration process, and associated costs and schedule. The EXPRESS Attached Payload Program is modeled after

⁵ Note: final number and configuration of the attached payload sites and ULC locations under study at time of publication. The platforms displayed in Figure 4 represent a concept for EXPRESS Attached Payload Pallets and are not meant to represent any actual payload manifest.

the EXPRESS Rack Program and Space Shuttle Get-Away-Special concept. The objective is to develop an EXPRESS Attached Payload platform that can support the accommodation and integration of EXPRESS Attached Payloads in less than one year.

Under the study, MDA considered the use of existing Space Shuttle and Space Station Freedom equipment capabilities to minimize development cost. Also considered were the existing attached payload operational envelopes, Space Station Logistics Elements, STS hardware, and provisions for EVA and robotic servicing.

The resulting EXPRESS Pallet System (See Figure 5) provides a cost-effective, flexible pallet that incorporates standard, available hardware, and emphasizes the minimization of interfaces and integration time. The pallet consists of three main components, the EXPRESS Carrier (comparable to Rack Drawers and Mid-deck Lockers), the EXPRESS adapter (comparable to the EXPRESS Rack) and the EXPRESS Pallet (comparable to the US. Lab).

Figure 6 shows an EXPRESS Pallet with two EXPRESS Adapters mounted to the center of the pallet. The Pallet is designed to be the EXPRESS Attached Payload facility. Similar to the laboratory modules, the pallet will be launched once and remain on orbit. EXPRESS payloads will arrive on Adapters and changed out robotically.

The three segmented Pallet is a 13' 9" by 6' Aluminum Space Frame, weighs approximately 1000 lbs and can accommodate 3000 lbs of payload. The Pallet is designed to accommodate 6 EXPRESS Adapters and a total of up to 24 payloads. The Station interface is through the Attached Payload Attach Structure (APAS). The Pallet contains the attach structure passive interface (e.g., guide pins and latch bar), and the Pallet distributes secondary power and data using wire harnesses with blind mate connectors routed from the APAS to the EXPRESS Adapters. In addition to EXPRESS use, the Pallet can be modified to accommodate large attached payloads simply by removing the guide rails.

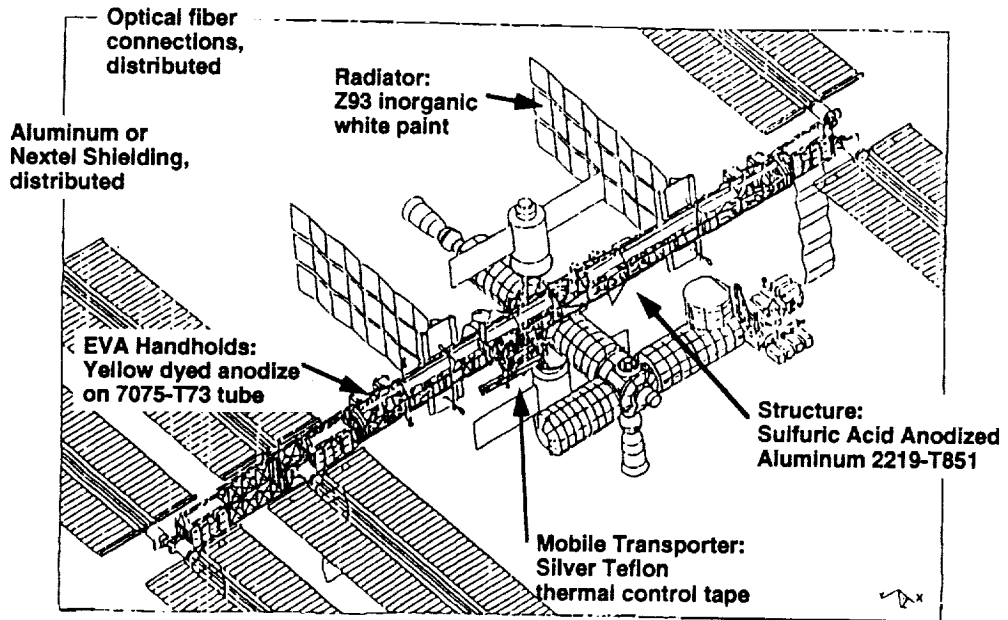
The EXPRESS Carrier depicted in Figure 5 is designed to be the equivalent to the EXPRESS Drawer or Middeck Locker. The EXPRESS Carrier will be robotically compatible and could be available in two sizes. It will be launched on the EXPRESS Adapter on the Unpressurized Logistics Carrier or directly to the STS side-wall.

The large and small Carriers are ~34" x 25" x 30" and 16" x 25" x 30" Aluminum chassis, weigh approximately 75 and 30 lbs and can accommodate ~140 and 70 lbs respectively. The Carriers are designed to accommodate one payload each. Power and data connections are made through blind mate connectors from the Adapter. Each Carrier will receive up to 420 watts of power at 120 Vdc, a 1553B Local Bus Connection and a High Rate Data Link (HRDL) fiber-optic interface. Other features include optional sides for viewing, Anodized coated sides to create custom thermal environment, heat pipes for maximum heat rejection, and micro meteoroid shielded sides for protection of sensitive instruments.

The Carriers interface to the Adapter using guide vanes and fine alignment pins. Options for using non-robotic or fixed EXPRESS carrier, or the Hitchhiker Canister are also being considered. The Carriers are designed to follow a standard integration process that requires the Payload Integration Agreement (PIA) Main Volume as the only Space Station integration documentation. The integration process starts 1 year prior to launch with the completion of the PIA.

SUMMARY

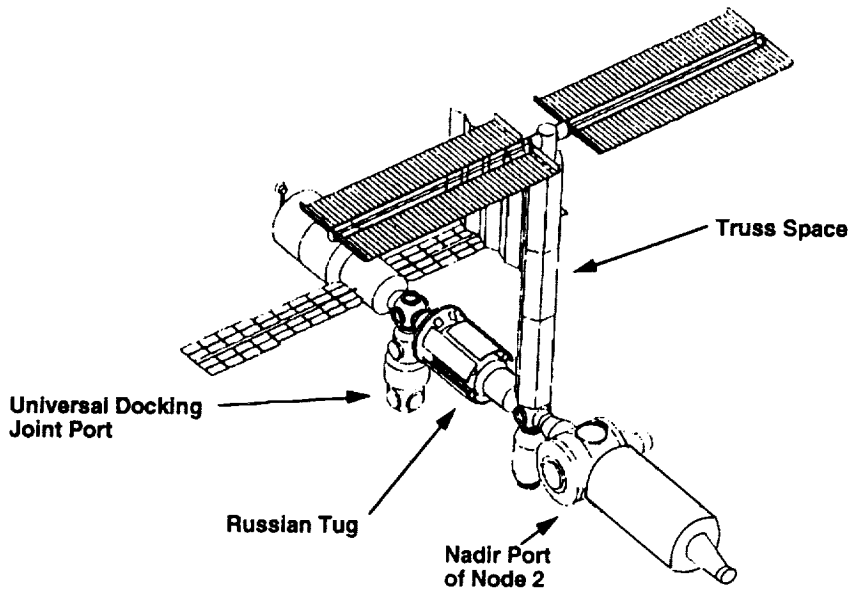
The Space Station can be considered a follow-on experiment to LDEF. Many of the Space Station's designs have taken advantage of LDEF results. Yet, advanced materials and systems used in Space Station design carry some uncertainty as to their long duration performance in the complex environment of an active spacecraft. A variety of opportunities is provided to space exposure experimenters to assess the performance of advanced technologies. Payload developers will be able to attach experiments on a variety of locations and environments on the Space Station, from small locations distributed along the truss, to the dedicated attached payload ports that can accommodate large exposure facilities. The EXPRESS pallet concept being developed will provide payload developers a cost effective method for launching less complicated experiments to get the maximum utilization from the Space Station facility.



*Reference configuration only

McDonnell Douglas Aerospace
Space Station Division

Fig. 1: Space Station is an Experiment in Long Duration Exposure



*Reference configuration only

McDonnell Douglas Aerospace
Space Station Division

Fig. 2: Potential Early Attached Payload Sites Russian-Alpha configuration

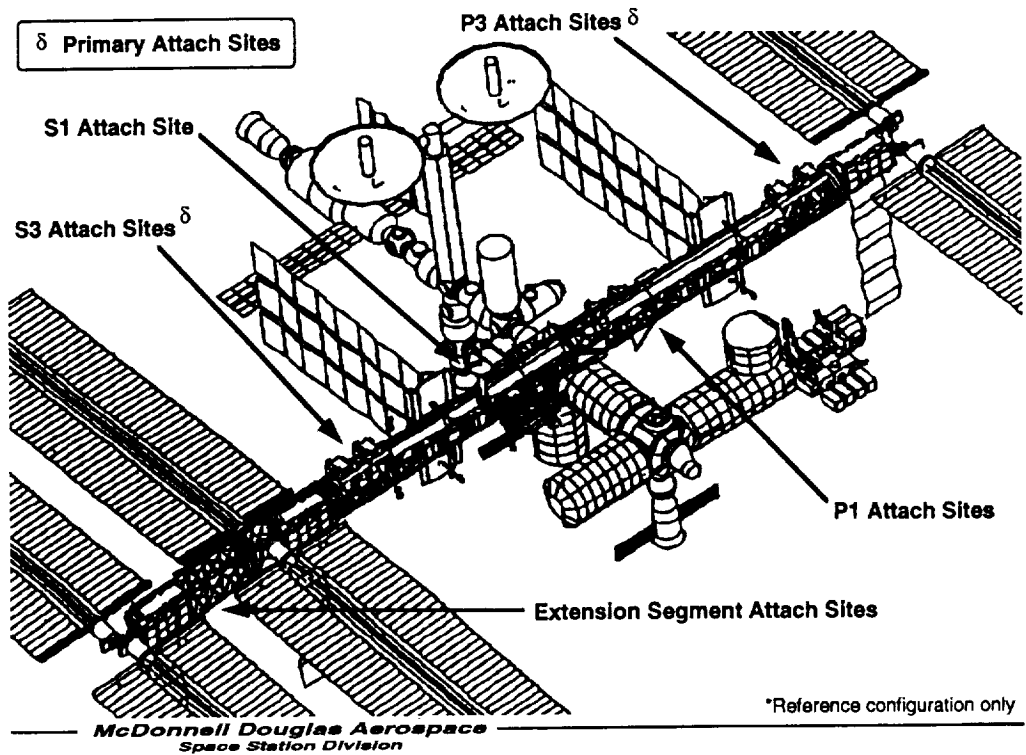


Fig. 3: Space Station Alpha Configuration with Russian Participation

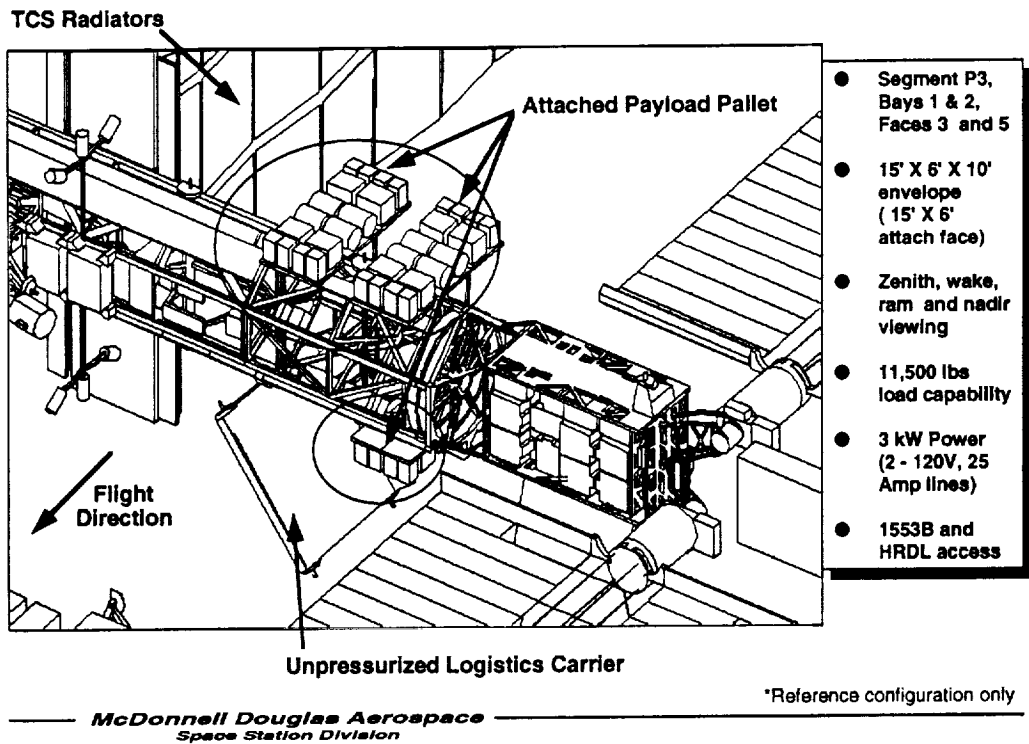


Fig. 4: P3 Attached Payload Sites

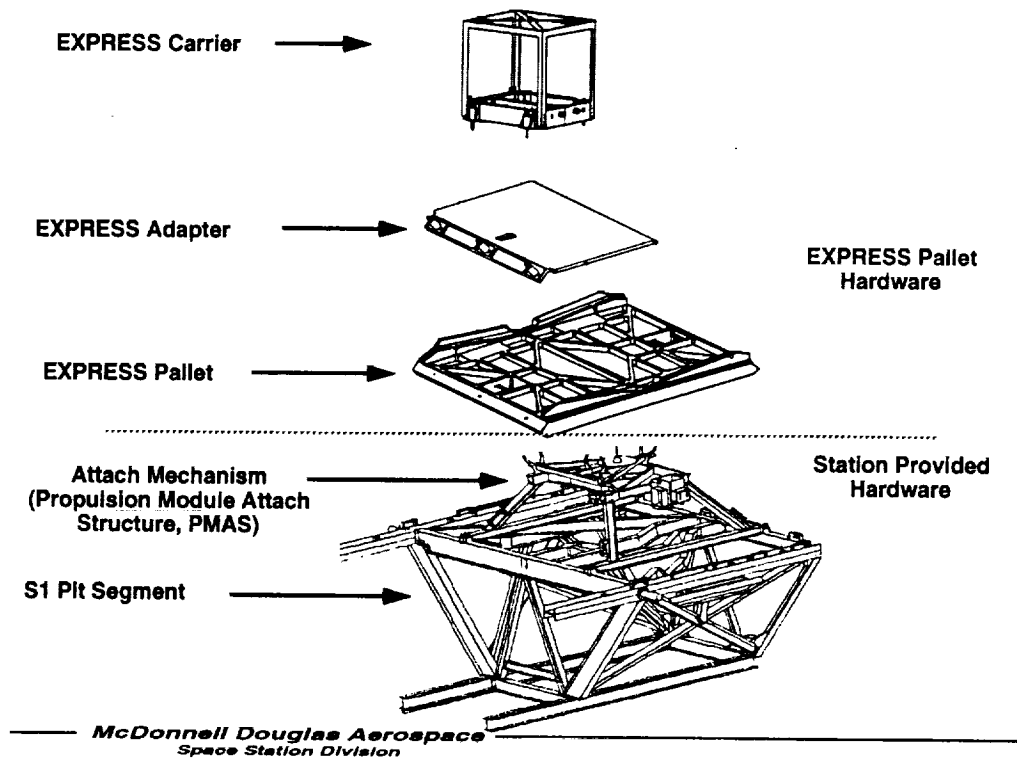


Fig. 5: EXPRESS Attached Payload Pallet Concept

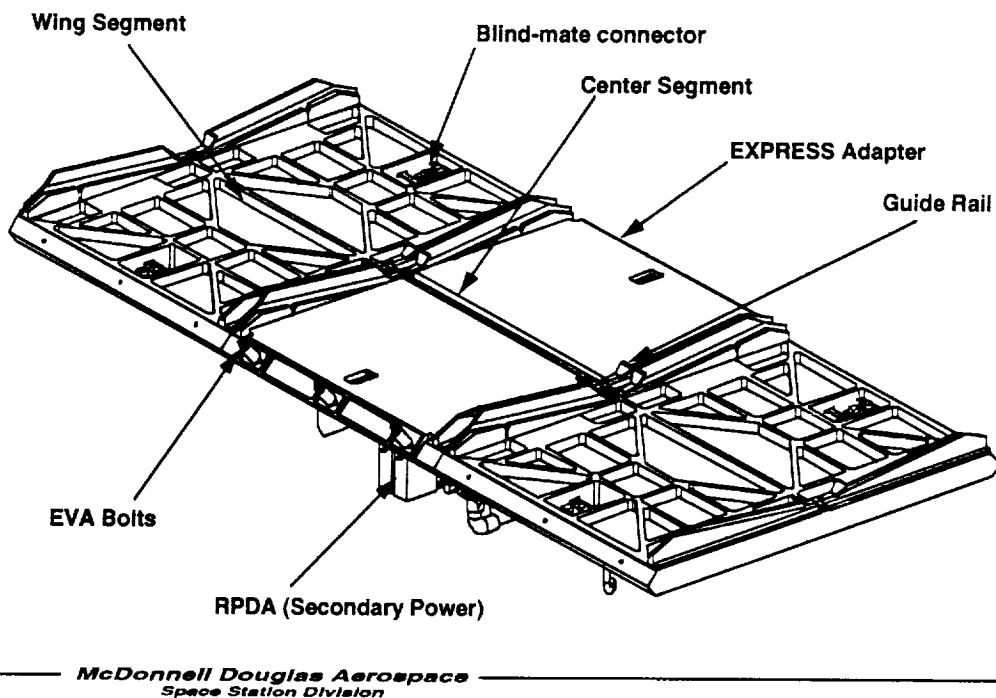


Fig. 6: EXPRESS Attached Payload Pallet

A Materials Exposure Facility

Wayne S. Slemp and Don E. Avery
NASA Langley Research Center
Hampton, VA 23681-0001

The objective of the Materials Exposure Facility (MEF) is to provide a test bed in space for conducting long-term (> one year) materials experiments which require exposure to the low Earth orbit (LEO) space environment. The proposed MEF is planned to be an integral part of the agency's Space Environments and Effects Research Program. The facility will provide experiment trays similar to the Long Duration Exposure Facility (LDEF). Each tray location is planned to have a power and data interface and robotic installation and removal provisions. Space environmental monitoring for each side of the MEF will also be provided. Since routine access to MEF for specimen retrieval is extremely important to the materials research, Space Station Freedom (Figure 1) has been chosen as the preferred MEF carrier.

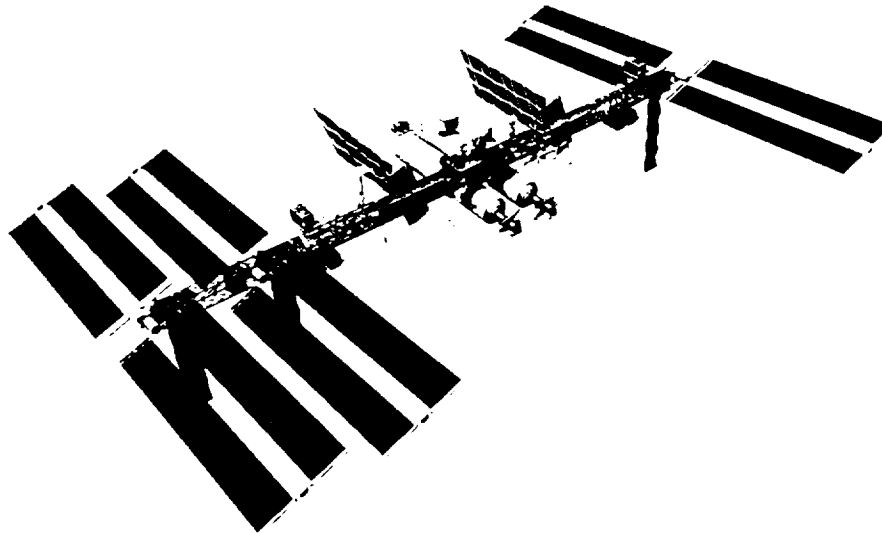


Figure 1 Space Station Freedom

The parameters in the LEO environment which affect materials are atomic oxygen, solar ultraviolet radiation, high vacuum (10^{-7} torr), electron and proton radiation, micrometeoroid and debris impacts, and orbital temperature cycling. Because of the cost and complexity of operation, it is impractical to simulate these parameters simultaneously in ground-based laboratories. Also, the lack of

knowledge of the influence of each of these parameters on materials degradation, makes ground-based accelerated testing difficult to interpret.

The results of the LDEF flight experiments point out the subtle, unique differences between long-term (five-year) materials experiments and accelerated, short term (40 hours at 120 nmi altitude which equaled 1-year exposure at normal LEO operational altitude) Shuttle-based flight experiments. The Effects of Oxygen Interactions with Materials-2 (EOIM-2) flight experiment results predicted that graphite-epoxy composites would lose 0.0105 inches in thickness in the Ram fluence of LDEF, but these lost only 0.0055 inches in thickness or about 1/2 the predicted loss. In the case of fluoropolymers like FEP Teflon, the effect was reversed. The EOIM-2 data predicted only a 0.00025-inch thickness loss from the LDEF fluence of AO, but in real-time on LDEF, the actual thickness loss was over four times the predicted value. These two examples serve to illustrate the need for long-term (>1 year), real-time space exposure in conducting flight experiments for design of future long-life spacecraft.

The MEF is being proposed as the first long-term exposure facility with the capability for real-time interaction with materials exposure experiments in actual conditions of orbital space flight. To better understand the mechanisms of materials degradation in space, real-time effects must be evaluated without the annealing effects caused by exposure to Earth's atmosphere and the long delay of three to six months before evaluation due to experiment de-integration. With power and data capability available active experiments can be conducted to evaluate the physical, chemical, and optical changes in materials as these changes occur. This should provide significant insight into space environmental effects mechanisms. Since these materials will also be returned to Earth for further evaluation, additional studies of the effects this environmental change has on material properties can be conducted. This type of materials research should provide the data needed to design materials and coatings that are resistant to the LEO environment for use in the next generation of spacecraft as well as for long-term performance prediction of current materials in the LEO environment.

The current concept for the MEF is shown in figure 2 with eight experiment trays on the leading and trailing faces, four trays on each side, and two trays on the Earth facing, bottom side for a total for 26 experiment trays. The experiment trays will be 39.4 inches (1m) by 39.4 inches (1m) by 12 inches (0.3 m) in depth and designed for robotic removal and exchange. The MEF is proposed to utilize Space Station Freedom's payload attachment site P1-F6-B1&B2 (Port Truss Segment 1-Truss Face 6-Truss Bays 1 and 2) to provide nearly full Ram, Wake, and Nadir exposure.

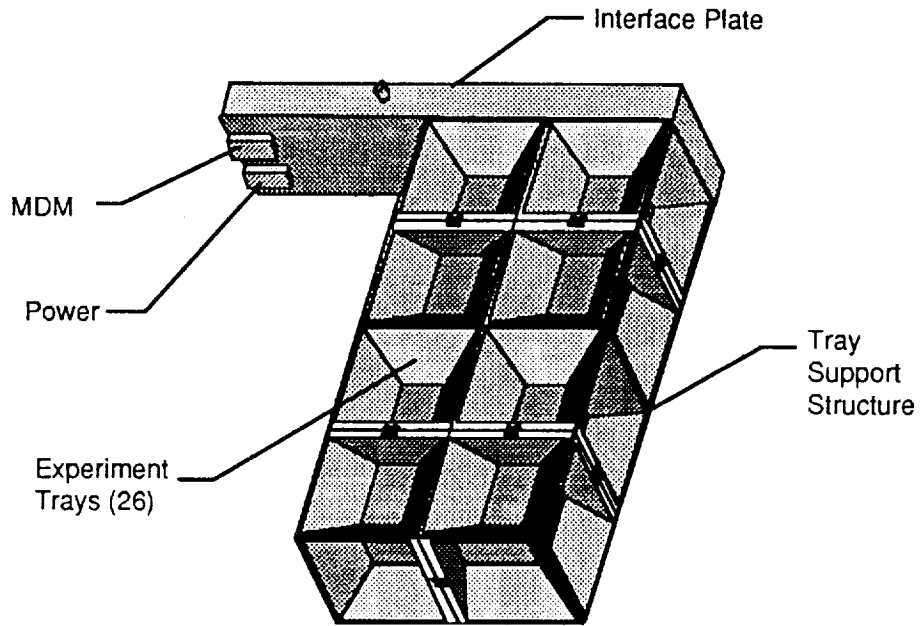


Figure 2 Materials Exposure Facility

The MEF is proposed to be launched on Utilization Flight UF-2, currently scheduled for late 1997. This facility will be fully integrated with experiments prior to launch and be robotically attached to Space Station Freedom (Figure 3) at which time power and data interfaces will be established. Change-out of individual experiments can be scheduled for intervals of six months to several years.

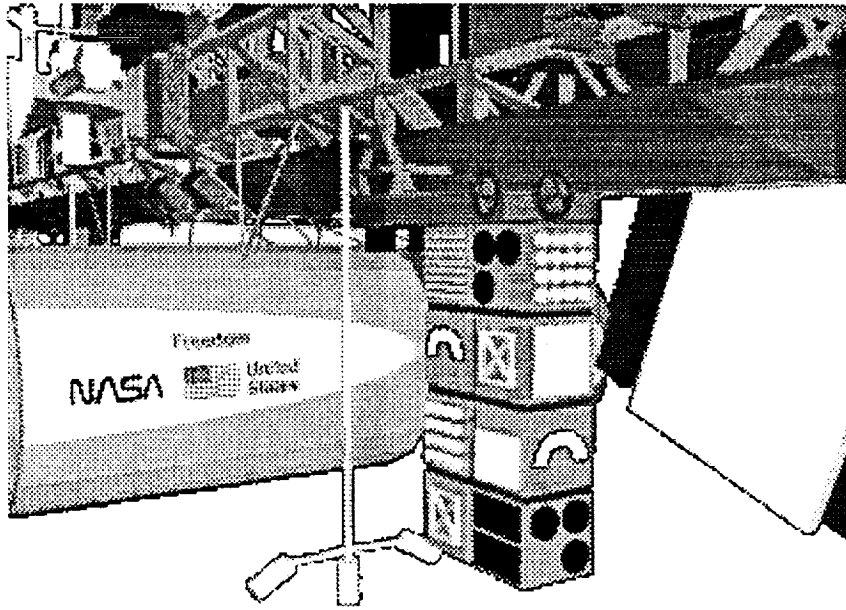


Figure 3 Space Station payload attachment site P1-F6-B1&2

Langley Research Center will design, fabricate and manage the MEF project. The electrical and data systems design teams will utilize standard Space Station Freedom developed components where possible. The project office will sponsor an MEF Announcement of Opportunity to select MEF experiments. The cost proposal includes the design, fabrication, integration through launch and initial operations but does not include experiment development funding, long-term facility operations, integration facilities, data collection facilities or data archiving.

Considerable Phase A MEF conceptual design work has been completed. However, Phase A funding is being requested to complete definition of requirements for engineering, contamination, documentation, integration, data retrieval and operations. These studies are required to develop the planning documentation needed for efficient MEF development and operation.

OTHER SPACECRAFT

AN LDEF FOLLOW-ON SPACECRAFT CONCEPT

Vernon Keller, Larry Breazeale, and Don Perkinson
NASA Marshall Space Flight Center
Marshall Space Flight Center, AL 35812
Phone: 205/544-2470; Fax: 205/544-5861

William H. Kinard
NASA Langley Research Center
Hampton, VA 23681-0001
Phone: 804/864-3796; Fax: 804/864-8094

ABSTRACT

The successful flight, retrieval, and analyses of the Long Duration Exposure Facility (LDEF) experiments demonstrated the value of long duration space exposure for a broad spectrum of science and engineering investigations. The original LDEF was an excellent gravity gradient spacecraft, but because of its 9 m length and 9,700 kg mass it was difficult to manifest on the Shuttle, for either launch or retrieval, in conjunction with other payloads.

This paper discusses an LDEF follow-on spacecraft concept whose short stowed length (~3 m) greatly improves Shuttle manifesting opportunities while still providing very large surface area exposure for experiments. Deployable 'wings' on each end of the short, 'cylindrical' main body of this new spacecraft provide the means for gravity gradient stabilization while greatly increasing the spacecraft surface area. The center section of the spacecraft is oriented with the end faces of the twelve sided, 4.2 m diameter 'cylinder' perpendicular to the velocity vector thus providing large areas for experiments in both the ram and anti-ram directions as well as additional exposure area around the periphery of the cylinder. When deployed and properly oriented with the Shuttle's Remote Manipulator System (RMS), both wings of the spacecraft are oriented edge on to the direction of motion and lie in the plane which contains the local gravity vector. The relatively thin wings readily accommodate dual side exposure of glass plate stacks for cosmic ray detection. Flat surfaces mounted normal to and on the periphery of the wings provide additional areas in both the ram and anti-ram directions for cosmic dust, micrometeoroid, and orbital debris collection free of contamination from 'splatter' off secondary surfaces. The baseline concept provides enhancements not available on the original LDEF such as solar array generated electrical power and data telemetry.

Status of the efforts to promote support for and ultimately space flight of this concept will be presented. Suggestions for improvements in the spacecraft design and proposed utilization are solicited.



LONG DURATION EXPOSURE FACILITY POST-FLIGHT DATA
AS IT INFLUENCES THE
TROPICAL RAINFALL MEASURING MISSION

Sharon A. Straka
NASA Goddard Space Flight Center
Greenbelt, MD 20771

SUMMARY

The Tropical Rainfall Measuring Mission (TRMM) is an earth observing satellite that will be in a low earth orbit (350 kilometers) during the next period of maximum solar activity. The TRMM observatory is expected to experience an atomic oxygen fluence of 8.9×10^{22} atoms per square centimeter. This fluence is ten times higher than the atomic oxygen impingement incident to the Long Duration Exposure Facility (LDEF). Other environmental concerns on TRMM include: Spacecraft glow, silicon oxide contaminant build-up, severe spacecraft material degradation, and contamination deposition resulting from molecular interactions with the dense ambient atmosphere. Because of TRMM's predicted harsh environment, TRMM faces many unique material concerns and subsystem design issues. The LDEF data has influenced the design of TRMM and the TRMM material selection process.

INTRODUCTION

The Tropical Rainfall Measuring Mission (TRMM) is a joint United States and Japan observatory program that will conduct systematic measurements of tropical rainfall required for weather and climate research. NASA's Goddard Space Flight Center (GSFC) in Greenbelt, Maryland will design, build, and test the observatory. The observatory will be 3.6 meters in diameter and 4.6 meters in length and has a mass of 3334 kilograms. Figures 1 and 2 show the observatory configuration. The observatory will carry five instruments: Precipitation Radar (PR) supplied by the National Space Development Agency of Japan (NASDA), TRMM Microwave Imager (TMI) built by Hughes in El Segundo, Visible Infrared Scanner (VIRS) built by Santa Barbara Research Corporation, Clouds and the Earth's Radiant Energy System (CERES) managed by NASA Langley Research Center and built by TRW, and Lightning Imaging Sensor developed by NASA Marshall Space Flight Center.

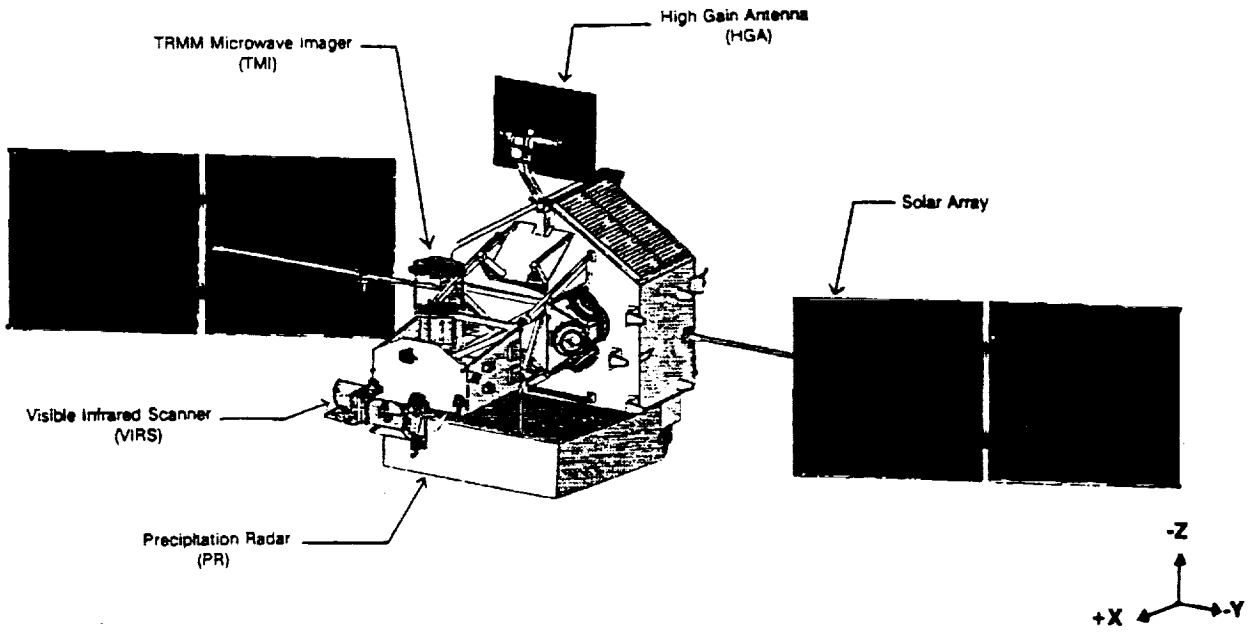


Figure 1. Tropical Rainfall Measuring Mission

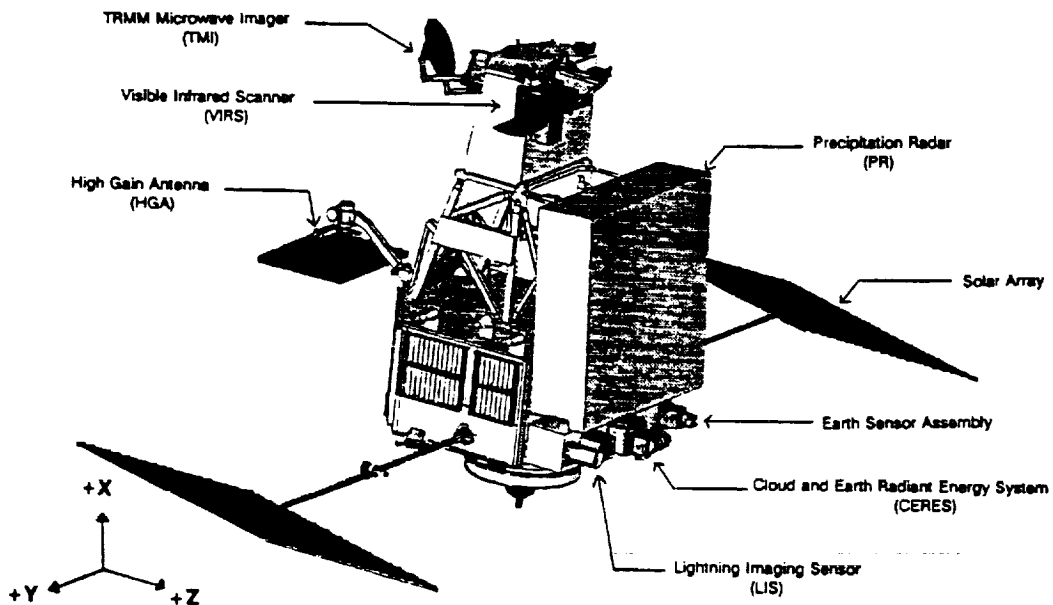


Figure 2. Tropical Rainfall Measuring Mission

TRMM is scheduled for launch in August 1997 from Tanegashima Space Center in Tanegashima, Japan. The launch vehicle is a Japanese H-II rocket. The observatory will fly in a circular orbit having an inclination of 35 degrees and an altitude of 350 kilometers (189 Nautical miles, just 10 nautical miles higher than the LDEF retrieval). TRMM's +Z axis is nadir pointing. The observatory performs a 180 degree yaw maneuver every 2 to 4 weeks to limit exposure of direct sunlight on the +Y side of the observatory.

TRMM will be in orbit during the next period of maximum solar activity (April 2000) and is predicted to experience an atomic oxygen fluence of 8.9×10^{22} atoms per square centimeter. This fluence is ten times higher than the atomic oxygen impingement incident to the Long Duration Exposure Facility (LDEF) and is almost double the space station atomic oxygen design fluence. Severe material degradation is expected resulting from material interactions with atomic oxygen or synergetic effects between atomic oxygen, solar ultra violet, and temperature. Most commonly used spacecraft outer layers will not survive TRMM's three and a half year mission. Table 1 lists the material thicknesses of common spacecraft materials required to survive the mission. The erosion rates used to calculate the material losses are based on LDEF and Shuttle erosion data^{1,2}. All exterior surfaces of the observatory need to be protected against atomic oxygen since the observatory has no true "wake".

Table 1

Approximate Material Thicknesses Required for TRMM Mission

Spacecraft Material	Material Thickness Required
Kapton	>105 Mil
Chemglaze Z306	>12 Mil
Teflon	>13 Mil
Graphite Epoxy	>91 Mil
Unprotected Silver	>368 Mil

TRMM has several other low earth orbit environmental concerns. The atomic oxygen is expected to react with outgassed silicones to produce a permanent contaminant layer. This phenomena was widely observed on LDEF and has been seen on other missions like the Solar Maximum Mission (SMM), the Evaluation of Atomic Oxygen Interactions with Materials (EOIM-3) Experiment, and the European Retrieval Carrier (EURECA). Silicone oxide build-up is TRMM's major on-orbit contamination concern. Not only will the contaminant itself degrade sensitive surfaces but the mechanism exists

for the silicone oxide to form in several different oxidation states making it difficult to predict the extent of degradation. In addition the silicone oxide contaminants can trap carbon based contaminants on sensitive surfaces further degrading those surfaces.

The contamination deposition problem is compounded by the dense ambient atmosphere. The ambient atmosphere at 350 km is approximately 26 times the density experienced at 600 km (a typical earth observing satellite orbit). Because of the dense ambient atmosphere, the TRMM thrusters need to fire approximately every two days during the last portion of the mission just to maintain orbit. TRMM will also experience localized pockets of ambient density build-up between the solar array and the spacecraft. As a result, outgassed contaminants from the observatory have a higher probability of colliding with the ambient atmosphere and returning back to the spacecraft. This phenomena is called return flux.

Another low earth orbit phenomena which TRMM is susceptible to is spacecraft glow. Glow is observed on shuttle flights especially after engine firings. Glow is a result of a reaction of contaminants or coatings with atomic oxygen and nitrogen. The mechanisms for glow to occur are not well defined. The impact of glow on the TRMM instruments and earth sensor will be evaluated in fiscal years 1994 and 1995.

DESIGN ISSUES

Multi-Layer Insulation Outer Layer

The TRMM Material Selection Working Group is responsible for approval of all external materials on TRMM with one of its main responsibilities being selection and testing of the observatory's multi-layer insulation (MLI) outer layer. The group consists of representatives from Contamination Engineering, Thermal Engineering, Thermal Coatings, and Materials. The group has evaluated over 50 candidate multi-layer insulation materials for use on TRMM. The materials included both instrument and spacecraft materials. The LDEF data was used in the preliminary screening process. Unfortunately, because of lack of applicable data and TRMM's harsh environmental constraints, selection of MLI outer layers has been difficult.

After preliminary screening, all candidate materials undergo environmental testing. The MLI outer layer testing program includes flex tests, optical property measurements, atomic oxygen testing, ultraviolet exposure tests, thermal cycling, and atomic oxygen testing in combination with ultraviolet irradiation. Flex tests involve flexing the materials sample over a 1/4 inch mandrel in two directions. Optical property measurements are performed by GSFC and include absorptance and emittance measurements. Atomic oxygen testing is performed at NASA Lewis Research Center (LeRC) using a directed atomic oxygen beam facility. The effective atomic oxygen fluence in this facility is calculated based on LDEF erosion rates for kapton and teflon. Ultraviolet exposure tests

are performed by the GSFC. The materials are tested to 3000 solar equivalent hours in this facility. Thermal cycling tests are also performed by GSFC. The samples are cycled from -100°C to +100°C for 3000 cycles. Atomic oxygen testing in combination with ultraviolet irradiation tests will be performed by LeRC. The tests are expected to start in January 1994. Pre-test chamber characterizations have been completed.

The TRMM primary multi-layer insulation outer layer is an Optical Coating Laboratories, Inc. (OCLI) proprietary coating over VDA backed white tedlar. This selection was driven by the desire to have a diffusely reflective outer layer. The OCLI coating is custom made to the TRMM mission specifications. The proprietary coating consists of multilayers of three different types of inorganic oxides. The substrate on the MLI outer layer is white tedlar. White tedlar is a polyvinylfluoride film manufactured by DuPont in a 1.5 mil thickness. White tedlar has an absorptance value of 0.301 and an emittance of 0.890. Vapor deposited aluminum is applied to the back of the substrate for conductivity. A scrim will also be attached to the material to provide added strength. The OCLI coating over tedlar has an absorptance ranging from 0.377 to 0.612 and an emittance ranging from 0.762 to 0.778 depending on the thickness on the coating and its state of oxidation.

Several back-up materials are also being considered in case the primary material fails to pass all environmental tests. They include beta cloth with vapor deposited aluminum backing, Sheldahl silicon oxide (SiO_x) over kapton, or a composite consisting of Kapton coated with chemglaze Z306 to roughen the surface, then coated with a layer of vapor deposited aluminum, followed by aluminum oxide, and completed with an over-coat of silicon oxide. The back-up materials are not perfect solutions. The thermal properties of beta cloth woven with silicones degrade with ultraviolet radiation causing the properties to exceed observatory thermal requirements. The silicones in the beta cloth can be transferred by touch and handling of the beta cloth produces particulates. Beta cloth without silicones tends to be more brittle. Also, the teflon in the beta cloth can be eroded with atomic oxygen exposure, thus increasing its transmittance. The Sheldahl SiO_x over kapton may contain pinhole defects in the material making it susceptible to atomic oxygen erosion. Also it is difficult to detect microcracks in the SiO_x coating as a result of handling. The composite material has end of life thermal properties that exceed the spacecraft limits.

Special Radiator Surfaces

Radiator material selection is also controlled by the TRMM Material Selection Working Group. The spacecraft will use MS 74 white silicate paint on its radiator surfaces. MS 74 white silicate paint is UV and atomic oxygen stable and exhibits low outgassing properties.

Silver teflon is not an acceptable radiator material for the TRMM mission. Based on the LDEF measured erosion rates, 13 mil of teflon will be eroded during the mission.

Because the erosion of teflon is a synergetic effect between atomic oxygen, UV, and temperature and cannot be accurately reproduced in ground testing, the exact erosion rate of teflon for the TRMM mission is difficult to extract from the LDEF measured rates (the LDEF data represents only one low earth orbit long exposure data point). Rather than design teflon radiators to degrade at a certain rate and leave enough teflon to maintain the correct thermal properties, the risk of failure has been reduced by eliminating unprotected teflon from the spacecraft. Protective coatings do not adhere well to teflon.

Other radiator surfaces on the observatory include optical solar reflectors, IITRI Z-93P white silicate paint, and vapor deposited aluminum.

Blanket and Radiator Attachment Methods

Current plans are to attach the spacecraft blankets with fiberglass or stainless steel buttons. The possibility of using velcro in some protected areas of the spacecraft that are not contamination sensitive is being investigated. The edges of blankets must be turned under to prevent AO erosion of the blanket materials. The concept of joining two blankets with a french seam is being considered.

The use of tapes on external surfaces will be minimized or eliminated. There is concern that the acrylic adhesive backed tapes will experience AO undercutting and possible lifting. Silicone based adhesives represent a contamination source and need to be minimized. Silicone adhesives are currently being used to bond solar array cells to the substrates and to attach optical solar reflectors.

Future testing includes both acrylic and silicone adhesion tests in an AO environment. Undercutting of adhesives will be measured. Optical solar reflector degradation will be measured as a result of adhesive outgassing and oxidizing in an AO/UV environment. In addition, a test needs to be performed to measure the efficiency of the silicone/atomic oxygen reaction.

Solar Array Harness Protection

The baselined wire on the solar array harness has 8 mil of teflon insulation and therefore needs protection from atomic oxygen. Alternative insulations either have higher AO erosion rates or are too stiff for three dimensional deployment. Protective coatings will not adhere to the wire insulations.

Several protection methods have been proposed for the solar array harnesses. The boom harness which moves three dimensionally during deployment will be covered with a beta cloth sleeve sewn with an AO resistant thread. The interconnect harnesses will

also be covered with beta cloth sleeves. The front side wire bundles with less than 10 wires will be coated with NUSIL CV1-1142. Larger bundles on the front side will be wrapped with germanium coated kapton tape. The backside wires (which experience some UV as a result of feathering the solar arrays to reduce drag) will be protected with germanium coated kapton sheets bonded with silicone adhesive or OCLI over white tedlar sheets bonded with a silicone adhesive. The terminal boards and diode boards will be covered with MS 74 painted metal covers. The backside of the arrays will be painted with MS 74 white silicate paint.

The above solar array harness protection methods need additional testing including outgassing tests, adhesion tests, thermal cycling and AO erosion tests. In addition, a study is being performed to determine if another suitable insulation is available.

Earth Sensor Concerns

The earth sensor is expected to experience several unique contamination concerns. The earth sensor has four lenses. Two of the lenses face 45° from the +X direction and two of the lenses face 45° from the -X direction. Because the observatory flies 50 percent of the time in the +X direction and 50 percent of the time in the -X direction, all lenses will face the ram direction making them susceptible to contamination and atomic oxygen environmental effects.

The earth sensor lens exterior consists of multiple layers of proprietary coatings. A sample of the lens will be tested in an atomic oxygen facility to verify the coating will remain intact in TRMM's predicted environment without pitting, eroding, or fogging. It is also planned to measure the effects of glow at the earth sensor wavelength region (12 to 18 microns) by exposing a lens sample to silicone and hydrocarbon contaminants while in the presence of atomic oxygen and nitrogen.

To determine the earth sensors susceptibility to contamination, GSFC will measure the lens sample transmittance loss as a function of SiO_x thickness, amorphous carbon thickness, and a combination of the two. There is concern that the earth sensor lenses will experience the same lens fogging problem³ as observed on the TIROS and DMSP ram facing earth sensor lenses. The fogging phenomena is believed to be a combination of environmental and contamination effects.

External Contamination Limitations

To minimize molecular contaminants such as those observed on LDEF, the amount of silicone based materials on the observatory exterior will be limited. Outgassed silicones react with atomic oxygen to produce silicon oxide (SiO_x). Silicon oxide is a permanent contaminant layer which cannot be "baked-off" a surface. In addition, silicon

oxide build-up can trap carbon based contaminants on a surface causing further degradation. Current external sources of silicones on the observatory include solar arrays (largest source), adhesives on tapes and optical solar reflectors, and protection of the TMI graphite epoxy support structure. Unfortunately, because of the lack of material alternatives and supporting flight data, silicones are being used to protect surfaces known to react with atomic oxygen.

Analytical predictions of contaminant flux to sensitive surfaces was performed using on-orbit contamination analyses and propulsion contamination analyses. Outgassing limits have been assigned to various spacecraft components. The outgassing rates of instruments, solar arrays, blankets, high gain antenna, harnesses, and electronic boxes will be certified during thermal vacuum testing using a quartz crystal microbalance. If the outgassing rates of those subsystems exceed the outgassing requirements, the respective subsystem will be baked-out. Spacecraft and instrument venting will be controlled and/or directed away from sensitive surfaces.

Internal Contamination Limitations

Contaminants originating from inside the spacecraft will be controlled. Outgassing rates of TRMM hardware will be monitored during component level thermal vacuum tests. Hardware not meeting the outgassing requirements will be baked-out.

The use of Chemglaze Z306 has been eliminated in the spacecraft cavity except for small quantities. The "nicotine" stains observed on LDEF have been attributed to outgassing from Chemglaze Z306. The equipment panels and electronic boxes will be either anodized or painted with MSA-94B black silicate paint.

Sources of silicones in the spacecraft interior will be controlled with a special spacecraft vent design. The spacecraft cavity will be tightly sealed with a layer of kapton or mylar under the thermal blankets. The vent effluent will be directed out a single vent in the least contaminating position on the spacecraft. Figure 3 shows the location of the spacecraft vent. The vent effluent will pass through a series of baffles coated with a molecular adsorber which has a high efficiency for adsorbing silicone based contaminants. The molecular adsorber is being developed by JPL. A similar venting concept was used in the Hubble Space Telescope Wide Field Planetary Camera II.

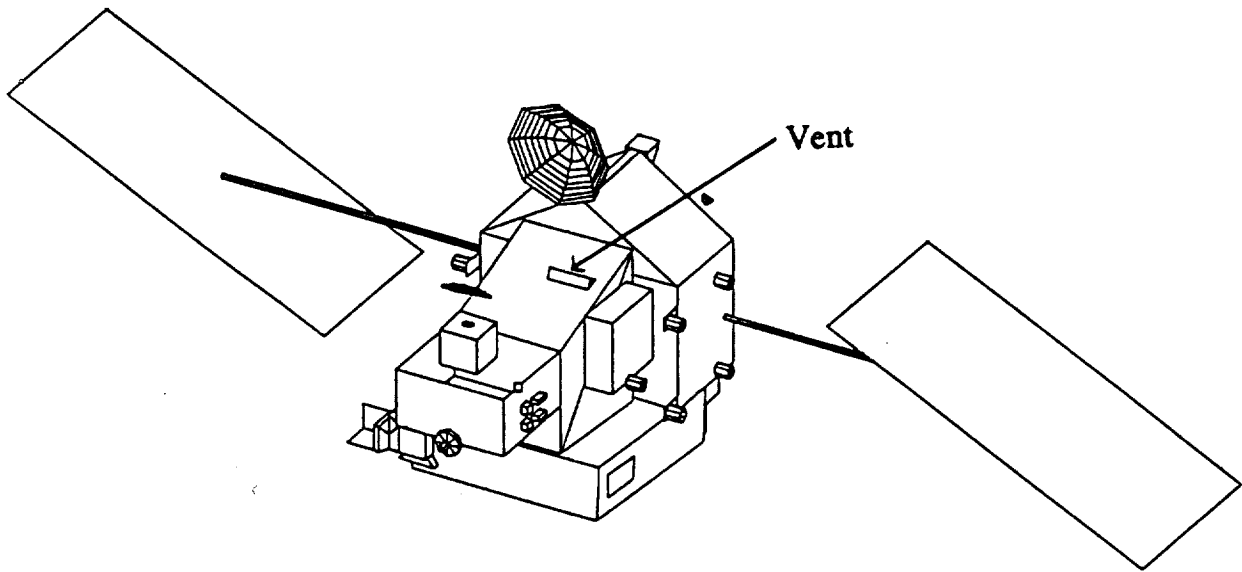


Figure 3. TRMM Vent Location

CONCLUSIONS

In conclusion, the knowledge obtained from LDEF post-flight data has been valuable in designing TRMM with respect to contamination control and material integrity. However, there exists a need for more long term data on materials, coatings and adhesives from orbits such as LDEF and TRMM, especially materials which erode by synergetic interactions with AO and UV. Because of the limited understanding of synergetic material interactions, extrapolating erosion rates from one orbital environment to another may be risky.

In addition, there are large voids in understanding how silicone based materials react with the environment, which silicones are hazardous, the efficiency of the silicone/silicon oxide reaction, and the relationship between atomic oxygen flux and silicone residence time. These material unknowns make material selection and behavior predictions difficult.

As a result of the uncertainties, the current design approach forces large margins, resulting in over-design, increased weight and increased cost. Efforts should be made to obtain environmental effects flight data from TRMM to make the follow-on mission more efficient as well as assisting in the design of similar low earth orbit satellites.

REFERENCES

1. Banks, B. A., Dever, J.A., Gebauer, L., and Hill, C.M.: Atomic Oxygen Interactions with FEP Teflon and Silicones on LDEF. NASA Conference Publication 3134, June 1991.
2. Banks, B. A.: Atomic Oxygen Interaction with Materials on LDEF. Presented at the LDEF Post-Retrieval Kick-off Meeting, 1991.
3. Predmore, R. E., Jacobowitz, H., and Hickey, J.R.: Exospheric Cleaning of the Earth Radiation Budget Solar Radiometer during Solar Maximum. SPIE Vol. 338, Spacecraft Contamination Budget, May 1982, pp 104-113.

ACKNOWLEDGEMENTS

The author would like to acknowledge the key members of the TRMM contamination engineering effort: Ms. Larissa Graziani, Mr. Jack Triolo, and Mr. Shaun Thomson. Larissa and Shaun work for Swales and Associates, Incorporated. Jack is a consultant contracted through Swales and Associates.

EXPERIMENTS

ELEMENT MATERIAL EXPOSURE EXPERIMENT BY EFFU

Yoshihiro Hashimoto and Masaaki Ichikawa
Ishikawajima-Harima Heavy Industries Co.,Ltd.
Tokyo,190-12,JAPAN
Phone: 81/425-68-7184; Fax: 81/425-68-7575

Mitsuru Takei,Yoshihiro Torii and Kazuo Ota
National Space Development Agency of JAPAN
Tsukuba,305,JAPAN
Phone: 81/298-52-2943; Fax: 81/298-50-1480

SUMMARY

National Space Development Agency of JAPAN(NASDA) is planning to perform "Element Material Exposure Experiment" using Exposed Facility Flyer Unit(EFFU). Several materials which will be used on JEM(Japanese Experiment Module for the Space Station) will be exposed. Space environment monitoring is also planned in this experiment. Several ground based tests are now being performed and getting useful data.

INTRODUCTION

EFFU(Exposed Facility Flyer Unit) is a module of SFU(Space Flyer Unit) which is shown in Figure 1. SFU is promoted by three Japanese organizations: National Space Development Agency of Japan (NASDA) on behalf of the Science and Technology Agency (STA); the Institute of Space and Astronautical Science (ISAS) on behalf of the Ministry of Education, Culture and Science(MOE); and New Energy and Industrial Technology Development Organization(NEDO) on behalf of the Ministry of International Trade and Industry (MITI). SFU system parameters are the following:

Dimensions 4.7[m] dia., 2.5[m] height
 Solar array paddle 24.4[m] length, 2.36[m] width
 Weight 4.0[ton] at launch, 3.2[ton] at retrieval
 Attitude Sun pointing
 Control 3-axis stabilized
 Microgravity 10-4[g] condition
 Mission orbit 300 - 500[km]
 Launch H-2 Rocket Test Flight#3
 Retrieval NASA Space Shuttle

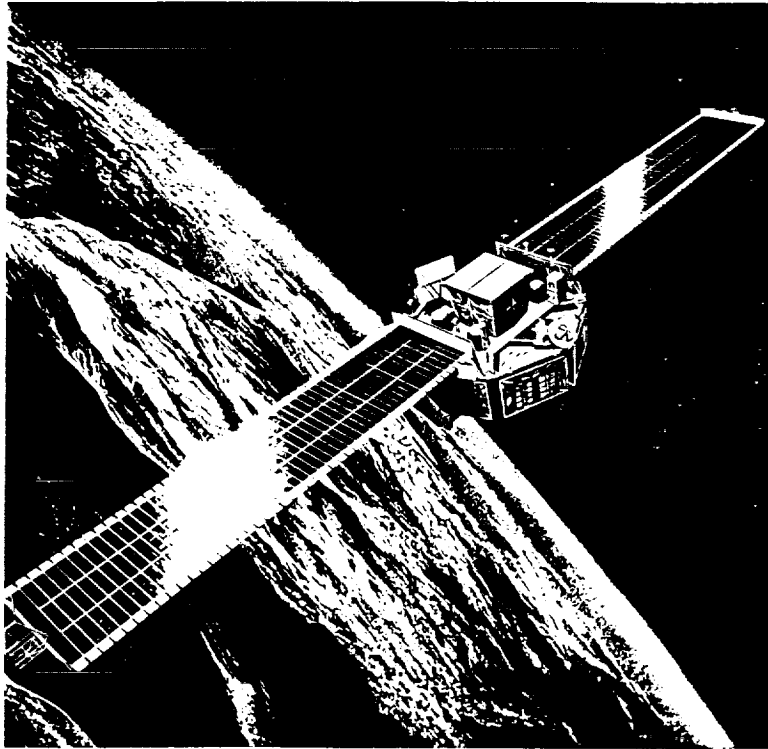


Figure 1: Space Flyer Unit (SFU)
(original figures unavailable)

EFFU is developed to improve the reliability of the JEM exposed facility. The missions are the following:

- 1. Equipment Exchange Mechanism Test**
- 2. Active Thermal Control System Test**
- 3. Element Material Exposure Experiment**
- 4. Physical Experiment by Gas Dynamics Experiment Facility**

SFU will be launched in the beginning of 1995. The operational orbit is almost the same as the Space Station. The nominal exposed period of EFFU is about 6 months. Some element materials of JEM will be exposed as "ELEMENT MATERIAL EXPOSURE EXPERIMENT" which is one of the EFFU missions. The degradation of the materials is due to atomic oxygen (AO), ultra-violet rays (UV), and radiation, including high energy ions. The other materials will also be installed to monitor these environments quantitatively. Several ground based tests are now being performed in order to select the most suitable materials for monitoring and to get data for estimating each fluence after retrieval.

EXPERIMENT

EFFU configuration is shown in Figure 2. The materials for the exposure experiment and for the monitoring will be attached on the side of the radiator panel facing the sun and on the truss without facing the sun.

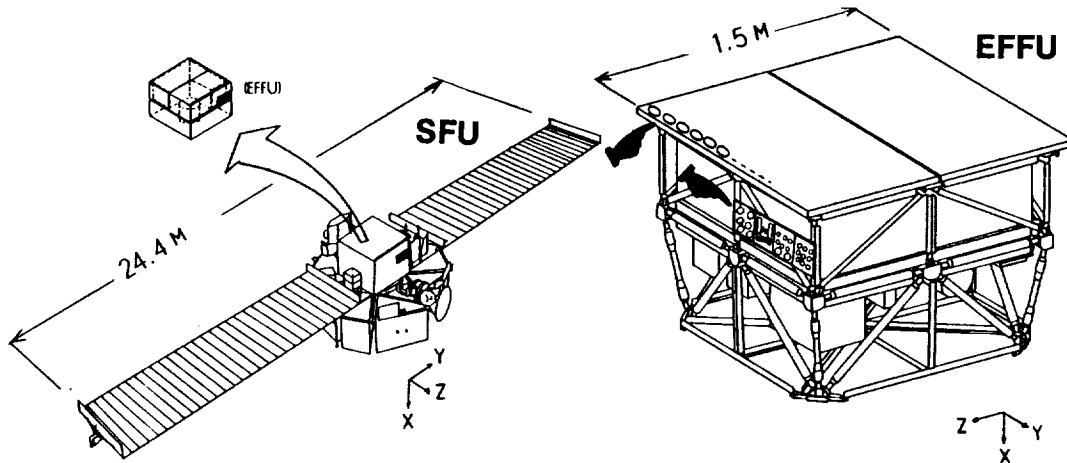


Figure 2: EFFU Configuration

Kawasaki Heavy Industries Co.,Ltd.;Nissan Motor Co.,Ltd;and Toshiba Co.,Ltd. are joining in the exposure experiment with NASDA and IHI. The purpose of the experiment is to investigate the degradation of material exposed for 6 months. The Materials for the exposure experiment are the following:

- (1)Solid Lubricant(HMB-34(MoS₂))
base:Aluminum Alloy,Stainless Steel,and Titanium Alloy
- (2)CFRP
- (3)Glass for Camera Lens
- (4)Thermal control materials
 - Anodized Aluminum
 - ITO coated Polyimide
 - SiO₂ coated Polyimide
 - Beta-Cloth
 - Flexible OSR
 - Silicone Paint
- (5)Electric Wire Covering
- (6)Glass for Solar Cell

The ground based tests are now being performed concerning AO,UV,and Electron Beam before the flight exposure experiment.

MONITORING

IHI is preparing some materials for the monitoring of space environments, atomic oxygen (AO), ultra-violet rays (UV), and radiation, including high energy ions that degrade an exposed material. The monitoring of AO and UV will be done passively; that is, each fluence will be estimated from the mass loss of material or optically changed material after retrieval, compared with ground based test data. CR-39 will be mounted for measuring LET distribution of high energy heavy ions.

Thermo luminescent dosimeter(TLD) and Alanine($C_3H_7NO_2$) dosimeter will be mounted for dose measurement.

AO MONITORING

The Polyimide film, KAPTON-HN, is a strong candidate for AO measuring material. The ground based tests were performed using two facilities in order to obtain the flight fluence evaluation data. IHI's AO test facility was used at first. AO is produced by the direct current arc dissociating method in the facility. The system diagram is shown in Figure 3. The merit of the facility is to be able to perform simulation tests in a short time. The $3.6E20$ [atoms/cm²] simulation test needs only an hour. The disadvantage is that produced AO has small translational energy about 0.2[eV]. The SEM photograph of KAPTON-100HN film specimen after AO irradiation is shown in Figure 4. The reaction efficiency R_e was $1.2E-24$ [cm³/atom] which is about a third of Space. Another test was performed at well-known PSI (Physical Science Inc.) to verify data obtained by IHI. The SEM photograph after irradiation is shown in Figure 5, which is Christmas tree-like and looks like the STS SEM photograph. The two test results are shown in Figure 6.

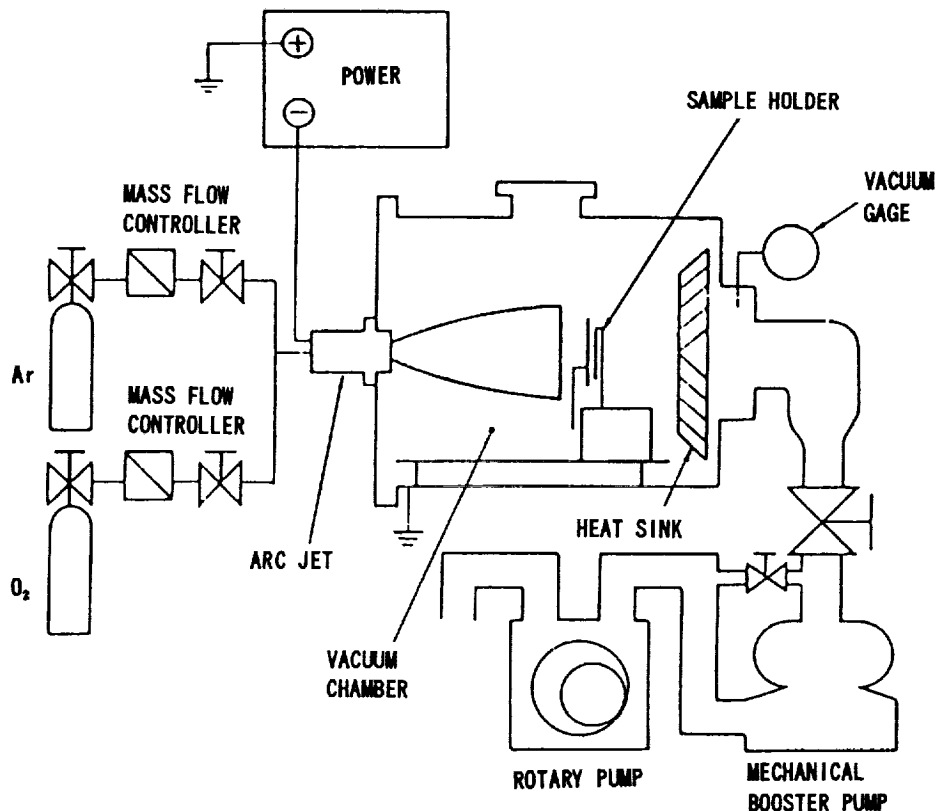
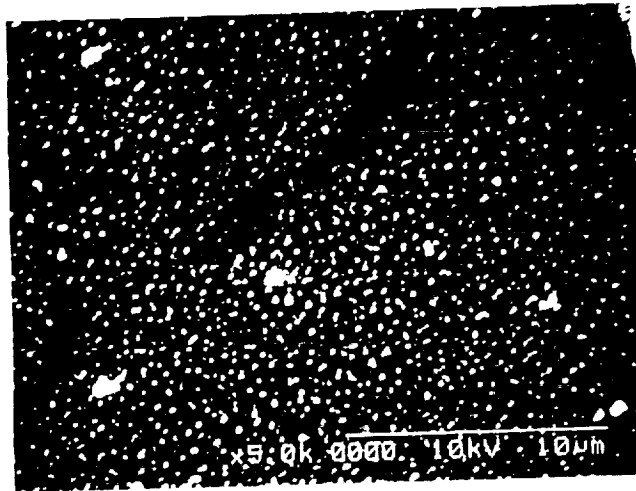
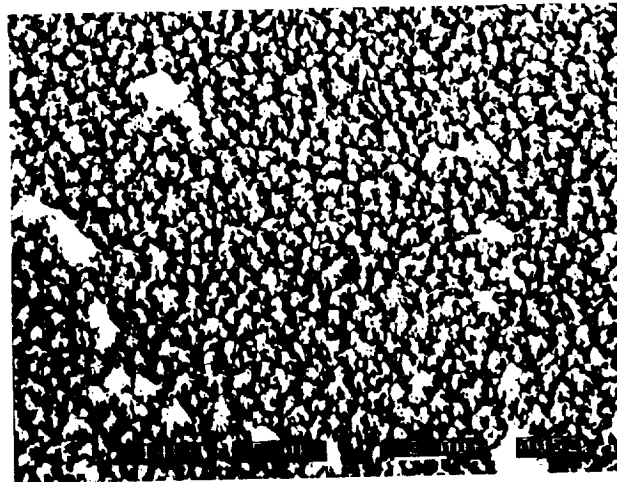


Figure 3: IHI Atomic Oxygen Irradiation Test Facility System Diagram



Irradiated A0 3.6×10^{20} [atoms/cm²]

Figure 4: SEM Photograph Of KAPTON-100HN Film
(IHI AO Testing)



4.51×10^{20} [atoms/cm²]

Figure 5: SEM Photograph Of KAPTON-100HN Film
(PSI AO Testing)

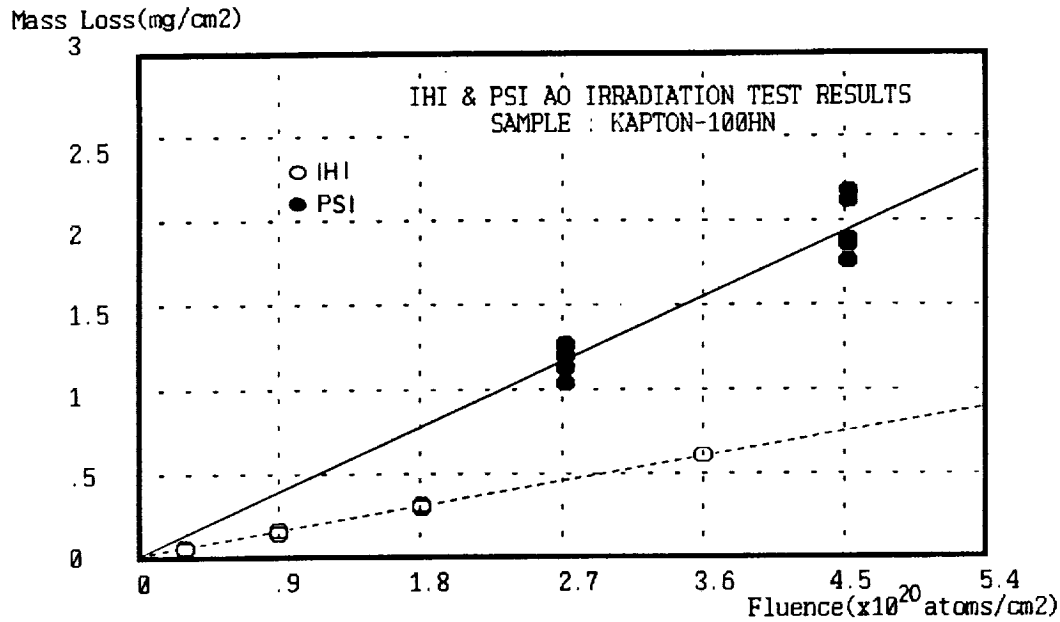


Figure 6: Atomic Oxygen Test Results
Mass Loss Versus AO Fluence

UV MONITORING

The UV fluence on orbit is planned to be estimated from optically changed material. The ground based tests to select the most suitable material for monitoring are under way. The four materials: Silvered Teflon (TEF) 2[MIL] and 5[MIL] thickness; KAPTON-100HN; and acrylic urethane based white paint made in Japan were tested at NASDA Tsukuba Space Center In 1993. The test results are shown in Figure 7. As shown in the figure, no change in emissivity of all materials was recognized, and obvious change was recognized in only solar absorptance of the white paint. The reflection spectrums of the paint are shown in Figure 8, but the change was almost saturated, irradiating about 300 equivalent solar days, so this white paint is not suitable for monitoring in orbit for more than 6 months. The other materials, urethane based white paint, silicon based white paint, which has a stronger bond than urethane based paint, and fluorine based white paint and so on are now being tested.

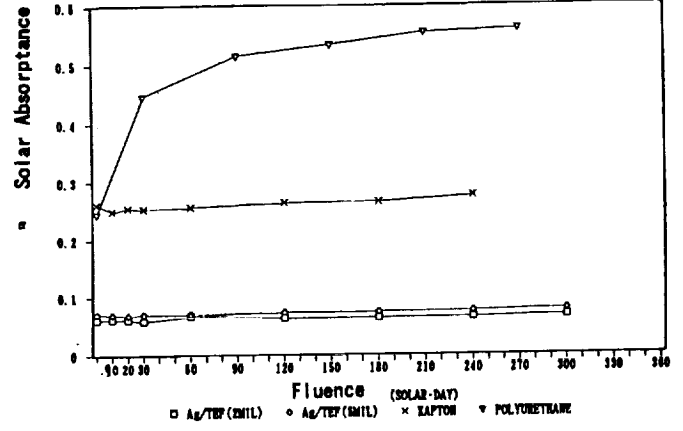
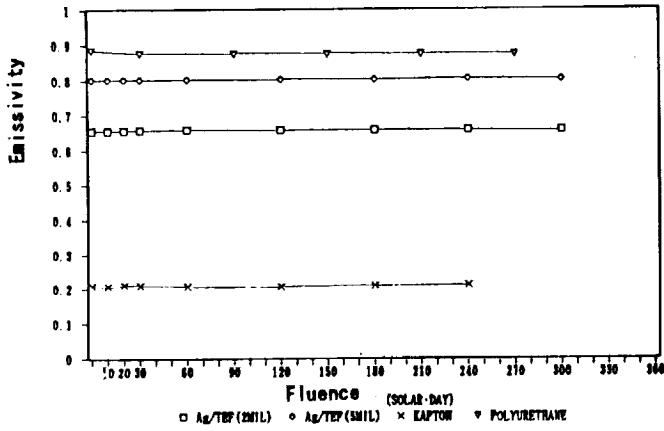
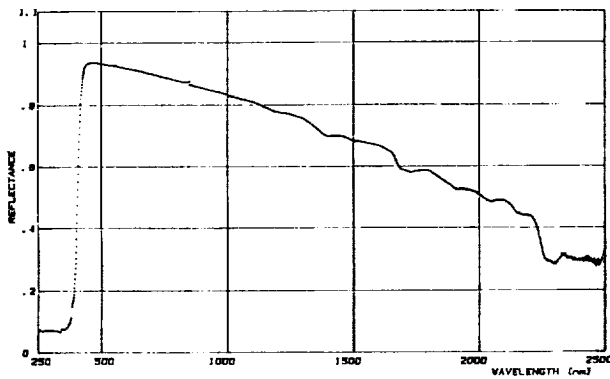
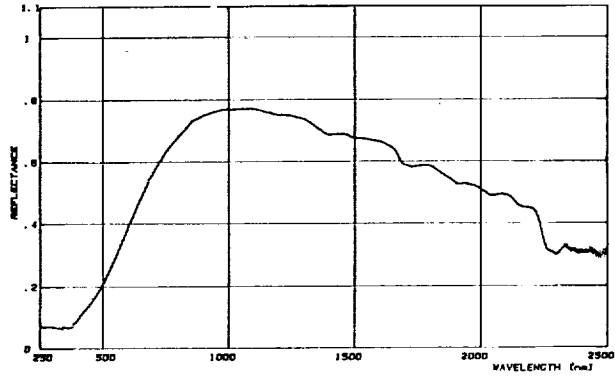


Figure 7: Ultraviolet Ray Irradiation Test Results
Optical Property Versus UV Fluence



Before UV Irradiation



After UV Irradiation (180[solar.day])

Figure 8: Ultraviolet Ray Irradiation Test Results
Reflection Spectrum Of Acrylic Urethane

RADIATION MONITORING

The radiation dose measurement will be made using Thermo luminescent dosimeters(TLD) and alanine dosimeters which are well-known dosimeters. TLDs are MSO (Mg₂SiO₄:Tb) and packed with CR-39 in an airtight aluminum box. The alanine dosimeters will be located completely exposed.

HIGH ENERGY HEAVY IONS MONITORING

CR-39 will be mounted on EFFU for measuring LET distribution of high energy heavy ions. The ground based tests are under way in order to obtain the calibration data.

SYNERGIC EFFECTS

It is important for each monitoring material to avoid other environment. The UV monitor has a UV passing glass cover which is about 2[mm] thick to avoid AO attack. But AO and UV monitors can't avoid electrons. The total number of electrons irradiated on EFFU orbit is estimated as follows:

Energy[MeV]	Number[/m ²]
0.04-0.1	1.363E16
0.1 - 1	2.368E16
1 -	6.730E13

The electron beam irradiation tests are under testing to evaluate synergic effect at Japan Atomic Energy Research Institute. The reflection spectrums of acrylic urethane based white paint are shown in Figure 9. There is no effect recognized in optical property of the paint. The other materials including KAPTON are under testing now.

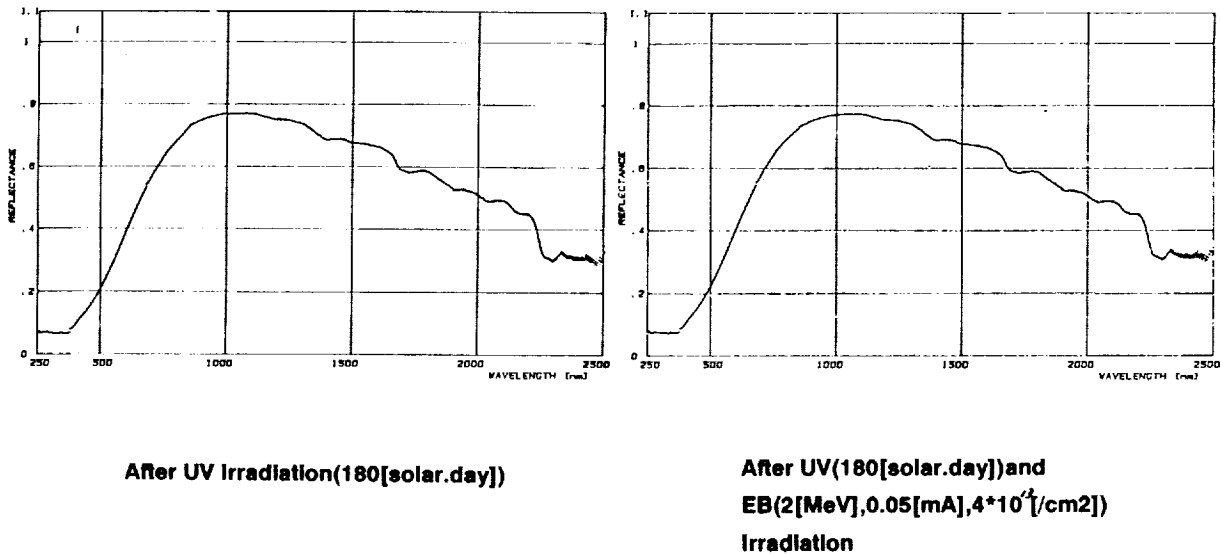


Figure 9: Synergic Effect Of Ultraviolet Ray And Electron Beam
Reflection Spectrum Of Acrylic Urethane

CONCLUSION

The material exposure experiment by EFFU is going to start in 1995. It is very important to obtain ground based test data before flight, especially for the monitor. The synergic effects are not ignored to evaluate material degradation and estimate AO and UV fluences accurately.

Lastly we greatly appreciate NASA Langley Research Center's precious advice.

REFERENCE

1. J.T.Visentine, L.J.Leger, J.F.Kuminecz and I.K.Spiker "STS-8 Atomic Oxygen Effects Experiment", AIAA-85-0415, Jan., 1985
2. L.J.Leger and J.T.Visentine "A Consideration of Atomic Oxygen Interactions with the Space Station", SPACECRAFT, Vol.23, No.5, Sept.-Oct., 1986

Orbiting Meteoroid and Debris Counting Experiment

William H. Kinard ¹, Dwayne Armstrong ², Sharon K. Crockett ³,
James L. Jones, Jr. ⁴, and Philip C. Kassel, Jr. ⁵
NASA, Langley Research Center
Hampton, VA

J. J. Wortman ⁶
North Carolina State University
Raleigh, N. C.

Abstract

The Orbiting Meteoroid and Debris Counting Experiment (OMDC) flew for approximately 90 days in a highly elliptical Earth orbit onboard the Clementine Interstage Adapter (ISA) Spacecraft. This experiment obtained data on the impact flux of natural micrometeoroids, and, it provided limited information on the population of small mass man-made debris as a function of altitude in near Earth space. The flight of the OMDC Experiment on the ISA Spacecraft also demonstrated that the ultra lightweight, low-power, particle impact detector system that was used is a viable system for flights on future spacecraft to monitor the population of small mass man-made debris particles and to map the cosmic dust environment encountered on interplanetary missions. An overview of the ISA Spacecraft mission, the approach to the OMDC Experiment and the data obtained by the experiment are presented.

I. Introduction / Background

Orbital debris represents an inescapable hazard for all space activities. Over the past several years the U.S. and international communities have recognized this present and growing threat as a dominant space environment concern in low altitude earth orbits and a growing concern in higher altitude orbits - particularly in synchronous orbits. The U.S. Congress Office of Technology Assessment has concluded that uncontrolled growth of space operations, including operations by the private sector, could eventually result in a debris population that will inflict severe limitations on space missions.¹ Other investigative organizations, including the National Security Council and the General Accounting Office, as well as NASA and the European Space Agency, have also addressed this problem.²⁻⁵ At issue is not just the possibility of catastrophic collisions of large debris objects with spacecraft, but also surface damage to instruments and systems on spacecraft which can result from

¹ Senior Research Scientist, NASA Langley Research Center, Hampton VA

² Electronic Engineer, NASA Langley Research Center, Hampton VA

³ Mechanical Engineer, NASA Langley Research Center, Hampton VA

⁴ Research Engineer, NASA Langley Research Center, Hampton VA

⁵ Electronic Engineer, NASA Langley Research Center, Hampton VA

⁶ Professor, Electrical Engineering, North Carolina State University, Raleigh NC

impacts of very small debris particles. In fact, surface damage resulting from small particle impacts may become more of a concern in the future with the current trend to fly more and more smaller spacecraft. These small spacecraft will have a very low probability being impacted by debris large enough to inflict catastrophic damage; however, the continuous bombardment of small debris can result in surface alterations that will limit their useful lifetime on orbit.

A prerequisite to establishing the controls needed to limit future growth in the man-made debris population and to getting these controls accepted by all space faring nations is the development of adequate data bases and models to define the sources of debris and the populations, sizes and orbits of the particles that are generated by these sources. Terrestrial measurements made by the Goldstone and Haystack ground-based radars, the GEODSS telescopes, along with data from USSPACECOM are providing adequate information on the population and orbits of debris objects that are a centimeter and larger in size near the Earth. Adequate measurements of the populations of smaller debris particles are not yet being made.

To date the LDEF experiments have provided the best indications of the small mass debris populations; however, separating the man-made debris impacts on these experiments from the natural meteoroid impacts has proven to be difficult. Also the LDEF provided data on debris only at the altitude of its near circular orbit (approximately 430 km). Prior to the Clementine mission there had been essentially no measurements that were focused on the populations of small mass debris at high altitudes and particularly near the synchronous orbits.

The Clementine ISA spacecraft, which flew in a highly elliptic orbit with a perigee altitude of approximately 127,000 km, spent most of its orbiting lifetime at altitudes above the orbits of man-made debris; thus, it provided an opportunity to obtain data on the natural meteoroid environment with no confusion introduced by man-made debris impacts. The ISA spacecraft's low perigee altitude, approximately 290 km, also allowed limited times to obtain data on the population of debris as a function of altitude. The OMDC Experiment was flown on the ISA spacecraft to take advantage of these opportunities and to establish whether or not the new detectors used in the experiment are a viable candidate for future spacecraft flights to monitor changes in man-made debris populations and to measure the natural meteoroid environments encountered during interplanetary missions.

The OMDC Experiment development, integration and post flight analysis were funded by the NASA Office of Advanced Concepts. The NASA Langley Research Center (LaRC) provided the overall management of the experiment and LaRC personnel designed and manufactured in-house all elements of the experiment hardware with the exception of the detectors. The impact detectors were developed and manufactured by faculty and students at North Carolina State University. Personnel at the Institute of Space Science and Technology generated the science requirements to supported the experiment development.

It is worthy to note that the OMDC Experiment was designed, manufactured, tested, and integrated on the ISA Spacecraft in less than 4 months and at a cost of only \$200,000, and that the experiment hardware meet all Clementine Program requirements including requirements that it weigh approximately 460 grams and use less than 10 milli watts of power.

II. General Approach

The basic approach to the OMDC Experiment was to measure the impact frequencies of sub micron particles as a function of time and spatial position. It was assumed that the impacts detected at altitudes above 46,000 km, the altitude of satellites in synchronous orbits, will be the result of collisions

with natural meteoroids only. Knowing the effects of the Earth's gravitational focusing of these meteoroids, it was also assumed that the natural meteoroid impact fluxes at lower altitudes can be established from flux measurements made at altitudes above 46,000 km. At altitudes below 46,000 km impacts of both natural meteoroids and man-made debris particles will be detected. The debris impact fluxes at these altitudes can be established by subtracting the calculated natural meteoroid impact flux from the combined meteoroid and debris flux measurements obtained by the OMDC Experiment.

III. MOS Detectors

The OMDC Experiment utilized improved ultra-light weight MOS (metal-oxide-silicon) impact detectors that are a derivative of the MOS detectors flown earlier in the Interplanetary Dust Experiment (IDE)⁶ on the Long Duration Exposure Facility (LDEF) and on the Meteoroid Technology Satellite (MTS)⁷. The improved MOS detectors, which were rectangular 3.9 cm wide and 7.7 cm long, were manufactured from 10.2 cm diameter silicon wafers cut 0.3 mm thick. A schematic of the detector and electrical connections is illustrated in Figure 1.

The surfaces of the 10.2 cm silicon wafers were oxidized to produce a silicon dioxide layer 1.0 μm thick. The wafers were then masked to the rectangular detector shape and aluminum was vapor deposited to a thickness of 0.1 μm on the silicon dioxide layer on the front. The aluminum and the silicon substrate thus formed the plates of a capacitor. The silicon dioxide layer formed the capacitor dielectric. These capacitors were charged to a nominal 43 volt bias. Impacts of particles having sufficient mass and velocity to penetrate the silicon dioxide dielectric layer will discharge the capacitor and the discharge current flow will burn the vapor deposited aluminum layer away from the region surrounding the impact site, thus allowing the capacitor to be recharged. The capacitor discharges are monitored to detect the particle penetration events. Extensive laboratory calibrations of the MOS detectors have established the impacting particle mass and velocities that are required for detection.⁸ The detectors weighed approximately .5 gram each, an order of magnitude less than the similar MOS detectors that were used earlier on the LDEF IDE and on the MTS. Figure 2. shows photographs of an OMDC detector and for comparison an earlier IDE detector.

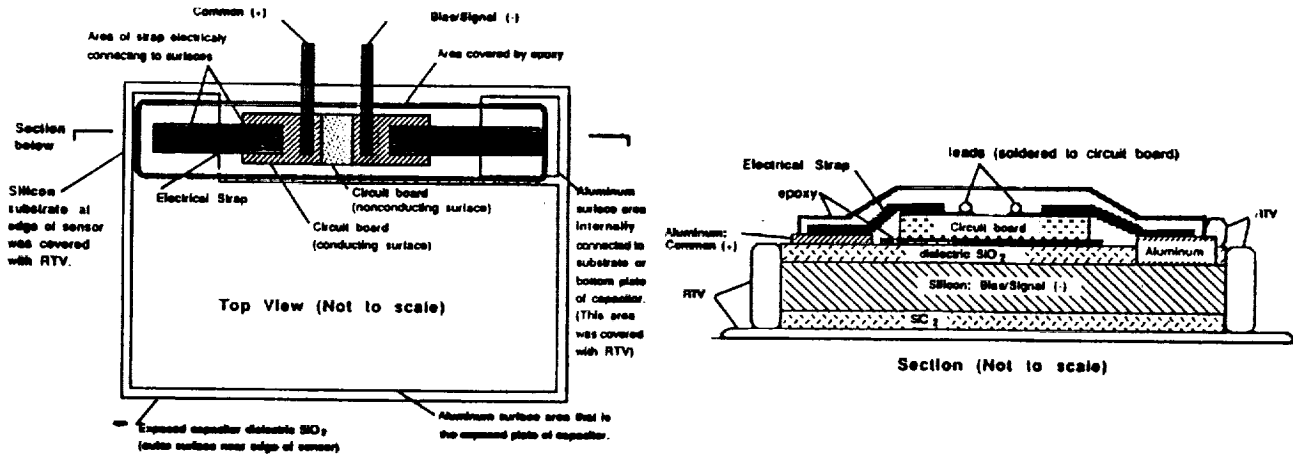
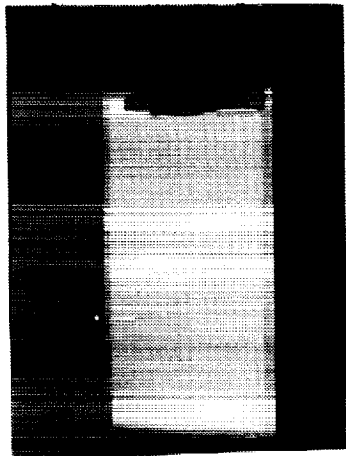
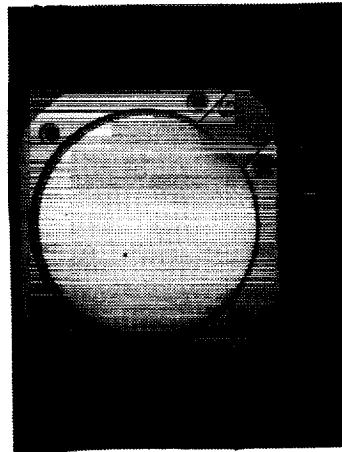


Figure 1. Schematic of the MOS detectors and electrical connections used on the OMDC Experiment. (Not to scale)

A photograph of an OMDC detector and, for comparison, a photograph of an earlier IDE detector are shown in Figure 2.



OMDC Detectors



LDEF IDE & MTS Detectors

Figure 2. Photographs of the MOS detector used on the OMDC Experiment and the MOS detector used on the LDEF IDE and the MTS.

IV. Detector Installation

A total of 54 of the MOS detectors were installed, using RTV 566 adhesive, in a ring on the exterior of the ISA Spacecraft structure at the same time and in the same manner as the spacecraft solar cells were installed. The bonding of the detectors directly to the spacecraft surface, rather than installing the detectors in a mount that is mechanically fastened to the spacecraft, as was done on LDEF, resulted in significant weight savings. Photographs of the detectors mounted on the ISA Spacecraft are shown in Figure 3.



Figure 3. Photographs of OMDC Experiment detectors installed on the ISA Spacecraft.

After installation, the edges of the detectors were sealed with RTV 142 to prevent current leakage through any plasma that may exist on orbit around the spacecraft. Later, based on data from electrical status checks and on the observations that some of installed detectors were badly shadowed by other spacecraft parts, 48 of the 54 installed detectors were selected to be actively connected to the OMDC Experiment electronic system. The wiring harness connecting the selected detectors and the experiment electronics was also tacked to the spacecraft structure with RTV 142 adhesive. Both the RTV 566 and the RTV 142 were chosen for their low-outgassing properties and previous space use qualifications.

V. Electronic System

The selected 48 active detectors were electrically connected to form 3 arrays of 16 detectors each. Each array covered a 120° segment of the spacecraft surface. The 16 detectors in each array were electrically partitioned into 2 groups - one having 9 detectors and one having 7 detectors. This partitioning of one array of the detectors and the block diagram for the electronics associated with that array is shown in Figure 4.

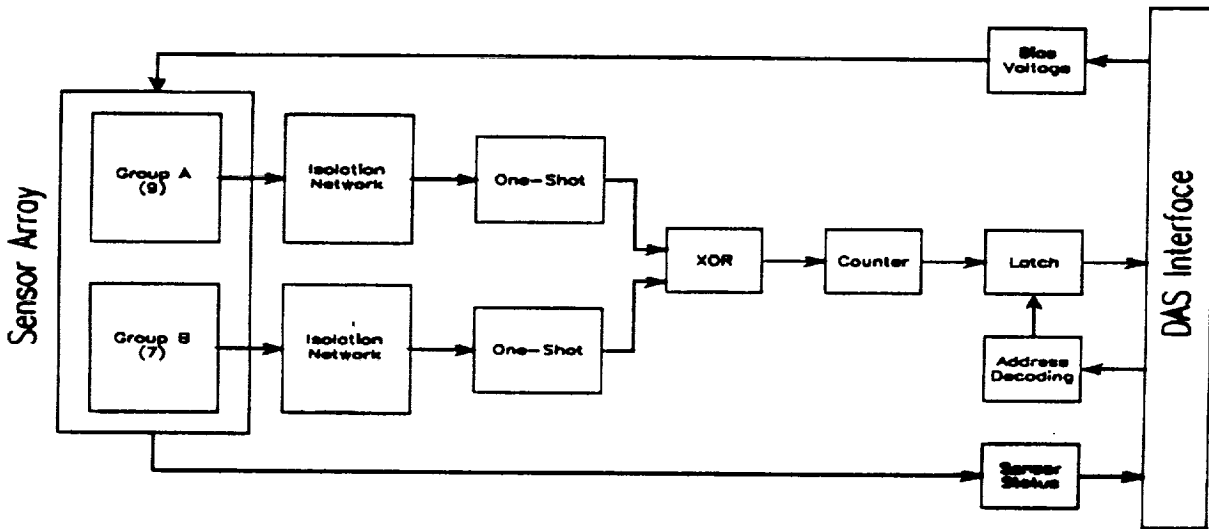


Figure 4. Block diagram of electronics associated with each of the 3 arrays of detectors.

Laboratory test data has shown that the MOS detectors require a minimum bias of 30 volts and a nominal operating bias of 43 volts. Since the load presented by the detectors was essentially capacitive, little drive current was required to achieve the bias. A 12 volt oscillator was created for use in the OMDC as an input to a voltage quadrupler. The output of the voltage quadrupler was then regulated to be the required 43 volt bias source. The bias supplied to each detector was current limited by a 2.2 meg. ohm resistor to prevent overloading of the bias supply in the event a detector was permanently shorted.

The signal leads from each group of detectors were paralleled. A particle impact on one detector causes a temporary short which discharges that detector. An isolation network was used to prevent the other detectors in the group from also being discharged through this temporary short. A one-shot was used to sense the temporary shorting of an impacted detector. The output of this one-shot in each group, which was XORed to allow simultaneous detection of impacts on the other group in the same array, clocked a counter to record the total number of impacts for the entire array.

Each array was memory mapped by the ISA spacecraft Data Acquisition System (DAS). Each counter was isolated from the data bus by a Class C radiation hardened HCS245 to prevent the OMDC Experiment from seizing control of the data bus in the event of an experiment system failure. When the correct address for an array was decoded, the appropriate HCS245 latched the data and put it on the data bus to be read by the DAS.

The health of all of the OMDC Experiment in terms of the number of detectors that developed shorts was monitored by a status circuit. The leakage current of each array of detectors was converted to a voltage by a trans-impedance amplifier. Each status voltage was inputted to a passive summer whose output was buffered by a voltage follower. This signal was read by the DAS and converted to a digital word representing the overall health of the detectors.

The fault tolerance that could be built into the experiment electronic system was limited by the extremely severe power, size and weight constraints. Redundancy in the ground wiring of the detector harness was, however, implemented such that two breaks of ground wires would be required to lose more than one detector.

The ISA Spacecraft DAS sampled the array counters once every 5 seconds. If an impact was detected, the value of the counters and the value of the system clock was written to memory. The detector status was sampled by the DAS every 10 minutes and written to memory. The OMDC Experiment data was broadcast with the other ISA Spacecraft telemetry signals upon ground commands.

VI. Testing

The method used to install the MOS detectors on the ISA Spacecraft structure was verified in thermal/vacuum test and in vibration test that were run on a test assembly. The experiment electronic system was also subjected to thermal/vacuum and vibration test, and, it underwent complete functional, workmanship and acceptance testing as a unit before it was integrated into the spacecraft DAS. After the OMDC Experiment electronic system was installed in the DAS, it underwent further environmental, acceptance and performance testing as a part of the ISA Spacecraft.

VII. Data Obtained

The originally planned apogee altitude for the ISA Spacecraft was approximately 195,000 km and with that perigee the prelaunch orbiting lifetime was predicted to be greater than 1 year. The ISA Spacecraft actually achieved an apogee of only 127,000 km. With this lower apogee the spacecraft orbiting lifetime proved to be only 3 months and thus the data sample obtained by the OMDC Experiment was reduced. There were also other situations that developed with the ISA Spacecraft that have created some difficulties in analyzing the OMDC Experiment data. First, there were spacecraft telemetry command and receiving problems that resulted in the loss of precise timing data and thus the orbit position for some of the impact events that were detected. No impacts were lost however. The data obtained was more than adequate to demonstrate the excellent performance of the new MOS detectors that were used. The data was also adequate to provide valuable information on the natural meteoroid environment near the Earth and an indication of the variation in the man-made debris population with altitude.

The OMDC Experiment health status circuit indicated that all of the 48 active detectors probably remained operational for the entire mission duration - even the last several orbits when the perigee altitude was rapidly dropping. In a worse case scenario, no more than one or two of the detectors could have developed permanent shorts. Thus for analysis purposes, the active sensing area for the experiment during the mission was a well defined quantity. All other ISA Spacecraft

housekeeping data that related to the OMDC Experiment indicated nominal performance of the experiment. The complete data set that was obtained is presented in Table I. The first column of the Table I presents the calendar date and time of broadcasts that contained new impact counts. The second and third columns lists the day of the year and the orbit respectively that new impact counts were recorded. The fourth and fifth columns lists the accumulated counts transmitted from each of the three array counters and the number of new events indicated by each array counter respectively. The sixth column lists the radial distance from the center of the Earth to the spacecraft location when a new event was detected. In those situations where multiple events were transmitted in a single transmission, the radial distance to the point of impact of the last of the multiple events only is known. The seventh and eighth columns lists the angle from perigee and the hours from perigee.

It should be mentioned that the ISA Spacecraft had no attitude control or attitude measuring systems, and the attitude motions of the spacecraft could not be predicted analytically. It was hoped that ground observations of the ISA Spacecraft during perigee passages would provide some indications of the orientation, but they did not. Since the detectors on the OMDC Experiment did not present equal detecting areas in all directions around the spacecraft, the unknown ISA Spacecraft orientation results in uncertainties in the analysis.

The early analysis of the data from the OMDC Experiment have been made and published.^{9, 10}

VIII. Conclusions

The flight of the OMDC Experiment on the ISA Spacecraft has demonstrated that useful data can be obtained with small, light weight, low power and inexpensive instruments that are developed and flown in a short period of time. The experiment is evidence of the positive side of the trend to smaller, cheaper and quicker spacecraft. The OMDC Experiment has also demonstrated that the ultra-light weight new MOS detectors that were used are excellent detectors for use on future near Earth spacecraft to monitor the small mass man-made debris population and on interplanetary spacecraft to monitor map the natural meteoroid environments encountered during the mission.

TABLE I
Accumulated Impacts - OMDC Experiment on ISAS

Date	DOY	Orbit	Accumulated				New Counts			radial dist	Pengee Angle	Hours from Pengee
			C1	C2	C3	Total	C1	C2	C3			
02/04/94 07:12	35.3005	138	1	2	2	5	1	2	2	1.33E+05	179.3	24.89
02/04/94 15:14	35.6348	138	2	2	2	6	1			1.27E+05	186.1	32.71
02/04/94 16:45	35.6981	138	3	2	2	7	1			1.23E+05	187.5	34.23
02/04/94 18:40	35.7780	138	3	2	3	8			1	1.18E+05	189.4	36.15
02/19/94 15:36	50.6500	145	5	3	4	12	2	1	1	1.22E+05	187.9	34.80
04/03/94 00:19	93.0133	165	8	6	6	20	3	3	2	1.33E+05	181.4	27.30
04/03/94 05:42	93.2379	165	8	6	7	21			1	1.27E+05	186.1	32.68
04/05/94 01:41	95.0707	166	8	6	8	22			1	1.33E+05	179.9	25.43
04/21/94 00:48	111.0336	173	11	8	8	27	3	2		2.28E+04	240.7	50.15
04/29/94 14:51	119.6189	178	11	8	14	33			6	1.19E+04	87.3	0.40
04/29/94 15:03	119.6274	178	11	8	15	34			1	1.57E+04	103.1	0.61
04/29/94 15:41	119.6535	178	11	8	16	35			1	2.60E+04	125.1	1.23
04/29/94 16:01	119.6676	178	11	8	17	36			1	3.09E+04	131.2	1.57
04/29/94 18:00	119.7505	178	11	8	18	37			1	5.39E+04	148.0	3.56
04/29/94 23:23	119.9749	178	11	8	19	38			1	9.30E+04	162.8	8.95
04/30/94 16:50	120.7014	178	11	8	20	39			1	1.33E+05	180.7	26.38
04/30/94 22:56	120.9562	178	11	8	21	40			1	1.27E+05	185.9	32.50
05/01/94 03:55	121.1635	178	11	8	22	41			1	1.13E+05	190.9	37.47
05/01/94 15:01	121.6261	178	11	8	23	42			1	4.24E+04	216.8	48.58
05/04/94 15:31	124.6467	180	12	8	24	44	1		1	1.27E+05	174.5	19.00
05/05/94 23:55	125.9968	180	12	9	24	45		1		1.32E+04	93.6	0.47
05/06/94 01:02	126.0435	180	12	10	24	46		1		3.12E+04	131.5	1.59
05/06/94 05:26	126.2264	180	12	11	24	47		1		7.43E+04	158.7	5.98
05/06/94 07:12	126.3005	181	12	11	25	48			1	8.62E+04	160.7	7.77
05/06/94 08:38	126.3603	181	12	12	25	49			1	9.44E+04	163.3	9.20
05/06/94 10:50	126.4519	181	12	13	25	50			1	1.05E+05	166.5	11.40
05/06/94 13:22	126.5573	181	12	13	26	51			1	1.15E+05	169.6	13.93
05/07/94 02:10	127.0909	181	12	13	27	52			1	1.33E+05	181.0	26.73
05/07/94 03:07	127.1300	181	12	13	28	53			1	1.32E+05	181.8	27.67
05/07/94 05:50	127.2435	181	12	14	28	54			1	1.30E+05	184.1	30.40
05/07/94 06:52	127.2865	181	12	15	28	55			1	1.28E+05	185.0	31.43
05/07/94 07:48	127.3250	181	12	16	28	56			1	1.27E+05	185.8	32.35
05/07/94 09:52	127.4114	181	12	17	28	57			1	1.22E+05	187.8	34.43
05/07/94 10:01	127.4178	181	12	18	28	58			1	1.22E+05	187.9	34.58
05/07/94 14:12	127.5923	181	12	19	28	59			1	1.08E+05	192.5	38.77
05/07/94 14:33	127.6067	181	12	19	29	60			1	1.07E+05	193.0	39.11
05/07/94 15:41	127.6538	181	12	19	30	61			1	1.02E+05	194.5	40.24
05/07/94 15:54	127.6629	181	12	19	31	62			1	1.01E+05	194.8	40.46
05/07/94 16:04	127.6698	181	12	20	31	63			1	9.99E+04	195.0	40.63
05/07/94 17:11	127.7165	181	12	21	31	64			1	9.42E+04	196.7	41.75
05/07/94 18:21	127.7650	181	12	22	31	65			1	8.78E+04	198.8	42.91
05/07/94 19:30	127.8125	181	12	23	31	66			1	8.05E+04	201.1	44.05
05/07/94 20:29	127.8537	181	12	24	31	67			1	7.35E+04	203.6	45.04
05/07/94 23:27	127.9773	181	12	25	31	68			1	4.72E+04	215.8	48.01
05/07/94 23:42	127.9678	181	12	25	32	69			1	4.45E+04	217.3	48.26
05/07/94 23:55	127.9969	181	12	25	33	70			1	4.20E+04	219.1	48.48
05/08/94 04:35	128.1915	182	12	25	36	73			3	3.39E+04	134.5	1.79
05/08/94 04:57	128.2067	182	12	25	37	74			1	3.86E+04	138.6	2.18
05/08/94 05:03	128.2111	182	12	25	38	75			1	3.98E+04	139.6	2.26
05/08/94 06:01	128.2512	182	12	25	39	76			1	5.05E+04	146.4	3.23
05/08/94 10:55	128.4555	182	12	26	39	77			1	8.82E+04	161.6	8.13
05/08/94 15:12	128.6339	182	12	27	39	78			1	1.09E+05	167.9	12.41
05/10/94 00:20	130.0143	182	12	28	39	79			1	6.57E+04	206.4	45.54
05/10/94 00:38	130.0287	182	12	28	40	80			1	6.32E+04	207.4	45.84

References

1. U.S. Congress, Office of Technology Assessment, *Orbiting Debris: A Space Environment Problem--Background Paper*, OTA-BP-ISC-72, Washington, DC: U.S. Government Printing Office (September 1990).
2. European Space Agency, "Space Debris", SP-1109, Paris (1988).
3. R.C. Reynolds and A.E. Potter, Jr., "Orbital Debris Research at NASA Johnson Space Center," Tech. Memo. 102155, National Aeronautics and Space Administration, Houston, TX (1989).
4. U.S. National Security Council, "Report on Orbital Debris," Washington, DC (1989).
5. U.S. Congress, General Accounting Office, "Space Program: Space Debris a Potential Treat to Space Station and Shuttle," Washington, DC (1990).
6. J. Derral Mulholland, S. Fred Singer, John P. Oliver, Jerry L. Weinberg, William J. Cooke, Nancy L. Montague, Jim J. Wortman, Philip C. Kassel and William H. Kinard, "IDE Spatio-Temporal Impact Fluxes and High Time-Resolution Studies of Multi-Impact Events and Long-Lived Debris Clouds," LDEF-69 Months in Space, First Post-Retrieval Symposium, NASA Conference Publication 3134 Part 1 (1991).
7. P.C. Kassel, "Characteristics of Capacitor-Type Micrometeoroid Flux Detectors when Impacted with Simulated Micrometeoroids," NASA TND 7359, (1973).
8. P.C. Kassel and J.J. Wortman, "Metal Oxide Silicon Capacitor Detector for Measuring Micrometeoroids and Space Debris Flux," Accepted for publication in *AIAA Journal of Spacecraft and Rockets* (1994).
9. John P. Oliver, "A First Look at the Clementine Interstage Adaptor Satellite Orbital Meteoroid and Debris Counter (OMDC) Results," Accepted for publication in *AIAA Journal of Spacecraft and Rockets* (1994).
10. John N. Thomas, Dave F. Medina and Henry B. Garrett, "Measurements of Interplanetary Dust and Orbital Debris on Clementine Interstage Adaptor Satellite," Accepted for publication in *AIAA Journal of Spacecraft and Rockets* (1994).

**THE STRATEGIC TECHNOLOGIES FOR AUTOMATION
AND ROBOTICS (STEAR) PROGRAM
PROTECTION OF MATERIALS IN THE SPACE ENVIRONMENT SUBPROGRAM**

L.R. Schmidt and J. Francoeur, Canadian Space Agency, STEAR Program¹

A. Agüero, Cametoid Advanced Technologies Inc.

M.R. Wertheimer, J.E. Klemberg-Sapieha, and L. Martinu, École Polytechnique

J.W. Blezius and M. Olivier, MPB Technologies Inc. and A. Singh, National Optics Institute

SUMMARY

Three projects are currently underway for the development of new coatings for the protection of materials in the space environment. These coatings are based on vacuum deposition technologies. The projects will go as far as the proof-of-concept stage when the commercial potential for the technology will be demonstrated on pilot-scale fabrication facilities in 1996. These projects are part of a subprogram to develop supporting technologies for automation and robotics technologies being developed under the Canadian Space Agency's STEAR Program, part of the Canadian Space Station Program.

1.0 INTRODUCTION

The Protection of Materials in the Space Environment subprogram is part of a larger Canadian Space Agency (CSA) program called STEAR (Strategic Technologies for Automation and Robotics). The STEAR Program was established to encourage the participation of Canadian companies, universities and research organizations in automation and robotic technologies which will have the potential to be used on advanced versions of the Mobile Servicing System (MSS). Canada is responsible for the development of the MSS for the international Space Station. "Protection of Materials in the Space Environment" was initiated as a supporting technology development for the automation and robotics technologies. It aims to identify, develop and demonstrate through detailed testing and evaluation, effective means of protecting structural materials and finishes used for the MSS, which will maintain their physical and functional integrity in the Low Earth Orbit (LEO) environment for 10 to 30 years. Three protection of materials research and development projects have commenced and will proceed over the next two years through to proof-of-concept and prototype development. This paper discusses the objectives and status of the Protection of Materials in the Space Environment subprogram and introduces the work being done by the three participating companies.

1. Addresses and phone numbers are provided in footnotes throughout the paper.

2.0 PROTECTION OF MATERIALS IN THE SPACE ENVIRONMENT SUBPROGRAM

2.1 STEAR Program Objectives

2.1.1 Specific STEAR Program Objectives

The STEAR Program's specific objectives are to:

- identify for development advanced strategic technologies which offer potential for incorporation into advanced versions of the MSS;
- support research and development of selected technologies in the private sector, until proof-of-concept is demonstrated;
- encourage the collaboration and networking of industries, universities and nonprofit research organizations;
- promote commercial exploitation of the strategic technologies developed within the Program by joining STEAR contractors to the MSS prime contractor/team and to government programs which support future product development and marketing; and
- ensure the regional distribution of STEAR developed activities across Canada.

2.1.2 STEAR Program Technology Emphasis

Emphasis is placed on strategic technologies which support the technical and operational advancement of the MSS and, in particular, its capability to:

- maximize the productivity of the Space Station's resources;
- minimize the operating costs;
- minimize extra-vehicular activities by the Space Station's flight crew; and
- maximize the service life of the MSS materials and structures.

2.1.3 The Need for the Protection of Materials on the MSS

The LEO environment in which the MSS will operate has proven to be very hostile. Recent experience has shown that many important materials used on the exterior of spacecraft, such as thermal control blankets, are rapidly attacked and eroded by atomic oxygen. Some of the features of the LEO environment which could prove hazardous to the MSS include: atomic oxygen, ultraviolet radiation, charged particle radiation, temperature extremes, thermal cycling, micrometeoroids, long term exposure to vacuum, and combined effects.

The flight segment of the Space Station MSS (see Figure 1) consists of three main elements: the Mobile Servicing Centre (MSC) - which includes the Space Station Remote Manipulator System (SSRMS) and the Mobile Base System (MBS); the Special Purpose Dexterous Manipulator (SPDM); and the MSS Maintenance Depot. The SSRMS is a versatile, 17 metre long manipulator arm, capable of moving more than 100,000 kilograms in space. It is an enhancement of the Shuttle's highly successful Remote Manipulator System (the "Canadarm"). A seventh joint will allow the SSRMS to mimic most of the movements of the human arm as it sweeps through space to grasp, place or move objects, or to manoeuvre astronauts. The SSRMS is a symmetrical design with either end being capable of acting as the shoulder or the wrist. The shoulder joint is attached to a rigid base through Power Data Grapple Fixtures (PDGFs) which also provide the electrical power, data and video interfaces. The wrist's end effector will be able to grasp tools, payloads, the SPDM or even the Shuttle Orbiter. The SPDM is equipped with two manipulator arms and will incorporate innovative technologies such as machine vision and force feedback to handle delicate work such as replacing components and working on the Space Station's electrical connections. The robotic manipulators will access specially designed tools and spare parts from the MSS Maintenance Depot.

The MSS will be constructed of standard space-rated materials as well as advanced composite materials such as graphite/epoxy and PEEK/graphite (poly ether ether ketone). Multi-layer thermal blankets will be used in some areas of the MSS and other areas of the Space Station to protect composite, aluminum and other metallic and non-metallic components. Thermal blankets are typically thick and heavy; for example, the blankets used on the Canadarm have an outer layer of Beta cloth, two layers of single-goldized Kapton², and two layers of double-goldized Kapton with each layer separated by a Dacron scrim cloth.

The protective coatings being developed on the STEAR Program offer the potential of being able to provide at least the same amount of protection as thermal blankets currently planned for use on the MSS and other areas of the Space Station at a significantly lower weight and thickness. These coatings also have potential for the protection of other space hardware systems such as Canada's RADARSAT which is an advanced Earth observation satellite project to monitor environmental change and to support resource sustainability.

2. Kapton is a registered trademark of DuPont.

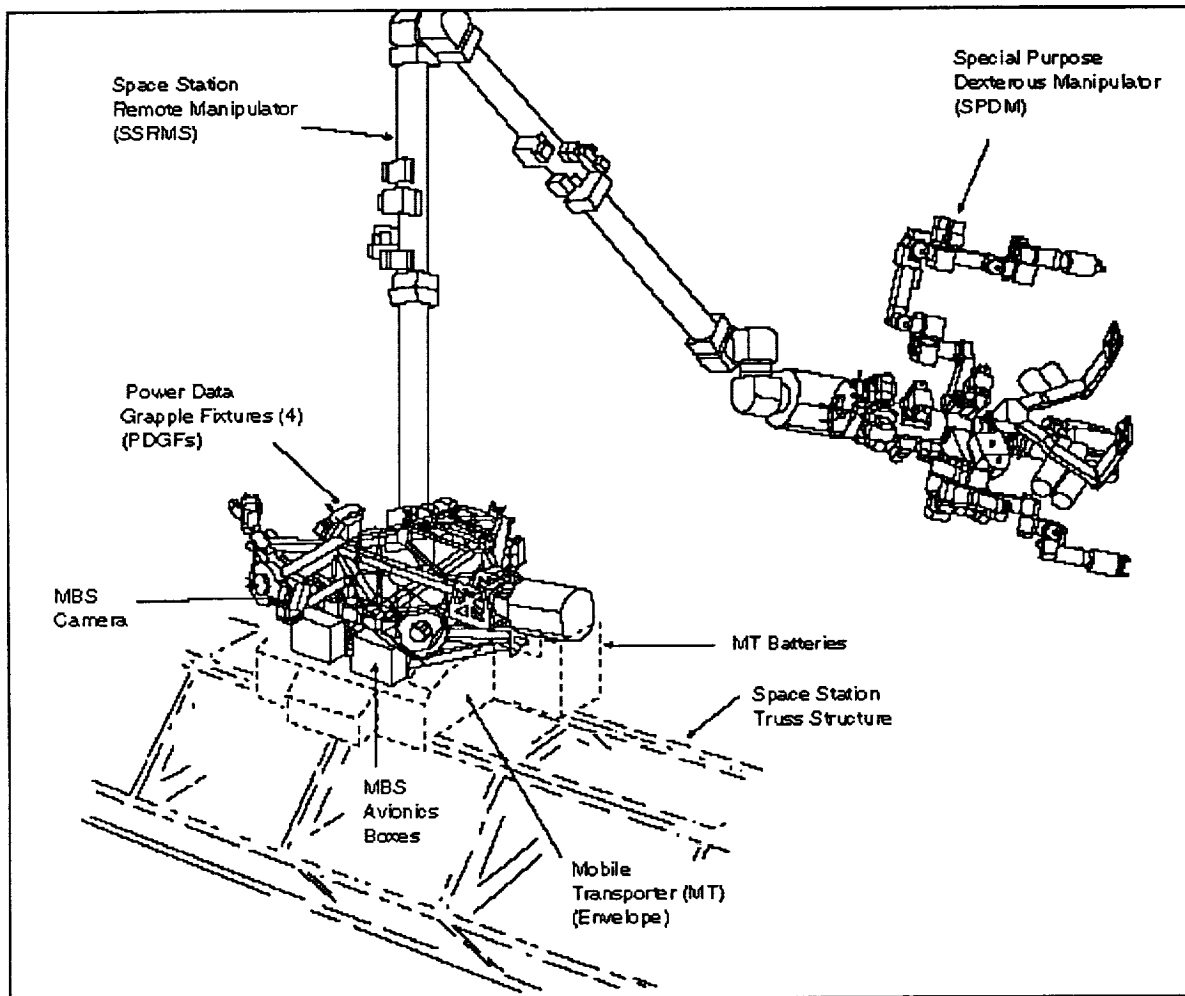


Figure 1.
The Mobile Servicing System

Some of the advantages being sought from the development of new protective coatings include:

- light weight
- strong adherence to the substrate
- resistance to attack by atomic oxygen
- tolerance to ultraviolet radiation while not changing the optical or thermal properties of the underlying substrate material
- antistatic properties, to prevent the build-up of harmful potential gradients
- ability to minimize the thermal cycling effects within the substrate
- ability to withstand temperature extremes

2.2 Protection of Materials in the Space Environment Subprogram

2.2.1 Subprogram Overview

The Protection of Materials in the Space Environment Subprogram is being conducted in two phases. During Phase I (July 1991 to May 1992), six companies won competitive bids to conduct feasibility studies to identify, develop and demonstrate through test and evaluation, effective means of protecting structural materials and finishes used for the MSS in the LEO Environment for 10 to 30 years. At the end of Phase I, each of these companies submitted a feasibility study report and a proposal for a Phase II development. Phase II projects (November 1992 to April 1996) will further develop the technology to the proof-of-concept stage including a demonstration of a prototype fabrication capability.

2.2.2 Phase I - Feasibility Study

The companies selected in a competitive bid process for the six, one-year, \$100,000 Phase I projects were:

- Aastra Aerospace Incorporated of Downsview, Ontario
- Cametoid Advanced Technologies Incorporated of Whitby, Ontario
- Ceramics Kingston Incorporated of Kingston, Ontario
- Datco Technology Limited of Mississauga, Ontario
- FRE Composites Incorporated of Saint-André, Québec
- MPB Technologies Incorporated of Pointe Claire, Québec

During Phase I, the contractors investigated the deposition of a number of different coatings, by various methods, on a number of substrates and then characterized the performance of the system using a standardized mandatory test plan set by CSA, and non-mandatory tests as selected by each of the contractors for their own unique processes. Substrates for the standardized testing were supplied to the contractors, including Aluminized Kapton, Aluminized Teflon, Beta Cloth, Carbon/Epoxy and Carbon/PEEK. The mandatory tests included:

- High Energy Atomic Oxygen and Ultraviolet Radiation
- Thermal Cycling
- Outgassing
- Solar Absorptivity and Emissivity
- Scanning Electron Microscope: Topography
- Scanning Electron Microscope: Defect Density
- Adhesion: Peel Tape Test
- Flexibility

2.2.3 Phase II - Technology Development

Three of the Phase I feasibility study contractors were selected to proceed to three-year, \$900,000 Phase II development projects based upon:

- the performance of their specimens on the Phase I mandatory tests;
- an understanding of the effects of the LEO environment on materials and the requirements of a protective coating;
- the technical merit of the Phase II proposals;
- the management abilities of the project team; and
- the potential to commercialize the technology in both space and terrestrial applications.

The companies selected for Phase II contracts include:

- Cametoid Limited: Development of Novel Composite Coatings for Material Protection in LEO Environment
- FRE Composites: Plasma-Deposited Protective Coatings for Spacecraft Applications
- MPB Technologies: ECR-Plasma Deposition of Silicon Dioxide

Specimens from Phase I contractors were also provided for the CANadian EXperiment (CANEX-2), Materials Exposure in Low Earth Orbit (MELEO) experiment which was part of the STS-52 shuttle mission in October, 1992. Since this mission occurred several months after the completion of Phase I, the results were not available or used for the selection of Phase II contractors.

The primary objectives of Phase II of the Protection of Materials in the Space Environment Subprogram is to demonstrate a prototype fabrication capability using a full scale component for a commercially viable process for the protection of materials from the space environment, and to demonstrate compliance with a set of performance requirements. Each of the three projects is well underway with positive results beginning to show promise for the new coating technologies. The remainder of this paper provides brief summaries of the three specific projects (in alphabetical order by company) with some discussion of the preliminary results of testing. The full results of scale-up capabilities for each coating technology will not be known until the end of the subprogram in 1996.

Further information on the STEAR Program or the Protection of Materials in the Space Environment Subprogram can be obtained by contacting the Canadian Space Agency³. Further information on the individual projects described below can be obtained directly from the companies involved.⁴

3. Contact Lorne Schmidt at the Canadian Space Agency, Space Station Program Office, STEAR Program, 6767 Route de l'Aéroport, St. Hubert, Québec, Canada, J3Y 8Y9, Tel: 514-926-4462, Fax: 514-926-4448.

4. See the relevant sections for contact names and addresses.

3.0 CAMETOID ADVANCED TECHNOLOGIES INCORPORATED PROJECT⁵

3.1 Development of Novel Composite Coatings for Material Protection in LEO Environment

Cametoid Advanced Technologies Inc. has developed a composite coating for the protection of Kapton from the Low Earth Orbit (LEO) environment. The coating is deposited by simultaneous electron beam (EB) evaporation of two materials. Extensive testing has been carried out according to CSA, NASA and ESA specifications, and the results have indicated excellent performance as presented in the next paragraphs.

Adhesion. The coating was subjected to the tape peel test, and optical microscopy at 400X magnification showed no sign of cracking or delamination.

Flexibility. Strips of coated Kapton were bent around a 0.125" mandrel without cracking or delamination as determined by optical microscopy at 400X magnification.

Thermal Shock. Coated Kapton specimens were submerged into liquid nitrogen for 1 minute, then into boiling water immediately after for another minute and finally back into liquid nitrogen for 1 minute. Optical microscopy evidenced no cracks or delamination at 400X magnification.

Optical Properties. Table 1 shows that the absorptivity (α) and emissivity (ϵ) of the coating are very close to the α and ϵ values of aluminized Kapton.

	α	ϵ	α/ϵ
Cametoid LEO Coating	0.37	0.62	0.59
Kapton	0.37	0.68	0.54

Table 1
Optical Properties of Cametoid LEO Coating

Defect Density. A scanning electron micrograph at 5000X magnification is presented in Figure 2. No evidence of cracks or pin hole defects was found.

Thermal Cycling. Coated Kapton samples were subjected to thermal cycling between +100°C and -100°C and for 10 cycles with 1-2 minute dwell at each temperature; the heating and cooling rates were 10°C/min and 13.8°C/min, respectively. No evidence of cracking was observed by SEM at 10,000X magnification. The tested samples were subjected to and passed the adhesion test (see above).

5. For further information on Cametoid's technology, contact Dr. Alina Agüero or Dr. Kam Yan, Cametoid Advanced Technologies Inc., 1449 Hopkins Street, Whitby, Ontario, Canada, L1N 2C2, Phone: 905-666-3400, Fax: 905-666-3413.

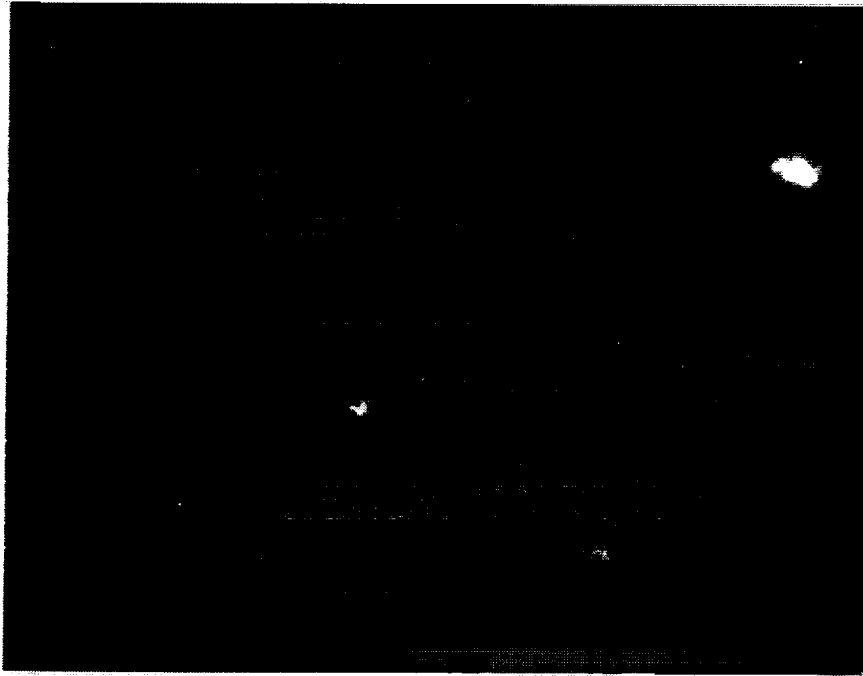


Figure 2
SEM image of the surface of the coating (5,000X)

Atomic Oxygen (AO) and Ultraviolet Erosion Resistance. The coating was tested at the AO beam facility of the University of Toronto Institute for Aerospace Studies (UTIAS). Real time mass loss data was collected with a dual quartz crystal microbalance (QCM) system. Some of the characteristics of the system are summarized below:

<u>Atomic Oxygen:</u>	energy	2.3eV	
	flux	$> 10^{17}$ atoms/cm ² s	
	angle	0-90°	
<u>Vacuum Ultraviolet:</u>	flux	10 ES (120-200 nm)	(ES: Equivalent Sun)
	angle	0-90°	

The reaction efficiency (RE) was calculated by the formula: $RE = \frac{\text{mass loss rate}}{\text{flux} \times \text{area} \times \text{coating density}}$

Table 2 shows the results as well as the minimum thickness required for 30 years in orbit. The test was also performed employing coated Kapton specimens and no weight loss could be detected on a microbalance (with a sensitivity of 10^{-6} g) for the same fluence. Further, no signs of under-cutting could be observed by SEM.

	Coating Mass (μg)	Coating Density (g/cc)	Mass Calibration (ng/Hz)	Time Exposed (sec)	Mass Loss Rate (ng/sec)	Reaction Efficiency (cc/atom)	Thickness (30 yrs) (μm)
Cametoid LEO Coating	90	3.59	707	21000	0.013	1.1E-28	0.2

Table 2
Atomic Oxygen & UV Test Results

The coating has been analyzed and characterised by a number of techniques including Electron Energy Loss Spectroscopy/Transmission Electron Microscopy (EELS/TEM), X-rays Photo-electron Spectroscopy (XPS), Electron Probe Micro-Analysis (EPMA), Energy Dispersion Spectroscopy (EDS) and Auger Electron Spectroscopy (AES). A TEM image of the coating cross-section is shown in Figure 3. The sectioning process required for sample preparation caused fracturing normal to the sectioning direction (a common artefact in the sectioning of brittle materials). The coating is amorphous, uniform and very dense.

Another interesting feature offered by Cametoid's coating process lies in the fact that by varying the composition of the coating, different optical properties can be obtained. Further, the composition can be varied as a function of the coating depth allowing a large range of values for both absorptivity and emissivity to be obtained. An example of such variations is presented in Table 3 where the α/ϵ values are shown as a function of the composition for homogeneous coating formulations on Kapton. Since both components (A and B) are essentially atomic oxygen resistant, it is possible to produce LEO resistant coatings for other substrates and applications requiring specific thermal and solar characteristics.

A (at. %)	09	13	19	30	32	38	40	50	60	76
B (at. %)	91	87	91	70	68	62	60	50	40	24
α/ϵ	0.50	0.50	0.50	0.54	0.53	1.0	1.1	1.4	2.3	6.6

Table 3
Optical Properties of Coated Kapton as a Function of the Coating Composition

Presently, a pilot scale coater for deposition on Kapton rolls is being built. The coating will be deposited by electron beam evaporation and a proprietary masking design and implementation process have been developed to ensure thickness and composition uniformity. An example of the masking effects on the thickness uniformity is illustrated in Figure 4.

In conclusion, Cametoid has developed a new, proprietary coating material for the protection of Kapton in the LEO environment. Preliminary observations indicate that this film outperforms any existing commercially available coatings, specifically in flexibility and resistance to cracking and delamination [1]. Further, the process can be employed to produce different coatings formulations, expanding its potential space applications.

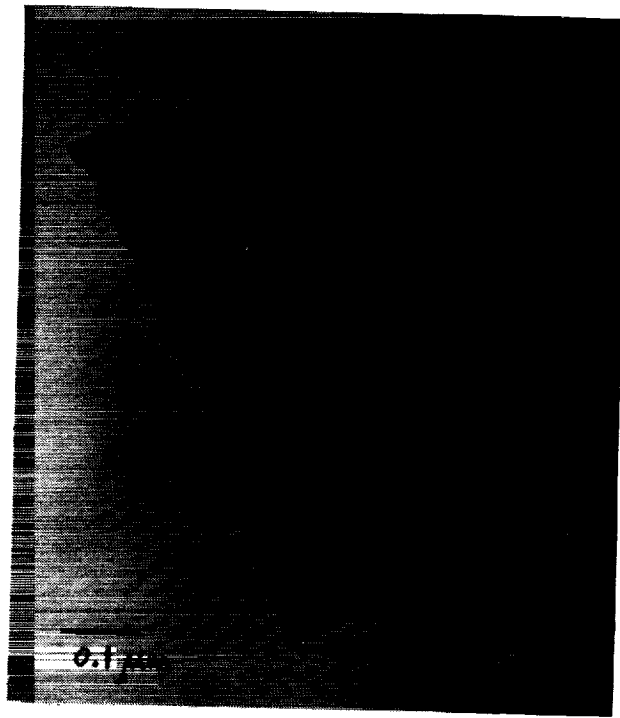


Figure 3
Transmission Electron Microscopy image of the cross-section of the coating

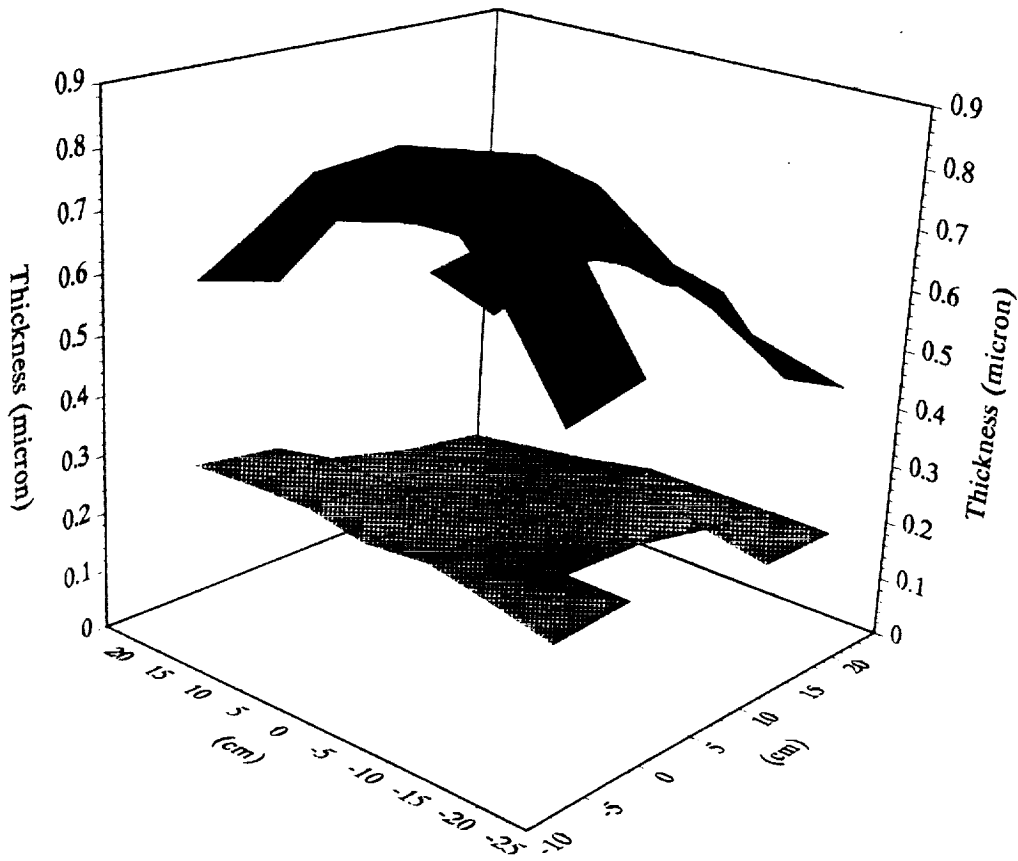


Figure 4
3-D plot of the coating thickness distribution with (grey) and without (black) masking

4.0 FRE COMPOSITES INCORPORATED PROJECT⁶

4.1 Plasma-Deposited Protective Coatings for Spacecraft Applications

In 1987, we commenced work in this laboratory (École Polytechnique, Département de génie physique) on the project "Multipurpose Protective Coatings for Spacecraft Materials", a theme which is still being pursued diligently to this day [2-5]. The objective is to coat both rigid (e.g. carbon/epoxy or carbon/PEEK composites) and flexible (e.g. polyimide) polymeric materials commonly employed in space technology with thin protective layers, using plasma enhanced chemical vapour deposition (PECVD) processes [6]. Our particular PECVD technique, dual-frequency plasma deposition, uses proprietary large area microwave (MW, 2.45 GHz) excitation combined with radio frequency (RF, 13.56 MHz) bias applied to the substrate. This MW/RF process allows one to deposit dense, flawless films onto substrates maintained at ambient temperature, a key feature when dealing with polymeric substrates [7,8].

The protective layers we have examined are the following: plasma-polymerized hexamethyldisiloxane (PP-HMDSO), amorphous hydrogenated silicon (a-Si:H), and inorganic silicon compounds (silicon dioxide p-SiO₂, nitride p-SiN, and oxynitride p-SiON), typical coating thicknesses being between 0.3 µm and 1.5 µm. Current work is focussed on p-SiO₂ which can be obtained both from inorganic or organic volatile Si compounds (SiH₄ and HMDSO).

The performances of coated substrates have been studied in depth with regard to the following criteria:

- resistance to atomic oxygen/vacuum ultraviolet (AO/VUV) exposure;
- charging and discharging characteristics;
- "other" characteristics, such as thermal radiative properties, ageing under thermal cycling and other mechanical stressing...

So far, coated specimens have flown on several Shuttle missions:

- STS 32 (December 1989)
- STS 40 (November 1991)
- STS 46 (July 1992, EOIM III)
- STS 52 (October 1992, MELEO)

Far more detailed evaluations have been conducted in laboratory simulations, as discussed below.

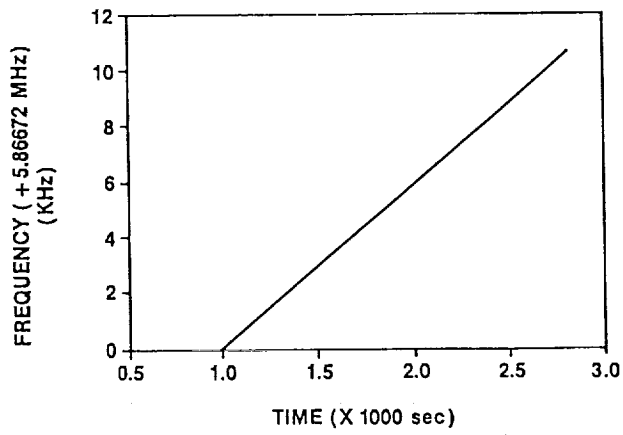
6. For further information on FRE Composite's Project, contact Rhéal Comte, FRE Composites Inc., 75 Rue Wales, St-Andre-Est, Québec, Canada, J0V 1X0, Tel: (514) 537-3311, Fax: (514) 537-3415 or Dr. Michael Wertheimer at École Polytechnique, Département de génie physique, 2900 Blvd. Édouard-Montpetit, C.P. 6079, succ. Centre-Ville, Montréal, Québec, Canada, H3C 3A7 Tel: (514) 340-4749, Fax: (514) 340-3218.

Protection of organic substrates against AO/VUV exposure is probably the most important among the above-cited criteria for low Earth orbital (LEO) applications; it is routinely tested in this laboratory by subjecting samples for long durations to dual-frequency MW/RF oxygen plasma, following which the samples are examined for mass loss, and for possible undercutting erosion under defects such as pinholes or cracks [9]. The latter test is accomplished by peeling away the coating over undercut areas; this can reveal the number density and spatial distribution even of microscopic (sub- μm) coating defects by optical microscopy. The advantage of MW/RF plasma is that it combines a very efficient AO/VUV source with energetic particle bombardment, simulating the reactive particle flux in the ram direction during LEO space flight.

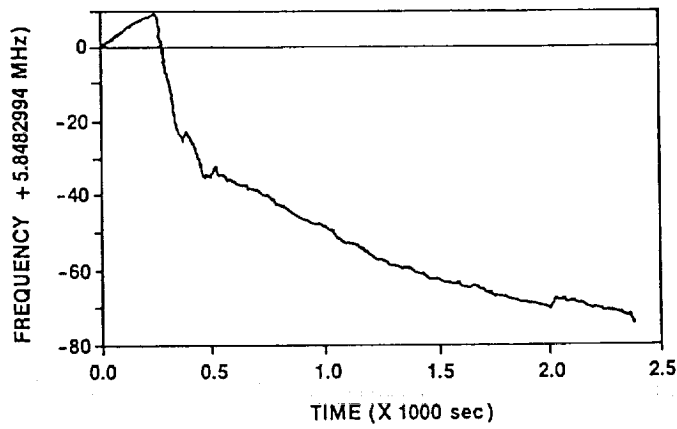
Even more realistic LEO simulation can be achieved in the well-known UTIAS beam facility [10], since there a well-characterized AO flux with 2.5 eV of kinetic energy can be directed at a VUV-illuminated sample surface at 10^{-5} Torr. Figure 5 shows the results of experiments in which quartz crystal microbalances (QCMs) coated with very thin (a few μm), solution-deposited layers of polyimide (PI) are exposed to an AO flux of $5.6 \times 10^{16} \text{ cm}^{-2}\cdot\text{s}^{-1}$. In Figure 5a, which was obtained using an unprotected PI surface, the linear rise in frequency after an induction period of about 17 minutes reflects the expected mass loss due to AO/VUV-induced erosion ("etching") of the polymer. In the case of Figures 5b and 5c, the PI has been overcoated with 0.5 μm layers of p-SiO₂ and a-Si:H, respectively. Noting the change in scales of the ordinates (in Hz, versus kHz for Fig. 5a), one first observes a brief period of mass loss (removal of absorbed water vapour and organic contaminant), followed by periods of slight mass gain (total $\Delta m \leq 10^{-8}$ g). Using Auger Electron Spectroscopy (AES) we have shown [4,5] that the surface region of the protective layer becomes fully oxidized to a depth of a few tenths of a nm, thereason for the observed mass gain, following which $dm/dt \rightarrow 0$ (i.e., the frequency response becomes time-invariant). This result strongly suggests that the protective PECVD layers are essentially defect-free over the roughly 1 cm² surface area of the QCM. Undercutting through microscopic defects (pinholes, microcracks), as reported by Banks [9], would give rise to a measurable positive slope on the QCM response curve.

Space limitations do not permit us to describe the other attributes of PECVD protective coatings, for example, their antistatic characteristics [4,5,11] which will be particularly advantageous in geosynchronous orbit. However, we do wish to say at least a few words about terrestrial spin-off applications and scale-up. First, regarding the latter, Figure 6 shows a pilot-scale MW/RF PECVD roll-coater now being commissioned in this laboratory. This machine will soon be able to coat 12 inch-wide (30 cm) rolls of flexible substrate materials in a "batch-continuous", roll-to-roll mode, for example, one-side metallized polyimide thermal blanket material.

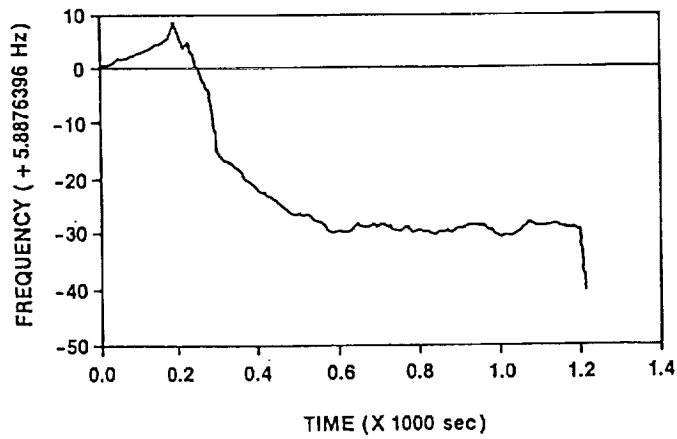
p-SiO₂ displays excellent barrier characteristics not only against the permeation of AO, but also against molecular O₂, H₂O vapour, and other gases or vapours of interest in plastic packaging applications of Earth. This technology is also being pursued vigorously in this and other laboratories [12,13].



a) POLYIMIDE



b) SiO₂ OVER POLYIMIDE



c) a-Si:H OVER POLYIMIDE
 FREQUENCY SHIFT OVER TIME
 FOR AO EXPOSURE OF COATINGS

Figure 5



Figure 6
Pilot-scale MW/RF PECVD roll-coater

5.0 MPB TECHNOLOGIES INCORPORATED PROJECT⁷

5.1 ECR-Plasma Deposition of Silicon Dioxide

Given the objective of protecting space structures against the Low Earth Orbit (LEO) environment for a life of 30 years, a deposition process for thin protective films of silicon dioxide is being developed.

Glass, particularly fused quartz alias silicon dioxide (SiO_2), is known for its inertness to all but the most reactive of chemical species. It is ideal for protection against Atomic Oxygen (AO), the dominant threat of LEO. The AO radical, being a stronger oxidizing agent than any chemical compound, has oxidation as its major route of attack. SiO_2 , being already in its highest oxidation state, is quite unaffected by this affront. The secondary route of attack by AO in LEO is by sheer kinetic energy. SiO_2 , having a bond energy of 8.3 eV⁸ is equally well equipped to resist the attack of LEO AO which is typically at 5 eV, with a distribution tail up to 8 eV.

Producing a thin, adherent coating of p- SiO_2 ⁹ is achieved by ECR-PECVD (Electron-Cyclotron-Resonant Plasma-Enhanced Chemical-Vapour Deposition). An important aspect of depositing high-quality p- SiO_2 is the activation energy available to the reactive species. With a CVD process, that energy can be made available by heating the substrate to 400°C or more, or by impinging the reactive surface with kinetically energetic species. The plasma enhancement of the CVD process achieves the latter. Even so, the substrate must be heated to 200°C to achieve a reasonable quality. A magnetic field in the plasma activation region so as to obtain the ECR condition allows more energy to be imparted to the reagents, in turn allowing deposition of high-quality film on actively cooled room-temperature substrates. This is important for depositing on organic substrates such as Kapton or composite materials such as graphite/PEEK.

The task remained to develop a facility that could implement this process on industrial-scale substrates. It is planned on this project to manufacture an apparatus capable of depositing coatings of p- SiO_2 on 5-foot-wide rolls of Kapton at MPB Technologies. There are two basic approaches to the scale-up problem. One is to increase the size of the plasma source so as to be able to deposit simultaneously across the 5-foot-width of the substrate. It was decided that a previously developed plasma source would be used. The size of the substrate was accommodated instead by raster scanning it under the plasma beam.

The principle of raster scanning has been verified with a miniature substrate manipulating

-
7. For further information on MPB Technologies' project, contact Dr. Jeff Blezius, MPB Technologies Inc., 151 Hymus Blvd., Pointe-Claire, Québec, Canada, H9R 1E9, Tel: (514) 694-8751, Fax: (514) 695-7492.
 8. The 8.3 eV Si-O bond energy is large as compared to the 3 to 4 eV bond energy found commonly in materials.
 9. The prefix "p-" refers to the plasma source and is an acknowledgement that the material is distinguishable from natural SiO_2 upon careful study.

device that fits into the existing facility. The resulting thin film has been verified to be at least as good as that produced without the manipulating device.

The AO erosion rate of the p-SiO₂ film has been measured on the UTIAS (University of Toronto Institute of Aerospace Studies) AO facility which produces a beam of 2.3 eV¹⁰ oxygen atoms. A total fluence of 1.4x10²¹ atoms/cm², combined in the latter half of the exposure with 7 equivalent sun days of UV, produced a mass loss of less than 1.1x10⁻²⁹ cm³/atom, as measured by the in-situ quartz crystal microbalance (QCM). The measurement was limited by the resolution of the QCM. At that rate, the erosion of the thin film due to a 30-year AO fluence in LEO of 1.5x20²³ atoms/cm³ would be less than 16 nm, a thickness that is easy to obtain.

The solar emissivity, ϵ , and absorptivity, α , of p-SiO₂ on aluminized Kapton have been tested according to ASTM-E-408-71 and ASTM-E-490-73a. Upon coating, the ratio α/ϵ changed from 0.45 to 0.48¹¹. Upon AO exposure of a coated QCM in the UTIAS facility, the ratio α/ϵ changed from 1.98 to 1.90. The same measurements were made for p-SiO₂ on Kapton before and after exposure to in-situ AO on the Canadarm, as a part of the "MELEO" experiment of the Canadian Space Agency: the changes in thermo-optical properties, as well as the resistance to LEO AO, were corroborated. Thus, the effect of the p-SiO₂ coating on the thermo-optical properties is only just measurable.

A preliminary qualitative test has been performed to verify the adhesion of the coating to the substrate. Adhesive tape 3M-610 (45 oz/in of tape width on steel) was pressed to the coating surface and removed. Examination of the coating and the tape under an optical microscope with polarized lighting revealed absolutely no removal of the film, indicating a good qualitative adhesion.

The coating flexibility has been measured based on ASTM-D-522-88. The coating on 25 μ m thick Kapton flexed successfully around a 0.038" diameter mandrel. At this small diameter, it was necessary to press the specimen to the mandrel with a gloved hand to ensure complete flexure. Examination of the coating under an optical microscope with polarized lighting revealed no cracking of the film. An analysis of the tensile stress imposed on the coating by this test yielded a tensile strength of at least 240 psi. This can be compared to that of fused silica with 7.1 psi, quartz fibres with 130 psi, and a p-SiO₂ film prepared by B. Banks [14] with 205 psi. Thus, the tensile strength of p-SiO₂ and its resistance to cracking are good.

The p-SiO₂ film on Kapton withstood preliminary thermal cycling and shock tests. The temperature was cycled ten times between +155°C and -135°C. The sample was also immersed for 1 minute in liquid nitrogen followed by 1 minute in boiling water, repeated twice. Examination under optical microscope revealed no change in the film, indicating good resistance to the LEO thermal environment.

10. Less than the 5 eV encountered in LEO, but nonetheless one of the best Earth-based simulations.

11. The short-term repeatability of these thermo-optical measurements is $\pm 2\%$. However, the long-term (months) repeatability seems to be double that. Thus, the variations reported here are all just above the level of resolution.

Because of the long mean free path in the plasma at the deposition pressure, the reactive gas can diffuse around a three-dimensional substrate. The result is coating on all surfaces. A preliminary deposition on a surface which did not have a direct line of sight to the plasma source has verified this principle with film of good quality.

The defects in the applied thin film were counted. There were, however, defects in the Kapton substrate before the p-SiO₂ coating was deposited. It is, therefore, difficult to distinguish between a well coated defect in the substrate and a defect in the coating. For this reason, the Substrate Undercutting Enhancement Test (SUET) was developed. This test consists of three steps. The coated substrate is first exposed to AO from a plasma source to a fluence of 10²⁰ atoms/cm² at 10 eV as measured by Kapton mass loss on a simultaneously exposed uncoated sample. During this exposure, the AO penetrates any defect in the film and reacts with the Kapton underneath.

Secondly, the sample is subjected to peel tape 3M-610 (45 oz./in of tape width adherence to steel) to remove areas of coating that are unsupported due to undercutting by the AO. Thirdly, the sample is examined by SEM, looking for the characteristic pattern of eroded Kapton. This technique was taken from reference [15]. Not only does this technique distinguish between well coated defects in the substrate and defects in the coating, it also renders the defects in the coating more visible.

In a preliminary test, 0.7 cm² of a sample was completely scanned by SEM and 10 film defects were found, typically of a diameter less than 5 μm. The SEM resolution was 0.1 μm. This yields a defect density of 15/cm² which is much lower than the 1000 defects/cm² [16] of commercially available sputtered SiO₂ film. The defect density can also be compared to the debris impact rate in LEO: the 1988 impact rate for debris of 2 μm diameter is 5×10⁷/year/(5000m²), or 1/year/cm². Thus the film defect count will be overcome by debris impacts in the first 15 years of flight, without even considering the growing debris population and the factor of 5 of crater size with respect to impacting particle size, indicating that this pin-hole density is insignificant with respect to protection against LEO.

It is informative to compare the resolution of this SUET technique to an equivalent one based on a mass loss measurement of the undercut Kapton substrate. With the UTIAS facility in mind, one would need to test a coating which is 10 times thicker than the proposed coating in order to meet the quartz microbalance requirements. Such a coating gives only the minimum step resolution of 5 ng; over 6 hours one could resolve a mass loss of about 20 ng.

Based on 1.45×10²¹ oxygen atoms/cm², a 100% reaction efficiency with the Kapton (13% is more realistic until the undercutting becomes pronounced), and an exposed sample area of 0.75 cm², the resolution limit would be five 5-μm (diameter) defects/cm² and that is still for a film which is 10 times thicker than the one of interest. This is to be compared to the SUET resolution of about 1 defect/cm² (any defect larger than about 0.1 μm). Thus, the defect density that has been easily observed by the SUET would probably have gone unresolved by a mass-loss detection method.

Thus, a facility for the large-scale deposition of thin-film protective coatings of p-SiO₂ on three-dimensional substrates is being constructed. The resulting film has already been shown

to have a very low erosion rate in atomic oxygen, to have a pin-hole (less than 5 μm diameter) density of only 15/cm², to have only a small effect on the thermo-optical properties of the substrate/coating system, to adhere well to the substrate, to be flexible to less than 1/8 inch diameter, and to be resistant to thermal cycling. In short, it is a good candidate as a protective coating for long-term protection against the LEO environment.

6.0 CONCLUSIONS

The three projects in the Protection of Materials in the Space Environment Subprogram have completed their first year of a three year development. The results from previous feasibility studies and the early experimental results from the current projects have already demonstrated that good quality coatings can be produced to address a variety of requirements for the protection of materials, not only in the space environment, but also in terrestrial applications. The development of pilot-scale fabrication facilities over the next two years will demonstrate the commercial viability of reproducing these coatings on an industrial scale.

7.0 REFERENCES

1. M. Raja Reddy, N. Srinivasamurthy and B.L. Agrawal, *Surface and Coating Technology*, 58 1 (1993).
2. J.E. Klemberg-Sapieha, M.R. Wertheimer, and D.G. Zimcik, "Plasma-Deposited Multi-Purpose Protective Coatings for Space Applications", Proc. ESA 4th Int. Symposium on Spacecraft Materials in Space Environment, Toulouse, France, Sept. 1988.
3. J.E. Klemberg-Sapieha, M.R. Wertheimer, and D.G. Zimcik, "Plasma-Deposited Multi-Purpose Protective Coatings for Space Applications", *ESA Journal* 13, 117 (1989).
4. D.G. Zimcik, M.R. Wertheimer, K.G. Balmain, and R.C. Tennyson, "Plasma-Deposited Protective Coatings for Spacecraft Applications", *AIAA Journal of Spacecraft and Rockets* 28, 652 (1991).
5. R.C. Tennyson, K.G. Balmain, M.R. Wertheimer and D.G. Zimcik, "Evaluation of Plasma-Deposited Protective Coatings for Spacecraft Applications", Proc. 5th Int. Symp. "Materials in Space Environment", Cannes, France, Sept. 1991. Cépaduès-Éditions, Toulouse, p. 385 (1992).
6. J. Mort and F. Jansen, "Plasma Deposited Thin Films", CRC Press, Boca Raton Fl, 1986.
7. J.E. Klemberg-Sapieha, O.M. Kuttel, L. Martinu and M.R. Wertheimer, "Dual Microwave/Radio Frequency Plasma Deposition of Functional Coatings", *Thin Solid Films* 193/194, 965 (1990).

8. L. Martinu and M.R. Wertheimer, "Ion Assisted Thin Film Growth in Dual Microwave/Radio Frequency Plasmas", in "Plasma Processing of Materials", J. Pouch and S.A. Alterovitz, Eds., Trans. Tech. Publications, Aedermannsdorf-Switzerland (in press).
9. B.A. Banks and S.K. Rutledge, "Low Earth Orbital Atomic Oxygen Simulator for Materials Durability Evaluation", Proc. ESA 4th, Int. Symp. on Spacecraft Materials in Space Environment, Toulouse, France, Sept. 1988.
10. R.C. Tennyson and W.D. Morison, "Atomic Oxygen Effects on Spacecraft Materials Degradation", Proc. "Materials Degradation in Low Earth Orbit", V. Srinivasan and B.A. Banks, Eds., Pub. TMS, ISBN No. 0-87339-152-7, 1990.
11. K.G. Balmain and M.R. Wertheimer, "Electron-Beam Charging of Plasma-Coated Spacecraft Dielectrics", Proc. IEEE Int. Symp. on Electrets (ISE7), Berlin, FRG, September 1991, IEEE Doc. 91CH3029-6, p. 747.
12. J.E. Klemberg-Sapieha, L. Martinu, O.M. Kuttel, and M.R. Wertheimer, "Transparent Gas Barrier Coatings Produced by Dual-Frequency PECVD", Proc. 36th Tech. Conf., Society of Vacuum Coaters, Dallas TX, Apr. 1993, p. 445.
13. M.R. Wertheimer and H.P. Schreiber, "Process for Modifying Large Polymeric Surfaces", Can. Pat. 1,226,591; US. Pat. 5,041,303.
14. B. Banks, Forum on Protection of Materials and Surface Finishes from the LEO Space Environment, Toronto, Canada, Feb. 20-21, 1992.
15. S.K. Rutledge, "Atomic Oxygen Effects on SiO_x , Coated Kapton for Photovoltaic Arrays in Low Earth Orbit", IEEE Photovoltaic Specialists Conference, Las Vegas, Nevada, Oct. 7-11, 1991.
16. B.A. Banks, S.K. Rutledge, K.K. de Groh, "Low Earth Orbital Atomic Oxygen Micrometeoroid, and Debris Interactions with Photovoltaic Arrays", Eleventh Space Photovoltaic Research and Technical Conference (SPRAT XI), NASA Lewis Research Center, Cleveland, Ohio, May 7-9, 1991.

THE ORBITAL DEBRIS DETECTOR CONSORTIUM: SUPPLIERS OF INSTRUMENTS FOR *IN-SITU*
MEASUREMENTS OF SMALL PARTICLES IN THE SPACE ENVIRONMENT

C. G. Simon¹

Institute for Space Science and Technology
Gainesville, FL (904) 371-4778 Fax: 372-5042

¹current address: AC Engineering, Inc.
2106 NW 67th PL, Gainesville, FL 32606
Phone: (904) 335-1889 Fax: (904) 335-1891

R. Münzenmeyer

Technical University of Munich
Richard-Wagner Str. 18/III,
D-80333 Munchen, Germany
Phone:(49) 89-2105-2578 Fax:(49) 89-2105-2468

W. G. Tanner, Jr.

Baylor University Space Science Laboratory
P.O. Box 97303, Waco, TX 76798-7303
Phone: (817) 755-3404 Fax (817) 755-3409

O. M. Uy

Applied Physics Laboratory
Johns Hopkins University
Johns Hopkins Road, Laurel, MD 20723-6099
Phone: (301) 953-5334 Fax:(301) 953-6119

R. A. Skrivanek

Visidyne, Inc.
10 Corporate Place, S. Bedford Street,
Burlington, MA 01803
Phone: (617) 273-2820 Fax: (617) 272-1068

A. J. Tuzzolino

Laboratory for Astrophysics and Space Research
The University of Chicago,
933 East 56th Street, Chicago, IL 60637
Phone: (312) 702-7798 Fax: (312) 702-6645

C. Maag

T & M Engineering, Inc.
2605 East Foothill Blvd., Suite R,
Glendora, CA 91740
Phone: (818) 852-9772 Fax: (818) 335-9968

J. J. Wortman

Department of Electrical and Computer Engineering
Campus Box 7911, North Carolina State University
Raleigh, NC 27695-7911
Phone: (919) 515-5255 Fax: (919) 515-3027

SUMMARY

The Industry and University participants listed above have joined together to form the IMPA:Ct consortium (In-situ Monitors of the Particulate Ambient: Circumterrestrial) which offers a broad range of flight qualified instruments for monitoring the small particle (0.1 micron to 10 cm) environment in space. Instruments are available in 12 months or less at costs ranging from 0.5 to 1.5 million dollars (US) for the total program. Detector technologies represented by these groups are: impact-induced capacitor-discharge (MOS, metal-oxide-silicon), cratering or penetration of electroactive thin film (polyvinylidene fluoride (PVDF), impact-plasma detection, acoustic detection, ccd tracking of optical scatter of sunlight, and photodiode detection of optical scatter of laser light. The operational characteristics, general spacecraft interface and resource requirements (mass/power/ telemetry), cost and delivery schedules, and points of contact for 7 different instruments are presented.

INTRODUCTION

The IMPA:Ct consortium was formed in response to customer information needs. All consortium members offer flight-qualified instruments. (New members are actively sought, just contact any consortium member if your group has, or is developing, a flight qualified system.) Our intention is to present information on existing technologies in a useful, customer-friendly format that will encourage further contact with consortium members for more detailed information. Customers should find this paper a useful resource for evaluating existing technologies that can meet their mission-specific requirements. The seven flight-qualified instruments described in the following pages are available in relatively short time periods (<12 months) and for modest total mission costs (U.S.\$ 0.5 to 1.5 million). Instrument configurations and capabilities range from ultra-thin, surface mountable capacitor-discharge sensors that detect submicron and larger particle impacts, to briefcase size optical scatter instruments that scan large volumes of space for particles in the mm to 10 cm size range. Most of the participating groups are also involved with research and development programs aimed at upgraded and/or hybrid technologies.

Data on the small particle environment produced by consortium instruments can be displayed in a variety of formats, including multi-dimensional phase-spaces relevant to specific missions. The data can also be used to predict the near-term future particle environment that spacecraft will experience, including short-term, high-flux time periods associated with debris ring and wake trail crossings. [LDEF data showed that nearly 2/3 of the estimated 7 million microparticle impacts on the ram, north and south sides of the spacecraft occurred in less than 1% of the mission time at predictable intervals associated with debris-ring crossings (refs. 1, 2). Data from particle monitors on board Space Shuttle flights have detected a 100 fold increase in the small particle flux associated with the crossing of a wake trail behind an old, spent Soviet (liquid-fueled) upper stage (ref. 3).] Information on the particle environment can be used by operators to minimize damage to sensitive surfaces or institute operational alerts. This situation is entirely analogous to the first use of information from meteorological instruments by aircraft operators. Indeed, a near term goal of present-day military spacecraft operators is the development and deployment of small, lightweight, non-intrusive sensors for monitoring a host of space environment conditions that affect the operations and degradation of their systems.

A consortium affiliate, POD Associates, Inc. of Albuquerque, NM [Contact: Mr. Dale Atkinson (505) 243-2287, FAX (505)243-4677] offers additional pre- and post-mission analytic support for sensor systems and data that includes: incorporation of spacecraft subsystem damage criteria and mission success and/or degradation (probability) criteria into environment predictions; comparison of new data sets with standard and current environment subsystem damage models; and incorporation of new data sets into improved particle environment models.

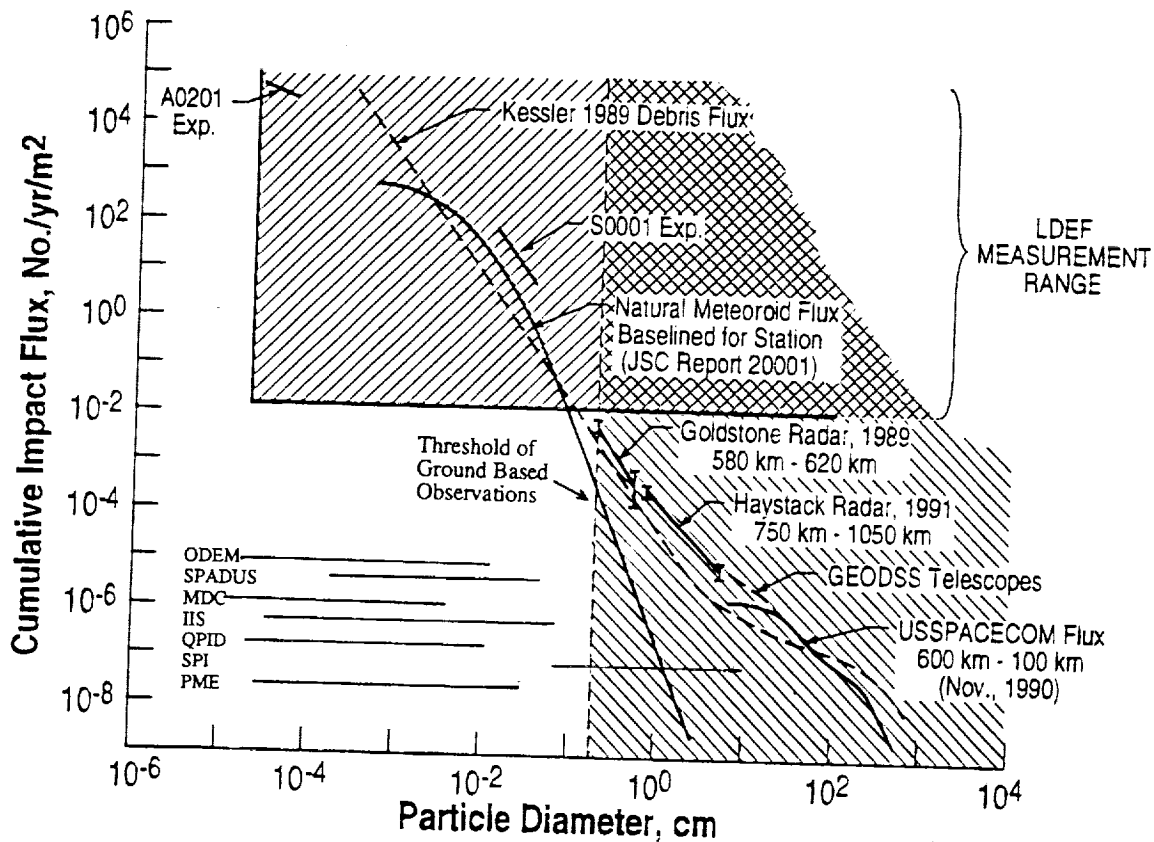


Figure 1. Present knowledge of the circumterrestrial meteoroid and debris environment based on LDEF and ground-based radar and optical data. Particle size detection ranges for all 7 of the IMPA:Ct consortium instruments are shown just above the x axis in this plot. All instruments are capable of detecting the maximum annual flux of particles in their respective detection ranges. Note the broad ranges and high degree of overlap of these instruments.

SENSOR TECHNOLOGY:

Instrument Generic Name:
Detection Method:
Particle Size Detection Range:
Field of View:
Consortium Contact:

MOS (metal-oxide-silicon) capacitor-discharge

ODEM-MOS, (Orbital Debris Environment Monitor)
impact on electrically active surface induces discharge
0.1 - 100 μm (10^{-15} to 10^{-6} g), no size discrimination except
for variable threshold sensitivities
180°, dependent on mounting location
Jim Wortman, North Carolina State University
Phone: (919) 515-5255 Fax: (919) 515-3027

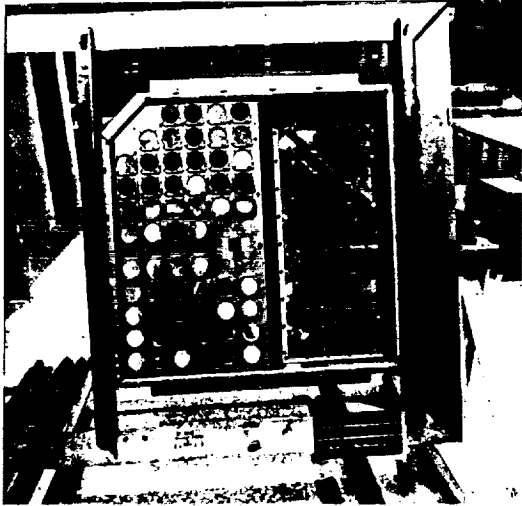


Figure 2. One of 6 MOS sensor arrays that flew on board LDEF for 5.8 years, from April 1984 to Jan. 1990 as the Interplanetary Dust Experiment.

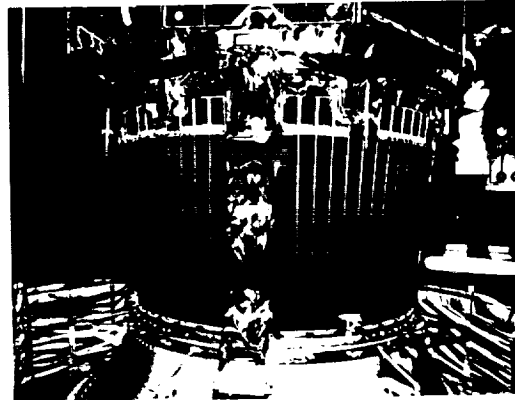


Figure 3. The Orbiting Meteoroid and Debris Counter on the Clementine-1 Interstage Adapter has 48 current-generation MOS sensors on board (Jan 1994- Apr 95).

Nominal Instrument Specifications

dimensions

active sensing area

mass

spacecraft electrical interface
mounting requirements

power requirements

telemetry requirements

Sensors: 38 x 76 x 0.05 mm, Electronics: 10 x 20 x 2 cm
3000 cm², nominal, variable up to the limit of available
spacecraft mounting area including solar panel back sides
<1 kg, includes sensors, electronics and wiring harness
compatible with all buses
sensors are bonded to rigid surfaces using solar cell mounting
techniques: electronic controller board can be mounted
in an existing box, or can have its own box (add 0.5 Kg mass)
2 watts
no special requirements, data rate <250 kbit/day

Nominal cost estimates (U.S. \$1000)

delivered hardware (only) costs
pre-launch mission support costs

software development costs

post-launch mission support (data
interpretation and report) costs

400-600

TBD, dependent on program/documentation requirements;
typical range is 250-400.

TBD, dependent on phase space requirements;
typical range is 25-100.

TBD, dependent on requirements;
typical range is 100-150/year.

Nominal delivery schedule

hardware (only) delivered

mission specific software development time

3-6 months

1-3 months (concurrent)

TECHNOLOGY DESCRIPTION AND FLIGHT HISTORY

The MOS capacitor-type impact detectors, originally designed and fabricated by J. J. Wortman (co-inventor) at North Carolina State University, have flown successfully on the Explorer 46 Meteoroid Technology Satellite (MTS) in 1977, and on LDEF in 1984-1990 as the Interplanetary Dust Experiment, which discovered the extreme anisotropic nature of orbital debris and tracked several debris clouds and rings (Fig. 4)^{1, 4-7}. An MOS-based instrument called the Orbiting Meteoroid and Debris Counter (OMDC) is currently operating on the BMDO Clementine-1 interstage adapter (Fig. 3)⁸.

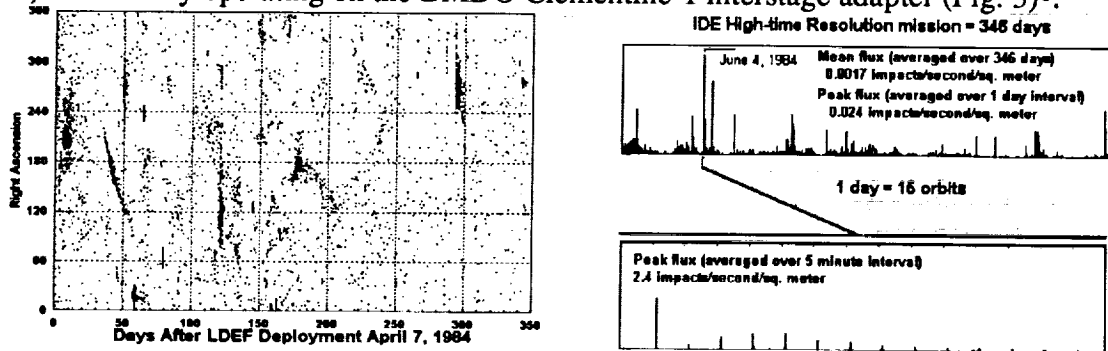


Figure 4. Impact flux data from IDE detectors on the ram side of LDEF showing examples of displays and the orbital periodicity of debris ring intercepts. Evidence indicates a continuous source for these rings.

The MOS detector (or sensor) is based on the fact that a charged parallel plate capacitor will partially discharge when struck by an energetic enough particle. The impact is detected by measuring the voltage transient due to the discharge. Transient power consumption due to impacts is on the order of milliwatts. A schematic drawing of the detector (Fig. 5) shows that the capacitor consists of a thin top metal electrode layer, a thin dielectric layer of silicon dioxide, and a bottom substrate, or electrode, of p-type silicon. They are fabricated utilizing standard silicon integrated circuit manufacturing processes and photo lithography. Threshold sensitivity of the detectors is dependent on the top electrode and dielectric layer thicknesses. Dimensions and shape can be varied from 2.5 cm squares to 10 cm diameter rounds. Sensors are typically bonded directly to rigid external spacecraft surfaces using solar-cell mounting techniques. Extensive ground simulation tests and orbital empirical calibration studies⁹⁻¹¹ have shown that the MOS detector sensitivity can be expressed as a function of particle mass in grams, velocity in m/s and impact angle (β) in degrees from normal. These data indicate that the MOS detectors respond to submicron Fe particles with a lower size limit of 0.1-0.2 μm ($\sim 10^{-14}$ to 10^{-15} g) for impact velocities ≥ 10 km/s (Fig. 6).

$$S = [(mass)^{0.33}(velocity)(\cos\beta)^{1.5}][e^{(-0.90T)}] - 0.13$$

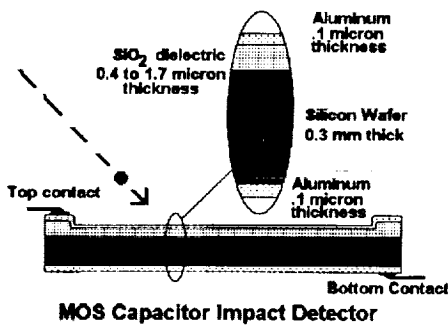


Figure 5. The current generation MOS sensor.

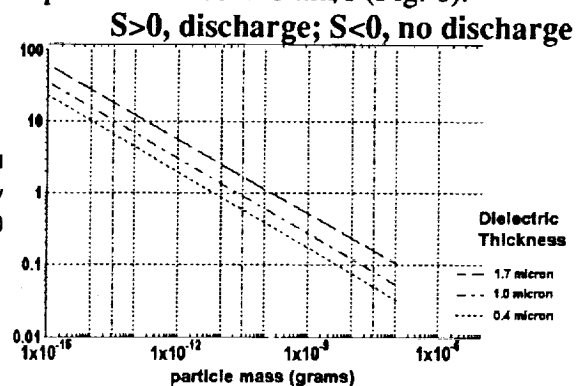


Figure 6. MOS detector threshold response curves.

New Developments

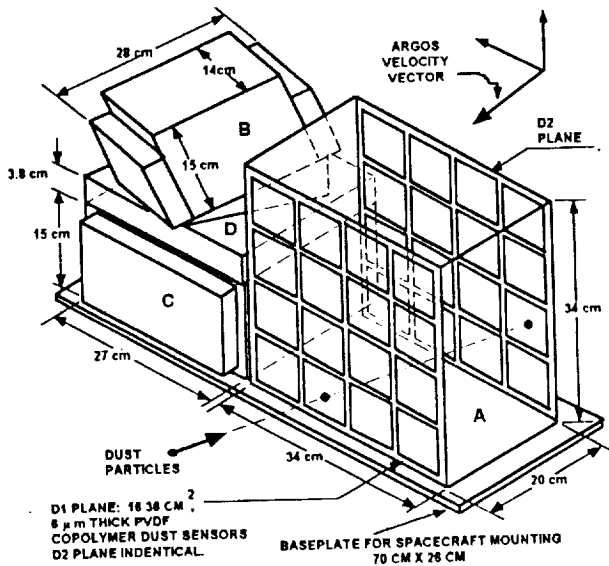
- (1) Combined MOS/PVDF array for detection of submicron particles and measurement of size/velocity/trajectory of particles $> 10 \mu\text{m}$ (under development: NASA/LARC, U. Chicago, NCSU, ISST, Visidyne).
- (2) Hybrid MOS/Acoustic sensor array for satellite health monitoring and impact detection. Senses all induced vibrations on a spacecraft and, using acoustic spectroscopy, provides information on spacecraft subsystem performance and impactor sizes, velocities, angles, and locations. (C.G. Simon, inventor)

SENSOR TECHNOLOGY:

Instrument Generic Name:
Detection Method:
Particle Size Detection Range:
Field of view:
Consortium Contact:

PVDF Electroactive Thin Film

SPADUS, Space Dust Monitor
 impact on or penetration of electrically active thin films
 2-200 μm (10^{-12} to 10^{-5} g); measures size, velocity ($\pm 5\%$),
 trajectory ($\pm 7^\circ$) of particles $> 10 \mu\text{m}$ with 2 parallel arrays
 180° for flux, 120° for trajectory
 Tony Tuzzolino, University of Chicago
 Phone: (312) 702-7798 Fax: (312) 702-6645



- A: Dust trajectory system consisting of two identical dust sensor arrays (D1 plane and D2 plane).
- B: Digital electronics.
- C: Analog electronics box.
- D: Power supply box.

Figure 7. The Space Dust Instrument (SPADUS) for flight on the ARGOS spacecraft (launch, Jan. 1996).

Nominal Instrument Specifications
dimensions

active sensing area

mass

spacecraft electrical interface
mounting requirements

power requirements

telemetry requirements

Nominal cost estimates (U.S. \$1000)

delivered hardware (only) costs
pre-launch mission support costs

software development costs

post-launch mission support (data interpretation and report) costs

Nominal delivery schedule

hardware (only) delivered

mission specific software development time

Sensor Module: 34 x 34 x 20 cm

Electronics Module: 30 x 27 x 20 cm

1200 cm², nominal, variable up to the limit of available spacecraft mounting area

8 kg, includes sensors, electronics and wiring harness compatible with all buses

external rigid mount required for box-shaped sensor array

Electronic controller box can be mounted external or internal

6.5 watts

no special requirements, data rate 1-10 Mbit/day

500-750

TBD, dependent on program/documentation requirements; typical range is 250-500.

TBD, dependent on phase space requirements, typical range is 50-150

TBD, dependent on requirements, typical range is 100-150/year

9-12 months

3-6 months (concurrent)

TECHNOLOGY DESCRIPTION AND FLIGHT HISTORY

PVDF dust sensors consist of 2-28 μm thick polarized (dipole-aligned) PVDF (or PVDF copolymer) foils mounted in circular or square frames. Vapor deposited aluminum films over the mounted foils serve as electrodes. When an impacting particle removes material due to cratering or penetration, a signal is generated which depends on the particle mass and velocity (Figs. 8, 9). PVDF sensors flew on the VEGA 1 and 2 spacecraft which encountered comet Halley in 1986 where they made the first direct measurements of the dust structure of a cometary coma (refs. 12-15). The current SPADUS instrument uses 5 μm thick copolymer sensors (36 cm^2) grouped in two 16-sensor arrays spaced 20 cm apart (Fig. 7, ref. 16).

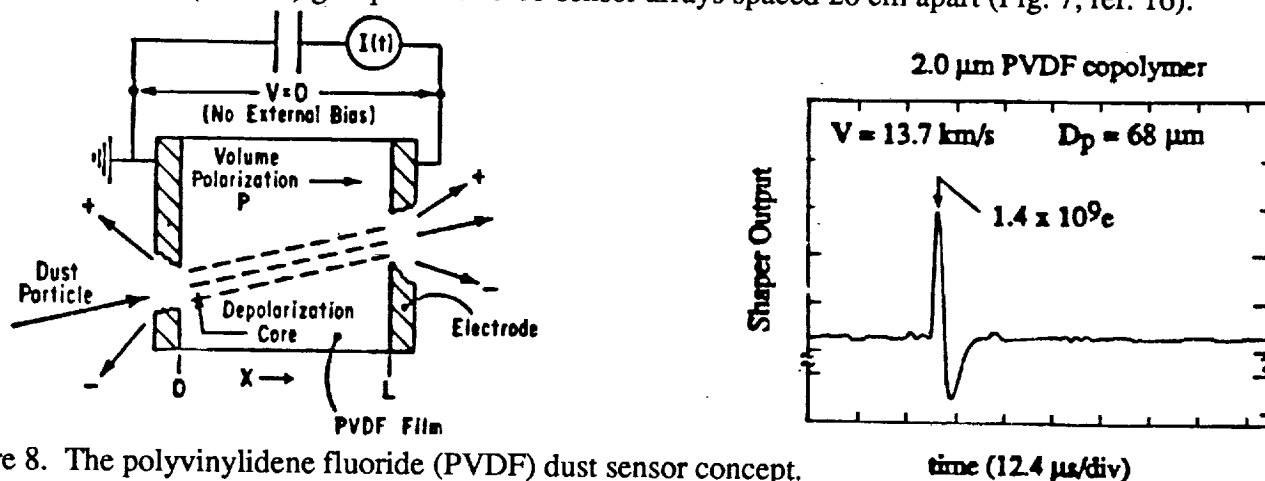


Figure 8. The polyvinylidene fluoride (PVDF) dust sensor concept.

For each impact, SPADUS data include:

- Impact time on D1 for correlation with spacecraft clock to obtain spacecraft attitude and orbital position,
 - Identification of D1 sensor and D2 sensor impacted to determine particle trajectory ($\pm 7\%$),
 - Time of flight between D1 and D2 ($0.25\ \mu\text{s}$ resolution) to determine particle velocity,
 - Pulse-height-analysis (PHA) of D1 and D2 signal amplitudes (32 channel PHA for each of the 32 sensors plus signal waveform storage with 2000 time points at 256 channel PHA/point) to determine particle mass.
- These data permit discrimination between orbital debris and natural particles. The time-velocity-trajectory capabilities of SPADUS also permit identification of orbital debris cloud and meteor stream encounters.

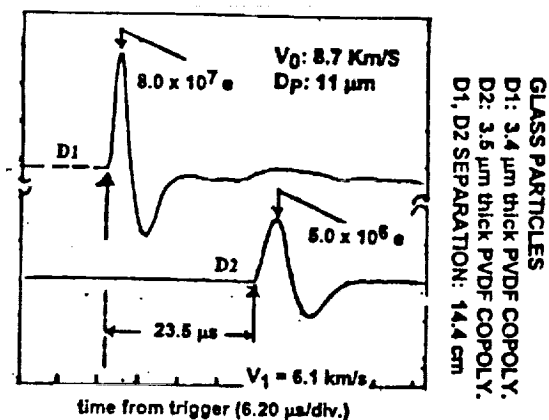


Figure 9. PVDF copolymer response curve.

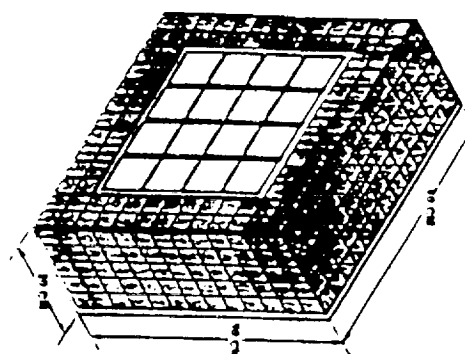


Figure 10. Combined MOS/PVDF instrument (IMOD).

New Developments

The University of Chicago has teamed with NASA/LaRC, the University of North Carolina, Visidyne, Inc. and ISST, Inc. to construct a combined MOS/PVDF instrument (Fig. 10) for detection of submicron to mm size particles and measurement of size/velocity/trajectory of particles $>10\ \mu\text{m}$ in size. This combined instrument is known as IMOD (*In-situ* Monitor of Orbital Debris).

SENSOR TECHNOLOGY:

Instrument Generic Name:
Detection Method:

Particle Size Detection Range:

Field of view:
Consortium Contact:

Impact-Plasma Detection

MDC, Munich Dust Counter
 measures electron and ion charges and times of arrival to electrodes from impact-plasmas generated from particles striking gold surfaces
 0.1 to 50 μm (10^{-15} to 10^{-7} g), measures mass ($\pm 430\%$), velocity ($\pm 150\%$), and trajectory ($\pm 70\%$)
 140°
 Ralf Münzenmeyer, Technical University of Munich
 Phone:(49) 89-2105-2578 Fax:(49) 89-2105-2468

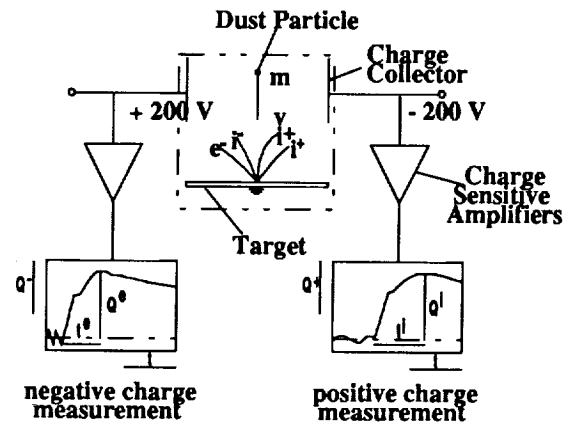
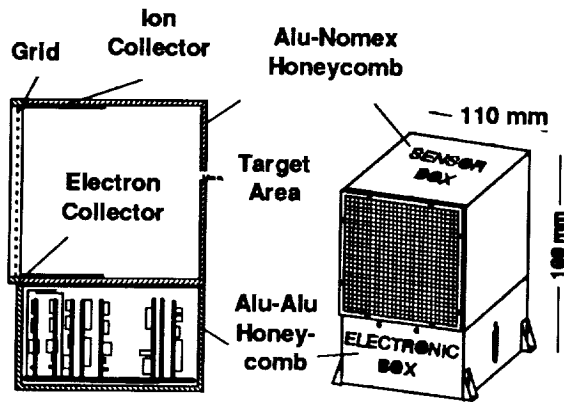


Figure 11. Outline of MDC mechanical design.

Figure 12. MDC measurement principle.

Nominal Instrument Specifications

dimensions	11 x 11 x 16 cm
active sensing area	100 cm ²
mass	0.6 kg, includes sensor, electronics and internal wiring
spacecraft electrical interface	compatible with all buses
mounting requirements	external or internal rigid mount required for box-shaped combination sensor and electronic controller
power requirements	2 watts
telemetry requirements	no special requirements, data rate 1-10 kbit/day

Nominal cost estimates (U.S. \$1000)

delivered hardware (only) costs	TBD
pre-launch mission support costs	TBD
software development costs	TBD
post-launch mission support (data interpretation and report) costs	TBD

Nominal delivery schedule

hardware (only) delivered	9-12 months
mission specific software development time	3-6 months (concurrent)

TECHNOLOGY DESCRIPTION AND FLIGHT HISTORY

The Munich Dust Counter consists of two honeycomb boxes that are typically mounted together (Fig. 11). The lower box houses all electronics and is fixed to the satellite platform. The upper box serves as the particle detector, or "sensor", and has a 100 cm² electrically grounded open steel grid at the front. The five gold plated inner sides, including electron and ion collector areas shown in Fig. 11, serve as target areas. The MDC measures the electrical charges generated by high velocity particle impacts into the gold surfaces. The amplitude and rise time of each charge signal are used to determine the mass and velocity of the particle using the empirical relationships:

$$t = (c_g)(v^n) \quad \pm Q/m = (c_r v^\beta)$$

where m is particle mass, v is velocity, Q is the maximum charge, t is the signal rise time, and c_r , c_g , n and β are calibration constants (refs. 17, 18, Figs. 13 and 14).

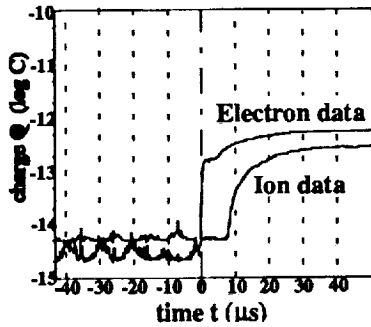


Figure 13. A typical impact induced plasma signal detected by the MDC.

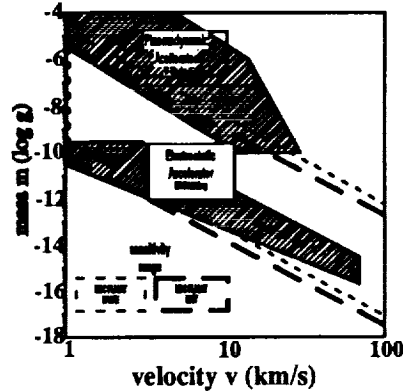


Figure 14. Sensitivity range of the MDC and particle accelerators used in calibration.

The MDC plasma dust sensor first flew on the Japanese MUSES-A (HITEN) Spacecraft in 1990-1993 (refs. 19, 20) where it measured the flux of natural particles in cislunar space and beyond. This mission provided valuable data on the mass, velocity and distribution of cosmic dust particles and β -meteoroids in the Earth-Moon system. Swarms, groups and random particles were detected and enormous variations in the instantaneous fluxes and impact rates were observed. Measurements of dust flux at the Lagrangian points L4 and L5 showed no indications of the presence of dust clouds.

A second MDC is currently flying in low Earth orbit (400 km, 58°, circular) on board the BREM-SAT, (Fig. 15), a microsatellite dedicated to dust detection. BREM-SAT was designed and constructed at the Center for Applied Space Technology and Microgravity (ZARM) in Bremen, Germany. It was launched from a Space Shuttle Getaway Special canister in February 1994 with a nominal mission duration of 2-6 months (ref. 20). Calculations using the ESABASE Meteoroid / Debris software predict that 360 meteoroids and 600 debris particles >0.5 μ m in size will strike the BREM-SAT MDC sensor per year.

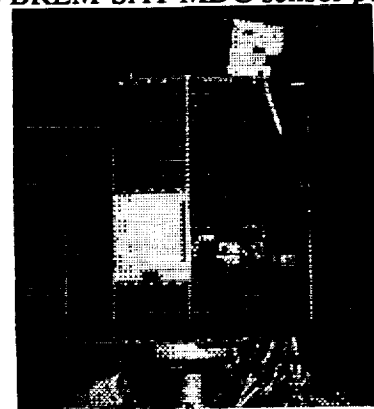


Figure 15. The BREM-SAT microsatellite for meteoroid and debris detection in low Earth Orbit.

SENSOR TECHNOLOGY:

Acoustic Impact Detection

Instrument Generic Name:
Detection Method:

IIS, Impact Impulse Sensor
 detects impact induced phonon displacements; derives
 impactor size and velocity of particles from momentum
 0.5 μm to 1 mm (10⁻¹³ to 10⁻³ g), measures momentum
 to ±20%

Particle Size Detection Range:

160°

Field of view:
Consortium Contact:

Bill Tanner, Baylor University
 Phone: 817-755-3404 Fax: 817-755-3409

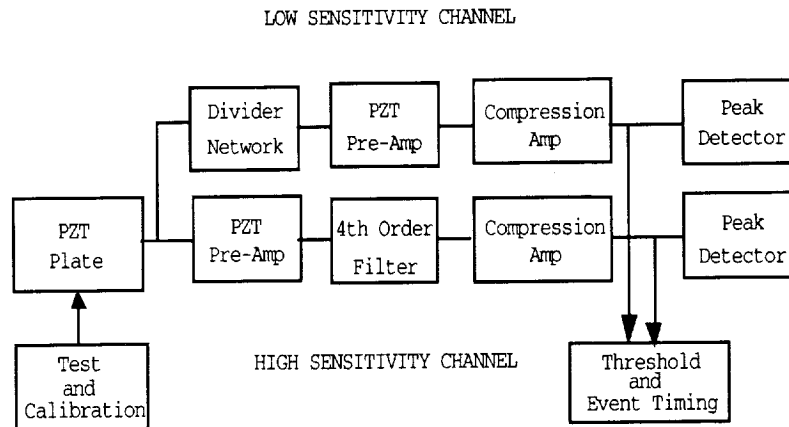


Figure 16. Impact Impulse Sensor functional block diagram. PZT = lead-zirconate-titanate sensor.

Nominal Instrument Specifications

dimensions

Sensors: 2 x 10 x 10 cm
 Controller: 2 x 14 x 16 cm

active sensing area
mass

100 cm²/sensor, up to 8 sensors (800 cm²) per controller
 5 kg, includes 8 sensors with housings, controller and wiring harness

spacecraft electrical interface
mounting requirements

compatible with all buses, (1553 standard)
 sensors - external rigid mount
 controller box - internal or external rigid mount

power requirements
telemetry requirements

10 watts (8 sensor array)
 no special requirements, data rate 1-8000 bps

Nominal cost estimates (U.S. \$1000)

delivered hardware (only) costs
pre-launch mission support costs

300-400
 TBD, dependent on program/documentation requirements;
 typical cost is 300

software development costs

TBD, dependent on phase space requirements;
 typical cost is 50

post-launch mission support (data interpretation and report) costs

TBD, dependent on requirements;
 typical cost is 75/year.

Nominal delivery schedule

hardware (only) delivered 6-8 months
mission specific software development time 2-4 months (concurrent)

TECHNOLOGY DESCRIPTION AND FLIGHT HISTORY

First proposed in the pre-satellite era, acoustic detectors later comprised the main thrust of early sensor development in the U.S. The piezoelectric sensor has high mass sensitivity at medium velocities and outperforms other impact related sensors. The reliability of early piezoelectric sensors was questioned due to the electronic controller limitations of the era. Current high-speed analog to digital (A/D) converters and CPU's have eliminated these earlier difficulties. A piezoelectric acoustic sensor system called DIDSY (The Dust Impact Detection SYstem) was included as one of ten major components of the Giotto Comet Halley scientific payload (ref. 21). Several piezo sensors have also flown on Shuttle missions (ref. 22).

Lead zirconate titanate (PZT) piezoelectric crystal sensors have a threshold momentum sensitivity of 5×10^{-11} Ns, which implies that an ~ 10 picogram grain (density = 0.8 g/cm^3) with a diameter of $\sim 2.9 \mu\text{m}$ and a velocity of 5 km/s will be detected. The PZT responds only to the normal component of the impulse delivered to the impact surface regardless of the obliquity of the impact.

The Impact Impulse Sensor consists of a PZT crystal bonded to a thin plate. Dust particles striking the plate give rise to acoustic waves which propagate radially from the point of impact, inducing transient charge separations in the PZT crystal. A charge-sensitive amplifier is used to detect these waves and the first few hundred μs of the analog signal are routed through a high-speed A/D converter and stored for processing (Fig 16.). The maximum PZT response is proportional to the particle momentum, and the slope and rise-time of the first acoustic wave is related to the size and velocity of the particle (ref. 23). The dynamic range of an IIS covers six orders of magnitude (Figs. 17, 18).

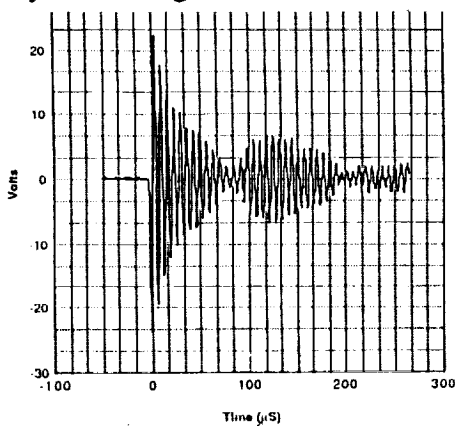


Figure 17. A typical impact-induced acoustic wave detected by the IIS.

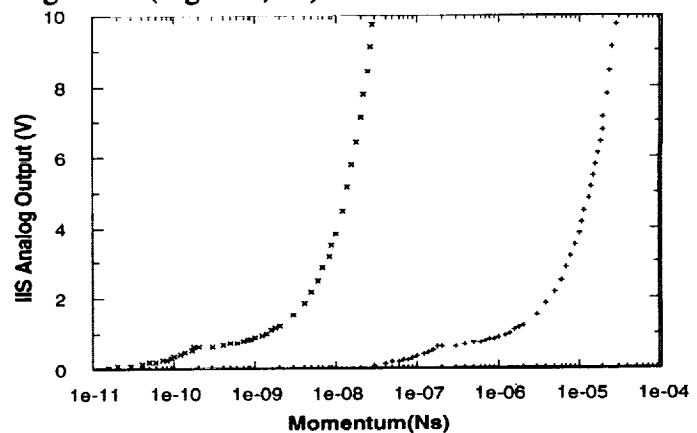


Figure 18. Peak amplitude versus momentum relationship for high and low sensitivity IIS .

New Developments

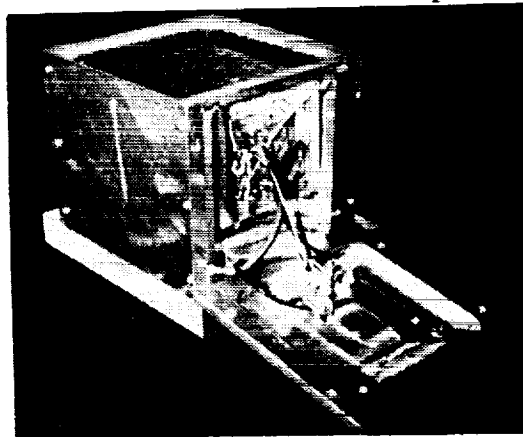


Figure 19. The Cometary Dust Environment Monitor experiment (CoDEM), selected for flight on the CRAF/Cassini mission, uses piezoelectric and plasma-charge sensor arrays to measure mass, velocity and trajectory of particles. Contact Bill Tanner for more information on this highly capable instrument.

SENSOR TECHNOLOGY:

Instrument Generic Name:
Detection Method:
Particle Size Detection Range:
Field of view:
Consortium Contact:

Acoustic Impact Detection

QPID, Quartz Particle Impact Detector
impact on electrically active surface
0.4 μm to 100 μm (10^{-12} to 10^{-3} g), measures momenta
ranging from 6×10^{-13} to 6×10^{-8} kg-m/s
150°
Carl Maag, T&M Engineering, Inc.
Phone: (818) 852-9772 Fax: (818) 335-9968

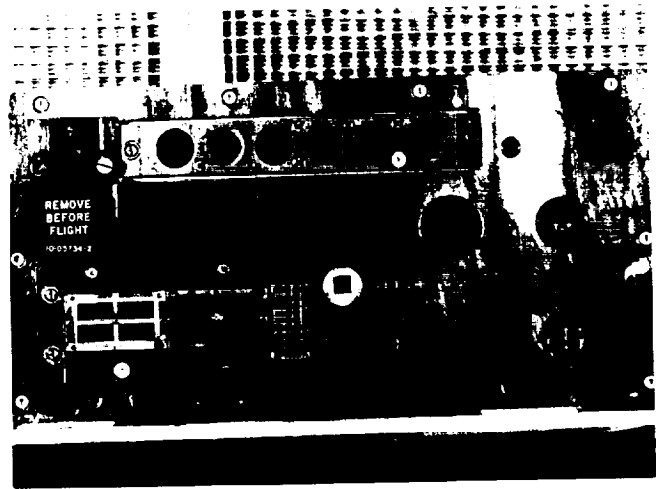
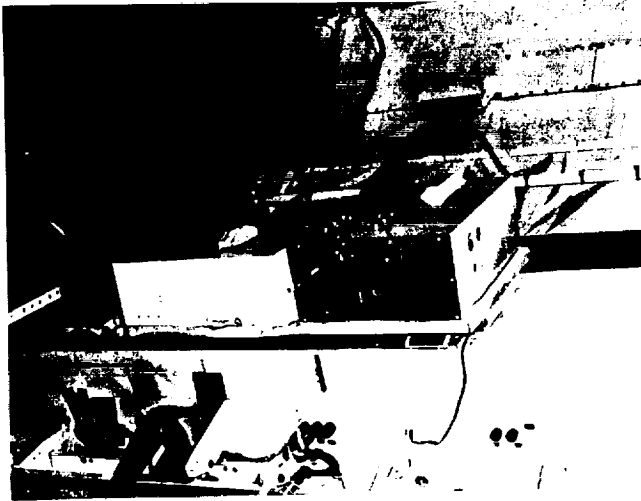


Figure 20. QPID detector mounted in STS-44/IOCM. Figure 21. Close-up view of QPID on STS-44.

Nominal Instrument Specifications

dimensions

active sensing area

mass

spacecraft electrical interface

mounting requirements

power requirements

telemetry requirements

Detector: 20 x 9 x 10 cm, Electronics: 12 x 10 x 10 cm
64 cm² (8 cm²/sensor, 8 sensors/detector)
1.5 kg, includes detector package, electronics and wiring
harness
compatible with all buses
external or internal rigid mount
3 watts
no special requirements, data rate 100-200 kbit/day

Nominal cost estimates (U.S. \$1000)

delivered hardware (only) costs

pre-launch mission support costs

software development costs

**post-launch mission support (data
interpretation and report) costs**

200-250

TBD, dependent on program/documentation requirements;
typical range is 100-150

TBD, dependent on phase space requirements;
typical range is 50-150

TBD, dependent on requirements;
typical range is 100-150/year.

Nominal delivery schedule

hardware (only) delivered

mission specific software development time

4-6 months

2-4 months (concurrent)

TECHNOLOGY DESCRIPTION AND FLIGHT HISTORY

The utility of the Quartz Particle Impact Detector (QPID) is based on the piezoelectric response of quartz when struck by a dust particle. The advantages of the QPID include direct counting (as with all impact detectors) and the avoidance of some difficulties associated with accumulation sensors such as collection efficiency, spallation of detector material, release of previously collected material and saturation. The QPID measures the amplitude of the impact induced oscillation of a quartz crystal. Timing the decay of the "ringing" against the crystal frequency eliminates the need for fast pulse electronics.

The fundamental component of the QPID is a Y-cut quartz crystal detector. When impacted, the crystal rings at its base frequency with an amplitude dependent on the momentum transfer. The damping of the crystal and its mounting cause the ringing to decay. By counting the cycles above a fixed amplitude threshold with a scalar, the momentum of the impacting particle may be determined (after proper calibration). The impacts are counted by a separate scalar. When the momentum scalar is replaced by a multichannel analyzer, the momentum spectrum may be obtained directly.

This detector is capable of measuring momenta ranging from 6×10^{-13} to 6×10^{-8} kg-m/s. The high momentum channel also includes counts with momenta greater than the upper limit. A typical system can process at least 100 impacts per second. This limit is set by the duration of the ring for the largest momentum discretely measured. In terms of Divine's model for comet Kopff (ref. 24) at 100 km distance sunward of the comet at perihelion, a single detector could count dust particles as small as 3×10^{-15} kg (at 295 m/s) and as large as 1×10^{-9} kg (at 73 m/s).



Figure 22. QPID detectors mounted on Galileo.

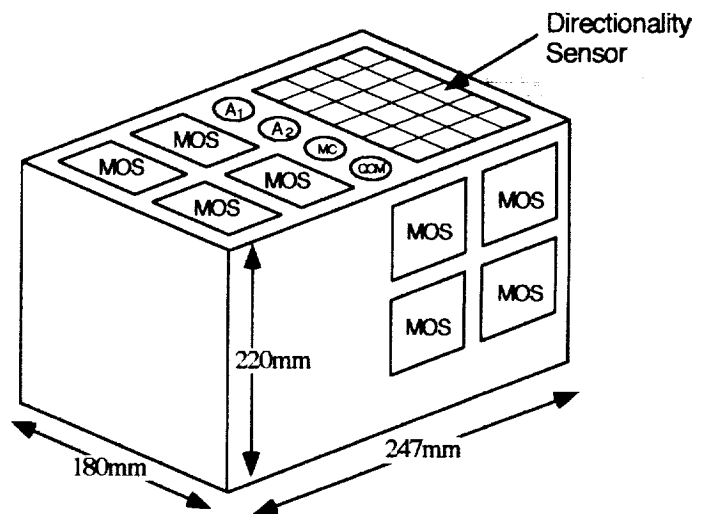


Figure 23. The COMRADE instrument for MIR.

QPID is a flight qualified detector. It has flown on two Shuttle missions for low earth orbit (LEO) debris detection. It aided in determining the scope of the debris cloud encountered during the STS-44 collision avoidance maneuver (ref. 3). In addition to these flights, an earlier version flew on the Galileo mission. The sensors were located on the body and on the RTG outriggers.

New Developments

An instrument for the detection of cometary dust has been accepted for integration onto the Priorda module of MIR. The instrument is known as COMRADE (Collection of Micrometeoroids, Residue and Debris Experiment). The instrument contains both active and passive sensors (Fig. 23).

SENSOR TECHNOLOGY:

Instrument Generic Name:
Detection Method:
Particle Size Detection Range:
Field of view:
Consortium Contact:

CCD Tracking of Scattered Sunlight

SPI, Space Particle Imager
 CCD detection of sunlight scattered from particles
 0.1 to 10 cm, measures size and orbital parameters
 30° conical FOV, 4 sensors can be grouped to give 60° FOV
 R. A. (Bob) Skrivanek, Visidyne, Inc.
 Phone: (617) 273-2820 Fax: (617) 272-1068

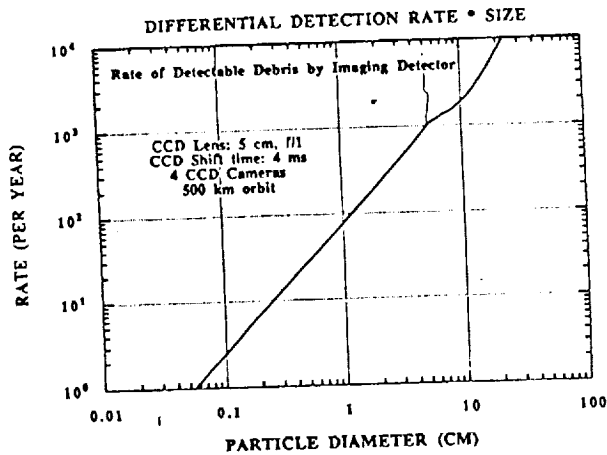


Figure 24. SPI detection rate.

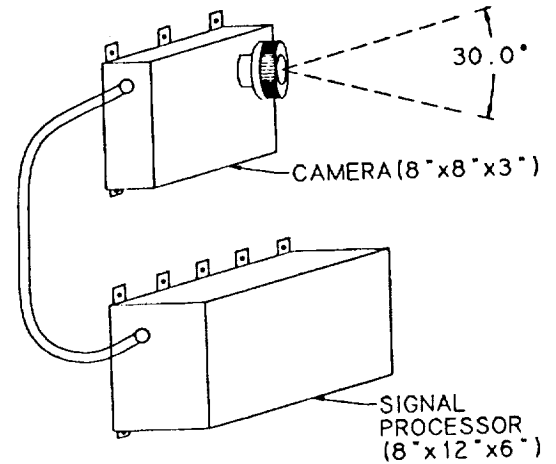


Figure 25. SPI debris detector schematic.

Nominal Instrument Specifications
 dimensions

- active sensing volume
- mass
- spacecraft electrical interface
- mounting requirements
- power requirements
- telemetry requirements

Sensor Module: 16 x 21 x 31 cm
 Electronics Module: 16 x 21 x 31 cm
 sensing volume is dependent on particle size; larger particles can be seen at very great distances (Fig. 24)
 16 kg, includes sensor, electronics and wiring harness
 compatible with all buses
 external, forward looking (into RAM) mount for sensor module; external or internal mount for electronics box
 35 watts
 1.5 x 10⁷ bits per orbit, 40 kbps nominal/100 kbps maximum.

Nominal cost estimates (U.S. \$1000)

- delivered hardware (only) costs
- special quality assurance reqmnts.
- special spacecraft interface reqmnts
- pre-launch mission support costs

500
 TBD
 TBD
 TBD, dependent upon mission requirements, designated spacecraft, schedule and required documentation; typical range is 250-500.
 TBD, dependent on requirements; typical range is 100-200
 TBD, dependent on requirements; typical cost is 200/year.

- software development costs
- post-launch mission support (data interpretation and report) costs

Nominal delivery schedule

- hardware (only) delivered
 - software development
- 12 months
 3-6 months (concurrent)

TECHNOLOGY DESCRIPTION AND FLIGHT HISTORY

The Visidyne Space Particle Imager has been designed to detect particles in the 0.1 to 10 cm size range, a size range that has the potential for causing serious impact associated problems for any spacecraft and for which there is very little data concerning fluxes. The Visidyne instrument uses a charge-coupled-device (CCD) focal plane array detector that monitors the conical volume in the RAM direction of the spacecraft looking for the sunlight scattered from debris or meteor particles as they pass through the active volume.

The flight instrument consists of two modules, a sensor module that houses the lens, CCD focal plane and pre-processing electronics; and the electronics module that holds the microprocessor. The sensor module must be externally mounted such that the lens has an unimpeded view of the RAM direction. The electronics module can be mounted anywhere within or on the spacecraft.

The instrument measures the sunlight scattered from a particle as it passes through the large field of view. The typical time (t) for a particle to pass through the field of view is given by:

$$\Delta t = [np/fl]r/v$$

where $(np)/fl$ is the angular width of the field of view (n is the number of pixels across the CCD, each of physical size p , and fl is the focal length of the imaging lens), and r is the distance of the particle from the image as it crosses through the field of view with a speed of v . If time tags are placed along the track, crucial distance information can be obtained. The angular velocity, which can be determined from time tags along the track, is given by $\Omega = v/r$, where v is the particle speed in the spacecraft reference frame. If the trajectory angle of the particle in the spacecraft frame of reference is known, then a very good estimate of v can be made. The distance r is then obtained from the measured value of Ω and inferred value of v .

Using a sensor with camera focal length of 5 cm and a 5 cm diameter lens, and using particle albedos as proposed by Henize (ref. 25), in a 500 km orbit, assuming reasonable system parameters such as signal strength and background noise, and using fluxes as predicted by the NASA standard model, this sensor will measure between 8 and 10 particles/year in the 0.5 to 1.0 cm size range, between 25 and 50 particles/year in the 1 to 2 cm size range and between 250 and 500 particles/year in the 5 to 10 cm size range.

The microprocessor in the electronics module performs many of the calculations on board the spacecraft, eliminating false alarm rates, etc., and only telemetering data to the ground that has been partially analyzed.

The first flight instrument of this design is currently being fabricated and tested by Visidyne and will be delivered to the United States Air Force Phillips Laboratory in mid 1994. Space flight, as part of the USAF Space Test Program (STP), is planned for the 1996 time frame.

SENSOR TECHNOLOGY:

Instrument Generic Name:
Detection Method:
Particle Size Detection Range:
Consortium Contact:

Photocell detection of scattered laser light

(PME) Particle Monitor Experiment
 Near-forward scattering of AlGaAs laser light
 0.5 to 10 μm (Type A); 10 to 250 μm (Type B)
 Dr. O. Manuel Uy, JHU/APL, 301/953-5334, Fax 953-6119

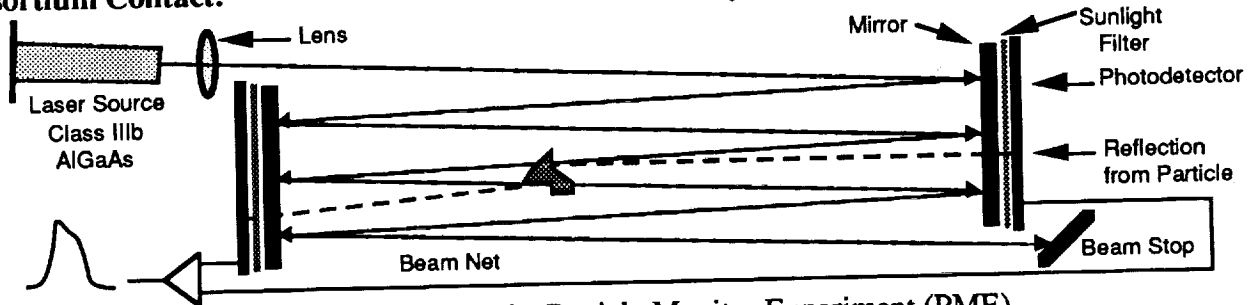


Figure 26. Optical design of the sensor for the Particle Monitor Experiment (PME)..

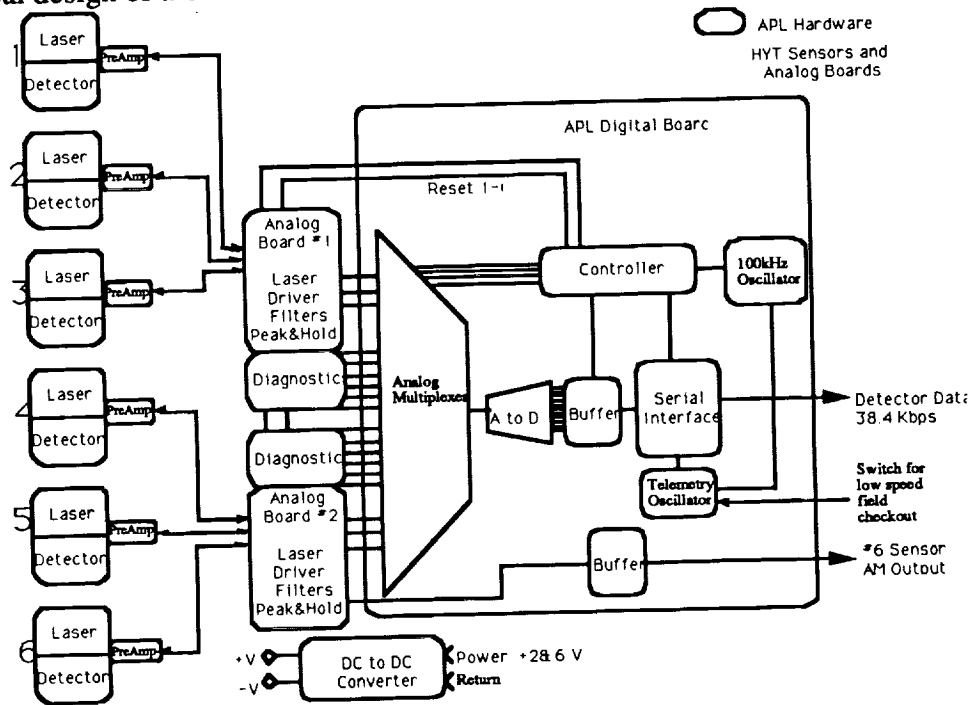


Figure 27. Particle Monitor Experiment (PME) Block Diagram

Nominal Instrument Specifications

dimensions

active sensing area

mass

spacecraft electrical interface

mounting requirements

power requirements

telemetry requirements

Sensors: 6 x 18 x 2 cm, Electronics: 20 x 33 x 9 cm
 42 cm² (6 sensors at 7 cm²/sensor), 421 samps/sec, 12 bit res.
 20 Lbs, includes 6 sensors, electronics, and wiring harness
 28V \pm 6V, no system control required
 sensors and electronics bolted to rigid surfaces
 18 Watts
 no special requirements, 4 kbits/sec or 38.4 kbit/sec

Nominal Cost Estimates (U.S. \$1000)

delivered hardware (only) costs

pre-launch mission support costs

software development costs and time

post-launch mission support

Nominal hardware (only) delivery

200-300, dependent on program requirements

50, dependent on program requirements

50, dependent on program requirements; 3-6 months

100, dependent on program requirements

9-12 months, dependent on program requirements

TECHNOLOGY DESCRIPTION AND FLIGHT HISTORY

The Particle Monitoring Experiment (PME) satisfies a requirement for real-time monitoring of the particle environment around an actual operating spacecraft. Particles consist of dust and aerosols associated with retrorockets and other attitude-control systems, water droplets, ice crystals, and other forms of condensation emanating from the spacecraft, dusts and fibers from ground operations, and even particles associated with surface erosion caused by atomic oxygen. It has been suggested that particles are generated by the rubbing of two different materials' surfaces that are in intimate contact with each other each time the spacecraft crosses the day/night terminators as a result of differential thermal expansion.

The objectives of the PME are to record the density of particles around the spacecraft, measure particulate flux (number of particles per unit area), determine their size distribution, obtain their velocity distribution, and, if possible, determine their chemical composition. In less than one year Applied Physics Laboratory developed the PME to satisfy the above objectives for the VIP launch known as the "Piggyback Flight".

The basic particulate sensor is a light-scattering device built by High Yield Technology (HYT) of Sunnyvale, California. The sensor contains an AlGaAs laser diode source (Class IIIb) that projects a 20 mW laser beam at a wavelength of 780 nm, a beam-forming lens, two reflecting mirrors, a beam stop, and two photocell detectors with sunlight filters (Fig. 26). The mirrors reflect the laser beam back and forth to produce a nearly continuous plane of laser light between the two mirrors with a Gaussian beam profile. When a particle crosses this plane of light it scatters the laser to either or both of the photo-detectors located just above the mirrors. The count rate of the particles crossing the light plane of the sensor is directly related to the particulate flux, $J = nv$, where n is the particle number density and v is the particle velocity. After calibration of the PME using latex spheres of known sizes, densities and velocities, particle fluxes can be measured and velocities inferred. Particle sizes can be binned according to peak heights or intensities of the photo-detector signals. This approximation is based on the assumption that all detected particles are spherical in shape and have the same index of reflection as the latex calibration spheres. Velocities may also be inferred by measuring the peak width of the signal outputs. Because of the assumptions involved, we cannot infer any information about the composition or shape of the particles.

The sensors were manufactured and calibrated by HYT for detection of particles within a size range of 0.5 to 10 μm (Type A), and 10 to 250 μm (Type B). Each sensor contains two photo-detectors whose outputs are summed and amplified. The signal is then sent to a peak-and-hold circuit which saves the largest peak during each 2.3 ms sampling interval. The "peak" value is digitized to 12 bit resolution and inserted into the telemetry stream. The sample and hold then resets and begins holding for the next interval. If multiple particles scatter light during a 2.3 ms interval, only the largest signal will be counted.

Six PME sensors were mounted on the VIP spacecraft and controlled by one Flight Electronics Box (Fig. 27). Four of the sensors were located on booms and the other two were located on the main payload structure. In addition to the digital signals used to measure particulate flux, an analog output from one sensor was telemetered to the ground via a separate analog channel and correlated to the digital measurement to determine pulse height and width. Statistics from the pulse height and width are used to estimate the particle size and velocity distributions around the VIP spacecraft. The PME was flown in the Fall of 1991 at an altitude of 1200 km and a flight duration of approximately 30 minutes and performed as advertised. The unit proved extremely robust and even survived a vehicle hardware malfunction. Data was collected from lift-off through reentry. The particle measurement data is currently classified but appears to confirm payload physicists theories. The digital data correlated well with the analog channel.

New Developments

- (1) A self-contained monitor and sensor in a sensor-sized housing is being developed. This would utilize self-contained on-board Analog-to-Digital conversion and bit-streaming compatible with standard space flight telemetry systems. This will entail flight hybridization in which APL has extensive experience and promises to produce a low cost, versatile PME.
- (2) A "daisy-chained" unit is also being analyzed to allow several modules on a flight vehicle. APL is also investigating pulsed sheet lasers for higher resolution and speed measurements.

REFERENCES

1. J. P. Oliver, S. F. Singer, J. L. Weinberg, C. G. Simon, W. J. Cooke, P. C. Kassel, W. H. Kinard, J. D. Mulholland and J. J. Wortman, "LDEF Interplanetary Dust Experiment (IDE) Results", *NASA CP-3275* (1995).
2. C. G. Simon, J. P. Oliver, W. J. Cooke, K. I. Downey and P. C. Kassel, "Long-term Microparticle Impact Fluxes on LDEF Determined from Optical Survey of Interplanetary Dust Experiment (IDE) Sensors.", *NASA CP-3275* (1995).
3. C. R. Maag, W. G. Tanner, T. J. Stevenson, T. J. Borg, J-P. Bibring, W. M. Alexander and A. J. Maag, "The Effect of an On-orbit Near Encounter on the Number Flux Density of Micron Sized Particles", *Lunar and Planetary Sci. XXIV*, 915-916, (1993).
4. F. Singer, J. E. Stanley, *et al.*, "First Spatio-Temporal Results from the LDEF Interplanetary Dust Experiment", *Adv. Space Res.*, **11**, No.12, pp. 115-122, (1991).
5. J. D. Mulholland, S. F. Singer, *et al.*, "IDE Spatio-Temporal Impact Fluxes and High Time-Resolution Studies of Multi-Impact Events and Long-Lived Debris Clouds", *NASA CP 3134*, pp. 517-527 (1992).
6. J.P. Oliver, J.L. Weinberg, S.F. Singer, C.G. Simon, W.J. Wortman, W.J. Cooke, J.D. Mulholland and P.C. Kassel, "Estimation of Debris Cloud Temporal Characteristics and Orbital Elements". *Adv. Space Res.*, **13**, No. 8 (1993).
7. W. J. Cooke, J. P. Oliver and C. G. Simon, "The Orbital Characteristics of Debris Particle Rings as Derived from IDE Observations of Multiple Orbit Intersections with LDEF", *NASA CP-3275* (1995).
8. W. H. Kinard, "Description of the Orbital Meteoroid and Debris Counting Experiment to Fly on the (OMDC) on board the Clementine Inter-Stage Adapter Spacecraft", *NASA CP-3275* (1995).
9. P. C. Kassel, "Characteristics of Capacitor-Type Micrometeoroid Flux Detectors When Impacted With Simulated Micrometeoroids", *NASA TN D-7359* (1973).
10. J. J. Wortman and P. C. Kassel, "Metal-Oxide-Silicon Capacitor Detectors for Measuring Micrometeoroid and Space Debris Flux" (submitted to *J. Spacecraft and Rockets* (1994).
11. C. G. Simon, J. D. Mulholland, J. P. Oliver, W. J. Cooke and P. C. Kassel, "Long-term Particle Flux Variability Indicated by Comparison of Interplanetary Dust Experiment (IDE) Timed Impacts for LDEF's First Year in Orbit with Impact Data for the Entire 5.77 Year Orbital Lifetime", *NASA CP-3194*, pp. 693-702 (1993).
12. J. A. Simpson and A. J. Tuzzolino, "Polarized Polymer Films as Electronic Pulse Detectors of Cosmic Dust Particles", *Nucl. Inst. and Meths.* **A236**, **187** (1985).
13. M. A. Perkins, J. A. Simpson and A. J. Tuzzolino, "A Cometary and Interplanetary Dust Experiment on the VEGA Spacecraft Missions to Halley's Comet", *Nucl. Inst. and Meths.* **A239**, **310**, (1985).
14. J. A. Simpson, D. Rabinowitz, A. J. Tuzzolino, L. V. Ksanfomality and R. Z. Sagdeev, "The Dust Coma of Comet P/Halley: Measurements on the VEGA 1 and VEGA-2 Spacecraft", *Astron. and Astrophys.*, **187**, **742** (1987).
15. J. A. Simpson, A. J. Tuzzolino, L. V. Ksanfomality, R. Z. Sagdeev and O. L. Vaisberg, "Confirmation of Dust Clusters in the Coma of Comet Halley", *Adv. Space Res.*, **3**, **259** (1989).
16. A. J. Tuzzolino, J. A. Simpson, R. B. McKibben, H. D. Voss and H. Gursky, "An Instrument for Discrimination Between Orbital Debris and Natural Particles in Near-Earth Space", *Adv. Space Res.*, **13**, No. 8, **133** (1993).
17. J. F. Friichtenicht and J. G. Slattery, "Ionization Associated with Hypervelocity Impact", *Nasa Tech. Note D-2091*, 1962.
18. H. Iglseeder, "Ladungsemission beim Hochgeschwindigkeitseinschlag", Dissertation, Lehrstuhl für Raumfahrttechnik, TU-München, 1986.
19. H. Iglseeder, R. Münzenmeyer, H. Svedhem, and E. Grün, "Cosmic Dust and Space Debris measurements with the Munich Dust Counter on board the Satellite HITEN and BREM-SAT", *Adv. Space Res.*, **13**, No. 8 (1993).
20. R. Münzenmeyer, H. Iglseeder and H. Svedhem, "The Munich Dust Counter MDC - An Experiment for the Measurement of Micrometeoroids and Space Debris", ESA SD-01, *Proceedings of the First European Conference on Space Debris*, Darmstadt, Germany, 5-7 April (1993).
21. W. M. Alexander, H. S. Goad, R. A. McDonald, W. G. Tanner and J. A. M. McDonnell, "Giotto Comet Halley dust impact experiments: Studies of discrete impact events", *Adv. Space Res.*, **6**, (1988).
22. W. M. Alexander, W. G. Tanner, R. A. McDonald, G. E. Schaub and S. L. Stephenson, "The status of Measurement Technologies Concerning Micron and Submicron Space Particulate Matter Capture, Recovery, Velocity and Trajectory", (in press) M. Zolenski, ed., *Proceedings of Workshop on Particle Capture, Recovery, Velocity/Trajectory Measurement Technologies*, Houston, Texas, Sept. (1993).
23. W. G. Tanner and W. M. Alexander, "Impulse Calibration of DIDSY PZT Sensors: 1 m/s to 7 km/s" in GCHP-BUSSL 003, Baylor University, 76 (1986).
24. N. Divine, "Dust Flux for Mariner Mark II CRAF mission to P/Kopff", from *JPL PD 699-10*, vol. 12, (1985).
25. Karl Henize, personal communication (October, 1993).



A NEW TECHNIQUE FOR GROUND SIMULATION OF HYPERVELOCITY DEBRIS

R. Roybal, J. Shively, C. Stein,
C. Miglionico, R. Robertson
Air Force Phillips Laboratory
Kirtland Air Force Base
Albuquerque, New Mexico 87117
(505) 846-4798 FAX (505) 846-7345

SUMMARY

A series of hypervelocity damage experiments were performed on spacecraft materials. These experiments employed a technique which accelerates micro flyer plates simulating space debris traveling at 3 to 8 km/sec. The apparatus used to propel the micro flyer plates was compact and fit well into a space environmental chamber equipped with instrumentation capable of analyzing the vapor ejected from the sample. Mechanical damage to the sample was also characterized using optical and scanning electron microscopy.

Data for this work was obtained from hypervelocity impacts on a polysulfone resin and a graphite polysulfone composite. Polysulfone was selected because it was flown on the Long Duration Exposure Facility (LDEF) which spent several years in low Earth orbit (LEO).

Chemistry of the vapor produced by the impact was analyzed with a time of flight mass spectrometer, (TOFMS). This represents the first time that ejected vapors from hypervelocity collisions were trapped and analyzed with a mass spectrometer. With this approach we are able to study changes in the vapor chemistry as a function of time after impact, obtain a velocity measurement of the vapor, and estimate a temperature of the surface at time of impact using dynamic gas equations. Samples of the vapor plume may be captured and examined by transmission electron microscopy.

Studies were also conducted to determine mechanical damage to a graphite polysulfone composite and a polysulfone resin. Impact craters were examined under optical and scanning electron microscopes. The collision craters in the matrix were typical of those shown in conventional shock experiments. However, the hypervelocity collisions with the graphite polysulfone composite were remarkably different than those with the resin.

INTRODUCTION

The effects of hypervelocity collisions on the structural integrity of materials have been the subject of numerous studies (Refs.1 through 5). Two different damage effects were looked at in this work. First the chemistry of vapor produced by the impact was studied. Also mechanical damage to a resin target and a resin/fiber target was studied and compared.

The collision process vaporizes the resin and causes it to de-polymerize as would be expected from the pressures and temperature present during the early stages of the collision. The chemistry of the vapor generated by the hypervelocity impact was characterized using a TOFMS. This allows for the studying of the vapor in a time resolved manner. The mass species produced, generation times of different mass species, and velocities of different species may be characterized with this technique, giving insight into the damage mechanisms involved with hypervelocity impact. Characterization of vapor deposited on TEM grids was conducted in a parallel research effort in which vapor deposits were produced by laser ablation of graphite polysulfone. Examination under high magnification revealed that the vapor deposited as very small spheres, many of which were single crystal graphite.

Questions as to the origin of some of the different contamination found on LDEF may be explained by the deposition of vapor caused by the impact of space debris on polymer samples flown on LDEF. An example of this was seen on our aluminum samples adjacent to our polysulfone samples. The deposits on aluminum samples contained sulfur which could have been vapor deposited from impacts on our polysulfone samples. Secondary debris are of importance when considering space environment effects on spacecraft optics and electronics susceptible to contamination damage originating from this source.

The phenomena of damage, while well documented, is not well understood. Most of the work on damage to composites was conducted at low velocities, less than 100 m/s. The usual way to produce damage at hypervelocities involves the use of air guns and rail guns which has made it difficult to look at damage caused by small particles. The technique used in this work has made it possible to produce hypervelocity impact of resin and composite samples with relative ease. The different damage effects, which were seen for the resin and for the composite targets is attributed to changes in density within the materials. Much of what happens inside a material after a hypervelocity collision apparently occurs after the initial compressive shock wave has passed through the material and has reflected back as a rarefaction wave. Reflective rarefaction waves occur when the density suddenly changes as at the back surface or at internal discontinuities such as precipitates or fibers. The nature of the damage observed in composites and resins is the focus of ongoing studies.

EXPERIMENTAL

The flyer-plate technique used in this experiment has several advantages over conventional methods of producing hypervelocity particles. This technique has the following advantages. The method is compact and fits conveniently into the chamber of the TOFMS. It produces very little chemical contamination when accelerating a flyer plate as compared to the electric gun or explosives. Aim is accurate and the flyer may be directed from outside of the vacuum chamber used to simulate space. Finally, the target can be oriented relative to the flyer to maximize the ejecta plume entering a diagnostic device such as an ionization chamber of a TOFMS.

Flyer plates 5 μ thick and 700 μ in diameter were accelerated at targets in this work which was carried out in the ultra high vacuum chamber within a TOFMS. A detailed description of the flyer plate accelerator is found in REF (6). While we generally used an aluminum flyer, materials other than aluminum have been launched; however, aluminum is preferred since it closely represents that of the average particle of space debris (Ref.7). The velocities of the flyer plates are measured using a VISAR System which is a laser interferometric technique (Ref.8)

Figure 1 shows the configuration used to study the chemical species produced by hypervelocity collisions of space structural materials by simulated particles of space debris. In the configuration shown, the flyer plate struck the polysulfone target at an angle of 45° relative to the direction of flight. This arrangement provides a favorable orientation for the vapor ejecta to escape and to enter the mouth of the TOF mass spectrometer.

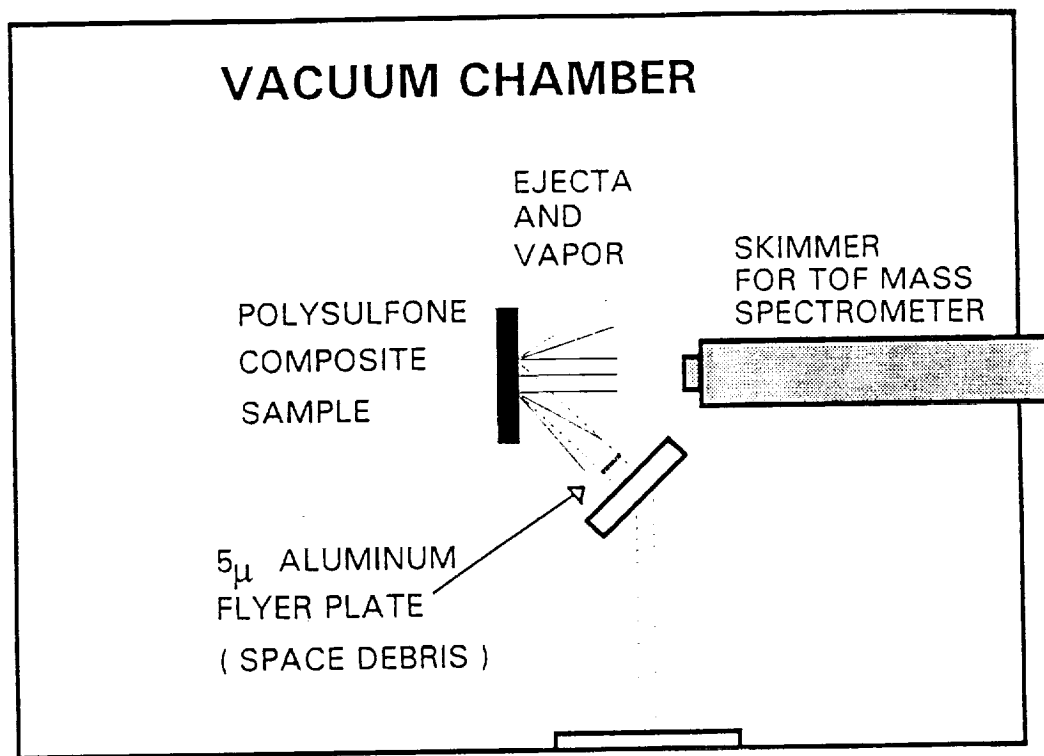


Figure 1. Experimental arrangement used to study chemical reactions from hypervelocity particle collisions.

The TOF mass spectrometer is capable of evaluating a complete mass spectrum from mass 1 to 200 in 12 ms. A hypervelocity collision adiabatically heats the polysulfone and ejects chemical species in the form of vapor. The ejected chemical species generated by the impact travel from the polysulfone target to the throat of the mass spectrometer where the vapor is ionized and accelerated toward the mass spectrometer detector. The chemical species are scanned as a function of time to produce a mass spectrum. Chemical species arriving later than 12 ms will be detected in the next spectral scan. This has the advantage that the chemical species generated first after impact can be differentiated from those which form at later stages.

In order to study the damage mechanism, some preliminary collisions were made in air apart from the TOFMS. In these experiments, an aluminum flyer was fired at a polysulfone resin target and at a polysulfone composite target. The velocities of the collisions ranged from 3 to 7 km/s. The impacted samples were then examined using optical and scanning electron microscopy at the Phillips Laboratory. Samples were first examined and photographed using the Nikon optical system at 50X and 100X. After optical studies, the specimens were sputter coated with a thin conductive layer of gold-palladium alloy for viewing in the scanning microscope. The coating prevents excessive charging during the bombardment with the electron beam of the microscope. The samples were also examined using the energy dispersive analysis of X-rays produced by the electron beam excitation of the atoms (EDAX).

RESULTS AND DISCUSSION

The effort to measure chemical species produced by hypervelocity collisions of aluminum with polysulfone resin were successful. The spectrum produced is shown in Figure 2 and is averaged over several scans to provide better statistical results. Essentially no changes in the spectrum were observed once the species were detected, which would have affected the averaging. As can be seen, the spectrum covers masses 1 through 100, and the relevant species are identified on the chart. The mer of polysulfone is also shown for reference. Sulfur, which is one species easily removed from the polysulfone mer, shows up at 32 amu on the spectrum. The sulfur species could have been overshadowed by the oxygen molecule which also has the same mass, 32 amu. However, the amount of oxygen present should be quite small in the vacuum chamber and the oxygen that is present is already combined with the aluminum. Therefore, the peak, at 32 amu is an indication of sulfur and is therefore positive verification that the polysulfone de-polymerized.

Plume From Aluminum Projectile Impacting Polysulfone Target

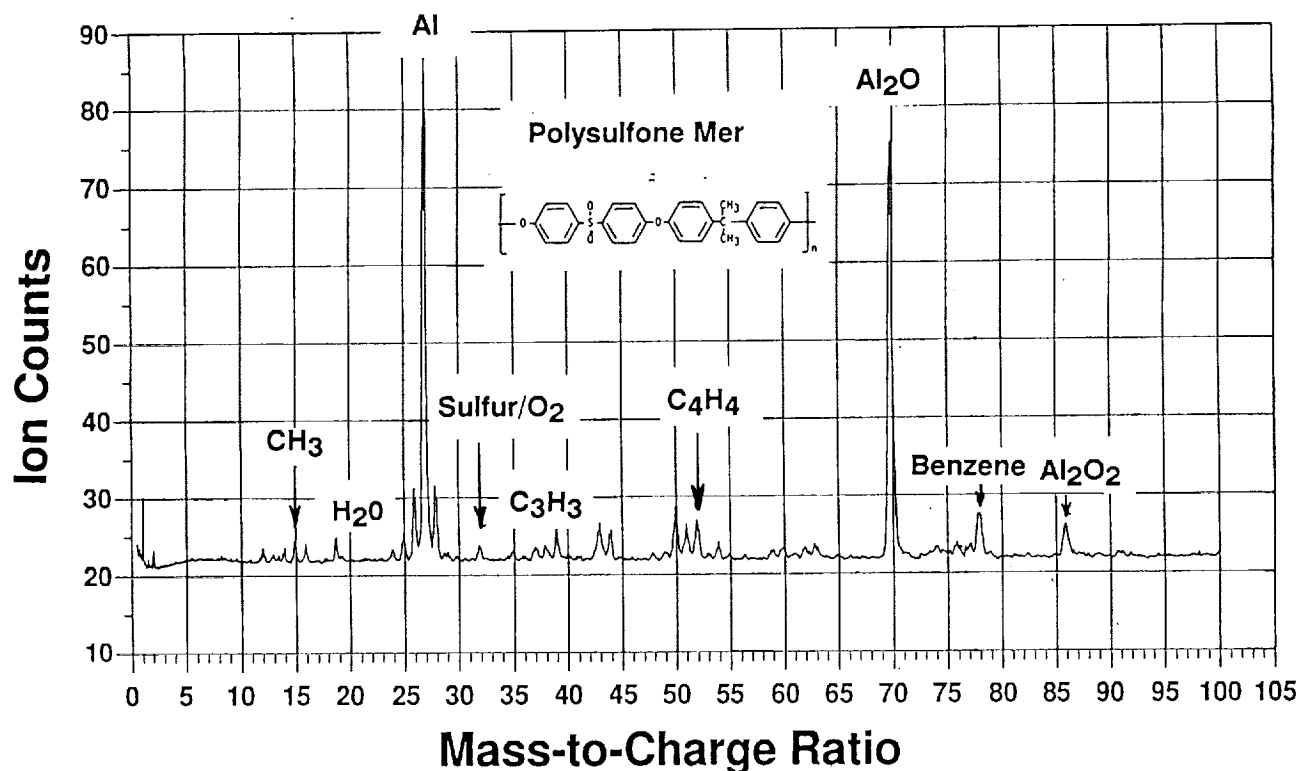


Figure 2. The spectrum produced from hypervelocity collision of aluminum with polysulfone.

Other species which were present undoubtedly came from the de-polymerization of the polysulfone and included the aromatic species, C_6H_x , and monomers of carbon-hydrogen species, such as C_2H_2 . In short, the spectrum seen is the direct result of the collision of a hypervelocity particle with the resin. This is the first time shock induced chemical changes from simulated space debris have been observed.

The mechanical damage caused by hypervelocity collisions is also striking. In the case of the resin without fibers, the results are quite similar to those observed in the collision of other homogeneous materials. The impact produces a crater on the surface, the depth and extent of which matches the size of the aluminum particle launched from the quartz. As can be seen, debris from the collision coats the neighboring surface with small sub-particles of aluminum from the flyer plate. The crater in the resin exhibits evidence of melting and a crack, due to shrinkage after melting, forms around the edge of the crater. See Figures 3 through 5. There is nothing unusual about the collisions that has not been observed in shock studies on other materials, except that the scale of these tests is small, leaving the surrounding material in a relatively undisturbed state.

The shock damage in the composite materials is quite different. Craters from the collision are presented in Figures 6 and 7. As can be seen, in all cases except at the very highest velocity, little evidence of the melting of the resin is evident. This suggests that the energy associated with the compression is not totally absorbed by the resin but that it is partly dissipated by the underlying fibers. Moreover, considerable fracture damage to both the matrix and the fibers as a result of the collisions is evident. The matrix is observed to spall off the surface exposing the fibers underneath. Below this matrix layer, the graphite fibers fractured in tension. This fracture process penetrated deep into the composite while surface craters observed in the pure resin were not so deep. Fibers around the edges of the craters were also severely fractured. Thus, damage in a composite material after a hypervelocity collision is fundamentally different than damage in the resin itself.



Figure 3. Top view of the crater in polysulfone photographed optically after collision at 6 km/s.

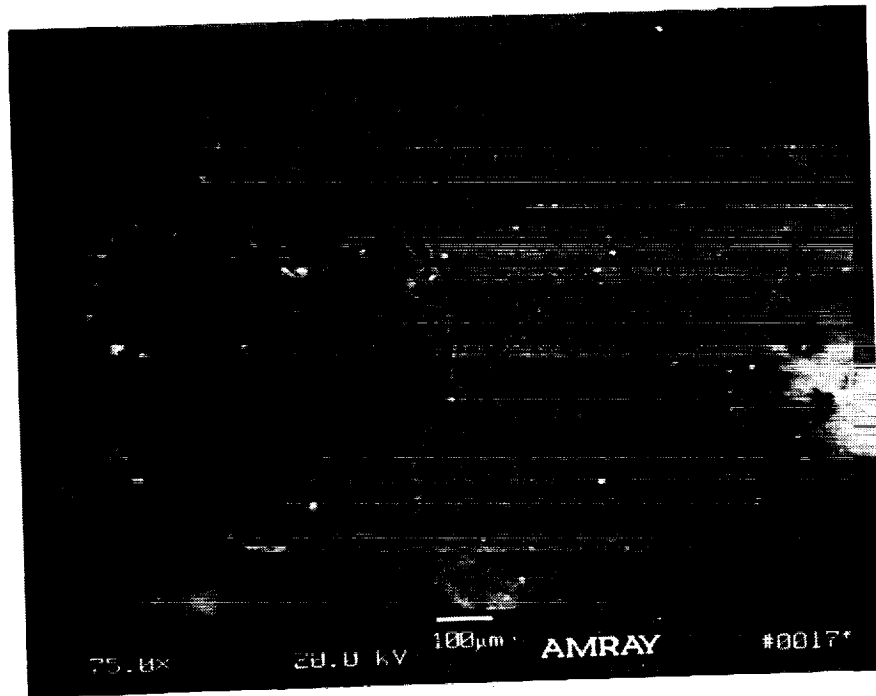


Figure 4. Scanning electron microscope top view of crater formed in polysulfone after collision at 6 km/s.

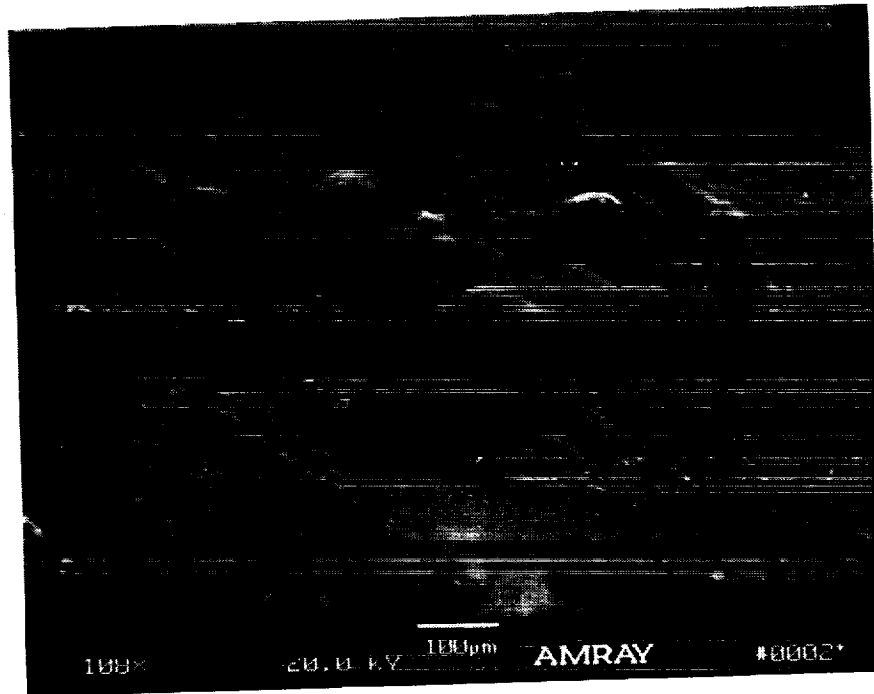


Figure 5. Scanning electron microscope tilt angle view of crater in polysulfone after collision at 6 km/s.

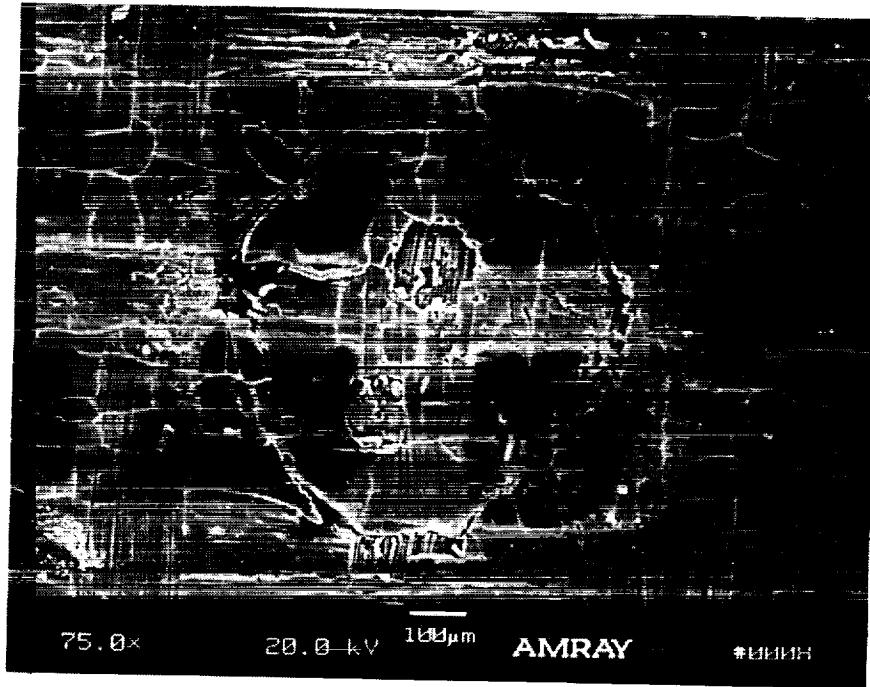


Figure 6. Scanning electron microscope top view of crater formed on polysulfone composite after collision at 5 km/s.

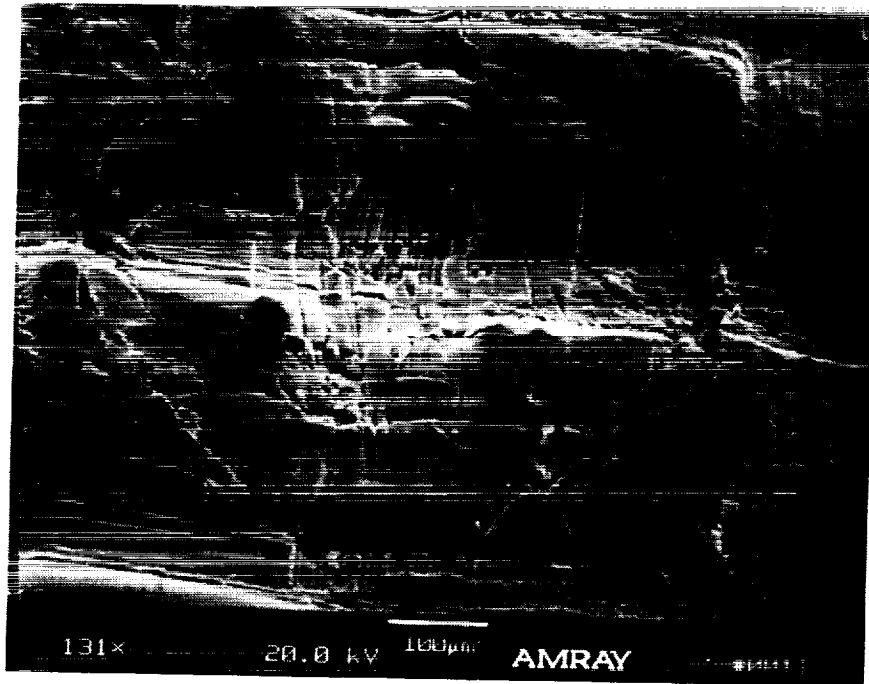


Figure 7. Scanning electron microscope tilt angle view of the crater formed on polysulfone composite after collision at 6 km/s

5.0 CONCLUSIONS AND RECOMMENDATIONS

The use of micro-flyer plates to simulate the effects of space debris has been demonstrated. The damage produced matches damage found on LDEF specimens. The presence of debris over the surface was observed in typical hypervelocity collision experiments. The use of the micro-flyer plate produced sufficient damage in the resin to cause the material to de-polymerize, to vaporize, and to melt. The technique used to produce the small hypervelocity plates is quite convenient and inexpensive compared to the use of the electric guns or mechanical methods such as air-guns, rail-guns, or explosives. The size of the particles launched with this technique are smaller than those launched with other techniques but are still convenient for macroscopic materials such as composites. This micro-flyer method is compatible with space environmental chambers since they can be accelerated from outside the chamber.

The mechanical damage observed differs substantially between the pure resin and the resin-fiber composite in that the resin is seen to melt, and material is ejected from the crater, while in the composites, front surface spalling and fracture of individual fibers dominates. The collisions cause little melting of the matrix on the surface of the composite.

A comparison of the data obtained from LDEF with the data produced by the space debris simulation, points to a conclusion that much of the contamination found on LDEF may have been produced by hypervelocity impact of micrometeorites on hydrocarbon materials depositing ejecta on adjacent surfaces. Mechanical damage comparison is very difficult because the impact craters on the LDEF sample were subsequently subjected to erosion and ashed.

Further studies will be initiated using the micro-flyer plates to cause damage in composites, so that internal examination in the region of the collision can be carried out to determine the depth of the fiber fractures. Specimens will be examined for evidence of delamination between layers which is observed when composites experience low-velocity impacts. Other resins and fibers will be studied, since the matrix and fibers used in these initial experiments are brittle. More ductile fibers are expected to resist breakage during impact, suggesting that the use of thermoplastic resins could partly reduce the brittleness in the matrix. In addition, particulate metal matrix composite materials, such as SiC or graphite particles in an aluminum matrix are expected to be good candidates for future shock studies.

REFERENCES

1. Dein, J., Tokheim, R., Curran, D., Chau, H., Weingart, R., and Lee, R., "Aluminum Damage Simulation in High-Velocity Impact", in Shock Wave in Condensed Matter, 1983, p.171, J.R. Asay, R.A.Graham, and G.K. Straub, Eds., Elsevier Science BV, 1984.
2. Rajendran, A.M., Dietenberger, M.A., and Grove, D.J., "A Void Growth-based Failure Model to Describe Spallation", Journal of Applied Physics 65, p.1521, 15 Feb 1989.
3. Riney, T.D., and Halda, E.J., "Effectiveness of Meteoroid Bumpers Composed of Two Layers of Distinct Materials", AIAA Journal 6, No.2, p.338, Feb 1968.
4. Fowles, G.R., "Shock Wave Compression of Hardened and Annealed 2024 Aluminum", Journal of Applied Physics, Vol 32, No. 8, p.1475, Aug 1961.
5. Curran, D.R., Shockley, D.A., and Seamann, L., "Dynamic Fracture Criteria for a Polycarbonate", Journal of Applied Physics, Vol 44, No. 9, p. 4025-38, September 1973.
6. Roybal, R.E., Shively J. H., " Chemical and Structural Effects Caused By Hypervelocity Impacts To Polysulfone Graphite Reinforced Composite And Its Resin", Air Force Phillips Lab Tech. Report PL-TR-92-1076, 1992.
7. Johnson, N.L., and McKnight, D.S., Artificial Space Debris, p.25ff, Orbit Enterprises Inc., Glen Ellyn, IL, 1991.
8. Barker, I.M., and Hollenbach, R.E., "Shock-Wave Studies of PMMA Fused Silica and Sapphire," Journal of Applied Physics, 41, No. 10, p.4208, September 1970.

REPORT DOCUMENTATION PAGE

Form Approved
OMB No. 0704-0188

Public reporting burden for this collection of information is estimated to average 1 hour per response, including the time for reviewing instructions, searching existing data sources, gathering and maintaining the data needed, and completing and reviewing the collection of information. Send comments regarding this burden estimate or any other aspect of this collection of information, including suggestions for reducing this burden, to Washington Headquarters Services, Directorate for Information Operations and Reports, 1215 Jefferson Davis Highway, Suite 1204, Arlington, VA 22202-4302, and to the Office of Management and Budget, Paperwork Reduction Project (0704-0188), Washington, DC 20503.

1. AGENCY USE ONLY (Leave blank)		2. REPORT DATE February 1995	3. REPORT TYPE AND DATES COVERED Conference Publication	
4. TITLE AND SUBTITLE 69 Months In Space: Third LDEF Post-Retrieval Symposium			5. FUNDING NUMBERS 233-03-02-03	
6. AUTHOR(S) Arlene S. Levine, Editor				
7. PERFORMING ORGANIZATION NAME(S) AND ADDRESS(ES) NASA Langley Research Center Hampton, VA 23681-0001			8. PERFORMING ORGANIZATION REPORT NUMBER L-17430C	
9. SPONSORING/MONITORING AGENCY NAME(S) AND ADDRESS(ES) National Aeronautics and Space Administration Washington, DC 20546-0001			10. SPONSORING/MONITORING AGENCY REPORT NUMBER NASA CP-3275, Part 3	
11. SUPPLEMENTARY NOTES				
12a. DISTRIBUTION/AVAILABILITY STATEMENT Unclassified—Unlimited Subject Category 99			12b. DISTRIBUTION CODE	
13. ABSTRACT (Maximum 200 words) This volume is a compilation of papers presented at the Third Long Duration Exposure Facility (LDEF) Post-Retrieval Symposium. The papers represent the data analysis of the 57 experiments flown on the LDEF. The experiments include materials, coatings, thermal systems, power and propulsion, science (cosmic ray, interstellar gas, heavy ions, micrometeoroid, etc.), electronics, optics, and life science. In addition, papers on preliminary data analysis of EURECA, EOIM-3, and other spacecraft are included.				
14. SUBJECT TERMS Space Experiment			15. NUMBER OF PAGES 546	
			16. PRICE CODE A22	
17. SECURITY CLASSIFICATION OF REPORT Unclassified	18. SECURITY CLASSIFICATION OF THIS PAGE Unclassified	19. SECURITY CLASSIFICATION OF ABSTRACT Unclassified	20. LIMITATION OF ABSTRACT	

